'5

A Qualitative and Quantitative Study of the Distribution of Pelagic Sediment in the Atlantic Basin

by

Helen Faith Webb

B. S., Worcester Polytechnic Institute, 1988

Submitted in Partial Fulfillment of the Requirements for the Degree of Doctor of Philosophy

at the

Massachusetts Institute of Technology

and the

Woods Hole Oceanographic Institution

February, 1997

Signature of Author_____
MIT/WHOI Joint Program in Oceanography/
Applied Ocean Science and Engineering

Certified by_____
Thomas H. Jordan
Thesis Supervisor

Accepted by_____
Deborah K. Smith
Chair, Joint Committee for Marine Geology and Geophysics
Massachusetts Institute of Technology/
Woods Hole Oceanographic Institute

A Qualitative and Quantitative Study of the Distribution of Pelagic Sediment in the Atlantic Basin

by

Helen Faith Webb

Submitted to the Department of Earth, Atmospheric and Planetary Sciences
Massachusetts Institute of Technology, and the
Department of Marine Geology and Geophysics, Woods Hole Oceanographic Institution
February 7, 1997
in partial fulfillment of the requirements for the degree of Doctor of Philosophy

ABSTRACT

Pelagic sedimentation is the primary modifier of topography generated by ridge-associated volcanic and tectonic processes. This thesis represents an effort to understand the processes of, and the general distribution of, pelagic sedimentation on rough topography, particularly in the Atlantic Basin but with applications to the world ocean as a whole.

This study utilizes a simple numerical model of sedimentation which, when applied to models of rough basement topography, allows us to study sedimentation effects in terms of commonly-measured stochastic parameters including seafloor RMS height, abyssal hill spacing, and slope distribution. We also address the effect of sediment compaction on seafloor morphology, and the impact of long-wavelength topography on stochastic measures of sedimented seafloor.

Understanding gained allows the construction of inverse problems to obtain information about sediment distribution and basement morphology from multibeam bathymetric data in regimes where backscatter from rough, reflective basement highs obscures returns from wide-beam seismic systems. By using maximum likelihood estimation to compare slope distribution functions calculated from data to those from filtered model topographies, we estimate average sediment thickness L, basement RMS height H, and a measure of sediment mobility κ.

Using data from near-ridge surveys and off-axis transit lines, we invert for L, H, and κ for 3-29 Ma seafloor from the western flank of the Mid-Atlantic Ridge (MAR) near 26° N, 2-45 Ma seafloor from the western flank of the MAR near 26° S, 2-40 Ma seafloor from the eastern flank of the MAR near 25° S, and 1-38 Ma seafloor from the western flank of the MAR near 35° S. Variations in L with seafloor age allow us to constrain sediment rain rate and the corrosivity of bottom waters to calcite since the Oligocene. We hypothesize that sediment rain rates during much of the early and middle Miocene were only 10-50% of the average rate for the past ~10 m.y. Variations in H suggest correlation between tectonic setting and topographic variability. A relatively narrow range of κ is needed to describe intrahill sedimentation patterns.

Thesis Supervisor: Thomas H. Jordan, Professor of Geophysics

TABLE OF CONTENTS

ACKNOWLEDGEMENTS

Financial support for this thesis was provided by ONR grants N00014-90-J-1584, N00014-93-1-0344, and N00014-93-1-0896 as part of the Acoustic Reverberation Special Research Project (ARSRP), and by an NSF Graduate Fellowship. Computational support was provided by the Center for Computational Science at the Naval Research Laboratory.

I thank Tom Jordan for taking me as a graduate student, handing me a fascinating project, and guiding me in making complex problems tractable. I thank Marcia McNutt, Brian Tucholke, Kelin Whipple, Bob Detrick, and John Grotzinger for serving on my thesis committee, and Tom Herring for serving as the chair of my defense. Of these individuals, I especially thank Marcia McNutt for advising one of my Generals projects, giving me a home on the 8th floor, and taking me to sea, and Brian Tucholke for guidance in the interpretation of single channel seismic records and for information on many aspects of pelagic sedimentation. I also thank Debbie Smith for serving as my WHOI advisor.

My work has been built upon the groundbreaking seafloor models of John Goff. John's willingness to share code and give advice have been much appreciated. Johan Robertsson's employment of our seafloor models also provided some of the motivation for the work within this thesis. I have also benefited from interactions with other participants in the ARSRP, and have extensively used data collected as part of this program. The RIDGE Program has provided easy access to other useful data sets. My work has benefited from the efforts of Paul Wessel and Walter Smith to provide convenient tools for processes and displaying geophysical data.

There are many other people who contributed to the scientific aspects of this thesis. In the body of this text, they are rewarded with references, while the people who have made this thesis possible by their example or by their support, or who simply have made life a little more pleasant, get no recognition, which I suppose is why thesis acknowledgements are the creatures they are. This one is no different...

I never would have come to graduate school if David Kaplan, my supervisor at the Naval Research Laboratory, hadn't convinced me that one's work in life should be intriguing, and if Peter Vogt hadn't introduced me to a field worth being intrigued by. I thank them both heartily. Other people who have had large impacts are Garrett Ito, who insisted that we actually understand all of our class notes, thereby teaching me how to approach graduate-level study; Carolyn Ruppel, who always took time to explain the computer system or to answer science questions, providing an example I have tried hard to emulate; Lynn Smith, who let me explain what I was trying to do until I understood it; and Mousumi Roy and Yu Jin, who have cheerfully kept me company during the final push to bring this thesis to completion.

I couldn't have asked for a better graduate student home than the 8th floor of the Green Building, what Yu Jin terms "the floor of women and dogs." Among the present and former denizens who have been a continual source of friendship and support are Tom Burbine, Jen Carlson, Jean Chu, Carrie Friedman, Jen Georgen, Emilie Hooft, Allegra Hosford, Kelsey Jordahl, Peter Kaufman, Laura Magde, Mike Pope, Bev Saylor, Feng Shen, Odin Smith, D'arcy Straub, Dawn Sumner, Jessica Sunshine, Paula Waschbusch, Sheri White, and Zhou Yu.

The Joint Program student community is also extremely supportive of its members, and I am grateful for the friendship of fellow students not yet mentioned including Einat Aharonov, Jess Adkins (to whom I owe my introduction to marine geochemistry), Susan Alderman, Gail Christeson (whose code I used heavily in one of my Generals projects), Hedy Edmonds, Javier Escartin, Debbie Hassler, Stefan Hussenoeder, Gary Jaroslow (who has been a continual source of advice on matters sedimentological), Rafi Katzman, Ken Koga, Li Lin, Danny Sigman, and Carl Wolfteich.

The intramural sports program at MIT is simply incredible and has given me the opportunity to try a number of different sports. I've been teammates with dozens of people but a couple of us often ended up on the same teams. I thank, in particular, Yu Jin, Peter Kaufman, Pat McGovern, John Olson, Mousumi Roy, Steve Shapiro, Bonnie Souter, and Paula Waschbusch for sometimes passing/volleying/throwing me the ball.

Greta Eckhardt, Gunter Siddiqi, Shane Pelechaty, and Peter Puster have also enriched life inside and outside the Green Building.

More official aspects of life at MIT have been facilitated by a number of people who also deserve mention. These include the staff of the Lindgren Library, especially Kathy Keefe and Garrett Eastman; administrative personnel on the 5th, 8th, and 9th floors including Kristin Barges, Dan Burns, Stacey Frangos, Beverly Kozol-Tattlebaum, Ronni Schwartz, and Deb Sykes; and those who have kept the computers up and running, including Linda Meinke and Michael Batchelder.

Outside of school, the E40 crowd has allowed me to take space at their lunch table daily, and has put up with a lot of pent-up silliness and the occasional show tune. The folks at College Ave. United Methodist Church also don't seem to mind my singing, and I thank them for forming my spiritual home for the past several years.

Finally, I'd like to thank those closest to me who have provided love, support, and loads of ego gratification through the years. My parents, Ralph and June Webb, and my brother, Matthew, have made me who I am. What more can I say? Betsy Linstrom has been a great email pen-pal and confidant, Karen Grant has been a link to normality throughout my time at MIT, and Nitin Garg continues to ask the most interesting questions whenever he gets a chance. And, I gratefully acknowledge the constant love and support provided by my husband, Chris. Again, what more can I say?

Chapter 1

Introduction: Studying Pelagic Sedimentation on Young Abyssal Hills

INTRODUCTION

Pelagic sedimentation is a ubiquitous feature of the world ocean floor. Although the total sediment supply of much of the seafloor is dominated by high-volume flows from nearby continents, approximately 20% of the Earth's surface, including the flanks of most of the world mid-ocean ridge system, receives sediment only from the gradual rain of biogenic, lithogenic, and hydrogenic detritus through the water column, at average rates ranging from less than one to greater than 100 m/m.y. Over millions of years, the accumulation and redistribution of pelagic sediments reshapes the seafloor, filling in small crevices, flattening valleys and, ultimately, completely burying all but the highest hills.

The morphology of hilly seafloor topography varies locally and regionally. Steep hillslopes range from being very rough, with little evidence of sediment accumulation, to being smoothed by the infilling of small cracks or, in extreme cases, to supporting sediment covers of substantial thickness with surface slopes of 12°-15° or more [*Moore*, 1961]. Where down-slope transport occurs, the surfaces of larger valley-filling sediment ponds may be flat, concave, or tilted. They may be composed of convex accumulations of benthic sediment and basement-derived debris, or have sediment accumulations which decrease in thickness as they ramp up hillsides. Sediment ponds are sometimes asymmetrically distributed around seafloor features [*Johnson and Johnson*, 1970], and may show scour marks where topography has focused bottom currents. In a few regions, particularly where topographic relief is low or where sediment rain rates are especially high (such as in the high latitudes subject to the accumulation of ice-rafted debris or beneath the equatorial high-productivity zones), seismic records show that the shape of the basement is followed even after hundreds of meters of sediment have accumulated.

Knowledge about the distribution of sediments on hillsides is necessary for the interpretation of low-angle acoustic backscatter from the seafloor [e.g. *Makris and Berkson*, 1994; *Robertsson and Levander*, 1995]. This thesis has been motivated, in part, by a need for models of sedimented abyssal hill topography which feature a realistic balance between sediment ponds and basement outcrops, and reasonable pond curvatures in both small hillside ponds and larger valley-filling deposits, for use in numerical calculations of acoustic backscatter. Specifically, we have attempted to generate models which resemble topography within the Office of Naval Research Acoustic Reverberation Corridor (ARC), as part of the Office of Naval Research Acoustic Reverberation Special Research Project (ARSRP). The ARC, located on 0 to 26-29 Ma crust on the western flank of the Mid-Atlantic Ridge to the north of the Kane Fracture Zone (25°25' - 27°10' N), serves as a natural laboratory for understanding acoustic reverberation in the deep sea. Bathymetric, sidescan, single-channel seismic, 3.5 kHz, and nearbottom data collected in the ARC have yielded much information about how seafloor develops and ages in a slow-spreading-rate regime, as well as allowing the interpretation of low-frequency acoustic data collected in the region. However, with the exception of several locales where near-bottom photographic surveys were run, the sidescan, single-channel seismic, and 3.5 kHz data have only been able to provide information on how sediments are distributed in relatively large ponds which extend several kilometers along-track.

The construction of realistic seafloor models has required the quantification of the spatial distribution of sediments within the ARC, as well as a measure of their mobility. In *Webb and Jordan* [1993], we presented the results of an inversion methodology in which the cumulative slope distributions of models of sedimented topography were compared to cumulative slope distributions calculated from bathymetric data from the ARC. The results of this inversion allowed us to, in collaboration with basement modelers and acousticians, produce models of topography which have allowed specific problems related to acoustic backscatter from rough topography to be addressed [e.g. *Goff et al.*, 1993; *Robertsson and Levander*, 1995, *Robertsson et al.*, submitted].

The specific models of topography we generated for use in numerical calculations of acoustic backscatter are not included in this thesis. Instead, we use the knowledge and

methodologies gained in the production of these models to address fundamental questions of marine geology. Among the questions we at least partially answer in this thesis are:

- What are the present-day rates of sediment rain and accumulation in the vicinity of the mid-ocean ridge system? How do these rates vary with geographical position? What constraints do these rates place on sources of pelagic sediments?

- How have the rates of sediment rain and accumulation throughout the world ocean varied since the middle of the Cenozoic?

- Are there significant regional variations in the mobility of pelagic sediments? How does sediment mobility depend on seafloor morphology?

- Is the local distribution of sediments consistent with a linear, down-slope diffusion model? Are bathymetric data better explained by a non-linear diffusion law, where lateral flux is proportional to some power of the local slope? A transport model in which mass movement events are explicitly parameterized?

- Can regional sedimentation patterns be interpreted in terms of post-depositional transport processes that operate on scales larger than those set by local sediment diffusion? Under what conditions do turbidity currents dominate sediment redistribution?

- Are there significant intraregional variations in the RMS variability of basement topography? What controls this variability?

REVIEW: METHODS OF STUDYING PELAGIC SEDIMENTATION

Basic questions about pelagic sedimentation persist because it has been difficult to obtain quantitative information about the geometry of thin accumulations of pelagic sediments; despite the intensive study of a few regions within the abyssal hill regime, the relationship between seafloor processes, sediment content, and topography remains elusive.

Consider, for example, the problem of determining the volume and rate of accumulation of sediments where the sediment average thickness is only a fraction of hill height. Since basement returns in seismic records are clear only for large (> 1 km wide) sediment ponds, due to backscatter from rough, reflective basement highs (Fig. 1.1), the volume of sediments in young, high relief topography, is difficult, if not impossible, to

accurately determine from seismic data. Additionally, seismic profiles offer only a two-dimensional view of the ocean floor, while topography and sedimentation patterns may be very different across the space of only a few kilometers.

Sediment cores and drill holes are also of limited utility for determining the volume of pelagic sediment on rough topography. While holes drilled into regions where thick sediments drape low-relief topography, such as at DSDP site 522 in the eastern South Atlantic [*Hsü, LaBrecque et al.*, 1984] and the drill holes of DSDP legs 5, 8, 9, 16, and 85 in the eastern equatorial Pacific, provide information about sediment accumulation rate and paleoceanographic conditions which probably hold for fairly large areas, most DSDP and ODP holes in hilly regions have been deliberately sited over local sediment thickness maxima or minima, and so may not be used to draw conclusions about average sediment rain or accumulation rate or sediment thickness. Holes drilled into "draped" hillsides, such as many of the holes drilled during DSDP Leg 3 in the South Atlantic, are also not appropriate to use to measure sediment rain or accumulation rate, since it seems likely that patterns of deposition in these locales are determined by small topographic features not resolvable in the bathymetric or seismic data collected by surface ships.

In the relatively few regions within the abyssal hill regime which have been the focus of intensive geological investigations, workers have learned how sediments behave within specific environments. These studies have involved the collection of some combination of seismic, bathymetric, side-scan sonar, photographic, gravitational, and magnetic data from both ship-mounted and deep-towed sources, as well as bottom samples from drill cores, piston cores, and dredge hauls. A few of these studies have focused on pelagic sedimentation, establishing that the rate of accumulation decreases with distance from continents [*Moore et al.*, 1973] and that current winnowing and gravity flows both transport sediment [*Moore et al.*, 1973; *Van Andel*, 1973]; that bioturbation plays a major role in the reworking and eventual downslope transport of sediment [*Marks*, 1981]; and that in some regions along the Mid-Atlantic Ridge, hillsides can be almost completely stripped of sediments by turbidity currents, which may rebound off the walls of enclosed valleys [*van Andel and Komar*, 1969]. A positive correlation between high clay content and slope failure has been observed in the Indian Ocean [*Abbott et al.*, 1981]. Sediment

redistribution processes are by no means ubiquitous, however, with radiocarbon analysis from sediments from some samplings of the highly seismic Reykjanes Ridge showing a monotonic increase in age with depth, indicating that minimal post-depositional transport occurs there [*Kuptsov and Barteneva*, 1988].

To understand the range of sedimentation patterns observed in the deep sea environment, the mechanics of individual processes have been studied. Researchers have investigated the conditions under which slumps and turbidity currents develop [e.g. *Moore*, 1961; *Pykhov*, 1972; *Embley and Jacobi*, 1977; *Parker*, 1982; *Abbott et al.*, 1981, 1984], how they entrain material [e.g. *Parker et al.*, 1987], and how they interact with pre-existing channels [e.g. *Komar*, 1972; *Dade and Huppert*, 1994]. Particle behavior within the benthic boundary layer has also been studied, to understand the patterns of grain size differentiation seen on the ocean floor [e.g. *Komar and Reimers*, 1978; *McCave and Swift*, 1976; *McLean*, 1985; *McLean and Yean*, 1987]. Another approach has been to study the motion of water in the deep ocean [e.g. *Flood*, 1978 *Richardson et al.*, 1981; *Gross and Dade*, 1991] and how bottom currents interact with topography such as isolated basement outcrops [*Gould et al.*, 1981].

With the exception of studies of the geology of major fracture zones [e.g. *Kastens et al.*, 1986; *Jaroslow and Tucholke*, 1994], most investigations of sediment redistribution have been conducted on continental shelves and abyssal plains. However, controls of sediment among abyssal hills are probably very different than in those that operate in near-shore regimes. In the abyssal hill regime, outcrops of basement rock and topographic gradient, not pre-existing channels, probably act to direct and limit large-scale sediment movements. It is likely that rough abyssal hill topography complicates water currents, intensifying them in some places while sheltering other locations.

In this thesis, we adopt a different approach to the study of pelagic sedimentation on young, rough topography. Our goal is not necessarily to understand individual processes, but rather to interpret sedimented seafloor topography in terms of total sediment thickness, general sediment mobility, and basement structure. To do so, we develop a simple model of pelagic sedimentation and apply this model to realistic renderings of basement topography to study how sediments alter observable features of abyssal topography

(Chapter 2). We then construct inversion problems to obtain basement and sedimentological parameters, specifically basement RMS variability H, apparent diffusivity κ, and average sediment thickness L, from bathymetric data from the North Atlantic (Chapter 3) and the South Atlantic (Chapter 4 and Chapter 5). Information about sediment thickness from seafloor of various ages allows us to study how surface productivity, sediment composition, and ocean chemistry have varied in the central gyres of the Atlantic since near the Eocene/Oligocene boundary (Chapter 6).

NUMERICALLY MODELING SEAFLOOR TOPOGRAPHY (CHAPTER TWO)

Often, one of the first steps in the study of geological features is the development of descriptive models which allow different regions to be compared so that geological controls can be determined. For instance, the study of seamounts benefits from an understanding of the characteristics of their distributions developed by *Smith and Jordan* [1988], which provides a common framework for the comparison of seamounts within [*Jaroslow*, 1997] and between [*Magde and Smith*, 1995] regions. In another example, the many processes that contribute to landscape denudation in the subaerial environment are frequently described simply by an erosion rate, with more sophisticated models allowing spatial changes to this rate with slope [e.g. *Cullings*, 1960] and, most recently, by parameterizing mass movement on hillsides differently than in streams [e.g. *Howard et al.*, 1994]. These process models do not generate exact replicas of real topographies; rather, they allow the study of how uplift and erosional processes interact to create topography, so that actual landscapes can be better understood.

Similarly, in the study of abyssal hill topography, workers have attempted to classify the character of ridge flanks throughout the world ocean. For example, *Goff and Jordan* [1988], building on previous work by *Krause and Menard* [1965], *Bell* [1975], and *Fox and Hayes* [1985], model young abyssal hills by assuming that small-scale (< 10-50 km) bathymetry is a realization of a zero-mean, stationary, Gaussian random field completely specified by a two-point covariance function $C_{hh}(\mathbf{x})$. The Goff-Jordan model of topography has provided a basis for investigating the morphological processes that generate and reshape abyssal hills, allowing the establishment of correlations between morphology

and spreading style [*Goff*, 1991; *Bird and Pockalny*, 1994] and assisting in the tracking of changes in ridge-axis volcanic and tectonic processes through time [*Goff et al.*, 1991, 1993; *Macario et al.*, 1994].

The importance of incorporating sedimentation into models of seafloor morphology has been recognized for some time. With few exceptions [e.g., *Cao and Lerche*, 1994], however, sedimentation has not been incorporated into comprehensive models of seafloor evolution, and workers in need of reasonable models of pelagic sedimentation have assumed that sediments are either evenly distributed [*Mitchell*, 1993] or form horizontal surfaces in local lows [e.g., *Bard and Bouchon*, 1985; *Mitchell*, 1993].

One approach to studying sedimentation on rough topography has been to parameterize the stochastic character of sedimented seafloor. *Goff* [1993] gives a methodology for using moments greater than 2 in the characterization of asymmetric (possibly sedimented) topography, but the utility of applying this sort of methodology to data is limited. *Bird and Pockalny* [1994] take a much simpler approach, relating decreases in seafloor RMS variability to increases in sediment thickness.

In this thesis, instead of approaching the problem of characterizing the effects of sedimentation upon topography in a purely statistical manner, we borrow from the efforts of modelers of subaerial and nearshore topography [e.g. *Cullings*, 1960; *Koons*, 1989; *Howard et al.*, 1994]. Based on the observation that the processes which redistribute seafloor sediments result in preferential downslope transport at horizontal scales ranging from centimeters [*Heezen and Hollister*, 1971], to meters [*Marks*, 1981], to kilometers, and that the resulting accumulations of sediment often have surface shapes which resemble solutions to the diffusion equation (as shown in *Mitchell* [1995]), we use gravity-driven diffusive transport as a first-order model for sediment redistribution processes. In Chapter 2, we describe the forward model of pelagic sedimentation in detail; then, using basement models generated following the methodology of *Goff and Jordan* [1988], we model how sediments accumulate on rough topography, and investigate how various basement bathymetries, sediment rain rates, and sediment mobility parameters affect the morphology of the seafloor through time. We also demonstrate the sensitivity of local sediment accumulation rate, as might be measured from a drill or piston core, to topographic setting.

We then study how the forward model of sedimentation predicts that sediments affect frequently-measured Goff-Jordan stochastic parameters and other measures of topography such as the distribution of seafloor slope. In particular, we find that slope statistics are a sensitive indicator of both basement and sedimentological parameters. Finally, we show examples of model topographies which are similar in character to hilly regions in the western North Atlantic.

SEDIMENTATION ON YOUNG NORTH ATLANTIC SEAFLOOR (CHAPTER THREE)

Seafloor slope distributions are extremely sensitive to both basement and sedimentological parameters. In Chapter 3 of this thesis, we use the understanding of slope statistics derived in Chapter 2 to invert for L, H, and κ, from bathymetric data collected within the ARC.

A preliminary version of the methodology used in this Chapter was published in *Webb and Jordan* [1993]. In that paper, we inverted bathymetric data for L, H, and κ by comparing cumulative slope distributions of models of sedimented topography (Chapter 2) to cumulative slope distributions computed from bathymetric data from the ARC. Major improvements of the methodology presented in this thesis over *Webb and Jordan* [1993] include compensating for sampling effects in the data, using slope distributions instead of cumulative slope distributions, and using maximum likelihood estimation to determine the likelihood of model parameters.

We group data into stochastically homogeneous groups of hills (hill-centered regions), and separately into regions around common catchment basins (basin-centered regions). Inverted values of L from the basin-centered subregions show thinner sediments near-axis, thickening westward with maximum values found on 10-20 Ma seafloor and lower values on the oldest seafloor in the ARC. The paleoceanographic implications of the observed variations in L are discussed in Chapter 6. Values of L on young seafloor, when corrected for the effects of compaction, suggest a sediment accumulation rate of 5.9 ± 2.0 m/m.y. since ~10 m.y.B.P.

Inverted values of H, as computed from hill-centered regions, range from 220 to 310 m, with an average of 267 ± 28 m. Hills are generally higher to the north of a low which runs through the study area.

Inverted values of κ range from 0.1 to 0.78 m^2/yr, with an average of 0.32 ± 0.20 m^2/yr. This is somewhat above values which well-describe the surface shapes of individual high-standing ponds, probably due to our inclusion of sediments deposited by a wider variety of processes, including pond-leveling turbidity currents.

NEAR-RIDGE SEDIMENTATION IN THE SOUTH ATLANTIC (CHAPTER FOUR)

In Chapter 4, we use the methods developed in Chapter 3 to determine how L, H, and κ vary on young seafloor at moderate latitudes in the South Atlantic. We invert multibeam bathymetric data from 0 to 8-11 Ma crust on the east and west sides of the MAR between 25°S and 27.5° S (near the intersection of the Rio Grande fracture zone and the MAR), and from 0 to 5-8 Ma crust from both sides of the MAR between 31°S and 35°S (near the intersection of the Cox fracture zone and the MAR). Based on inverted values of L after correction for the effects of compaction, we estimate that sediment is accumulating at 4.9 ± 0.5 m/m.y. in the Rio Grande study area and at 5.9 ± 1.0 m/m.y. in the Cox study area. RMS basement roughness H shows an average of 206 ± 29 m in the Rio Grande study area and 199 ± 11 m in the Cox study area, somewhat lower than the values found in the ARC, which is associated with crust produced at lower spreading rates. Inverted values of κ have a mean of 0.29 ± 0.25 m^2/yr in the Rio Grande study area and 0.14 ± 0.11 m^2/yr in the Cox study area, similar to the values observed in the ARC.

Since the South Atlantic seafloor does not feature the degree of spreading segment reorganization seen in, for example, the ARC, and since tracklines tend to be oriented perpendicular to hill-strike direction, we are able to group seafloor by tectonic setting prior to the inversion for model parameters. In the Rio Grande region in particular, we are able to classify seafloor as being strictly inside corner or outside corner. We find that H correlates strongly with crustal type, with inside corner crust having an average H of 222 ± 23 m, while H for outside corner crust averages 189 ± 22 m. Fixing H at 220 m for inside corner crust and 190 m for outside corner crust produces estimates of L which show less

scatter than those achieved when H is allowed to vary. Fixing H at 200 m prior to inversion for L and κ in the Cox study area also produces values of L which correlate strongly with crustal age.

Off-Axis Sedimentation in the South Atlantic (Chapter Five)

In Chapter 3 and Chapter 4, we study sedimentation using high-quality multibeam bathymetric data, which contains data sampled every 60-180 m along-track, from regions which have been extensively mapped. However, very little of the world ocean floor has been surveyed by multiple closely-spaced tracklines. A considerable amount of bathymetric data has been collected along single transit lines, but only 1-minute samples of the center beam return, which are typically spaced 250 to 400 m apart (as determined by ship speed and the exact sampling criteria used), are generally available.

In Chapter 5, we modify our inversion methodology to study sedimentation patterns using transit line data from the Angola, Brazil, and Argentine basins in the South Atlantic. The data we examine extends off-axis from near the Rio Grande and Cox study areas of Chapter 4. We find that all three inverted parameters fluctuate greatly between subregions, but that when H is fixed at geologically reasonable values prior to inversion, L shows less variability with seafloor age.

Sediment thickness appears to increase with seafloor age on young crust, but shows a non-monotonic relationship with seafloor age on older seafloor in the Angola and Brazil basins. The complex relationship between L and seafloor age we observe is used in Chapter 6 to study the paleoceanography of the region. Sediment accumulation is more rapid off-axis in the Argentine Basin. We find that seafloor older than 20 Ma in that basin has sediments sufficiently thick that the original abyssal hill signature no longer dominates topography, and sedimented stretches seem to possess features not related to basement structure, which may be related to current activity. Thus, we do not have confidence in our inversion results from older seafloor in the Argentine Basin.

Results suggest that 1-minute samples of centerbeam data are a useful source of information about sedimentation patterns, provided that H can be independently constrained and that the seafloor sampled is representative of the local topography.

PALEOCEANOGRAPHY IN THE ATLANTIC BASIN (CHAPTER SIX)

Marine paleoclimate and deep water circulation patterns are usually investigated through analysis of drill cores. However, the relatively sparse spatial distribution of drilling sites has made it difficult to determine how surface productivity and bottom water corrosivity have varied geographically in the world ocean through time. The methodology we present in this thesis to invert bathymetric data for average sediment thickness L provides a new source of data to use in addressing these issues.

Where estimates of average sediment thickness are obtainable at nearby sites of varying ages, variations in paleoceanographic conditions can be bounded through modeling the response of L to temporal variations in sediment rain rate, sediment composition, the lysocline, and the CCD. In Chapter 6, we use such modeling, as well as data from traditional sources, to constrain temporal variations to these parameters in the Atlantic basin since at least the Oligocene. Our methodology is to assume that the dissolution of calcite at the sediment-water interface is linearly related to the depth of the seafloor below some surface, which we term the U-lysocline, with the CCD representing the bottom of the zone of dissolution. This is an extreme simplification of a complex process; however, the current state of understanding of how the factors which regulate calcite dissolution interact precludes more complex modeling at this stage.

Our inversion results suggest that the lack of preserved early and middle Miocene sediments in the Atlantic is due not only to an uplifted CCD during that period but also to reduced biological productivity. We also may recognize latitudinal differences in sediment rain rate in the South Atlantic, although our findings are not conclusive.

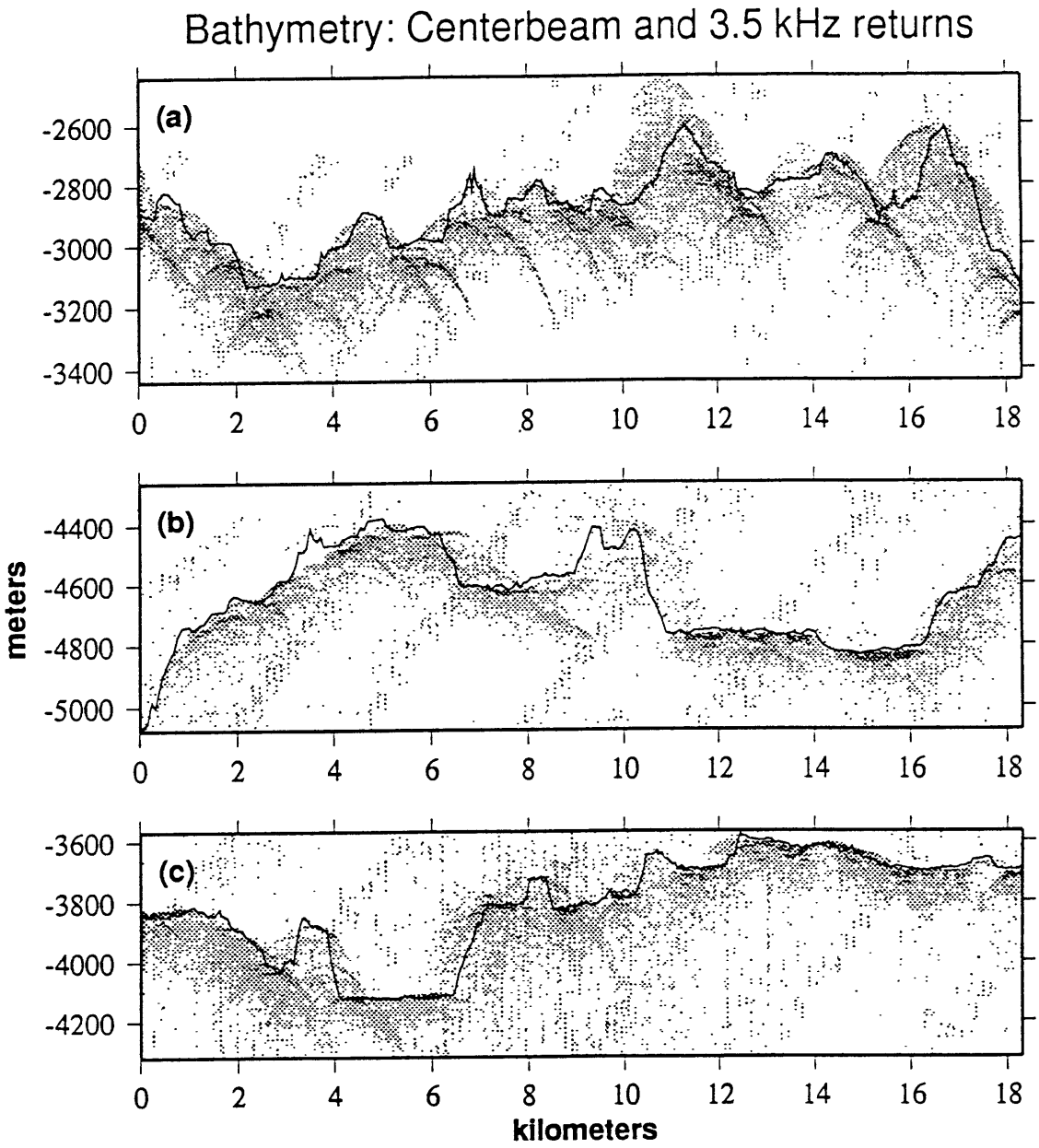

Fig. 1.1: Comparison of Hydrosweep centerbeam bathymetry (solid line) with digitally recorded 3.5-kHz returns for three profiles on the western flank of the Mid-Atlantic ridge north of the Kane Fracture Zone. Average sediment thicknesses estimated by inverting the bathymetric data (Chapter 3) are (a) 10 m, (b) 40 m, and (c) 60 m. The data were collected during the large-scale geophysics reconnaissance of the ARSRP study area by the *R/V Maurice Ewing* (EW9208; July-August, 1992). The center beam bathymetry is from the *Ewing's* Krupp Atlas Hydrosweep system; the 3.5-kHz data is from a DAT-based recording system.

Chapter 2

A Forward Model of Pelagic Sedimentation On Rough Seafloor Topography

INTRODUCTION

Pelagic sedimentation is the primary modifier of the topography of the world mid-ocean ridge system. Over millions of years, sediments slowly arrive at the seafloor from the water column and smooth the rough basement generated by ridge-associated volcanic and tectonic processes. The resulting topography varies locally and regionally, reflecting differences in (but not limited to) pre-existing topography, the pelagic sediment rain rate through the water column, and local transport processes.

Basic questions persist about sedimentation in the abyssal hill regime: How much sediment is present in a given region? How fast is sediment accumulating? What controls this rate? How has it varied in the past? How rapidly do post-depositional transport processes move sediment? What controls these rates? These questions could be answered if we better understood how the seafloor reflects the processes that have shaped it. Unfortunately, quantitative information about the structure of thin accumulations of pelagic sediments is rare. In seismic records from regions where the average thickness of pelagic sediments is a fraction of hill height, basement returns are clear only for large (greater than 1 km wide) sediment ponds (see Fig. 1.1). Sediment cores are also of limited utility for determining the regional rate at which sediment has accumulated. While large-scale mass-movement events such as slumps and turbidites can be identified in cores, and their input exempted from the computation of sediment accumulation rate, the effects of non-catastrophic mass movement processes, such as current winnowing or soil creep, are difficult to quantify.

Numerical process models have been used extensively in recent years to the study the evolution of topography in the subaerial environment. Instead of attempting to fully model individual processes, workers use simplistic models to explore the relationship between the

magnitude of various processes and large-scale, long-timelength characteristics of the resulting topography [e.g. *Kooi and Beaumont*, 1994]. In this chapter, we take a similar approach to the study of sedimentation on abyssal hills. Observing that, at all scales, sediments lie thicker in local lows than on highs, we model post-depositional sediment transport as a diffusive process in which the downhill flux of material is proportional to seafloor slope. This model allows us to explore how the pelagic sediment rain rate and post-depositional sediment mobility affect the resulting topography for a wide range of basement topographies. Since sedimentation is a three-dimensional process, with sediments moving down steep scarps into local lows and then shifting position within these lows, we primarily model sedimentation on three-dimensional surfaces, although we employ a two-dimensional version of the methodology in several numeric experiments.

We generate sedimented topographies at variety of scales, including scales appropriate for comparing models with multibeam bathymetric data. Multibeam bathymetric imaging systems, which have footprint widths of 50-200 m (depending on water depth and beam position within a swath as well as system design), are able to recover the surface shape of sediment accumulations in locations that are not well imaged by wider-beam systems. Multibeam bathymetric imaging systems have been used during the last 20 years to map fairly large sections of abyssal hill terrain, making data from such systems a source of information about the how topography ages and the role sedimentation plays in this process. By generating forward models at resolutions similar to multibeam bathymetric data, the influences of sediment on common measures of topography can be quantified, so that both sedimentation and basement information can be derived from data.

To construct our forward models, we use a number of different basement morphologies. Most, however, at least in part incorporate bathymetry models generated using the methodology of *Goff and Jordan* [1988]. Goff-Jordan models contain many of the features researchers [e.g. *Malinverno and Gilbert*, 1989] commonly associate with abyssal hill topography, including characteristic values of RMS variability, hill spacing, hill length-to-width ratio and orientation, and topographic roughness at small scales.

We begin this chapter by discussing the requirements of models of abyssal hill bathymetry. Then we introduce our forward model and show examples of model

topographies generated using various parameters. We explore how our model predicts that sedimentation changes the stochastic character of topography, as is commonly measured in studies of the world-wide variability of basement structure, and we observe the rate at which sediments accumulate at specific locations within models, as would be encountered by a sediment core. Then we modify the forward sedimentation model slightly to allow sediments to experience compaction, and observe how this affects the character of the resulting seafloor. We also explore how long-wavelength topographic signals affect sedimentation patterns and stochastic measures of topography. Finally, we compare model bathymetries to actual topography and discuss the strengths and weaknesses of the forward sedimentation model.

The forward sedimentation model introduced in this thesis has been used to generate very high resolution models of topography in support of numerical studies of acoustic backscatter conducted as part of the Office of Naval Research's Acoustic Reverberation Special Research Project (ARSRP). Experiments conducted using specially-designed basement models (*Webb, Goff and Jordan*, in prep.) have shown that, on sedimented hillsides, the character of backscattered energy is regulated by the distribution of small sediment ponds and bare outcrops [*Robertsson and Lavander*, 1995; *Robertsson et al.*, submitted]. The forward sedimentation algorithm has also been used to study sediment dispersal in the filling of the Hawaiian and Marquesan flexural moats [*Wolfe et al.*, 1994].

MODELING SEDIMENTED ABYSSAL HILLS

The height $h(\mathbf{x},t)$ of topography at position $\mathbf{x}$ and time t may be expressed

$$h(\mathbf{x},t) = b(\mathbf{x},t) + s(\mathbf{x},t) \tag{2.1}$$

where $b(\mathbf{x},t)$ is the height of the hard-rock basement and $s(\mathbf{x},t)$ is sediment thickness. Basement height $b(\mathbf{x},t)$ reflects the near-axis constructional processes that formed the seafloor, as well as the effects of subsidence and off-axis degradation, while $s(\mathbf{x},t)$ is a function of deposition rate, dissolution by bottom waters, and sediment redistribution processes. We separate the basement height into a static term $b_r(\mathbf{x})$ and a time-variable term $\bar{b}(\mathbf{x},t)$, such that

$$b(\mathbf{x},t) = \bar{b}(\mathbf{x},t) + b_r(\mathbf{x}). \tag{2.2}$$

The corresponding residual height may be expressed

$$h_r(\mathbf{x},t) = b_r(\mathbf{x}) + s(\mathbf{x},t). \tag{2.3}$$

During its first several million years of existence, as crust is rafted from rift valleys onto ridge flanks, hard-rock topography changes as faults grow and talus slopes develop [e.g. *Le Pichon*, 1969; *McKenzie and Bowin*, 1976]. Evidence exists for some further basement degradation off-axis (*Tucholke et al.*, in press). However, the magnitude of off-axis basement degradation is not large enough to affect the RMS variability of the topography significantly [*Bird and Pockalny*, 1993]. Because off-axis basement variability at small length-scales is (probably) relatively unimportant to large-scale sediment transport, we take $\bar{b}(\mathbf{x},t)$ to be a function only of long-wavelength changes in average basement depth, such as that due to lithospheric cooling, with

$$\left|\nabla \bar{b}(\mathbf{x},t)\right| << \left|\nabla b_r(\mathbf{x})\right| \tag{2.4}$$

for virtually all $\mathbf{x}$.

Basement model requirements

For modeling how sediments accumulate on abyssal hills on the flanks of the mid-ocean ridges, ideal models of basement topography would explicitly incorporate the pillows, rough fault scarps of lengths of centimeters to hundreds of meters, and talus slopes which make up abyssal hills. Fault spacing distributions would vary along the length of hills [*Shaw and Lin*, 1993]. Models would reflect the tectonic settings of the seafloor, with hills on outside corner crust trending downward into lows extending out from on-ridge spreading-center segment boundaries, while inside corner crust hills would rise as they near segment boundaries, then drop dramatically into lows [*Severinghaus and Macdonald*, 1988; *Tucholke and Lin*, 1994]. Perhaps the best models would be based on actual surveys of young topography, with faults placed where indicated by bathymetric and sidescan sonar data. Talus slopes of pillow fragments would be ramped against large faults; as time progressed, these slopes would accumulate more material.

Unfortunately, information required to generate models with this degree of detail is only now beginning to become available, and only for a few, intensely studied locations. For most of the world mid-ocean ridge flank, only a limited amount of information is

available, such as the RMS variability of sedimented topography, and the orientation and, perhaps, typical spacing of hills. And, even in the most well studied areas, only very small regions, on the order of 10-100 km^2, have been mapped at high enough resolutions to make the deduction of small-scale sediment redistribution processes possible.

To study sedimentation on abyssal hills in enough detail to determine its contribution to topography at the resolution of multibeam bathymetric data, accuracy down to the scale of meters or fractions of meters is probably not needed. Bathymetric models should, however, reflect the character of abyssal hills at length scales ranging from meters to tens of kilometers. The structure of unsedimented abyssal hills at these length scales varies greatly between regions, but in general hills within an area tend to have characteristic regional heights, spacings, lengths, and strikes.

Goff and Jordan [1988] introduce a model of rough seafloor topography, based on the stochastic character of young abyssal hills, which allows prominent aspects of morphology to be parameterized. They assume that small-scale (< 10-50 km) bathymetry is a realization of a zero-mean, stationary, Gaussian random field completely specified by a two-point covariance function $C_{hh}(\mathbf{x})$. The three-dimensional form of this function has five parameters which correspond to root-mean-squared (RMS) height H, characteristic along- and across-flowline corner wave numbers k_n and k_s, local strike ζ_s, and fractal dimension D, which governs the roughness of topography at wave numbers above k_n and k_s. Profiles are parameterized simply by H, corner wave number k, and D. Corner wave numbers and fractal dimension are related to hill spacing λ through

$$\lambda = \frac{2\sqrt{7-2D}}{k}. \tag{2.5}$$

Goff-Jordan models have provided a basis for investigating the processes that generate and reshape abyssal hills, allowing correlations between morphology and spreading style [*Goff*, 1991; *Bird and Pockalny*, 1994] and assisting in the tracking of changes in ridge-axis volcanic and tectonic processes through time [*Goff et al.*, 1991, 1993; *Macario et al.*, 1994].

One weakness of Goff-Jordan models is that they do not include topographic asymmetry caused by listric faulting [*Shaw and Smith*, 1990]. They also do not include

the regional highs and lows associated with spreading center offsets, or long-wavelength curvature associated with thermal subsidence. And, they may be too rough at scales less than 5-10 m (John Goff, pers. comm., 1995).

Despite these drawbacks, Goff-Jordan models possess much of the character of abyssal hill topography in three dimensions at scales relevant to the sediment transport problem. And, since they are based on studies of seafloor greater than 1-2 Ma in age, these models incorporate the early phase of crustal degradation during which talus slopes develop. Therefore, we choose to use Goff-Jordan models for $b_r(\mathbf{x})$ for most of the sedimented bathymetries discussed in this thesis. Modified Goff-Jordan models are used to study how long-wavelength structure affects sediment transport and the stochastic character of sedimented topography.

Modeling sediment transport as a diffusive process

In the subaerial and near-shore environments, material transport processes are commonly modeled as obeying the diffusion equation [e.g. *Culling*, 1960; *Flemings and Jordan*, 1989; *Montgomery and Deitrich*, 1994]. This model assumes that, to first order, the flux of material may be modeled by

$$f(\mathbf{x},t) = -\kappa(\mathbf{x},t)\nabla h(\mathbf{x},t). \tag{2.6}$$

To use (2.6) to model sediment transport processes, we substitute (2.1) and (2.2), so that

$$f(\mathbf{x},t) = -\kappa(\mathbf{x},t)\nabla\left(\bar{b}(\mathbf{x},t) + b_r(\mathbf{x}) + s(\mathbf{x},t)\right). \tag{2.7}$$

Because of the relationship given by (2.4), (2.7) can be approximated by

$$f(\mathbf{x},t) = -\kappa(\mathbf{x},t)\nabla\left(b_r(\mathbf{x}) + s(\mathbf{x},t)\right). \tag{2.8}$$

Using (2.3), this can be restated

$$f(\mathbf{x},t) = -\kappa(\mathbf{x},t)\nabla h_r(\mathbf{x},t). \tag{2.9}$$

To calculate changes to $s(\mathbf{x},t)$ through time, we observe that, from (2.3),

$$\frac{\partial s(\mathbf{x},t)}{\partial t} = \frac{\partial h_r(\mathbf{x},t)}{\partial t}. \tag{2.10}$$

Changes to $h_r(\mathbf{x},t)$ are caused both by the lateral transport of matter, described by (2.9), and by the introduction of new sediment from the water column, with

$$\frac{\partial h_r(\mathbf{x},t)}{\partial t} = -\nabla \cdot f(\mathbf{x},t) + F(\mathbf{x},t)$$
$$= \nabla \cdot \kappa(\mathbf{x},t)\nabla\big(h_r(\mathbf{x},t)\big) + F(\mathbf{x},t), \tag{2.11}$$

where $F(\mathbf{x},t)$ is the sediment rain rate through the water column. If $\kappa(\mathbf{x},t)$ is constant,

$$\frac{\partial h_r(\mathbf{x},t)}{\partial t} = \kappa\nabla^2 h_r(\mathbf{x},t) + F(\mathbf{x},t). \tag{2.12}$$

This is a modification of the classic diffusion equation, and is solvable analytically for simple formulations of $b_r(\mathbf{x})$ [*Mitchell*, 1995].

Is (2.9) a reasonable model for sediment transport on the seafloor? Hundreds of thousands of sediment samples have been collected to determine the composition and general distribution of pelagic sediments and the mechanisms of post-depositional transport in the world ocean. However, detailed small-scale studies that attempt to describe all the factors that influence sediments in a given region have only been undertaken in a few places, most notably in the Panama Basin [*Kowsmann*, 1973; *van Andel*, 1973]; in the Mid-Atlantic Ridge (MAR) rift valley in the FAMOUS area [*Marks*, 1981]; and along the MAR between the Azores and Iceland [e.g. *Grousset and Chesselet*, 1986]. These studies indicate that the primary agents of pelagic sediment transport include highly variable benthic currents and periodic mass-wasting events.

Grain-by-grain movements of sediment usually result from small-scale resuspension processes. These can be currents, including those associated with high-energy benthic storms [e.g. *Richardson et al.*, 1981], or bioturbation [e.g. *Ruddiman and Glover*, 1972]. Although some resuspended particles may settle higher than their initial point of contact with the seafloor, gravitational forces insure that, on average, there is a net downward flux of sediment into more sheltered locations [e.g. *van Andel*, 1973; *Kowsmann*, 1973].

Larger-scale mass wasting events are caused by the liquidation of susceptible layers of sediment, such as unconsolidated sands or clays, due to excess pore pressure. In the abyssal hill regime, rapid pore pressure changes are most commonly caused by earthquakes [*Pykhov*, 1972]. As classified by *Embley and Jacobi* [1977], sediment transport events often start as slumps, in which blocks either rotate in place or travel short distances. Slumps may trigger slides, which can travel for kilometers down very shallow slopes. Slumps and slides often result in hummocky deposits at slope breaks.

If a slump or slide involves relatively unconsolidated sediments, water can be entrained, causing a debris flow or turbidity current to develop. Debris flows have some internal cohesion and may form convex deposits at the edges of sediment ponds. In contrast, turbidity currents, dilute suspensions of clay, silt, and sand, rush to fill topographic lows. In enclosed abyssal valleys, turbidity currents can rebound off hillsides multiple times, eroding and redepositing the same material several times over the course of a few hours [*van Andel and Komar*, 1969].

The resulting morphology of sedimented seafloor varies locally and regionally. Steep hillslopes range from being very rough, with little evidence of sediment accumulation, to being smoothed by the infilling of small cracks or, in extreme cases, to supporting sediment covers of substantial thickness with surface slopes of 12°-15° or more [*Moore*, 1961]. The surfaces of valley-filling sediment ponds may be flat, concave, or tilted; composed of convex accumulations of benthic sediment and basement-derived debris; or have sediment accumulations which grade evenly into slightly thinner hillside sediments. In some regions, particularly where sediment rain rates are high or basement variability is low, sediments may drape topography, exhibiting little if any signs of ponding. On the whole, however, the net result of both gradual and rapid transport processes is downward movement of sediment, producing thicker sediment accumulations in lows than in highs, at horizontal scales ranging from centimeters [*Heezen and Hollister*, 1971], to meters [*Marks*, 1981], to kilometers.

Of the various shapes taken by sediment pond surfaces, a symmetrical concavity is most common. This has been attributed to compaction effects, the presence of slump deposits on pond edges, and the influence of talus slopes on the shape of sediment pond edges. All of these factors probably do have some effect. However, *Mitchell* [1995] has found that the surface concavity of many sediment ponds in the FAMOUS region resembles solutions to the diffusion equation for the infilling of rectangular basins, suggesting that some concavity is due to the gradual transport of sediments downward from pond edges, with the rate of this within-pond transport determined by local slope. Particularly convincing is Mitchell's observation that convex sediment deposits in highstanding regions also resemble solutions to the diffusion equation.

Based on the above observation, (2.9) seems a reasonable approximation for sediment transport within the confines of sediment ponds. There are several problems, however, with using (2.9) to model the movement of sediments near where $s(\mathbf{x},t)$ is 0. First, since oceanic basement topography is fractal at scales of millimeters to kilometers, $\nabla h_r(\mathbf{x},t)$ has, theoretically, no meaning for bare seafloor. It can, of course, be measured using a ruler of finite length, but the measured value is a function of this length. Thus, $\nabla h_r(\mathbf{x},t)$ is an average gradient of a region of seafloor, not of a specific point.

The second problem is that, in order for (2.9) to be obeyed, there must be sufficient sediment present to supply the entire flux of material, because bedrock is not subject to transport in our model. Flux away from a region of steep topography can be positive because of the input of material from the water column, but the amount of sediment thus available is a function of the local geometry.

Apparent diffusivity and sediment transport processes

The apparent diffusivity $\kappa(\mathbf{x},t)$ regulates the volume of sediments that are transported downslope, with higher values of $\kappa(\mathbf{x},t)$ modeling more energetic sediment transport than lower values. If the nature of sediment transport processes throughout a region were known, $\kappa(\mathbf{x},t)$ could be modeled as varying so as to reflect the efficiency of the redistribution processes. However, since our understanding of sediment transport is insufficient to allow us to use more sophisticated formulations, we here assume $\kappa(\mathbf{x},t)$ is constant for all $\mathbf{x}$ and t. In so doing, we model processes ranging from soil creep to turbidity currents with one parameter, probably resulting in an overprediction of sediment movement in places sheltered from bottom currents and an underprediction of the volume of sediments removed from hillsides by large-scale slides and turbidity currents. We hope that the understanding of sediment transport processes we develop in this thesis will allow more sophisticated formulation of $\kappa(\mathbf{x},t)$, if not the entire transport model, in the future.

Algorithm description

We model the sedimentation of abyssal hills in both two and three dimensions using an explicit finite difference algorithm designed to take advantage of the massively parallel

architectures of computers such as Thinking Machines Corporation's CM-2 and CM-5. Topographies to be sedimented are discretized onto an evenly spaced grid of $d \times d$ cells, with the basement height of each cell taken to be the value of $b_r(\mathbf{x})$ at the center of the cell. Our basic procedure is to add sediment to each cell at a constant rate, then allow material to shift relative to local gradients (Fig. 2.1). The details of the three-dimensional version of the algorithm are given in Appendix A; a summary is presented below.

In some places, our methodology is an explicit solution of (2.12). Therefore, we use criteria for numerical solutions of (2.12) to choose the appropriate timestep Δt via

$$\Delta t = r\left(\frac{d^2}{\kappa}\right). \tag{2.13}$$

For numerical sedimentation of profiles (the two-dimensional version of our model), r may be as high as 0.5, while an r of 0.25 will provide stable solutions to (2.12) as $t \to \infty$ [*Gerald and Wheatley*, 1984, p.472-477]. However, accuracy is compromised.

To determine optimal values of r for our purposes, we illustrate the sensitivity of numerical solutions to (2.12) to r in two dimensions in Fig. 2.2. Assuming $b_r(\mathbf{x})$ is 0 for all x between -W/2 and W/2, and sediment is added at 0 at a flux rate (NOT sediment rain rate) of 200 m^2/yr, the height of the seafloor after t m.y. is given by

$$\begin{aligned} h_r(x,t) = {} & \frac{F(0,t)d}{2W}t - \frac{F(0,t)d}{\kappa}|x| + \frac{F(0,t)d}{4\kappa W}x^2 + \frac{F(0,t)dW}{6\kappa} \\ & + \frac{W}{\pi^2\kappa}\sum_{i=1}^{\infty} -\frac{F(0,t)d}{i^2}\cos\left(\frac{i\pi|x|}{W}\right)\exp\left(\frac{-i^2\pi^2\kappa t}{W^2}\right) \end{aligned} \tag{2.14}$$

where

$$F(x,t) = \begin{cases} 200 \text{ m}^2 / d & x = 0 \\ 0 & x \neq 0. \end{cases} \tag{2.15}$$

We model (2.14) by numerically applying sediment to the center cell of a 201-cell array in which each cell is 50 × 50 m^2 (d = 50 m, W = 10.05 m) at a rain rate of 4 m/m.y., using a κ of 0.2 m^2/yr. We find that using a Δt corresponding (via (2.13)) to an r of 0.05 produces a very close fit to (2.14), but that agreement between models and (2.14) decreases with increasing r. An r greater than 0.5 leads to instability. The same magnitude of error exists as t increases, but the value of error as a percentage of total $s(\mathbf{x},t)$ decreases.

As a compromise, we use an r of 1/3 for modeling sedimentation in two dimensions, the highest value for which the center of a spike of material subject to diffusion will always be a maximum. Using similar reasoning, we use an r of 1/5 when modeling sediment redistribution processes in three dimensions.

After an appropriate Δt is chosen, if we let $F(\mathbf{x},t)$ be constant then the volume of sediment to be added during each timestep is calculated as

$$n = F\Delta t d^2, \tag{2.16}$$

and the required number of timesteps is computed by

$$N = T/\Delta t. \tag{2.17}$$

For N timesteps, a volume n of sediment is added to each cell. Then, due to the requirement that sediment thickness always be positive, flux into and out of cells is considered separately. First we calculate the amount of sediment that would be transported between cells if it were always possible to obey (2.9). If the amount to be contributed to neighboring cells from any node is greater than $d^2 s(\mathbf{x},t)$, the amount each downhill cell receives is scaled so that no more than $d^2 s(\mathbf{x},t)$ sediment is sent. Then, transport is enacted, and the process repeats.

Sediment redistribution processes are limited to within the bounds of the model topographies. Sediment may neither enter nor leave models through edges. This is equivalent to assuming that the slope of the seafloor at all edges is 0 for all t.

The computational requirements of the algorithm are rather large: a 51.2×51.2 km^2 region with a spacing d of 50 m, sedimented at a rain rate of 4 m/m.y. for 25 m.y. of model time using diffusivity of 0.2 m^2/yr, takes 32.5 minutes to run on a 32 node CM-5. Reducing d by a factor of α results in an α^2 increase in required computer memory and an α^4 increase in computational time. Therefore, when choosing appropriate grid spacings for model topographies, we seek to maximize d.

Computational requirements are much less for two-dimensional models than for three-dimensional models. For example, a 51.2 km profile with a d of 50 m, sedimented at a rain rate of 4 m/m.y. for 25 m.y. of model time using diffusivity of 0.2 m^2/yr, uses 1/1024 as much memory as its three-dimensional counterpart, needs only 60% as many timesteps, and has 1/2048 as many intercell communication events per timestep. Intracell

computations are also simpler. The sedimentation of the profile takes 11.3 minutes on a Sun Sparc 5 desktop workstation. Reducing d by a factor of α results in only an α increase in required computer memory and an α^2 increase in computational time. Therefore, where very high resolution is required or where models are used to illustrate some feature of the forward methodology (as in Fig. 2.2 above and Fig. 2.3 below), not to specifically model a real topography, we model sedimentation in two dimensions.

As a practical matter, as long as d is less than about 10% of the typical across-strike hill spacing, the exact value of d does not much affect the distribution of sediments. We demonstrate this by sampling a Goff-Jordan model generated to have an H of 225 m, a corner wave number k of 0.6 km^{-1}, and a fractal dimension D of 1.2, using d of 10, 25, 50, 100, 250, and 500 m. For each d value, the profile is sedimented for 10 m.y. of model time using an F of 4 m/m.y. and a κ of 0.2 m^2/yr. In Fig. 2.3, we demonstrate that the shape of ponds is not sensitive to d for basement datapoint spacings of 250 m or less. Denser, as opposed to coarser, samplings of basement topography are generally desirable, however, when model topographies are to be used for stochastic analysis or for visual comparison to data. In this thesis, we use values of d ranging from 10 to 500 m.

An artifact of our forward sedimentation algorithm is that the volume of sediments on steep hillsides is dependent on d and r. On a hillside steep enough that all sediment available is moved during each timestep, seafloor below the crest of the hill is subjected to all of the sediment transported from uphill cells, as well input from the water column, during each timestep. Therefore, if a cell is subjected to the entire outflow of sediment from M uphill cells, it will have a sediment thickness of $MF\Delta t$ at the end of each timestep. For profiles sedimented using the two-dimensional version of our algorithm, this means that, if a location lies at a distance X from a hill crest, it receives sediment from approximately X/d uphill cells, for a sediment thickness of roughly Xn/d at the end of each timestep. From (2.16) and (2.13), the volume of sediments present is thus roughly $FXrd^3/\kappa$, corresponding to a sediment thickness of $FXrd/\kappa$ (Fig. 2.3(c)).

Where hillside basins are completely filled, sediment moves across the surfaces of perched ponds. The slope imposed on pond surfaces because of this effect (in the two-dimensional version of our algorithm) is Frd/κ. For r = 0.2, d = 50 m, F = 4 m/m.y.,

and $\kappa = 0.2$ m^2/yr, this causes a negligible excess slope of 0.0002. In three dimensions, the excess slope in a filled pond between adjacent cells acting as sinks to M and M' other cells is $(M' - M)Frd/\kappa$. In an extreme example, in an elongated valley in which the peaks are 5 km apart M and M' could differ by 100, imparting a slope of 0.02 between adjacent cells using the above values of r, d, F, and κ; this is sufficiently high to cause slope distributions (as discussed below) to be slightly overbroad at low slope.

The flow of sediments within a model is illustrated by Fig. 2.4. We sediment a three-dimensional Goff-Jordan model for 5 m.y. of model time at a rain rate of 4 m/m.y. using a diffusivity of 0.1 m^2/yr. The gradients shown indicate that sediment that lands on rough topography flows downhill perpendicular to the direction of hill strike. However, sediments that initially encounter ponds, along with sediment transported downslope from hillsides, primarily moves slowly along-pond (in the direction of hill strike). This change in the direction of travel underscores the importance of modeling sedimentation in three dimensions instead of just along profiles, despite the large computational requirements.

During numerical sedimentation, hard-rock locales will stay essentially bare of sediment as long as n is less than the amount requested by downstream nodes, i.e. where

$$F(\mathbf{x},t)d < \kappa \nabla b_r(\mathbf{x}). \tag{2.18}$$

Given typical parameter values of 1 to 10 m/m.y. for F, 10^2 m for d, 10^5 to 10^6 m^2/m.y. for κ, and an RMS variability of $\nabla b_r(\mathbf{x})$ of 0.1-1 (from equation A5 of *Goff and Jordan* [1988]), (2.18) is usually satisfied. Therefore, where models are bare of sediment, the downward rain of sediment from the water column is usually insufficient to both supply downhill cells and allow sediment to accumulate locally. This condition persists until a cell is incorporated into a growing sediment pond. Thus, the movement of sediment on rough topography is usually insensitive to κ. Within ponds, however, slopes are much lower, and κ controls the movement of sediments, and ultimately sediment pond width.

We do not expect that, in detail, actual transport within ponds follows solutions to (2.12). However, *Mitchell* [1995] finds good agreement between analytic solutions to the diffusion equation for simple U-shaped geometries and the surfaces of 150- to 400-m-wide sediment ponds imaged by deep-tow profilers in the FAMOUS region, with a κ of 0.04 to 0.11 m^2/yr. Similarly, we find that the general shape of a 2-km-wide sediment pond

located between highly lineated abyssal hills on the western flank of the MAR is well-matched by this algorithm, using a κ of 0.05 m^2/yr (Fig. 2.5).

Non-dimensional parameters

Several non-dimensional parameters are useful for the generation and evaluation of sedimented renderings built upon *Goff-Jordan* [1988] model basement topographies. These include hill length to spacing ratio

$$a = k_n / k_s; \tag{2.19}$$

height to spacing ratio

$$\eta = Hk_n; \tag{2.20}$$

normalized sediment thickness

$$\Lambda = L / H, \tag{2.21}$$

where L is the average regional sediment thickness; and non-dimensional diffusivity K, defined below.

We may non-dimensionalize (2.12) by assuming $F(\mathbf{x},t) \equiv F$ and letting $h_r'(\mathbf{x},t) = h_r(\mathbf{x},t)/H$, $\mathbf{x}' = k_n\mathbf{x}$, and $t' = t/T$, where T is seafloor age. Taking T to be L/F, we substitute into (2.12) to obtain

$$\frac{\partial h_r'}{\partial t'}(\mathbf{x}',t') = \Lambda K \nabla_{\mathbf{x}'}^2 h_r'(\mathbf{x}',t') + \Lambda \tag{2.22}$$

with non-dimensional K given by

$$K = \left(\frac{\kappa}{F}\right) H k_n^2. \tag{2.23}$$

Throughout this chapter, we use L and κ to refer to actual parameters used in models, but use Λ and K where possible to describe relationships we deduce between model parameters and topographic measures.

The ramifications of the above scaling relationships are illustrated by applying our sedimentation methodology to a two-dimensional Goff-Jordan model basement profile (Fig. 2.6). The basement shown in Fig. 2.6 (a) and (b) has H = 225 m, k = 0.6 km^{-1}, and D = 1.2. This topography, sedimented for 20 m.y. of model time at a rate F of 4 m/m.y. using a κ of 0.1 m^2/yr (Fig. 2.6(a)), is identical to one that has been sedimented for 10

m.y. at a rate of 8 m/m.y. using a κ of 0.2 m^2/yr (Fig 2.6(b)). For both of these profiles, Λ is 0.356 and K is 2.0. If the basement terrain shown in Figs. 2.6(a) and (b) spans 30 km instead of 20 km, corresponding to a k of 0.4 km^{-1}, hillslopes are uniformly lower, so a κ of 0.2 m^2/yr and F of 8 m/m.y. produce a topography with greater onlap of sediments onto hillsides (Λ = 0.356, K = 0.9). From (2.23), a higher diffusivity of 0.45 m^2/yr is needed to raise K to 2.0, which leads to the same amount of downslope transport as in Fig. 2.6(b), given an F of 8 m/m.y.

Example topographies

We demonstrate our forward sedimentation procedure more fully by numerically applying sediment to a variety of three-dimensional Goff-Jordan basement models, using a range of diffusivity values, and examining how topography differs through time and between models of the same age.

Here, we take the resolution of the Hydrosweep system, which has a centerbeam footprint ~100-200 m wide in 4000 m water, as an upper bound for d. Since the seafloor contains sediment-filled basins of every size, using a large d lessens the carrying capacity of the hillsides, so that ponds are slightly too broad (see Fig. 2.3). However, since Goff-Jordan basement models represent the character of actual seafloor topography at length scales above a few meters, but are too rough at high wave numbers (John Goff, pers. comm., 1995), there is little advantage to using d less than 5 m. Computational requirements make using a somewhat larger d desirable; we find that a d of 50 m resolves much of the structure of sediment ponds while allowing reasonably large areas to be numerically sedimented, and therefore use this value to generate example models.

The topographies shown in Figure 2.7 illustrate the impact of variations to K (via variations to κ, for fixed H, L, and F), fractal dimension D, and hill length to width ratio a. In Figure 2.8, the profiles, measured 60° from hill-strike direction, represent isochrons through the models used to generate Fig. 2.7. They display the effects of varying Λ (via variations to L, for fixed H, F, and K) on the shape of abyssal hills and sediment ponds.

The basement topography which underlies models A-C is statistically similar to young North Atlantic seafloor [*Goff*, 1991]. The Goff-Jordan parameters for this

basement are H = 225 m, k_n = 0.6 km^{-1}, k_s = 0.12 km^{-1}, D = 2.2, and ζ_s = 30°. H, k_n, k_s, and ζ_s are chosen based on values inverted from multibeam bathymetric data from thinly-sedimented topography using the methodology of *Goff and Jordan* [1988], while D is based on small-scale roughness estimates from deep-tow bathymetric data (John Goff, pers. comm., 1995). The values of k_n, k_s, and D used correspond to a typical hill spacing λ_n of 5.4 km and hill length λ_s of 27 km. A constant sediment rain rate F of 4 m/m.y., typical of mid-latitude Atlantic carbonate sedimentation [*Lisitzin*, 1972], is used for all of the models; we do not incorporate the effects of sediment dissolution or compaction. Areas shown are 20 × 20 km^2.

Models A-C explore the effects of various diffusivities on a fixed model basement. In A, a low κ of 0.01 m^2/yr causes sediments to drape hillsides. Higher values of κ in B (0.1 m^2/yr) and C (1.0 m^2/yr) yield more rapid downslope transport, exposing peaks and creating flat sediment ponds. The diffusivity values used for Model B and Model C bracket the range of sedimented morphologies seen for young mid-latitude North Atlantic seafloor, based on the inversion results of Chapter 3.

Model D shows the effect of a higher value of D on basement and sedimented topographies. Although D values greater than ~2.4 are not often found in nature [*Goff*, 1991; *Goff and Kleinrock*, 1991], for illustrative purposes we use a D of 2.5. The basement for Model D has higher slopes than the model used for models A-C, so downslope sediment transport is increased, leading to more level ponds in topographic lows, and sharper pond-hillside transitions.

In models E and F, we investigate the effect of varying hill aspect ratio a. We find that sediment is more rapidly removed from hillsides when hills are shorter (Model E); however, even when hills are long relative to their widths there is considerable along-strike sediment transport. This along-pond transport is more rapid in Model E because slopes in the along-strike direction are steeper, but is also very important in Model F.

Limits on lateral flux

In some locales, regions of interest have, on average, positive or negative values of $\nabla^2 b_r(\mathbf{x})$. This has important implications to the modeling of, and interpretation of, data

from regions of highstanding topography along inside corner highs, or lowstanding topography on outside corner crust or between inside corner highs in terms of regional sedimentation patterns and sediment volumes.

The amount of sediment a portion of a model imports or exports is dependent on the range of $\nabla^2 b_r(\mathbf{x})$ at the edges of the region and sediment availability. If the curvature of the seafloor is everywhere such that new sediments are immediately transported, i.e. if

$$\nabla^2 h(\mathbf{x}) \leq -F/\kappa \tag{2.24}$$

for all $\mathbf{x}$, then all new sediment is rapidly moved out of the area. However, on rough seafloor topography, even if the average curvature within a region is much less than $-F/\kappa$, there are likely to be many locations where the local curvature is greater than $-F/\kappa$, and even positive.

We explore the effect of non-zero regional average values of $\nabla^2 b_r(\mathbf{x})$ by adding curvatures of varying amounts to a 51.2×51.2 km^2 basement model statistically identical to the topography underlying models A-C in Fig. 2.7 and 2.8, with the exception that the hill-strike direction ζ_s is 0°. Various long-wavelength signals, such as is shown in Fig. 2.9, are imposed on the models in the hill-strike direction so that the central 11.25 km of the models have average values of $\nabla^2 h(\mathbf{x})$ ranging from 6.4×10^{-6} to -6.4×10^{-5} (Fig. 2.9(c)). Outside this range, slope is adjusted so that the average extending away from the center strip is equal to the slope at the edges of the center strip (Fig. 2.9(b)), with the average value of $\nabla^2 h(\mathbf{x})$ equal to 0. These models are sedimented using a κ of 0.2 m^2/yr and a F of 4 m/m.y. for 25 m.y. of model time, with sediment distributions examined at model times of 2.5, 10, and 25 m.y. These times correspond to average model-wide sediment thicknesses of 10, 40, and 100 m. Figs. 2.10 and 2.11 show the average sediment thickness within the center strip of the models and predictions based on a smoothly-curving surface which maintains the imposed average through time. Fig. 2.11 includes the amount of sediment gained within strips from models built on equal-sized smoothly-varying surfaces. This is useful because even where there is no small-scale roughness $\nabla^2 h(\mathbf{x})$ is gradually altered with the accumulation of sediment.

By equation (2.24), if curvature in the across-strip direction were equal everywhere and slope in the along-strip direction was uniformly 0 (i.e. if the topography were a

smoothly curving surface), curvatures of -2×10^{-5} or less would keep the center strip empty. However, seafloor roughness captures sediments, particularly at low *t*. After 2.5 m.y. of model time, sediment removal from the center strip is only ~20% of what would occur if the topography were smoothly curving. As more sediment accumulates, small basins fill with sediment and newly arriving sediment is more able to move longer distances without encountering local minima. When using a high negative (excess) curvature of -6.4×10^{-5}, half of the center-strip sediment present at the end of 10 m.y. of model time is present at the 2.5 m.y. mark, and only a few meters accumulate in the following 15 m.y. of model time. At lower excess curvature values, ~20% of the smooth-surface value is missing at 2.5 m.y., ~40% at 10 m.y., and ~55% at 25 m.y. (Fig. 2.10).

For models where positive excess curvatures are imposed, the filling of small basins allows more long-distance sediment travel, so, as model time passes, the amount of sediment accumulating with the center strip approaches that estimated for a smoothly-sloping seafloor devoid of small-scale roughness (Fig. 2.11). The percentage of the smooth-surface amount imported is a function of curvature (Fig. 2.12).

These experiments show that along-hillstrike curvature greatly influences rate at which sediment is accumulated within a region, particularly once small lows are filled. The greater the absolute value of average curvature, the greater the amount of long-distance transport. However, when seafloor is young, even where average curvature is large we find that enclosed basins absorb a large amount of the available sediment.

In the following section, we address how sedimentation affects the stochastic character topography built upon Goff-Jordan basement models, which are complex at wavelengths of less than ~10 km. This allows us to understand how sediments accumulate on, and change, the small-scale character of rough topography. In a later section, we more fully investigate the effects of a common source of long-wavelength topography, the along-strike flexure associated with differences between inside corner and outside corner crust, on sediment redistribution patterns.

SEDIMENTATION AND SEAFLOOR STATISTICS

Stochastic parameters have been used by many workers to characterize abyssal hills [e.g. *Menard*, 1967; *Goff and Jordan*, 1988; *Malinverno*, 1991]. For example, the RMS variability of topography and the Goff-Jordan hill-spacing parameter λ_n have been observed to positively correlate with seafloor spreading rate and crustal thickness [*Goff*, 1991; *Macario et al.*, 1994]. However, the effects of sedimentation on stochastic measures of topography have not been addressed except to note that sedimentation lowers hill RMS height [*Bird and Pockalny*, 1994] and causes the distribution of seafloor heights to loose its initial Gaussian character [*Krause and Menard*, 1965]. To quantify in detail how sediments change the stochastic character of the seafloor over time, we use our forward model of pelagic sedimentation to generate models of sedimented seafloor topography, from which we compute height distributions, autocovariance functions, and power spectra. We also explore how sedimentation affects inverted values of Goff-Jordan model parameters.

In these numerical experiments, we keep basement parameters constant and vary L and κ. Where possible, we interpret observations in terms of dimensionless parameters.

The basement models used for these numerical experiments are generated using the methodology of *Goff and Jordan* [1988] and are statistically identical to the basement model used for Models A-C in Figs. 2.7 and 2.8, with H = 225 m, k_n = 0.6 km^{-1}, k_s = 0.12 km^{-1}, D = 2.2, and ζ_s = 30°. Data point spacing d and model size vary between experiments, as detailed below. All models are sedimented at a constant rain rate F of 4 m/m.y. We again do not incorporate the effects of sediment dissolution or compaction.

Height distributions

The distribution of heights in a region of seafloor is the most basic statistical measure of topography, yielding information about average seafloor depth and topographic variability [e.g. *Krause and Menard*, 1965; *Malinverno*, 1991]. Here, we examine how the height distribution $G(h)$ of topography is altered by sedimentation, both within small (51.2 × 51.2 km^2, d = 50 m) and large (204.8 × 204.8 km^2, d = 200 m) regions.

Height distributions of Goff-Jordan topography models are, by design, Gaussian, with a predetermined RMS variability H. As the models accumulate sediment, the means

of the distributions shift upward by L, as expected, and the RMS variability of the topography decreases. This second effect as been noted from investigations of seismic data from sedimented topography [*Bird and Pockalny*, 1994].

The distributions calculated from our sedimented models are relatively symmetric about their means, and appear to be roughly Gaussian when averaged over large enough regions (Fig. 2.13). To quantify the relationship between these curves and Gaussian ideals, we apply the Kolmogorov-Smirnov test [*DeGroot*, 1986, p. 556]. This test determines whether variations between cumulative height distribution functions and cumulative Gaussian functions (i.e. error functions) are within appropriate bounds. If

$$c > m^{1/2} \sup \left| G_c(h) - \left(\frac{1}{2} + \frac{1}{2} \operatorname{erf}\left(\frac{h}{\hat{H}\sqrt{2}} \right) \right) \right|, \tag{2.25}$$

where m is the number of sample heights h used to generate cumulative height distribution function $G_c(h)$, $\hat{H}$ is the computed standard deviation of the heights, and c is as given below, then $G(h)$ resembles a Gaussian distribution at some level of confidence. From [*DeGroot*, 1986, p. 556], the relationship between c and confidence level ϕ is given by

$$c = 1 - 2\sum_{i=1}^{\infty} (-1)^{i-1} e^{-2i^2\phi^2}. \tag{2.26}$$

We find that, for moderate to high diffusivity values, the maximum possible ϕ is 80% for L below 5 m. For L between 5 and 15 m, there is a steady drop in maximum possible ϕ, with higher sediment thicknesses resembling ideal Gaussian distributions even less.

The details of the changes to $G(h)$ with increasing L vary with κ and with the size of the region under consideration. As individual regions acquire sediment, the heights of the lower-lying regions increase as lows are filled with sediments, with the rightmost (highest) part of the height distributions remaining constant. For the smaller model seafloor, the heights of individual sediment ponds show up as peaks in the height distribution function (Fig. 2.13(a)). These peaks are more pronounced at higher κ (Fig. 2.13(b)), reflecting more nearly level pond surfaces. The tendency of height distributions from small areas to form peaks is a function of pond shape, and thus scales with K if bin size scales with H. For the larger seafloor model, the effects of individual sediment accumulations on the distribution function are reduced, so that the height distribution is smoother (Fig. 2.13(c)).

As we model in a later section, height distributions are very sensitive to large-wavelength effects such as crustal subsidence and the curvature imposed on hills by spreading center segmentation. Thus, the RMS variation of seafloor height calculated from data may be greater than would be expected based on local peak-to-trough variations. Ideally, these long-wavelength effects can be removed [*Bird and Pockalny*, 1994]; in practice, this is difficult to perform systematically. Therefore, although examining how our forward pelagic sedimentation model changes height distributions helps us understand some of the features of height distributions calculated from bathymetric data, we consider them to be less useful than other measures we discuss in this chapter.

Sediment thickness distributions

The distribution of sediments on and between hills can be only approximately determined from seismic records. However, it has important consequences for the behavior of acoustic energy. Knowledge of the distribution of sediment thickness within a region is also important for determining how compaction has affected the average thickness of sediments, as is discussed in a later section.

We define $S(Z)$ as the portion of seafloor with sediment thickness $s(\mathbf{x},t)$ within $[Z - dZ/2, Z + dZ/2)$. Here, dZ = 1 m. In Fig. 2.14, we show how our forward sedimentation model predicts that average sediment thickness and characteristic diffusivity affect $S(Z)$ calculated from small (51.2 × 51.2 km^2, d = 50 m) regions of seafloor. We find that, where post-depositional transport is not vigorous enough to clear much of the basement of sediments ($K << 1$, in this model caused by a low κ as opposed to a high F), the distribution of sediment thickness resembles a normal distribution about the regional averages (L = 40 in Fig. 2.14(a)), truncated at 0. For higher κ (and K), increasingly more of the seafloor is essentially bare, while the deepest localities become the repository of most sediment. For $Z > L$ where $L \geq 40$ m, $S(Z)$ decreases approximately linearly with Z for higher κ. As sediment thickness increases, less of the seafloor is essentially bare, and the percentage of seafloor thickly covered increases (Fig. 2.14(b)). As sediments gradually decrease the variability of topography, the average rate of lateral transport decreases, and $S(Z)$ displays peaks at L.

The percentage of bare or very thinly sedimented seafloor ($Z < 1$ m) may be a useful to know when interpreting acoustic backscatter from partially sedimented topography. Therefore, we have developed an empirical expression of the percentage of seafloor with sediment cover of less than $(1/225)H$ m, as a function of K and Λ. We find that the percentage of essentially bare ($s(\mathbf{x},t) < (1/225)H$ m) seafloor is

$$p(K,\Lambda) = e^{\left(-3.4K^{-0.16}\Lambda^{0.5}\right)} \tag{2.27}$$

for $\Lambda \leq 0.4$, $K \geq 1$, as illustrated by Fig. 2.15.

Second-order statistics

Second-order statistics yield information about the distances across which topography is correlated, including the typical outer scale of topography, and about the roughness of small-scale topography. By sedimenting a 51.2×51.2 km^2 region of seafloor generated with a d of 50 m, we study how sedimentation affects seafloor autocovariance functions and power spectra. We find that sedimentation alters power spectra at wave numbers greater than the along-track corner wave number in particular, with the burial of some of the rough basement topography causing decreases in power at moderate and high wave numbers (Fig. 2.16). This shows that sedimentation alters the character of topography from being strictly self-affine, making the estimation of fractal dimension irrelevant even for fairly small L. However, the slope of the power spectra at high wave numbers in regimes with moderate to high κ reflects the roughness of bare peaks, and thus may be indicative of basement D.

Covariance functions illustrate how the RMS height $\hat{H}$ and along-track hill spacing $\hat{\lambda}_z$ of sedimented topography change through time (Fig. 2.17). As sediment accumulates, autocovariance functions decrease at low lag and broaden at high lag, indicating a decreasing $\hat{H}$ and increasing $\hat{\lambda}_z$, as lower ridges become buried. The primary effect to autocovariance functions of an increases to κ is a decreased covariance at low lag; near 0 lag, the covariance function is more peaked for high values of κ, reflecting the fractal character of basement outcrops.

Goff-Jordan parameters

Goff-Jordan parameterization has become a standard method for describing the morphology of sparsely-sedimented seafloor in the abyssal hill province [*Goff et al.*, 1991, 1993; *Macario et al.*, 1994]. Goff-Jordan parameters can be inverted from bathymetric data by comparing cross-covariance functions computed from data and model autocovariance functions $C_{hh}(\mathbf{x})$ using an iterative, weighted, least-squares technique described in *Goff and Jordan* [1988]. The Goff-Jordan inversion methodology assumes that the stochastic character of ridge-flank topography can be completely specified by second-order statistics. Sedimented topography, with smoothed lows and rough highs, obviously does not meet this criteria. However, even on moderately sedimented terrains, Goff-Jordan parameters may be effective for quantifying the typical spacing of hills and the RMS variability of topography, as long as measures of second-order statistics have forms similar to those of Goff-Jordan model topographies (see Fig. 2.16 and 2.17).

Here, we investigate how inverted values of Goff-Jordan parameters may be affected by sedimentation. We apply the parameter inversion technique of *Goff and Jordan* [1988], adapted to use gridded data sets (John Goff, unpub. code, 1995), to models of sedimented topography. Models are 51.2×51.2 km^2, and have a d of 50 m. We use a moderate diffusivity κ of 0.2 m^2/yr, corresponding here to a K of 4.

Inversion results are shown in Figure 2.18. We find that $\hat{H}$ decreases as L increases, such that

$$\hat{H} \approx 225 - 0.45L. \tag{2.28}$$

This can be generalized as

$$\hat{H} \approx H - \rho(K, D, a)L. \tag{2.29}$$

For $D = 2.2$, and $a = 5$, we find that a K of 20 yields a ρ of ~ 0.6, while for a K of 0.5 ρ is ~ 0.25. In general, we use, as a rule of thumb,

$$\hat{H} \approx H - L/2 \tag{2.30}$$

to estimate the RMS variability of sedimented hills where $L << H$.

Bird and Pockalny [1994] have measured the affect of sediment on $\hat{H}$ from seismic profiles from the South Australian Basin and Argentine Basin, but since most of their data is from regions which bear much greater amounts of sediment than we model in this

chapter, our results are not directly comparable. Their results do show that $\hat{H}$ continues to decrease as sediment thickness increases to thicknesses of many hundreds of meters.

Accumulating sediments gradually bury low ridges, so the distance between hills increases with increasing L. For low L, we find that inverted values of seafloor across-strike corner wave number $\hat{k}_n$ and hill spacing $\hat{\lambda}_n$ change very little, because the inversion algorithm preferentially reduces $\hat{D}$ instead of $\hat{k}_n$. For L greater than 20 m, the seafloor has lost its fractal character and inverted fractal dimension $\hat{D}$ goes towards 2.0, so for L in this range we set $\hat{D}$ at 2.05 to keep the inversion procedure stable. We find that, with $\hat{D}$ thus fixed, increases in $\hat{\lambda}_n$ follow the form

$$\hat{\lambda}_n = \lambda_n + 1.3\lambda_n \Lambda. \tag{2.31}$$

These relationships between inverted hill height, spacing, and sediment thickness allow the estimation of basement parameters from abyssal topography if L is approximately known. We make use of these relationships when inverting topography for both basement and sedimentation parameters in chapters 3 and 4. While the final estimation of a basement λ_n is based on visual comparison of models with topography, and H is inverted for as part of a methodology for estimating L and κ, (2.30) assists in determining the range of H to consider, and (2.31) provides an approximate starting point for the search for λ_n.

SLOPE STATISTICS

The stochastic measures discussed above are helpful for understanding how the statistical character of seafloor is affected by sedimentation. However, on the highly-segmented flanks of the MAR at least, seafloor can almost never be described as zero-mean over distances of more than ~10 km, due to long-wavelength topographic influences. Therefore, measurements of height distributions, power spectra, and covariance functions from actual data from regions of bare seafloor show substantial variability from their ideal forms. The distribution of seafloor slope, however, is fairly insensitive to long-wavelength topographic trends, while being a sensitive indicator of small-scale deviations from a Gaussian form.

We use sedimented Goff-Jordan models to investigate how sedimentation may affect slope statistics by addressing seafloor slope in the form of slope distribution functions. A

profile of constant strike ζ_s sampled at a constant horizontal interval u has a slope distribution function $g(\theta,u)$, where $g(\theta,u)$ is the portion of seafloor with slopes that fall within a bin centered at θ, when measured using a ruler of length u.

It should be emphasized that since (especially young) seafloor is rough at all length scales [*Bell*, 1975; *Fox and Hayes*, 1985], the measured slope υ at a given point increases as the length u across which the slope is measured decreases, with $\upsilon \rightarrow \infty$ as $u \rightarrow 0$. Therefore, the concept of "slope" on a fractal surface such as young oceanic crust is only meaningful in relation to u. This value must be much smaller than typical hill spacing λ_n to sufficiently sample smaller ponds and rough, high-standing topography. However, when used to analyzed real data, u should be several times greater than the typical data sampling interval, to allow multiple nearby data points to be incorporated into calculations of slope so that the effects of sampling system noise are reduced (discussed in Chapter 3), and to make slope calculations less sensitive to the presence of the inevitable data gaps.

We begin by examining slope distribution functions calculated from bathymetric data from young seafloor on the western flank of the MAR at ~25.75° N (Fig. 2.19). These functions display a peak near 0, a kink near 0.1, and a gradual decrease at higher slopes. The amplitude of the peak at 0 increases with seafloor age.

These functions resemble slope distribution functions computed from our model topographies, as shown in Fig. 2.20. Slope distribution functions shown are computed from 51.2 × 51.2 km^2 (d = 50 m) Goff-Jordan models which are numerically sedimented using a range of κ and L.

A Goff-Jordan model topography is a Gaussian random surface. Therefore, $g(\theta,u)$ of every basement in Fig. 2.20 is normally distributed about 0 with variance

$$\begin{aligned}\sigma_b^2(u) &= \frac{2\left[C_{hh}(0) - C_{hh}(u)\right]}{u^2} \\ &= 2\left(\frac{H}{u}\right)^2\left(1 - \frac{(k_z u)^\nu K_\nu(k_z u)}{\pi(1-\nu)}(2\sin\nu\pi)(0.5)^\nu\Gamma(2-\nu)\right)\end{aligned} \tag{2.32}$$

for u near 0, where $\nu = 3 - D$, K_ν is the modified Bessel function of order ν, and

$$k_z = \sqrt{k_s^2\cos^2\zeta + k_n^2\sin^2\zeta} \tag{2.33}$$

is the corner wave number of the power spectrum in direction ζ (measured from ζ_s) [*Goff and Jordan*, 1988]. For Goff-Jordan models, $C_{hh}(\mathbf{x})$ is a function of Goff-Jordan parameters H, D, k_n, k_s, and ζ_s as well as ζ and ruler length u. Therefore, all these parameters influence the shape of $g(\theta,u)$ for basement topographies. Slope distributions calculated from sedimented topographies built upon Goff-Jordan models increasingly deviate from a normal distribution as sediment accumulates (Fig. 2.20), with sharp kinks developing above some slope θ_0 (near 0.1), which separates slopes derived from ponds from those of hillsides. The shape of the basement is preserved by the slope distribution functions at θ greater than θ_0, but the magnitude of $g(\theta,u)$ at these values decreases.

If we take $g_b(\theta,u)$ to be the remnant basement signal in a slope distribution function $g(\theta,u)$, the slope distribution function of the sedimented regions can be represented as

$$g_s(\theta,u) = g(\theta,u) - g_b(\theta,u), \tag{2.34}$$

discounting the effects of slopes measured across outcrop-sediment pond transitions and from slopes which may sample seafloor from within two different sediment ponds. Examples of $g_b(\theta,u)$ and $g_s(\theta,u)$ are shown in Fig. 2.21. The width of $g_s(\theta,u)$ decreases as K increases, indicating flatter ponds (Fig. 2.21(a)). The magnitude of $g_s(\theta,u)$ at $\theta = 0$ increases with increasing average sediment thickness (Fig. 2.21(b,c)). Unfortunately, we have been unable to explicitly derive a functional form for $g_s(\theta,u)$.

Local Sediment Accumulation Rate in Hilly Topography

Non-turbidite pelagic sediments in cores are normally interpreted as having been continuously accumulated at a rate equal to the regional average sediment rain rate, minus any effects from dissolution prior to burial. Hiatuses in sediment cores are interpreted as representing times of increased dissolution, erosion by bottom currents, or decreased sediment supply.

Our forward sedimentation model allows us to observe how rapidly sediments in various topographic settings accumulate. To do so, we sediment the three-dimensional Goff-Jordan model basement underlying models A-C in Figs. 2.7 and 2.8 for 50 m.y. of model time at rate $F = 4$ m/m.y., using a diffusivity of 0.2 m^2/yr. Since the sediment rain rate is kept constant and our model does not incorporate the effects of dissolution or

compaction, the only influence on local sediment accumulation rate is the response of the post-depositional flux of sediments to the bottom topography.

Sedimentation is monitored at five locations located along a profile through the center of the region, shown in Fig. 2.22. We present the results of the experiment in the format commonly used to display sediment core data, giving the depth at which sediments would be found as a function of the time of their deposition.

At location i (Fig. 2.23), located in a pond perched high on a hillside, we find that sediments begin to accumulate rapidly soon after the beginning of the model run, but that after the accumulation of ~50 m the pond fills. Location i continues to accumulate sediments, which ramp up against the ledge to its left, but this happened very slowly, as most sediment is transported over the ledge to its right or out of plane. This continues for 20 m.y. of model time. Finally, the lower, larger pond to the right of location i fills with sediments, burying the ledge separating it from location i. Thereafter, location i accumulates sediments at slightly greater than the average regional rate.

Location ii (Fig. 2.24) is situated on the hillside which bounds the right side of the large pond which eventually incorporates location i. Since location ii is not in a local minima, it does not accumulate sediments until the level of the large pond reaches its location. It then accumulates sediments fairly rapidly for a few million years of model time, since it is then at a concave break in slope and receives sediments from uphill faster than they are removed into the rest of the pond. As the pond continues to expand and the slope break moves uphill to the right, the rate of accumulation at location ii continues to decrease. With the final burial of the hill upon which it resides, rate decreases to just the background rate, as sediments are no longer available from immediately uphill. The general flux of sediments at ii now probably shifts to the right, to fill the lower standing pond on the other side of the hill.

Location iii (Fig. 2.25) is situated just at the crest of this hill. Like location ii, its position keeps it from accruing sediments until a large pond incorporates it. For location iii, this takes 30 m.y. of model time. As it is being incorporated into the large pond, it experiences a brief period of a sediment accumulation rate of 2 m/m.y., meaning that other locations are also competing with it for sediment. Local accumulation rate soon drops to

1 m/m.y. Finally, as the pond expands to fully cover location iii and the rest of the top of the hill, sediment accumulation rates rise to near the downward rain rate.

Location iv (Fig. 2.26), in contrast, is situated near the bottom of a deep, fairly narrow trough. The geometry of the trough and surrounding hills allows location iv to accumulate sediments very rapidly as it is incorporated into the pond, then at a steady, high rate of 8 m/m.y. as the pond continues to expand.

Finally, location v (Fig. 2.27) is located in a fairly large, perched pond to the right of the pond of location iv. Located in the deepest part of the perched pond, it accumulates sediment rapidly at first, and more slowly as the pond expands and the downward-flowing sediment is spread across a larger area. By 35 m.y.B.P. (in model time), the perched pond fills, and sediments begin to flow over the ledge to the left towards location iv. However, location v continues to accumulate some sediments, as predicted for a shelf where sediment flow follows the diffusion equation [*Mitchell*, 1995].

SEDIMENT COMPACTION

The modeling exercises presented in this chapter thus far have not incorporated the effects of sediment compaction. Compaction, relatively unimportant for very thin accumulations, significantly decreases the thickness of sediment accumulations greater than 50-100 m [e.g. *Audet*, 1995]. As shown by the sediment thickness distributions in Fig. 2.14, even where average sediment thicknesses are thin, much of the sediment present resides in ponds which may be hundreds of meters thick.

We study the effects of compaction on observed average sediment thickness $\tilde{L}$ and dimensionless apparent diffusivity K by modifying our forward sedimentation model to allow gradual compaction and then numerically sedimenting model Goff-Jordan basement topographies, as above. We assume that porosity $\phi(z)$ varies with subbottom depth z as calculated using Equation 13 of *Audet* [1995] (Fig. 2.28), using an initial ϕ_0 of 0.71, a rock (carbonate) density ρ_r of 2750 kg/m^3, a water density of 1050 kg/m^3, and compaction parameters *Audet* [1995] derived for oozes at ODP site 806. Using $\phi(z)$, the total rock mass of a sediment column of length Z is given by

$$W(Z) = \int_0^Z (1 - \phi(z))\rho_r dz. \tag{2.35}$$

Sediment redistribution processes follow the procedure given in Appendix A, with the exception that rock mass $W(\mathbf{x},t)$ is tracked and moved instead of sediment thickness. Via (2.35), Z is determined based on W at the end of each timestep. (Implicit in this procedure is an assumption that compaction occurs instantaneously in response to increases in sediment thickness.)

Effect on average sediment thickness

We apply the modified forward sedimentation model to the Goff-Jordan basement topography of models A-C in Fig. 2.7 and Fig. 2.8, which has parameters H = 225 m, k_n = 0.6 km^{-1}, k_s = 0.12 km^{-1}, and D = 2.2, using K of 0.5, 1.4, 4.0, and 8.1. We also use a K of 3.2 to apply sediment to a basement with a higher H of 300 m and identical k_n, k_s, and D. For each model run, a downward sediment rain rate of 5 m/m.y. is used. The average (post-compaction) sediment thickness $\tilde{L}$ is measured after the passage of 1, 2, 4, 6, 8, 12, 16, and 20 m.y. of model time.

We find that the loss to L due to compaction

$$C = L - \tilde{L} \tag{2.36}$$

positively correlates with K and H (Fig. 2.29). The correlation with K reflects the effects of increased transport of sediments into thick accumulations in local lows. The correlation with increased H is due to the thicker nature of small ponds in higher-amplitude Goff-Jordan topographies, which are more effected by compaction.

The variation in C with L for K and Goff-Jordan basement parameters in the range examined are well-described by the empirical formula

$$C = 0.021\tilde{L}^{1.44}. \tag{2.37}$$

We use this relationship in later chapters of this thesis to correct for the effects of compaction on values of L inverted from bathymetric data.

Effect on pond morphology

Since compaction affects thick sediment accumulations more than thinner ones, it might be expected that compaction influences the concavity of sediment pond surfaces. However, using the forward model of sedimentation incorporating compaction described above, compaction does not markedly effect pond shape (Fig. 2.30). We find that, if the rate of lateral transport is governed by local slopes via (2.9), gradual increases to local slope due to compaction are compensated for by increased lateral transport rates. Consequently, a surface generated without compaction for X m.y. of model time using a sediment rain rate F and a moderate diffusivity κ will strongly resemble a surface generated with compaction for $(X + C/F)$ m.y. of model time using the same κ, where C as above is the decrease in average sediment thickness due to compaction.

This does not hold for all possible seafloor geometries. For example, two adjacent regions, one with a broad, shallow sediment sink and the other with a narrow, deep sediment sink, will experience different average reductions to L due to compaction. However, each catchment basin taken individually should follow this relationship internally, given an appropriately-chosen value of C for each basin.

Since the shape of sedimented Goff-Jordan model topographies is not much affected by compaction effects, we can use $W(Z)$ and sediment distribution functions as shown in Fig. 2.14 to calculate the pre-compaction average sediment thickness L independently of (2.37) for topographies where Goff-Jordan basement parameters and κ, T, and $\tilde{L}$ are known but details of the topography are unknown. First, a model basement with the same Goff-Jordan parameters is sedimented, without allowing compaction, at a rate F of $\tilde{L}/T$, using a diffusivity of κ, for T m.y. of model time. From the resulting surface, $S(Z)$, as discussed above, is computed. Then, using the expansion function $E(Z)$ given by

$$E(Z) = \frac{1}{Z(1-\phi_0)} \int_0^Z (1-\phi(z))\, dz, \tag{2.38}$$

the pre-compaction L for the topography in question can be computed via

$$L = \int_0^\infty S(Z)E(Z)dZ. \tag{2.39}$$

RIDGE-PARALLEL FLEXURE AND SEDIMENT TRANSPORT

Goff-Jordan basement models possess neither along-strike flexure nor regional deeps caused by spreading center segmentation, ubiquitous features of slow-spreading mid-ocean ridges. Here, we incorporate ridge-parallel flexure into basement models, to study how distributions of sediment thickness, basement height, and seafloor slope are affected.

Table 2.1. Sources of data

Segment Type	Example	Reference	Modeling Formula
Inside-inside	E. flank of S. MAR, 25.75° to 26.33° S, 13.18° to 13.51° W	*Grindlay et al.*, 1991	$-600(\sin(\pi x/70))^{0.5} - 2600$
Outside-outside	W. flank of S. MAR, 25.89° to 27.15° S, 14.72° to 15.05° W	*Grindlay et al.*, 1991	$800(\sin(\pi x/120))^{0.5} - 4000$
Inside-outside	W. flank of N. MAR, 25.51° to 26.41°N, 46.8° to 47.64° W	*Tucholke et al.*, 1992	left: $500(\sin(\pi x/86))^{0.5} - 4550$ right: $-500(\sin(\pi x/86))^{0.5} - 3550$

Model flexure patterns are developed by averaging across-strike over at least 30 km of ridge-parallel hills, as expressed in gridded bathymetric data from near-MAR surveys (Table 2.1). Fig. 2.31 illustrates that, where hills are bounded on both sides by inside corner crust, seafloor exhibits a saddle shape. In contrast, where the segment is entirely outside corner crust, curvature is convex, and valleys trend into segment-boundary lows. Where hills trend from inside corner to outside corner crust, the segment reaches maximum average heights near the inside corner segment boundary and hills trend downward across the outside corner crust into extra-segment lows. We find that, along-strike, both inside corner and outside corner curvature effects on the edge shape of a segment and an end may be described using the form

$$\Delta b_c(x) = A\sin^{0.5}(x\pi / B) + N, \tag{2.40}$$

where x is the distance from the segment boundary along-strike, $\Delta b_c(x)$ is the average change in basement height, A is the amplitude of the effect, B is the distance over which the seafloor is affected by curvature, and N is a normalization parameter. In the bathymetric data we examined (Table 2.1), A ranges from 500 to 800 m and the effects of flexure are felt along entire segments, which range in length B from 70 to 120 km.

We impose flexure using (2.40) on a 307.2 × 307.2 km^2 Goff-Jordan basement model with a sparse d of 300 m. As with many of the models we examine in this chapter, H = 225 m, k_s = 0.6 km^{-1}, k_n = 0.12 km^{-1}, and D = 2.2. We use $\zeta_s = 0°$, and impose the curvature along-strike. Each segment is 90 km long, with 9.15 to 9.45 km transition zone between segments. The imposed curvature, with $\Delta b_c(x)$ and x given in kilometers, is

$$\Delta b_c(x) = \begin{cases} 0.4 - (0.8/9.15)x & 0 \le x < 9.15 \\ -0.4 + 0.8\sin^{0.5}\pi(x - 9.15)/90 & 9.15 \le x < 54.15 \\ -0.4 + 0.8\sin^{0.5}\pi(99.15 - x)/90 & 54.15 \le x < 99.15 \\ -0.4 + (0.8/9.3)x & 99.15 \le x < 108.45 \\ 0.4 - 0.8\sin^{0.5}\pi(x - 108.45)/90 & 108.45 \le x < 153.45 \\ 0.4 - 0.8\sin^{0.5}\pi(198.45 - x)/90 & 153.45 \le x < 198.45 \\ 0.4 - (1/9.3)x & 198.45 \le x < 207.75 \\ -0.6 + 0.6\sin^{0.5}\pi(x - 207.75)/90 & 207.75 \le x < 252.75 \\ 0.6 - 0.6\sin^{0.5}\pi(297.75 - x)/90 & 252.75 \le x < 297.75 \\ 0.6 - (1/9.45)x & 297.75 \le x \le 307.2. \end{cases} \quad (2.41)$$

The shape of the curve defined by (2.41), and its impact on seafloor shape, are shown in Fig. 2.32. Model seafloor between 9.3 and 99.3 km long-strike is referred to below as the outside-outside segment; between 108.6 and 198.6 km as the inside-inside segment; and between 207.9 and 297.9 km as the outside-inside segment.

We use κ of 0.2, 1.0, and 10.0 m^2/yr and an F of 4 m/m.y. to sediment the model topography for 25 m.y. of model time. We also sediment the Goff-Jordan basement model absent the flexure of (2.41), and refer to the models thus generated as control models.

The lowest κ value we use is within the range of κ inverted from bathymetric data in Chapter 3 of this thesis, and the middle value is just slightly above the range we observe. Therefore, we use sedimented surfaces generated using these values to study how sedimentation changes stochastic measures of topography in the following sections.

Effect on sediment distribution

The magnitude of the curvature imposed by (2.41), when averaged over nearby cells, has a magnitude generally near 0.5-1.0 × 10^{-6} except at the very edges of segments, where curvatures have magnitudes of 10^{-5} or higher. As shown in Fig. 2.10 and 2.11, these

curvatures are too low to cause the large-scale movement of sediment from the centers of segments into boundary ponds. There is some preferential deposition in regional lows, however, and the highest-standing topography stays relatively devoid of sediment through time. These effects are more pronounced at higher κ (Fig 2.33). However, the middle 72 km of the outside-outside segment looses only a few meters of sediment, on average, compared to the control seafloor, and the middle of the inside-inside segment gains only a few meters of sediment. For the outside-inside segment, the sediment thickness in the middle 72 km of its length differs from that of the control model by is less than 0.1%.

The amount of sediment lost or gained positively correlates with model time, since small basement pockets are a factor limiting sediment transport. As they fill, sediments are able to move across their sedimented surfaces. The amount of sediment lost or gained by segment centers also is higher for the models generated using the higher diffusivity values.

In Fig. 2.33, some ponding is obvious at regional minima associated with outside corner crust. The counterparts to these lows in nature, referred to as outside corner lows, typically possess thick accumulations of flat-lying sediment. We find that a κ of 10.0 m^2/yr generates models with ponds as flat and as deep as the ponds seen in nature, as shown in Fig. 2.34. This value is well above those inverted in Chapter 3, which are thought to parameterize intrahill sedimentation processes. The failure of lower values of κ to adequately fill regional lows may be due to local variations in transport processes. Deep regional lows, at least on young seafloor, may be primarily filled by turbidity currents (e.g. *Van Andel and Komar* [1969] and at Site 519 in the South Atlantic [*Hsü, LaBrecque et al.*, 1984]), while a variety of processes may be reflected in deposits in shallower settings.

Using the lower values of κ which we believe are appropriate for modeling intrahill sediment redistribution, we find that there is little or no difference in $S(Z)$ between the models which incorporate flexure and control models, as shown in Fig. 2.35 and 2.36. Thus, long-wavelength curvature does not affect this measure of sedimented topography.

Effect on height distribution

In contrast to sediment thickness distributions, height distributions $G(h)$ from models which incorporate flexure are different from those of control models, as shown in

Figs. 2.37 and 2.38. Flexure expands the range of heights h of the basement, such that $G(h)$ for the outside-outside segment basement is positively skewed and the inside-inside segment's basement $G(h)$ is negatively skewed. The outside-inside segment's basement $G(h)$ is symmetric, but is more triangular than Gaussian. As sediments accumulate, $G(h)$ from the outside-outside segment becomes more evenly distributed, as the low tail is shifted up. Conversely, $G(h)$ from the inside-inside segment responds to sedimentation by becoming steeper at low values of height. Sedimentation affects the outside-inside segment by narrowing the range of height values seen. The height distribution maintains its symmetric shape. After 25 m.y. of model time, the height distribution for the outside-inside corner crust more closely resembles a Gaussian distribution than the height distributions from the model topography.

The most obvious diffusivity-caused difference to height distributions is that the range of heights seen decreases more rapidly with increasing L when κ is higher, an effect of the more rapid filling-in of lows. Higher-κ height distribution functions also contain more local highs; these would presumably disappear were a large enough model used.

Effect on slope distribution

We above advance slope distributions $g(\theta,u)$ as potential tool for evaluating topography, partially due to the small effect long-wavelength topography signals have on local slope distributions in other studies [*Shaw and Smith*, 1990]. If long-wavelength topography had a large effect on $g(\theta,u)$, the usefulness of using sedimented Goff-Jordan model basements to study $g(\theta,u)$ and, as in chapters 3, 4, and 5, invert topography by comparing model and data slope distribution functions, would be questionable.

In Figs. 2.39 and 2.40, we examine the effect of along-strike flexure on across-strike $g(\theta,u)$. We find that slope distributions from the flexure-affected segments and from the control topography to be practically identical, with the shape of $g(\theta,u)$ reflecting only variance of the basement slope distributions, L, and κ, as discussed above. We might, however, expect that $g(\theta,u)$ measured along-strike to be affected by the imposed flexure. We find that the effect on basement slopes is actually fairly slight, as shown in Figs. 2.41 and 2.42. However, as sedimentation progresses, ponds that develop between hills trend

down into imposed lows, causing the range of along-strike slopes to be greater on the segments which have imposed flexure than in the control models. This effect is more pronounced for the outside-outside and inside-inside segments than the outside-inside segments, especially when the higher κ value of 1.0 m^2/yr is used.

Implications for parameter inversion techniques

The sensitivity of seafloor height to flexural effects associated with crustal type makes the use of height distributions alone for quantifying topography problematical, at least on the flanks of the MAR. In the Pacific, where *Krause and Menard* [1965] first used height distributions to investigate basement topography, this is less of an issue, because while fracture zones are important topographic features in the Pacific, segment boundary effects on abyssal hill topography seem to be more minor, and hills maintain fairly constant heights along their strikes [e.g. *Cochran et al.*, 1993].

Slope statistics, the primary measure we utilize to invert topography for stochastic parameters in later chapters, seem to be relatively impervious to the effects of along-strike flexure when measured across-strike. When slope is measured along-strike, the main complication is a wider distribution at small θ. Thus, along-strike distributions through flexure-affected seafloor are likely to resemble distributions generated using lower κ on non-flexure-affected seafloor. This suggests that inversions of seafloor topography for L and H are likely to be insensitive to long-wavelength flexural affects, regardless of the direction along which $g(\theta,u)$ is measured. Apparent diffusivity, however, may be affected by measurement direction.

POTENTIAL MODEL MODIFICATIONS

Additional modifications to basement models and the pelagic sedimentation algorithm would be useful for addressing specific issues. In particular, basement models with greater accuracy at small wavelength would be useful for studying problems at very small scales.

Changes to the sedimentation distribution model could entail recasting (2.6), allowing bedrock to erode, or explicitly modeling sedimentation processes such as turbidity currents, asymmetric benthic currents, and sediment resuspension in the benthic boundary layer.

The relationship between lateral flux and seafloor slope in (2.6) has one of many possible forms. *Mitchell* [1995] explored non-linear relationships, but found that (2.6) best described the shapes of the small ponds he observed. However, non-linear relationships may be appropriate in other regimes. The relationship between sediment flux and slope may also vary with slope range and/or dominate local redistribution process. For instance, very little sediment transport could be allowed for slopes below some threshold. To model regions where turbidity currents dominate sediment redistribution, sediment could be completely removed from high-standing regions of young seafloor and placed in level accumulations in lows, by allowing very large κ.

Our forward sedimentation model assumes that basement is static and non-erodible. Recent investigations show that faults degrade continuously as seafloor ages (*Tucholke et al.*, in press). To study this phenomena and how sediments respond, basement failure could be incorporated into the forward model, perhaps also as a diffusive process.

The explicit inclusion of turbidity currents is also possible. One method would be to periodically allow massive failures to start on steeper slopes, clear away the uppermost sediments from downslope regions, and terminate by filling in lows. This is different than assuming a high value of κ, in that a location's position relative to upstream turbidity current sources, not local topography, would govern whether it is ever stripped of sediments. Another way to model turbidity currents is to allow the diffusivity of cells to increase with distance from drainage divides.

All of the above modifications would be simple to incorporate into the framework of our forward model of pelagic sedimentation.

EXAMPLE MODELS: NORTH ATLANTIC ABYSSAL HILLS

To evaluate our forward modeling methodology, we display gridded multibeam bathymetric data from three small regions in the North Atlantic and model bathymetries generated using regional values of κ, *Goff-Jordan* [1988] basement parameters H, k_n, k_s, ζ_s, and D, and average sediment thickness L, similar to values inverted from bathymetric data (Chapter 3). The models are built upon a constant Goff-Jordan basement, scaled to reflect the inverted values of H prior to sedimentation. After sedimentation, models are

filtered to simulate the effects of the Hydrosweep sampling system, including the addition of a normally-distributed random noise term with a variance of 15 m^2 (see Chapter 3).

The first region (Fig. 2.43), centered at 25.8° N, 46° W, we estimate to have an average sediment thickness L of 24 m on hills with H = 275 m, redistributed with an average diffusivity κ of 0.12 m^2/yr. In general, the higher regions in the data seem to be flatter than in the model we generate using these parameters. The model hills seem more regular, and perhaps more elongated. To more accurately model this region, regional lows should be introduced into the basement model prior to sedimentation. In addition, the value of RMS H imposed on the basement may be too high.

The models generated to resemble the character of more homogeneous regions look somewhat better. The second region we model (Fig. 2.44), centered at 25.9° N, 46.7° W, has inverted parameters L = 40 m, H = 245 m, and κ = 0.36 m^2/yr. The model generated using these parameters has similar-looking high and low sedimented surfaces, sharp ridges, and narrow deeper regions. The third region (Fig. 2.45), centered at 26.6° N, 46.1° W, has inverted parameters L = 78 m, H = 270 m, and κ = 0.78 m^2/yr. It is also well-matched by a model seafloor generated using the inverted parameters, which displays the same general height range and hill spacing. For the regions in Fig. 2.44 and 2.45, the major difference between data and models are that some valleys in the models seems to be more U-shaped across their narrowest extents, and have more tilt towards low regions, than is typically seen in the data.

These models illustrate some of the strengths and weaknesses of our methodology for modeling pelagic sedimentation. The general pattern of rough hills and smooth valleys is well-reproduced, but complexities in basement morphology not present in the Goff-Jordan basements used are evident. Long-wavelength topography associated with spreading-center segmentation causes abyssal hills to vary in depth across their lengths, and the strike of hills may not always be as parallel as Goff-Jordan models portray. The U-shape of valleys in highstanding portions of models may indicate that sediment redistribution processes in highstanding regions are modeled as being too energetic.

CONCLUSIONS

By modeling seafloor sedimentation as a gravity-driven diffusive process, we produce models of topography which allow us to study pelagic sedimentation at a level of detail not feasible using traditional methods.

We explore how sedimentation may change the stochastic character of topography at scales of 50-100 m, which is relevant to the interpretation of bathymetric data from multibeam swath mapping systems such as Seabeam or Hydrosweep. Our forward model of pelagic sedimentation predicts that power is lowered at high wave numbers as sediment accumulates. However, the distance across which topography is correlated increases with sediment accumulation. We find that relatively small (10 - 20 m) amounts of sediment are sufficient to alter topography to the extent that inversions for fractal dimension following the methodology of *Goff and Jordan* [1988] become unstable. Particularly useful may be our estimations of how sedimentation might influence the Goff-Jordan parameter values inverted from young topography, given by (2.30) and (2.31).

Our model predicts that much seafloor remains essentially bare, even where average thicknesses of sediment are 50 - 100 m. At the same time, much sediment resides in ponds many times thicker, at their thickest locales, than the average regional sediment thickness. Thus, compaction is likely to be important even where average sediment thicknesses are low. Via (2.37), we propose a correction factor for estimating the average sediment thickness in a region which would be seen if compaction did not occur, given an estimation of average post-compaction sediment thickness.

Using our forward model to study how variations in basement and sedimentological parameters affect the rate at which sediment accumulates at particular locales, we have found that sediment accumulation rate is heavily influenced by topography. The accumulation rate at a given location is commonly several times higher or lower than the average for a region. We find that some hiatuses in our model cores are due solely to temporary shifts in the locus of deposition.

We find that slope statistics are particularly sensitive to variations in average sediment thickness. We find that long-wavelength topography, which greatly influences height distributions, has little to no influence on slopes, particularly when they are measured perpendicular to the direction of long-wavelength topographic variability.

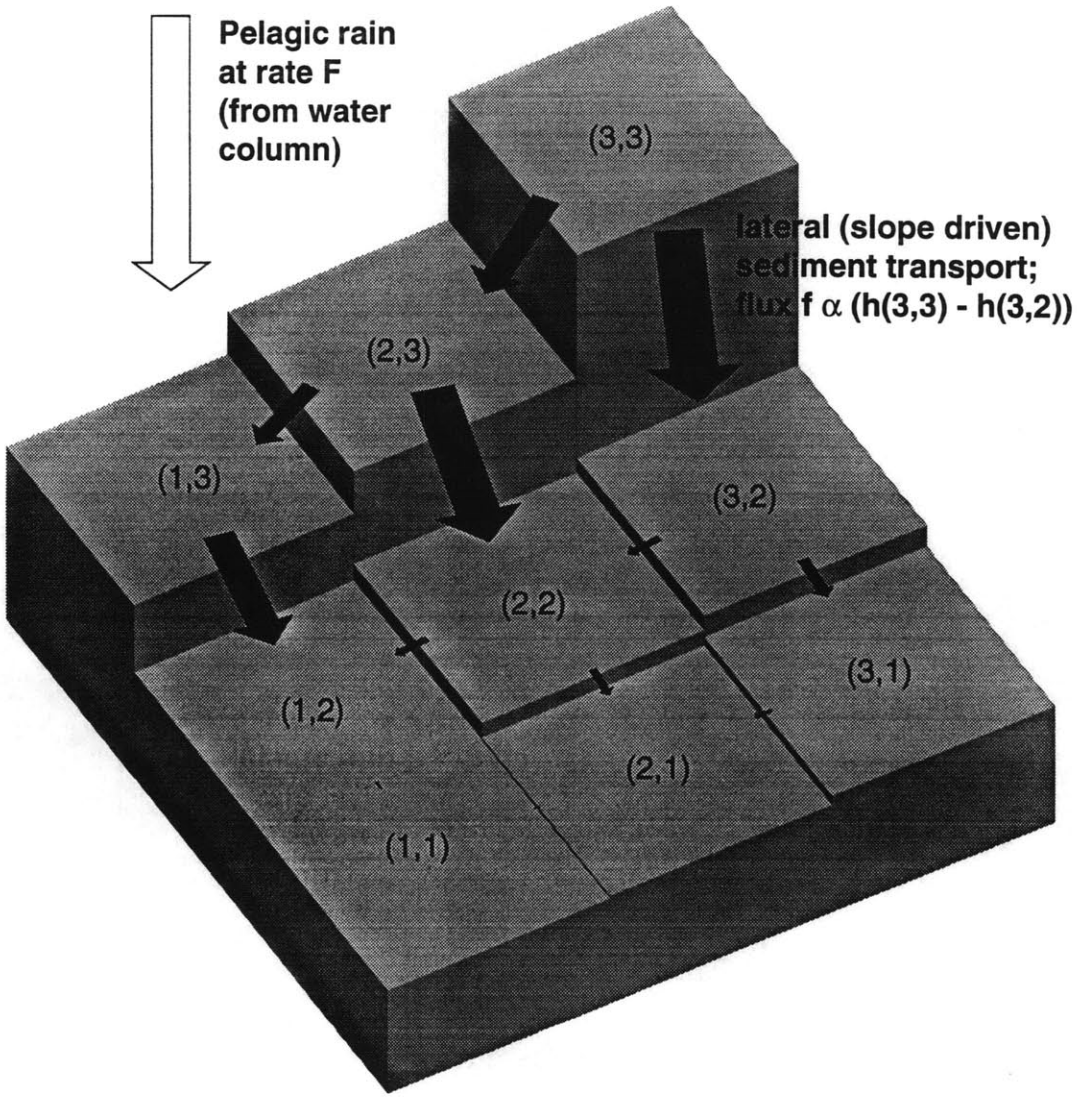

Fig. 2.1: Schematic illustrating the discrete-block algorithm used to redistribute sediment in our three-dimensional model. By apportioning sediments from high-standing blocks to low-standing nearest-neighbors, we can generate flow fields that obey the down-slope diffusion equation while honoring the hard-basement boundary condition. This boundary condition makes the problem highly nonlinear. This cellular-automaton algorithm can be easily generalized to include other sediment-transport processes.

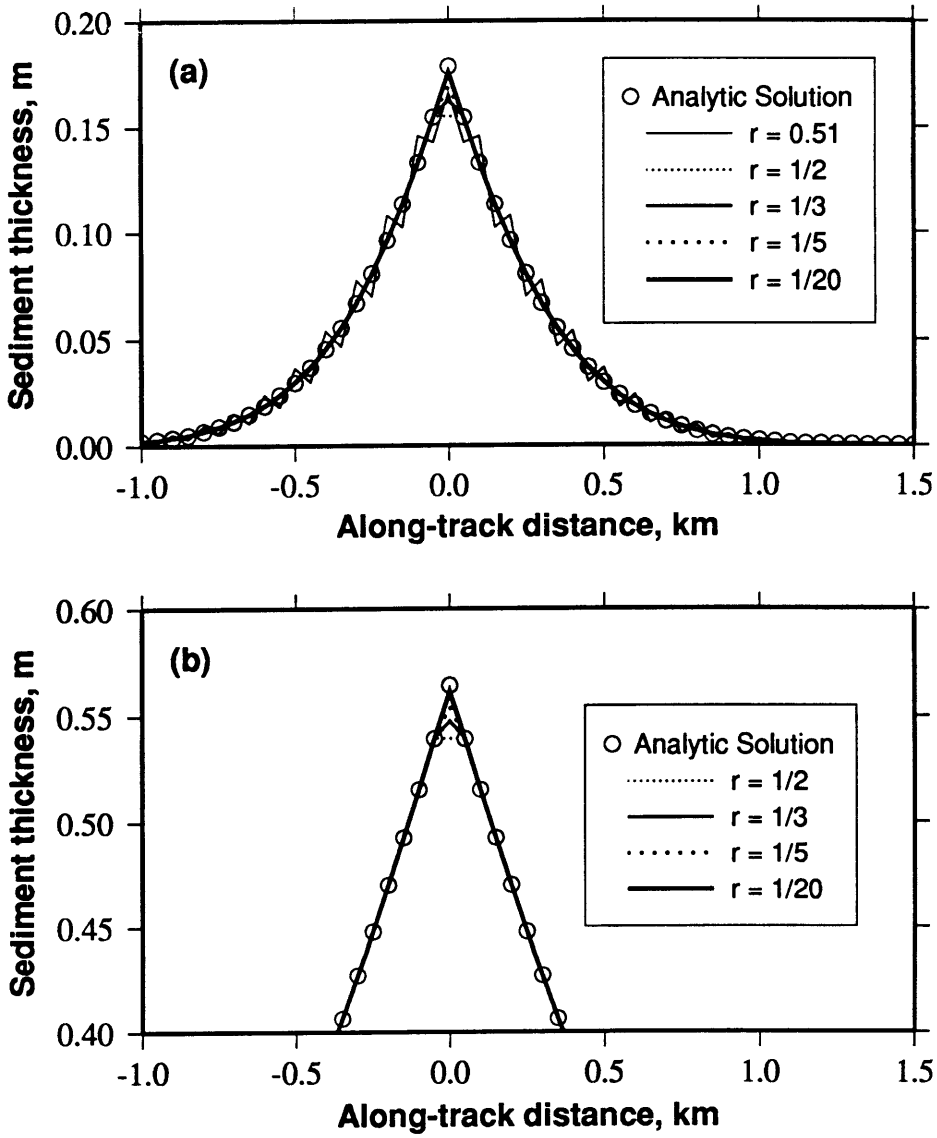

Fig. 2.2: Sediment is applied to the center of a 12-km long, level profile to illustrate the sensitivity of finite-difference solutions to parabolic partial differential equations such as (2.11) to the ratio r of Δt to d^2/κ. Small values of r provide the best fit to the analytic solution, while $r > 0.5$ lead to instability. Pictured are solutions corresponding to (a) 0.5 and (b) 5 m.y. of model time. The flux rate is 200 m^2/m.y., and the data point spacing is 50 m. This gives a sediment rain rate F of 4 m/m.y. to the center cell in the model, while F is 0 for the other cells. The diffusivity κ used was 0.2 m^2/yr.

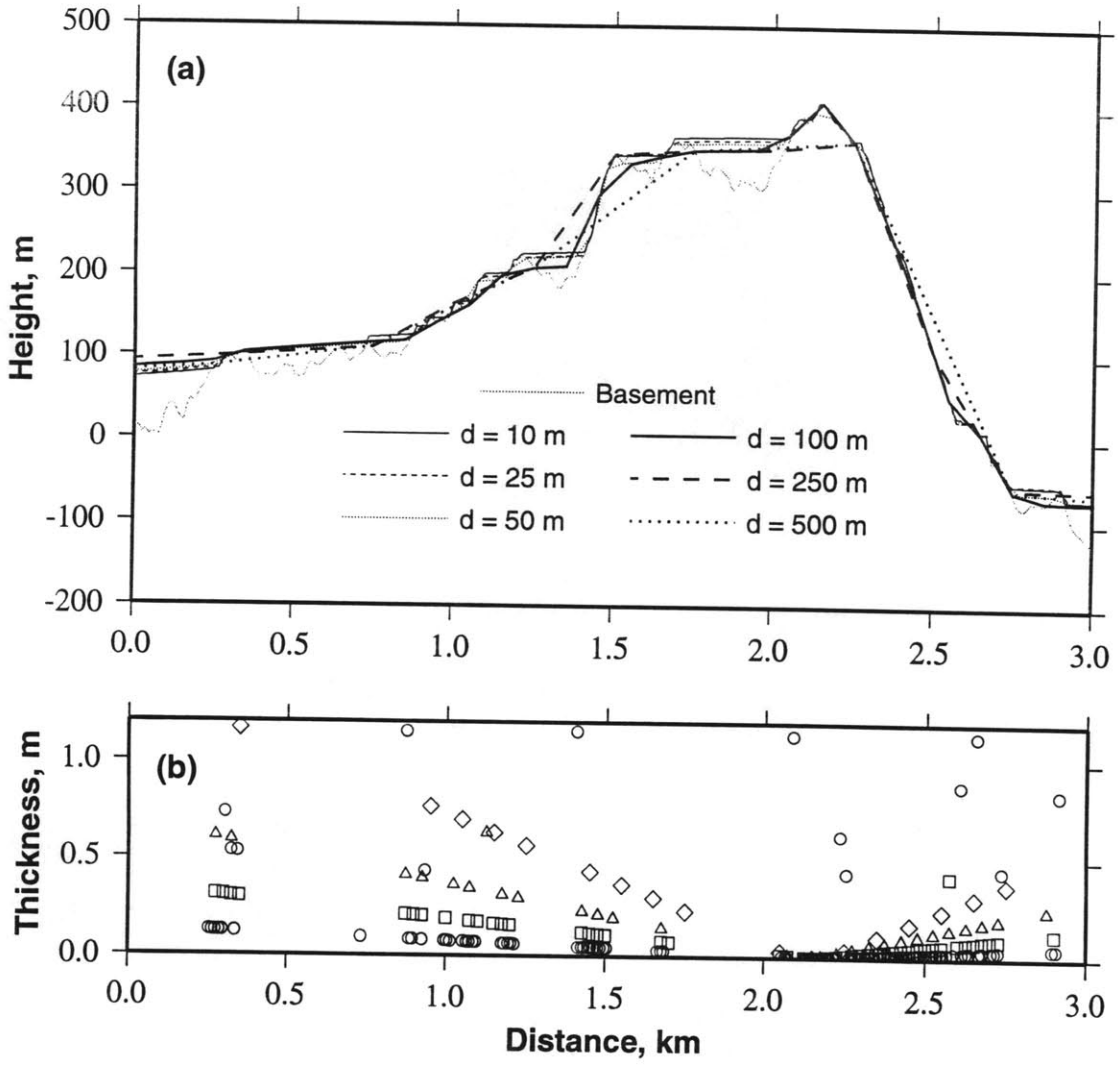

Fig. 2.3: Panel (a) illustrates the insensitivity of sedimented seafloor models to d, and (b) gives sediment thickness for almost-bare areas of (a). The basement was generated using an H of 225 m, k of 0.6 km^{-1}, and D of 1.2. (a) Basement (d = 10 m) and surfaces resulting from 10 m.y. of sedimentation using an F of 4 m/m.y and κ of 0.2 m^2/yr, using d of 10, 25, 50, 100, 250, and 500 m, as labeled. Correspondence between profiles is good for $d \leq 250$ m, but poor for d = 500 m. (b) Sediment thicknesses where $s(\mathbf{x},t) \leq 1.2$ m for the sedimented profiles in (a), for d = 10 (circles), 25 (squares), 50 (triangles), and 100 (diamonds) m. Where hillslopes are steep, all sediment available is passed during each timestep. For locations downhill of the crest at 2.15 km, each cell receives sediment originally deposited at its uphill neighbor. The resulting amount of sediment in each cell is a function of d and r (see text). Since the small ponds in this region are filled, sediment is also transported across their surfaces. The slope thus imposed on ponds is Frd/κ. For r = 0.2, d = 50 m, F = 4 m/m.y., and κ = 0.2 m^2/yr, the imposed slope is 0.0002.

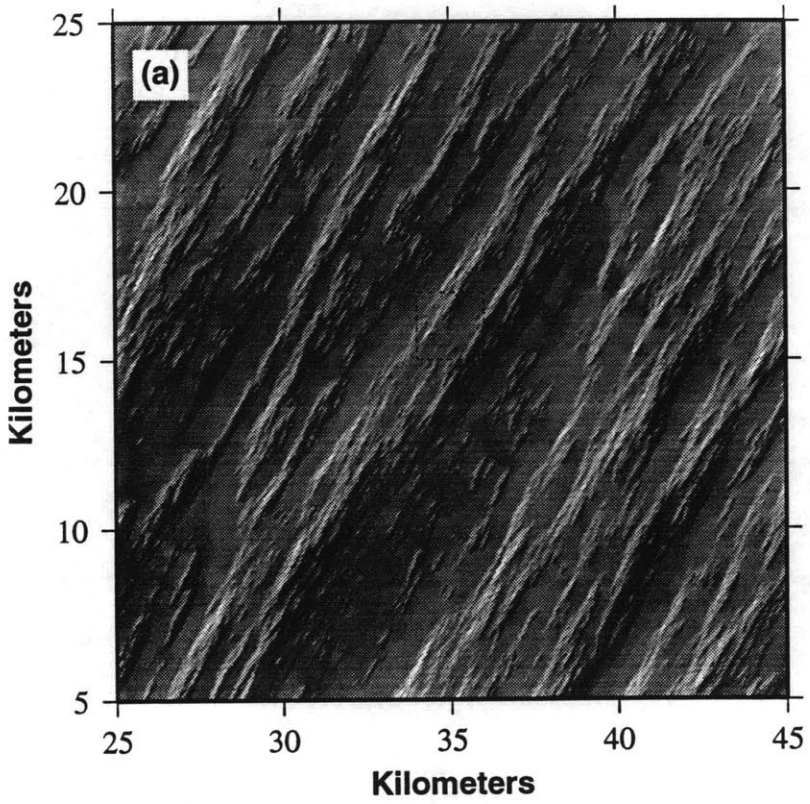

Fig. 2.4: Examination of directions of sediment transport, as approximated by seafloor gradient, on a sedimented Goff-Jordan topography. The basement used was generated using $H = 225$ m, $\zeta_s = 30°$, $k_n = 0.6$ km^{-1}, $a = 5$, and $D = 2.2$. Sedimentation proceeded for 5 m.y. of model time with $F = 4$ m/m.y. and $\kappa = 0.1$ m^2/yr. The total model size was 51.2×51.2 km^2. (a) Map view of a 20×20 km^2 region from the model, illuminated from the northeast. (b) Detail of (a), showing gradients for each cell calculated by taking directional derivatives to the north and east. For many of the cells, these indicate the mean direction of sediment flow from each cell at $t = 5$ m.y., and the line lengths corresponding to the amount which would be transported if sediment thickness was not limited to being greater than or equal to 0 m. However, the movement of sediment from cells on ridge peaks, such as those near the coordinates (35.6 km, 15.4 km), or at saddle points, is not well represented by this methodology. (c) Detail of (b), with contour lines (white). Contour interval is 5 m.

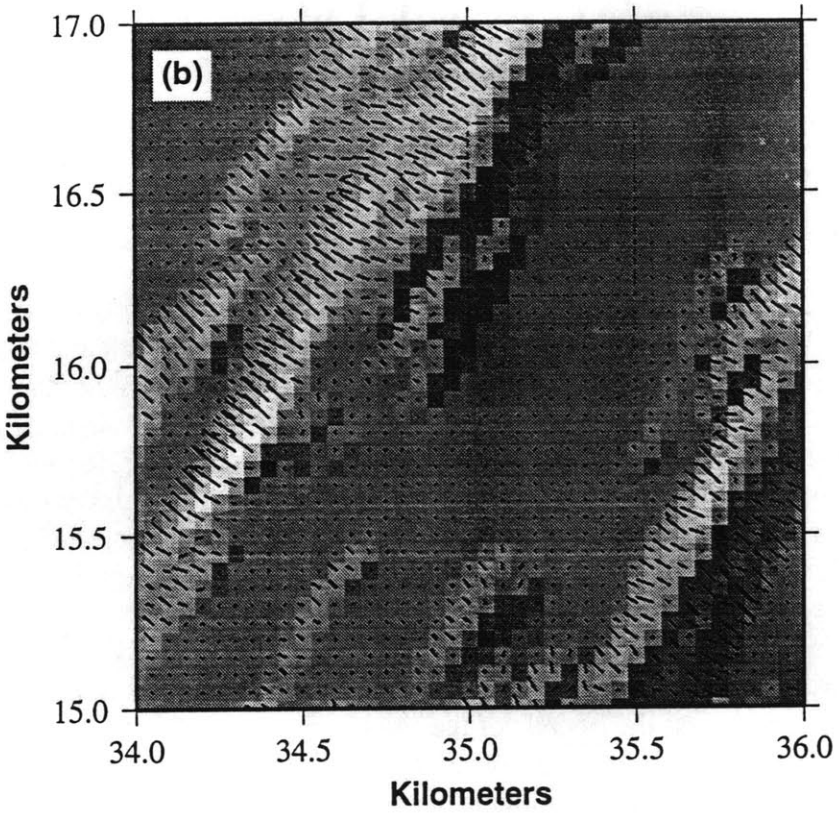
(b)
17.0
16.5
16.0
15.5
15.0
Kilometers
34.0
34.5
35.0
35.5
36.0
Kilometers

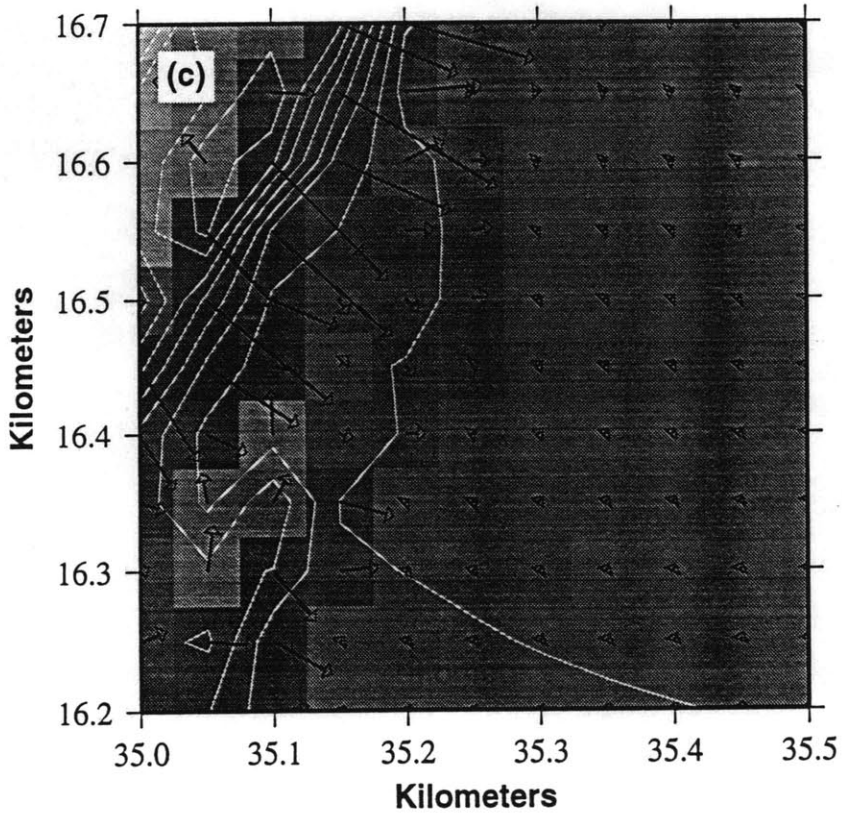
(c)
16.7
16.6
16.5
16.4
16.3
16.2
Kilometers
35.0
35.1
35.2
35.3
35.4
35.5
Kilometers

Fig. 2.5: Comparison between a very high resolution bathymetric profile and topographic models for 26 Ma seafloor located on the western flank of the Mid-Atlantic Ridge. Three-dimensional bathymetric data was collected by the DSL-120, a 120 kHz phase-difference sidescan sonar. A profile of high-resolution bathymetric data was obtained by a Mesotech profiling sonar, a 675-kHz single-beam sonar capable of cm-scale resolution. Model basement topography was constructed by assuming that triangular basins exist beneath flatter regions along the Mesotech profile. This basement was then projected perpendicular to the hill strike direction, sedimented using a variety of κ values, and projected back onto the track of the Mesotech profile. (a) Plan-view relief image of the area, from bathymetric data obtained by the DSL-120. The path of a Mesotech profiler is given by the solid black line, and the white line represents the continuation of the profiler track to the top of the hill. Points A and A' represent the bounds of the section modeled. Contour interval is 50 m. (b) Mesotech data, with DSL-120 continuance, with assumed basement structure between points A and A' (solid lines). Sediment was applied for 26 m.y. of model time at a constant rate of 2.8 m/m.y. (chosen so that resulting sediment volume is equivalent to the assumed volume of the basins) using diffusivity κ values of 0.025 (thick dashed line), 0.05 (dotted line), and 0.1 (thin dashed line) m^2/yr, here shown projected along the path of the Mesotech profiler. These profiles suggest a local apparent diffusivity of ~0.05 m^2/yr, within the range observed by *Mitchell* [1995] for small (150 to 400 m wide) ponds in the FAMOUS region. (c) Detail of (b).

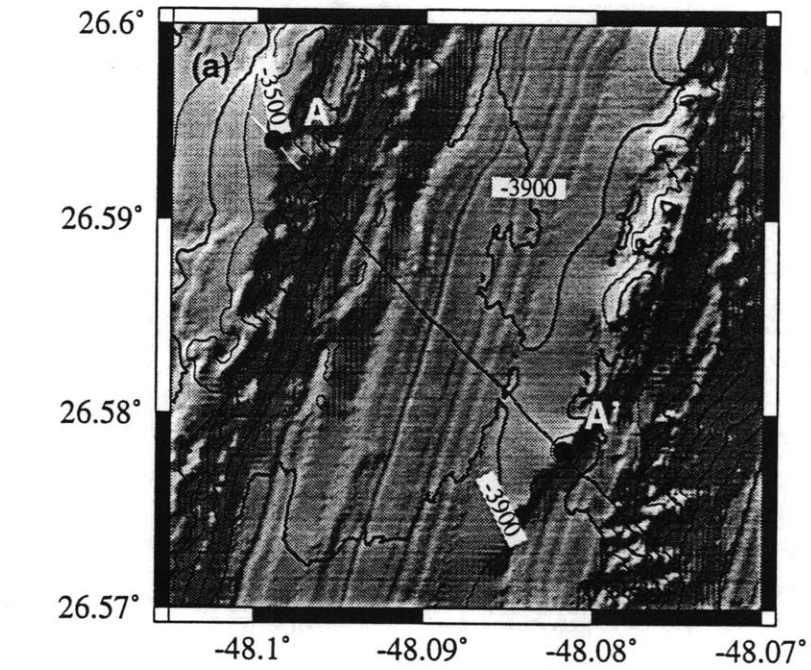
26.6°
26.59°
26.58°
26.57°
-48.1°
-48.09°
-48.08°
-48.07°
(a)
A
A'
-3500
-3900
-3900

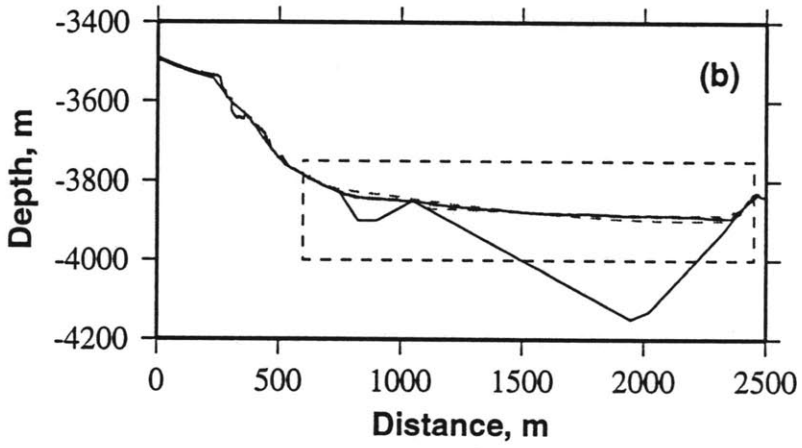
(b)
Depth, m
-3400
-3600
-3800
-4000
-4200
0
500
1000
1500
2000
2500
Distance, m

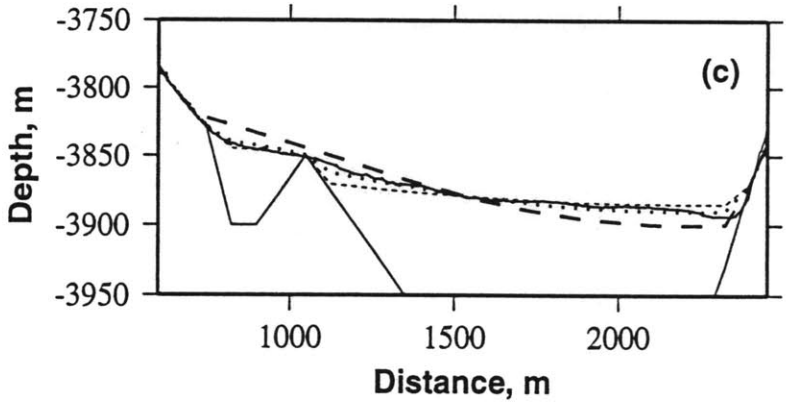
(c)
Depth, m
-3750
-3800
-3850
-3900
-3950
1000
1500
2000
Distance, m

Fig. 2.6: Examples of the application of the pelagic sedimentation model to a simple profile of topography, generated using the methodology of Goff and Jordan [1988]. Goff-Jordan parameters for the profile, as shown in (a) and (b), are H = 200 m, k = 0.6 km^{-1}, and D = 2.2, and as shown in (c) are H = 200 m, k = 0.4 km^{-1}, and D = 2.2. (a) Lines corresponding to basement and the predicted seafloor after the passage of T = 1, 2, 5, 10, and 20 m.y. of model time, corresponding to mean sediment thicknesses L of 4, 8, 20, 40, and 80 m, respectively, given κ = 0.1 m^2/yr and F = 4 m/m.y. (b) Lines corresponding to basement and the predicted seafloor after the passage of T = 1, 2, 5 and 10 m.y. of model time, corresponding to average sediment thicknesses L of 8, 16, 40, and 80 m, respectively, given κ = 0.2 m^2/yr and F = 8 m/m.y. The profiles for T = 1, 5, and 10 m.y. are identical to those for T = 2, 10, and 20 m.y. in (a). (c) If the basement used in (a) and (b) represented wider-spaced hills, a κ of 0.2 m^2/yr and F of 8 m/m.y. will produce sediment deposits which lap far onto hillsides (solid lines). Via (2.23), we calculate that a κ of 0.45 m^2/yr will produce a topography with the same amount of downslope transport as in (b) (dotted lines). Shown are profiles corresponding to T = 1, 2, 5 and 10 m.y. of model time, corresponding to average sediment thicknesses L of 8, 16, 40, and 80 m, respectively.

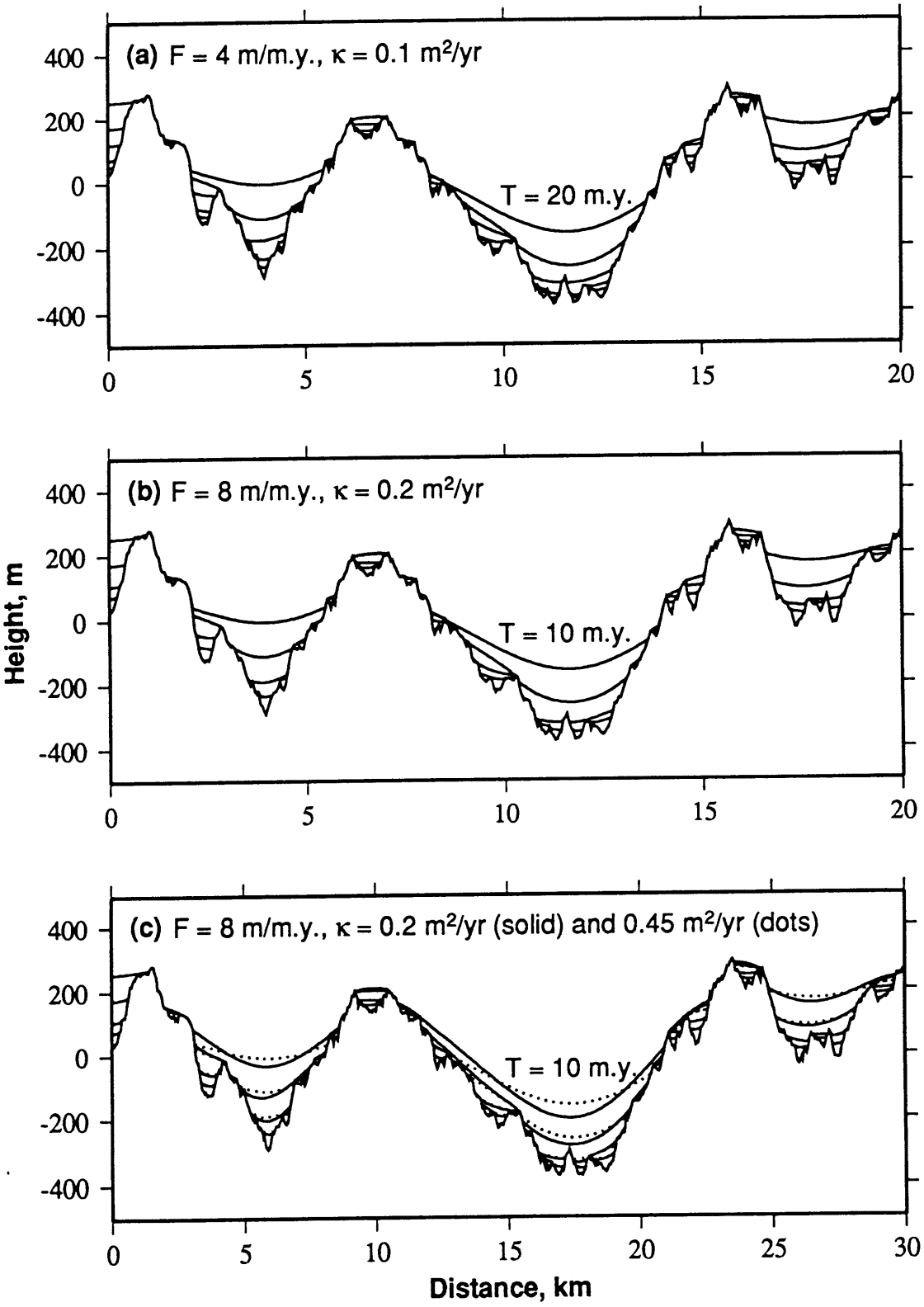
(a) F = 4 m/m.y., κ = 0.1 m²/yr
T = 20 m.y.
(b) F = 8 m/m.y., κ = 0.2 m²/yr
T = 10 m.y.
(c) F = 8 m/m.y., κ = 0.2 m²/yr (solid) and 0.45 m²/yr (dots)
T = 10 m.y.
Height, m
Distance, km
400
200
0
-200
-400
0
5
10
15
20
25
30

Fig. 2.7: Plan-view relief images of sedimented-seafloor models showing the effects of different diffusivities and basement parameters. Basement topographies are realizations of the stochastic model of Goff and Jordan [1988]. Dimensions of the images are 20 km × 20 km, and color changes occur at bathymetric levels of -200, 200, and 600 m. All surfaces correspond to an average sediment thickness of L = 50 m resulting from 12.5 m.y. of pelagic sedimentation at a rain rate of F = 4 m/m.y. Models A-C show the effects of varying the diffusivity (κ = 0.01, 0.1 and 1.0 m^2/m.y., respectively) on an abyssal-hill basement with parameters fixed at H = 225 m, ζ_s = 30°, k_n = 0.6 km^{-1}, a = 5, and D = 2.2. The low κ of Model A produces a morphology where sediments drape hillsides, while the higher values of κ for models B and C produce progressively flatter ponds and greater exposure of local topographic highs. In models D-F, we fix the diffusivity at κ = 0.2 m^2/m.y. and vary the basement parameters. Model D has a larger fractal dimension (D = 2.5), evident by the rough appearance of exposed peaks. Model E has a smaller abyssal-hill aspect ratio (a = 2), providing abundant paths for downslope sediment transport in all directions. The larger aspect ratio of Model F (a = 8) leads to long, linear hills that restrict the redistribution of sediments. Dashed lines correspond to the cross-sections shown in Figure 2.8.

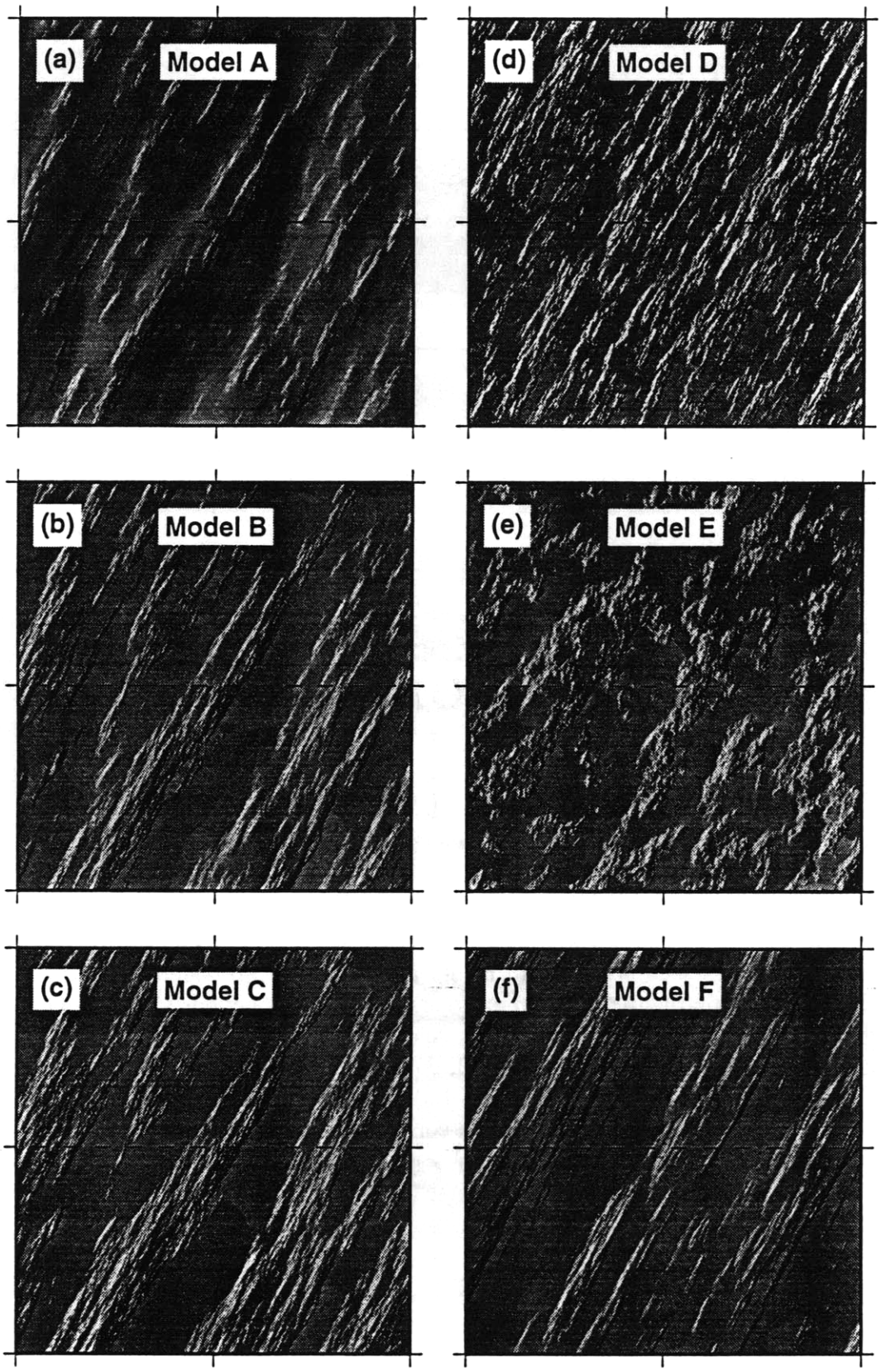
(a)
Model A
(d)
Model D
(b)
Model B
(e)
Model E
(c)
Model C
(f)
Model F

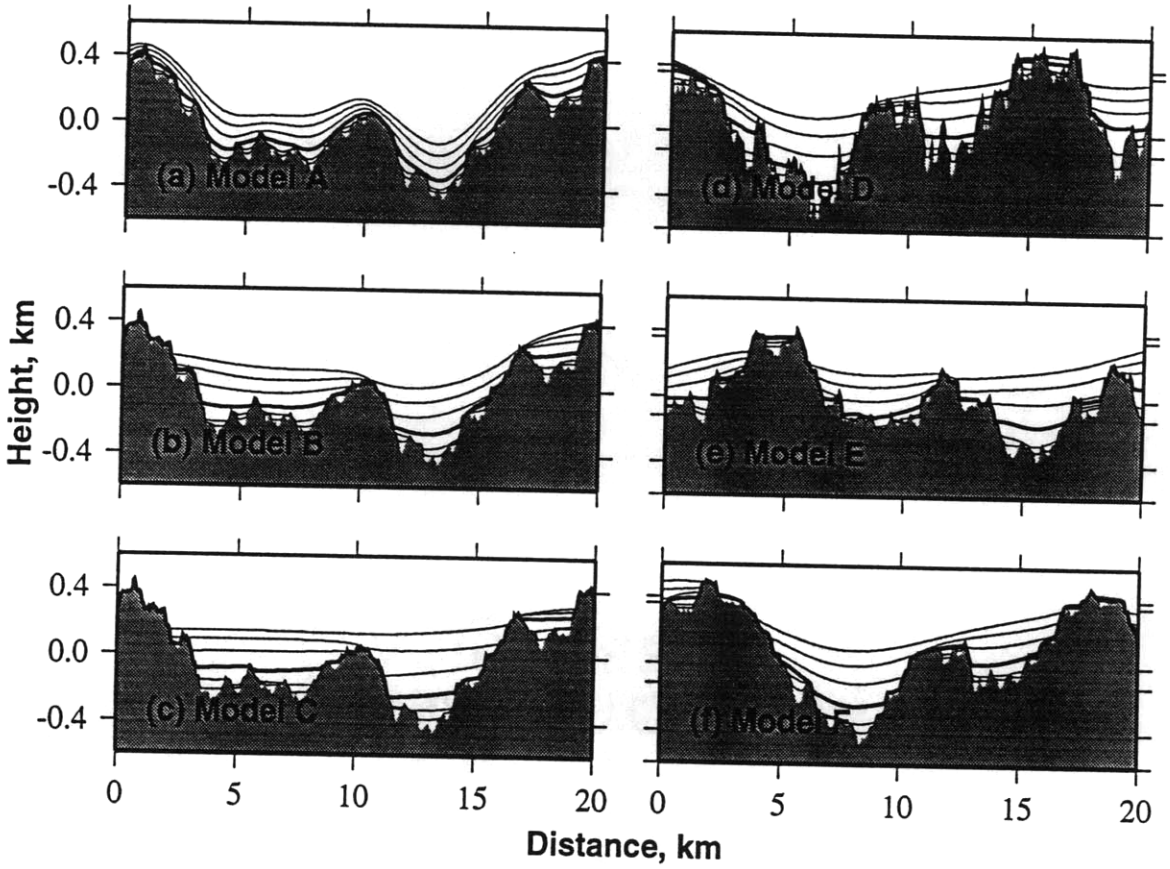

Fig. 2.8: Cross-sections of sedimented-seafloor models taken along the dashed lines in Figure 2.7, plotted with a vertical exaggeration of 6:1. Sections show the Goff-Jordan basement topography (lower thick lines) and the calculated sediment-water interfaces for seafloor ages of T = 2.5, 5, 12.5, 20, 37.5, and 50 m.y., corresponding to average sediment thickness of L = 10, 20, 50, 100, 150, and 200 m. The thicker lines are the 12.5-m.y. (L = 50 m) isochrons, which correspond to the surfaces shown in Figure 2.7. The degree of sediment drape and the flatness of the sediment ponds vary with diffusivity κ (models A-C). The fractal dimension of the underlying basement influences seafloor slope, with higher values resulting in increased downslope transport (Model D). The degree to which sediments are trapped by the fine-scale topography at the hilltops varies with the aspect ratio of the abyssal hills (models E-F). This demonstrates that for realistic basement parameters ($a \approx 5$), a two-dimensional ($a = \infty$) approximation is inadequate.

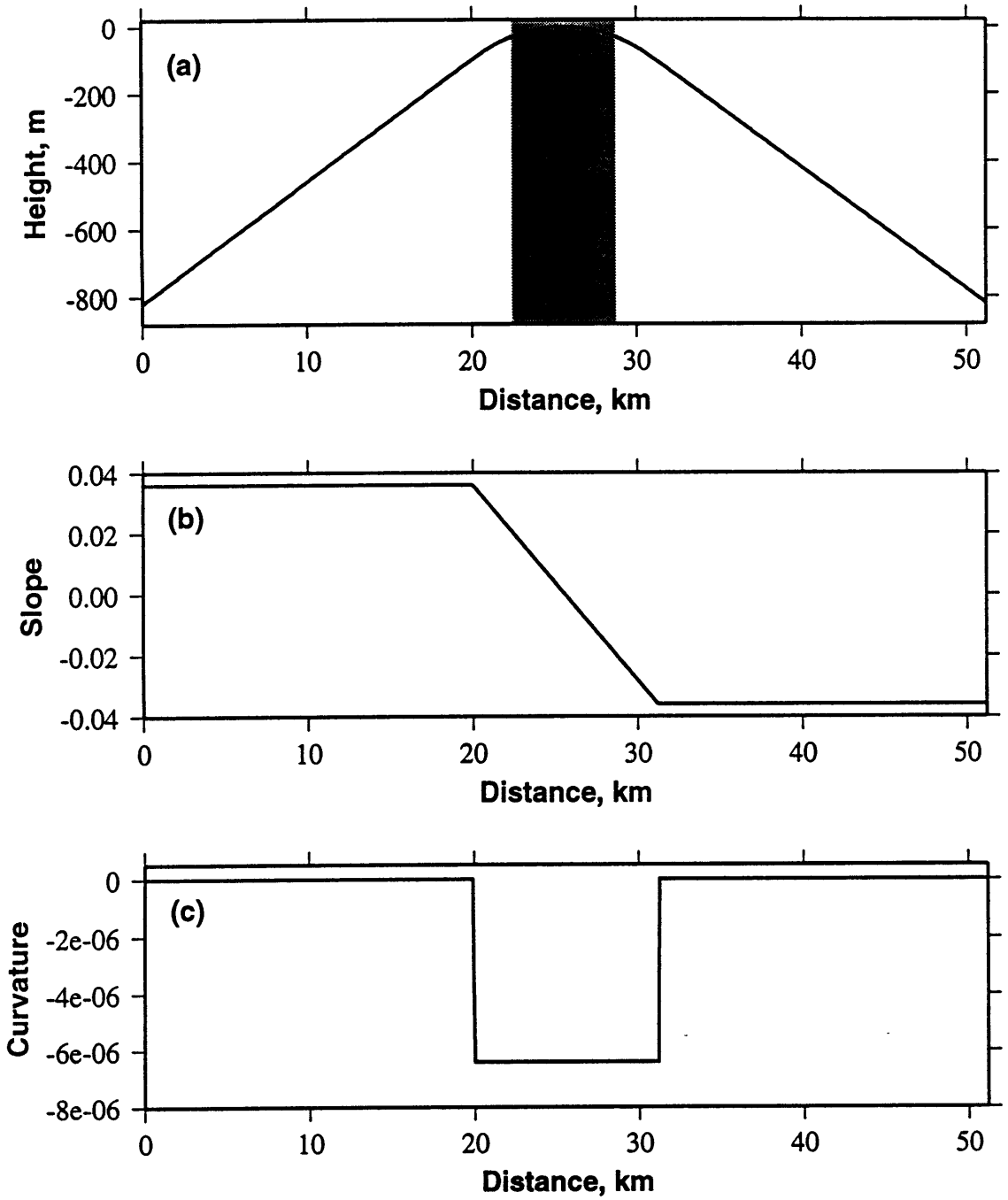

Fig. 2.9: (a) Example of curvature added to rough topographies in the direction of hillstrike. Shaded region indicates the 6.3 km-wide center strip from which average sediment thickness was calculated. (b) Slope of profile in (a). Since the average slope of the rough basement to which (a) was added is 0, (b) gives the average along-strike slopes of the model basements. (c) Slope of (b). This represents $\nabla^2 b_r(\mathbf{x})$ in the along-strike direction.

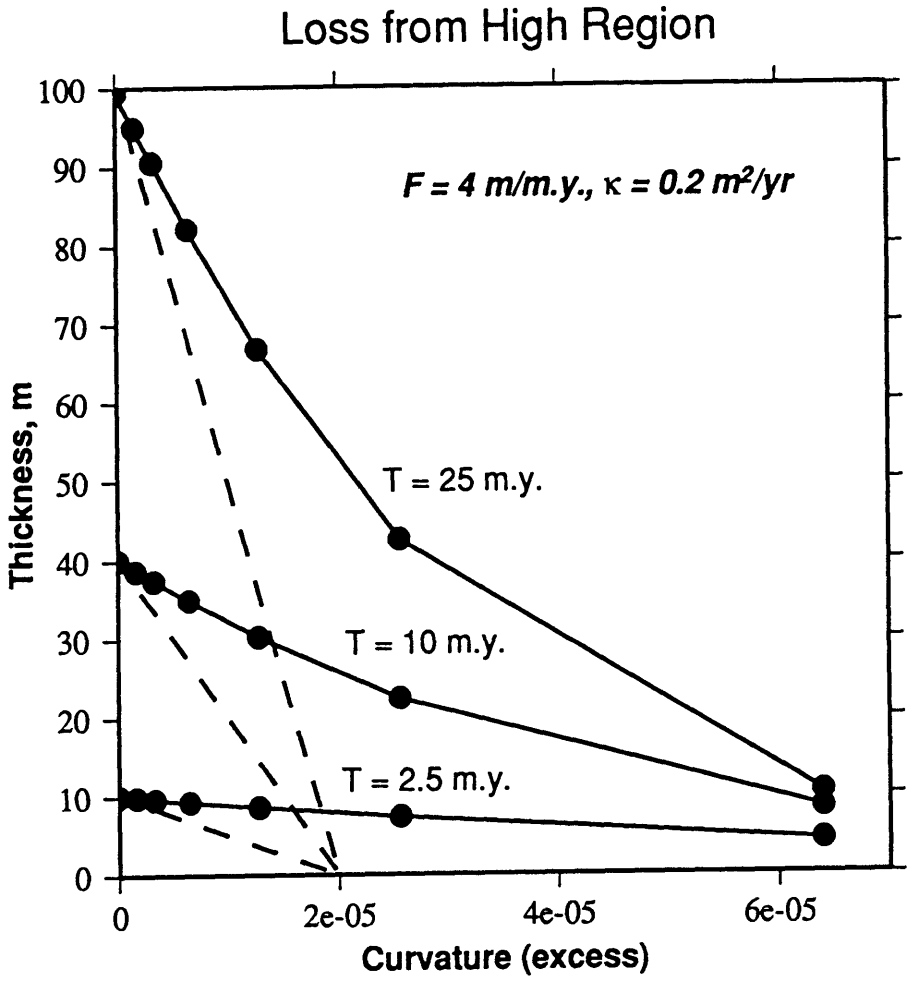

Fig. 2.10: Average sediment thicknesses (solid) for the center 6.3 km of sedimented Goff-Jordan model topographies, described in the text, which have had long-wavelength curvature imposed, after the passage of 2.5, 10, and 25 m.y. of model time. Dashed lines represent the average sediment thickness for the central strip when there is no short-wavelength topographic signal.

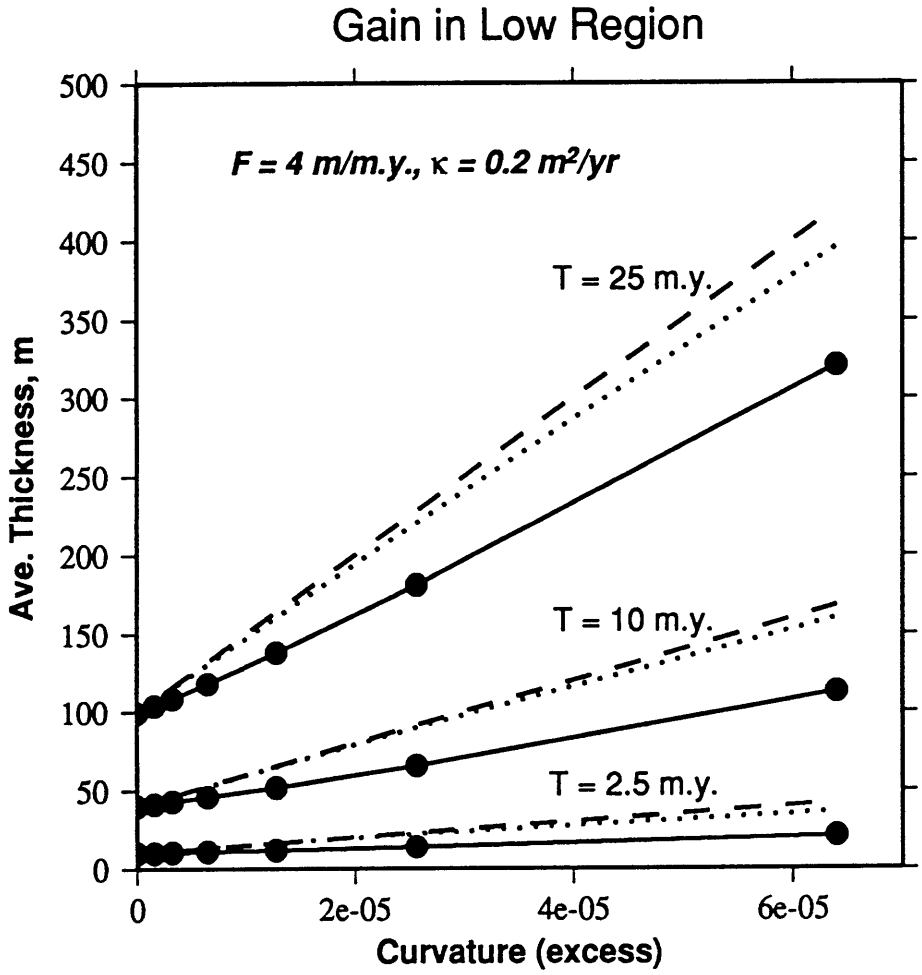

Fig. 2.11: Average sediment thicknesses (solid) for the center 6.3 km of sedimented Goff-Jordan model topographies, described in the text, which have had long-wavelength curvature imposed, after the passage of 2.5, 10, and 25 m.y. of model time. Dashed lines represent the average sediment thickness for the central strip when there is no short-wavelength topographic signal, if the imposed $\nabla^2 b_r(\mathbf{x})$ were maintained. Dotted lines represent the average sediment thickness for the central strip when there is no short-wavelength topographic signal, allowing $\nabla^2 b_r(\mathbf{x})$ to vary.

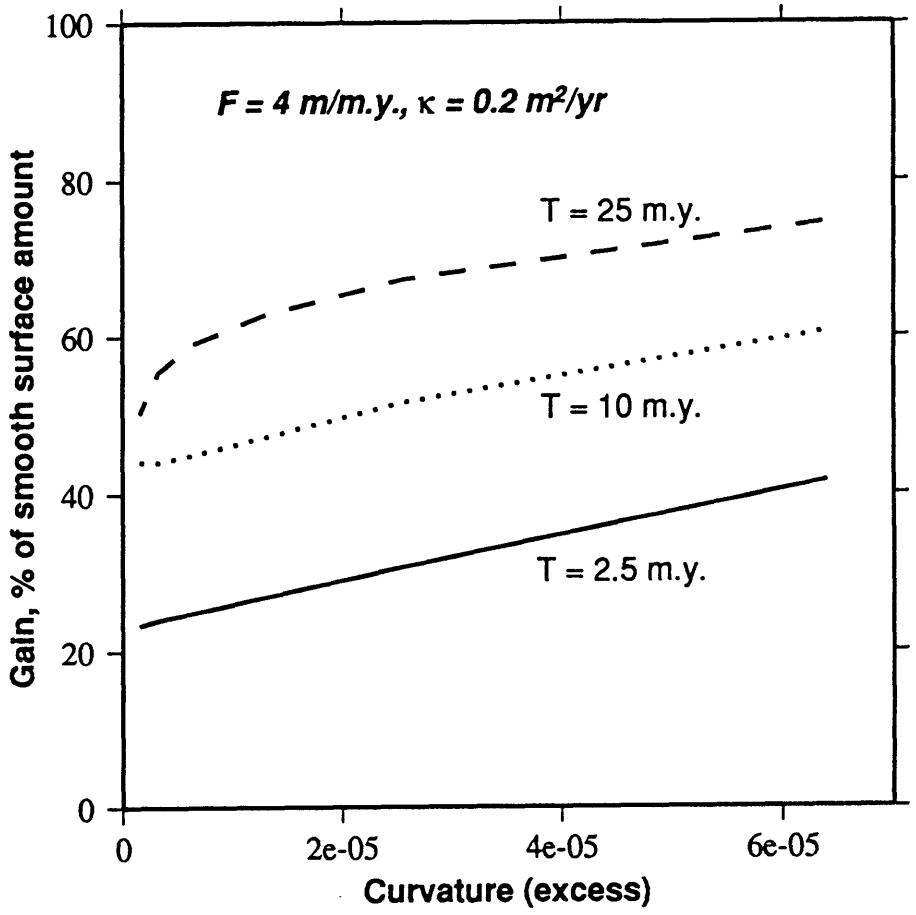

Fig. 2.12: Percentage of the smooth-topography import amount satisfied by sediment transport over tough terrain, as a function of excess curvature and model time.

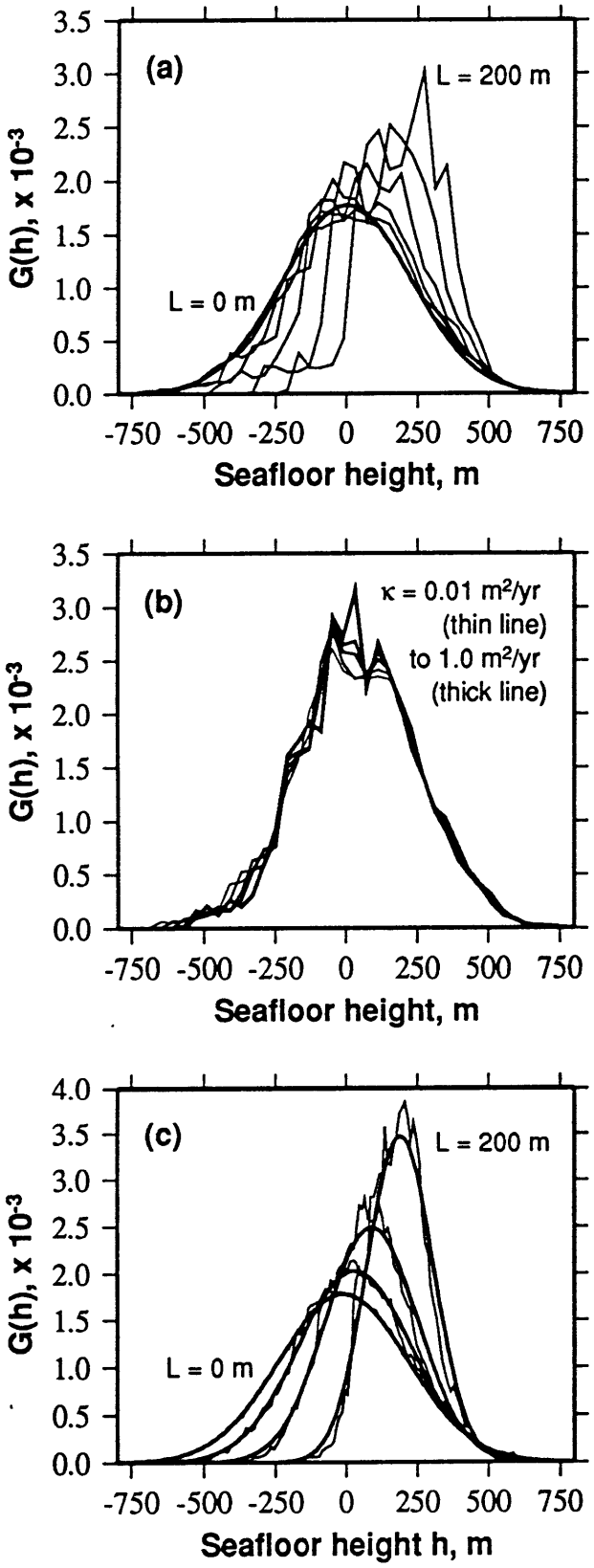

Fig. 2.13: Height histograms for sedimented models. Basement parameters are H = 225 m, k_n = 0.6 km^{-1}, k_s = 0.12 km^{-1}, ζ_s = 30°, and D = 2.2. The binning interval is 40 m for (a) and (b) and 10 m for (c). (a) Thin lines represent height histograms from 2500 km^2 model basement (L = 0 m) and surfaces with L = 20, 40, 80, 140, and 200 m, sedimented with κ = 0.2 m^2/yr and F = 4 m/m.y. Thick line represents the ideal height histogram predicted from the basement parameters. Peaks in histograms are caused by relatively level accumulations of sediment. (b) Height histograms for L = 40 m surface from 2500 km^2 models sedimented with κ = 0.01, 0.05, 0.2, 0.35, and 1.0 m^2/yr (K = 0.2, 1, 4, 7, 20) and F = 4 m/m.y. Line thickness increases with increasing K. Peaks in histograms are caused by relatively level accumulations of sediment, which are larger and flatter in high-K regimes. (c) Thin lines represent height histograms from 10000 km^2 model basement (L = 0 m) and surfaces with L = 0, 40, 100, and 200 m, sedimented with κ = 0.2 m^2/yr and F = 4 m/m.y. Thick lines represent normal distributions with variance equal to the variance of the model topographies, illustrating the deviation of topographic height distributions from Gaussian to non-Gaussian character as sediment thickness increases. Histograms are less rough than in (a) because the effects of level ponds are less significant due to the larger size of the models.

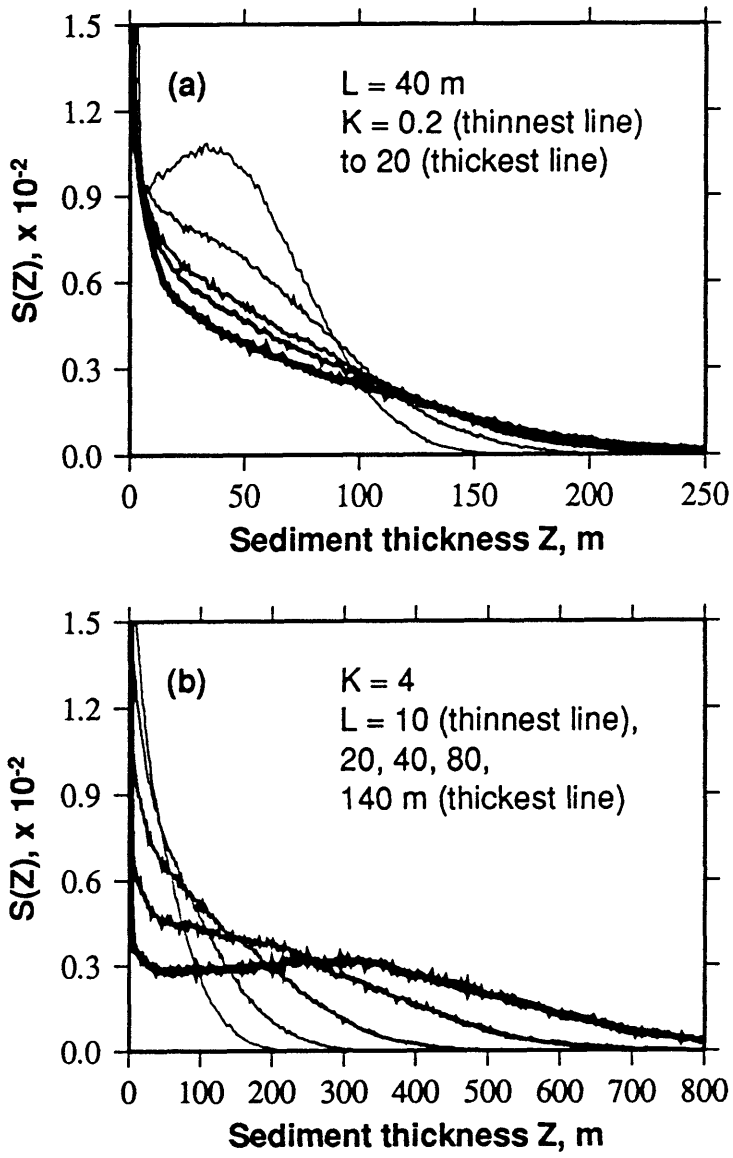

Fig. 2.14: Distribution of sediment thickness $S(Z)$ from sedimented models of seafloor topography. Basement parameters are H = 225 m, k_n = 0.6 km^{-1}, k_s = 0.12 km^{-1}, ζ_s = 30°, and D = 2.2. The binning interval is 1 m. (a) Distributions of sediment thickness for L = 40 m for model seafloor sedimented using F = 4 m/m.y. and κ = 0.0125 (thin line), 0.05, 0.2, 0.35, and 1.0 m^2/yr (thick line), corresponding to dimensionless diffusivities K of 0.2, 1, 4, 7, and 20. (b) Distributions of sediment thickness for F = 4 m/m.y., κ = 0.2 m^2/yr, and L = 10, 20 , 40, 80, and 140 m. In low-K regimes, sediments do not travel far from their original point of contact with the seafloor, and distributions display peaks at L. For $K \geq 1$, peaks at 0.5 m are off-scale. The proportion of seafloor represented in these peaks is given in Fig. 2.15(a).

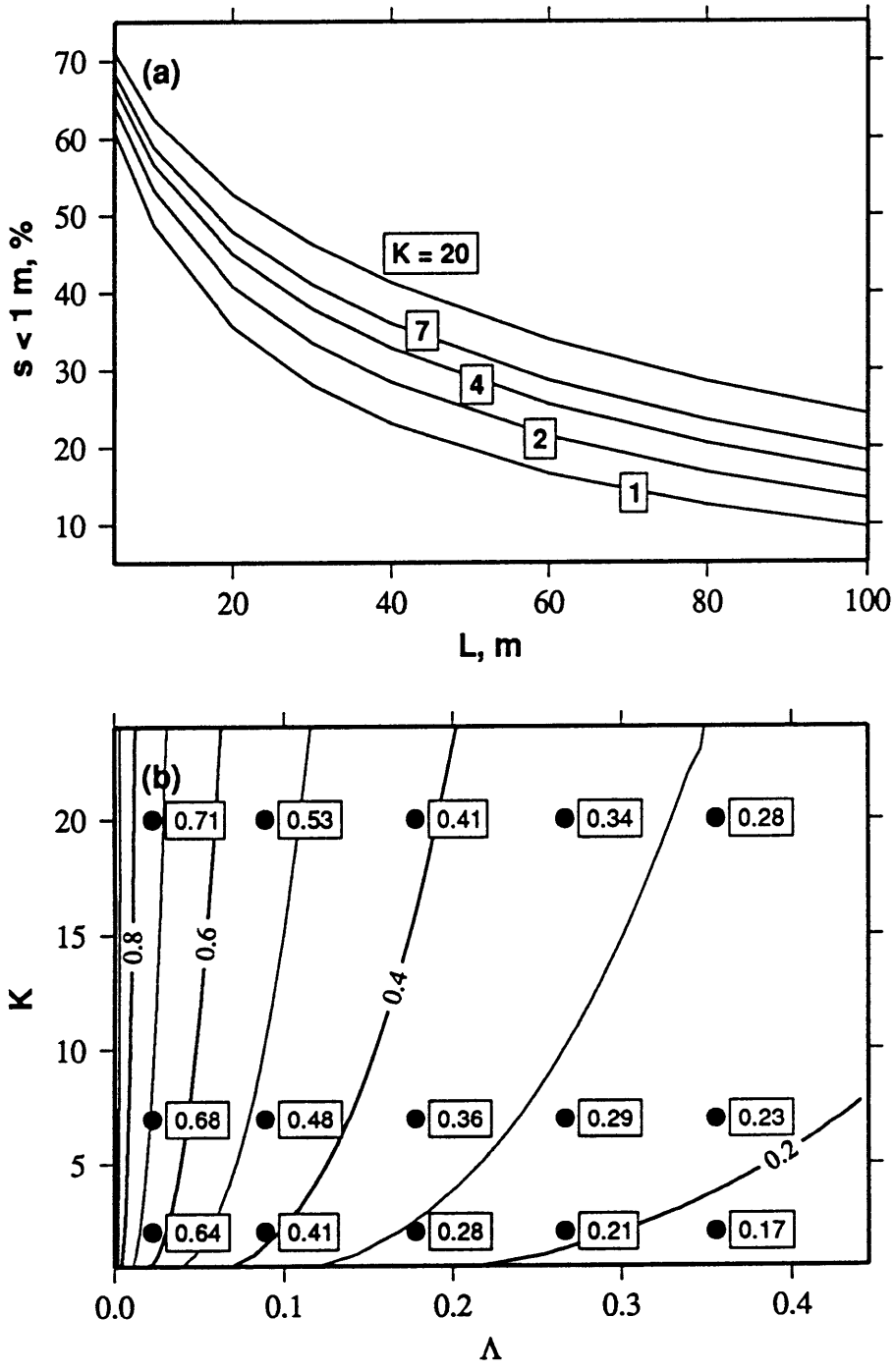

Fig. 2.15: (a) Percent bare ($s < 1$ m) seafloor, corresponding to the true heights of the off-scale peaks such as in Fig. 2.14. (b) For $K \geq 1$ and $\Lambda \leq 0.444$, the percent bare seafloor (boxed numbers) is well-described by (2.27) (contour lines).

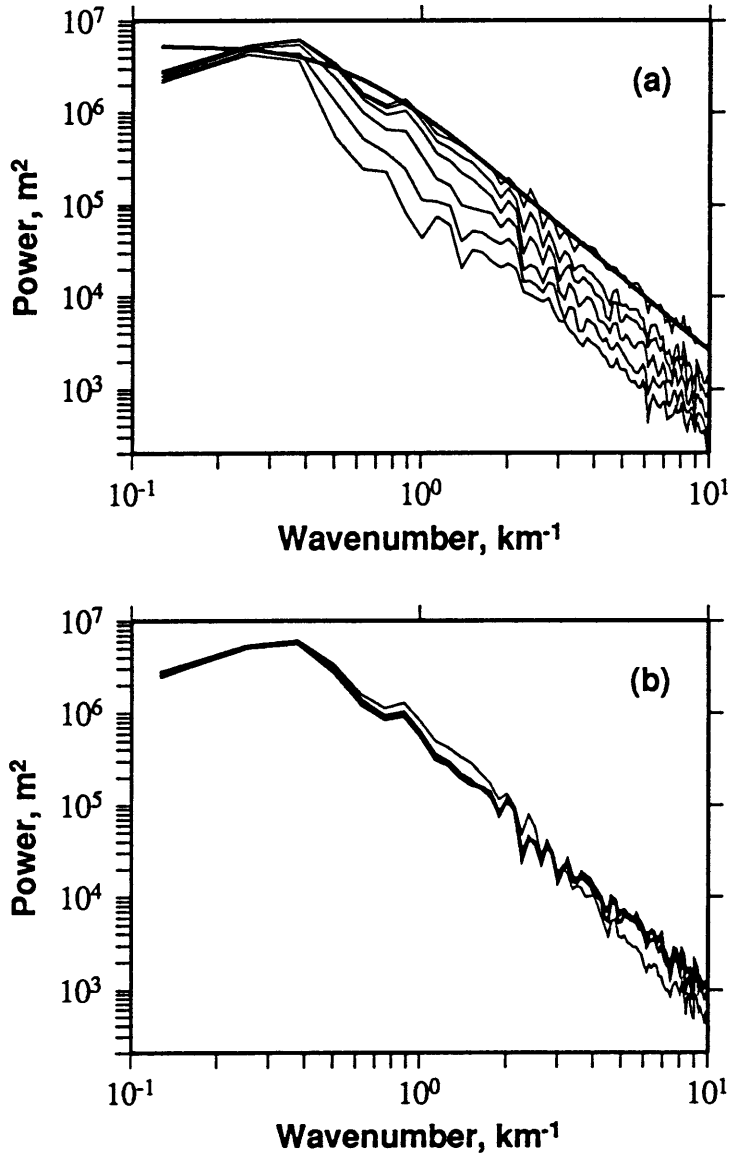

Fig. 2.16: Power spectra computed from sedimented models of seafloor topography. Basement parameters are H = 225 m, k_n = 0.6 km^{-1}, k_s = 0.12 km^{-1}, ζ_s = 30°, and D = 2.2. (a) Power spectra for L = 0, 20, 40, 80, 140, and 200 m for model seafloor sedimented using κ = 0.2 m^2/yr and F = 4 m/m.y. (thin lines). Power spectra were calculated from tracklines trending 30° from hill flow direction. Thick line corresponds to the predicted power spectrum of the basement topography, given the basement parameters. (b) Power spectra for L = 40 m for model seafloor sedimented using κ = 0.01 (thin line), 0.2, and 1.0 (thick line) m^2/yr and F = 4 m/m.y. Basement parameters are H = 225 m, k_n = 0.6 km^{-1}, k_s = 0.12 km^{-1} and D = 2.2. Power spectra were calculated from tracklines trending 30° from hill flow direction.

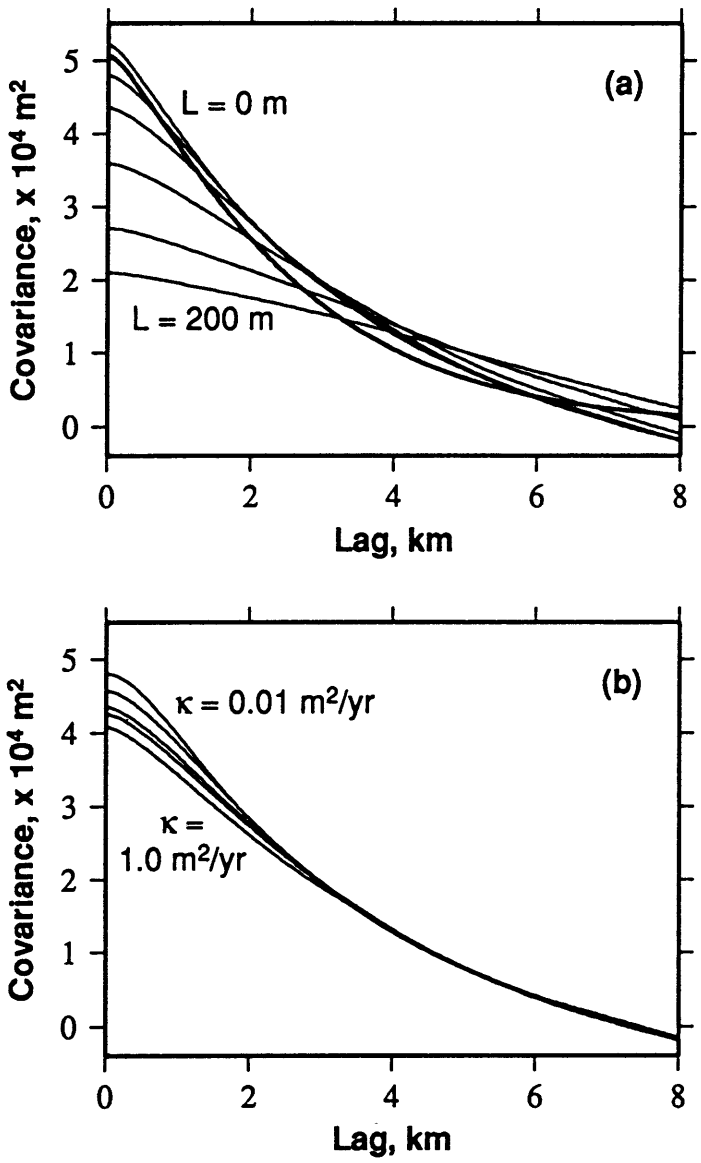

Fig. 2.17: Autocovariance functions computed from sedimented models of seafloor topography. Basement parameters are H = 225 m, k_n = 0.6 km^{-1}, k_s = 0.12 km^{-1}, D = 2.2, and ζ_s = 30°. (a) Covariance functions for L = 0, 20, 40, 80, 140, and 200 m for model seafloor sedimented using κ = 0.2 m^2/yr and F = 4 m/m.y. (thin lines). Autocovariance was calculated from tracklines trending 30° from hill flow direction. Thick line corresponds to the predicted covariance of the basement topography, given the basement parameters. (b) Autocovariance functions for L = 40 m for model seafloor sedimented using κ = 0.01, 0.05, 0.2, 0.35, and 1.0 m^2/yr (K = 0.2, 1, 4, 7, 20) and F = 4 m/m.y. Covariance was calculated from tracklines trending 30° from hill flow direction.

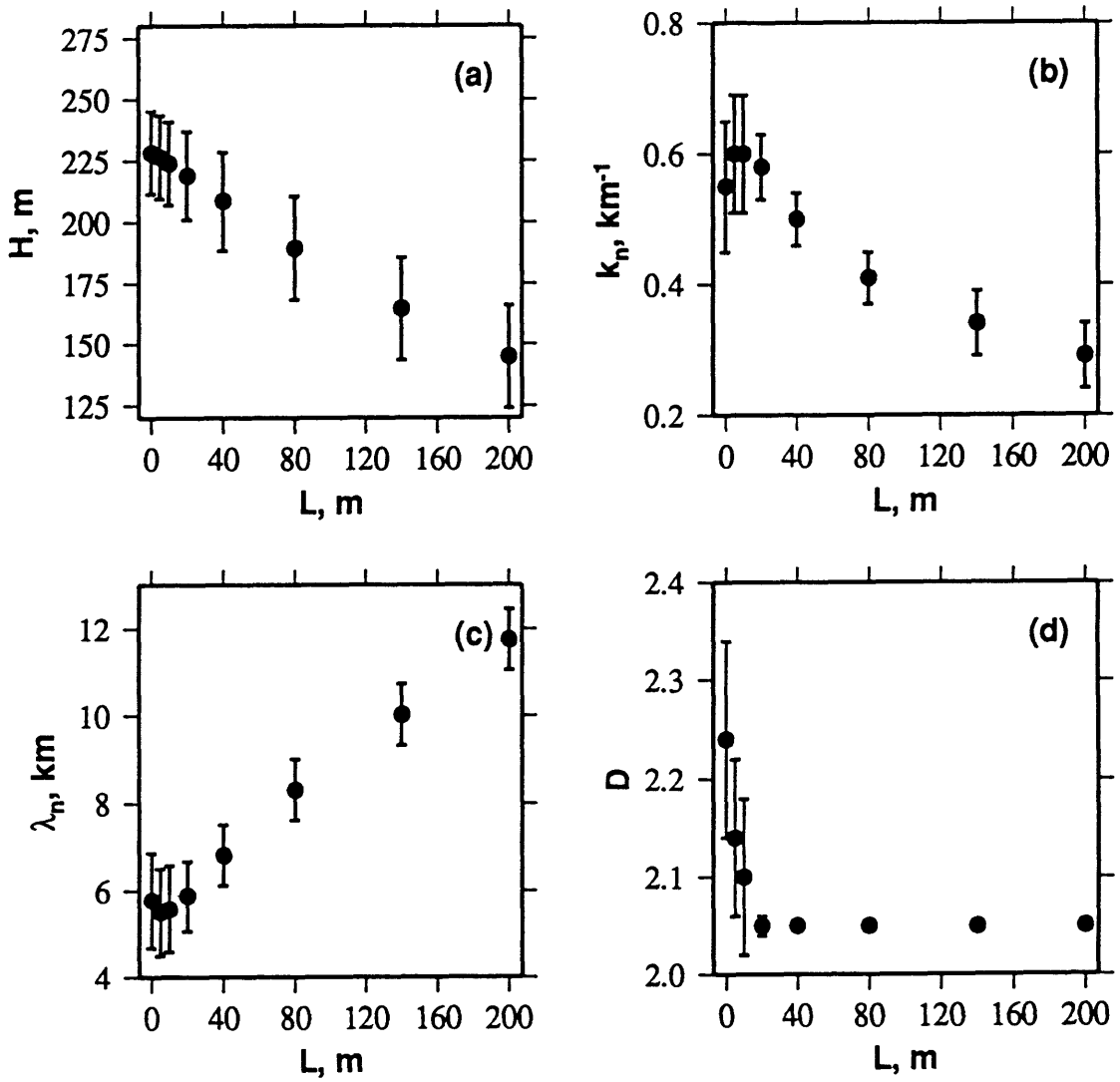

Fig. 2.18: Variations in *Goff-Jordan* parameters obtained from inversions of model sedimented seafloor bathymetries generated using $\kappa = 0.2$ m^2/yr and $F = 4$ m/m.y. upon a basement with $H = 225$ m, $k_n = 0.6$ km^{-1}, $k_s = 0.12$ km^{-1}, $D = 2.2$, and $\zeta_s = 30°$. Decreases in H and D with L are easily quantifiable; changes to k_n (and, hence, λ_n) are more complex, but indicate that pelagic sedimentation increases the characteristic spacing of abyssal topography. D was set to 2.05 for all inversions for $L > 20$ m.

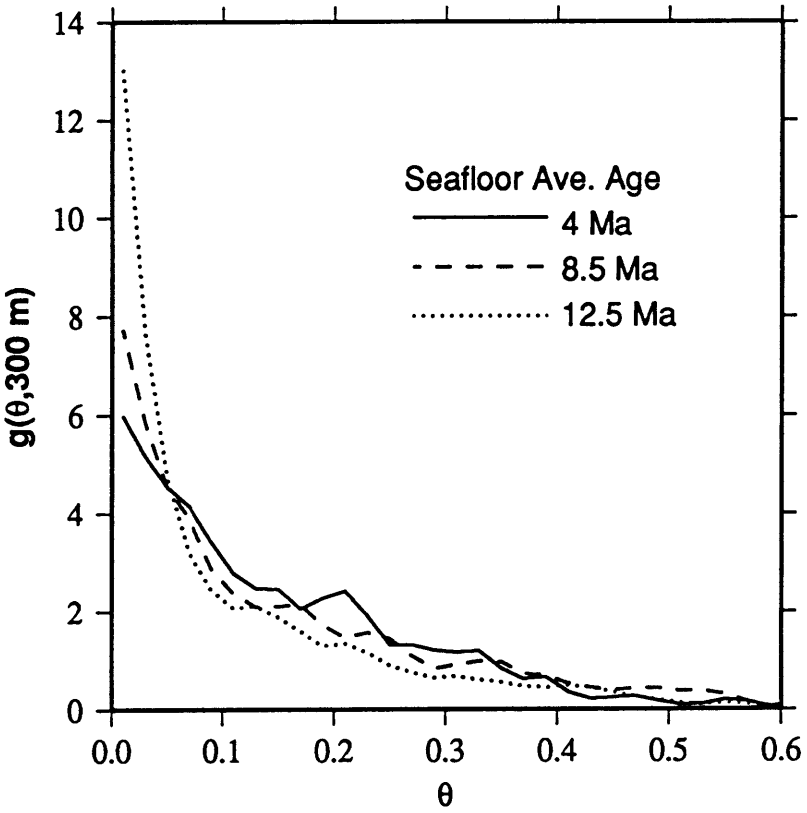

Fig. 2.19: Slope distribution functions, calculated from centerbeam bathymetric data from young seafloor on the western flank of the Mid-Atlantic Ridge at ~25.75° N. An average of 300 km of along-track data was used to compute each slope histogram. Note the increase in amplitude of the functions at $\theta = 0$ with increasing seafloor age.

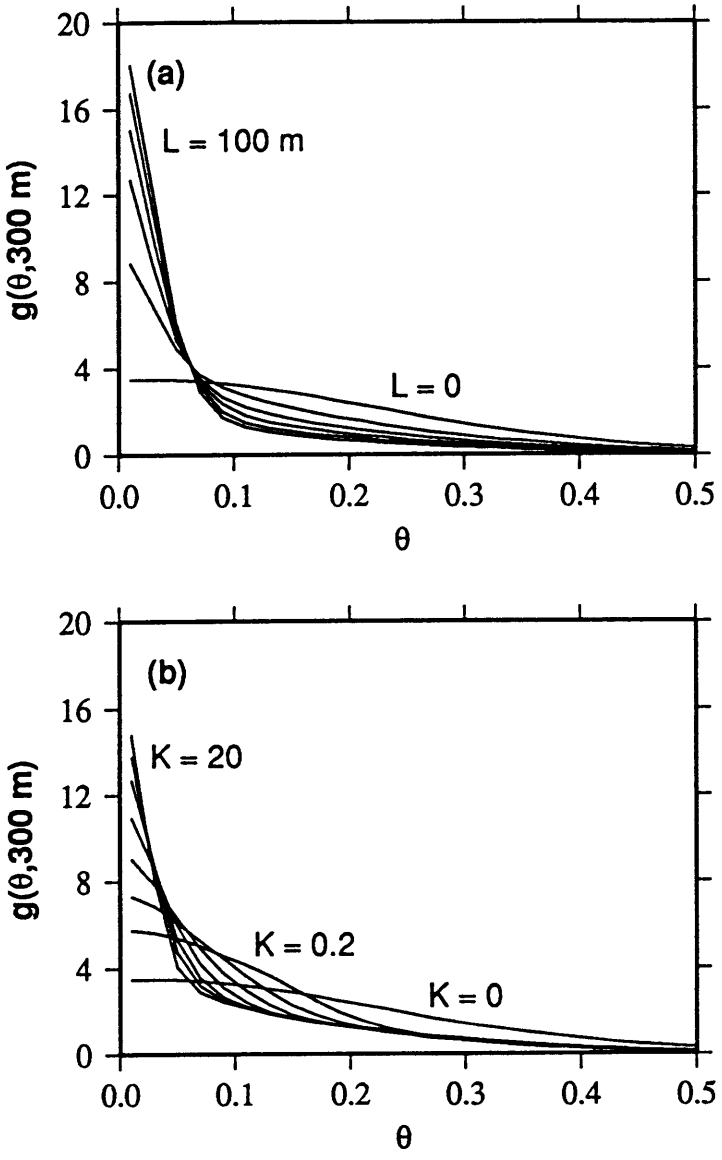

Fig. 2.20: Slope distribution functions calculated from profiles through model basement and sedimented topographies. Basement parameters are H = 225 m, k_n = 0.6 km^{-1}, k_s = 0.12 km^{-1}, D = 2.2, and ζ = 30°. Sediment was added at a rate F of 4 m/m.y. (a) Curves calculated from models with κ = 0.2 m^2/yr (K = 4), for L = 0, 20, 40, 60, 80, and 100 m. The width of the curve for $\theta < \theta_0$ is constant, indicative of the value of κ used, while g(0,300 m) is governed by L. (b) Curves calculated from model with L = 40 m and κ = 0.01, 0.05, 0.2, 0.35, and 1.0 m^2/yr (K = 0.2, 1, 4, 7, 20). The zero-diffusion case in (b) corresponds to the sediment-free case in (a), since sediments follow the topography exactly. For $K > 0$, the width of the curve at low θ is indicative of K. The shape of the curves at higher θ is caused by the distribution of slope of basement outcrops, and so is indicative of basement parameters.

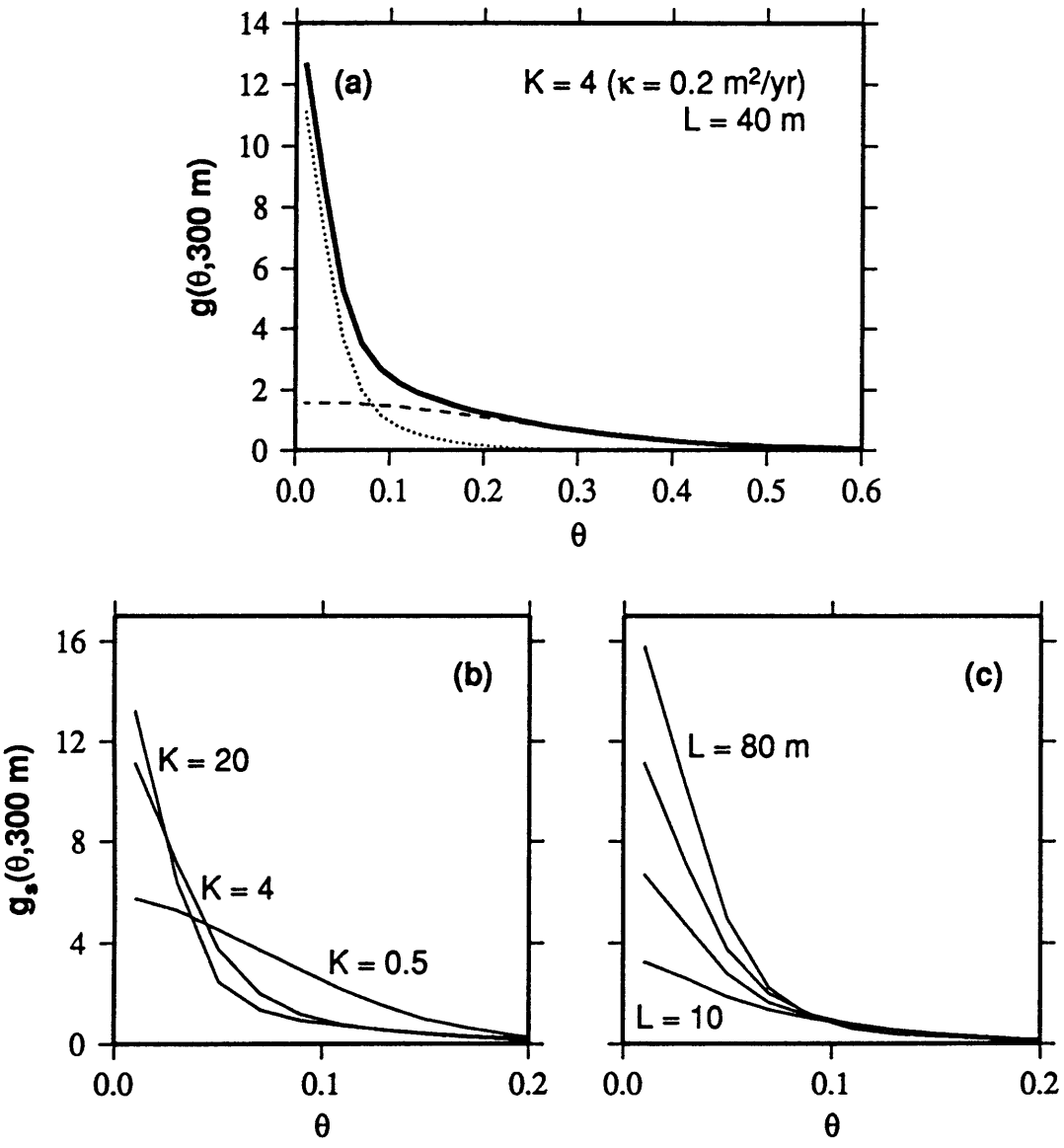

Fig. 2.21: (a) A slope distribution function $g(\theta,u)$ (solid line) may be separated into a basement signal $g_b(\theta,u)$ (dashed line) and a residual sediment signal $g_s(\theta,u)$ (dotted line). (b) The residual sediment signal $g_s(\theta,u)$ varies with diffusivity, with higher values leading to more downslope transport hand greater magnitude at $\theta = 0$, for constant L. (c) The residual sediment signal $g_s(\theta,u)$ varies with average sediment thickness, with higher values leading to more ponded regions and greater magnitude at $\theta = 0$, for constant κ.

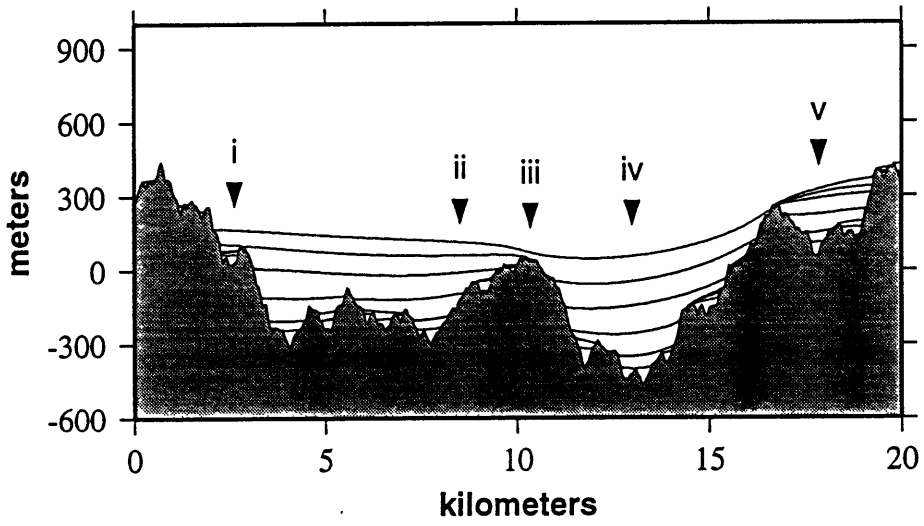

Fig. 2.22: Cross-section through a three-dimensional sedimented topography generated using the basements underlying Model A-C in Fig. 7 and 8. Sediment was applied at a rain rate of 4 m/m.y. for 50 m.y. of model time, using a diffusivity of $\kappa = 0.2$ m^2/yr. Lines correspond to isochrons of 2.5, 5, 12.5, 25, 37.5, and 50 m.y. (L = 10, 20, 50, 100, 150, 200 m). Roman numerals correspond to positions monitored to local determine sediment accumulation rate (Figs. 2.23 - 2.27).

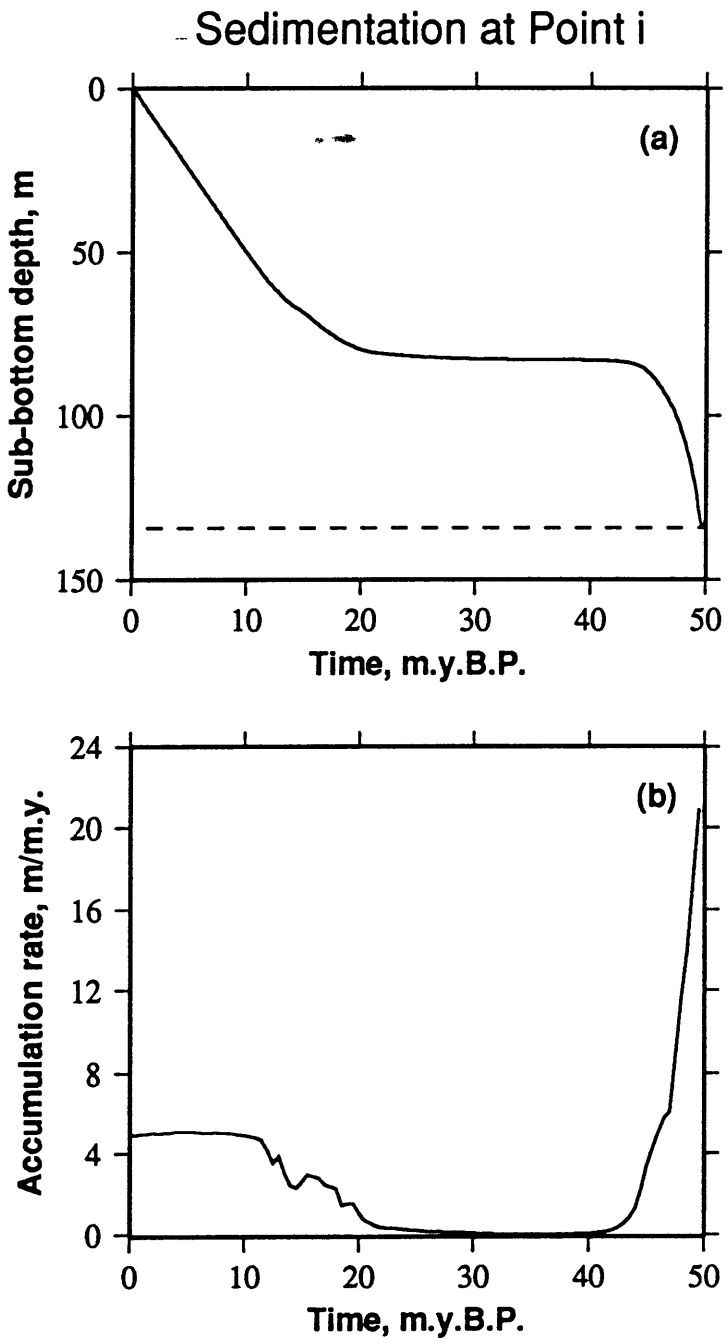

Fig. 2.23: (a) Subbottom depth vs. time of deposition for sediments at model point i. Dashed line corresponds to the thickness of sediments at point i at the end of 50 m.y. of model time. (b) Sediment accumulation rate vs. time of deposition for model point i.

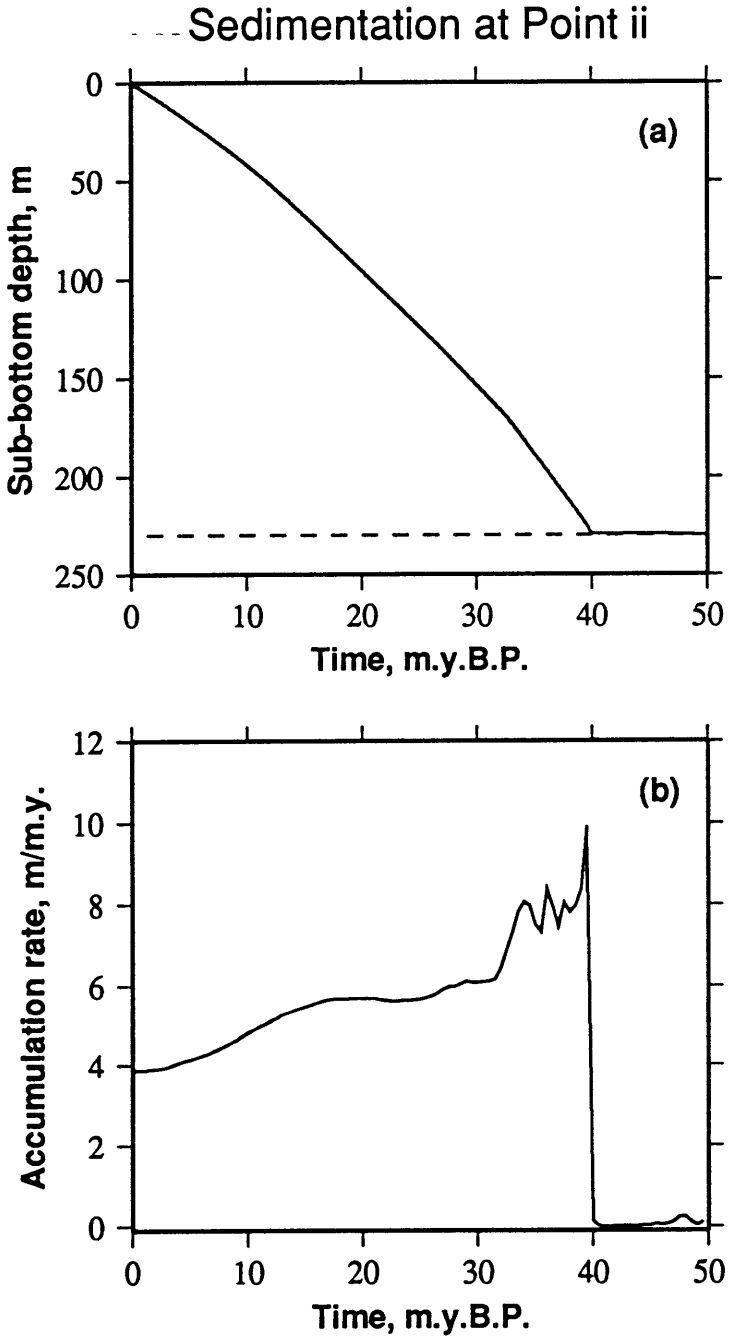

Fig. 2.24: (a) Subbottom depth vs. time of deposition for sediments at model point ii. Dashed line corresponds to the thickness of sediments at point ii at the end of 50 m.y. of model time. (b) Sediment accumulation rate vs. time of deposition for model point ii.

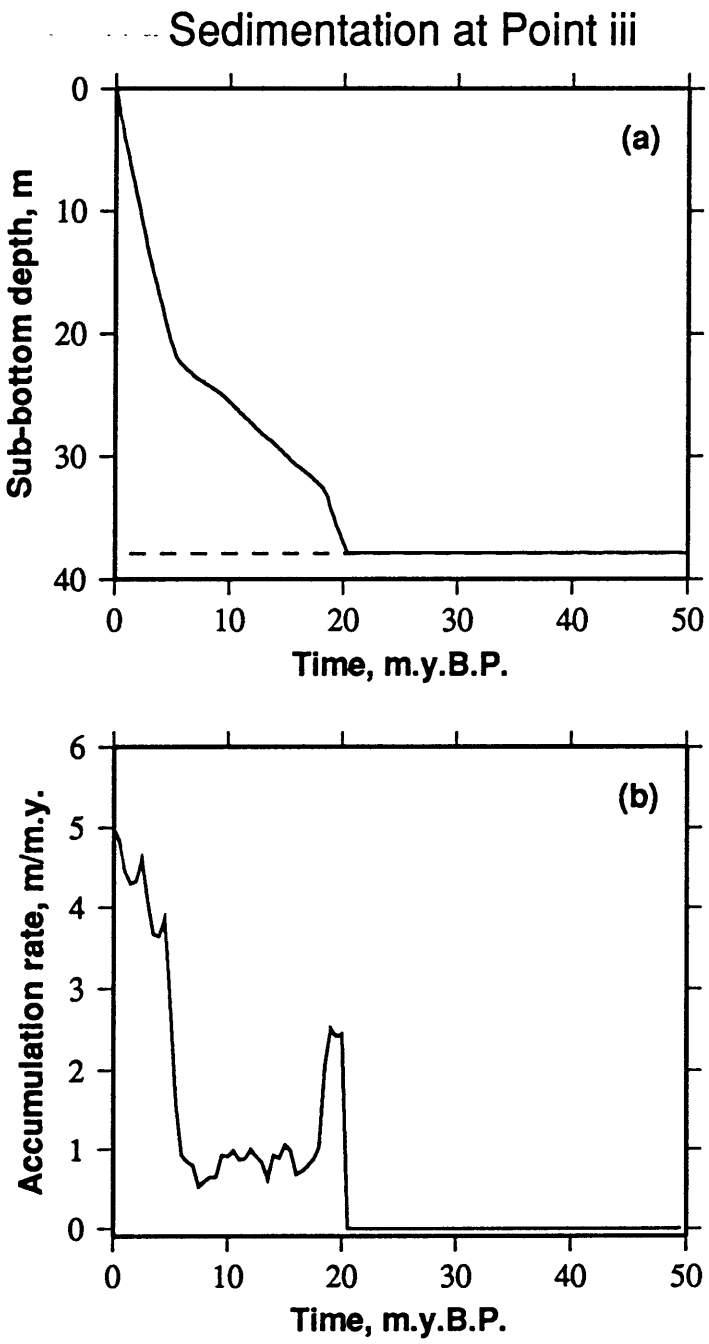

Fig. 2.25: (a) Subbottom depth vs. time of deposition for sediments at model point iii. Dashed line corresponds to the thickness of sediments at point iii at the end of 50 m.y. of model time. (b) Sediment accumulation rate vs. time of deposition for model point iii.

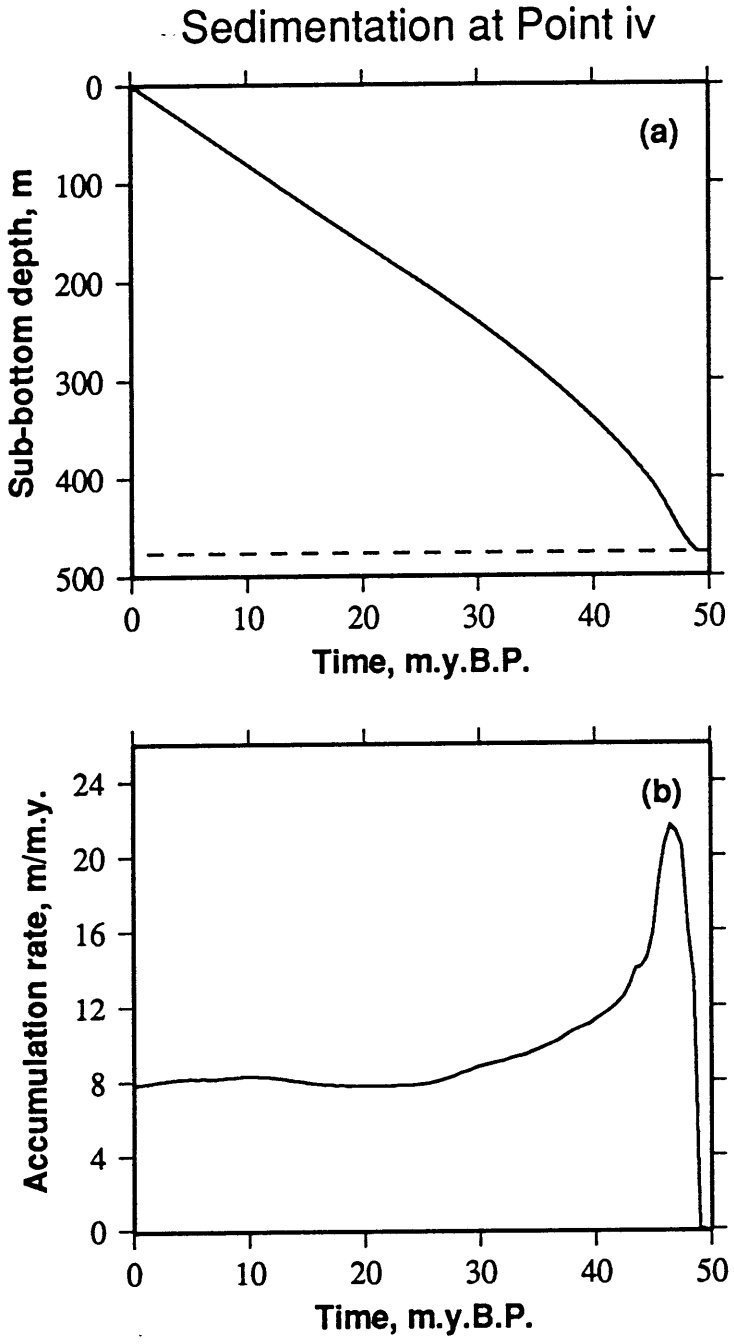

Fig. 2.26: (a) Subbottom depth vs. time of deposition for sediments at model point iv. Dashed line corresponds to the thickness of sediments at point iv at the end of 50 m.y. of model time. (b) Sediment accumulation rate vs. time of deposition for model point iv.

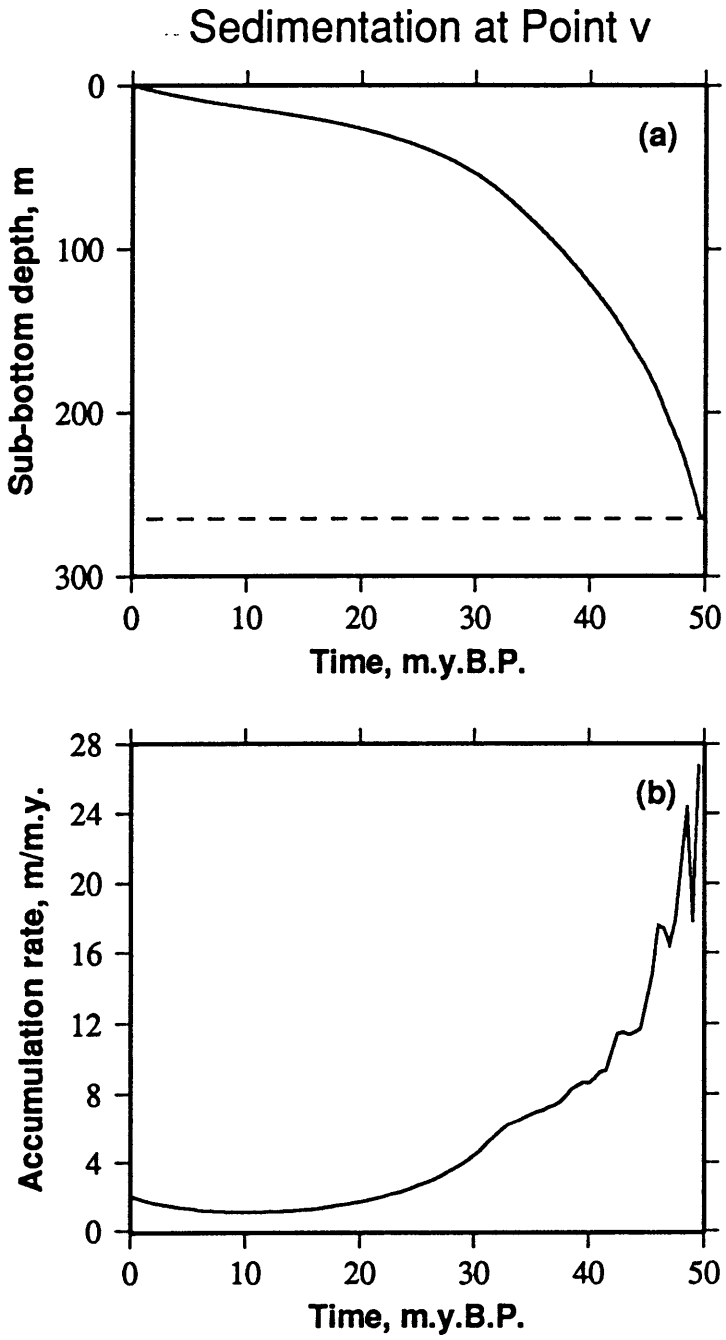

Fig. 2.27: (a) Subbottom depth vs. time of deposition for sediments at model point v. Dashed line corresponds to the thickness of sediments at point v at the end of 50 m.y. of model time. (b) Sediment accumulation rate vs. time of deposition for model point v.

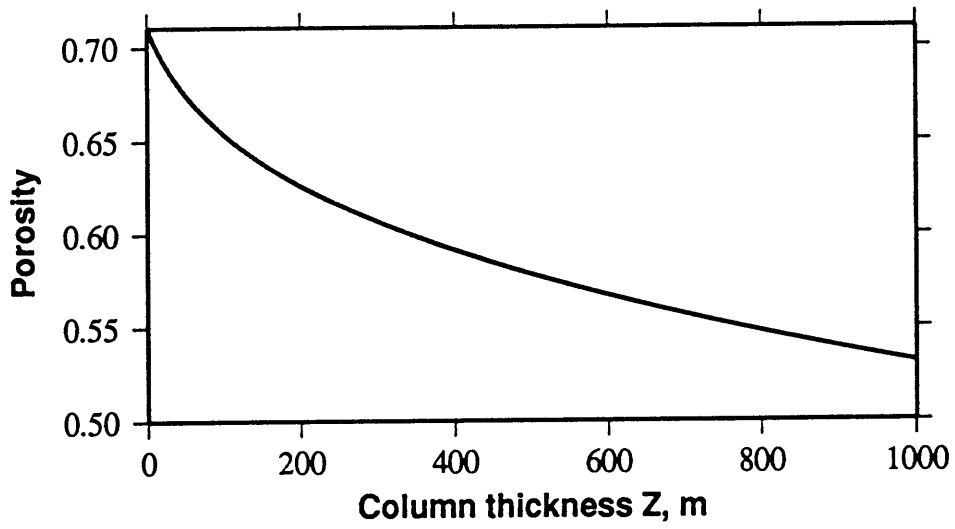

Fig. 2.28: Porosity for a column of sediments, based on equation (13) of *Audet* [1995], computed assuming using an initial $\phi(0) = 0.71$, $\rho_r = 2750$ kg/m^3, a water density of 1050 kg/m^3, and compaction parameters *Audet* [1995] derived for oozes at ODP Site 806.

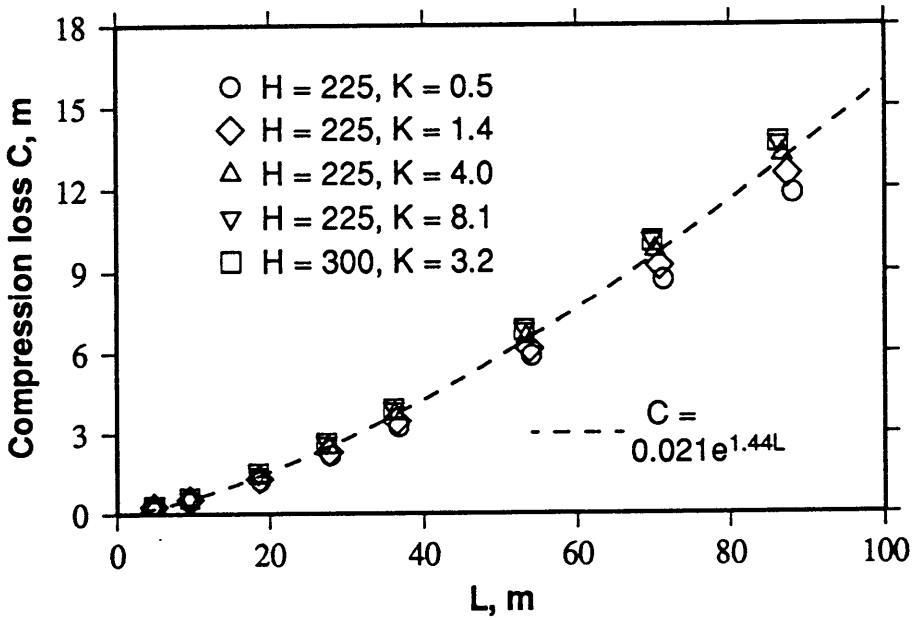

Fig. 2.29: Amount of compaction observed during numerical experiments in which a Goff-Jordan basement topographies with parameters $H = 225$ m or 300 m, $k_n = 0.6$ km^{-1}, $k_s = 0.12$ km^{-1}, $D = 2.2$, and $\zeta_s = 30°$, were sedimented using K of 0.5, 1.4, 4.0, and 8.1 (for the $H = 225$ m topography), and 3.2 (for the $H = 300$ m topography), at a rate F of 4 m/m.y. L corresponds to the average sediment thickness in the region after compaction, and C represents the loss in average sediment thickness due to compaction.

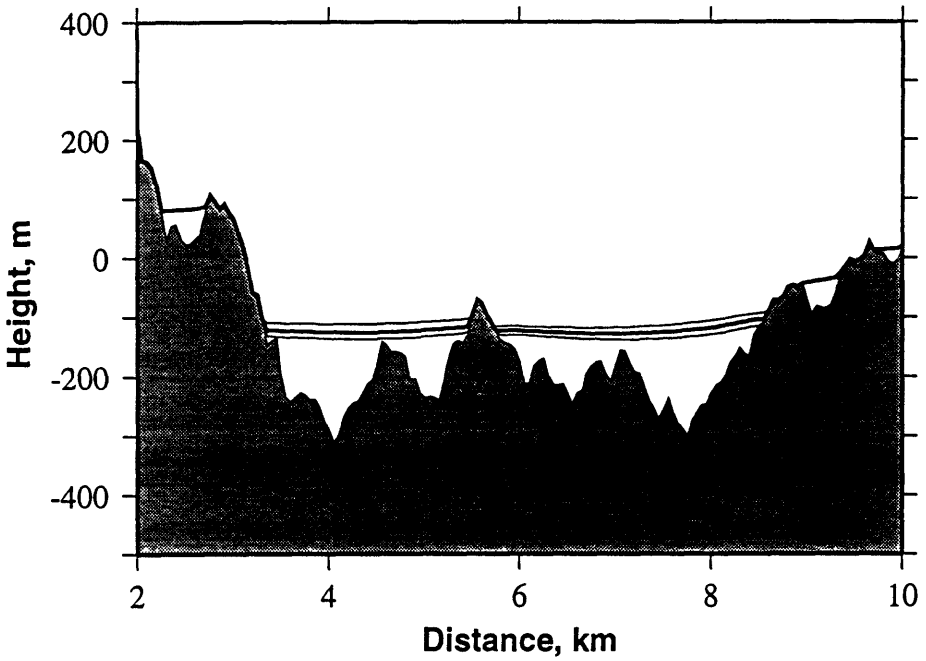

Fig. 2.30: Profile of seafloor generated using Goff-Jordan parameters H = 225 m, k_n = 0.6 km^{-1}, k_s = 0.12 km^{-1}, D = 2.2, and ζ_s = 30°, sedimented using a K of 4.0. Thin lines represent L = 40 m and L = 50 m surfaces generated assuming no compaction takes place (the standard forward sedimentation model). Thick line represents a surface generated allowing compaction, with an L of 44.9 m. Vertical exaggeration is 1:6.

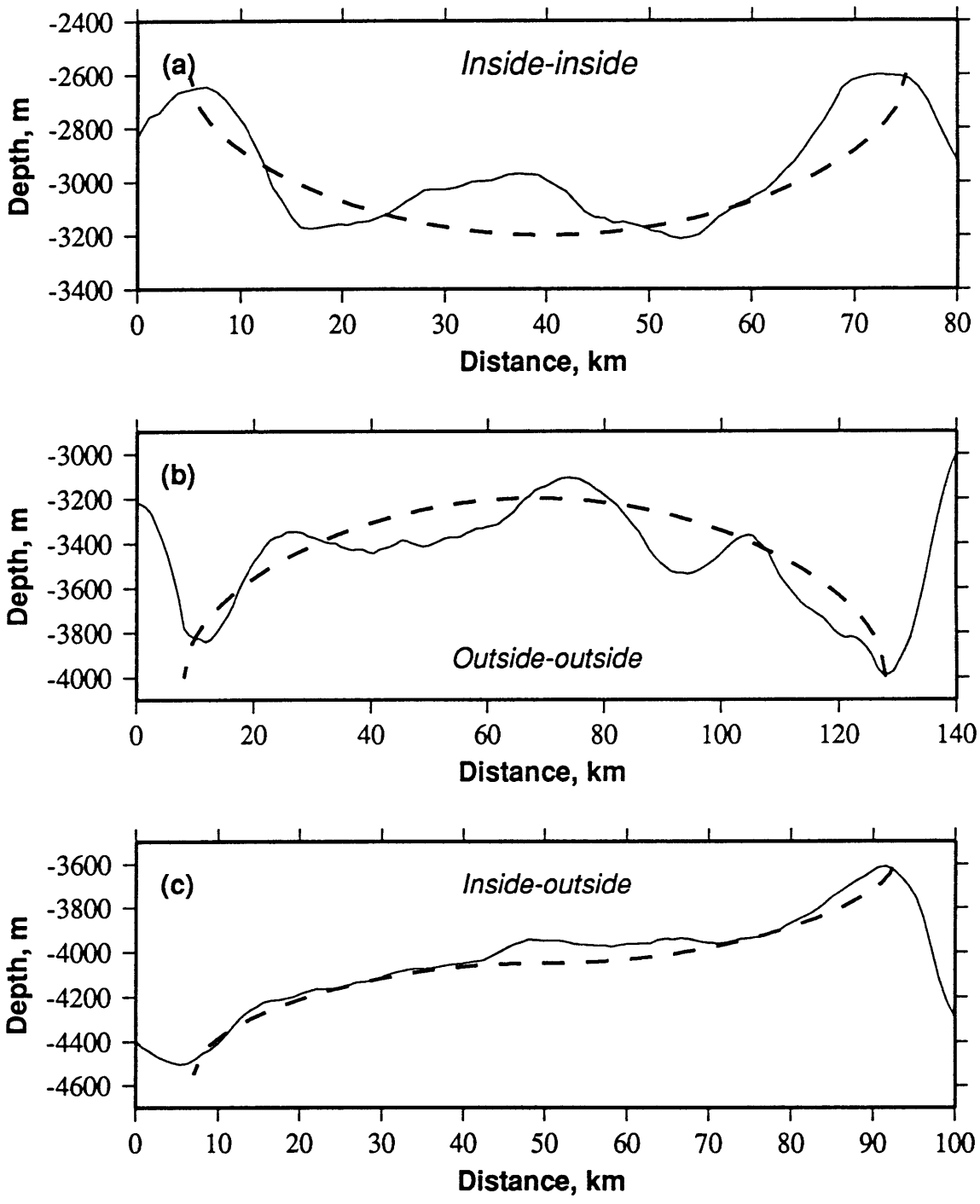

Fig. 2.31: Examples of (a) inside-inside, (b) outside-outside, and (c) inside-outside corner crust (solid lines) from near-MAR surveys in the North Atlantic and South Atlantic, compared to model curves (dashed lines) (see Table 2.1). Vertical exaggerations are 26:1 for (a), 37:1 for (b), and 27:1 for (c).

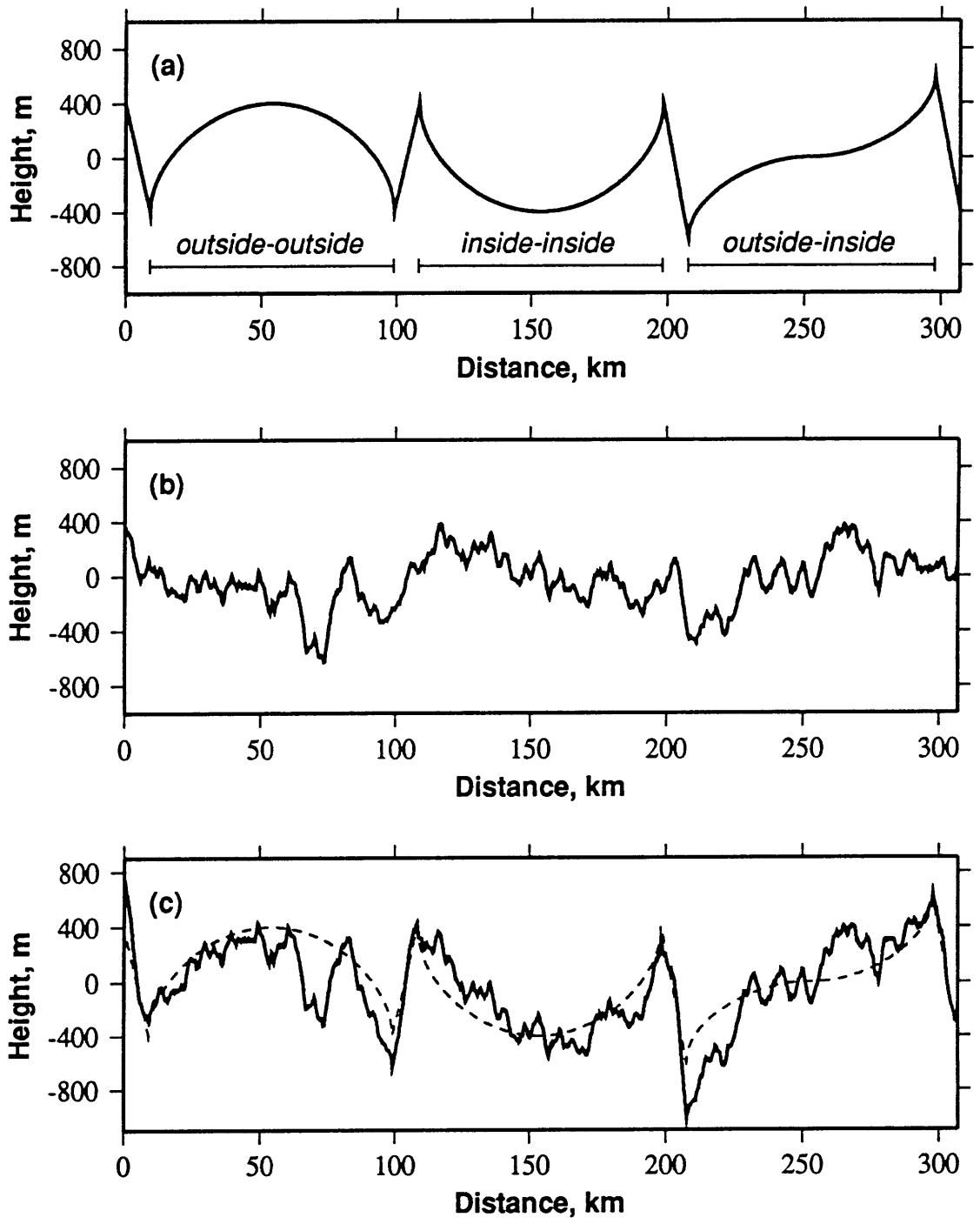

Fig. 2.32: (a) Flexure signal (2.41) added to model topographies prior to sedimentation. (b) Profile through center of the a 307.2 × 307.2 km^2 Goff-Jordan basement model generated using a datapoint spacing d of 300 m. Basement parameters are H = 225 m, k_n = 0.6 km^{-1}, k_s = 0.12 km^{-1}, and D = 2.2. We let $\zeta_s = 0°$, and impose the curvature in this, the along-hillstrike, direction. (c) Sum of profiles in (a) and (b). Vertical exaggeration for all three panels is 77:1.

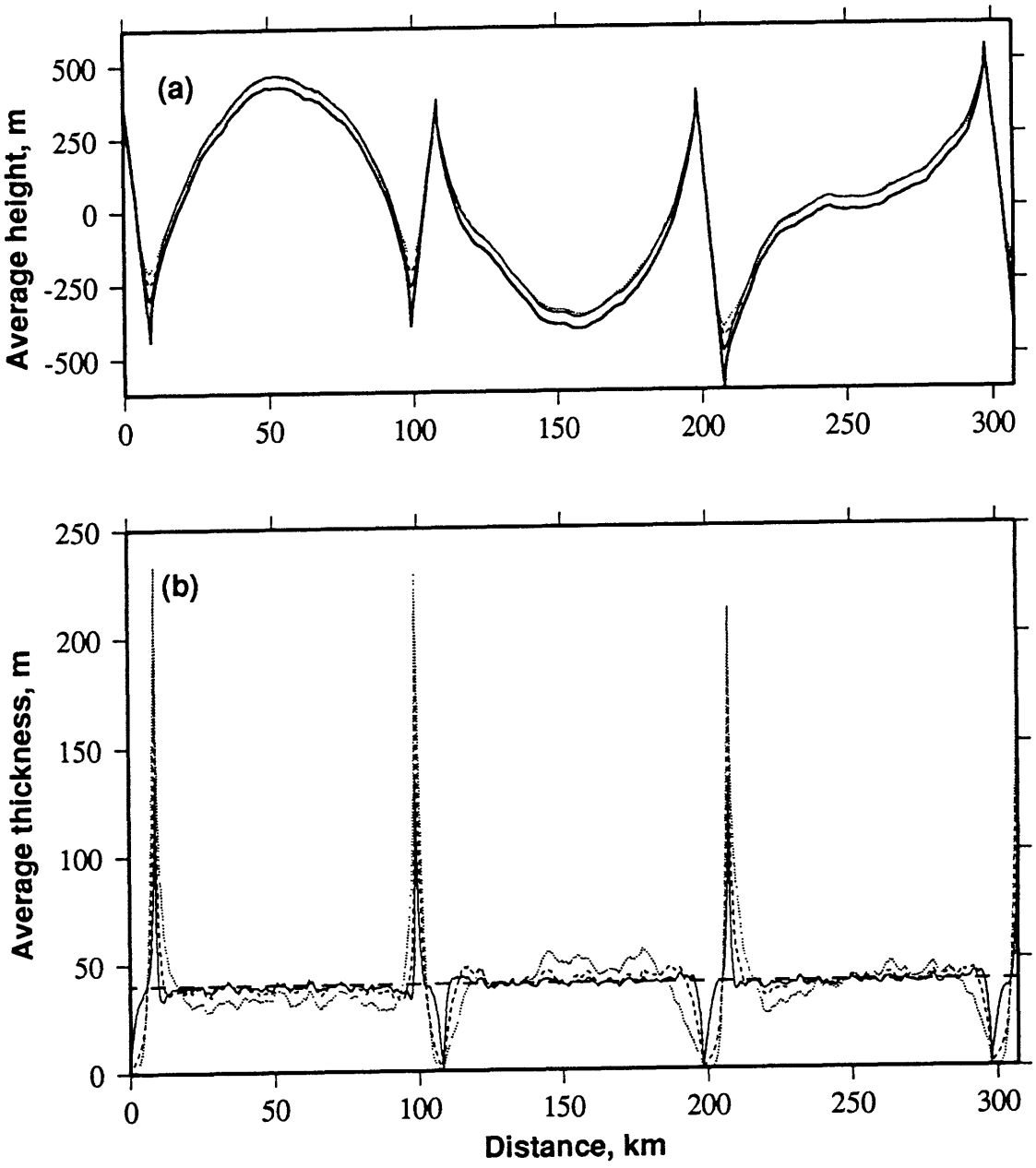

Fig. 2.33: (a) Average of along-strike basement and 10 m.y. (L = 40 m) surface generated using a κ of 0.2 (solid line), 1.0 (dashed line), and 10.0 (dotted line) m^2/yr and F of 4 m/m.y. Vertical exaggeration is 99:1. (b) Along-strike average sediment thicknesses for 10 m.y. (L = 40 m) surface, for κ = 0.2 (solid line), 1.0 (thin dashed line), and 10.0 (dotted line) m^2/yr and F = 4 m/m.y, as compared to L (thick dashed line).

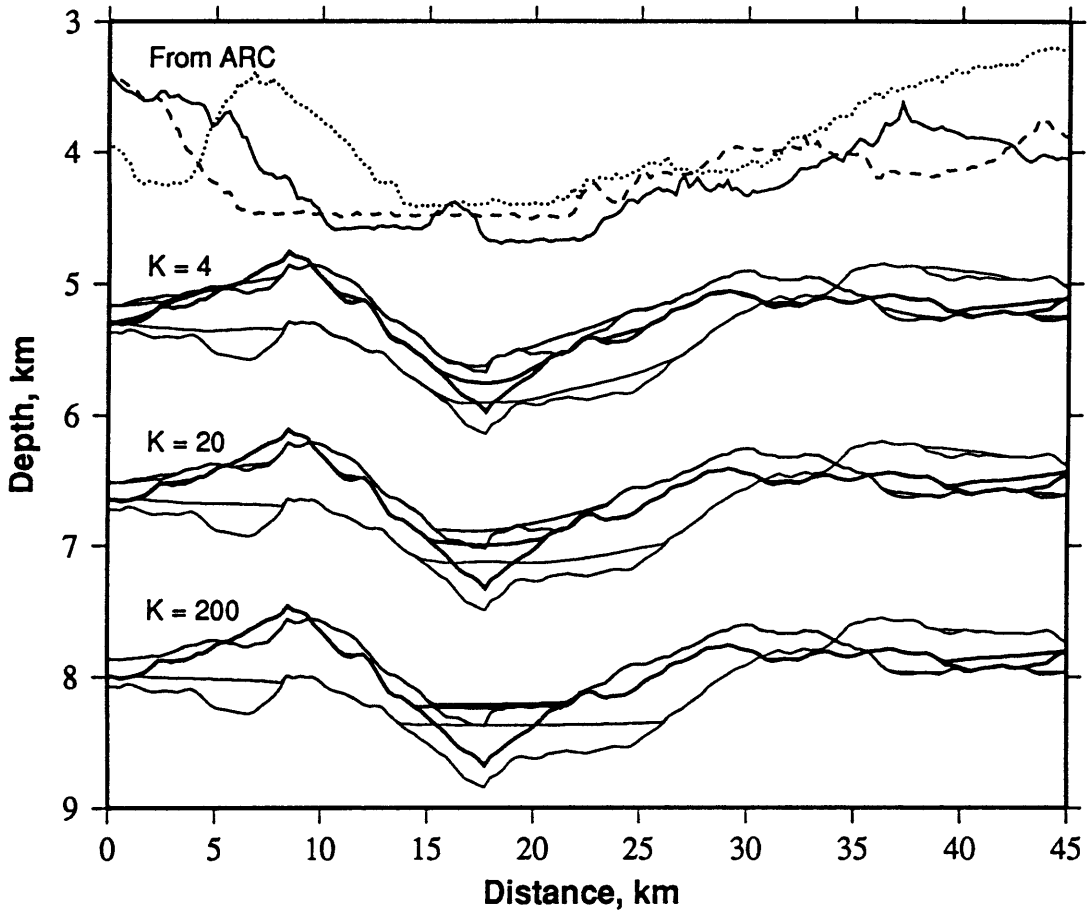

Fig. 2.34: Examples of north-south profiles from bathymetric data from the North Atlantic ARC discussed in Chapter 3. Profiles extend from 26.36° N, 46.05° W to 26.77° N, 46.06° W (dotted line), 26.23° N, 46.55° W to 26.64° N, 46.56° W (dashed line), and 26.05° N, 47.05° W to 26.45° N, 47.06° W (solid line). Also shown are profiles extracted from the sedimented long-wavelength flexure models, sedimented to an average thickness L of 40 m, with dimensionless diffusivities of 4, 20, and 200, as labeled. Given a sediment rain rate F of 4 m/m.y. and a seafloor age of 10 m.y., this corresponds to the use of apparent diffusivities κ of 0.2, 1.0, and 10.0 m^2/yr. Vertical exaggeration is 6:1.

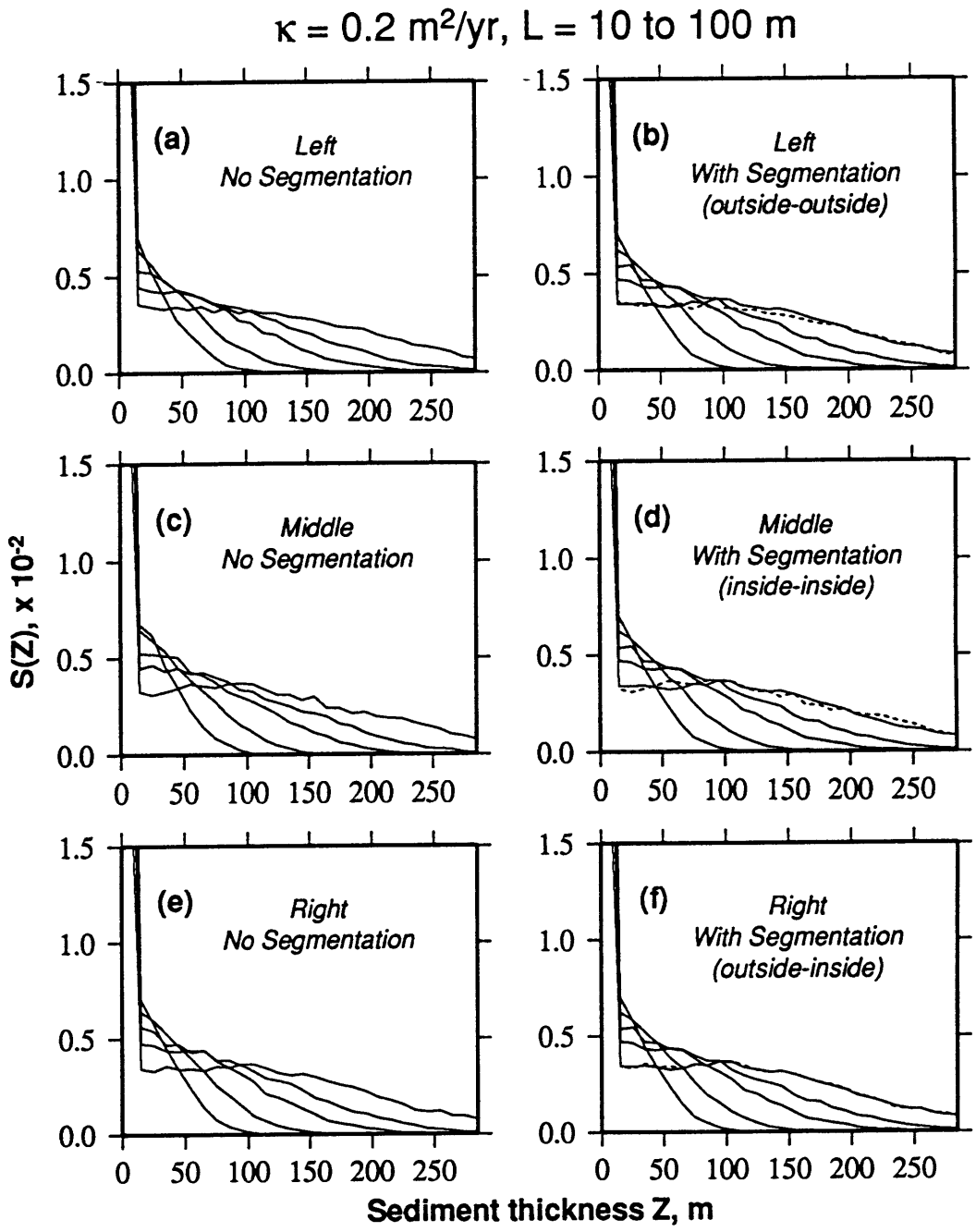

Fig. 2.35: Sediment thickness distribution functions $S(Z)$ for control model ((a), (c), and (e)) and model with long-wavelength flexure ((b), (d), (f)), for surfaces after the passage of 2.5, 5, 10, 15, and 25 m.y. of model time, for outside-outside, inside-inside, and outside-inside corner segments, as labeled. Models are generated using $\kappa = 0.2$ m^2/yr and F = 4 m/m.y. A large bin size of 10 m is used. Dashed lines in (b), (d), and (f) correspond to 25 m.y. surface $S(Z)$ from (a), (c), and (e), demonstrating that the imposed flexure does not exert much influence on sediment thickness distribution functions.

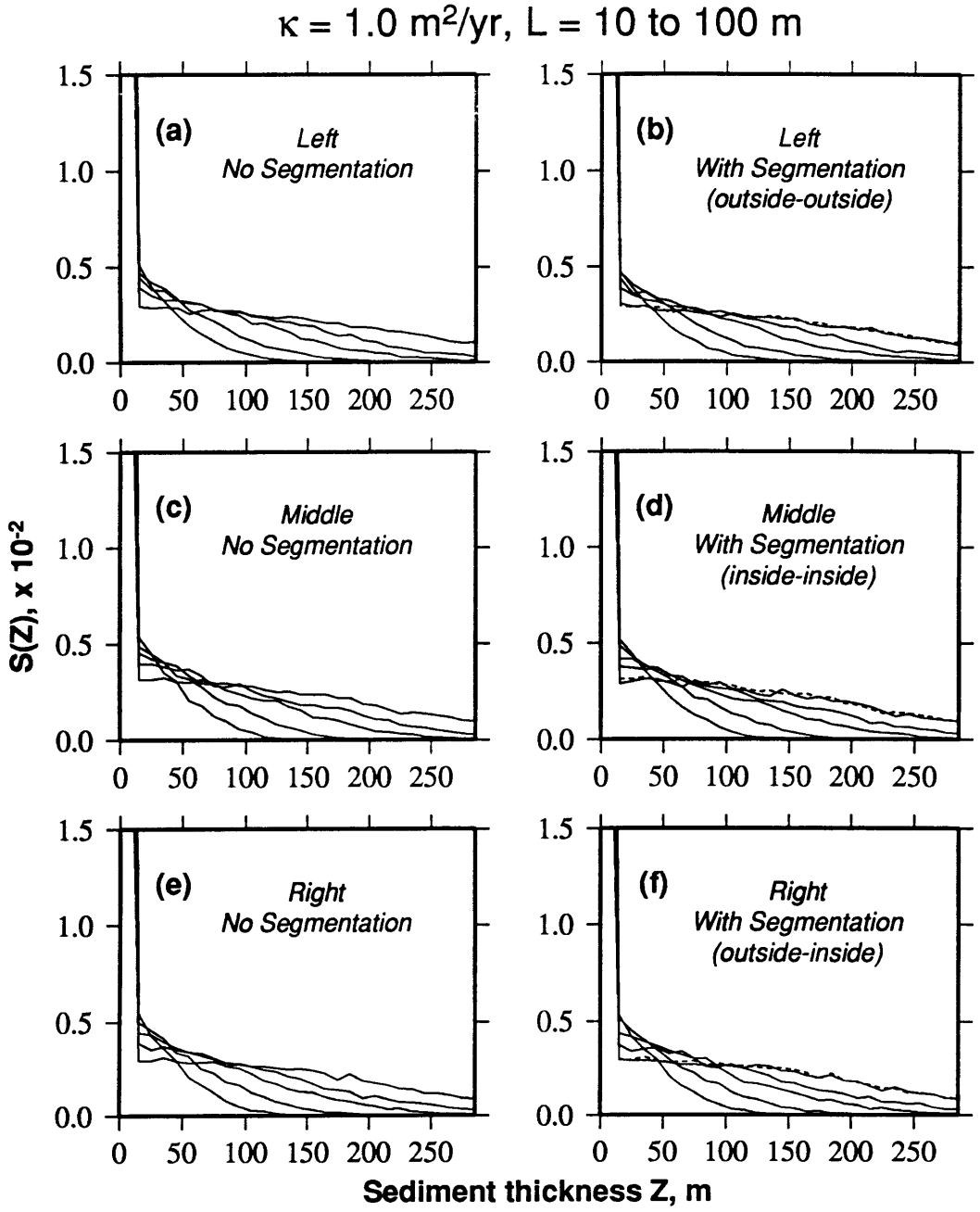

Fig. 2.36: Sediment thickness distribution functions $S(Z)$ for control model ((a), (c), and (e)) and model with long-wavelength flexure ((b), (d), (f)), for surfaces after the passage of 2.5, 5, 10, 15, and 25 m.y. of model time, for outside-outside, inside-inside, and outside-inside corner segments, as labeled. Models are generated using $\kappa = 1.0$ m^2/yr and F = 4 m/m.y. A large bin size of 10 m is used. Dashed lines in (b), (d), and (f) correspond to 25 m.y. surface $S(Z)$ from (a), (c), and (e), demonstrating that the imposed flexure does not exert much influence on sediment thickness distribution functions.

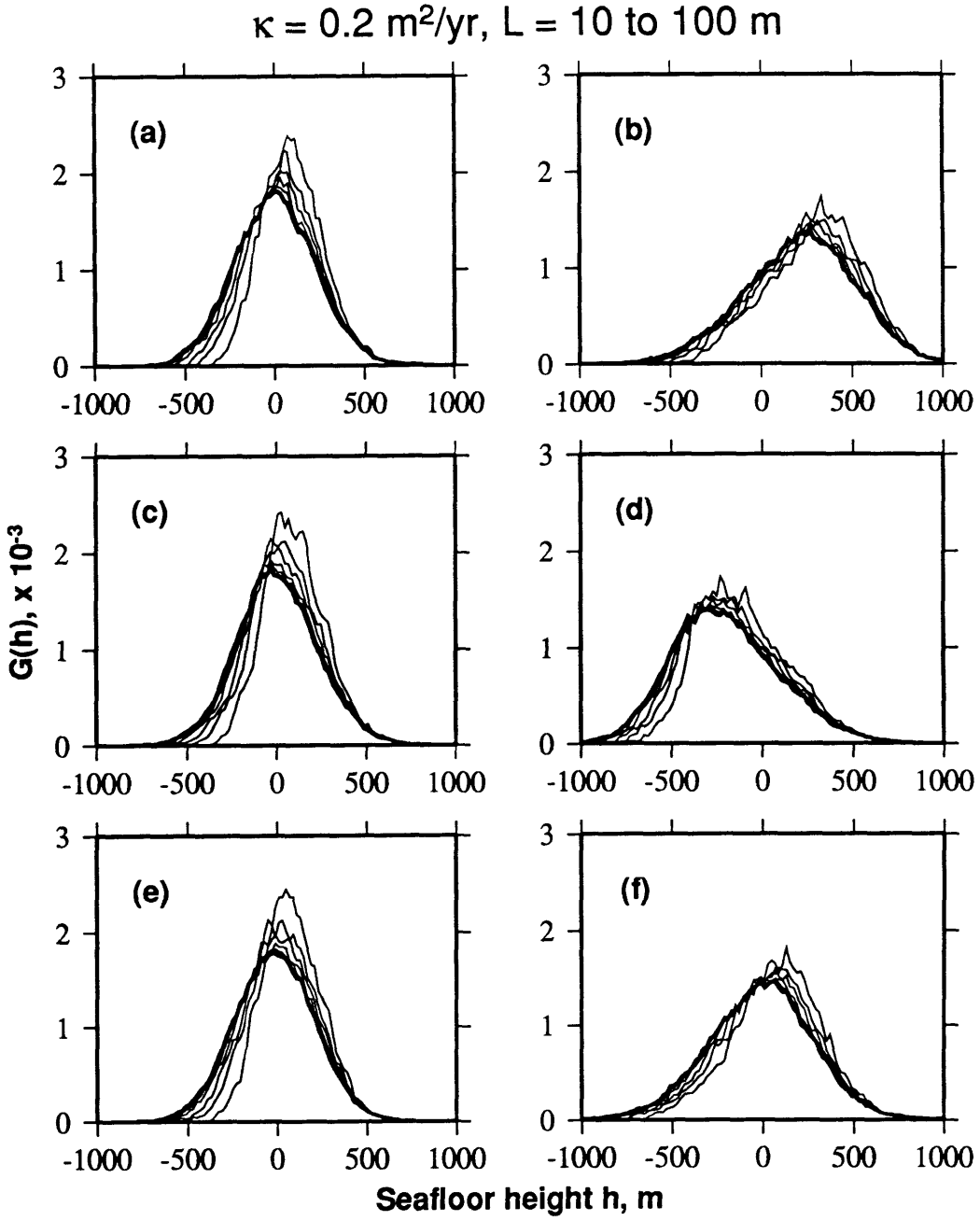

Fig. 2.37: Height distribution functions $G(h)$ for control model ((a), (c), and (e)) and model with long-wavelength flexure ((b), (d), (f)), for basement (thick lines) and surfaces after the passage of 2.5, 5, 10, 15, and 25 m.y. of model time, for outside-outside ((a) and (b)), inside-inside ((c) and (d)), and outside-inside ((e) and (f)) corner segments. Models are generated using $\kappa = 0.2$ m^2/yr and $F = 4$ m/m.y. A bin size of 20 m is used.

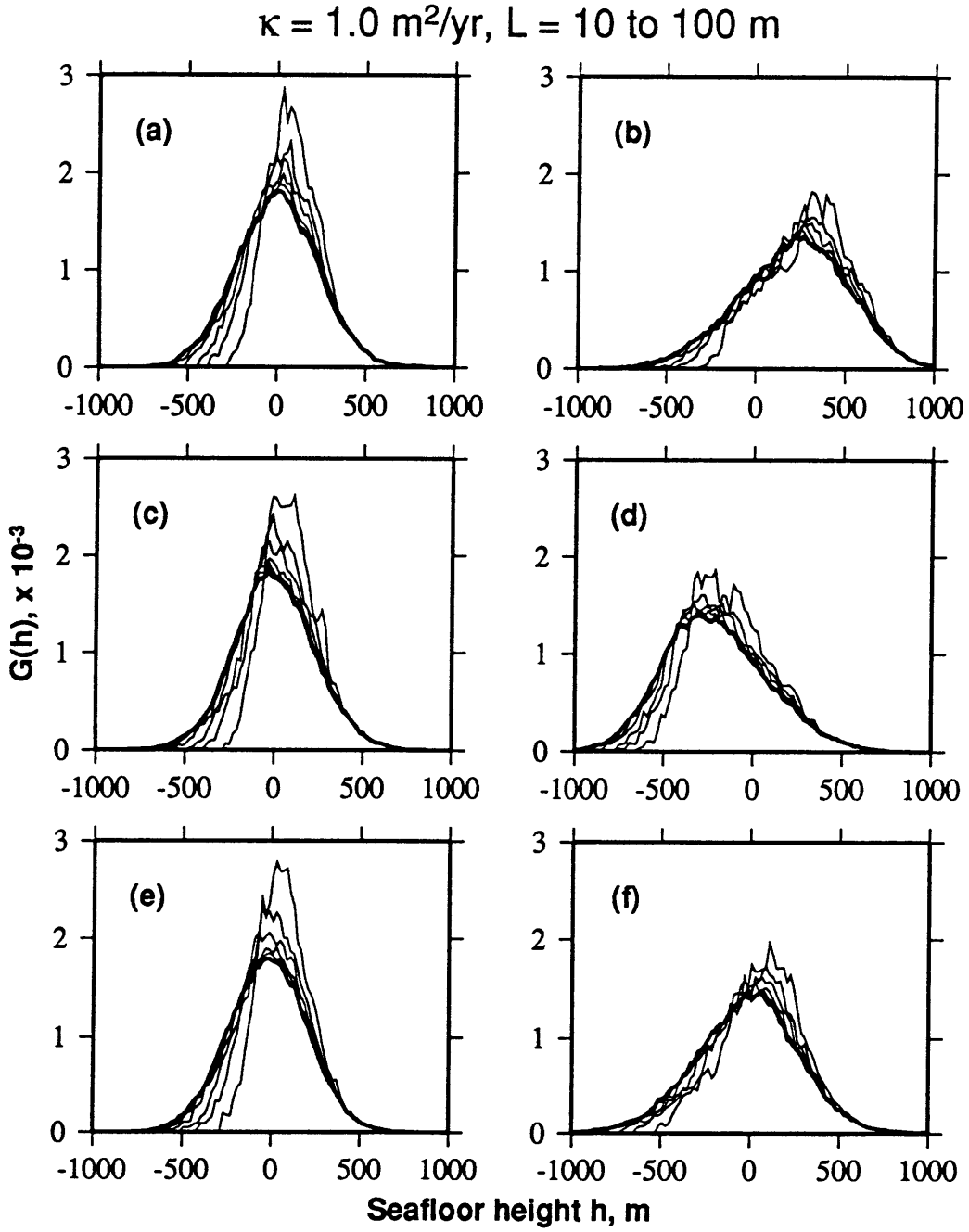

Fig. 2.38: Height distribution functions $G(h)$ for control model ((a), (c), and (e)) and model with long-wavelength flexure ((b), (d), (f)), for basement (thick lines) and surfaces after the passage of 2.5, 5, 10, 15, and 25 m.y. of model time, for outside-outside ((a) and (b)), inside-inside ((c) and (d)), and outside-inside ((e) and (f)) corner segments. Models are generated using $\kappa = 1.0$ m^2/yr and $F = 4$ m/m.y. A bin size of 20 m is used.

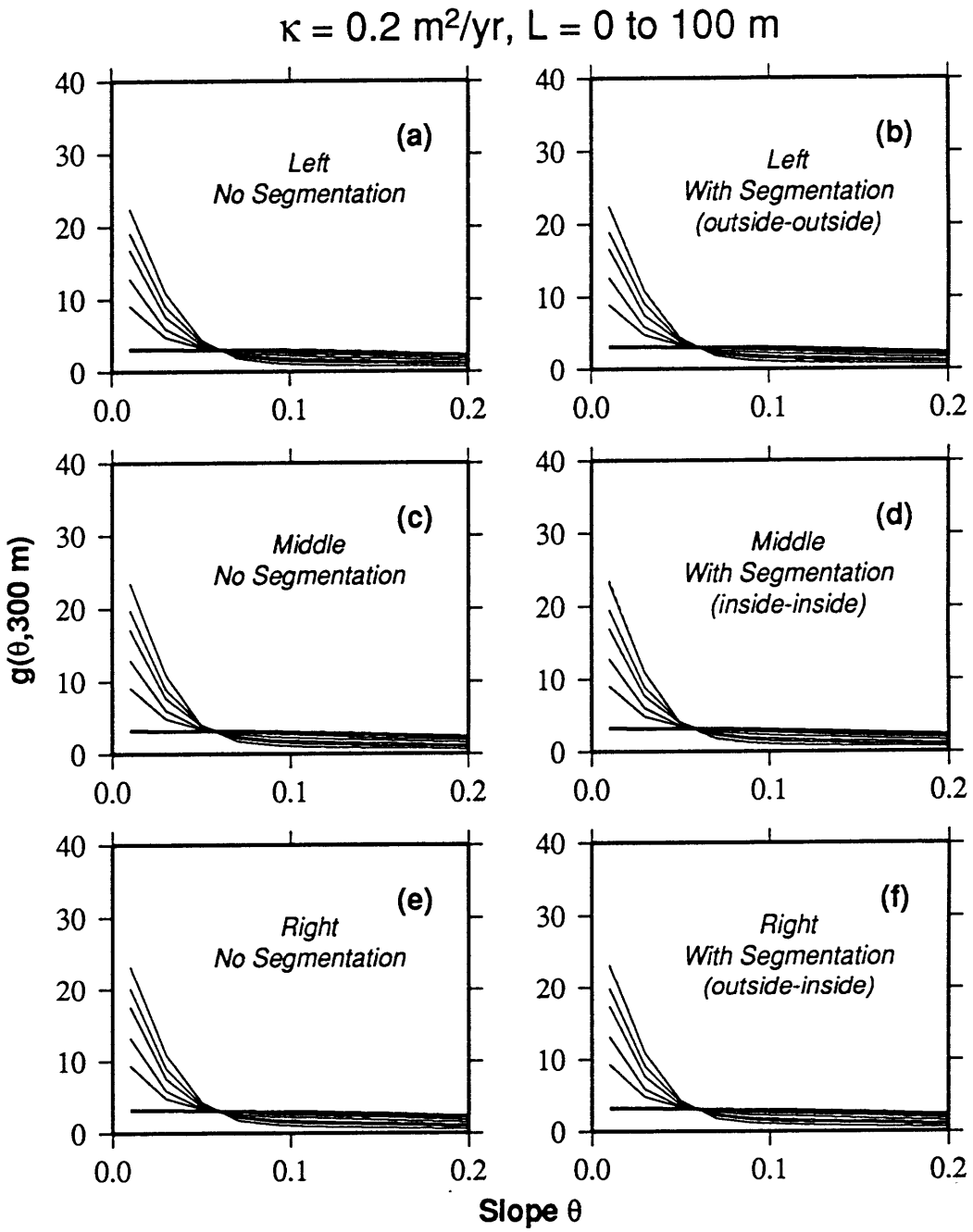

Fig. 2.39: Slope distribution functions $g(\theta,u)$, u = 300 m, measured perpendicular to the hillstrike direction for control model ((a), (c), and (e)) and model with long-wavelength flexure ((b), (d), (f)), for basement (thick lines) and surfaces after the passage of 2.5, 5, 10, 15, and 25 m.y. of model time, for outside-outside ((a) and (b)), inside-inside ((c) and (d)), and outside-inside ((e) and (f)) corner segments. Models are generated using $\kappa = 0.2$ m^2/yr and F = 4 m/m.y. A bin size of 0.02 is used. Dashed lines in (b), (d), and (f) correspond to $g(\theta,u)$ from the 25 m.y. surface as in (a), (c), and (e), demonstrating that the imposed flexure exerts almost no influence on hillstrike-perpendicular $g(\theta,u)$.

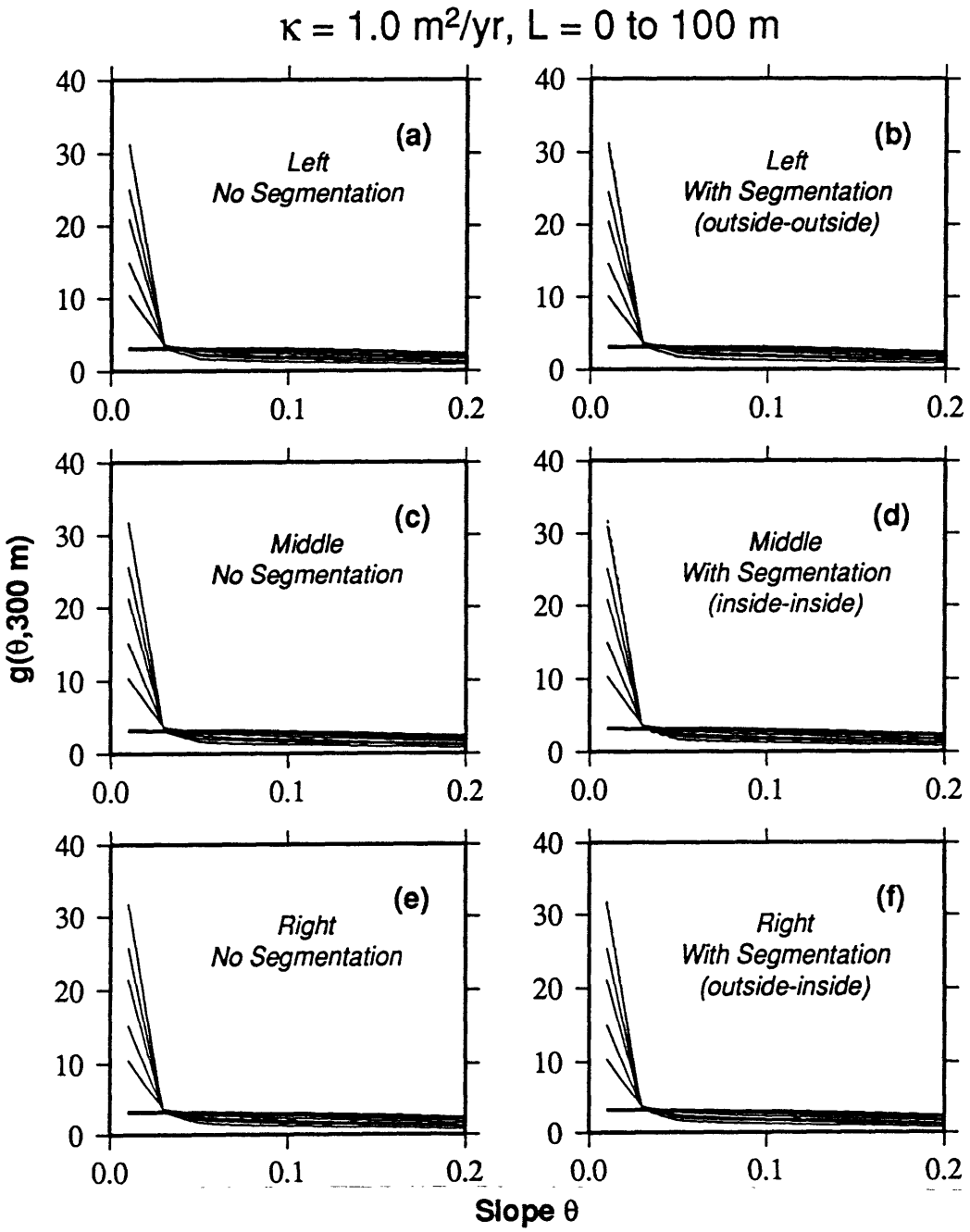

Fig. 2.40: Slope distribution functions $g(\theta,u)$, u = 300 m, measured perpendicular to the hillstrike direction for control model ((a), (c), and (e)) and model with long-wavelength flexure ((b), (d), (f)), for basement (thick lines) and surfaces after the passage of 2.5, 5, 10, 15, and 25 m.y. of model time, for outside-outside ((a) and (b)), inside-inside ((c) and (d)), and outside-inside ((e) and (f)) corner segments. Models are generated using κ= 1.0 m^2/yr and F = 4 m/m.y. A bin size of 0.02 is used. Dashed lines in (b), (d), and (f) correspond to $g(\theta,u)$ from the 25 m.y. surface as in (a), (c), and (e), demonstrating that the imposed flexure exerts almost no influence on hillstrike-perpendicular $g(\theta,u)$.

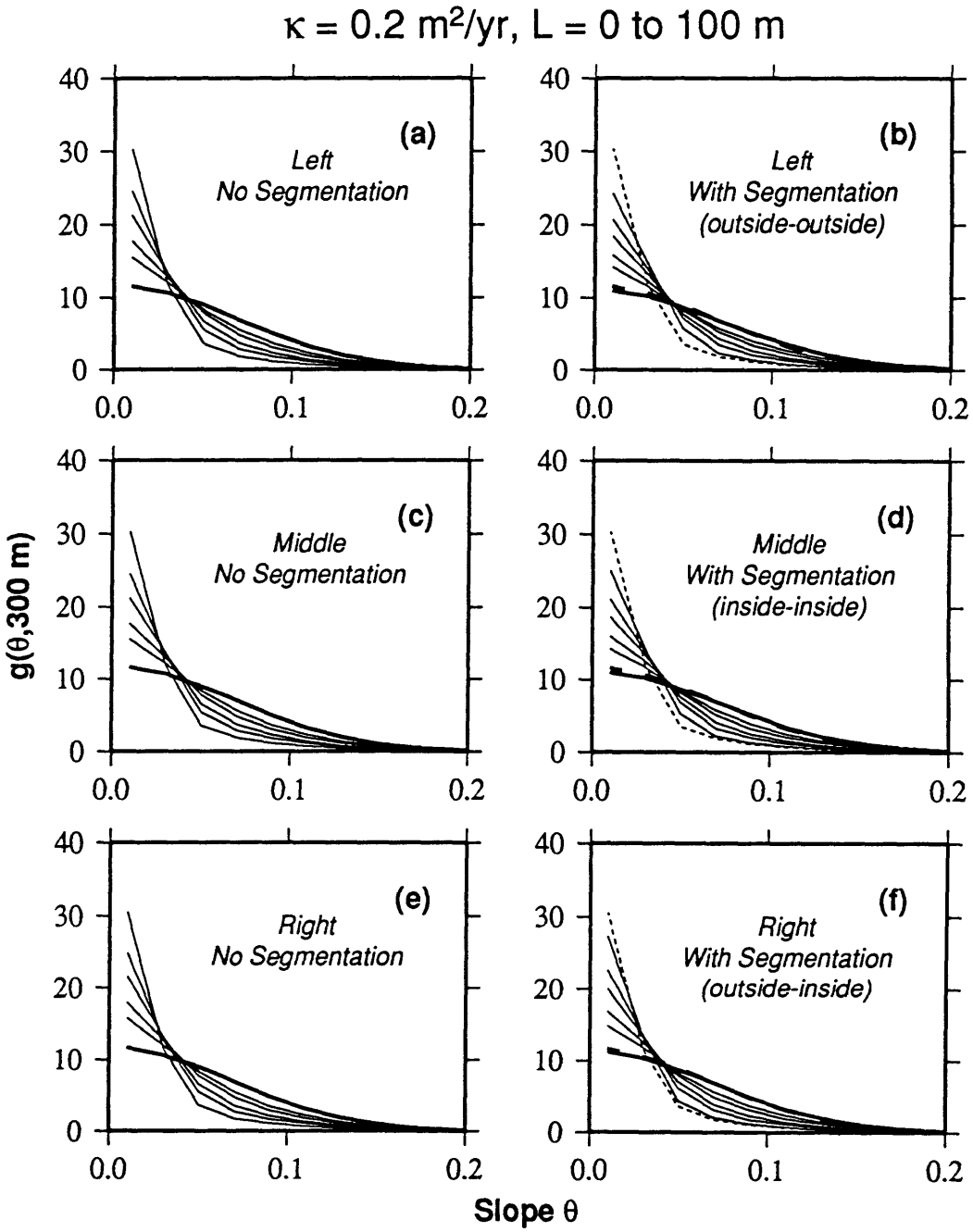

Fig. 2.41: Slope distribution functions $g(\theta,u)$, u = 300 m, measured along-strike for control model ((a), (c), and (e)) and model with long-wavelength flexure ((b), (d), (f)), for basement (thick lines) and surfaces after the passage of 2.5, 5, 10, 15, and 25 m.y. of model time, for outside-outside ((a) and (b)), inside-inside ((c) and (d)), and outside-inside ((e) and (f)) corner segments. Models are generated using $\kappa = 0.2$ m^2/yr and $F = 4$ m/m.y. A bin size of 0.02 is used. Dashed lines in (b), (d), and (f) correspond to $g(\theta,u)$ from the basement (thick) and the 25 m.y. (thin) surface as in (a), (c), and (e), demonstrating that the imposed flexure exerts some influence on along-strike $g(\theta,u)$.

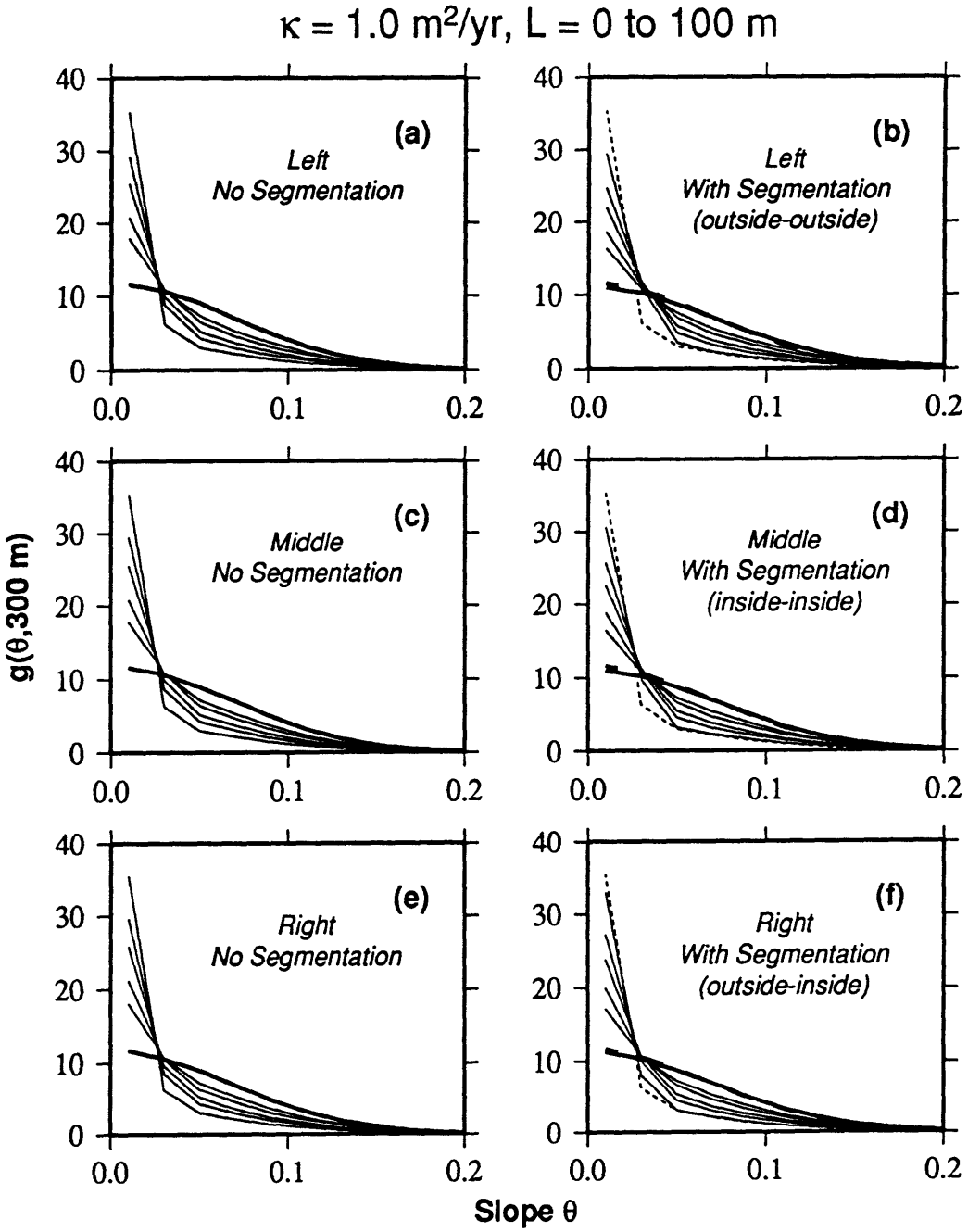

Fig. 2.42: Slope distribution functions $g(\theta,u)$, u = 300 m, measured along-strike or control model ((a), (c), and (e)) and model with long-wavelength flexure ((b), (d), (f)), for basement (thick lines) and surfaces after the passage of 2.5, 5, 10, 15, and 25 m.y. of model time, for outside-outside ((a) and (b)), inside-inside ((c) and (d)), and outside-inside ((e) and (f)) corner segments. Models are generated using κ = 1.0 m^2/yr and F = 4 m/m.y. A bin size of 0.02 is used. Dashed lines in (b), (d), and (f) correspond to $g(\theta,u)$ from the basement (thick) and the 25 m.y. (thin) surface as in (a), (c), and (e), demonstrating that the imposed flexure exerts some influence on along-strike $g(\theta,u)$.

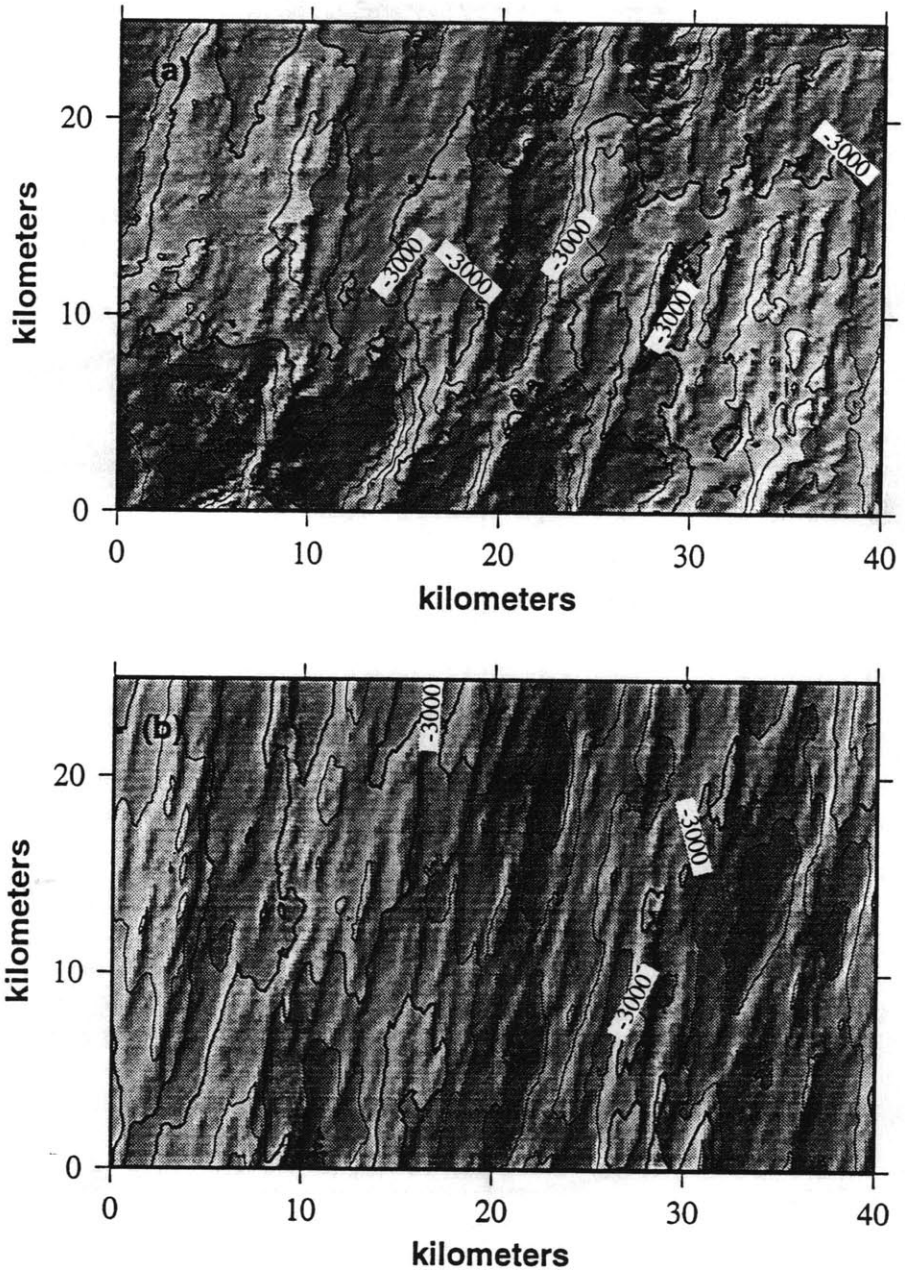

Fig. 2.43: Map-view renderings of bathymetric data centered at 25.8° N, 46.0° W (a) and a model bathymetry generated to have the same stochastic parameters including RMS height H (275 m), post-compaction sediment thickness L (24 m), and apparent diffusivity κ (0.12 m^2/yr) (b). Illumination is from the northwest, and the contour interval is 250 m.

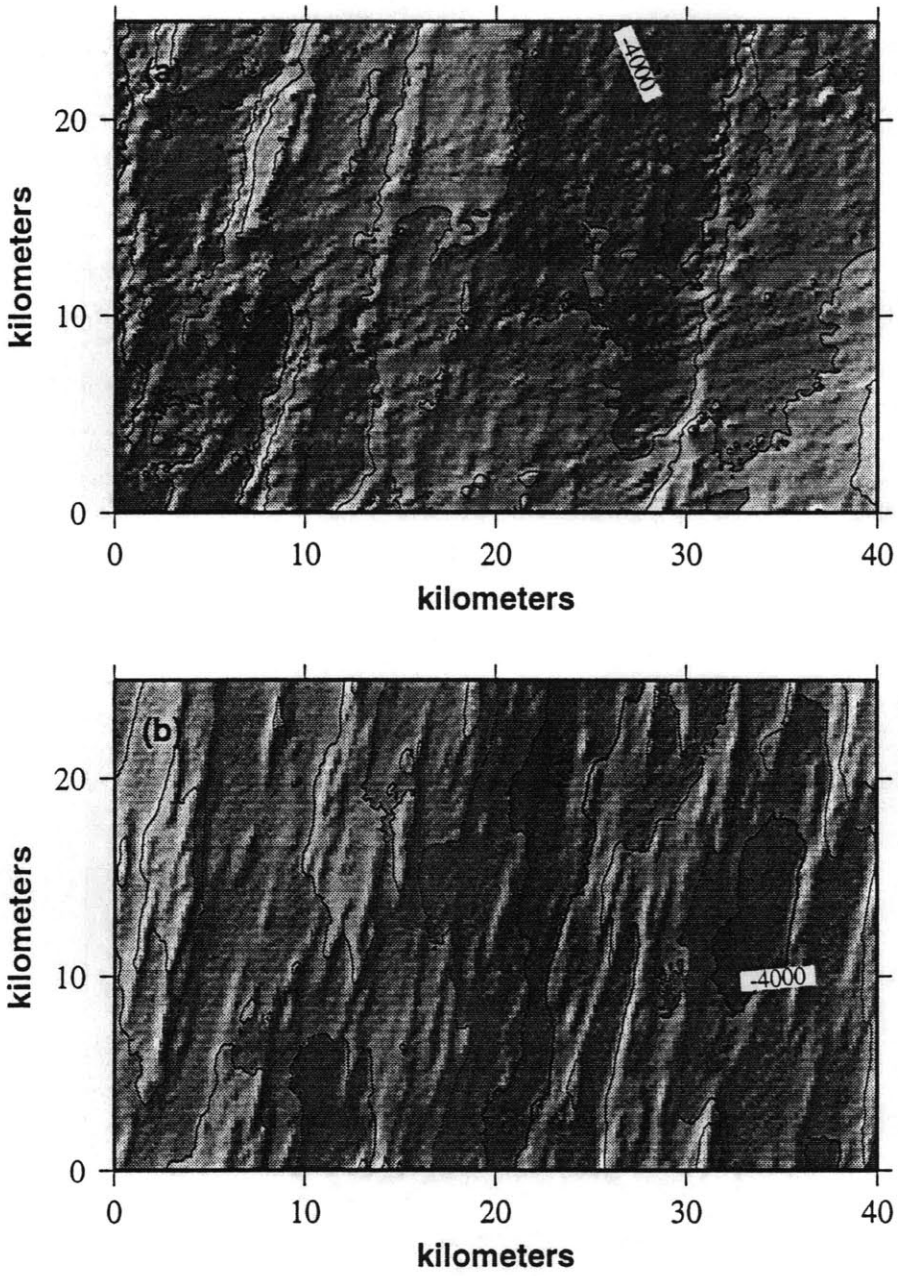

Fig. 2.44: Map-view renderings of bathymetric data centered at 25.9° N, 46.7° W (a) and a model bathymetry generated to have the same stochastic parameters including RMS height H (245 m), post-compaction sediment thickness L (40 m), and apparent diffusivity κ (0.36 m^2/yr) (b). Illumination is from the northwest, and the contour interval is 250 m.

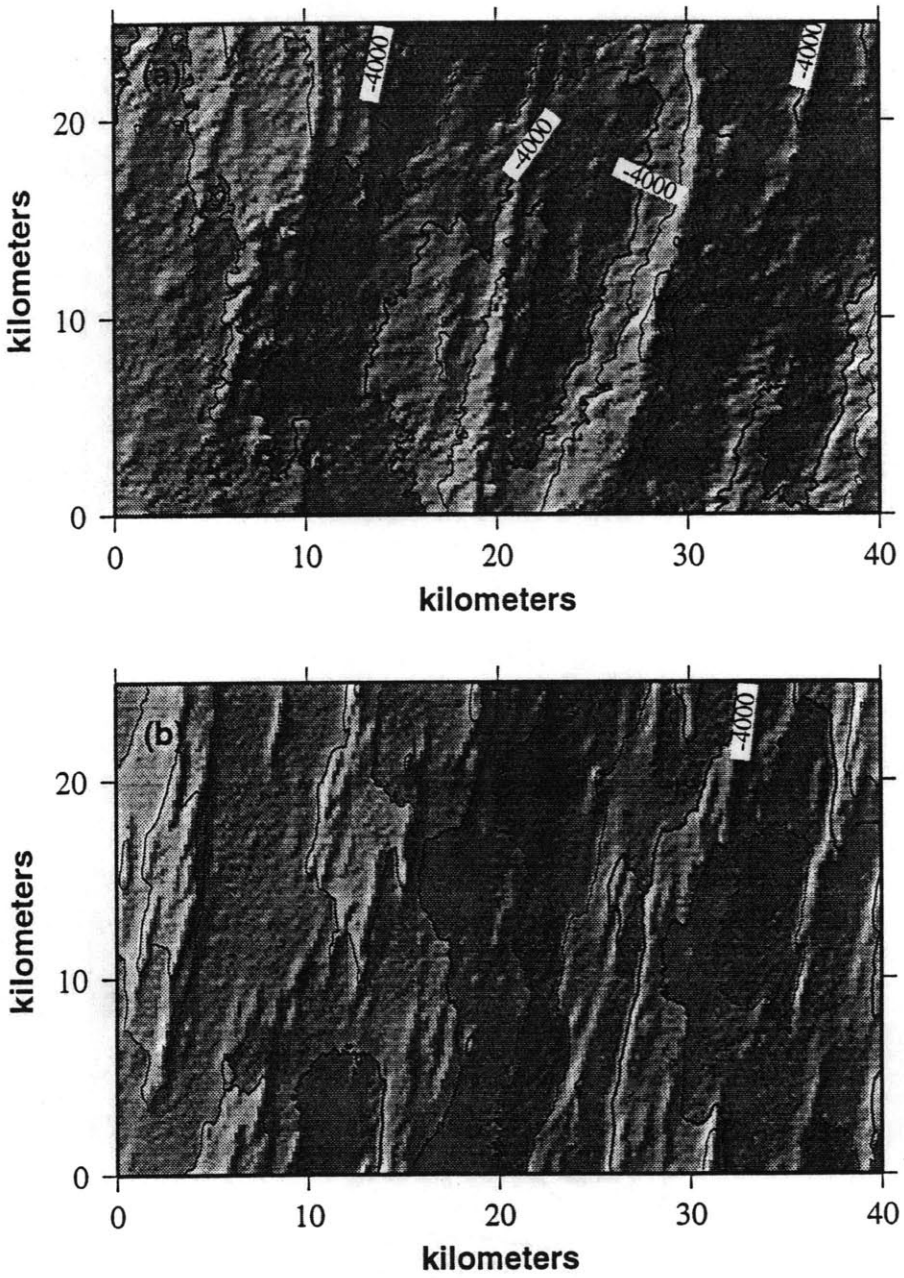

Fig. 2.45: Map-view renderings of bathymetric data centered at 26.6° N, 46.1° W (a) and a model bathymetry generated to have the same stochastic parameters including RMS height H (270 m), post-compaction sediment thickness L (78 m), and apparent diffusivity κ (0.77 m^2/yr) (b). Illumination is from the northwest, and the contour interval is 250 m.

Chapter 3

The Inversion of Bathymetric Data for Sedimentological and Basement Parameters in the ONR Acoustic Reverberation Corridor

INTRODUCTION

The topography of abyssal hills reflects basement constructional processes and the smoothing effects of pelagic sedimentation. While much work has been performed in an effort to understand the processes of volcanism and block faulting which construct abyssal hills [e.g. *Rona et al.*, 1974; *Shaw and Lin*, 1993], comparatively little has been done toward understanding the role of pelagic sediments in altering abyssal hill topography. Such an understanding would be useful for the study of paleoceanography, since the ability to determine the amount of sediment on rough topography would greatly expand our knowledge of how sediment accumulation rates, and, hence, biological productivity and bottom water corrosivity, have varied throughout the world ocean. Additionally, knowledge about the distribution of sediments on hillsides, at scales below the resolution of ship-based seismic systems, is necessary for the interpretation of low-angle acoustic backscatter [e.g. *Makris and Berkson*, 1994; *Robertsson and Levander*, 1995], since to properly interpret backscatter from a given area the extent of sediment cover and the roughness of basement outcrops must be known. And, an understanding of how sedimentation affects the stochastic character of seafloor is vital if we are to successfully map the variability of basement topography on the world mid-ocean ridge system, since even thin accumulations may alter the stochastic character of topography as measured using common measures such as height distribution and covariance functions (see Chapter 2).

Multibeam bathymetric data is an unexplored source of information about sediment accumulation patterns on rough topography. Multibeam bathymetric imaging systems record the surface shape of sediment accumulations in locations that are not well imaged by wider-beam sediment-penetrating acoustic sources. The surface shapes of small

accumulations in a region reflect whether sediments have been moved energetically into low, flat, level sediment ponds or whether individual grains of sediment tend to be deposited on pond edges and move slowly down-slope; whether a region has been subjected to recent block tilting; and the horizontal extent of sediment ponds.

In Chapter 2 of this thesis, we introduce a simple forward model of pelagic sedimentation on rough abyssal hill topography in which material derived from the water column is transported from topographic highs to lows with lateral flux equal to local seafloor slope multiplied by a diffusivity constant κ. This constant effectively serves to parameterize how much curvature the surfaces of sediment ponds in a region tend to exhibit, which we take as correlating with general sediment mobility. Using this model, we quantify the effects of sedimentation on topography through the use of common measures including height distributions, covariance functions, and power spectra. Theoretically, any of these measures could be used to quantitatively study pelagic sedimentation. However, second-order statistics are very sensitive to long-wavelength topographic effects, complicating the interpretation of variations seen in stochastic measures as calculated from bathymetric data. As shown in Chapter 2, the distribution of seafloor slope, in contrast, is sensitive to basement structure and the morphology of sedimented surfaces, but is insensitive to long-wavelength topographic signals. In this chapter, we develop a methodology for using the distribution of seafloor slope, as sampled by narrowbeam bathymetry measurement systems such as the multibeam swathmappers Hydrosweep and Seabeam, to study sedimentation patterns on rough topography. Specifically, we invert Hydrosweep centerbeam bathymetry data from small regions of topography for average regional sediment thickness (L), sediment apparent diffusivity (κ), and basement RMS variability (H). Our basic procedure is to compute slope distribution functions from the bathymetry data and from models, then determine, via maximum likelihood estimation, a range of models which are similar to data.

We apply our methodology to bathymetric data from the Office of Naval Research Acoustic Reverberation Corridor (ARC). The ARC serves as a natural laboratory for understanding acoustic reverberation in the deep sea, as part of the ONR Acoustic Reverberation Special Research Project (ARSRP). During several dedicated research

cruises, bathymetry, single-channel seismic (SCS), 3.5 kHz (recorded both to paper and DAT tapes), sidescan sonar, gravity, magnetic, and photographic data, from surface-based and/or deep-towed systems, have been collected in the ARC. This wealth of information makes it the most thoroughly studied region of abyssal hills in the world. However, despite the extensive amount of geological and geophysical data collected in the ARC, the distribution of sediments on and between hills is not immediately apparent even where very detailed near-bottom surveys have been performed.

Inversion results obtained in this chapter provide insight into how sedimentation processes interact with topography. We have used inverted parameters to produce model topographies in support of the needs of acoustic modelers, as part of the ARSRP (e.g. *Robertsson et al.*, submitted); these models are not presented in this thesis. The inverted values of L also yield information about changes to sediment supply rate and/or oceanic chemistry since the late Oligocene; this issue is addressed in Chapter 6 of this thesis.

In *Webb and Jordan* [1993], we employed an earlier version of the methodology given here to ARC bathymetry data. Major improvements of the methodology presented in this thesis over *Webb and Jordan* [1993] include compensating for data sampling effects of the multibeam bathymetric imaging systems, and making use of maximum likelihood estimation for the actual inversion for model parameters. While we still restrict our analysis to the centerbeam return of the bathymetric imaging system because this beam is least susceptible to data drops and has the least system noise, we use all data from that beam, not just 1-minute-spaced interpolated averages as in *Webb and Jordan* [1993].

THE ACOUSTIC REVERBERATION CORRIDOR

The ONR Acoustic Reverberation Corridor is a 82,000 km^2 region located on 0 - 29 Ma crust on the western flank of the Mid-Atlantic Ridge (MAR) to the north of the Kane Fracture Zone (25.5° - 27.25° N, 44.5° - 49° W) (Fig. 3.1). The ARC encompasses seafloor generated at several distinct ridge segments which are separated by right-lateral non-transform offsets [*Tucholke et al.*, 1992]. Topography within the ARC consists of thinly- to moderately-sedimented lineated abyssal hills, and sediment-filled deeps which follow relic spreading-segment boundaries. On the young seafloor near the MAR axis, the

hills are relatively short (20-50 km in length), and are several 100's of meters higher at their southern (inside corner crust) ends than at their northern (outside corner crust) ends, which dip down into the segment-boundary deeps. On older crust within the ARC, hills are longer, and, while there is some dip from the south to the north (see Fig. 2.31 (c)), this effect is less pronounced on older crust than on younger crust within the ARC.

Sedimentation patterns

Currently, the moderate latitudes of the North Atlantic are accumulating calcareous sediment at depths shallower than 5-5.5 km [*Biscaye et al.*, 1976], including the depth range of most of the ARC. Thus, the composition of sediment within the ARC is fairly uniform. The spatial distribution of sediments within the ARC, conversely, is highly heterogeneous, reflecting the effects of bottom currents, post-depositional transport processes, and dissolution on pelagic sediments. Detailed examination of SCS, 3.5 kHz, and side-scan sonar data [*Jaroslow and Tucholke*, 1995; *Jaroslow*, 1997] has found that much of the seafloor is essentially bare (at the resolution of these low- to moderate-resolution systems), while deeps associated with spreading center offsets may have 500-750 m of sediment. Between the ridge-parallel abyssal hills, elongated sediment ponds with widths of more than 1-2 km are common, and may be as deep as 250 m in the more heavily sedimented regions of the ARC. Smaller ponds are also found on hillsides and between hills. As these are poorly resolved by wide-beam acoustic sources, it difficult to determine how much of the ARC is covered by sediments and total sediment volume.

The character of sedimented topography varies throughout the ARC. The large, deep-set ponds on outside corner crust are extremely level, suggesting that they are mostly (or, most recently) filled by turbidites. In higher-standing regions, some ponds seem to lie flat, while others exhibit a fair amount of concavity, as imaged in 3.5 kHz and Hydrosweep data (Fig. 3.2).

A few locales within the ARC were studied in great detail during May-June 1993 using the deep-towed sonar DSL-120, which provided bathymetry as well as acoustic reflectivity data, and the *Jason* ROV, which was equipped with video and still cameras, the DSL-200 sidescan and DSL-300 forward scan sonar instruments, and the 675 kHz

Mesotech profiling sonar. The high-resolution studies found that small-scale topography is much rougher than is rendered by Hydrosweep bathymetry data. Fault scarps range in height from a few meters to up to 200 m, and slopes of greater than 60° are not uncommon. The bathymetry data obtained by the DSL-120 at ~26.59° N, 48.09° W show that sediment pond surfaces within the ARC can maintain curvature through time (see Fig. 2.5). The curvature exhibited at this location is similar to that observed by *Mitchell* [1995] in deep-towed bathymetric data from the FAMOUS area in the North Atlantic. We find that, if we assume that sediment transport follows the diffusion equation, a κ of 0.05 m^2/yr can explain the curvature seen in the profile shown in Fig. 2.5, while *Mitchell* [1995] found that surface shape of many 150- to 400-m-wide ponds in the FAMOUS area could be modeled using κ between 0.04 and 0.11 m^2/yr.

Data grouping for analysis

The abundance and small size of abyssal hills and sediment ponds makes the detailed study of the structure of numerous individual hills impractical. However, much can be learned about constructional processes by studying the statistical character of ensembles of abyssal hills [e.g. *Malinverno and Gilbert*, 1989; *Goff*, 1991]. We take this approach to the study of topography within the ARC.

In this chapter, we are attempting to answer two fundamental questions. First, how does sedimentation affect the character of abyssal hills throughout the ARC? Secondly, how does average sediment thickness vary throughout the ARC? The answer to the first question is necessary for developing general rules for interpreting topography in terms of basement structure and sedimentation effects, and for generating models for studying acoustic backscatter. The answer to the second question allows us to study the paleoceanography of the ARC, as revealed by the rate at which sediment has accumulated through time.

We address these questions primarily through the use of Hydrosweep bathymetry data collected by the *R/V Maurice Ewing* during July-August 1992 (cruise EW9208). This data set provides nearly 100% coverage of a 82,000 km^2 region of seafloor, at a trackline spacing of 4 to 9 km. Returns were collected every 11-15 seconds, resulting in an along-

track data spacing of 60-80 m. Single-channel seismic data, digitally-record 3.5 kHz data, and sidescan sonar data were collected concurrently.

We apportion the ARC into two separate families of subregion. To study processes within hilly regimes, we divide the seafloor into 15 1000–4000 km^2 highstanding areas within which the stochastic character of the abyssal hills appears homogeneous. We refer to these areas as *hill-centered* (Fig. 3.3). We avoid regions where the hills are interrupted by ridge-segment boundaries, which are typified by deeper bathymetry, thicker sediments, and inhomogeneous statistics. These subregions incorporate roughly half of the ARC.

We also divide the ARC into 35 generally smaller (500-2500 km^2) subregions, based on the placement of present-day catchment basins; we refer to these a being *basin-centered.* These subregions are chosen such that all sediment which is currently being deposited in these area stays within these subregions. Thus, these areas are useful for studying how L, and thus sediment accumulation rate now and in the past, varies throughout the ARC. These subregions cover most of the ARC, excluding all but the youngest crust and those regions which presently drain sediment into external sinks.

To construct the basin-centered subregions, we smooth a 0.5-minute gridded rendering of the ARC Hydrosweep bathymetric data, then select local lows and all uphill locations which would drain sediment into these lows, if sediments were limited to moving only north, south, east, or west, in the direction of maximum slope. An example of the procedure is shown in Fig. 3.4. In Fig. 3.5, we show the geographic extents of all 35 basin-centered regions.

Stochastic character

Goff et al. [1995] characterize the abyssal hills within the southern spreading center of the ARC in terms of five geomorphic parameters. These parameters, introduced in *Goff and Jordan* [1988], are estimated by assuming that abyssal hill bathymetry is a realization of a zero-mean, stationary, Gaussian random field completely specified by a two-point covariance function $C_{hh}(\mathbf{x})$. The parameters of this function correspond to root-mean-squared (RMS) variability H, characteristic along- and across-flowline corner wave numbers k_n and k_s, local hillstrike direction ζ_s, and fractal dimension D. In this chapter,

we make a distinction between these parameters as estimated for sedimented topography as opposed to basement topography. Therefore, as in Chapter 2, we refer to the Goff-Jordan parameters as inverted from sedimented topographies (whether actual or model) as $\hat{H}$, $\hat{k}_n$, $\hat{k}_s$, $\hat{\zeta}_s$, and $\hat{D}$. *Goff et al.* [1995] find that, off-axis along the southern segment, the average value of $\hat{H}$ from 4-m.y. spans of seafloor varies from 140 to 300 m, and that hill width $\hat{\lambda}_n$ (related to $\hat{k}_n$ and D through (2.5)) varies from ~6 to 12 km. They observe that $\hat{H}$ and $\hat{\lambda}_n$ correlate negatively with crustal thickness, with inside corner crust having higher, more widely spaced hills than outside corner crust, particularly where outside corner crust is associated with positive mantle Bouguer anomalies.

The inverted parameters of *Goff et al.* [1995] are functions both of basement structure and the distribution of sediment. Here, we attempt to determine how sediment has affected the stochastic character of the ARC, to gain an understanding of basement and sediment thickness variability within the ARC. In Chapter 2, we quantified how our forward sedimentation model predicts that sedimentation processes alter $\hat{H}$ and $\hat{\lambda}_n$; empirical relationships between height variability, hill spacing, and sediment thickness are given by (2.30) and (2.31). To make use of these relationships to study basement structure, knowledge of L to within a few meters is necessary. Similarly, we would need to know basement H to within a few meters, and $\hat{\lambda}_n$ to within a few tenths of kilometers, to use these measures to study L. As a general rule, if L were measurable precisely enough from seismic data to be useful, H and $\hat{\lambda}_n$ would also be easily measured, negating the need for (2.30) and (2.31). However, this level of information is available only from deep-towed high-frequency bathymetric and seismic data, which is extremely rare.

If we could assume that values of $\hat{H}$ and $\hat{\lambda}_n$ inverted from near-ridge (bare) topography using the methodology of *Goff and Jordan* [1988] are equal to H and λ_n for the ARC as a whole, these values could be used along with $\hat{H}$ and $\hat{\lambda}_n$ from sedimented topography to map L within the ARC. However, variability in $\hat{H}$ within the ARC, as measured by *Goff et al.* [1995], seems to be larger than could be explained solely by sedimentation effects. Additionally, even if we could assume that near-ridge basement character held for the entire region, the uncertainty in measurement of $\hat{H}$ and $\hat{\lambda}_n$ would complicate the application of (2.30) and (2.31) to determine L.

Therefore, we endeavor to interpret the effects of sedimentation directly from stochastic measures of topography. In Chapter 2, we investigate how the most common stochastic measures, including height distributions and second-order statistics, are affected sedimentation. We find that sedimentation affects the power spectra of model topographies by causing a drop in power at higher wave numbers, and that the wave number at which this drop occurs varies negatively with κ (Fig. 2.16). Covariance functions express these changes by a lowering of amplitude and a widening of wavelength with increasing L (Fig. 2.17). Power spectra and covariance functions calculated from centerbeam data from within the ARC, as shown in Fig. 3.6 and Fig. 3.7, resemble those of models with low to moderate average sediment thicknesses. However, it is unclear how we might distinguish variations from ideal forms due to sedimentation from those due to basement differences.

Numerical experiments in Chapter 2 show that sedimentation tightens the range of seafloor heights observed. However, this lowering of variability in heights is virtually indistinguishable from the effect of a smaller basement H (see Fig. 2.13). There are other, more subtle, effects of sedimentation on height distribution functions, such as a tendency for peaks to develop at the levels of sediment ponds and for distributions to become positively skewed. However, the skewness is not distinguishable from the effects of long wavelength topography on height distribution functions (see Fig. 2.37 and 2.38). The height distributions calculated from centerbeam data, shown in Fig. 3.8, may bear the results of sedimentation in their changing center values and standard deviations, but without knowledge of basement character they are not useful for studying sedimentation.

As discussed in Chapter 2, slope distribution functions are relatively immune to long-wavelength topographic signals. Slope distribution functions computed from bathymetric data from throughout the ARC are rather smooth, as shown in Fig. 3.9. Even at the small scale presented in this figure, similarities in shape are observable for functions computed from similarly-aged regions of seafloor. Most notably, the functions from young seafloor have low amplitudes at small slopes θ. Amplitudes at 0 are higher for seafloor in the center of the ARC, and lower again for the older (20-29 Ma) crust located in the westernmost portion of the ARC. There are also variations in the slope distribution functions at higher slope. Numerical experiments conducted in Chapter 2 indicate that the shape of slope

distribution at low θ is related to the morphology of ponded regions, while the slope at high θ is a function of the morphology of bare regions. We have found that we can exploit the sensitivity of slope distribution functions to both ponds and steeper regions to invert bathymetric data for information about the seafloor, as described below.

MODELING BATHYMETRIC DATA FROM YOUNG NORTH ATLANTIC SEAFLOOR

As in Chapter 2, we build model topographies upon basement models generated using the methodology of *Goff and Jordan [1988]*. By varying the parameters H, k_n, k_s, ζ_s, and D, basement models can be generated to resemble young seafloor with a variety of heights, roughnesses, and typical hill spacings. Goff-Jordan models lack some of the features of actual topography such as asymmetry due to listric faulting [*Shaw and Smith*, 1990] and long-wavelength topographic effects due to ridge segmentation and crustal thermal subsidence, and may be too rough at scales less than 5-10 m (John Goff, pers. comm., 1995). In this chapter, we assume that these weaknesses are unimportant. The assumption that long-wavelength topographic effects may be ignored is supported by the observation that they do not much influence slope distribution functions, as long as slopes are measured in directions close to plate flowline trends (see Figs. 2.39 and 2.40).

Choice of basement parameters

Goff et al. [1995] estimate that near-axis $\hat{H}$ in the ARC, computed inside elongated regions of gridded bathymetric data, ranges from 140 m to 390 m, that hill width $\hat{\lambda}_n$ ranges from 4 to 14 km (with narrower values associated with the centers of hills), and that aspect ratios vary from 1 to 6. As detailed above, they find similar values for off-axis regions within the ARC. However, visually, hill spacings within the ARC seem to be fairly uniform (see Fig. 3.1). Therefore, we choose to model basement throughout the ARC using a single along-flowline (across-strike) corner basement wave number k_n, fractal dimension D (and thus along-strike hill spacing λ_n), hillstrike direction ζ_s, and hill aspect ratio $a = k_n/k_s$. To choose k_n and D, we compare bathymetric data to model bathymetries generated using various values of these parameters, sedimented to various thicknesses, to bathymetric data. We find that a basement D values of 2.1 to 2.4 and k_n of 0.45 to 0.75

km^{-1} producing models which resemble data, with the best models being generated using a k_n of 0.6 km^{-1} and a D of 2.2. Our choice of D is within the range generally seen on rough seafloor, which has been calculated to be 2.13 from deep-towed data from the Galapagos Ridge [*Goff and Kleinrock*, 1991], and 2.25 from deep-towed data from several sites in the study area (John Goff, pers. comm., 1995). Since we utilize profiles taken horizontally through models (see Fig. 2.7), hillstrike direction ζ_s should be equal to the angle between tracklines and abyssal flowline direction to appropriately sample topography; we take this to be 30°. An a of 5 seems reasonable based on visual estimation of typical hill length-to-width ratios. Examples of the goodness of match between data and models produced using the fixed values of k_n, D, and a are shown in figures 2.43, 2.44, and 2.45.

Choice of grid size

In choosing the appropriate grid spacing at which to generate model topographies, we seek to minimize computational costs, which increase with decreasing d and increasing model size, while staying well below the ruler length u used to measure slope. Since models are subject to smoothing to simulate the effects of Hydrosweep, as described below, much of the difference between models generated with grid spacings less than the centerbeam sampling footprint width of ~200 m is eliminated prior to the measurement of slope. However, actual topography contains potential sediment catches of every size, and using a relatively large d lessens the carrying capacity of the model hillsides, which leads to an underestimation of the thickness of sediments during the inversion process.

To quantify this effect, we generate models with d values of 10, 20, 30, 50, 60, and 100 m, using basement parameters H = 225 m, k_n = 0.6 km^{-1}, k_s = 0.12 km^{-1}, ζ_s = 30°, and D = 2.2, and a variety of sediment thicknesses. We then smooth the models to simulate the sampling effects of Hydrosweep (detailed below), and compute slope distribution functions using a u of 300 m via the procedure described below. For all L, functions from models with d of greater than 10 m resemble histograms generated using a d of 10 m models which have slightly higher sediment thicknesses; thus, as expected, inversions based on the slope statistics of high-d models underestimated L. In our experiment, this offset is constant for L greater than 10 m, and increases with d (Fig.

3.10). We also conduct this experiment using higher values of D, and find that underprediction increases with D, but is not a major factor until $D \geq 2.5$. As a compromise, we use a d of 50 m for our model bathymetries.

We are unable to quantify how much sediment may reside in the many cracks, fissures, and intra-pillow lows that dominate the seafloor below the 10 m scale, but suspect that less than 1 m of sediment is required to smooth irregularities in microtopography. We estimate that this effect, combined with our choice of a relatively large d, leads to a systematic underestimation of sediment thickness of ~1.5-3 m.

Construction of model bathymetries

Using the basement parameters given above and an H of 225 m, sediment is repeatedly numerically added to a randomly-generated 51.1×51.1 km^2 Goff-Jordan model at a rain rate F of 4 m/m.y. for 50 m.y. of model time, using diffusivities κ of 0.01, 0.025, 0.05, 0.1, 0.14, 0.2, 0.25, 0.35, 0.5, and 1.0 m^2/yr. Surfaces are recorded at model times t of 0.625, 1.25, 1.875, 2.5, 3.75, 5, 6.25, 7.5, 8.75, 10, 12.5, 15, 20, 25, 35, and 50 m.y., corresponding to average sediment thicknesses L of 2.5, 5, 7.5, 10, 15, 20, 25, 30, 35, 40, 50, 60, 80, 100, 140, and 200 m. These surfaces may be described using nondimensional parameters K and Λ, introduced in Chapter 2. By (2.21) and (2.23), these sedimented surfaces can be used to produce models for any H and k_n, for $K \in \{0.2, 0.5, 1, 2, 2.8, 4, 5, 7, 10, 20\}$ and $\Lambda \in \{0.0111, 0.0222, 0.0333, 0.0444, 0.0667, 0.0889, 0.1111, 0.1333, 0.1555, 0.1778, 0.2222, 0.2667, 0.3556, 0.4444, 0.6222, 0.8889\}$, where $a = 5$, $D = 2.2$, and $\zeta_s = 30°$. Keeping k_n fixed at 0.6 km^{-1}, we let $H = 225/m_i$ m, $m_i \in \{0.4,0.45,0.5..1.8\}$, which results in H ranging from 125 to 562.5 m.

The range of H and L for which model topographies are generated is based on preliminary inversion results, with minimum and maximum values of H and L being well beyond the expected 95% confidence intervals of these parameters found in the ARC. The lower bound on K is similarly chosen. Choosing an upper bound for K, however, is more difficult. Increasing diffusivity values result in increasingly flat ponds, with all sediment within interconnected ponds reaching some constant value as $K \rightarrow \infty$. However, because long-wavelength topographic effects on actual seafloor tend to impart some tilt, this does

not occur in nature in most cases. Thus, we choose an upper limit for K of 20, observing that little change in across-strike pond curvature occurs for K above 10.

Using all chosen H values we calculate surfaces $h(\mathbf{x})$ for every recorded value of K and Λ. After calculating model surfaces, we simulate the effects of sampling by the Hydrosweep system. This is done by filtering $h(\mathbf{x})$ to form $\tilde{h}(\mathbf{x})$ via

$$\tilde{h}(\mathbf{x}) = \int_{-\infty}^{+\infty}\int_{-\infty}^{+\infty} h(x_1 + x_1', x_2 + x_2') B_p(x_1', x_2') dx_1' dx_2', \tag{3.1}$$

where $B_p(x_1', x_2')$ is a Hanning taper with form [*Goff and Jordan*, 1988]

$$B_p(x_1, x_2) = \begin{cases} \beta_p \cos^2\left((\pi/2)\psi_p(x_1, x_2)\right) & \psi_p \le 1 \\ 0 & \psi_p > 1, \end{cases} \tag{3.2}$$

and

$$\psi_p(x_1, x_2) = \frac{2\psi\sqrt{x_1^2 + x_2^2}}{\pi\delta\phi_{1/2} h_{AV}}, \tag{3.3}$$

$\psi = \arccos((1/2)^{1/4}) = 0.5718...$, $\delta\phi_{1/2} = 0.02$ rad [*Kleinrock*, 1992] is the half angle of a Hydrosweep beam at its half-power point, h_{AV} is the average seafloor depth of the region to which the model is to be compared, and β_p is a normalization constant chosen to make the kernel unimodular.

System noise is introduced into the bathymetric data by the Hydrosweep system. To estimate the variance E^2 of system noise, we examine the RMS variability of centerbeam bathymetric data from relatively low-standing, level regions within the ARC, such as the pond from 4 - 6.5 km along-track in Fig. 3.2. Detailed examination of this pond (Fig. 3.11) shows that the left hand side is flat-lying, with point-to-point variability with variance 5.43 m^2. We find that this variability is typical for data from relatively level regions throughout the ARC. We model this feature of the bathymetric data collection process by adding, to every model surface height, a randomly generated, normally-distributed noise term taken from a sample with a variance E^2 of 5 m^2.

Filtering via (3.1) - (3.3), and the addition of low-amplitude random noise, has relatively little effect on the visual character of topography. However, it does influence the shape of slope distribution functions, particularly at small θ. As a example of the effect of

(3.1) - (3.3) and the addition of random noise, in Fig. 3.12 we show profiles taken from sedimented three-dimensional seafloor models before and after filtering and noise introduction. The models are generated using Goff-Jordan basement parameters H = 225 m, k_n = 0.6 km^{-1}, k_s = 0.12 km^{-1}, ζ_s = 30°, and D = 2.2, sedimented at a rain rate of 4 m/m.y. for 10 m.y. of model time (L = 40 m) using a κ of 0.2 m^2/yr. We assume an h_{AV} of 4000 m and add noise with a variance of 5 m^2. At moderate scales (Fig. 3.12(a)), profiles which incorporate smoothing, with and without noise, are indistinguishable from the unfiltered model surface. Examined in detail, however, the smoothed profiles have degraded peaks, less steep scarps, and more curved sediment pond-hillside intersections (Fig. 3.12(b)). Slope distributions (Fig. 3.12(c)) are highly influenced by the filtering process. Since filtering makes higher slopes lower and lower slopes higher, the amplitude of slope distribution functions at high θ, and at $\theta = 0$, is less after filtering. The shape of the functions at low θ is broader, however, reflecting imposed curvature at the sides of ponds. The random noise term further degrades the amplitude of slope distribution functions at θ = 0, but has little additional effect. The effects of various filtering parameters on inversion results are discussed further below.

INVERSION TECHNIQUE

Slope distributions from models and bathymetric data are calculated so as to minimize the effects of system noise. Then, maximum likelihood estimation is used to choose the range of values of κ, H, and L which best model the data from each subregion of bathymetry.

Calculation of slope distribution functions

As in Chapter 2, we define a slope distribution function $g(\theta,u)$ as the portion of seafloor with slopes that fall within a bin centered at θ, when measured using a ruler of length u. Slope distribution functions are normalized so that

$$\int_0^{\theta_{MAX}} g(\theta,u)d\theta = 1. \tag{3.4}$$

To construct a slope distribution function, slope values $v_{i,i=1..N}$ are calculated so as to minimize and quantify the associated uncertainties $e_{i,i=1..N}$. In this chapter, we use a ruler length u of 300 m, large enough to insure that several soundings are available within $u/2$ of almost every point where slope is calculated, but small enough to sample intrahill ponds.

A bathymetric mapping system produces a rendering of topography

$$\hat{h}(\mathbf{x}) = \tilde{h}(\mathbf{x}) + \varepsilon, \tag{3.5}$$

where $\tilde{h}(\mathbf{x})$ is a smoothed version of actual topography and ε is uncorrelated system noise with RMS variance E^2. Since $\hat{h}(\mathbf{x})$ is not known at all $\mathbf{x}$, we calculate $v_{i,i=1..N}$ via

$$v_i = \frac{1}{u}\left(\sum_{j=1}^{3} \varphi_j \hat{h}\left(\mathbf{x}_i - \xi_{i,j}\right) - \sum_{j=4}^{6} \varphi_j \hat{h}\left(\mathbf{x}_{i+1} - \xi_{i,j}\right) \right) \tag{3.6}$$

where $\xi_{i,j=1..3}$ are the distances between the three closest locations where $\hat{h}(\mathbf{x})$ is known and $\mathbf{x}_i$ and $\xi_{i,j=4..6}$ are the distances between $\mathbf{x}_{i+1}$ and the three closest locations where $h(\mathbf{x})$ is known. We define $\tilde{v}_i$, the slope of the smoothed topography represented by $\tilde{h}(\mathbf{x})$, as

$$\tilde{v}_i = \frac{1}{u}\left(\tilde{h}(\mathbf{x}_{i+1}) - \tilde{h}(\mathbf{x}_i)\right), \tag{3.7}$$

and take e_i as the expected difference between v_i and $\tilde{v}_i$, given by

$$\begin{aligned} \left\langle e_i^2 \right\rangle &= \frac{1}{u^2}\left\langle \left(\left(\sum_{j=1}^{3} \left(\varphi_j \hat{h}\left(\mathbf{x}_i - \xi_j\right)\right) - \sum_{j=4}^{6} \left(\varphi_j \hat{h}\left(\mathbf{x}_{i+1} - \xi_j\right)\right) \right) - \tilde{h}(\mathbf{x}_i) + \tilde{h}(\mathbf{x}_{i+1}) \right)^2 \right\rangle \\ &= \frac{1}{u^2}\left\langle \left(\left(\sum_{j=1}^{3} \left(\varphi_j \tilde{h}\left(\mathbf{x}_i - \xi_j\right) + \varphi_j \varepsilon \right) - \sum_{j=4}^{6} \left(\varphi_j \tilde{h}\left(\mathbf{x}_{i+1} - \xi_j\right) + \varphi_j \varepsilon \right) \right) \right. \\ &\quad \left. - \left(\tilde{h}(\mathbf{x}_i) - \tilde{h}(\mathbf{x}_{i+1}) \right) \right)^2 \Bigg\rangle. \end{aligned} \tag{3.8}$$

Weights $\varphi_{i,i=1..6}$ which minimize (3.8) are chosen by solving

$$\begin{aligned} 0 = \frac{\partial}{\partial \varphi_j}\Bigg\langle & \left(\left(\sum_{j=1}^{3} \left(\varphi_j \tilde{h}\left(\mathbf{x}_i - \xi_j\right) + \varphi_j \varepsilon \right) - \sum_{j=4}^{6} \left(\varphi_j \tilde{h}\left(\mathbf{x}_{i+1} - \xi_j\right) + \varphi_j \varepsilon \right) \right) \right. \\ & \left. - \left(\tilde{h}(\mathbf{x}_i) - \tilde{h}(\mathbf{x}_{i+1}) \right) \right)^2 \Bigg\rangle \end{aligned} \tag{3.9}$$

for $\varphi_{i,i=1..6}$. To do so, we take $\tilde{h}(\mathbf{x})$ to be stationary [*Goff and Jordan*, 1988], such that

$$\left\langle \tilde{h}(\mathbf{x}-\xi_m)\tilde{h}(\mathbf{x}-\xi_n)\right\rangle = C_{\tilde{h}\tilde{h}}\left(\left|\xi_m-\xi_n\right|\right) \tag{3.10}$$

which can be estimated from smoothed model topographies with basement and sedimentation parameters close to the expected results of the inversion procedure. Using (3.10), equation (3.9) may be expanded, and the determination of $\varphi_{i,i=1..6}$ for use in (3.6) is straight-forward. The error estimates e_i are then calculated by expanding (3.8) and substituting in covariance values calculated via (3.10) and $\varphi_{i,i=1..6}$.

We use this procedure to determine slopes and error estimates from both data and models. When calculating the slope distribution from bathymetric data, distances $\xi_1..\xi_6$ are governed by the Hydrosweep sampling frequency. When calculating the slope distribution from model topographies, we simulate the effect of uneven sampling by letting ξ_1 = -50 m, ξ_2 = 50 m, ξ_3 = 100 m, ξ_4 = -100 m, ξ_5 = 0, and ξ_6 = 50 m. We find that the difference between u and its effective length, given by $|(\varphi_1\xi_1 + \varphi_2\xi_2 + \varphi_3\xi_3) - (\varphi_4\xi_4 + \varphi_5\xi_5 + \varphi_6\xi_6)|$, is usually less than 2 m and almost always less than 6 m, so we do not attempt to minimize this quantity.

Where data gaps occur, uncertainties in slope values are high. Thus, we are able to discard slope values highly influenced by data gaps by only incorporating slopes with uncertainties e less than some maximum e_{max}. In this chapter, we let e_{max} be 0.02. Slope values with associated e less than e_{max} are apportioned into bins of width w, here also 0.02. Uncertainties in the slope measurements are of the order of w, so each slope value may contribute to several bins. We calculate the contribution of slope value υ_i to the bin centered at $\theta_{j,j=-J..J}$ via

$$\gamma(\theta_j,\upsilon_i,e_i,w) = \frac{1}{2}\left(\operatorname{erf}\left(\frac{(\theta_j + \mathrm{w}/2)-\upsilon_i}{e_i\sqrt{2}}\right) - \operatorname{erf}\left(\frac{(\theta_j - \mathrm{w}/2)-\upsilon_i}{e_i\sqrt{2}}\right)\right). \tag{3.11}$$

Finally, the slope distribution function at positive values $\theta_{j,j=1..J}$ is computed as

$$g(\theta,u) = \frac{1}{Nw}\sum_{i=1}^{N}\gamma(\theta,\upsilon_i,e_i,w) + \frac{1}{Nw}\sum_{i=1}^{N}\gamma(-\theta,\upsilon_i,e_i,w). \tag{3.12}$$

A total of 50 bins are used for the slope distribution functions in this chapter, so that $g(\theta,u)$ is defined for θ of 0.01 to 0.99. The use of slope measurement errors in the

computation of slope distribution functions results in the smoothing of functions from data (Fig. 3.13(a)). The primary effect on functions from models is to lower the amplitude of the functions at $\theta = 0$ (Fig. 3.13(b)).

Using Maximum Likelihood Estimation to determine best-fitting parameters

The probability of a slope distribution function measured from data, $g_d(\theta,u)$, being equivalent to some model slope distribution function $g_m(\theta,u,\kappa,H,L)$ is equal to the product of the probabilities that the functions are equal at each θ_j. This product of probabilities is referred to as the *likelihood* of the parameters κ, H, and L given $g_d(\theta,u)$. Finding parameters for which likelihood is maximized for some $g_d(\theta,u)$, constructed from N slope values, is equivalent to maximizing

$$Lik(\kappa,H,L) = \prod_{j=1}^{J} p\left(Nwg_d\left(\theta_j,u\right) | Nwg_m\left(\theta_j,u,\kappa,H,L\right)\right). \tag{3.13}$$

If $Nwg_m\left(\theta_j,u,\kappa,H,L\right)$ is large (>50-100) for all θ_j and the expected variance is normally distributed and equal for all j, then solving (3.13) is equivalent to the familiar least-squares method. However, for θ_j > 0.2-0.3, $Nwg_m\left(\theta_j,u,\kappa,H,L\right)$ may be small (typically less than 10) even for large (>1000) N. Also, there is no reason to assume that the expected variances from $g_m(\theta,u,\kappa,H,L)$ are Gaussian, or even uniform. Therefore, we must use more complex analysis to determine likely ranges of κ, H, and L.

If we assume that, for any slope distribution function, $g\left(\theta_{j_1},u\right)$ and $g\left(\theta_{j_2},u\right)$ are independent for all $j_1 \neq j_2$, and $Nwg\left(\theta_j,u\right)$ is an integer and proportional to w, we may take $Nwg\left(\theta_j,u\right)$ to be Poisson distributed [e.g. *Smith and Jordan*, 1988] with mean $Nwg\left(\theta_j,u\right)$ and standard deviation $\left(Nwg\left(\theta_j,u\right)\right)^2$. However, since we allow individual slopes, via (3.11), to contribute to multiple bins, $Nwg\left(\theta_j,u\right)$ is not necessarily an integer. Therefore, we generalize the Poisson distribution, taking $Nwg_m\left(\theta_j,u,\kappa,H,L\right)$ at each θ_j to be the mean μ of a probability distribution given by

$$p(x;\mu) = \frac{e^{\mu}\mu^{x}}{\Gamma(x+1)}. \tag{3.14}$$

This function is equivalent to a Poisson distribution at all integer values of x (Fig. 3.14). The likelihood of parameters κ, H, and L given $g_d(\theta,u)$ is thus computed via

$$Lik(\kappa,H,L)=\prod_{j=1}^{J}\frac{e^{Nwg_m(\theta_j,u,\kappa,H,L)}\left(Nwg_m(\theta_j,u,\kappa,H,L)\right)^{Nwg_d(\theta_j,u)}}{\Gamma\left(Nwg_d(\theta_j,u)+1\right)} \tag{3.15}$$

with the best-fitting model values maximizing $Lik(\kappa,H,L)$. We term the maximum likelihood value M.

For each $g_d(\theta,u)$, we determine an average seafloor age T (Tivey et al., unpub. data, 1995), and estimate H and L. Then, taking F to be equal to sediment thickness divided by T, minimum and maximum κ values κ_{min} and κ_{max} are selected via substitution into (2.23) such that

$$\kappa_{min}=\frac{0.2(L/T)}{0.36\ \mathrm{km}^{-2}H} \tag{3.16}$$

and

$$\kappa_{max}=\frac{19.7(L/T)}{0.36\ \mathrm{km}^{-2}H}. \tag{3.17}$$

Then, for κ between κ_{min} and κ_{max} measured at an interval of $2.5\kappa_{min}$, H between 125 and 560 m measured at an interval of 5 m, and L between 3 and 200 m measured at an interval of 1 m, $Lik(\kappa,H,L)$ is calculated via (3.15) everywhere $K \in [0.2,20]$ and $\Lambda \in [0.0111,0.8888]$. Where K is less than 0.2 or Λ is less than 0.0111 or greater than 0.8888, we set $Lik(\kappa,H,L)$ to 0. Where K is greater than 20 and Λ is between 0.0111 and 0.8888, we set $Lik(\kappa,H,L)$ to $Lik\left(20(L/T)/0.36\mathrm{km}^{-2}H,H,L\right)$, the likelihood associated with the maximum possible value of κ given H and L.

Since $g_m(\theta,u,\kappa,H,L)$ is defined for only a limited number of model parameters, it is necessary to interpolate between defined slope distribution functions to compute (3.15) for many κ (or K), H, and L. To determine how this should be done, we examine how slope distribution functions (computed assuming an h_{AV} of 4000 m and an E^2 of 5 m^2) vary with L, K and H. We find that, for L values such that Λ is between 0.05 and 0.3, the amplitude of $g_m(\theta,u,\kappa,H,L)$ varies positively with $L^{1/2}$ for θ less than θ_0 (as defined in Chapter 2) and negatively with $L^{1/2}$ for θ greater than θ_0, as shown in Fig. 3.15. Variations to $g_m(\theta,u,\kappa,H,L)$ due to changes to K occur only for θ less than θ_0, with θ_0 varying negatively with K. As illustrated by Fig. 3.16, within relatively narrow ranges of K, $g_m(\theta,u,\kappa,H,L)$ varies positively with $K^{1/2}$ for low θ. Comparison of models generated

using constant K and L and varying values of H show that $g_m(\theta,u,\kappa,H,L)$ varies positively with H^{-1} for θ less than θ_0 and negatively with H^{-1} for θ greater than θ_0, as shown in Fig. 3.17, as would be expected given the inverse relationship between H and σ_b shown in (2.32). These relationships are incorporated into our methodology for interpolating between model slope distribution functions, as given in Appendix B.

Best values of κ, H, and L are taken to be those which maximized (3.15). We take the 95% confidence interval to include the models for which $Lik(\kappa,H,L) \geq m$, where m is defined as the value for which

$$\frac{\sum_{\kappa,H,L} Lik(\kappa,H,L)\rho}{\sum_{\kappa,H,L} Lik(\kappa,H,L)} = 0.95, \quad \rho = \begin{cases} 1, & Lik(\kappa,H,L) \geq m \\ 0, & Lik(\kappa,H,L) < m. \end{cases} \tag{3.18}$$

The 95% confidence interval for each model parameter $y \in \{\kappa,H,L\}$ is determined by summing over the probabilities of all models for discrete values of y and finding y_l and y_u such $p(y < y_l) < 0.025$ and $p(y < y_u) \leq 0.975$.

In this chapter, all bounds on inversion results represent a confidence level of 95%.

Uncertainties in inverted parameters

We explore sources of uncertainty inherent in this inversion methodology by inverting model slope distribution functions for model parameters using the model space constructed above. In Fig. 3.18, we show confidence ellipses that result from the inversion of two models with basement H = 225 m and κ = 0.2 m^2/yr, sedimented at a rate F = 4 m/m.y., for 5 and 15 m.y. of model time (L = 20 m and 60 m, respectively), and sampled using an h_{AV} of 4000 m and an E^2 of 5 m^2. For both models, we set N to 400, 800, and 1200, to examine the role that total sample number plays in the confidence assigned to inversion results. Inversion results, along with 95% confidence bounds on individual model parameters, are also given in Table 3.1. We find that uncertainties in H and L are positively correlated, reflecting that a lowering of H and a raising of L have similar affects on slope distributions. For L = 20 m, κ is unbounded by the 95% surface all three values of N used. Uncertainties in κ decrease as sediment cover increases, because the portion of the slope distribution function at low θ becomes more influential on

final likelihood values than the portion at high θ (Fig. 3.19). Conversely, uncertainties in L show an increase with L. Uncertainties in H are relatively insensitive to L for this range of values (see Fig. 3.18 (a) and (c)). Uncertainties in L and κ are uncorrelated, and uncertainties in H and κ show only a slight positive correlation.

Table 3.1. Inversion results/N and L varied.

	N = 400	N = 800	N = 1200
L = 20	H = 225 +50/-25 L = 20 +21/-9 κ = 0.2 +∞/-0.12	H = 225 +25/-20 L = 20 +10/-8 κ = 0.2 +∞/-0.11	H = 225 +20/-20 L = 20 +8/-7 κ = 0.2 +∞/-0.1
L = 60	H = 225 +65/-30 L = 60 +46/-18 κ = 0.2 + 0.37/-0.09	H = 225 +40/-20 L = 60 +26/-14 κ = 0.2 + 0.26/-0.07	H = 225 +25/-20 L = 60 +19/-12 κ = 0.2 + 0.11/-0.06

As shown in Table 3.1, the uncertainties associated with each parameter addressed separately also vary with both L and N. Uncertainties in all three parameters vary inversely with sample size. The confidence interval for κ shrinks with increasing L, while L and H uncertainties increase with L. To further study this effect, we examine error bounds on L and H, given the other Goff-Jordan basement parameters assumed in the construction of basement models, for a range of H, L, and κ, in terms of H and non-dimensional parameters Λ and K. For constant Λ and K, the uncertainties associated with inverted values of L and H scale with H. As seen in Fig. 3.18, uncertainties associated with inverted values of L and H are affected by the average sediment thickness of the topography being inverted. In Fig. 3.20, we explore how 95% confidence bounds on H and L vary with Λ, for K = 1 (very low), 4 (equivalent to a κ of 0.2 m^2/yr, for an H of 225 m, other Goff-Jordan parameters as defined above, and an F of 4 m/m.y.), and 20. In Fig. 3.21 we specifically examine the 95% confidence bounds on L when H is 225 m and F is 4 m/m.y. Uncertainties are greatest when K is low or when L is low. When both K and Λ are low, uncertainties are so large that the inverted values of L are useless, e.g. if H is 225 m then the 95% confidence bounds on an inverted sediment thickness of 10 m, from a model generated using a K of 1, extend from 3 to 59 m. Higher K values yield smaller confidence bounds, and while the absolute range in uncertainty increases with increasing

sediment thickness, uncertainty as a percentage of L stays constant for L from 20-30 through 100 m, for constant K between 1 and 20.

We find that κ is least reliably determined parameter. Even when model seafloors are inverted, the 95% confidence interval is unbounded when L is low, at moderate κ. This is partially caused by the upper limit of 20 imposed on K. Also, as shown in Fig. 3.16, model slope distribution functions do not change much in response to increasing κ, indicating that, even if we produced models with very high K, it is unlikely that they would produce likelihoods much less than those of models with K of 20.

This raises the question of the meaning of confidence intervals when one parameter is unboundable. By (3.18), m, the cutoff likelihood for the 95% confidence interval, expands as the range over which parameters are calculated grows. $Lik(\kappa, H, L)$ is much less than maximum likelihood M for L and H beyond our model bounds, so m should not be changed by the expansion or moderate contraction of the bounds on these parameters. However, if likelihoods along the maximum κ boundary for a given inversion are not much less than M, an expansion or decrease of the range over which κ is examined will change total likelihood, and thus m and the 95% confidence region for all three model parameters.

We find, in contrast, that the 95% confidence intervals for H and L are not very sensitive to the upper value of κ. A 25% reduction in the maximum value of κ considered does not alter the confidence intervals on H, as shown in Table 3.1, and changes the confidence intervals of L by at most one meter. Decreasing the range of κ also does not effect the lower bounds on the confidence intervals for κ for the L = 20 m model for all N but does shrink the confidence intervals for the L = 60 m model by 0.01-0.04 m^2/yr. The relative insensitivity of the confidence intervals to the range of κ considered occurs because, although decreasing the maximum κ boundary will decrease the likelihood of any particular L or H, the decrease in likelihood for a L or H will be roughly proportional to the original likelihood of the values.

Sensitivity of results to basement and sampling parameters

In our inversion methodology, we assume that, of the five Goff-Jordan basement parameters, only H is variable. In this section, we investigate systematic errors in our

inversion results caused by misestimation of basement Goff-Jordan parameters k_n, k_s, D, and ζ_s, average regional seafloor depth h_{AV}, and the variance E^2 of systemic noise.

As discussed in Chapter 2, the slope distribution function of an unsedimented Goff-Jordan model topography is Gaussian, with variance σ_b^2 determined by the length of the measuring ruler u and Goff-Jordan parameters H, k_n, k_s, D, and ζ_s. As sediment is added to Goff-Jordan models, slope distribution functions maintain the form of those of basement models for θ above 0.1-0.2, and are functions of the basement parameters as well as κ and L at lower θ. The balance in amplitude between high and low θ is primarily a function of the percentage of bare seafloor, which, from Fig. 2.15, is strongly dependent on Λ but is also sensitive to K. When k_n, k_s, D, or ζ_s are misestimated, the inversion procedure, in essence, tries to balance achieving appropriate values of σ_b^2, percent bare seafloor, and the curvature of pond surfaces. Thus, if the actual value of along-track corner wave number, k_z', is different than the preset model k_z of 0.5231 (via (2.32)), the result of the inversion procedure will estimate an H different from true H' so that

$$\sigma_b\left(k_z = 0.5231 \text{ km}^{-1}, H\right) \approx \sigma_b\left(k_z', H' = 225 \text{ m}\right). \tag{3.19}$$

Simultaneously, the inversion technique attempts to match the amplitude of the slope distribution functions at higher θ. Amplitudes at high θ are similar where similar amounts of seafloor are free of sediments From (2.27), for $D = 2.2$ and $a = 5$, this occurs when the relationship between true L', κ', and H' and inverted values L, H, and κ follows

$$(K')^{-0.16}(\Lambda')^{0.5} \approx (K)^{-0.16}(\Lambda)^{0.5}. \tag{3.20}$$

The inversion algorithm also attempts to match model to data slope distribution functions at low θ through the manipulation of L and κ as well as the other Goff-Jordan basement parameters. Where L/H and L'/H' are equal, this is achieved when

$$\left(\frac{\kappa'}{F'}\right)H'k_z' \approx \left(\frac{\kappa}{F}\right)Hk_z. \tag{3.21}$$

To illustrate how inverted values of H, L, and κ are affected by the misestimation of k_n, we generate model topographies built upon basements with parameters H' = 225 m, D = 2.2, $\zeta_s = 30°$, and $a = 5$ and with k_n' of 0.4, 0.5, 0.7, and 0.8 km^{-1}. Fixing a at 5, k_s' for these models is 0.08, 0.1, 0.14, and 0.16 km^{-1}, respectively. These basements are sedimented at a rate F of 4 m/m.y. for 25 m.y. of model time, using a diffusivity κ' of 0.2

m^2/yr. Surfaces are recorded at model times of 2.5, 5, 10, 15, and 25 m.y., corresponding to L' values of 10, 20, 40, 60, and 100 m. We refer to these models as test models; slope distribution functions calculated from the test models are referred to as test slope distribution functions. Calculations of all slope distribution functions assume an h_{AV} of 4000 m and an added random system noise with variance E^2 of 5 m^2. The test slope distribution functions are then inverted for H, L, and κ as above. In this inversion and all following inversions in this section, we assume an N of 800.

The results of the inversion procedure are shown in Fig. 3.22. Primarily driven by (3.19), test models with k_n' above 0.6 km^{-1} resulted in H greater than H', and k_n' below 0.6 km^{-1} resulted in H less than H'. When hill spacing is misestimated by 50% (k_n' = 0.4 km^{-1}), the underprediction of H may be as large as 25%.

The inverted values of L from the test models can be best understood by recasting (3.20). Given the assumed Goff-Jordan basement parameters,

$$L \approx H\left(\frac{L'}{225\text{ m}}\right)\left(\frac{0.6\text{ km}^{-1}}{k_n'}\right)^{1/2}\left(\frac{\kappa}{0.2\text{ m}^2/\text{yr}}\right)^{1/4}. \qquad (3.22)$$

When k_n' is greater than 0.6 km^{-1}, the effect of an overlarge H from (3.19) is damped by the $\left(0.6\text{ km}^{-1}/k_n'\right)^{1/2}$ term. Similarly, this term partially counteracts the effect of the underestimation of H on L when k_n' is less than 0.6 km^{-1}.

We found that κ is also very sensitive to misestimations in basement parameters. However, since L/H and L'/H' are rarely equal, (3.21) does not reliably determine κ.

We illustrate matches between models with differing basement parameters in Fig. 3.23 and 3.24. In Fig. 3.23, a test model generated with a k_n' of 0.4 km^{-1}, bearing an average sediment thickness L' of 100 m after 25 m.y. of model time, has an inverted L of 91 +46/-23 m, an H of 170 +40/-25 m, and an apparent diffusivity of 0.16 +0.10/-0.07 m^2/yr. These inverted values correspond to a seafloor with lower, more closely spaced hills. However, using a ruler of 300 m, the underlying basement topographies have very similar slope distributions, with σ_b = 0.185 and σ_b' = 0.184. Via (3.21) and (3.22), an L of 88 m and κ of 0.16 m^2/yr are predicted, well within the uncertainty bounds on L and κ.

In Fig. 3.24, a test model generated with a k_n' of 0.8 km^{-1}, with an average sediment thickness L' of 40 m after 10 m.y. of model time, has an inverted L of 38 +18/-10 m, an

H of 260 +40/-25 m, and an apparent diffusivity of 0.38 +.52/-.21 m^2/yr. The underlying basement topographies have less similar slope distributions than those of Fig. 3.23, with σ_b = 0.284 and σ_b' = 0.298. Equations (3.21) and (3.22) predict an L of 46 m and κ of 0.22 m^2/yr. The discrepancy between these values and the most likely inversion results is due to the underprediction of H, represented by the low value of σ_b. Because the model basement associated with an H of 260 m is lower at high θ than the test model basement, more bare seafloor is required to match the shape of the test slope distribution function at high θ than is predicted by (3.21) and (3.22).

Goff et al. [1995] estimate that a varies from 2.5 to 5. To investigate the effect of a misestimation of a, we generate test models using Goff-Jordan basement parameters of H' = 225 m, D = 2.2, ζ_s = 30°, and k_n' = 0.6 km^{-1}, and with k_s' of 0.3 and 0.075 km^{-1}, corresponding to a values of 2 and 8. Sediment is applied for 10 m.y. of model time at a rain rate of 4 m/m.y. using a κ' of 0.2 m^2/yr. Slope distribution functions are computed from the resulting surfaces, assuming an h_{AV} of 4000 m and an added random system noise with variance E^2 of 5 m^2, and inverted for H, L, and κ. Results, along with those expected for a standard a of 5, are given in Table 3.2.

Table 3.2. Inversion results/a variable; bold denotes model generated with correct parameters. % Bare is the percent of seafloor where sediment thickness is less than 1 m.

a	2	**5**	8
k_z'	0.5408	**0.5231**	0.5210
σ_b'	0.2508	**0.2451**	0.2445
σ_b	0.2560	**0.2451**	0.2506
H	235 +50/-35 m	**225 m**	230 +30/-25 m
L	38 +29/-17 m	**40 m**	43 +16/-11 m
κ	.06 +.02/-.04 m^2/yr	**0.2 m^2/yr**	.33 +.49/-.14 m^2/yr
% Bare	40.2%	**32.7%**	30.3%

We find that misestimation of a does not much affect H, although the small effect that is seen is opposite to what would be predicted, were the satisfaction of (3.19) the primary driver of the inversion procedure. For the test model in which a is set to 2, an H of 235 m corresponds to a σ_b of 0.2560, close to the value of 0.2508 exhibited by the test model.

Since hills for this test model are relatively short relative to their lengths, the ζ_s value of 30° causes some along-pond tilt to be included in slope measurements, which leads to a wide slope distribution function at low θ and a low inverted value of κ. At the same time, since hills are relatively stubby in map view, sediment is efficiently removed from highs. Thus, slope distribution functions from this test model resemble those from higher-a models produced using a slightly lower L. For the test model in which a is set to 8, an H of 220 or 225 m would have produced inverted values of σ_b closer to σ_b'. However, even given the inverted H value of 230 m, the variation between σ_b and σ_b' is not large. Since hills for this test model are long, less along-pond tilt is measured by slope distribution functions, leading to the overestimation of κ. The somewhat lower percentage bare seafloor leads to an overestimation of L.

To examine how the misestimation of D would affect inversion results, we generate test models using parameters of H' = 225 m, ζ_s = 30°, k_n' = 0.6 km^{-1}, k_s' = 0.12 km^{-1}, and D of 2.075, 2.35, and 2.5. Sediment is applied for 10 m.y. of model time at a rain rate of 4 m/m.y. using a κ' of 0.2 m^2/yr. Slope distribution functions are computed from the resulting surfaces, assuming an h_{AV} of 4000 m and E^2 of 5 m^2, and inverted for H, L, and κ. Results, along with those expected for a standard D of 2.2, are given in Table 3.3.

Table 3.3. Inversion results/D variable; bold denotes model which agrees totally with model assumptions.

D	2.075	**2.2**	2.35	2.5
λ_n'	5.6 km	**5.4 km**	5.1 km	4.7 km
σ_b'	0.2047	**0.2451**	0.3114	0.4042
σ_b	0.2234	**0.2451**	0.2833	0.3160
H	205 +25/-20 m	**225 m**	260 +40/-30 m	290+30/-35 m
L	42 +15/-12 m	**40 m**	37 +18/-12 m	28 +12/-12 m
κ	.23 +.28/-.09 m^2/yr	**0.2 m^2/yr**	.21 +.59/-.10 m^2/yr	.11 +∞/-.06 m^2/yr

As with misestimated corner wave numbers, small misestimations of D' lead to large errors in H but have relatively little effect on the inverted value of L for D between 2.075 and 2.35. Apparent diffusivity κ is also relatively impervious to D.

Equations (3.19)-(3.22) were developed using a D of 2.2, and so cannot be used to interpret the inversion results directly, but the underlying relationships, based on attempts to match percentages of bare seafloor between test functions and model space, hold. Generalizing (3.22) and substituting in parameters from the above experiments produces

$$L \approx H\left(\frac{40\text{ m}}{225\text{ m}}\right)\left(\frac{\lambda_n'}{5.4\text{ km}}\right)^B\left(\frac{\kappa}{0.2\text{ m}^2/\text{yr}}\right)^C \tag{3.23}$$

where λ_n' is the along-flowline hill spacing of the test models. Where D' is greater than 2.2, H is overestimated. However, via (2.5), λ_n' is less than 5.4 km and the effect of the large H on L is dampened. Where D' is less than 2.2, the opposite occurs, and L is again only slightly changed. In the case where $D' = 2.5$, even the high inverted H value is not large enough to allow σ_b to equal σ_b', so that L is further underestimated because not as much sediment cover is required to match the shape of the test slope distribution function.

We also make assumptions about ζ_s and E^2, and round h_{AV} to the nearest kilometer. We investigate the effects of the misestimation of these parameters by again generating test models with Goff-Jordan model parameters $H' = 225$ m, $k_n' = 0.6$ km^{-1}, k_s' of 0.12 km^{-1}, and $D' = 2.2$, and varying ζ_s, h_{AV}, and E^2. The resulting test slope distribution functions are inverted assuming a constant ζ_s of 30°, h_{AV} of 4000 m, and a system noise variance of 5 m^2. The results are given in Table 3.4.

Table 3.4. Inversion results: ζ_s, h_{AV}, and RMS system noise E^2 variable; bold denotes model which agrees totally with model assumptions; italics indicate value altered from model assumptions.

ζ_s	**30°**	*0°*	30°	30°	30°	30°	30°
h_{AV}	**4000 m**	4000 m	*3000 m*	*5000 m*	4000 m	4000 m	4000 m
noise variance E^2	**5 m^2**	5 m^2	5 m^2	5 m^2	*1 m^2*	*10 m^2*	*25 m^2*
σ_b'	**0.2451**	0.2692	0.2451	0.2451	0.2451	0.2451	0.2451
σ_b	**0.2451**	0.2833	0.256	0.2342	0.2451	0.2451	0.2451
H	**225 m**	260 m	235 m	215 m	225 m	225 m	225 m
L	**40 m**	46 m	44 m	35 m	40 m	40 m	39 m
κ (in m^2/yr)	**0.2**	0.48	0.24	0.16	0.28	0.16	0.11

When $\zeta_s = 0°$ instead of 30°, the measured value of along-track σ_b' is less than σ_b, so H is overestimated in compensation. However, since $k_n = k_n'$, the hill-spacing term $\left(0.6\ \text{km}^{-1}/k_n'\right)^{1/2}$ in (3.22) does not act as a damper. Via (3.21), κ has a good chance of being overestimated since k_n' is greater than $k_{\zeta=30°}'$. Therefore, L/H is likely to be greater than or equal to L'/H'. In our experiment, this is the case. The inversion methodology make matters worse by overpredicting the minimum H required to match σ_b'.

When h_{AV} is mischosen, different problems occur. The amount of smoothing which topography is expected to have undergone is determined by h_{AV}, with less expected for lower h_{AV} and more expected for higher h_{AV}. As shown in Fig. 3.13, the major effect of smoothing is that higher slopes are lowered and lower slopes are raised. Therefore, smoothed slope distribution functions have lower amplitudes both at high θ and at $\theta = 0$. When h_{AV} is overestimated, as in the inversion in which the test model generated with h_{AV}' = 3000 m is inverted, the higher amplitude of the test slope distribution function is misinterpreted as corresponding to a seafloor with higher H and, via (3.22), higher L. The overestimation of L is increased because κ is also overestimated in our numerical experiment. Likewise, when h_{AV} is underestimated, as in the inversion in which the test model generated with h_{AV}' = 5000 m is inverted, the lower amplitude of the test slope distribution function is misinterpreted as corresponding to a seafloor with lower H and, via (3.22), a lower L. The underestimation of L is decreased because κ is also underestimated.

Small misestimation of random noise has no influence on inverted values of H or L, but does affect inverted values of κ. When too much noise is expected, κ is overestimated because slopes are lower than anticipated. Likewise, when too little noise is expected, κ is underestimated because slopes are too high. When random noise is greatly underestimated (i.e. when true E^2 is 25 m^2), L, H, and κ are all slightly underestimated.

Some subregions probably consist of areas with varying values of L, κ, and basement parameters. To investigate how having seafloor of varying character within a single subregion might influence inversion results, we average model slope distribution functions (h_{AV} = 4000 m, E^2 = 5 m^2) associated with different values of L, κ, and H, and invert for these parameters. We take the other four basement parameters to be equal to the values we use to model the ARC, as described above. We find that if we average the slope

distribution functions associated with equal values of L and H and two different values of dimensionless diffusivity K, K_u and K_l, where $K_u \leq K_l \leq 3K_u$ and K_u and K_l are between 1 and 20, the inverted value of H is not affected, L is subject to an underestimation of 2% or less, and the inverted value of κ is with a few percent of $(\kappa_u \kappa_l)^{1/2}$, the form suggested based on how the amplitude of slope distribution functions vary with K in Fig. 3.16, where κ_u and κ_l are the diffusivity values corresponding to K_u and K_l, respectively. If, instead, we average the slope distribution functions associated with equal values of H and K and two different values of L, L_u and L_l, for $K \geq 1$, we find that the inverted value of L is within a few meters of $(L_u L_l)^{1/2}$, the form suggested based on how the amplitude of slope distribution functions vary with L in Fig. 3.15, and that H and K are misestimated by at most a few percent.

Since σ_b is inversely related to H (see (2.32)), one might expect that the average of slope distribution functions associated with equal values of L and K and two different values of H, H_u and H_l, would be within a few meters of $0.5(1/H_u + 1/H_l)$. We actually find that, for an H_u of 180 m and H_l of 250 m, the inverted value of H is 220 m, 11 m higher than would be expected if the basement topography drove the parameter inversion procedure, but fortuitously close to the average of H_u and H_l, for all L. We find that, for these values of H, L and κ are misestimated by at most a few percent.

While the values of H, L, and κ we invert here suggest that, where different values of a parameter are represented with a subregion, the inverted value does not represent an average, as long as the variation is not large the inversion result is not extremely far from the regional average. Again, however, an underestimation, albeit rather small, of the varying parameter occurs.

The experiments discussed within this section show that L is relatively insensitive to small misestimations of basement and sampling parameters. However, since the majority of possible errors tend to result in the underestimation of L, effects can be compounded resulting in significant misestimation of L. For example, a basement with parameters H' = 225 m, k_n' = 0.6 km^{-1}, k_s' = 0.2 km^{-1}, D = 2.35, and ζ_s = 30°, numerically sedimented for 10 m.y. of model time using a κ of 0.2 m^2/yr, filtered using an h_{AV}' of 5000 m and assuming a system noise E^2 of 25 m^2, and inverted for H, L, and κ using a h_{AV} of 4000

m, is subject to the underestimation of L from the underestimation of ship-to-seafloor distance, system noise, and D and the overestimation of a. The inversion results are H = 235 +40/-25 m, L = 28 +21/-11 m, and κ = 0.08 +0.12/-0.04 m^2/yr, with the underestimation of L large enough to affect conclusions about sediment distribution.

The inverted values for H are shown to be even more sensitive to other basement parameters, making the correct interpretation of this parameter somewhat problematical.

Apparent diffusivity κ is very sensitive to the misestimation of basement parameters. These experiments show that greater understanding of seafloor stochastic character, in general, will be necessary before inverted values of κ can be reliably interpreted. This, however, does not preclude the usage of inverted values of κ for the construction of realistic models of topography, but simply indicates that, for slightly different geometries, a different κ would perhaps be called for to recreate seafloor with the same character.

RESULTS: HILL-CENTERED REGIONS

Using the procedure described above, apparent values of H, L, and κ are inverted for each of the 15 hill-centered subregions we construct to study how the stochastic character of hilly topography varies throughout the ARC. The inversion results are given in Fig. 3.25 and Fig. 3.26 and in Table 3.5, along with region center locations, 95% confidence bounds, and the number of points N at which slope is measured in each subregion.

Table 3.5. Inversion results from hill-centered subregions within the ARC

Site	Location	N	T, Ma	H, m	κ, m^2/yr	L, m
H1	25.80°N, 45.55°W	1117	4.14	220 +15/-15	.30 +∞/-.24	8 +5/-3
H2	25.80°N, 46.05°W	525	8.43	275 +70/-35	.12 +∞/-.06	24 +22/-10
H3	25.84°N, 46.60°W	1157	12.44	245 +20/-25	.38 +∞/-.17	40 +12/-9
H4a	25.94°N, 47.35°W	1367	17.38	240 +25/-20	.30 +.15/-.09	82 +23/-15
H4b	26.26°N, 47.35°W	843	18.05	250 +40/-30	.15 +.15/-.06	56 +24/-16
H5	26.27°N, 48.05°W	1689	23.70	255 +20/-20	.18 +.17/-.08	44 +11/-9
H6	26.26°N, 48.53°W	961	26.11	260 +25/-25	.10 +∞/-.04	31 +10/-9
H7	26.86°N, 48.37°W	691	27.48	300 +50/-30	.28 +∞/-.18	42 +20/-10
H8	26.86°N, 47.87°W	1181	24.73	300 +35/-25	.28 +∞/-.16	38 +12/-8
H9	26.92°N, 47.27°W	1547	20.32	280 +25/-25	.30 +∞/-.12	49 +14/-10
H10	27.00°N, 46.36°W	1222	14.39	230 +25/-15	.15 +.16/-.05	42 +14/-9
H11	26.60°N, 46.00°W	979	11.21	270 +40/-30	.78 +∞/-.3	78 +27/-17
H12	26.94°N, 45.60°W	923	9.31	300 +60/-30	.48 +∞/-.19	61 +29/-15
H13	26.70°N, 45.10°W	891	5.57	275 +45/-25	.32 +∞/-.24	15 +12/-4
H14	26.22°N, 45.25°W	466	4.24	310 +75/-35	.70 +∞/-.57	17 +16/-6

Sediment thickness

Average sediment thickness L is clearly a function of seafloor age. The same-age variations in sediment thickness are probably partially due to differences in the sediment flow characteristics between regions, with anomalously low L values in regions which lose sediments into external deeps and high values in locations which receive sediments from external sources. Because of the potential for medium- and long-distance flow, we do not use L inverted from these subregions to study sediment thickness variability with seafloor age, instead using inverted values of L from the basin-centered data groupings, as discussed below.

Basement variability

Inverted values from hill-centered regions are appropriate for studying variability in H and κ. We find that H varies from 220 m to 310 m, with a mean $\overline{H} = 267 \pm 28$ m. The variation in H correlates with the ridge-segment boundary that passes through the center of the corridor. The average abyssal hill amplitude in the eight areas north of the segment boundary is somewhat higher ($\overline{H} = 283 \pm 26$ m) than in the seven areas to the south ($\overline{H} = 249 \pm 17$ m), implying a persistent discontinuity in the ridge-crest constructional processes. (The confidence bounds given for mean values of H, L, and κ in this section, and throughout this thesis, represent the standard deviations of the distributions of the quantities included in the calculations.)

Apparent diffusivity

Apparent diffusivity values range from 0.1 to 0.78 m^2/yr, with an average apparent diffusivity $\overline{\kappa} = 0.32 \pm 0.20$ m^2/yr. The average apparent diffusivity south of the major segment boundary, 0.22 ± 0.11 m^2/yr, is lower than north of the boundary (0.41 ± 0.22 m^2/yr), though not significantly so. This mainly reflects the observed correlation between inverted values of H and κ. Like L, κ seems to also vary with seafloor age, with higher values on younger seafloor than on older seafloor. This could, in part, also be caused by a correlation between H and κ, discussed below. This might also be a side effect of the relationship between κ and F for seafloor with a given amount of curvature, as

parameterized by K (see (2.23)). Since we calculate F as L divided by T, if L is low and T is high then F is also low; such is the case for the older seafloor within the ARC. Practically speaking, since the maximum value K we allow is 20, 25 Ma seafloor with an H of 250 m and an average sediment thickness of 40 m can have an inverted κ of at most 0.35 m^2/yr. Thus, given the range of uncertainty in the inversion results, κ of the older seafloor could possibly exhibit the range seen on younger topography.

Comparisons between models and data

The confidence intervals as given in Table 3.5 are not much larger than those calculated when models themselves are inverted, as discussed above and shown in Fig. 3.20 and 3.21. This indicates that good matches are achieved between model and data slope distribution functions.

In Fig. 3.27, we show $g_d(\theta,u)$ and best-fitting $g_m(\theta,u,\kappa,H,L)$ for the regions shown in figures 2.43 (H2), 2.44 (H3), and 2.45 (H11) and for the region centered at 27.0° N, 46.4° W (H10), one of the few for which κ is well-bounded. The model slope distribution functions are able to match most of the features of the $g_d(\theta,u)$, including amplitude at $\theta = 0$ and slope at low and high θ. In Fig. 3.28, we show that power spectra computed from the data and from best-fitting model topographies also seem reasonably similar, particularly for subregions H2 and H3. However, there is marked differences between power spectra from data and models for wave numbers above ~2 for subregions H10 and H11. Unfortunately, despite our investigations of Chapter 2, our understanding of how sedimentation affects power spectra is not sufficient to determine whether this high wave number discrepancy is due to misestimation of basement parameters, errors in the inversion procedure, long-wavelength topographic effects, differences between basement character and Goff-Jordan models, or other causes.

The 95% confidence intervals of inverted values of H, L, and κ for these subregions vary in magnitude (Fig. 3.29), with that of region H10, with slope calculated from N = 1222 data points, the smallest, and region H2, with slope calculated from N = 525 data points, the largest. The error ellipses show similar tradeoff between H and L to that observed in Fig. 3.18. Although the error ellipses seem rather large, models within the

ellipses do not differ much from ideal models, particularly when N is large. In Fig. 3.30, we show $g_d(\theta,u)$, $g_m(\theta,u,\kappa,H,L)$, and four slope distribution functions whose H, L, and κ lie on the 95% confidence contour for H10.

Confidence bounds

All but four of the hill-centered regions are unbounded above for κ at the 95% confidence level. This occurs because, for K above 10, $g_m(\theta,u,\kappa,H,L)$ change little with increasing κ (see Fig. 3.16), and because we bound model space such that only κ less than or equal to κ_{max}, as defined by (3.17), are considered. As shown above, this truncation of possible κ models does not much affect confidence intervals for H or L.

We demonstrate this for subregions H2, H3, H10, and H11 by computing the likelihood of L (Fig. 3.31) and H (Fig. 3.32) for the entire model space and for κ below $15(L/T)/\left(0.36\text{km}^{-2}H\right)$, which shrinks model space by 25%. The likelihoods computed using all of model space, shown by solid lines, are greater than the likelihoods from the smaller model spaces, shown by dashed lines, for regions H2, H3, and H11. Shrinking the model space does not effect the likelihoods of various H and L for H10. For H2 and H3, the basic form of the likelihood functions is not changed, so the 95% bounds on H and L are not altered. For H11, where κ is fairly high, shrinking the range of κ considered reduces the width of the likelihood functions of L and H, but 95% confidence intervals are only slightly affected, reducing the upper bound on L by 3 m and on H by 5 m.

It might be expected that changing the range of κ considered would have a fairly large effect on the lower bounds on confidences for κ. Examining $Lik(\kappa)$ for these same four subregions (Fig. 3.33) shows that our upper bounding of κ does seem to truncate off much of the tails of the likelihood functions for higher κ for H2, H3, and H11, while H10 is well-bounded at both high and low κ. However, for H2, H3, and H11, decreasing the range over which $Lik(\kappa)$ is defined by 25% lowers the minimum bound on κ by only 0.005, 0.01, and 0.01 m^2/yr, respectively, and has no effect on the bounds on H10. Therefore, we do not expect that increasing the range over which κ is modeled would much increase the lower bounds on the 95% confidence interval for κ.

Correlations between parameters

In Fig. 3.34, we investigate whether correlations exist between inversion results. Inverted values of H and L appear to be totally uncorrelated, with correlation coefficient r = -0.0436. Correlation does exist, however, between H and κ, at the 86% confidence level, with r = 0.403. There also may be some correlation between L and κ, but only at a confidence level of 56%. The correlation between H and κ may indicate that sediment mobility scales non-linearly with seafloor slope. We also note that the highest diffusivity values seem to lie over subregions dominated by inside corner crust, though the necessarily large size of the subregions makes this effect impossible to quantify using our present inversion methodology.

Comparison with Goff-Jordan methodology inversion results

Goff et al. [1995] study seafloor RMS height $\hat{H}$ and along-flowline hill spacing $\hat{\lambda}_n$ along the ARC's southern segment. To compare our inversion results to theirs, we must compensate for the effects of sedimentation on their inverted values of $\hat{H}$ and $\hat{\lambda}_n$ for our hill-centered regions which lie in the southern segment of the ARC (H1, H2, H3, H4a, H4b, H5, and H6). In Chapter 2, we find that, for model parameters typical of the ARC, an average sediment thickness L reduces the RMS height of the seafloor by roughly $L/2$. Subtracting $L/2$ from our inverted values of H reveals that we observe the same trends in height variability with seafloor age as *Goff et al.* [1995] (Fig. 3.35), although there is some offset between our best estimates and those of *Goff et al.* [1995].

Goff et al. [1995] measure along-flowline hill spacings as range from 5.7 to 12.5 km. In Chapter 2, we develop an empirical relationship for how sediment changes hill spacing through time, which allows us to compare estimates of seafloor hill spacing based on our λ_n, L, and H to the inversion results of *Goff et al.* [1995]. Our empirical relationship estimates that, for K and Λ within the range of the values we find in the ARC, sedimentation increases hill spacings by $1.3\lambda_n\Lambda$. Applying this relationship to the inversion results from the southern section of the ARC (assuming, via (2.5), a basement hill spacing of 5.37 km), we find that for five of the seven southern hill-centered regions, our estimates of hill spacing are near those of *Goff et al.* [1995] (Fig. 3.36). For the two

regions where our results are significantly different, one is from 8-12 Ma crust within our subregion H3 which *Goff et al.* [1995] find to have a very high H and to be non-lineated. In our experience with this region, in which lineated topography is interrupted by a pseudofault, we have found that inversion results using the methodology of *Goff and Jordan* [1988] are very sensitive to how data is subdivided, and that, except for where they are interrupted, the hills within this area resemble topography from throughout the ARC, so we feel that our choice of k_n, and thus our other inversion results, is valid for this region.

There is also a large difference between our prediction of hill spacing and the inversion results of *Goff et al.* [1995] for the oldest seafloor within the ARC that they examined. This may have implications for our inversion results, as we discuss in the following section. In general, though, we find that the results of *Goff et al.* [1995] support our inversion methodology for basement and sedimentation parameters.

Corrections to inverted parameters

The model basement parameters k_n, k_s, ζ_s, and D used to generate the topography which underlies all sedimented models used during the inversion process are somewhat arbitrarily chosen. The observations above that inverted Goff-Jordan parameters do not always equal those values predicted from our inversion methodology suggests that, in some parts of the ARC at least, the basement parameters as we have chosen them do not well-model actual topography. Of these parameters, we are most concerned about k_n. In particular, from Fig. 3.36, and from the covariance functions given in Fig. 3.7, hill spacing for the oldest seafloor seems larger than can be assumed using a k_n of 0.6 km^{-1}, particularly since this region is not particularly heavily sedimented. This also holds for subregion H1 and, based solely on Fig. 3.7, subregion H13. Fig. 3.7 also suggests that the heavily-sedimented region H11 may have hills which are more closely spaced than can be expected for a seafloor where k_n is 0.6 km^{-1}, while power spectra in Fig. 3.28 can be interpreted as showing a higher corner wave number than 0.6 km^{-1}.

For regions H1, H6, and H13, if k_n is actually less than 0.6 km^{-1}, then H should be adjusted upward so that σ_b, computed via (2.32), is unchanged. Similarly, if k_n is actually greater than 0.6 km^{-1} in subregion H11, H for that region should be adjusted downward

using the same procedure. Sediment thickness should also be adjusted so that the amount of bare seafloor remains the same, as discussed above. Assuming that κ is unchanged, we can compute adjusted average sediment thickness $\underline{L}$ by recasting (3.23) as

$$\underline{L} = \underline{H}\left(\frac{L}{H}\right)\left(\frac{\underline{k}_n}{0.6\ \mathrm{km}^{-1}}\right)^{1/2}, \tag{3.24}$$

where $\underline{H}$ and $\underline{k}_n$ are the adjusted values of H and k_n.

To determine if other values of $\underline{k}_n$ better describe the variations in hill spacing observed by *Goff et al.* [1995], as shown in Fig. 3.36, we use (2.32) to determine $\underline{H}$, then use the alternate $\underline{k}_n$ and $\underline{H}$ to compute $\underline{L}$ via (3.24). We then use (2.5) to compute adjusted hill spacing $\underline{\lambda}_n$, and apply (2.31) to predict the spacing of sedimented hills $\hat{\underline{\lambda}}_n$. We find that most of the seafloor is best modeled using a corner wave number k_n of 0.6 km^{-1}, as shown in Fig. 3.37, but that the westernmost portion of the ARC seems to be better modeled using a values of 0.4-0.5 km^{-1}. Based on this process, we let $\underline{k}_n$ for region H6 be 0.45 km^{-1}. Due to the shapes of the covariance functions in Fig. 3.7, we also set $\underline{k}_n$ for regions H1 and H13 to this value. For H11, we somewhat arbitrarily adjust $\underline{k}_n$ upward to 0.75 km^{-1}, based on the location of its covariance function somewhere between the 0.6 and 0.8 km^{-1} lines in Fig. 3.7 despite a large amount of sediment within the region. We do not attempt to reconcile our results with the anomalous inverted Goff-Jordan parameters from 8-12 Ma seafloor in Fig. 3.37.

The inverted value of L is also affected by compaction. In Chapter 2, we explore how compaction alters model topographies, deriving an empirical equation (2.37) for determining the average thickness loss for a region given its post-compaction average sediment thickness. This equation allows us to estimate L_u, the average sediment thickness which would be present if sediments were not subject to compaction, for all of the hill-centered regions.

In Table 3.6, we give adjusted values for H, L, and k_n, and then adjust all values for the effects of compaction. Note that the adjusted value of $\underline{H}$ for H1 is even further from the value estimated by *Goff et al.* [1995] (see Fig. 3.35). The alternate values of $\underline{k}_n$ do not greatly change any of the estimates of average sediment thickness, similar to our results from the inversion of models. Adjusting L for compaction has a much larger effect.

Table 3.6. Adjusted inversion results from hill-centered subregions

Site	T, Ma	H, m	L, m	k_n, km^{-1}	$\underline{H}$, m	$\underline{L}$, m	L_u, m
H1	4.14	220	8	0.45	269	8.5	9
H2	8.43	275	24	-	-	-	26
H3	12.44	245	40	-	-	-	44
H4a	17.38	240	82	-	-	-	94
H4b	18.05	250	56	-	-	-	63
H5	23.70	255	44	-	-	-	49
H6	26.11	260	31	0.45	318	32.8	36
H7	27.48	300	42	-	-	-	47
H8	24.73	300	38	-	-	-	42
H9	20.32	280	49	-	-	-	55
H10	14.39	230	42	-	-	-	47
H11	11.21	270	78	0.75	232	74.9	85
H12	9.31	300	61	-	-	-	69
H13	5.57	275	15	0.45	336	15.9	17
H14	4.24	310	17	-	-	-	18

(- indicates no change)

If we were limited to using inverted parameters from hill-centered regions to study sedimentation, we would use the values of L_u, as given in Table 3.6, as our estimates of how sediment thickness varies with seafloor age. However, since the resolution of the bathymetric data available is good enough for us to construct basin-centered regions based on probable lateral sediment flux constraints, we instead use the inverted values of L from these regions. These inversion results are discussed in the following section.

RESULTS: BASIN-CENTERED REGIONS

Following the same procedure as for the hill-centered regions, apparent values of H, L, and κ are inverted for each of 35 basin-centered regions (see Fig. 3.5), constructed as shown in Fig. 3.4. We use these regions primarily to study how the average thickness of sediments varies throughout the ARC. The inversion results are shown in Fig. 3.38 and Fig. 3.39 and are given in Table 3.7, along with region center locations, 95% confidence bounds, and the number of points N at which slope is measured per region.

Twelve of these regions are positioned over relic spreading center offsets, which bound segments of abyssal hills. Especially in the eastern parts of the ARC, these locales tend to contain deep basins which are not well-modeled by Goff-Jordan realizations of topography. In Fig. 3.39, parameters inverted from these subregions are depicted by white circles, while parameters from all other basin-centered subregions are represented by black

circles. We find that inverted values of L from these subregions tend to be lower than those from seafloor of similar age, presumably because their ponds are thicker in proportion to their surface widths than the ponds that occur with the sedimented models. We therefore limit our interpretation of L to the values inverted from the 23 other subregions, which primarily contain lineated topography. H and κ from the subregions over the relic offsets also tend to be lower than those from the other subregions.

Table 3.7. Inversion results from basin-centered subregions within the ARC

Site	Location	N	T, Ma	H, m	κ, m^2/yr	L, m
B1	25.86°N, 48.44°W	1173	23.57	270 +25/-30	.11 +.17/-.05	(40 +14/-11)
B2	26.32°N, 48.31°W	558	25.05	225 +30/-25	.12 +∞/-.06	38 +19/-12
B3a	26.58°N, 48.46°W	651	27.19	330 +65/-35	.16 +∞/-.08	40 +22/-11
B3b	26.65°N, 48.03°W	833	24.67	255 +35/-20	.22 +∞/-.13	(37 +17/-8)
B4	26.02°N, 47.94°W	954	21.37	265 +35/-25	.16 +∞/-.09	37 +14/-9
B5	26.61°N, 47.80°W	584	23.19	295 +75/-35	.10 +∞/-.05	(42 +31/-14)
B6a	25.99°N, 47.60°W	654	19.28	230 +50/-20	.24 +.29/-.09	66 +35/-14
B6b	26.40°N, 47.47°W	296	19.37	200 +50/-25	.09 +∞/-.04	(33 +29/-13)
B7	26.68°N, 47.52°W	1014	21.32	255 +35/-25	.20 +∞/-.08	44 +16/-10
B8	25.88°N, 47.34°W	433	17.28	230 +70/-25	.30 +∞/-.11	70 +54/-17
B9	25.92°N, 47.04°W	882	15.18	250 +35/-20	.55 +∞/-.21	64 +24/-12
B10	26.85°N, 47.16°W	677	19.33	285 +45/-25	.47 +∞/-.27	47 +20/-11
B11	26.38°N, 47.25°W	668	17.88	220 +30/-20	.16 +.30/-.06	(37 +17/-10)
B12	26.78°N, 46.91°W	576	18.02	215 +45/-25	.08 +.08/-.04	40 +28/-13
B13	26.84°N, 46.68°W	598	16.20	235 +50/-20	.10 +.22/-.03	(37 +25/-11)
B14	26.90°N, 46.40°W	509	14.47	240 +65/-30	.18 +.25/-.07	60 +41/-18
B15	26.60°N, 46.46°W	880	14.85	255 +40/-25	.36 +.40/-.14	64 +25/-15
B16	26.15°N, 46.67°W	1117	13.44	220 +25/-15	.22 +.19/-.07	(50 +17/-10)
B17	25.87°N, 46.40°W	358	11.38	295 +80/-40	.45 +∞/-.26	49 +38/-16
B18	26.20°N, 46.38°W	466	12.42	220 +55/-25	.20 +.45/-.09	(45 +33/-13)
B19	26.37°N, 47.00°W	448	16.45	205 +40/-25	.12 +.34/-.06	(31 +22/-11)
B20	26.12°N, 46.09°W	936	10.29	215 +20/-20	.22 +.43/-.10	(31 +11/-8)
B21	25.91°N, 45.94°W	272	7.74	275 +85/-35	.58 +∞/-.46	(25 +28/-9)
B22	25.91°N, 45.73°W	595	6.19	235 +40/-25	.14 +.57/-.06	(20 +14/-8)
B23	25.87°N, 45.47°W	593	3.85	210 +70/-30	.04 +.91/-.01	18 +38/-12
B24	26.37°N, 45.53°W	722	7.24	265 +45/-25	.64 +∞/-.33	38 +19/-9
B25	26.66°N, 46.08°W	503	11.96	270 +60/-35	.48 +∞/-.23	55 +33/-16
B26	27.00°N, 46.06°W	563	12.20	260 +60/-30	.41 +∞/-.18	57 +32/-15
B27	26.64°N, 45.88°W	473	10.47	295 +50/-40	1.0 +∞/-.6	59 +25/-17
B28	26.45°N, 45.77°W	462	9.56	240 +55/-30	.30 +.67/-.13	44 +28/-14
B29	26.81°N, 45.57°W	678	8.83	305 +70/-40	.48 +∞/-.20	64 +36/-18
B30	26.99°N, 45.78°W	376	10.50	305 +90/-50	.30 +∞/-.12	66 +50/-23
B31	26.42°N, 45.24°W	615	4.98	305 +90/-45	.24 +.31/-.10	48 +42/-19
B32	26.86°N, 45.25°W	1088	6.70	280 +50/-30	.15 +.36/-.06	31 +19/-11
B33	26.66°N, 44.99°W	655	4.17	245 +45/-25	.10 +∞/-0.07	14 +14/-7

() Indicate regions centered over deep basins which are poorly modeled using our forward modeling technique. Thus, inverted values of L, as well as H and κ, are suspect.

As shown by Fig. 3.40, inverted values of L, H, and κ from basin-centered subregions show the same general variations with seafloor age as values inverted from hill-centered subregions. Since N is generally lower than for the hill-centered regions, the 95% confidence intervals are larger, leading to larger variabilities. Despite this, basin-centered inverted values of L show less variability with seafloor age, presumably because there has been minimal inter-regional transport. In contrast, more variability in H and κ is seen in values inverted from basin-centered subregions, probably due to smaller region sizes.

There is, however, some same-age variability in L. For instance, the small region centered at 26.42°N, 45.24°W (B31) has an anomalously high inverted value for sediment thickness, given its average age of only ~5 Ma. We believe that this a consequence of the geometry of the seafloor in this region, which includes a low which trends in the ship track direction, and is therefore oversampled.

Correlations between parameters

Correlations exist between all three inverted parameters when all 35 basin-centered regions are considered (Fig. 3.41). When only the 23 regions which do not include segment boundaries are examined (Fig. 3.42), the correlation between H and L is greatly reduced in significance ($r = 0.193$, $\alpha = 0.38$). However, H and κ have a correlation coefficient r of 0.393, significant at the $\alpha = 0.06$ level, and the correlation coefficient between L and κ is 0.478, significant at the $\alpha = 0.02$ level. Since the tradeoff in significance between L and κ in the inversion process is minimal (see Fig. 3.18), we attribute the observed correlation to generally low values of κ on the youngest seafloor of the ARC where sediments are very thin, and the practical upper boundary on κ for older seafloor, where average sediment thickness is also rather low. Higher diffusivities and sediment thicknesses are both inverted from ~10 Ma seafloor, but whether the high sediment thickness contributes to the high inverted values of κ is unknown.

Variations to L with seafloor age

Basin-centered regions are ideal for studying variations to L. As seen in Fig. 3.38 and 3.39, sediment thickness seems to be primarily a function of seafloor age. To use

inverted values of L in studies of sediment accumulation rate through time, it is desirable to correct both for the effects of post-depositional compaction and for any inaccuracies in the estimation of k_n during the parameter inversion procedure. Correcting for compaction effects may be performed via the application of (2.37). Correcting for the effects of inaccurately chosen k_n is less straightforward. Our technique is to assume that the true k_n for a region is equal to the value we estimate for hill-centered regions covering the same topography. Thus, a k_n of 0.6 km^{-1} is assumed for most of the basin-centered regions, but a k_n of 0.45 km^{-1} is assumed for regions B2, B3a, B23, B32, and B33, and of 0.75 km^{-1} is assumed for regions B25, B27, and B28. For regions where we assume a k_n other than 0.6 km^{-1}, we use (2.32) to estimate $\underline{H}$, the value H would be if we had correctly chosen k_n, and (3.24) to determine $\underline{L}$, the adjusted value of L. Adjusted L values for the 23 basin-centered regions which do not contain segment-boundary lows are given in Table 3.8.

As seen for the hill-centered regions, adjustments for the effects of misestimated k_n have very little effect on L values, but large impact on H values. For most of the adjusted regions, $\underline{L}$ are moved closer to the values found on comparably-aged seafloor, while $\underline{H}$ for several of the locations seem to be moved outside the typical range of H (Fig. 3.43). This may mean that the adjustments made to k_n are too large.

Correcting for compaction effects leads to larger adjustments to L. The resulting estimates of average sediment thickness, L_u, represent our best estimates of sediment thickness within the ARC (Fig. 3.44).

The variability seen in L_u with seafloor age probably reflect changes in sediment supply, composition, and/or dissolution rate through time. *Jaroslow and Tucholke* [1991] attribute age-dependent variations in average sediment thickness, evident in seismic data obtained in the ARC, in part to variations in the North Atlantic CCD since the late Oligocene [*Tucholke and Vogt,* 1979; *Tucholke and Mountain*, 1986].

For near-axis seafloor in the ARC and in chapters 4 and 5, we compute the average accumulation rate A by minimizing the sum of the squares of residuals from lines of the form

$$L = AT. \tag{3.25}$$

The values of L_u for younger seafloor with the ARC, as given in Table 3.8, suggest that sedimentation in the ARC has occurred at a rate of 6.3 ± 2.5 m/m.y. since at least the late Miocene if data from questionable subregion B31 is included, and at a rate of 5.9 ± 2.0 m/m.y. if it is excluded. In Chapter 6, we derive information about sediment supply as well as bottom water paleochemistry by using L_u to assess models of surface productivity and bottom water corrosiveness since the late Oligocene.

Table 3.8. Adjusted inversion results from basin-centered regions within the ARC

Site	T, Ma	H, m	L, m	k_n, km^{-1}	$\underline{H}$, m	$\underline{L}$, m	L_u, m
B2	25.05	225	38	0.45	275	40.2	44
B3a	27.19	330	40	0.45	403	42.8	47
B4	21.37	265	37	-	-	-	41
B6a	19.28	230	66	-	-	-	75
B7	21.32	255	44	-	-	-	49
B8	17.28	230	70	-	-	-	80
B9	15.18	250	64	-	-	-	72
B10	19.33	285	47	-	-	-	52
B12	18.02	215	40	-	-	-	44
B14	14.47	240	60	-	-	-	68
B15	14.85	255	64	-	-	-	72
B17	11.38	295	49	-	-	-	55
B23	3.85	210	18	0.45	257	19.1	21
B24	7.24	265	38	-	-	-	42
B25	11.96	270	55	0.75	232	52.8	59
B26	12.20	260	57	-	-	-	64
B27	10.47	295	59	0.75	253	56.6	64
B28	9.56	240	44	0.75	206	42.2	47
B29	8.83	305	64	-	-	-	72
B30	10.50	305	66	-	-	-	75
B31	4.98	305	48	-	-	-	54
B32	6.70	280	31	0.45	342	32.8	36
B33	4.17	245	14	0.45	299	14.8	16

(- indicates no change)

CORROBORATION OF RESULTS

Due to the lack of high-resolution sediment thickness information such as might be obtained from a deep-towed vehicle outfitted with, for instance, a 3.5 kHz sonar system, it is impossible to directly verify our estimates of sediment thickness, seafloor variability, or apparent diffusivity. However, the internal consistency of our results, and the favorable comparison of our results with those from other studies of sedimentation and basement

parameters from the ARC, such as the investigation of *Goff et al.* [1995], suggest that our inversion methodology is both accurate and precise.

Uniformity in L with age

One indication of the precision of our inversion methodology is the similarity in L inverted from regions of similar seafloor age, particularly when long-distance, extra-regional sediment transport is minimal. For example, the four westernmost basin-centered regions (B1, B2, B3a, and B3b) all have inverted values of average sediment thickness between 37 and 40 m. However, the slope distribution functions from which these values are inverted (Fig. 3.45) look quite different, reflecting a wide range of basement structures. Results such as this lead us to believe that our error estimations may be overly pessimistic.

Comparison with estimates from seismic data

Variations in L with seafloor age are similar in magnitude to those estimated by Jaroslow and Tucholke [*Jaroslow and Tucholke*, 1995; *Jaroslow*, 1997] from the single-channel seismic and 3.5 kHz data collected in the ARC (Fig. 3.46). Quantitatively, we estimate, on average, 50% more sediment than Jaroslow and Tucholke throughout the ARC. We attribute this to differences in sampling methodologies. Jaroslow and Tucholke were able to measure the volume of sediment in broader ponds within the hilly regions of the ARC, but were unable to well-image sediment accumulations less than ~1 km in width, or less than 50 m thick (although sidescan backscatter data was used to identify low-sediment (<10 m) crust, and sediment thickness was interpolated between 50-m contours and the low-sediment regions.) The slope values we measure also may not explicitly sample small ponds, but since the model topographies to which we compare slope statistics do contain them, their influence is included in inverted values of L.

CONCLUSIONS AND DISCUSSION

Apparent diffusivity

Apparent diffusivity κ for hill-centered study areas ranges from 0.10 to 0.78 m^2/yr, with an average of 0.32 ± 0.20 m^2/yr. For basin centered areas, the distribution of values is slightly broader, ranging from 0.04 to ~1 m^2/yr with an average of 0.28 ± 0.20 m^2/yr.

The variations in apparent diffusivity κ seen throughout the ARC have proven difficult to explain. Single-channel seismic and 3.5 kHz records from areas with lower apparent diffusivities show more hillside drape and sediment pond surface concavity, in general, than data from areas with higher apparent diffusivities, as calculated for hill-centered regions. However, this phenomena is difficult to quantify using means other than statistical methods such as we have employed.

The weak correlation between κ and H for both hill-centered and basin-centered regions may indicate that sediment mobility scales non-linearly with seafloor slope. This could be caused by several effects. For instance, transport could follow the form

$$f(\mathbf{x},t) = -\kappa(\mathbf{x},t)\left(\nabla h(\mathbf{x},t)\right)^n, \tag{3.26}$$

$n > 1$, as opposed to (2.6). Or, steep hillsides might increase the chance of slides or turbidity currents developing, which form flatter accumulations in lows than those which occur due to gradual across-pond grain-by-grain transport.

We note that the highest diffusivity values seem to lie over regions dominated by inside corner crust, though the necessarily large size of the study areas makes this effect impossible to quantify using our present inversion methodology.

Diffusivity values in the ARC are generally higher than the recent estimates of 0.04 to 0.11 m^2/yr derived for the central Atlantic by *Mitchell* [1995] from a detailed analysis of sediment ponds in narrow valleys, imaged in deep-tow data, and our own rough estimate of 0.05 m^2/yr for κ within a single narrow valley within the ARC (see Fig. 2.4) well-imaged in DSL-120 and DSL-300 data. Even lower values of κ, between 0.002 and 0.015 with an average of ~0.007 m^2/yr, have been found by *Mitchell* [1996] to model sediment transport, probably in the form of creep, within 100-200 of the tops of scarps on the Galapagos Ridge. At the opposite extreme, in Chapter 2 we find that a κ on the order of 10

m^2/yr is needed to model the transport of sediment tens of kilometers into the deep, level ponds which often fill relic spreading segment boundaries (see Fig. 2.34). This suggests that, in some sense, the value of κ inverted from a given setting increases with the characteristic length scales of the features which dominate locally, as shown in Fig. 3.47. The locally dominate topography may not control the sediment processes, but instead determine which processes are preserved in the shapes taken by sediments. For example, creep may be active on slopes immediately above large ponds, but periodic turbidity currents obliterate the signal of such less energetic processes. Higher uphill, high-energy events may transport sediment so efficiently in places that no deposits remain, such that κ is only measurable from those places which are isolated for some reason.

Sediment thickness

Inverted values of sediment thickness, as given in Table 3.5 and Table 3.7, range from 8 to 82 m for hill-centered regions and from 14 to 70 m for basin centered regions. The larger range in values from hill-centered regions is probably caused because some regions, such as the high-L regions H4a and H11, import sediment from external regions, while the low-L region H1 (along with H2 and H3) loses sediment into a large pond to its north. The basin-centered regions, in contrast, entirely contain all catchment areas they contact. Therefore, we use inverted values from these areas to study L.

Allowing for corrections due to potential misestimation of hill spacings during the inversion process and the effects of compaction, we find that sediment has accumulated on young seafloor within the ARC at ~6 m/m.y since the late Miocene. The relatively low sediment thicknesses (~40 m) we observe for older seafloor within the ARC is caused by variabilities in biological productivity and/or bottom water chemistry since the late Oligocene, and is discussed in detail in Chapter 6.

RMS height

Basement H, as calculated from hill-centered regions, varies from 220 m to 310 m, with a mean $\overline{H} = 267 \pm 28$ m. Variations in H correlate with the ridge-segment boundary that passes through the center of the corridor, with hills north of the boundary having a

mean of 285 ± 26 m and hills south of the boundary having a mean of 249 ± 17 m. Inverted values of H agree, in general, with the inversion results for sedimented topography of *Goff et al.* [1995], after correction for the effects of sedimentation.

Adjustments to inverted values of H in response to possible misestimation of basement hill spacings have a fairly large effect on H. This sensitivity of H to basement hill spacing leads us to doubt the usefulness of this inversion methodology to draw conclusions about H when k_n is not well constrained.

Summary

Slope distribution functions calculated from bathymetric data provide a new source of information on how sediments are distributed on rough near-ridge abyssal hill topography. Inverted values of H, L, and κ also allow us to produce realistic models of topography shown in figures 2.43, 2.44, and 2.45.

The spatial resolution of inverted values of L suggests that this methodology could prove useful for determining the distribution of sediments from narrowbeam bathymetric data wherever average sediment thickness is less than roughly half the RMS variability of the basement.

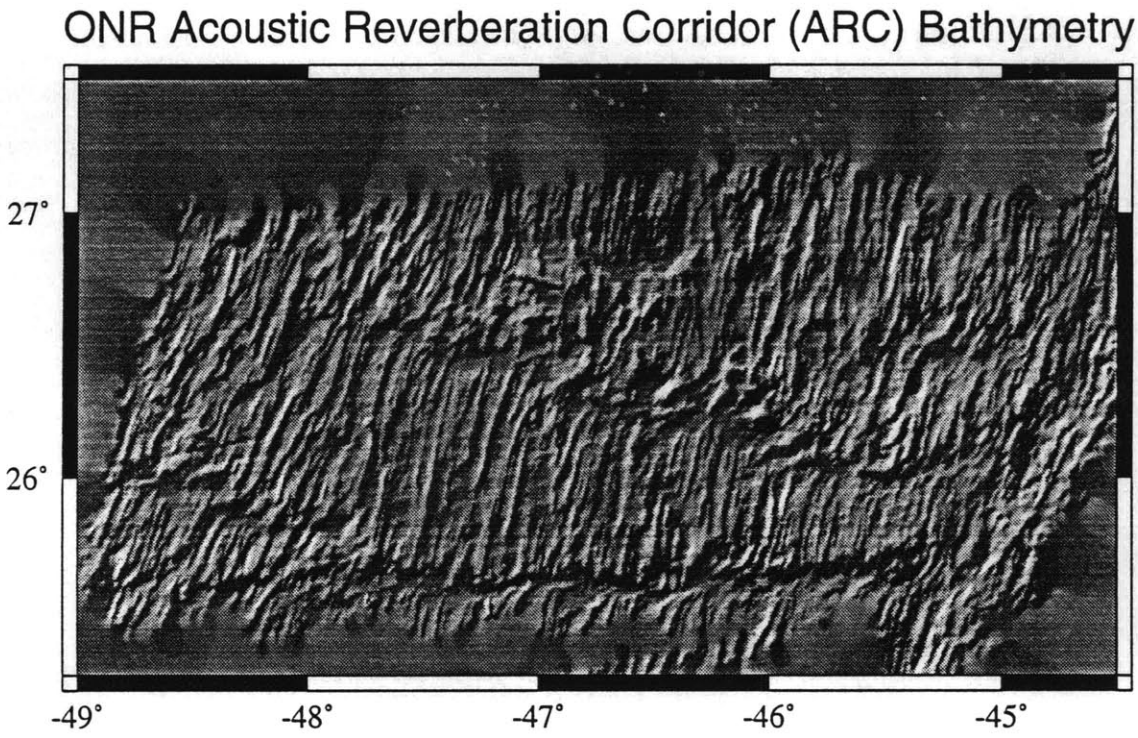

Fig. 3.1: Gridded Hydrosweep bathymetry data [*Tucholke et al.*, 1992] from the Acoustic Reverberation Corridor, located on 0-29 Ma crust on the western flank of the Mid-Atlantic ridge north of the Kane Fracture Zone, collected by the *R/V Maurice Ewing* (EW9208; July-August, 1992) as part of the Office of Naval Research Acoustic Reverberation Special Research Project. Shading is from the northwest. The deep running east-west through the middle of the area corresponds to a small spreading-center offset.

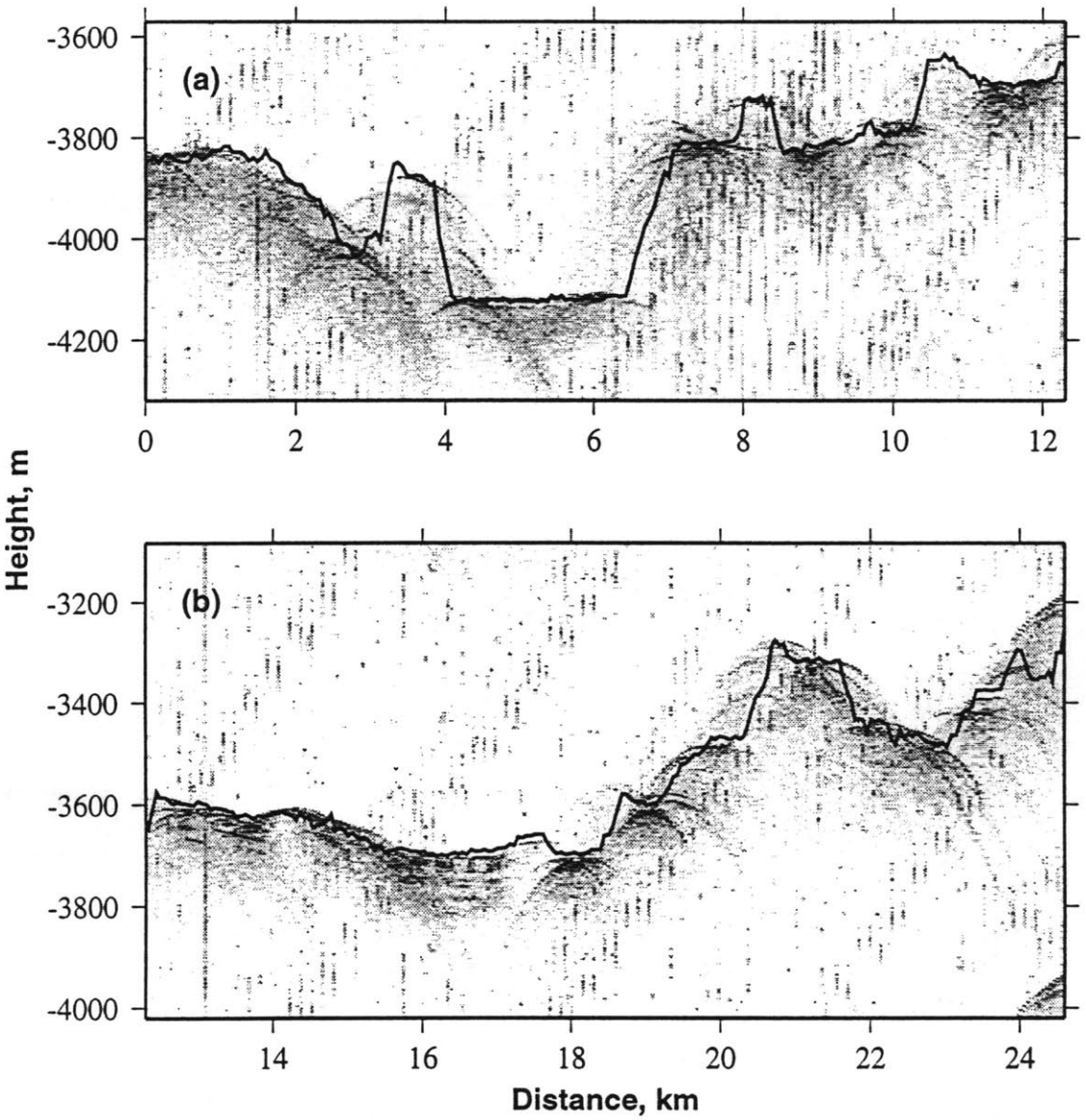

Fig. 3.2: Comparison of Hydrosweep centerbeam bathymetry (solid line) with digitally recorded 3.5-kHz returns for one 24.6-km stretch within the ARC, between 26.695° N, 46.237° W and 26.661° N, 46.481° W, collected *R/V Maurice Ewing* (EW9208; July-August, 1992) as part of the Office of Naval Research Acoustic Reverberation Special Research Project. The center beam bathymetry is from the *Ewing's* Krupp Atlas Hydrosweep system; the 3.5-kHz data is from a DAT-based recording system. Note that the first half of the profile, given in (a), is situated roughly 400 m lower than the second half of the profile, given in (b). Vertical exaggeration is 7:1.

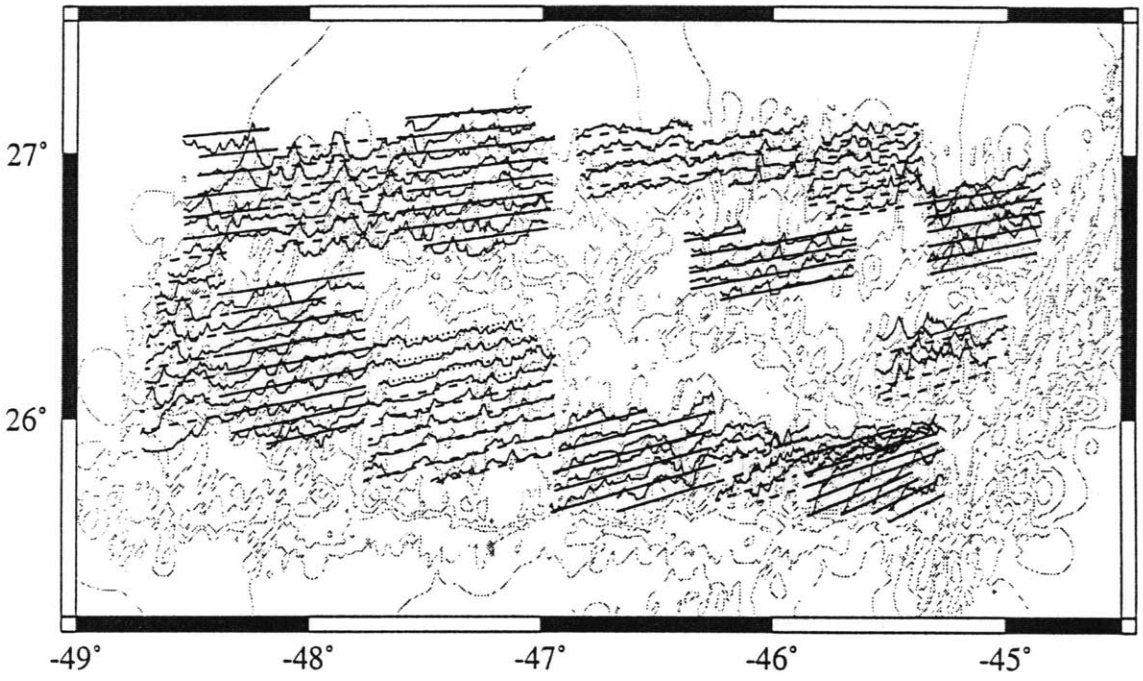

Fig. 3.3: Contours (500 m interval) of ARC bathymetry data as in Fig. 3.1, and tracklines and centerbeam data from within 15 hill-centered regions, chosen to avoid intersegment lows. Differences in trackline patterns denote separate regions. Vertical exaggeration of the centerbeam data is 12:1.

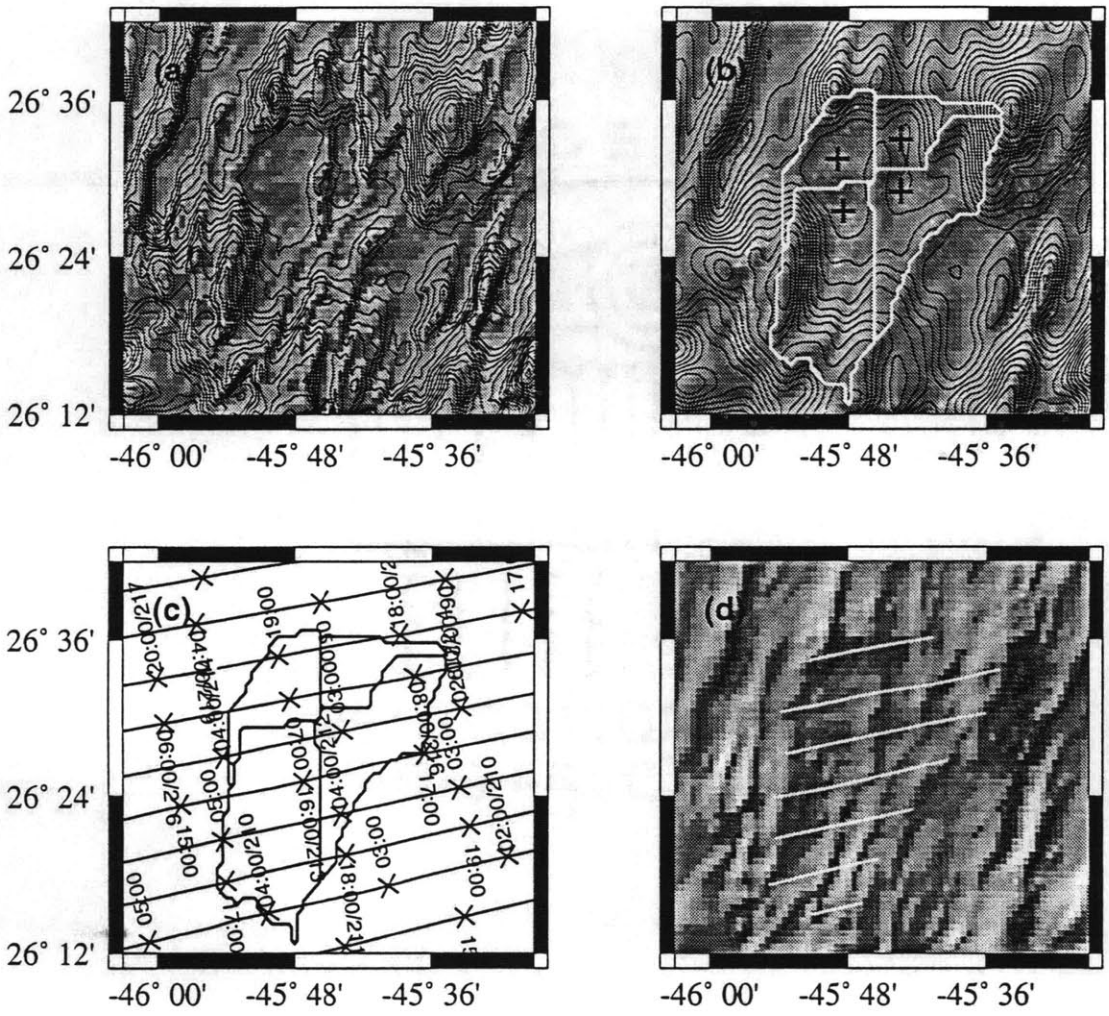

Fig. 3.4: Methodology for choosing basin-centered regions such that all sediment which arrives in the area stays within the area, assuming transport is in the direction of maximum slope. Since gridded renderings of Hydrosweep bathymetry data are rough, and contain many local minima, as in (a), the detection of separate basins is difficult. Therefore, we smooth the gridded data set, eliminating all small-scale lows (b). We find persisting lows within the topography (crosses, in (b)) and determine the bounds of basins which contribute sediment to these lows. We group small basins together based on proximity, being careful to group basins which might have been artificially separated by ridges imposed by the smoothing process. We then overlay tracklines (c), and determine centerbeam data which samples the groupings. These segments span the topography which forms the subregion (d).

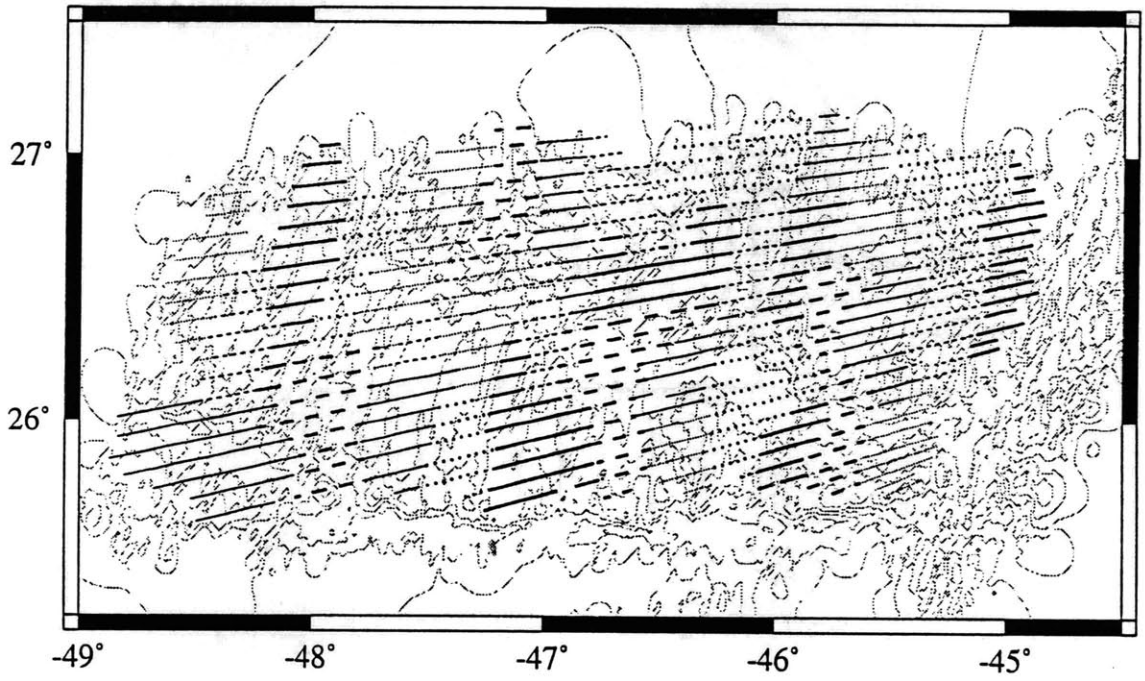

Fig. 3.5: Contours (500 m interval) of ARC bathymetry data as in Fig. 3.1, and tracklines from within 35 basin-centered subregions. Trackline patterns denote subregions.

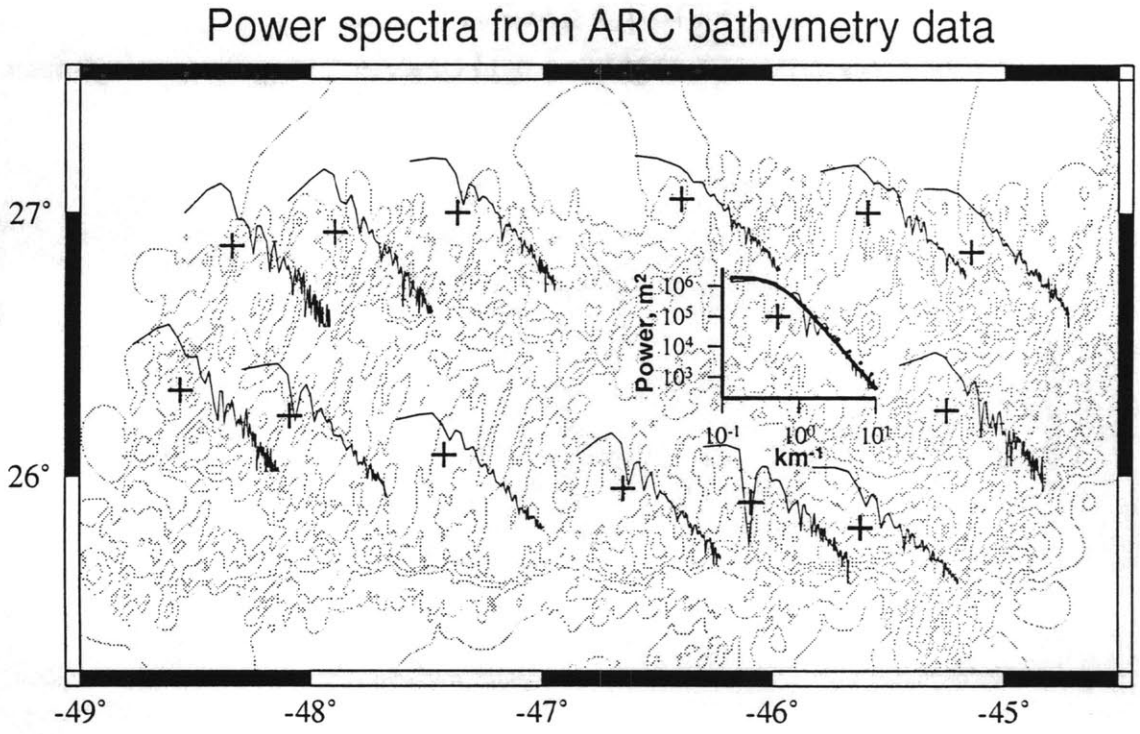

Fig. 3.6: Contours (500 m interval) of ARC bathymetry data as in Fig. 3.1, and power spectra computed from centerbeam data from within the 15 hill-centered subregions of Fig. 3.3. (Data from the two hill-centered regions near 26° N, 47.5° W have been combined, giving a total of 14 power spectra). Crosses are for purposes of scale, and denote a wave number of 0.5231 km^{-1}, the assumed basement corner wave number in the direction of travel, and a power of 10^5 m^2. For the region at 26.60° N, 46.00° W (H11), power spectra models are also shown. These models have corner wave numbers of 0.5231 km^{-1} and D of 2.05 (solid line) and 2.2 (dotted line).

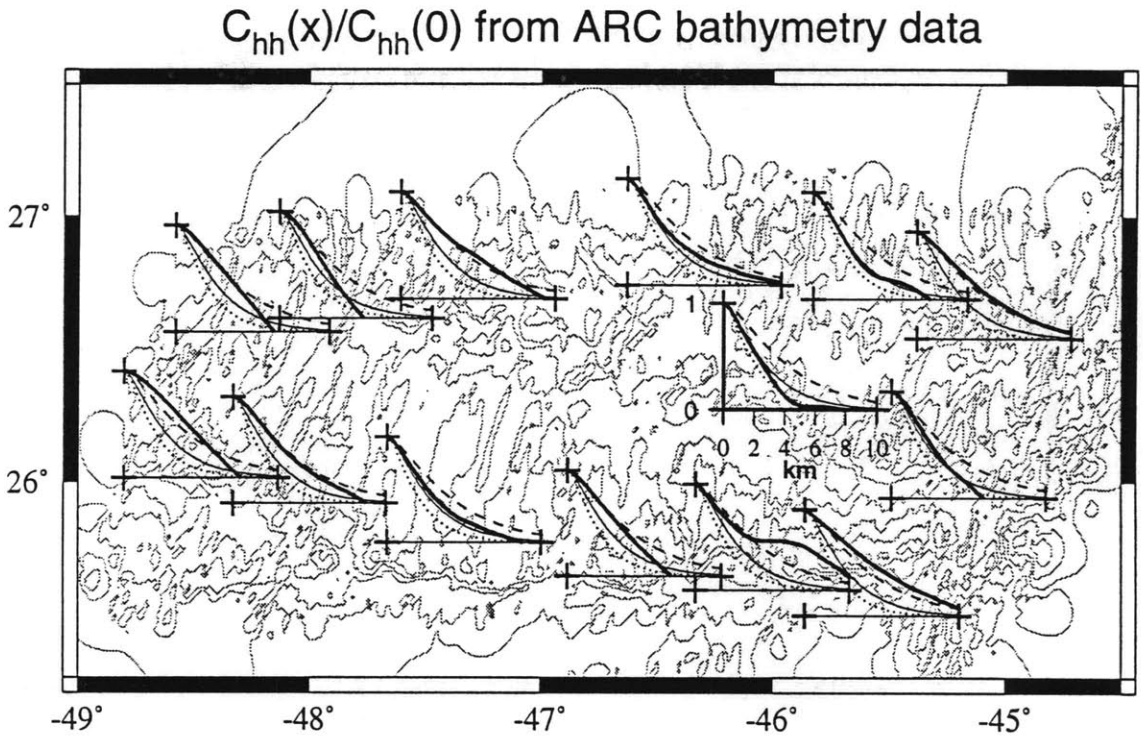

Fig. 3.7: Contours (500 m interval) of ARC bathymetry data as in Fig. 3.1, and scaled covariance functions $C_{hh}(x)/C_{hh}(0)$ (thick lines) computed from centerbeam data from within the 15 hill-centered subregions of Fig. 3.3. (Data from the two hill-centered regions near 26° N, 47.5° W have been combined, giving a total of 14 scaled covariance functions). Crosses are for purposes of scale, and denote the origins of the charts, the x-axis at 10 km, and the location (0 km,1). Additional lines correspond to scaled slope distribution functions following the form of *Goff and Jordan* [1988]. These models have D of 2.05 and corner wave numbers of 0.6975 (dotted lines), 0.5231 (thin solid lines), and 0.3487 (dashed lines) km^{-1}. These values correspond to k_z for an a of 5 and k_n of 0.8, 0.6, and 0.4 km^{-1}, respectively.

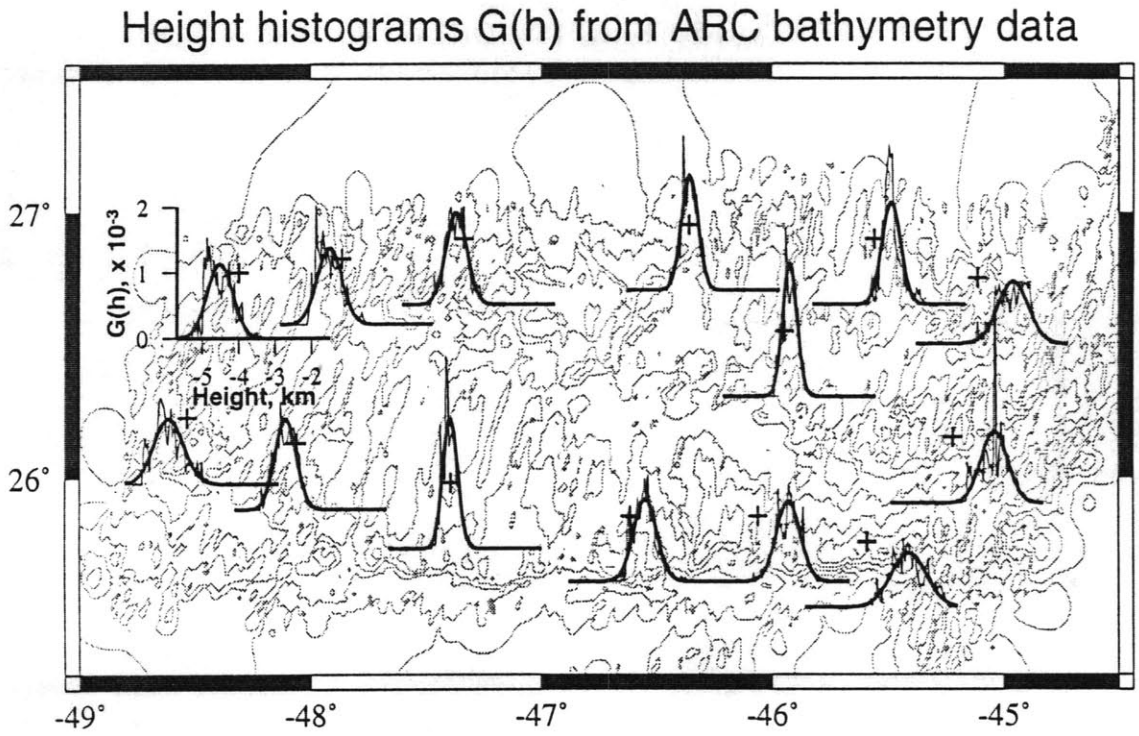

Fig. 3.8: Contours (500 m interval) of ARC bathymetry data as in Fig. 3.1, height distribution functions $G(h)$ computed from centerbeam data from within the 15 hill-centered subregions of Fig. 3.3 (thin lines), and Gaussian distributions with means and standard deviations calculated from these functions (thick lines). Crosses are for purposes of scale, and denote a mean height of -4000 m and function value of 0.001. Data from the two hill-centered regions near 26° N, 47.5° W have been combined, giving a total of 14 height distribution functions.

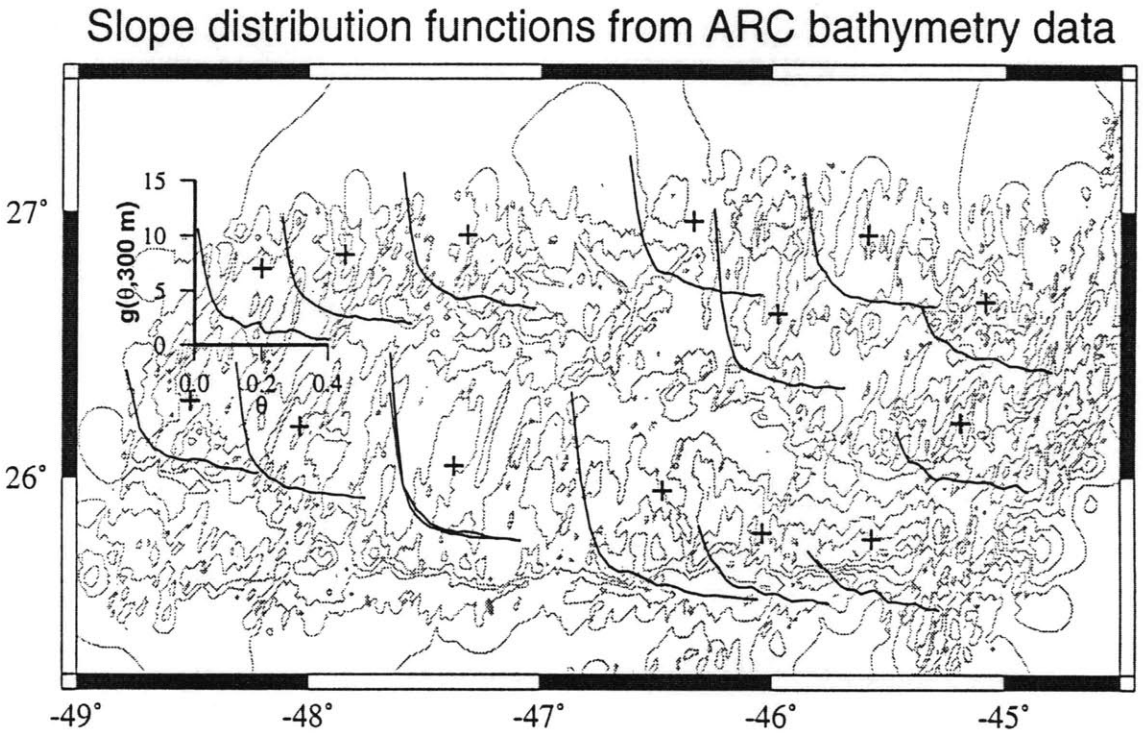

Fig. 3.9: Contours (500 m interval) of ARC bathymetry data as in Fig. 3.1 and slope distribution functions computed from centerbeam data from within the 15 hill-centered subregions of Fig. 3.3. Crosses are for purposes of scale, and denote a slope of 0.2 and a function value of 7. Slope distribution functions from the two hill-centered regions near 26° N, 47.5° W are plotted together.

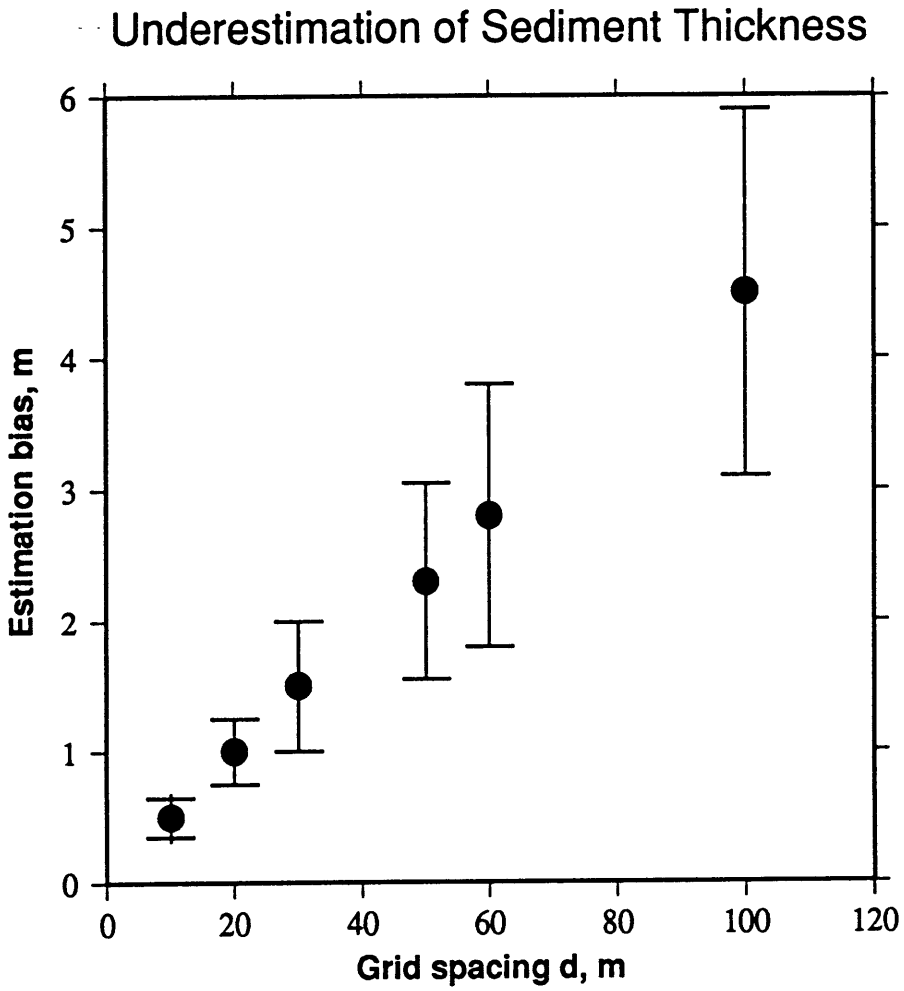

Fig. 3.10: Apparent offset between slope distribution functions computed from models generated using a data point spacing *d* of 10 m and models generated using less dense grid spacings.

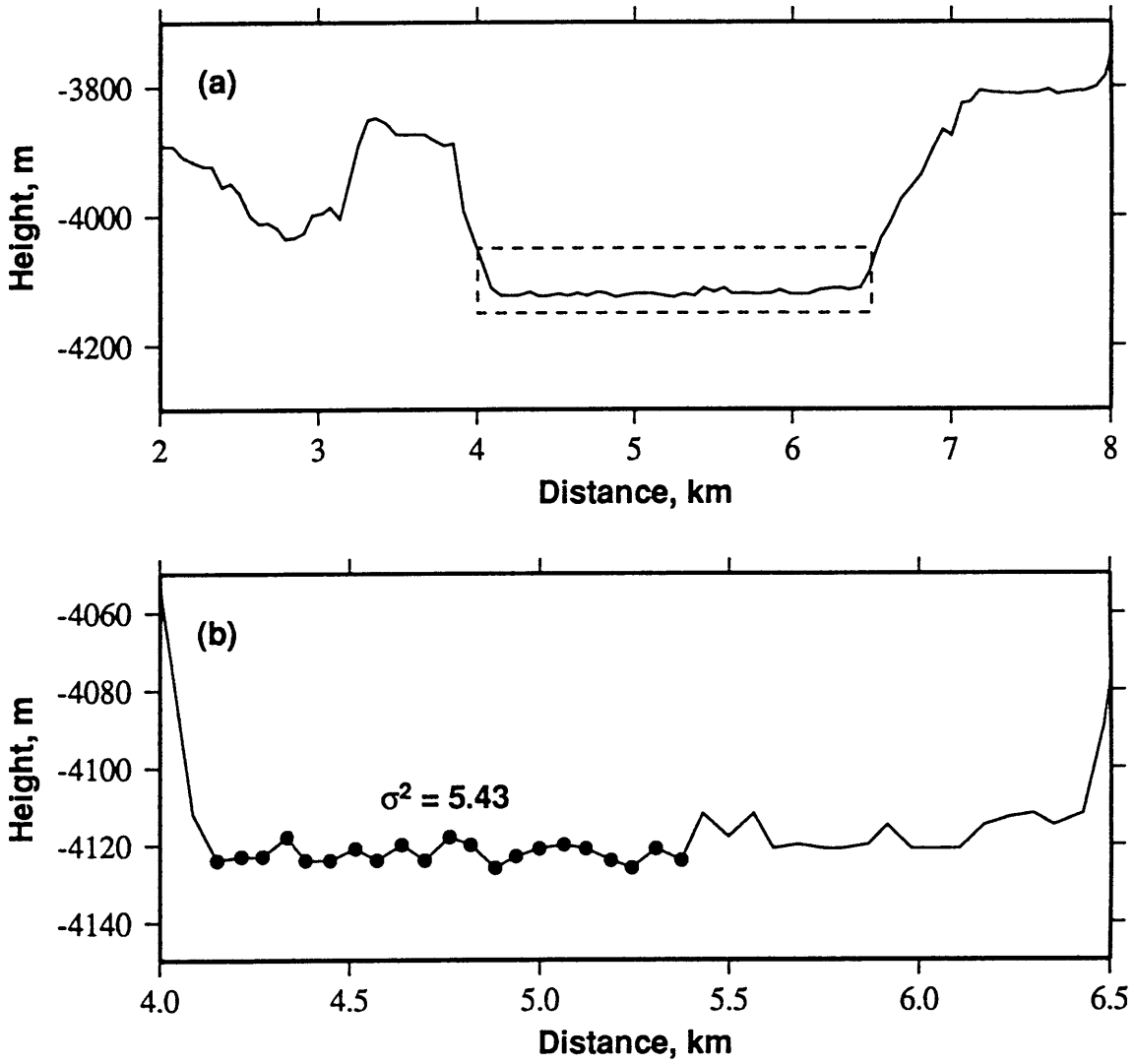

Fig. 3.11: Example of procedure used to determine the variance of system noise introduced by the Hydrosweep sampling system. Flat lying ponds such as are found from 4 to 6.5 km along-track in Fig. 3.2 are found (a). Expanding the dashed region in (a) allows the selection of extremely flat region (b), from which the variance of small-scale roughness is calculated (b). Here, $\sigma^2 = 5.43$; this is typical of such values throughout the ARC. Vertical exaggerations are 4:1 in (a) and 10:1 in (b).

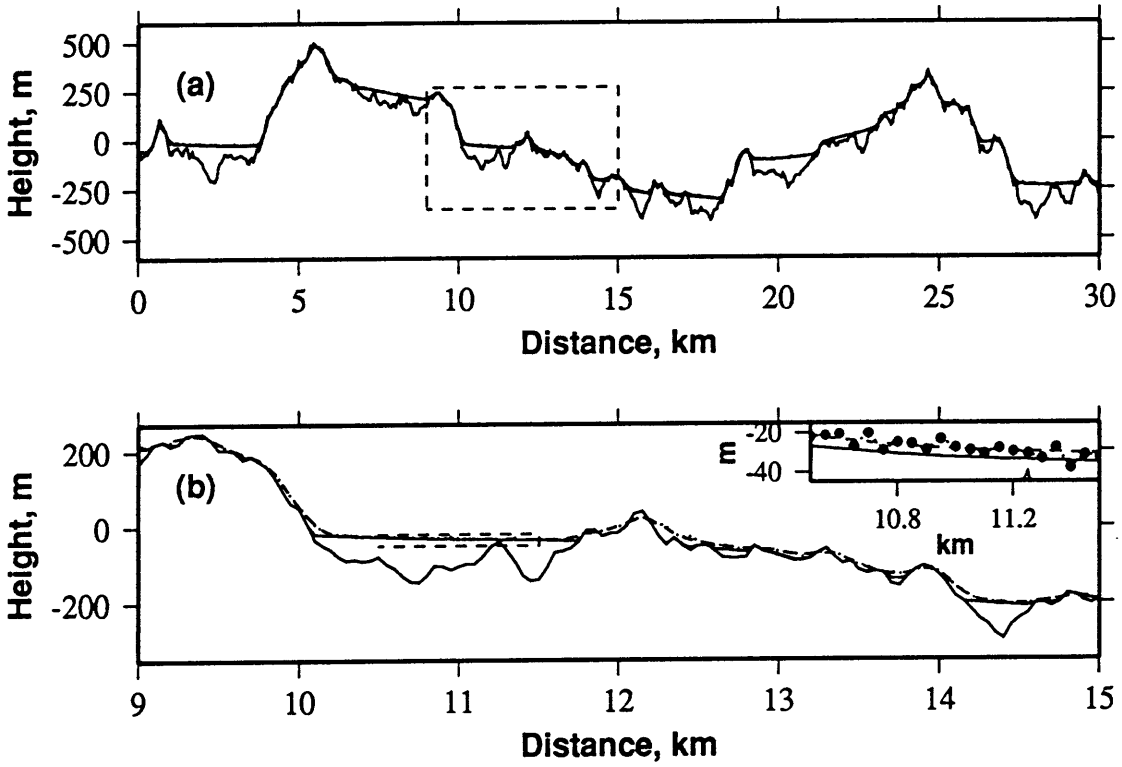

Fig. 3.12: (a) Original model surface (solid line), smoothed version of this model (dashed line), and smoothed version to which normally-distributed random noise with a variance of 5 m^2 has been added (dotted line) (vertical exaggeration 6:1). (b) Expansion of dashed region of (a) showing degradation of hillside slopes, narrowing of ponds, and lowering of peaks due to smoothing (vertical exaggeration 2:1). Inset shows small-scale roughness (vertical exaggeration 7:1). (c). Slope distribution functions of the unfiltered model (solid line), the smoothed model prior to the addition of noise (dashed line), and the smoothed model after the addition of noise (dotted line).

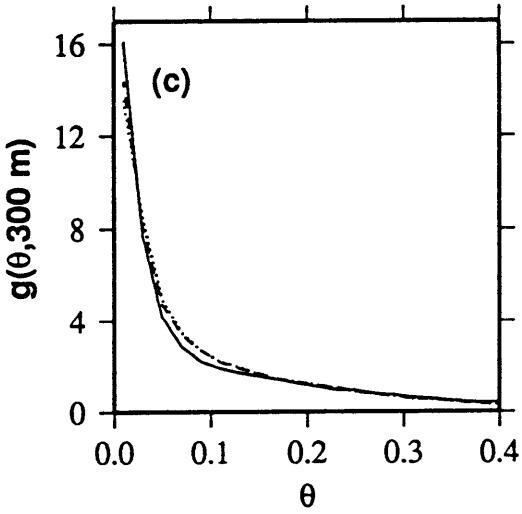

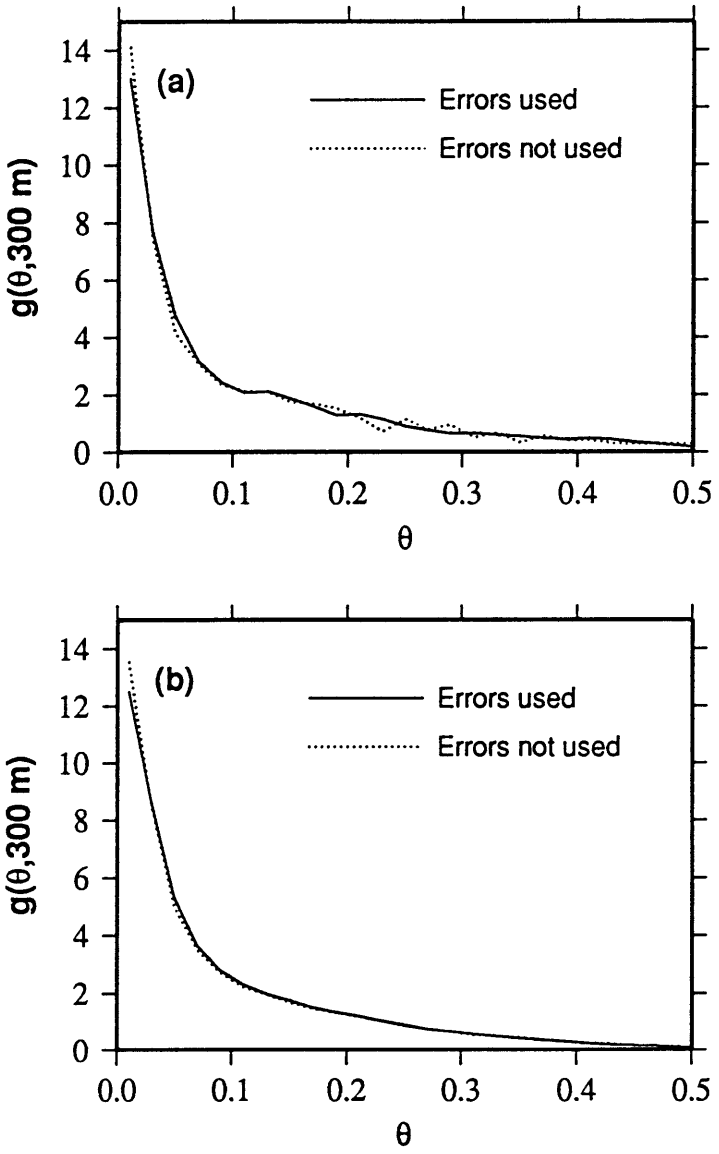

Fig. 3.13: (a) Slope distribution functions $g(\theta,u)$ of hill-centered subregion H3, calculated allowing for (solid line), and not allowing for (dotted line), smoothing due to the incorporation of error terms via (3.11). (b) Slope distribution functions calculated from a model topography computed using basement parameters H = 225 m, k_n = 0.6 km^{-1}, k_s = 0.12 km^{-1}, D = 2.2, and ζ_s = 30°, sedimented for 10 m.y. of model time at a rate F of 4 m/m.y. using a κ of 0.2 m^2/yr. The model is filtered assuming an h_{AV} of 4000 m and a variance E^2 of 5 m^2. The function represented by the solid line is computed allowing for the uncertainties in computed slope to be incorporated into $g(\theta,u)$ via (3.11), while the function represented by dotted line is computed without allowing for this smoothing. As in (a), if error terms are used the amplitude of $g(\theta,u)$ is reduced at very low θ, and $g(\theta,u)$ experiences a slight widening at θ of 0.05-0.1. Both $g(\theta,u)$ are smoother at high θ than in (a), due to the use of a large number of points in the calculation of $g(\theta,u)$.

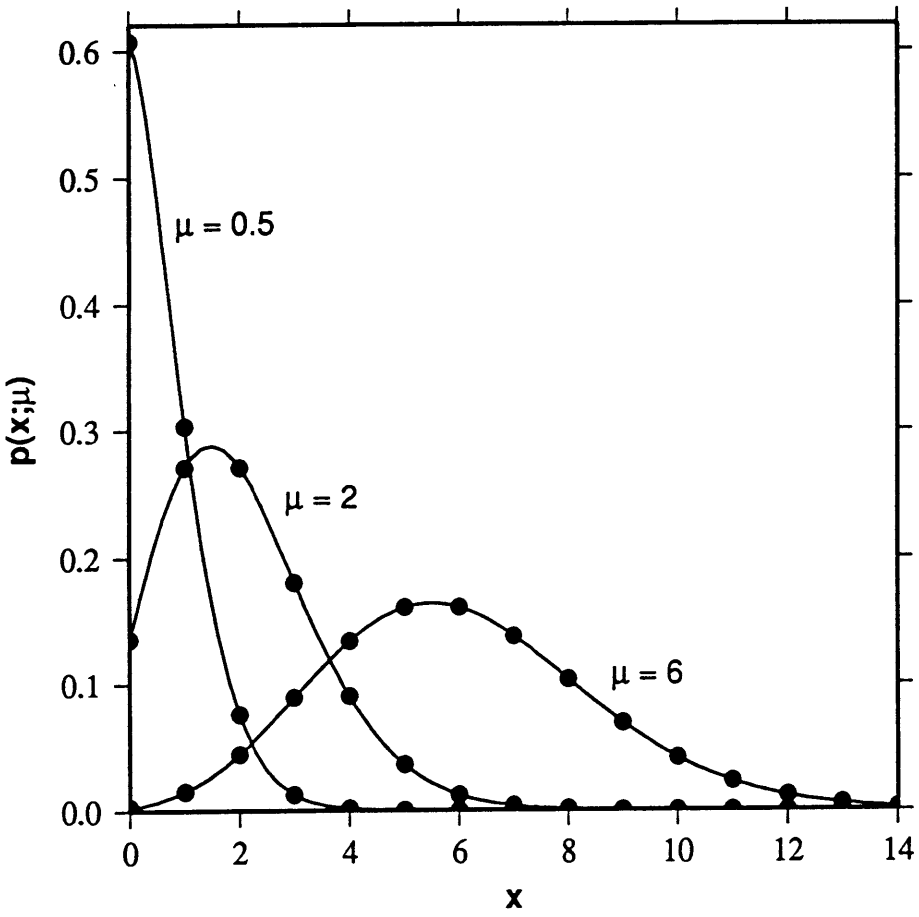

Fig. 3.14: Poisson distribution values (dots) and values of (3.14), for $\mu = 0.5$, 2, and 6.

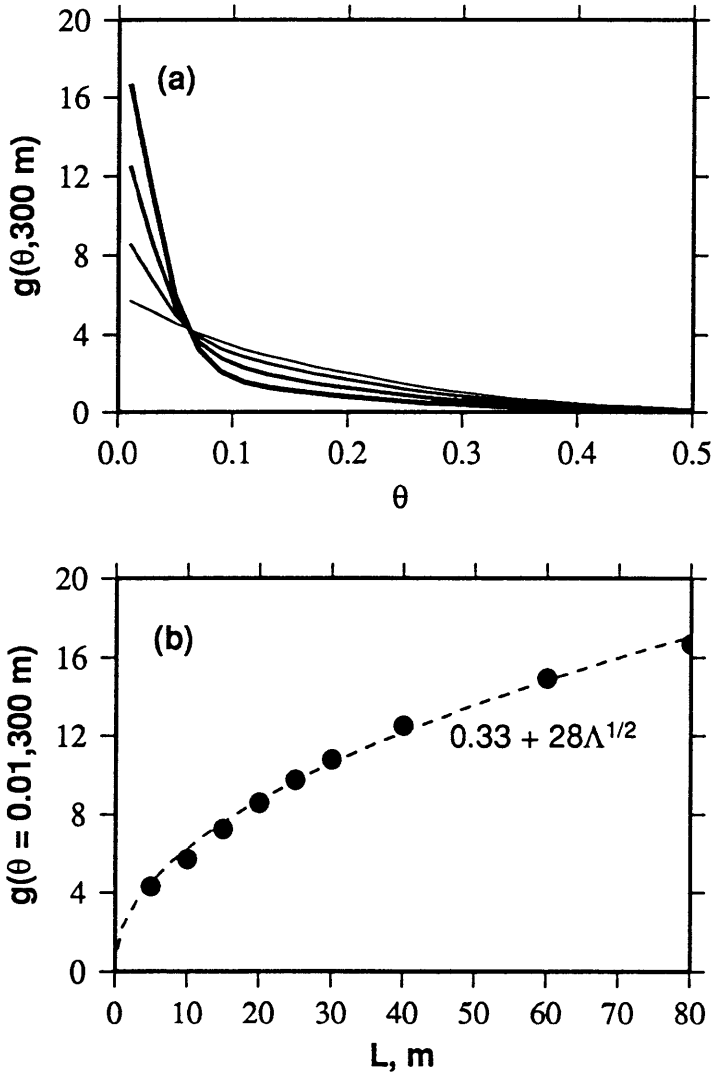

Fig. 3.15: (a) Slope distribution functions from models generated using basement H = 225 m, k_n = 0.6 km^{-1}, k_s = 0.12 km^{-1}, D = 2.2, and ζ_s = 30°, sedimented for 2.5, 5, 10, and 20 m.y. of model time at a rate F of 4 m/m.y. (for L of 10, 20, 40, and 80 m) using a κ of 0.2 m^2/yr, and filtered assuming an h_{AV} of 4000 m and a random system noise variance E^2 of 5 m^2. The thicknesses of the lines increase with increasing values of L. (b) The amplitude of the slope distribution function at θ = 0.01, the lowest value we record, for slope distribution functions from models generated using basement H = 225 m, k_n = 0.6 km^{-1}, k_s = 0.12 km^{-1}, D = 2.2, and ζ_s = 30°, sedimented for 1.25, 2.5, 3.75, 5, 6.25, 7.5, 10, 15, and 20 m.y. of model time at a rate F of 4 m/m.y. (for L of 5, 10, 15, 20, 25, 30, 40, 60, and 80 m) using a κ of 0.2 m^2/yr, and filtered assuming an h_{AV} of 4000 m and a random system noise variance E^2 of 5 m^2 (dots) and a functional form which well-models these values, as given in the figure.

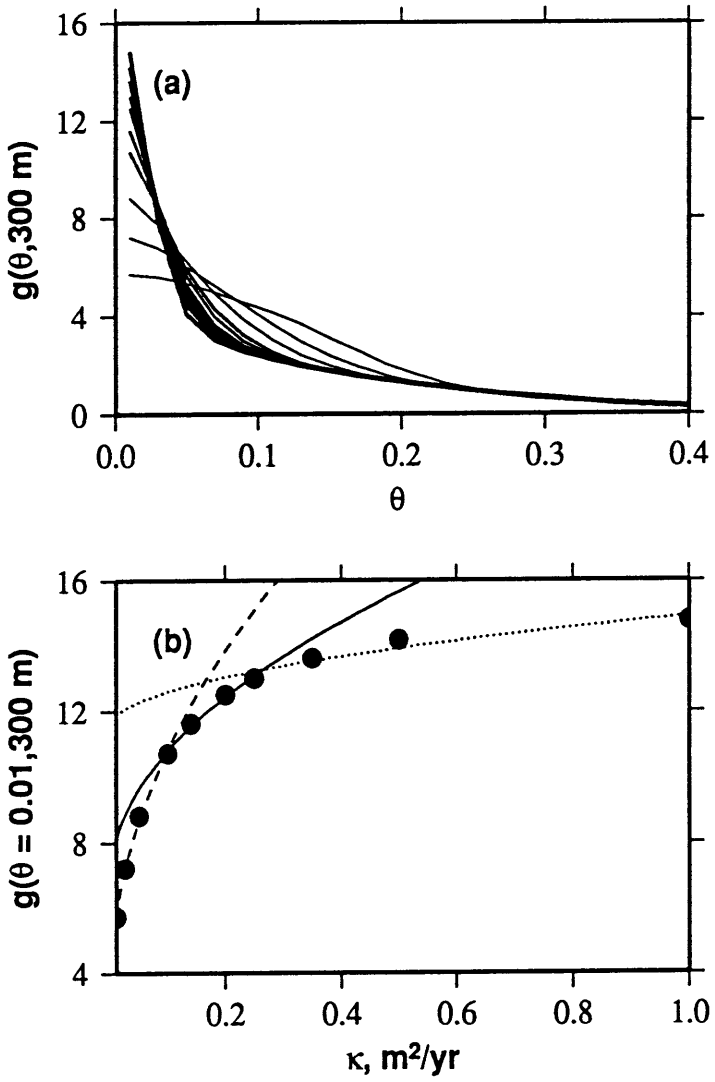

Fig. 3.16: (a) Slope distribution functions from models generated using basement H = 225 m, k_n = 0.6 km^{-1}, k_s = 0.12 km^{-1}, D = 2.2, and ζ_s = 30°, sedimented for 10 m.y. of model time at a rate F of 4 m/m.y. using κ of 0.01, 0.025, 0.05, 0.1, 0.14, 0.2, 0.25, 0.35, 0.5, and 1.0 m^2/yr (for K of 0.2, 0.5, 1.0, 2.0, 2.8, 4.0, 5.0, 7.0, 10.0, and 20.0), and filtered assuming an h_{AV} of 4000 m and a random system noise variance E^2 of 5 m^2. The thicknesses of the lines increase with increasing values of K. (b) The amplitude of the slope distribution function at θ = 0.01, the lowest value we record, for the slope distribution functions in (a) (dots) and functional forms which well-model portions of these values. The dashed line follows 3.487 + 5.186$K^{1/2}$, the solid line follows 6.882 + 2.772$K^{1/2}$, and the dotted line follows 11.524 + 0.758$K^{1/2}$.

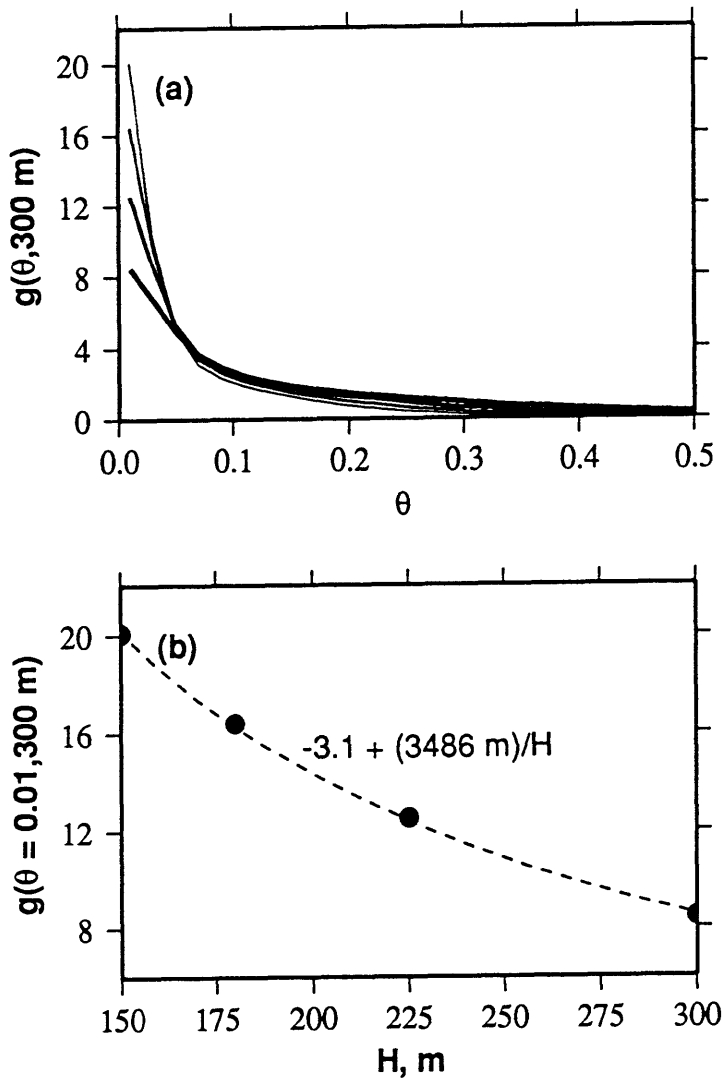

Fig. 3.17: (a) Slope distribution functions from models generated using basement k_n = 0.6 km^{-1}, k_s = 0.12 km^{-1}, D = 2.2, and ζ_s = 30°, and H of 150, 180, 225, and 300 m, sedimented for 10 m.y. of model time at a rate F of 4 m/m.y. (for an L of 40 m) using κ such that K is uniformly 4, filtered assuming an h_{AV} of 4000 m and a random system noise variance E^2 of 5 m^2. The thicknesses of the lines increase with increasing values of H. (b) The amplitude of the slope distribution function at θ = 0.01, the lowest value we record, for slope distribution functions from the models in (a) (dots) and a functional form which well-models these values, as given in the figure.

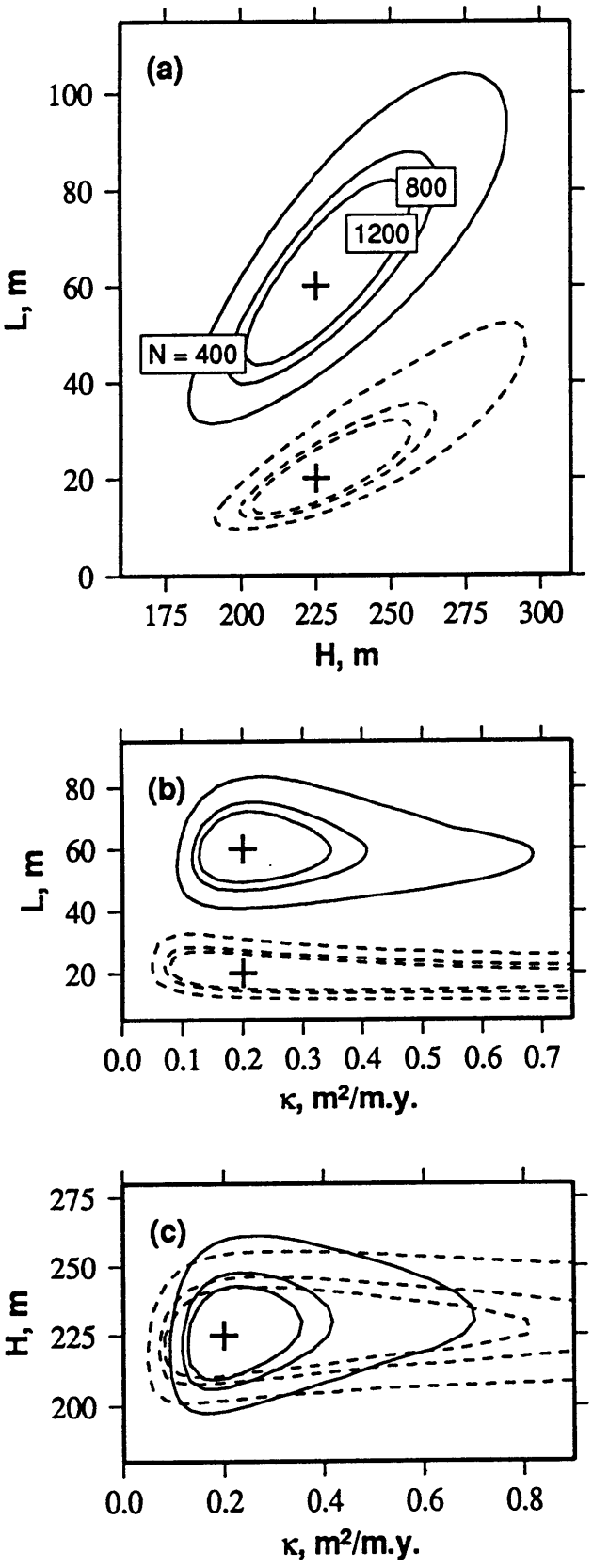

Fig. 3.18: Slices through 95% confidence regions of model parameters. Slope distribution functions inverted to determine parameters are assumed to have been computed using 400, 800, and 1200 300-m-spaced sampling points. Model topographies are built assuming basement H = 225 m, k_n = 0.6 km^{-1}, k_s = 0.12 km^{-1}, D = 2.2, and ζ_s = 30°, and are sedimented for 5 and 15 m.y. of model time at a rate F of 4 m/m.y. (for L of 20 and 60 m, respectively) using a κ of 0.2 m^2/yr, and filtered assuming h_{AV} = 4000 m and E^2 = 5 m^2. Contours for the L = 20 m surface are shown as dashed lines, and for the L = 60 m surface are shown as solid lines. In (a), the 95% confidence bounds on H and L and best estimates (crosses) are shown for cross-sections at κ = 0.2 m^2/yr. In (b), the 95% confidence bounds on κ and L and best estimates (crosses) are shown for cross-sections at H = 225 m. In (c), the 95% confidence bounds on κ and H and best estimates (crosses) are shown for cross-sections at L = 20 (dashed lines) and L = 60 (solid lines).

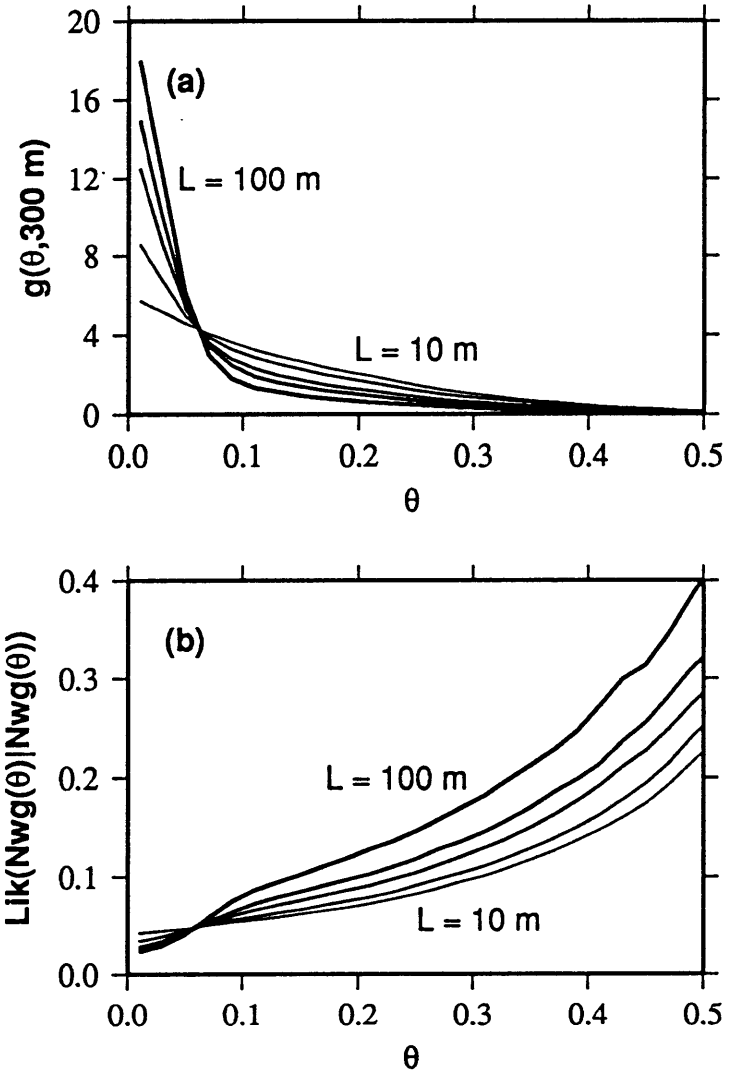

Fig. 3.19: (a) Slope distribution functions from models generated using basement H = 225 m, k_n = 0.6 km^{-1}, k_s = 0.12 km^{-1}, D = 2.2, and ζ_s = 30°, sedimented for 2.5. 5, 10, 15, and 25 m.y. of model time at a rate F of 4 m/m.y. (for L of 10, 20, 40, 60, and 100 m, respectively) using a κ of 0.2 m^2/yr, and filtered assuming an h_{AV} of 4000 m and a random system noise variance E^2 of 5 m^2. (b) Likelihood of each point of the functions in (a) being equal to itself. Since total likelihood is the cumulative product of likelihoods at each point, the farther likelihood values are from 1 the greater their influence on the final likelihood of a function. Therefore, higher values of $g(\theta,u)$ have a greater influence on total likelihood than lower values, and the inversion methodology preferentially attempts to match models at low θ. This effect increases with increasing L. However, since a relatively small portion of the function is high, its influence is balanced by the majority of points which represent $g(\theta,u)$ at $\theta > 0.1$.

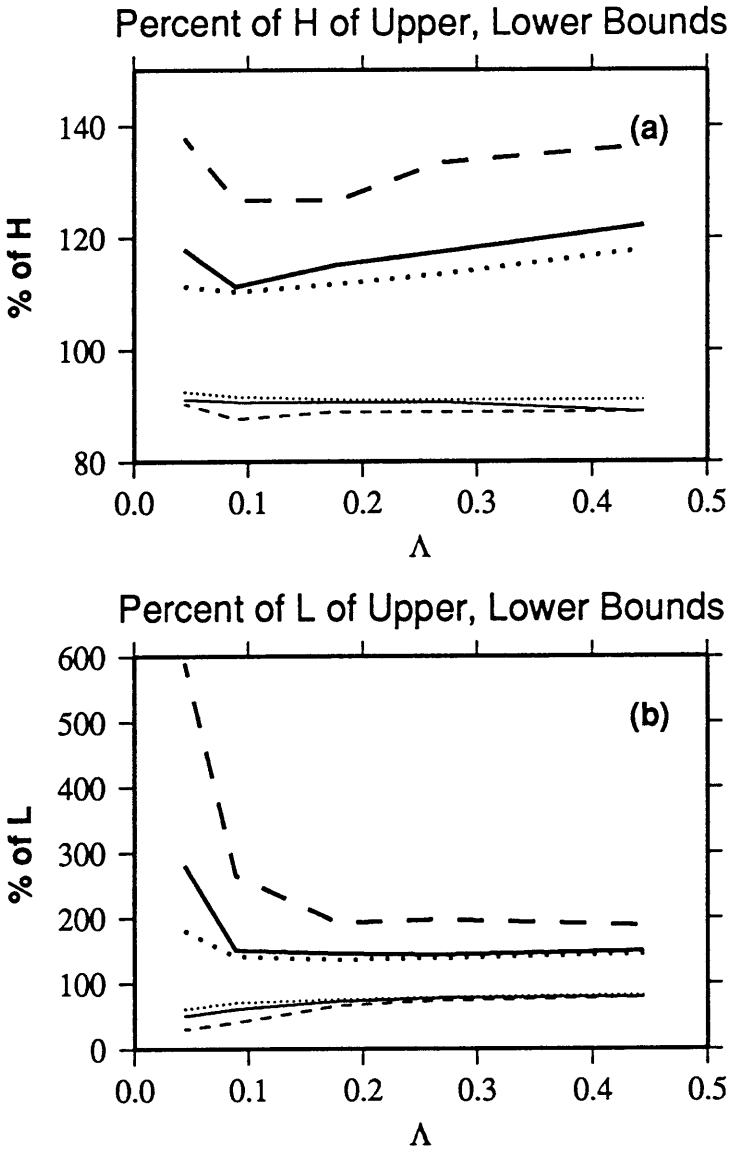

Fig. 3.20: (a) Upper (thick) and lower (thin) bounds on the 95% confidence interval for H as a percentage of H, as a function of Λ, for K of 1 (dashes), 4 (solid), and 20 (dots), for inversion results from model topographies as described in the text. (b) Upper (thick) and lower (thin) bounds on the 95% confidence interval for L as a percentage of L, as a function of Λ, for K of 1 (dashes), 4 (solid), and 20 (dots), for inversion results from model topographies as described in the text. Uncertainties are shown to be highest when K and L are both low.

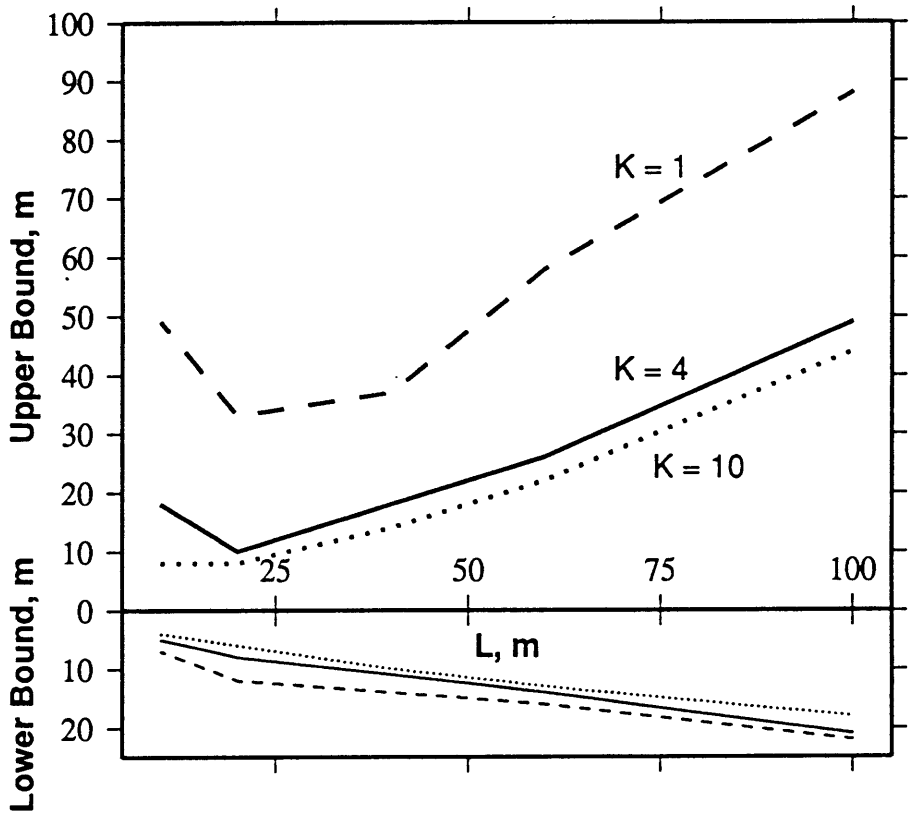

Fig. 3.21: Upper (thick) and lower (thin) bounds on the 95% confidence interval for L, as a function of L, for K of 1 (dashes), 4 (solid), and 20 (dots), for inversion results from model topographies as described in the text. Uncertainty in L is dependent on K, and increases as L increases.

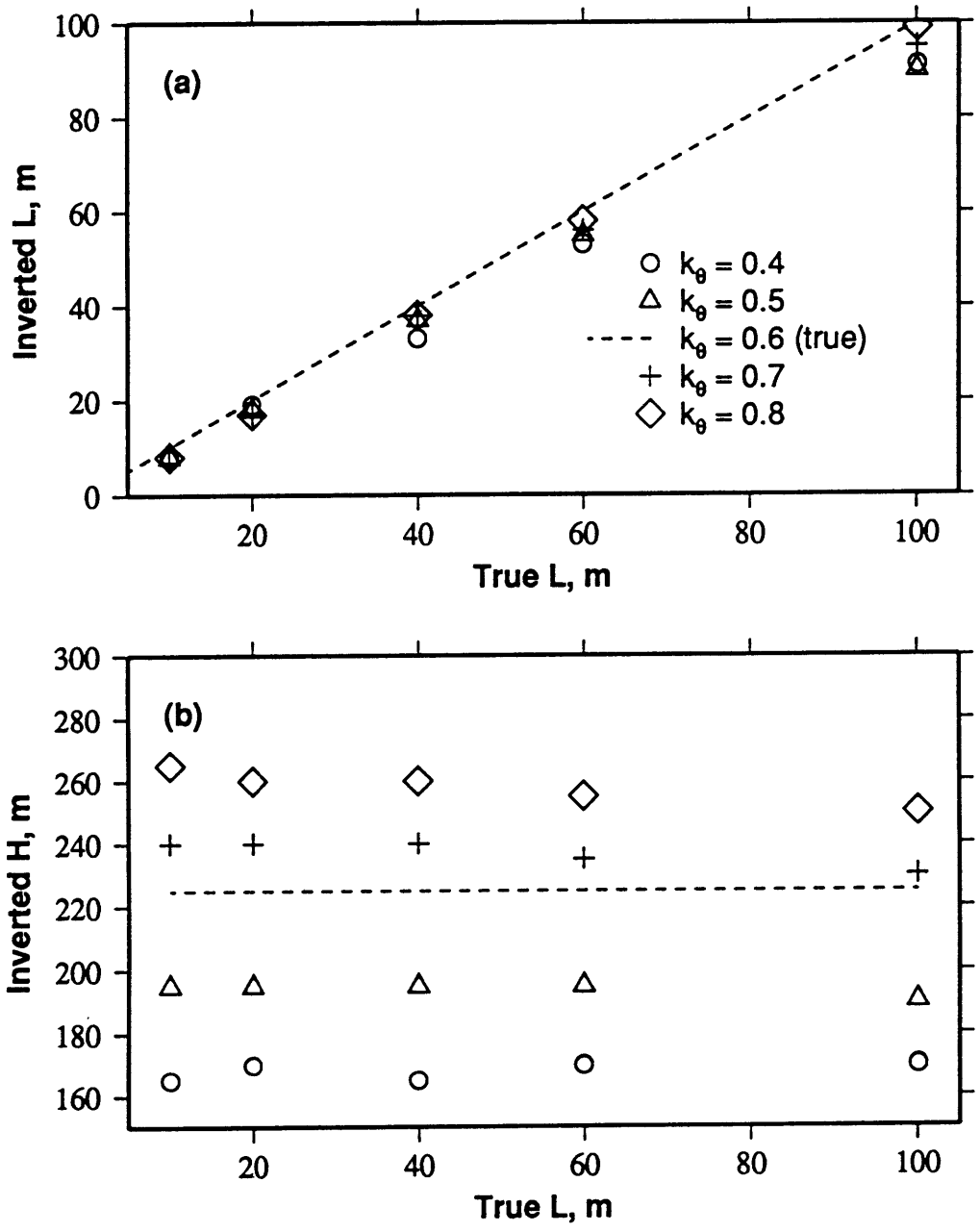

Fig. 3.22: Inverted values of L (a) and H (b) for models generated with a variety of corner wave numbers. The inversion procedure assumes k_n = 0.6 km^{-1} and k_s = 0.12 km^{-1}, leading to large errors in H but relatively little error in L.

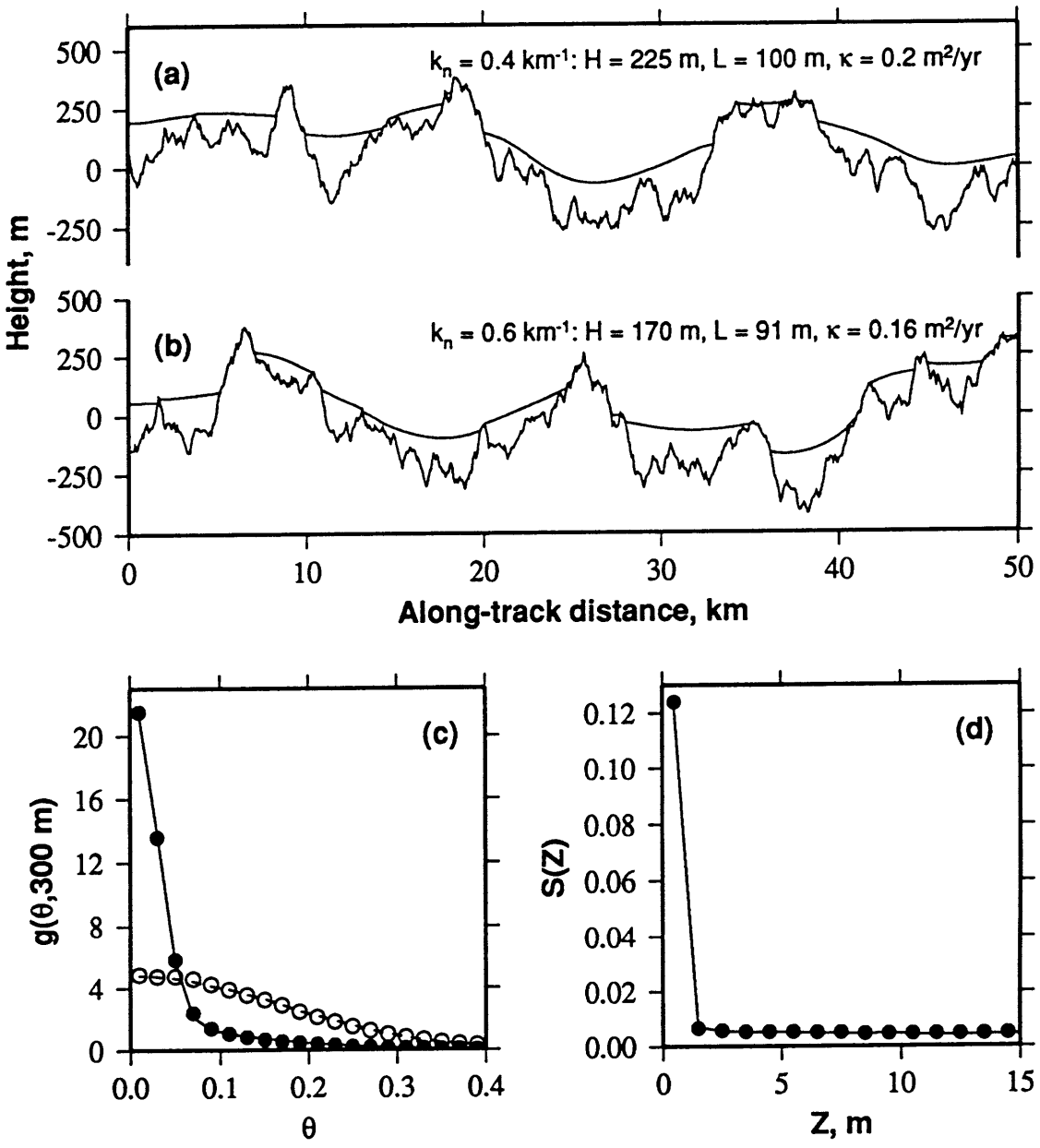

Fig. 3.23: Comparison of models with similar slope distribution functions. (a) Profile through a model generated with a k_n' of 0.4 km^{-1}, bearing an average sediment thickness L' of 100 m after 25 m.y. of model time. (b) Profile through a model generated using a k_n of 0.6 km^{-1} and parameters inverted from the model the profile in (a) is drawn from (L = 91 m, H = 170 m, κ = 0.16 m^2/yr). (c) Slope distribution functions for the sedimented surfaces of (a) (solid line) and (b) (black circles), and for the underlying basements (dashed for (a), clear circles for (b)). (d) Sediment thickness distribution functions for the sedimented surfaces of (a) (solid line) and (b) (black circles).

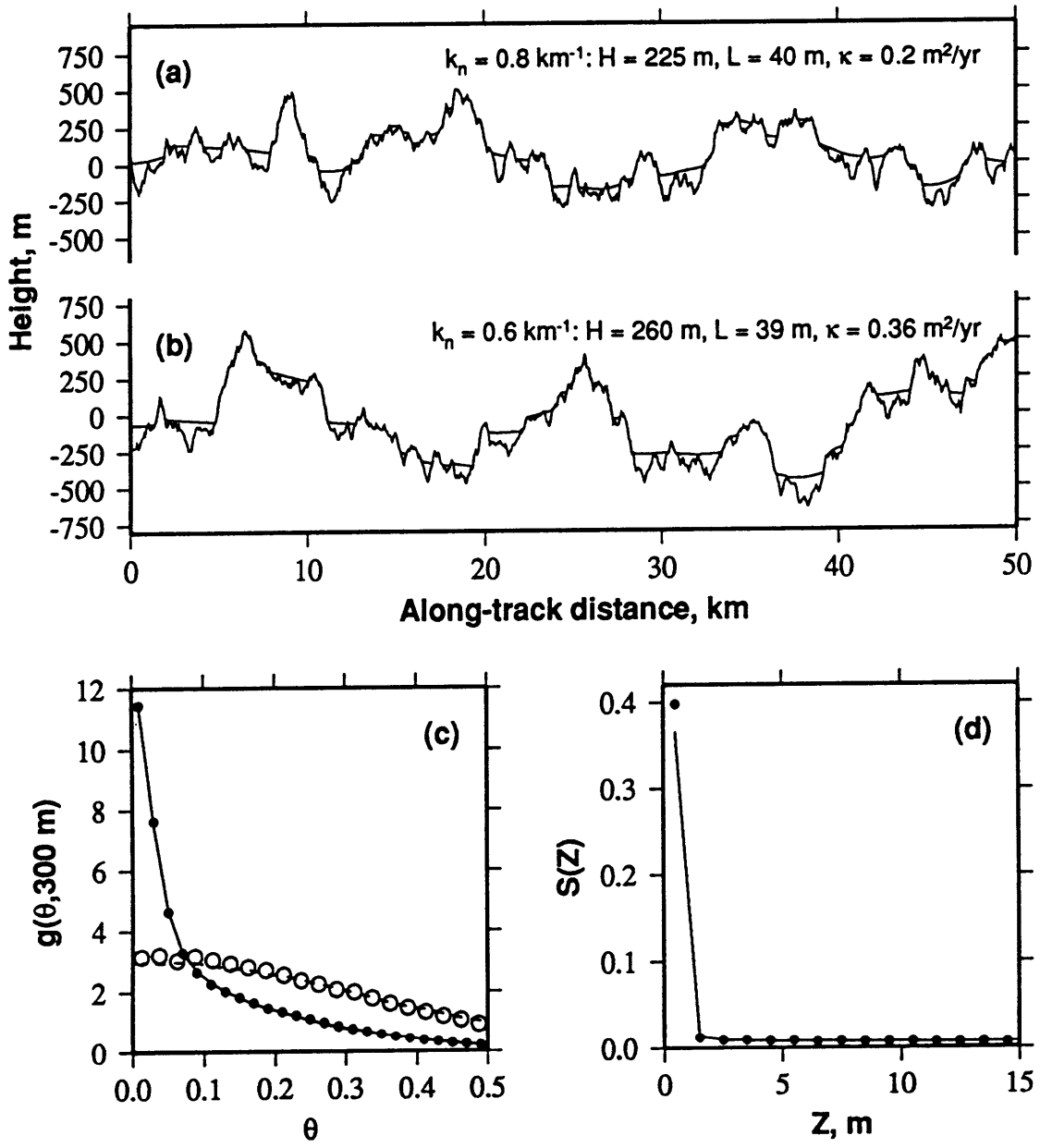

Fig. 3.24: Comparison of models with similar slope distribution functions. (a) Profile through a model generated with a k_n' of 0.8 km^{-1}, bearing an average sediment thickness L' of 40 m after 25 m.y. of model time. (b) Profile through a model generated using a k_n of 0.6 km^{-1} and parameters inverted from the model the profile in (a) is drawn from (L = 39 m, H = 260 m, κ = 0.36 m^2/yr). (c) Slope distribution functions for the sedimented surfaces of (a) (solid line) and (b) (black circles), and for the underlying basements (dashed for (a), clear circles for (b)). (d) Sediment thickness distribution functions for the sedimented surfaces of (a) (solid line) and (b) (black circles).

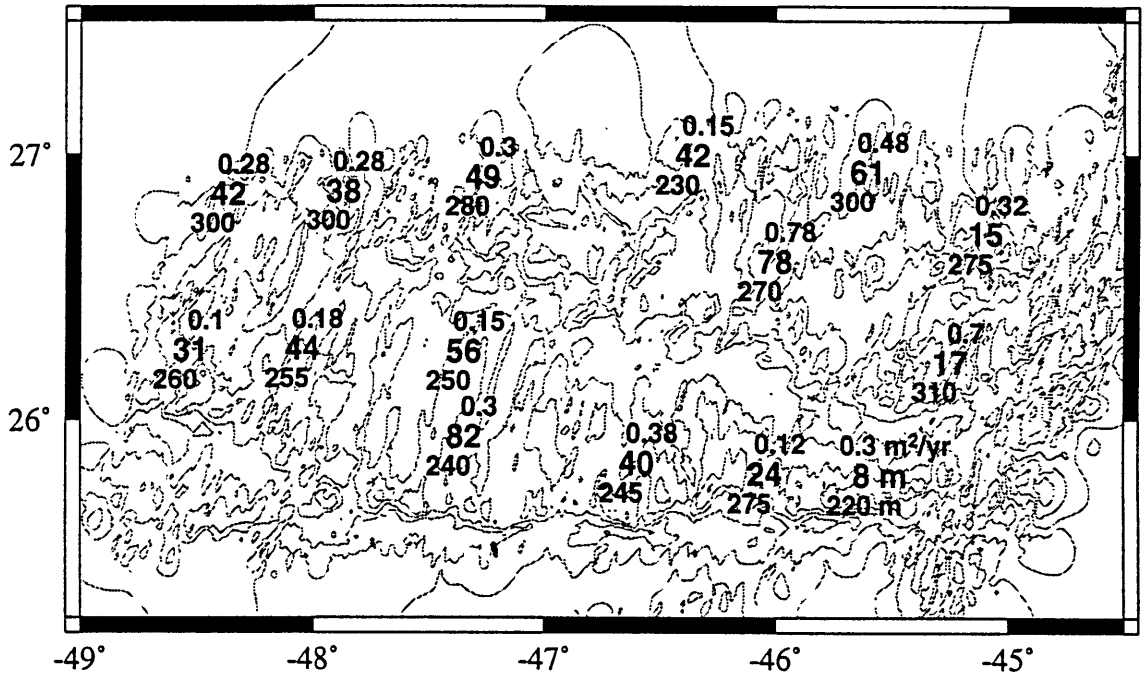

Fig. 3.25: Contour plot (interval = 500 m) of the ARC (as in Fig. 3.1) and inverted model parameters for the 15 internally-homogeneous hill-centered areas. For each of the 15 areas, the average sediment thickness L (in meters) (not corrected for the effects of compaction) is given by large number centered on the area, and the apparent diffusivity κ (in m^2/yr) and basement RMS height H (in meters) are listed as smaller numbers above and below.

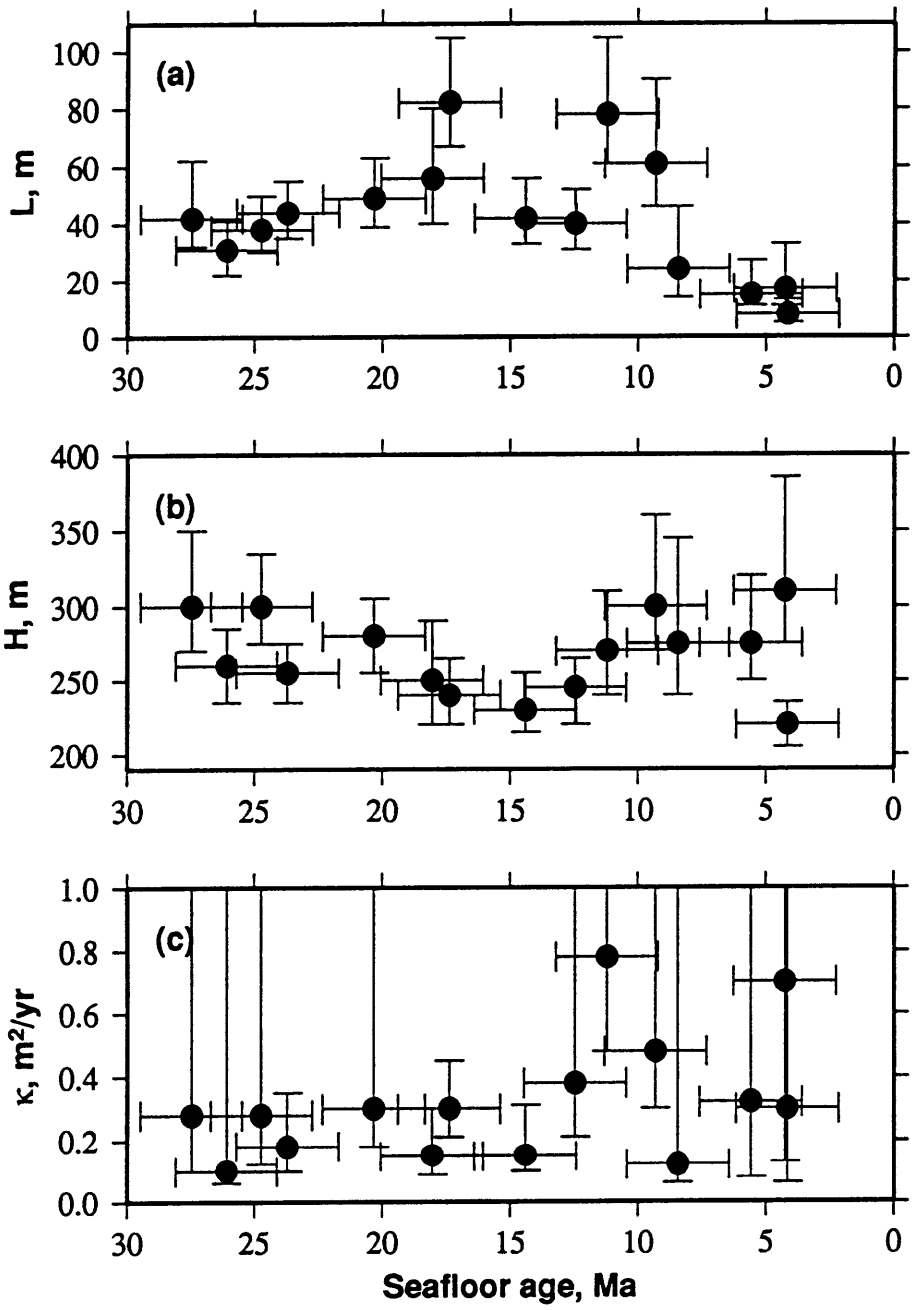

Fig. 3.26: Inverted values, and 95% confidence bounds, of L (a), H (b), and κ (c), as a function of seafloor age T. Bounds in horizontal direction indicate the range of seafloor ages that contribute to each inversion result.

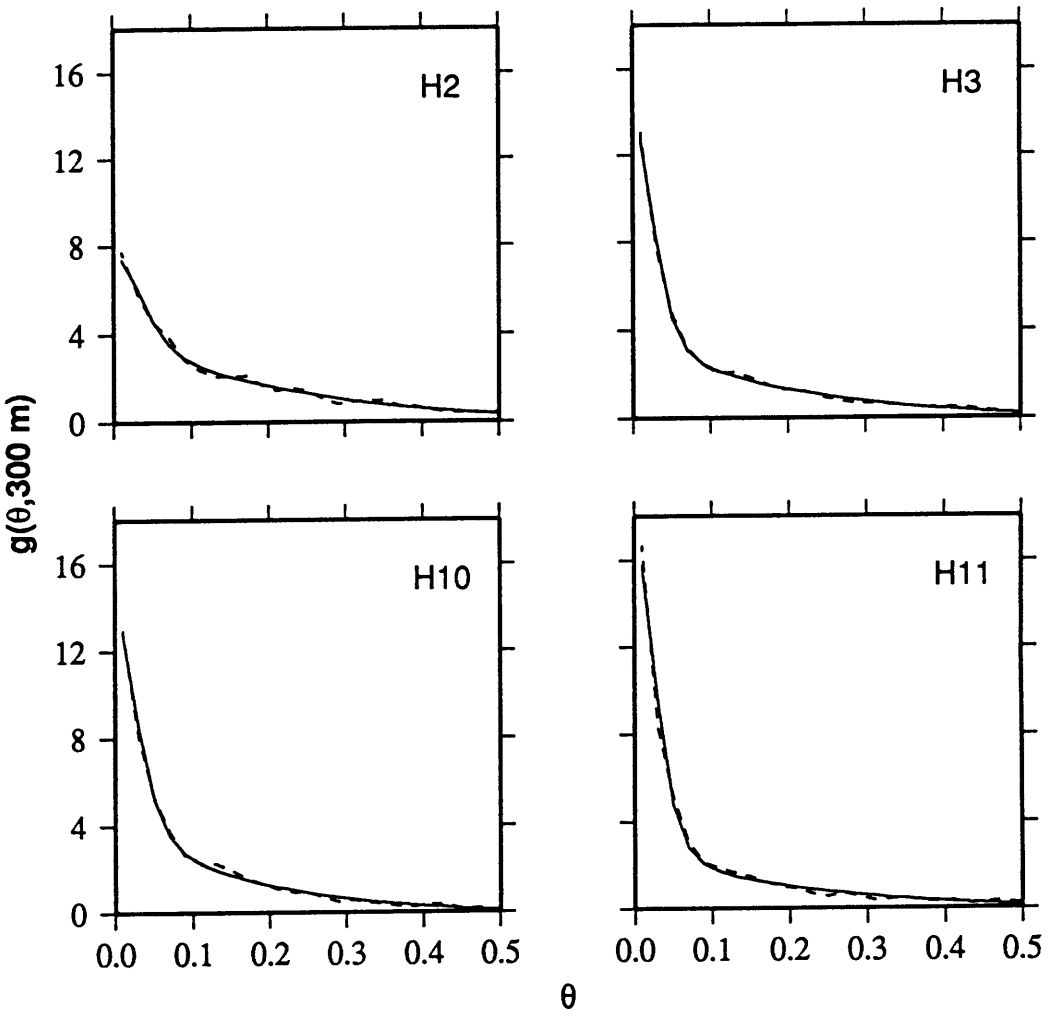

Fig. 3.27: Examples of fits between model slope distribution functions and slope distribution functions from data for hill-centered regions H2, H3, H10, and H11.

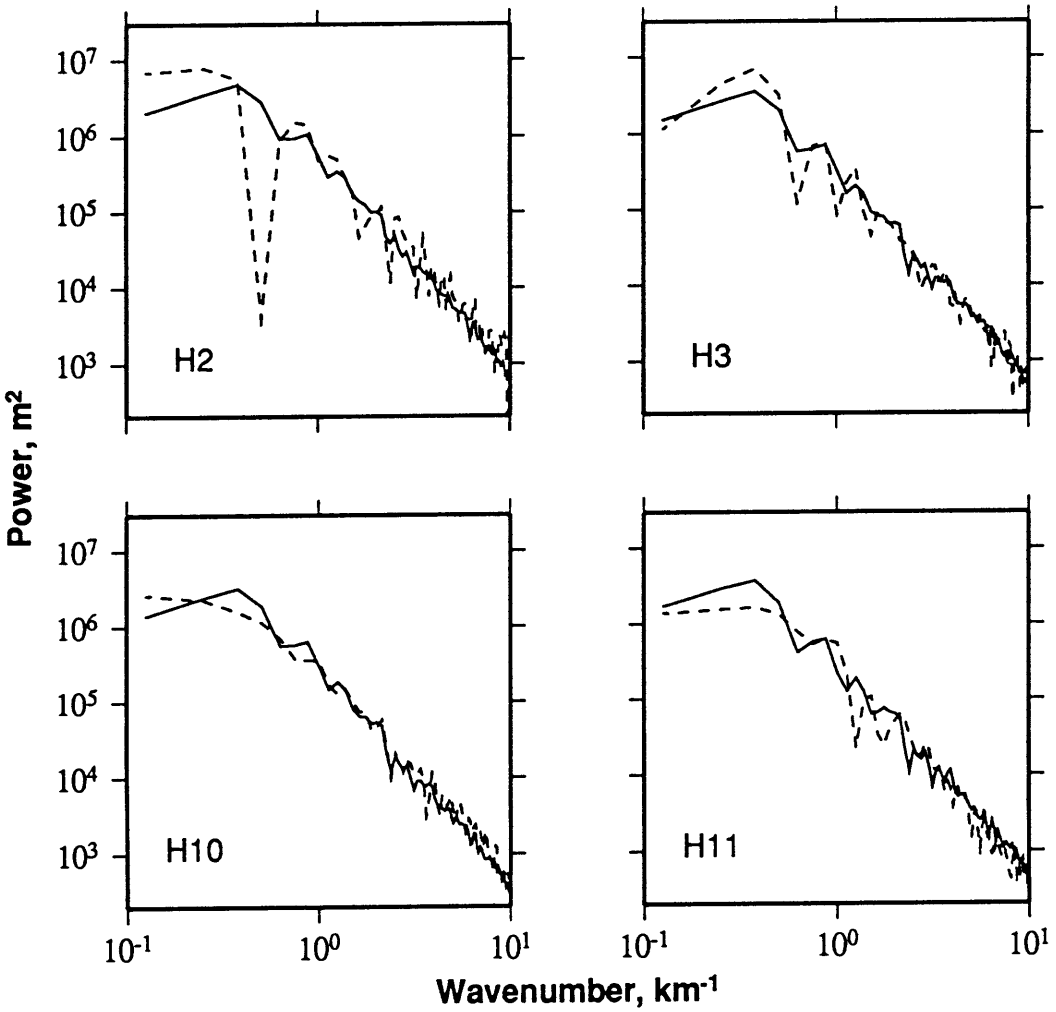

Fig. 3.28: Examples of fits between power spectra computed from data and from models generated using the best-fitting model parameters for hill-centered regions H2, H3, H10, and H11.

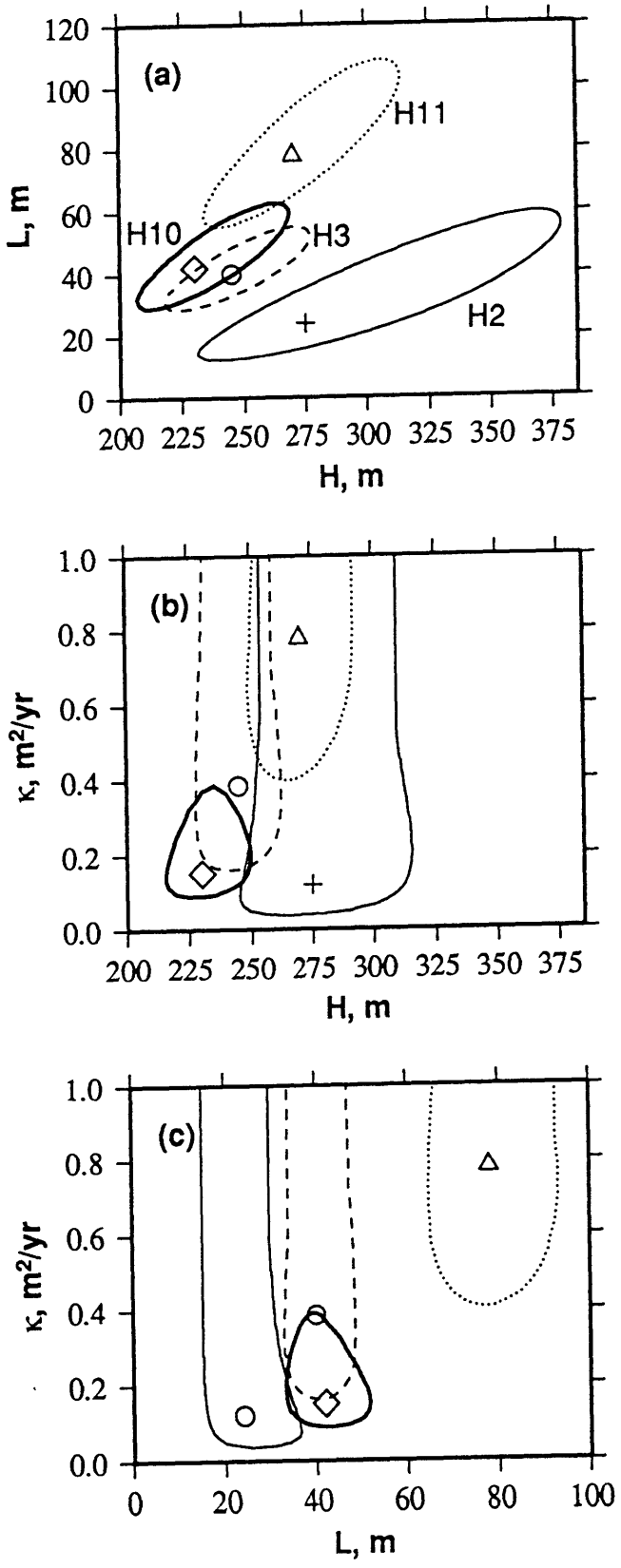

Fig. 3.29: Slices through 95% confidence regions resulting from the inversion of the slope distribution functions of hill-centered subregions H2 (thin solid lines, crosses), H3 (dashed lines, circles), H10 (thick solid lines, diamonds), and H11 (dotted lines, triangles). (a) 95% confidence bounds on H and L and best estimates (symbols) for cross-sections at best estimates of κ. (b) 95% confidence bounds on κ and H and best estimates (symbols) for cross-sections at best estimates of L. (c) 95% confidence bounds on κ and L and best estimates (symbols) for cross-sections at best estimates of H.

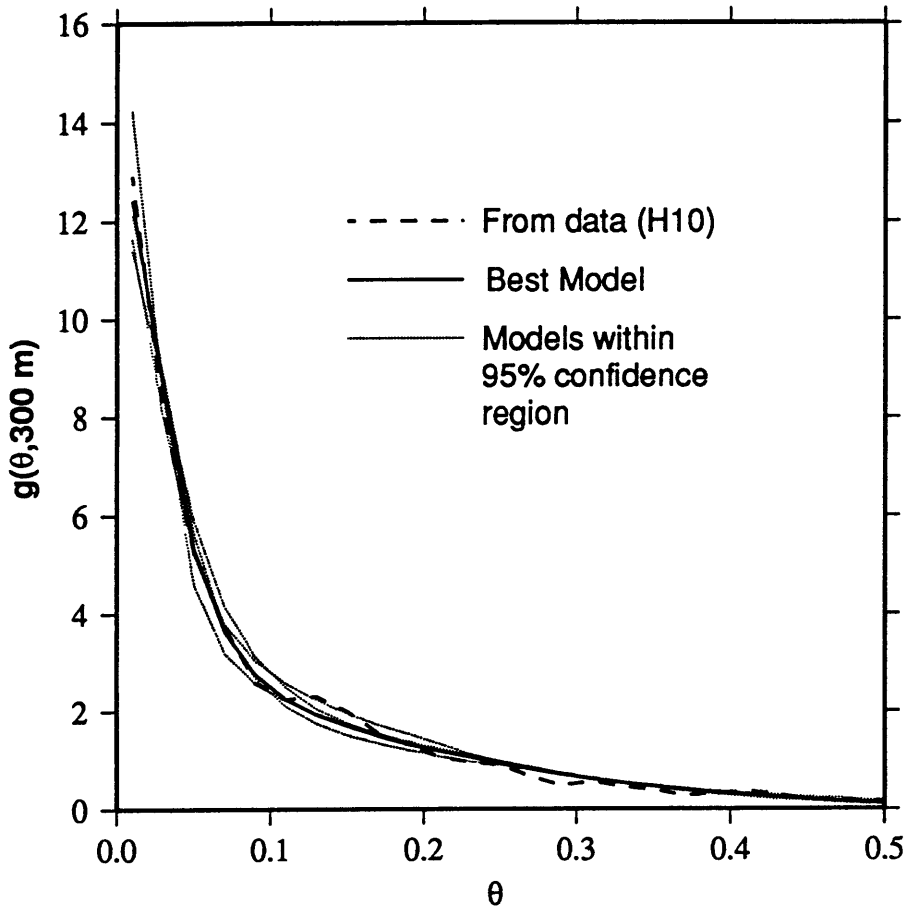

Fig. 3.30: Slope distribution function $g(\theta,300\text{ m})$ for the hill-centered subregion H10 (dashed line), best-fitting theoretical model ($H = 230$ m, $\kappa = 0.15$ m^2/yr, $L = 42$ m) (solid line), and other models which lie within the 95% likelihood bounds for the region (dotted lines).

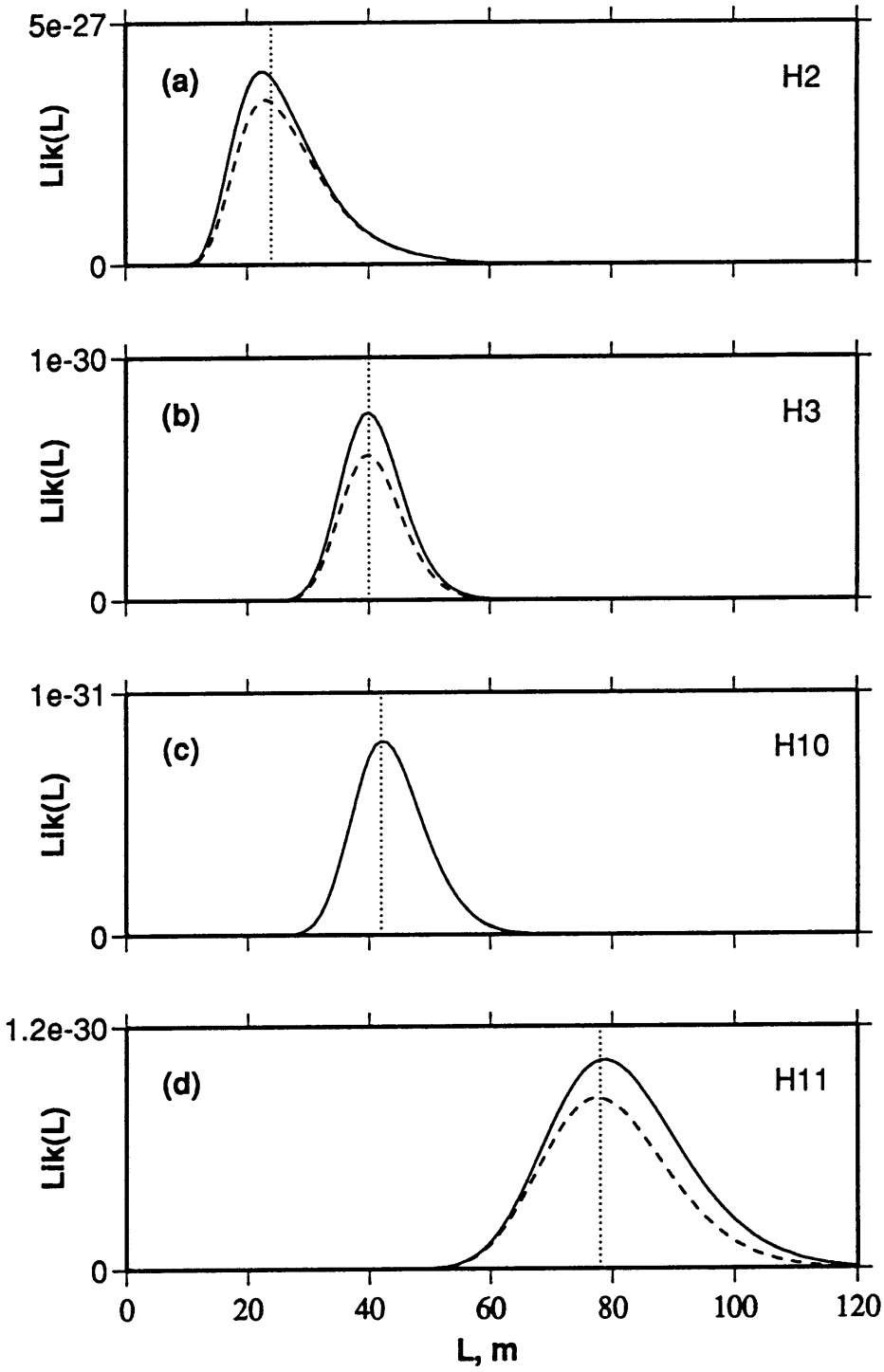

Fig. 3.31: Likelihood distribution of L for subregions H2, H3, H10, and H11, as labeled, for inversion computations in which κ ranged from $0.2(L/T)/(0.36\ \text{km}^{-2}H)$ to $20(L/T)/(0.36\ \text{km}^{-2}H)$ (solid lines) and $15(L/T)/(0.36\ \text{km}^{-2}H)$ (dashed lines). Dotted lines denote L.

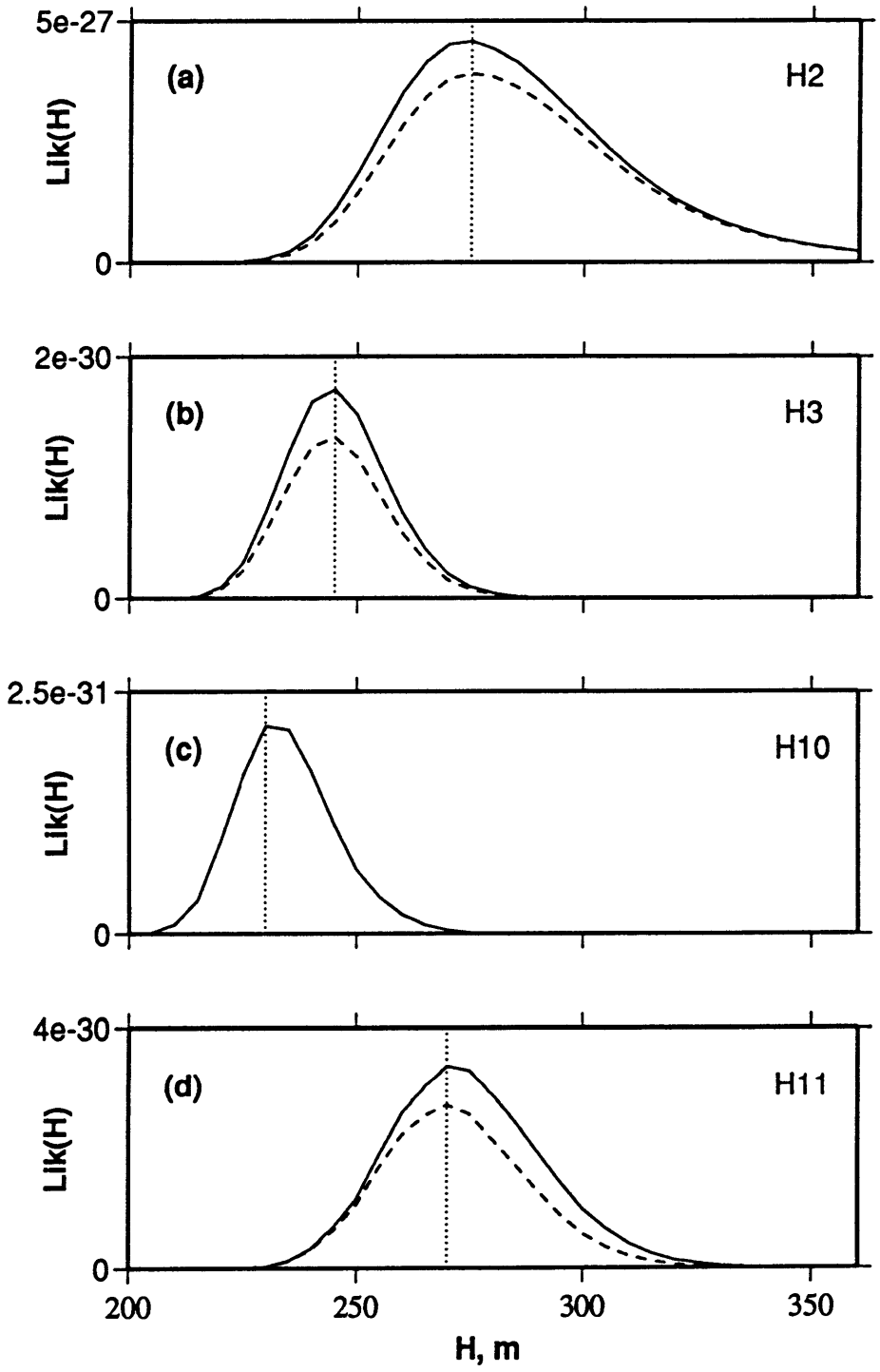

Fig. 3.32: Likelihood distribution of H for subregions H2, H3, H10, and H11, as labeled, for inversion computations in which κ ranged from $0.2(L/T)/(0.36\ \text{km}^{-2}H)$ to $20(L/T)/(0.36\ \text{km}^{-2}H)$ (solid lines) and $15(L/T)/(0.36\ \text{km}^{-2}H)$ (dashed lines). Dotted lines denote H.

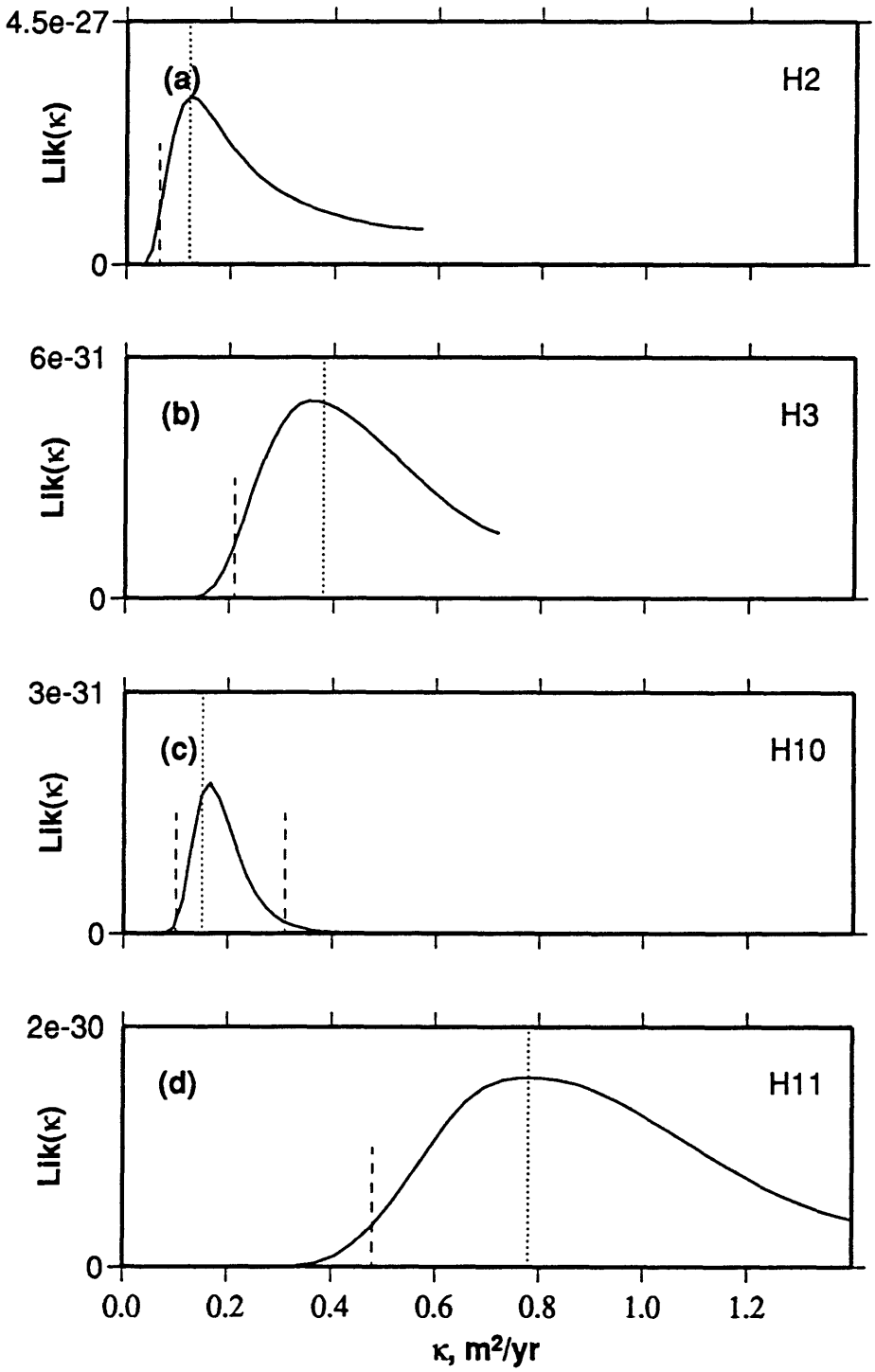

Fig. 3.33: Likelihood distribution of κ for subregions H2, H3, H10, and H11, as labeled. Dashed lines denote lower and, in (c), upper bounds on 95% confidence intervals of κ. Dotted lines denote κ.

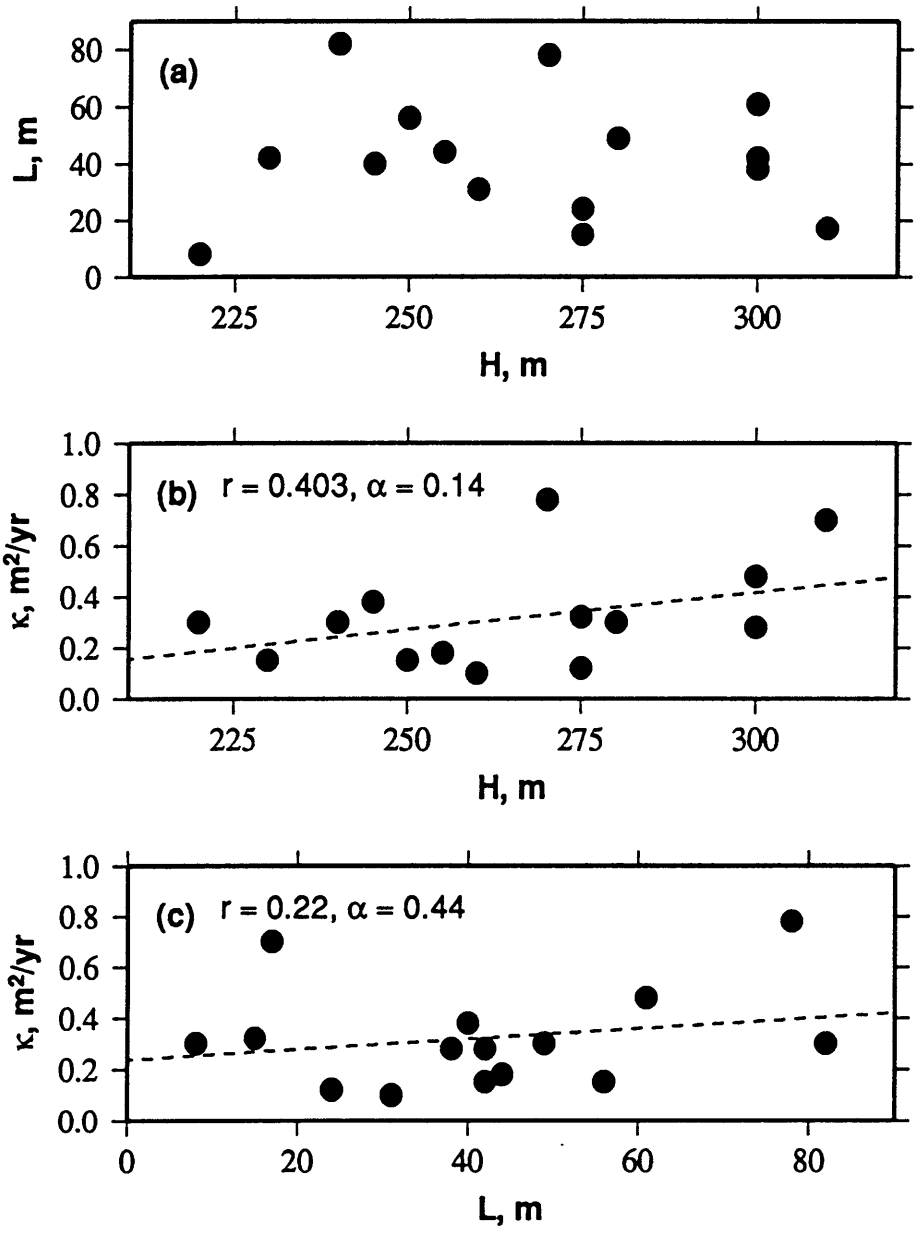

Fig. 3.34: (a) Inverted values of L vs. H for hill-centered regions. L and H are completely uncorrelated (sample correlation coefficient r = -0.0436). (b) Inverted values of κ vs. H for hill-centered regions, and best-fitting line (dashes). The sample correlation coefficient r is 0.403, equivalent to a z of 1.48 and a probability of correlation of 0.86. (c) Inverted values of κ vs. L for hill-centered regions, and best-fitting line (dashes). The sample correlation coefficient r is 0.221, equivalent to a z of 0.778 and a probability of correlation of 0.56.

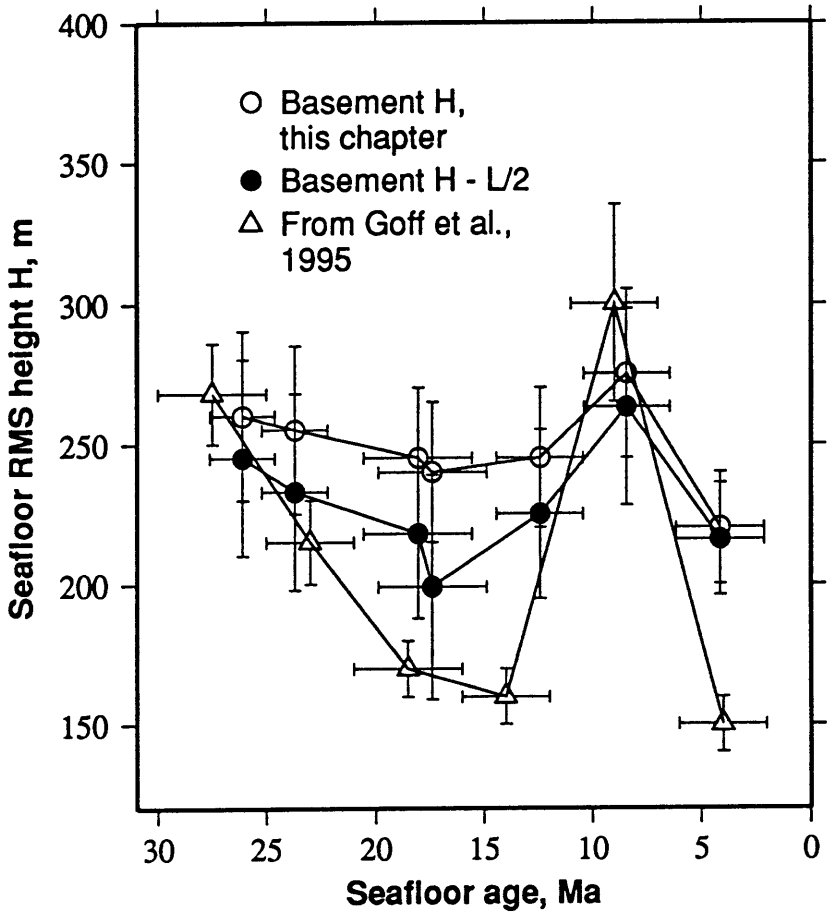

Fig. 3.35: Comparison between inversion results for seafloor RMS variability from *Goff et al.* [1995] (triangles) with our inversion results from regions H1, H2, H3, H4a, H4b, H5, and H6, which lie south of the discontinuity which trends east-west through the ARC, before (clear circles) and after (black circles) being adjusted for the effects of sedimentation on surface values of H, based our observations in Chapter 2. While our values are not quite as widely spread as those of *Goff et al.* [1995], they vary qualitatively with those of *Goff et al.* [1995] and cover much of the same range.

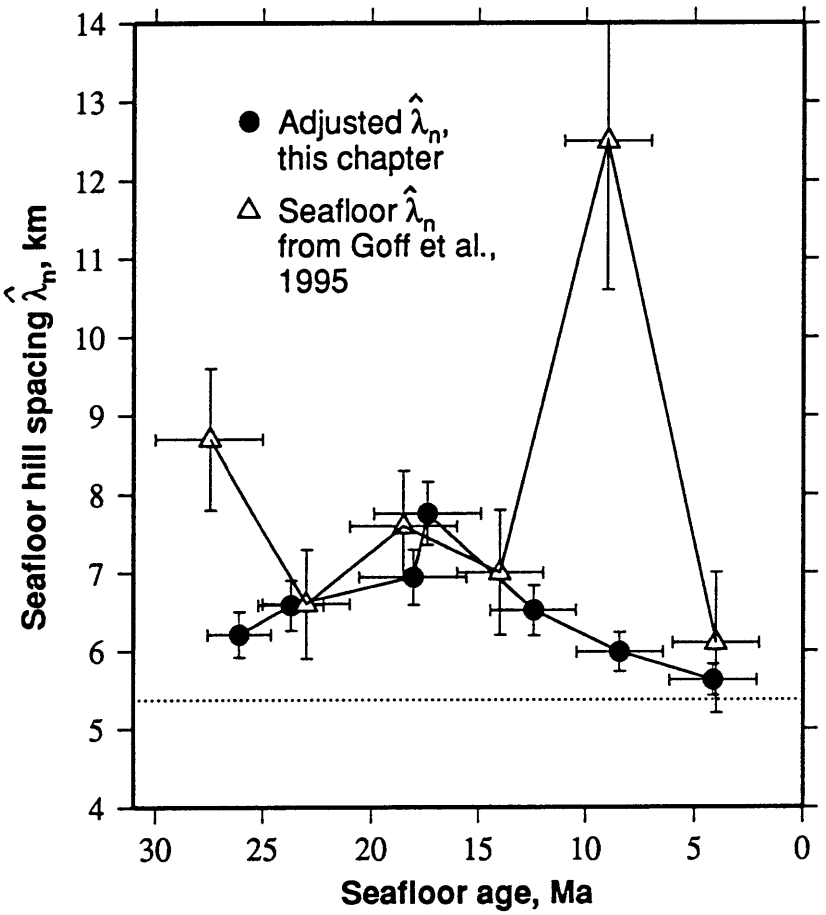

Fig. 3.36: Comparison between inversion results for along-flowline hill spacings from *Goff et al.* [1995] (triangles) with estimates calculated via (2.31) from regions H1, H2, H3, H4a, H4b, H5, and H6, which lie south of the discontinuity which trends east-west through the ARC (solid circles). Dotted line represents the assumed basement hill spacing of 5.37 km which correlates with a k_n of 0.6 km^{-1}.

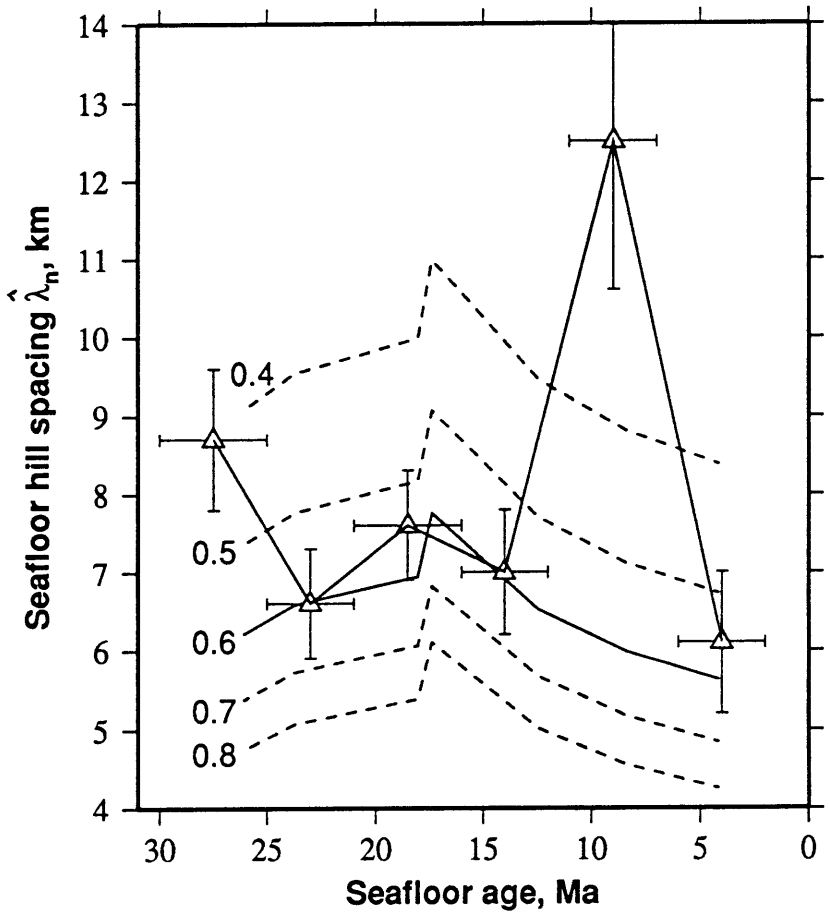

Fig. 3.37: Comparison between inversion results for along-flowline hill spacings from *Goff et al.* [1995] (triangles) with estimates calculated via (2.31) from regions H1, H2, H3, H4a, H4b, H5, and H6, given basement k_n of 0.4, 0.5, 0.6, 0.7, and 0.8 km^{-1}, as labeled.

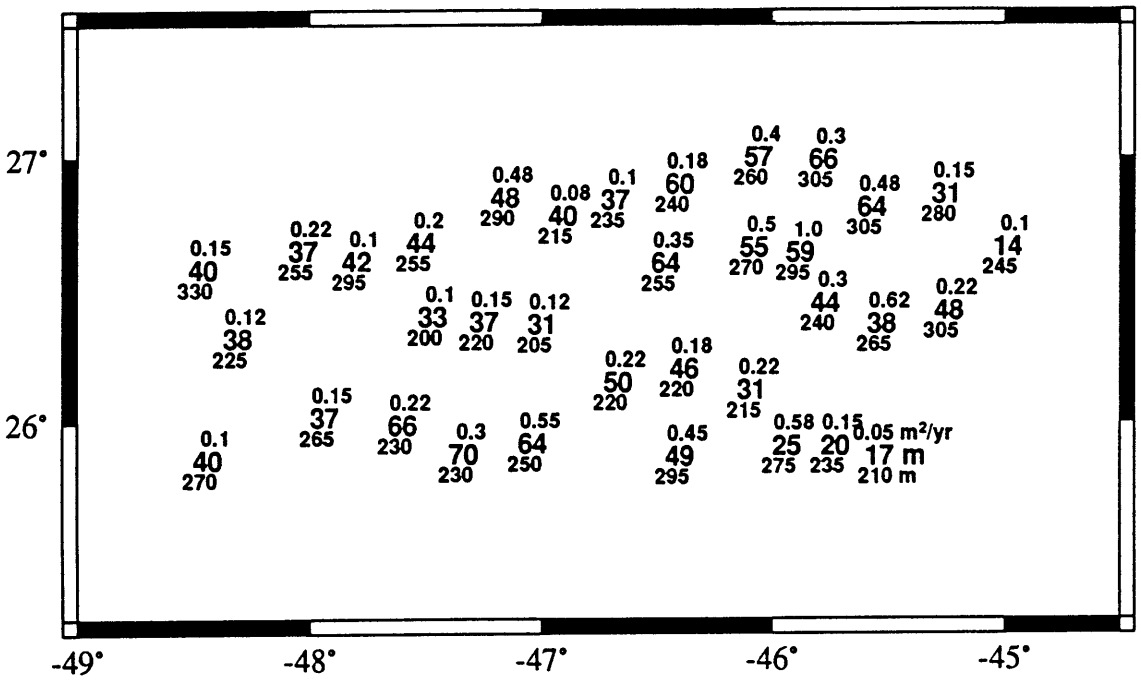

Fig. 3.38: Inverted model parameters for the 35 basin-centered regions. For each of the 35 areas, the average sediment thickness L (in meters) (not corrected for the effects of compaction) is given by large number centered on the area, and the apparent diffusivity κ (in m^2/yr) and basement RMS height H (in meters) are listed as smaller numbers above and below.

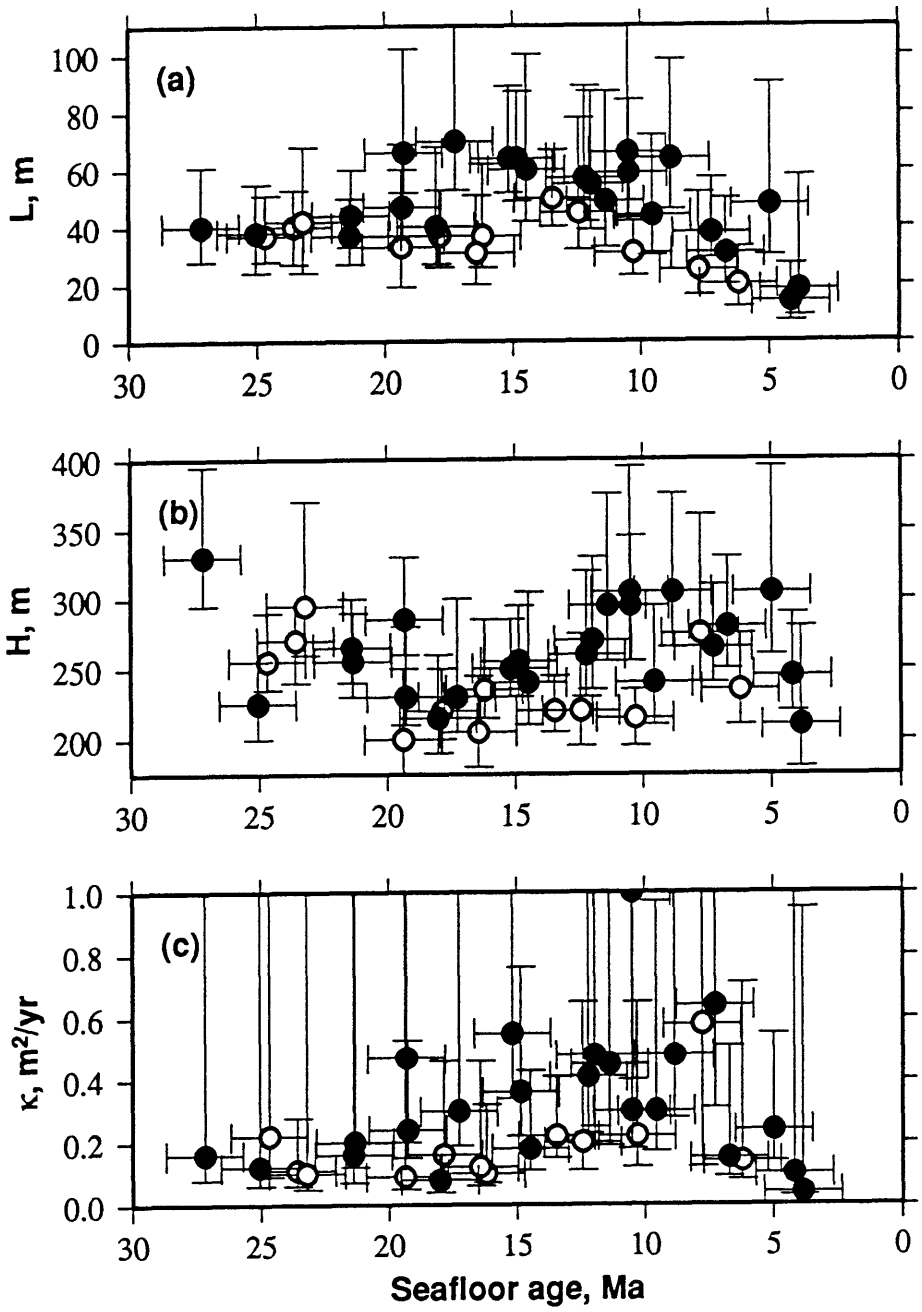

Fig. 3.39: Inverted values, and 95% confidence bounds, of non-compaction-corrected L (a), H (b), and κ (c), as a function of seafloor age T, from basin-centered regions. Results from the 23 regions which do not overlie relic spreading center boundaries are given by filled circles, while clear circles give results from the 12 areas which overlie relic spreading center boundaries. Bounds in horizontal direction indicate the range of seafloor ages that contribute to the inversion results.

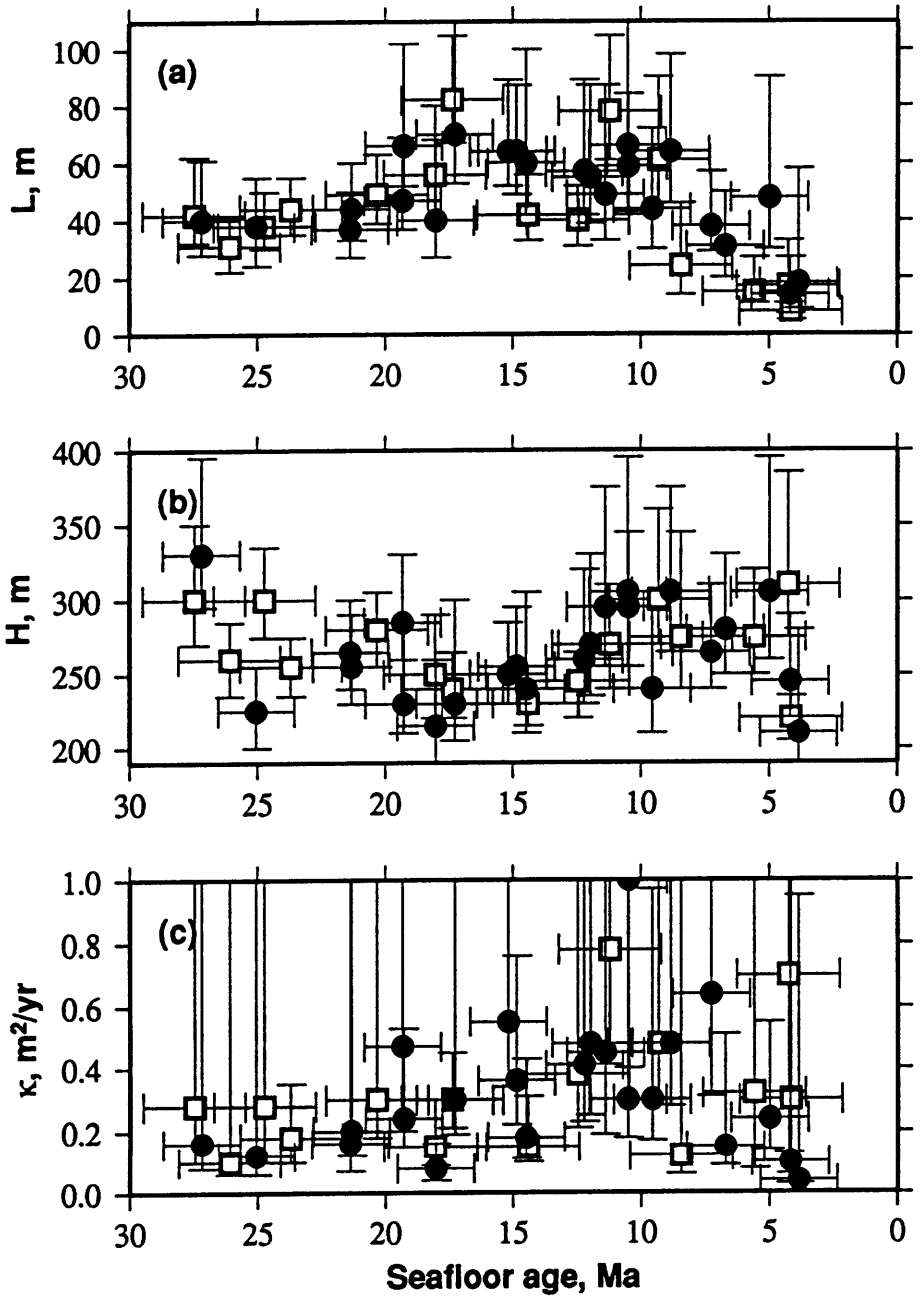

Fig. 3.40: Inverted values, and 95% confidence bounds, of non-compaction-corrected L (a), H (b), and κ (c), as a function of seafloor age T, from the 23 basin-centered regions which do not overlie relic spreading center boundaries (filled circles) and from hill-centered regions (clear squares). Bounds in horizontal direction indicate the range of seafloor ages that contribute to the inversion results.

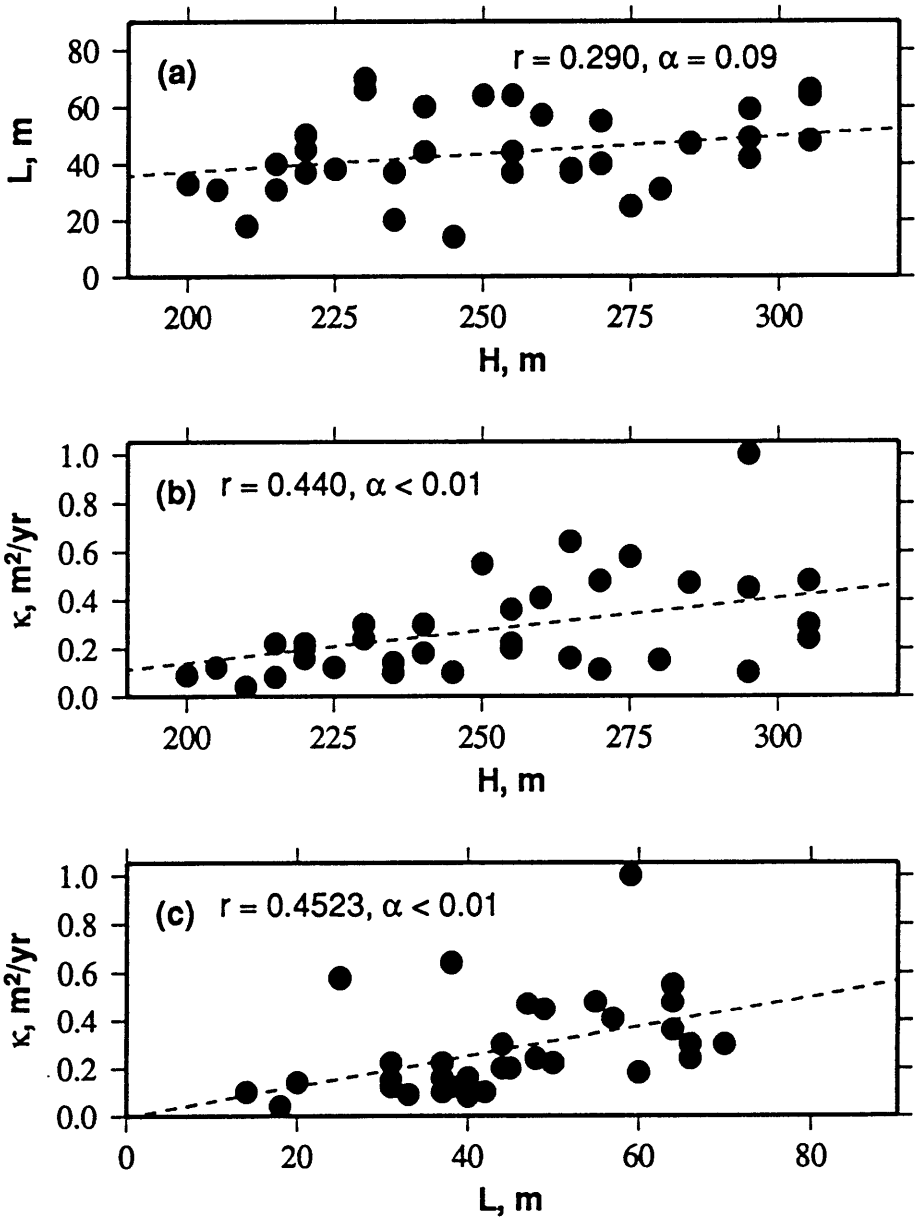

Fig. 3.41: (a) Inverted values of L vs. H for all 35 basin-centered regions, and best-fitting line (dashes). The sample correlation coefficient r is 0.290, equivalent to a z of 1.69 and a probability of correlation of 0.91. (b) Inverted values of κ vs. H for all 35 basin-centered regions, and best-fitting line (dashes). The sample correlation coefficient r is 0.440, equivalent to a z of 2.67 and a probability of correlation greater than 0.99. (c) Plot of inverted values of κ vs. L for all 35 basin-centered regions, and best-fitting line (dashes). The sample correlation coefficient r is 0.452, equivalent to a z of 2.76 and a probability of correlation greater than 0.99.

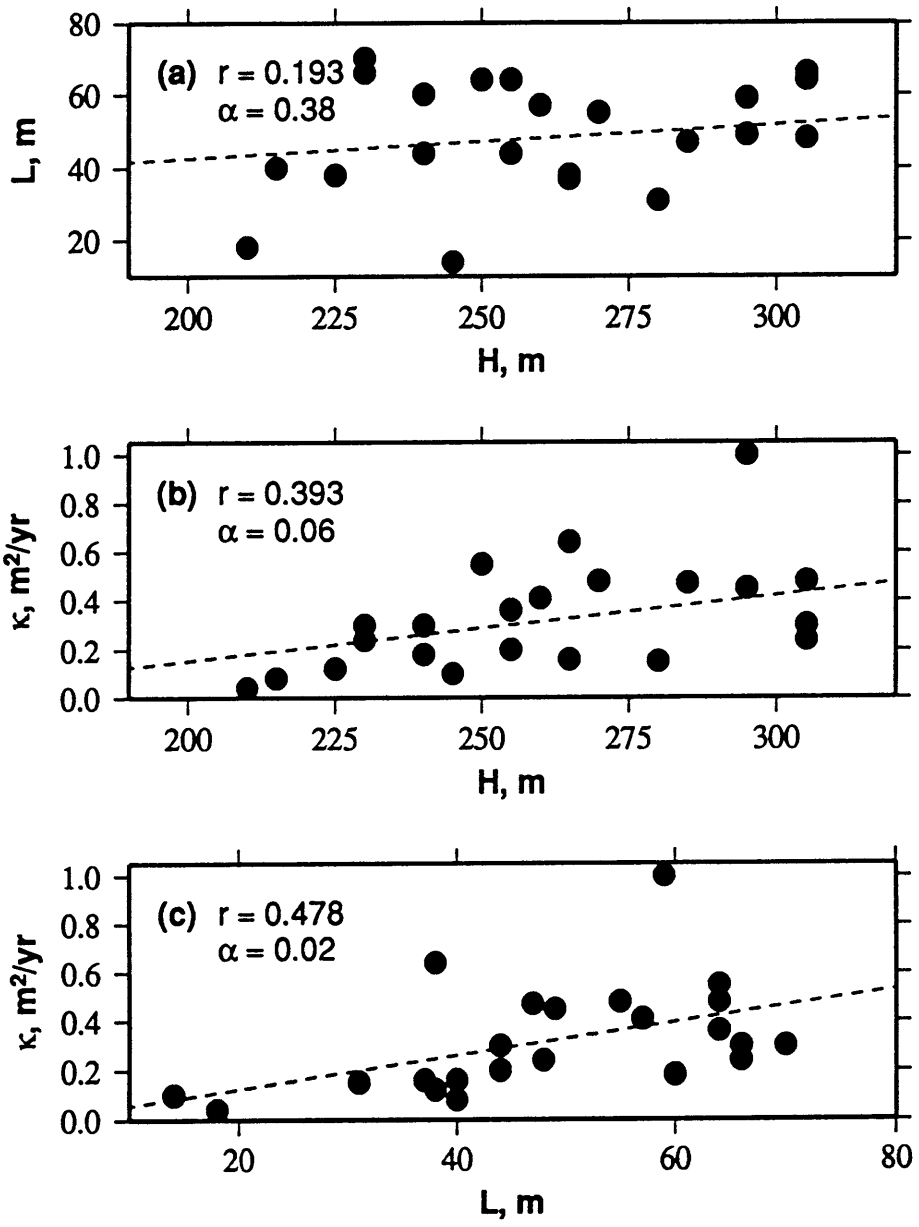

Fig. 3.42: (a) Inverted values of L vs. H for the 23 basin-centered regions which do not overly intersegment lows, and best-fitting line (dashes). The sample correlation coefficient r is 0.193, equivalent to a z of 0.87 and a probability of correlation of 0.62. (b) Inverted values of κ vs. H for the 23 basin-centered regions which do not overly intersegment lows, and best-fitting line (dashes). The sample correlation coefficient r is 0.393, equivalent to a z of 1.86 and a probability of correlation of 0.94. (c) Inverted values of κ vs. L for the 23 basin-centered regions which do not overly intersegment lows, and best-fitting line (dashes). The sample correlation coefficient r is 0.478, equivalent to a z of 2.33 and a probability of correlation of 0.98.

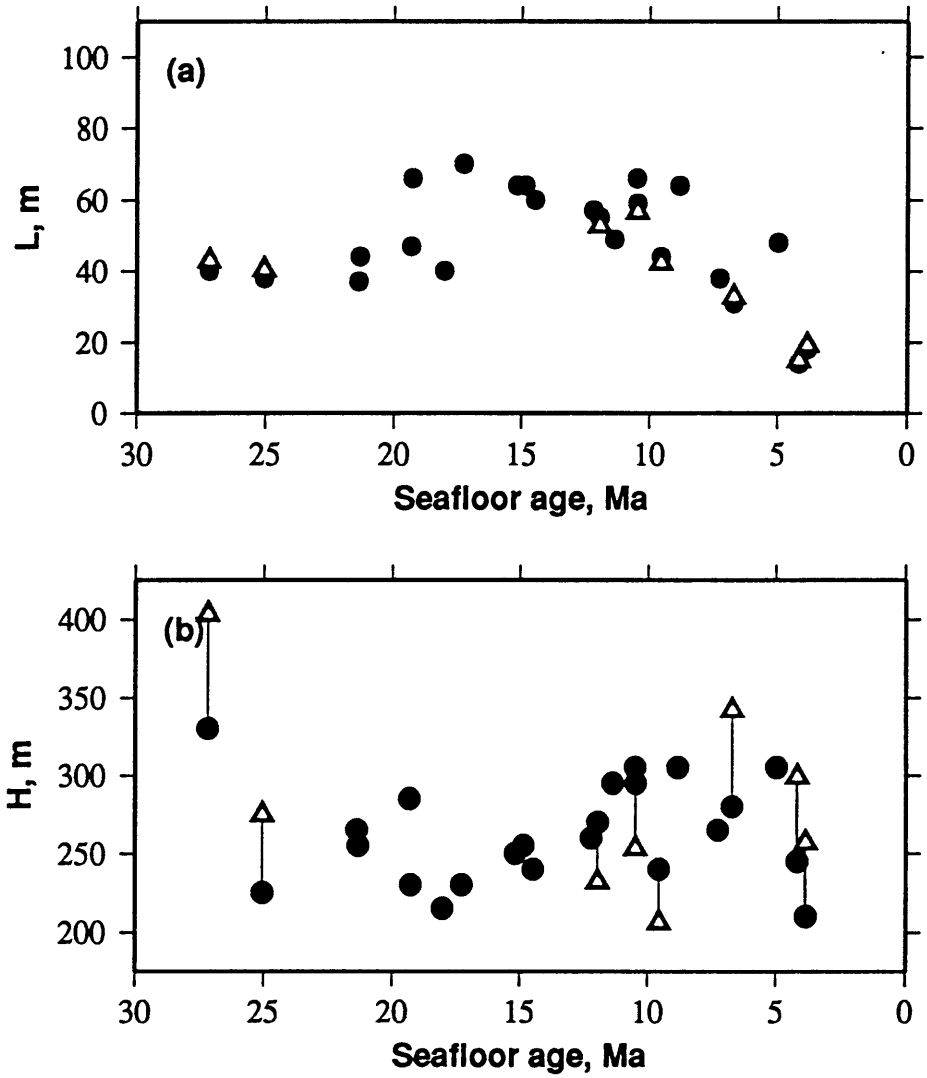

Fig. 3.43: (a) Inverted values of L for the 23 basin-centered regions which do not overly intersegment lows (filled circles), and values of L after adjustments due to alternate estimations of k_n (clear triangles) for the eight regions for which a k_n of 0.6 km^{-1} is suspect. (b) Inverted values of L for the 23 basin-centered regions which do not overly intersegment lows (filled circles), and values of L after adjustments due to alternate estimations of k_n (clear triangles) for the eight regions for which a k_n of 0.6 km^{-1} is suspect. Vertical lines link inverted values of H before and after adjustment.

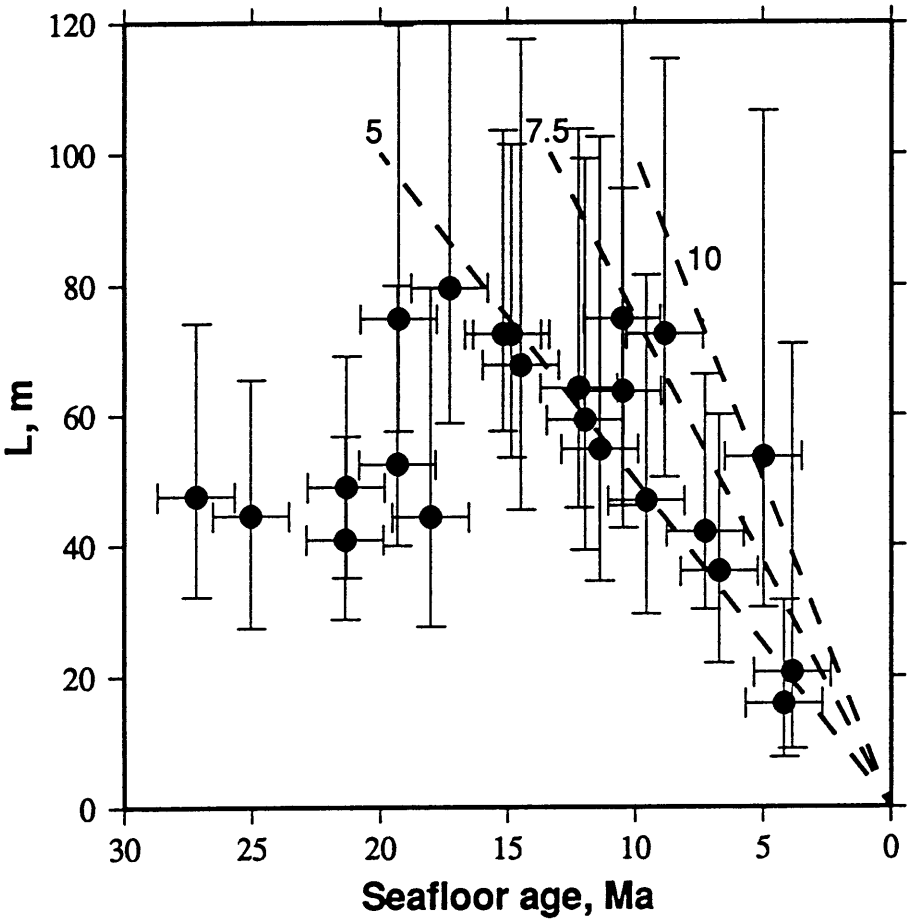

Fig. 3.44: (a) Inverted values of L for the 23 basin-centered regions which do not overly intersegment lows (filled circles), adjusted for the effects of the (possible) misestimation of k_n during the inversion procedure and for the effects of compaction. Dashed lines represent expected values of L given average sediment accumulation rates of 5, 7.5, and 10 m/m.y., as labeled.

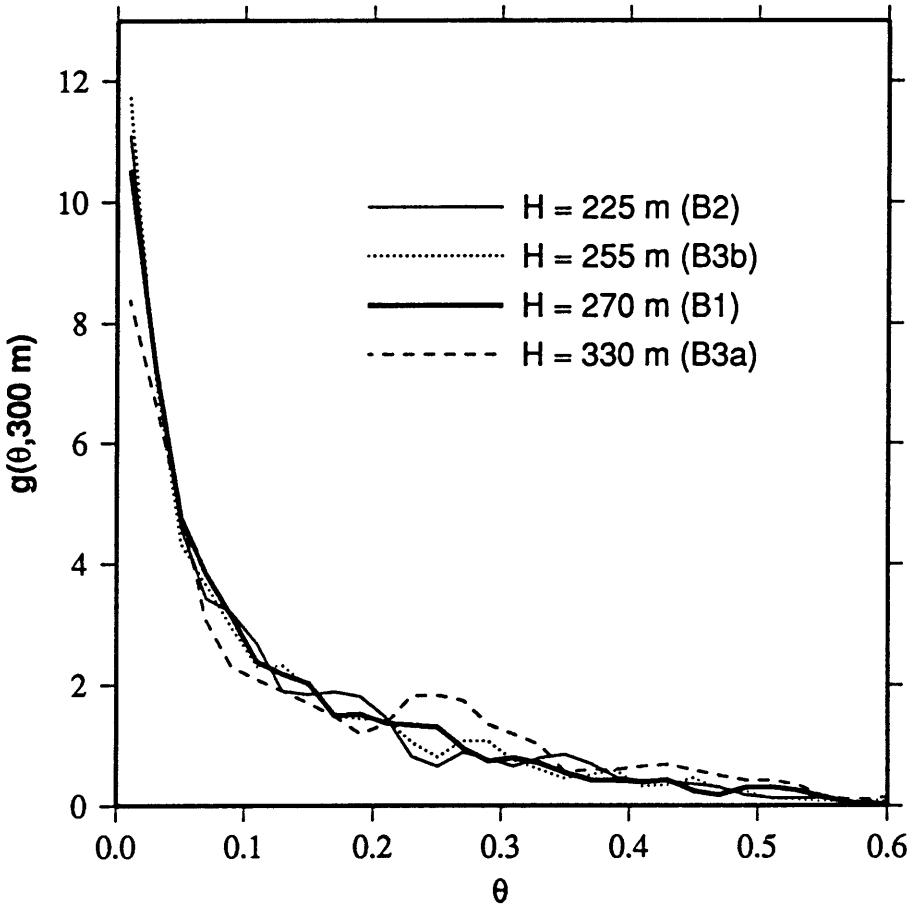

Fig. 3.45: Slope distribution functions computed from the four western-most basin-centered regions, as labeled, all of which have L between 37 and 40 m. The crossing of functions at moderate θ reflects the varying basement morphologies of the regions.

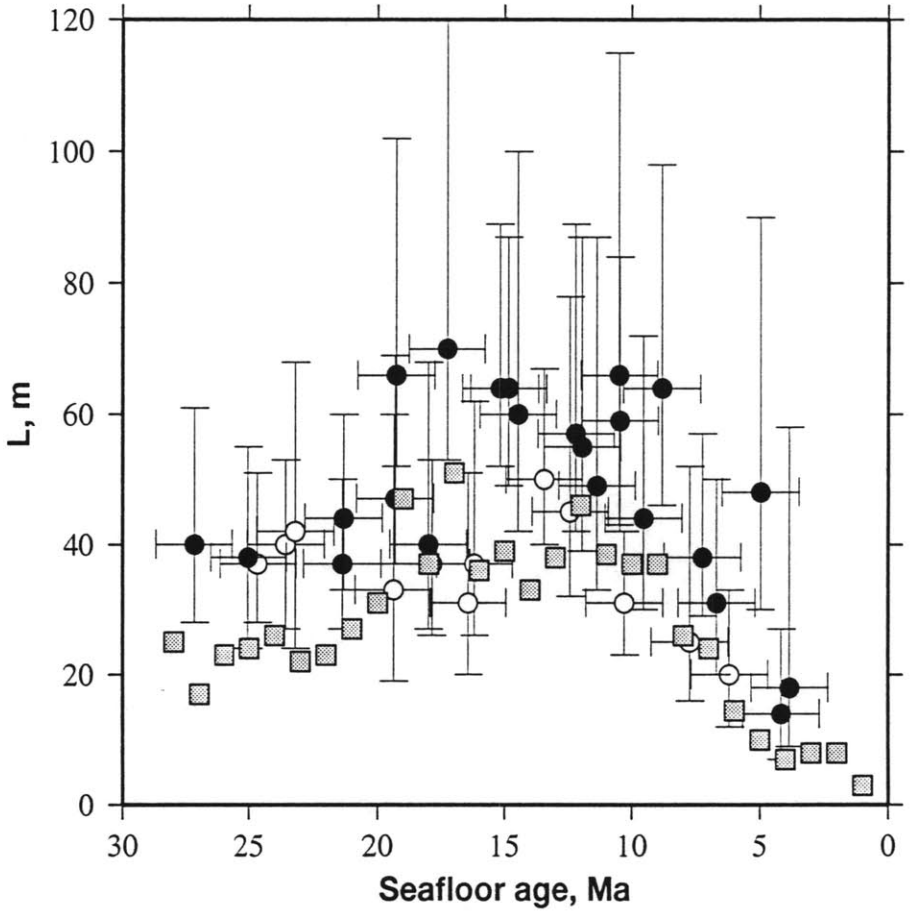

Fig. 3.46: Inverted values of L (not corrected for the effects of compaction) from the basin-centered regions, with values from the 12 regions which contain spreading-center boundaries in white and from the other 23 regions in black, and estimates of sediment thickness from seismic data measured by *Jaroslow and Tucholke* [1995] (gray squares). Our estimates are ~50% above the values of Jaroslow and Tucholke, but quantitatively the trends are very similar.

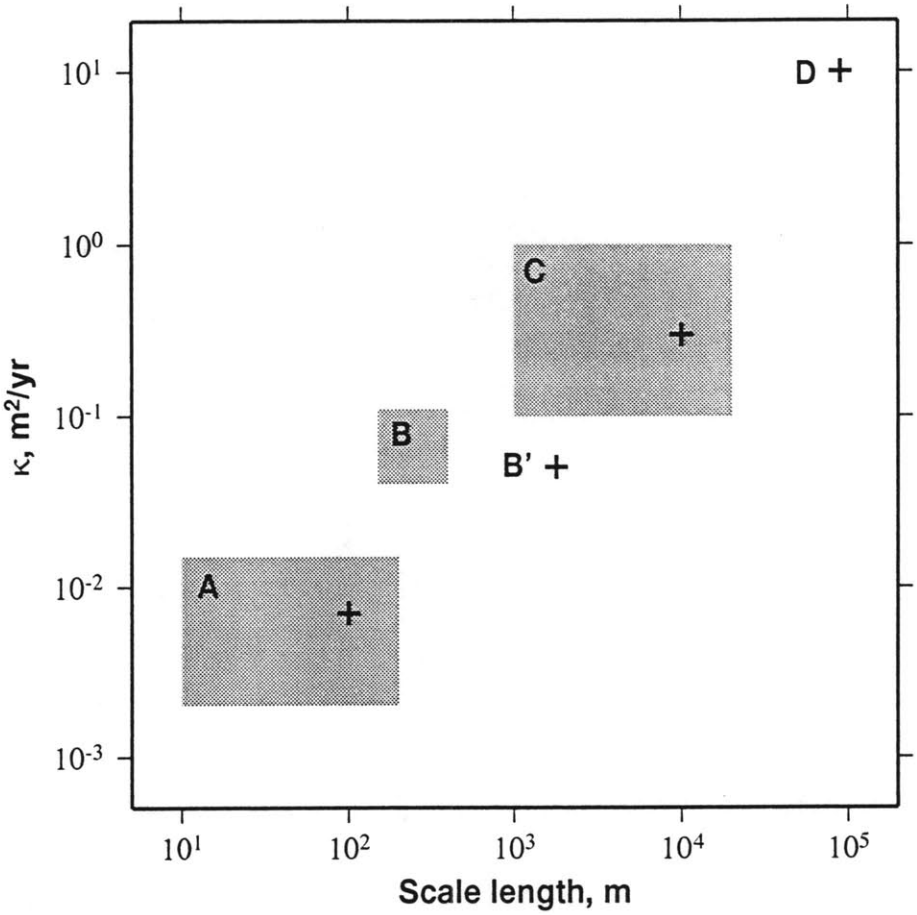

Fig. 3.47: Apparent diffusivity values inverted using techniques which observe sediment transport at scales ranging from meters to tens of kilometers. Box A shows the distances (10 m to 200 m) over which sediment creep is observable in deep-tow data from the Galapagos Ridge, and the range of values of κ (0.002 to 0.015 m^2/yr) which describe the shapes of the structures governed by creep, from *Mitchell* [1996]. The enclosed cross denotes the average κ of 0.007 m^2/yr and a typical length scale of 100 m. Box B shows the widths (150 to 400 m) of small basins observable in deep-tow data from the FAMOUS region and the ARC, and the range of values of κ (0.04 to 0.11 m^2/yr) which describe the shapes of pond surfaces in *Mitchell* [1995]. The cross labeled B' denotes the κ of 0.05 m^2/yr we infer for a 1.8-km-wide pond imaged by deep-tow data in Chapter 2. Box C shows the range of diffusivity values we invert in this chapter, and the range of hill-spacings seen in the Hydrosweep bathymetry data. The enclosed cross denotes the average κ of 0.3 m^2/yr and a hill spacing of 10 km, which takes into account along-pond transport. The cross labeled D is our estimate of the κ, 10 m^2/yr, required to form level, deep ponds in topography where spreading segments are 90-100 km wide, as modeled in Chapter 2.

Chapter 4

Distribution of Sediment and Basement Roughness on Young South Atlantic Crust, 25° - 35° S

INTRODUCTION

At scale lengths of 100 km or more, sediment thickness in the moderate latitudes of the South Atlantic has been mapped to ± 50 m, primarily from single channel seismic (SCS) data [e.g. *Divins and Rabinowitz*, 1990]. In broad terms, geographical differences in sediment thickness are qualitatively understood in terms of seafloor age, terrigenous material sources, biological productivity, and surface and bottom currents. Quantitative information about sediment thickness and mobility needed to develop and evaluate more complex theories about sedimentation has been largely unavailable, however. For example, the rate at which sediments accumulate in the central gyre, and how this rate has varied regionally and through time, is only roughly known except at a few Deep Sea Drilling Project (DSDP) sites (e.g. Site 522 [*Hsü, LaBrecque et al.*, 1984]). The processes by which jagged hills are transformed into the rolling, low-amplitude topography seen off-axis has never been studied. And, while the RMS variability along flow lines in the South Atlantic has been found to vary generally between 100 and 250 m [*Goff*, 1992; *Bird and Pockalny*, 1994], the controls of variations in roughness have not been determined.

In Chapter 3, we introduce a methodology for analyzing multibeam bathymetric data to determine information about basement structure and overlying pelagic sediments. Applying this methodology to Hydrosweep data collected from the Office of Naval Research's Acoustic Reverberation Corridor (ARC), a region of 0-29 Ma seafloor located on the western flank of the Mid-Atlantic Ridge (MAR) between 25.5° and 27.25° N, we estimate the average thickness L of sediments on much of this rough topography to a precision of ± 10-20 m at the 95% confidence level. These values allow us to, in Chapter 6, track how sediment rain rate and oceanic chemistry have varied since the late Oligocene. We also invert for the RMS variability H of the underlying basement topography and a

characteristic mobility parameter κ. Unfortunately, complexities in the structure of the study area associated with changes in spreading segment lengths through time hinder the interpretation of these variables in terms of geological phenomena.

The MAR in the moderate latitudes of the South Atlantic (25° - 35° S), which has a full spreading rate of ~35 km/m.y. [*Grindlay et al.*, 1991], has been the subject of numerous geophysical research cruises in recent years in an effort to understand crustal constructional patterns on ridges with spreading rates within the transition between slow and intermediate values. These cruises have provided much data on seafloor structure, but very little information on sedimentation patterns. In this chapter, we apply our inversion methodology to bathymetric data from two near-ridge regions where much attention has been focused (Fig. 4.1) [e.g. *Carbotte et al.*, 1991; *Grindlay et al.*, 1992], obtaining values for L, H, and κ for regions of seafloor generally spanning 2 m.y. in age. Observed variations in L with seafloor age allow us to determine the rate at which sediment has accumulated along the MAR since the late Miocene, which facilitates the interpretation of sediment thickness from off-axis tracklines (see Chapter 5) and assists in the development of whole-basin models of sediment accumulation (see Chapter 6). In addition, unlike in the ARC, we are able to relate inverted values of H to the constructional regime of the basement topography. Controls of κ, however, remain elusive.

GEOLOGICAL SETTING

The geophysical research cruises to the moderate latitudes of the South Atlantic concentrated on two regions near the Rio Grande and Cox fracture zones which span the MAR (Fig. 4.1) [e.g. *Carbotte et al.*, 1991; *Grindlay et al.*, 1992]. These regions consist of 0 to 10-12 Ma seafloor between 25° and 27° S (the Rio Grande study area) and 0 to 5-6 Ma seafloor between 31° and 35° S (the Cox study area).

Bathymetry

The bathymetry swath data, covering ~20-50% of the seafloor within the study areas, shows the topography to be primarily composed of ubiquitous elongated abyssal hills such as cover much of the floor of the world ocean. Fracture zones and other, smaller

discontinuities disturb perhaps 10% of the seafloor. Seafloor generated at inside corners, adjacent to active transform faults (to the northwest and southeast of right-lateral offsets, and to the southwest and northeast of left-lateral offsets), stands higher than comparably-aged outside corner seafloor.

As shown in Fig. 6.20, the rate of seafloor subsidence varies somewhat between and within study areas. Generally, however, the age-depth relationship of *Parsons and Sclater* [1977] is followed, which estimates that the height of seafloor x km from a ridge follows

$$\bar{h}(x) = -2500 - 350\sqrt{T(x)}, \tag{4.1}$$

where $T(x)$ is the age of the seafloor in millions of years, with $\bar{h}(x)$ given in meters. Given (4.1) and a seafloor spreading half-rate of 17.5 km/m.y., subsidence imparts an along-track average slope to topography of

$$\bar{h}'(x) = 0.01/\sqrt{T(x)}. \tag{4.2}$$

This predicts that an average slope of 0.01 is present in bathymetric data from 1 Ma seafloor, reduced to 0.003 for 11 Ma seafloor.

Typical seafloor RMS variability $\hat{H}$, as determined using the methodology of *Goff and Jordan* [1988], is less than is observed for the North Atlantic topography in Chapter 3, with 6 of 8 inverted values falling between 170 and 209 m [*Goff*, 1991].

Sedimentation patterns

Two DSDP legs (3 and 73) have sampled near-ridge seafloor between 25° and 31°S [*Maxwell et al.*, 1970; *Hsü, LaBrecque et al.*, 1984]. Deep sea drill cores and piston cores show that, on shallower topography, young sediments consist of calcareous oozes, while red clays fill the deeper regions of the off-axis basins. The depth of the transition from calcite-rich to calcite-free sediments, the Carbonate Compensation Depth (CCD), is shallower to the west of the MAR than to the east, probably due to the easy passage of corrosive Antarctic bottom water (AABW) into the Argentine and Brazil basins [*Ellis and Moore*, 1973]. In the Angola Basin, AABW is blocked by the MAR and the Walvis Ridge, and calcareous oozes are currently accumulating at depths of 4500 m, as seen at DSDP Site 522 [*Hsü, LaBrecque et al.*, 1984], with some carbonate present in sediments from as deep as 5400 m [*Ellis and Moore*, 1973].

Although SCS data has been collected during a number of regional surveys and transits across the MAR, the spacing of lines through near-ridge topography is very sparse, and the roughness of the topography makes the systematic study of sedimentation patterns on seafloor younger than ~10 Ma difficult using seismic data. In off-axis SCS data [e.g. *Neprochnov*, 1977] it can be seen that, despite the corrosivity of bottom waters to calcite deposition, sediments are fairly thick (greater than 100-200 m, on average) on seafloor older than 20 Ma in the Argentine Basin, while seafloor greater than 40 Ma in the Brazil Basin bears much less sediment [e.g. *Gamboa and Rabinowitz*, 1981]. This difference may be attributed to greater biological productivity in surface waters [*Berger*, 1991] and/or to increased terrigenous sediment input from the Antarctic shelf via the nepheloid layer, which is particle-rich as far east as 30° W at 30° S [*Biscaye and Eittreim*, 1977].

DATA ANALYSIS: RIO GRANDE REGION

The Rio Grande near-ridge study area covers ~70,000 km^2 of 0-12 Ma seafloor on the eastern and western flanks of the MAR between 25° and 27.5° S, 11.5° and 16.25° W. The region includes the prominent Rio Grande transform, the site of a 42 km right-lateral offset of the ridge crest, and a 9.5 km non-transform left-lateral offset known as the Moore Discontinuity [*Grindlay et al.*, 1992]. The region has been the site of multibeam bathymetric surveys by the *R/V Robert D. Conrad* (RC2711 and RC2802) [*Grindlay et al.*, 1992] and the *R/V Maurice Ewing* (EW9011) [*Grindlay and Fox*, 1991], which have found great intra-region variability in faulting styles despite long-term constancy in the spacing of discrete spreading centers [*Cande et al.*, 1988]. Single-channel seismic data was not collected during these surveys.

To determine H, L, and κ throughout the study area, we divide the seafloor older than 2 m.y. into 33 small (1000–4000 km^2) areas, avoiding the two fracture zones but including all other crust (Fig. 4.2). Gaps between areas covered prevent us from choosing regions based on catchment area, such as is done to construct the basin-centered areas of Chapter 3. Instead, regions are based solely on seafloor age and geographic position. Each region contains between 80 and 200 km of along-track data. Most regions contain an age range of 2 m.y., though several regions contain slightly larger ranges.

Inversion proceeds much as in Chapter 3. We estimate basement stochastic character, then generate a Goff-Jordan model topography [*Goff and Jordan*, 1988] as a model basement. This model is sedimented using a variety of values of apparent diffusivity, with surfaces recorded throughout model time. The sedimented surfaces are scaled to model a range of basement H values, then sampled to simulate the effects of the data collection systems Seabeam and Hydrosweep. Slope distributions are generated from these models and from the bathymetric data. Then, maximum likelihood estimation is used to determine best-fitting parameters for each subregion, both while allowing all three parameters to vary and while fixing H.

Construction of model topographies

Visually, topography throughout the Rio Grande study area appears to be fairly homogeneous, with long, narrow, regularly spaced hills, as shown in an enlargement of the western portion of the study area in Fig. 4.3. Based on this observation, we take k_n, a, D, and ζ_s to be constant for the entire Rio Grande study area; consequences of this decision are discussed in a later section.

We choose regional values of a and D based on *Goff* [1992], who inverted multibeam data from cruises RC2711 and RC2802 for all five Goff-Jordan parameters to study how seafloor constructional processes have varied through time and how seafloor changes as it ages. For seafloor less than 10 Ma, he found that H ranged from 125 to 322 m, hill spacings fell between 3.7 and 11.4 km, a values ranged from 1.3 to 5.1, and D ranged from 2.05 to 2.42. Based on the more common values of these parameters, we choose D to be 2.2 and set a at 3. Additionally, since most tracklines are perpendicular to the ridge crest, we take ζ_s to be 0°.

The results of *Goff* [1992] are not sufficient for determining k_n. In Chapter 3, we estimate basement parameters, including k_n, by visually comparing profiles and surfaces from sedimented models to actual topography. In the Rio Grande region, however, long-wavelength topographic effects and the wide data gaps between tracklines prevent us from producing three-dimensional gridded renderings which compare well visually to models. Therefore, in this chapter we instead constrain k_n by comparing along-track centerbeam

data to profiles through models. Unfortunately, as we see in along-track centerbeam data in Fig. 4.3 and, in more detail, Fig. 4.4, neighboring lines can appear very different, even where individual hills span the distance between lines.

To constrain k_n, we compare the topography data shown in Fig. 4.4(a)-(c) to profiles through model topographies, shown in Fig. 4.4(d). These profiles are taken from model topographies generated using basement parameters H = 200 m, D = 2.2, a = 3, ζ_s = 0°, and k_n of 0.4, 0.6, and 0.8 km^{-1}, which we have sedimented for 6.25 m.y. of model time at a rain rate F of 4 m/m.y, using κ such that non-dimensional diffusivity K (defined via (2.23)) is 2 for each profile. Constant slopes of 0.0015, 0.001, and 0.00075, respectively, have been added to each model profile such that 51.1 m is gained traveling from left to right. We find that, although each model resembles parts of the tracklines shown in Fig. 4.4(a)-(c), some parts of the tracklines are not well-modeled by any of the segments. In general, this approach suggests that k_n is between 0.4 and 0.6 km^{-1}.

A second approach we took to the estimation of k_n is based on the analysis of covariance functions, the stochastic measure used to determine Goff-Jordan parameters [*Goff and Jordan*, 1988]. Average scaled covariance functions for the Rio Grande study area subregions span a wide range of possible k_n values, but the majority fall between 0.4 and 0.6 km^{-1} if a seafloor $\hat{D}$ of 2.05 is expected (see Chapter 2), as shown in Fig. 4.5. To use this observation to estimate basement k_n, we must understand how both sedimentation and long-wavelength topography associated with subsidence affect k_n. To do so, we begin by inverting a basement Goff-Jordan topography generated using basement parameters H = 160 m, k_n = 0.6 km^{-1}, k_s = 0.2 km^{-1} (such that a = 3), D = 2.2, and ζ_s = 0°, for Goff-Jordan basement parameters using the methodology of *Goff and Jordan* [1988], then sediment this basement a rate of 4 m/m.y. for 5 m.y. of model time using a κ of 0.14 m^2/yr and invert the resulting topography for Goff-Jordan parameters. We then add a slope of 0.005, via (4.2) the amount expected for 4 Ma seafloor, to the model basement and the model sedimented topography and re-invert for Goff-Jordan basement parameters. We find that the added slope leads to a decrease of ~0.1 km^{-1} in the inverted values of k_n for the basement and the sedimented topography (Fig. 4.6). This suggests that true basement k_n probably ranges between 0.5 and 0.7 km^{-1}.

Based on these two approaches to the quantification of k_n, we believe that the best value is probably between 0.5 and 0.6 km^{-1}. Here, we choose k_n to be 0.6 km^{-1}, but investigate how misestimation of this parameter would affect inversion results.

Using the above basement parameters and an H of 160 m, sediment is numerically added to a randomly-generated 51.1 × 51.1 km^2 Goff-Jordan model (discretized with data point spacing d of 50 m) at a constant rain rate F of 4 m/m.y. for 50 m.y. of model time using diffusivities κ of 0.014, 0.024, 0.04, 0.08, 0.14, 0.24, 0.4, 0.8, and 1.4 m^2/yr. Surfaces are recorded at model times of 0.625, 1.25, 2.5, 3.75, 5, 6.25, 7.5, 10, 15, 20, 30, and 50 m.y., corresponding to average sediment thicknesses L of 2.5, 5, 10, 15, 20, 25, 30, 40, 60, 80, 120, and 200 m. By (2.21) and (2.23), these models can be used to produce models for any H and k_n (given $a = 3$, $D = 2.2$, and $\zeta_s = 0°$) for non-dimensional $K \in \{0.2, 0.34, 0.57, 1.14, 2.0, 3.4, 5.7, 11.4, 20.0\}$ and $\Lambda \in \{0.0156, 0.0312, 0.0625, 0.0935, 0.125, 0.156, 0.188, 0.25, 0.375, 0.5, 0.75, 1.25\}$, where Λ is the non-dimensional sediment thickness given by (2.21). Fixing k_n at 0.6 km^{-1}, we let $H = 160/m_i$ m, for $m_i \in \{0.4,0.45,0.5..1.8\}$, and produce models for H from 88.89 to 450 m.

Inversion Technique

Slope distribution functions for data and models are constructed much as in Chapter 3, although a slightly higher value of random system noise variance E^2, 10 m^2, is assumed based on the variability measured from flat-lying regions of the study area. The ruler length u we use for slope calculations is 300 m as in Chapter 3, but a less rigorous cutoff for uncertainties e, e_{max}, of 0.025 is used. Binning width w is again 0.02, and values of model slope distribution functions $g_m(\theta,u,\kappa,H,L)$ and slope distribution functions from data $g_d(\theta,u)$ are again calculated at slope θ values of 0.01 to 0.99.

We make one important modification to how the $g_d(\theta,u)$ are calculated. The accurate determination H requires that, for some i such that θ_i is between 0.15 and 0.3,

$$\sum_{j=i}^{50} g_d(\theta_j,u) = \sum_{j=i}^{50} g_m(\theta_j,u,\kappa,H,L). \tag{4.3}$$

Unfortunately, a model which maximizes likelihood, as described in Chapter 3, does not necessarily satisfy (4.3), especially if $g_d(\theta,u)$ shows variability at higher values of θ. In

this chapter, we are particularly interested in resolving H, so we force $g_d(\theta,u)$ to be smoother high θ than would be imposed by (3.11). To do so, the influence of individual slopes υ greater than υ_0 is spread among an increased number of bins by recasting (3.11), the contribution of an individual slope υ_i with associated error e_i on a bin centered at θ_j, as

$$\gamma(\theta_j,\upsilon_i,e_i,w)=\frac{1}{2}\left(\operatorname{erf}\left(\frac{(\theta_j+w/2)-\upsilon_i}{(e_i(\upsilon_i/\upsilon_0)\sqrt{2})}\right)-\operatorname{erf}\left(\frac{(\theta_j-w/2)-\upsilon_i}{(e_i(\upsilon_i/\upsilon_0)\sqrt{2})}\right)\right) \qquad (4.4)$$

for all υ_i greater than υ_0, given that e_i is below e_{max}. In this chapter, we let υ_0 be 0.15. We do not use this recasting of (3.11) to compute slope distributions from models; the implications of this for inverted values of model parameters are discussed below.

We find that slope distribution functions, as displayed in Fig. 4.7(a)-(b), resemble those of Chapter 3 (see Fig. 3.9). Functions calculated from near-ridge seafloor have low amplitudes at small slopes, with amplitude at zero slope increasing with seafloor age. In particular, the variations in $g_d(\theta,u)$ with age for the subregions extending eastward from the MAR between 25.5° and 26° S, as shown in Fig. 4.7(b), is striking.

For each slope distribution from data $g_d(\theta,u)$, we determine average seafloor age T based on the global compilation of *Müller et al.* [1993]. Initial estimates of H and L for each region are made; then, taking F to be equal to L divided by T, minimum and maximum κ values κ_{min} and κ_{max} are selected via (3.16) and (3.17). For κ between κ_{min} and κ_{max} measured at an interval of $2.5\kappa_{min}$, H between 90 and 350 m measured at an interval of 5 m, and L between 2 and 200 m measured at an interval of 1 m, $Lik(\kappa,H,L)$ is calculated via (3.15) for all models for which $K \in [0.2,20]$ and $\Lambda \in [0.0156,1.25]$. Where K is less than 0.2 or Λ is less than 0.0156 or greater than 1.25, we set $Lik(\kappa,H,L)$ to 0. Where K is greater than 20 and Λ is between 0.0156 and 1.25, we set $Lik(\kappa,H,L)$ to the likelihood associated with the maximum possible value of κ given H and L, as in Chapter 3.

Since model slope distribution functions $g_m(\theta,u,\kappa,H,L)$ are defined for only a limited, albeit large, number of values of κ, H, and L, it is necessary to interpolate between defined slope distribution functions to compute (3.15) for many κ, H, and L. As in Chapter 3, this is achieved using the methodology described in Appendix B. Inversion errors are calculated following the methodology given in Chapter 3.

Results

Results of the inversion methodology described above are displayed with geographic position in Fig. 4.8 and are listed in Table 4.1.

Table 4.1. Inversion results, Rio Grande area

Site	Location	N	T, m.y.	H, m	κ, m^2/yr	L, m
R1	25.92°S, 15.94°W	514	11	205 +60/-30	.10 +.24/-.04	36 +36/-15
R2	25.83°S, 15.47°W	417	9	260 +130/-45	.15 +.35/-.07	84 +100/-31
R3	25.66°S, 14.89°W	518	6	200 +40/-20	.35 +∞/-.19	25 +19/-8
R4	25.49°S, 14.31°W	401	3	*205 +115/-25	*.30 +∞/-.21	*15 +64/-7
R7	25.19°S, 13.09°W	420	3	**230	**0.06	**15
R8	25.19°S, 12.64°W	446	5	160 +25/-15	.24 +∞/-.17	12 +10/-5
R9	25.09°S, 12.12°W	626	7.5	165 +30/-20	.20 +.20/-.08	37 +20/-12
R10	26.47°S, 15.92°W	480	9	185 +40/-25	.13 +.58/-.07	26 +22/-12
R11	26.36°S, 15.50°W	606	7	165 +20/-20	.28 +.86/-.13	28 +13/-9
R12	26.26°S, 15.03°W	789	5	180 +25/-20	.18 +.75/-.09	23 +12/-10
R13	26.13°S, 14.62°W	880	3	210 +25/-20	.50 +∞/-.22	23 +11/-8
R16	25.85°S, 13.41°W	831	3	**200	**0.03	**8
R17	25.79°S, 13.00°W	632	5	240 +70/-40	.20 +1.1/-.10	30 +32/-14
R18	25.80°S, 12.60°W	769	7	210 +30/-25	.25 +.∞/-.10	29 +14/-9
R19	25.78°S, 12.20°W	664	9	230 +65/-30	.27 +.53/-.11	49 +35/-14
R20	25.71°S, 11.81°W	655	11	270 +85/-35	.37 +.71/-.14	76 +56/-20
R21	26.78°S, 15.86°W	414	9	205 +125/-35	.13 +.22/-.07	52 +98/-21
R22	26.70°S, 15.42°W	464	7	170 +25/-25	.20 +∞/-.10	22 +13/-9
R23	26.62°S, 14.98°W	392	5	185 +55/-25	.20 +1.0/-.10	25 +29/-11
R24a	26.47°S, 14.55°W	603	3	225 +125/-30	.20 +1.3/-.13	*25 +64/-12
R24b	26.69°S, 14.45°W	624	3	**200	**0.07	**34
R27a	26.19°S, 13.23°W	414	3	*220 +140/-40	*.11 +∞/-.05	*20 +73/-14
R27b	26.41°S, 13.22°W	460	3	225 +55/-20	.57 +∞/-.52	8 +14/-4
R28	26.20°S, 12.92°W	555	5	185 +25/-15	.83 +∞/-.63	14 +8/-5
R29	27.25°S, 15.86°W	356	11	205 +70/-30	.18 +.63/-.09	38 +39/-14
R30	27.20°S, 15.49°W	347	9	225 +120/-35	.20 +.75/-.09	47 +72/-19
R31	27.17°S, 15.04°W	249	7	255 +95/-45	1.0 +∞/-.68	45 +45/-17
R32	27.13°S, 14.62°W	723	5	240 +45/-30	.38 +∞/-.17	32 +18/-11
R33	26.91°S, 14.24°W	444	3	**205	**0.16	**4
R34	27.15°S, 14.19°W	404	3	210 +45/-20	1.1 +∞/-.96	13 +14/-5
R38	26.80°S, 12.98°W	803	3	**205	**0.05	**11
R39	26.83°S, 12.52°W	417	5	175 +45/-25	.25 +∞/-.11	32 +28/-13
R40	26.56°S, 11.84°W	594	8	170 +25/-20	.25 +∞/-.11	25 +14/-8

* Distribution of likelihood for each variable is non-Gaussian, making the given 95% confidence bounds suspect. ** Parameters not boundable. See text for explanation.

The inverted values of sediment thickness L show symmetry about the MAR, and seem to be linearly related to seafloor age, as shown in Fig. 4.9. This suggests that, at a resolution of 2 m.y., sediment has been accumulating at a constant rate for roughly the past

12 m.y. Via (3.25), this rate, A, is computed to be 4.9 ± 0.8 m/m.y. if all data from the study area is considered, with the western flank showing a rate of 4.8 ± 1.2 m/m.y. and the eastern flank a rate of 5.0 ± 1.0 m/m.y. (Uncertainties for A and compilations of inverted parameters represent standard deviations, not 95% confidence ranges).

There is considerable same-age variability in L. Much of this is probably due to the import or export of sediment into study areas, similar to that expected for the hill-centered regions discussed in Chapter 3. Furthermore, the sparseness of the data is such that we cannot state with confidence which regions are more likely than others to import or export sediment, or if, in any areas, peculiarities in hill orientation might lead to the undersampling or oversampling of ponds (such as we suspect for basin-centered region B31 in Chapter 3). Some scatter in sediment thickness estimations may also be simply due to estimation error; where this occurs, H should also be misestimated, since errors in L and H are correlated (see Chapter 3). This is discussed in detail in the next section.

Inverted values of H have a mean $\overline{H}_{all}$ of 206 ± 29 m, significantly lower than the value of 267 ± 28 m determined for abyssal hills in the North Atlantic in Chapter 3, as would be expected given the faster spreading rate within the Rio Grande study area (35 mm/yr vs. the ARC rate of 27 mm/yr [*Tucholke and Schouten*, 1988]), based on observed correlations between spreading rate and seafloor roughness [*Krause and Menard*, 1965; *Malinverno*, 1991]. The range of H values seen in both of these regions is smaller than the variability seen in other studies of seafloor roughness [e.g. *Malinverno*, 1991; *Goff*, 1992; *Bird and Pockalny*, 1994], perhaps because we are considering values from within single geographical locales, or because we are able to avoid crust associated with fracture zones. For reference, the mean values for the ARC and the Rio Grande region are near, though above, those predicted by the equation in the Fig. 2 caption of *Malinverno* [1991] for $\hat{H}$, based on his global compilation of spreading rates and seafloor RMS variability. *Malinverno*'s [1991] equation,

$$\hat{H} = 1296(\text{full spreading rate, in mm / yr})^{-0.539} \tag{4.5}$$

predicts that for spreading at the Rio Grande full rate of 35 mm/yr, $\hat{H}$ is 190 m, while seafloor being produced at the ARC rate of 27 mm/yr [*Tucholke and Schouten*, 1988] is predicted to have an average $\hat{H}$ of 219 m.

While there is relatively small variability in H in the Rio Grande region, we find that this parameter correlates with whether crust was produced in an inside corner or outside corner setting. In the Rio Grande study area, the right-lateral Rio Grande transform fault and the left-lateral Moore discordant zone produce inside corner crust to the west, north of the Rio Grande fracture zone; to the east, between the Rio Grande and Moore fracture zones; and to the west, south of the Moore fracture zone. The across-ridge complements of these three regions each feature outside corner crust, composed of lower hills which trend into the fracture zone lows. The three regions of inside corner crust yield average H values of, from north to south, 218 ± 28 m, 222 ± 26 m, and 223 ± 21 m, while the three complementary outside corner regions produced average H values of 185 ± 39 m, 192 ± 20 m, and 183 ± 19 m. Taken together, H of the outside corner regions have average $\overline{H}_{out}$ of 189 ± 22 m and the inside corner regions have average $\overline{H}_{in}$ of 222 ± 23 m. Thus, there is a 95% probability that the means of H from inside and outside corner crust differ by at least 20 m. The medians of H for inside corner and outside corner crust are 215 and 185 m, respectively, also suggesting that $\overline{H}_{in}$ and $\overline{H}_{out}$ are not unduly influenced by a few outlying values. The variation between $\overline{H}_{in}$ and $\overline{H}_{out}$ is large enough to suggest that much of the variability seen in H in global studies might be attributed simply to whether the crust being measured was generated near an inside corner or an outside corner.

In the inversion methodology, we have assumed a constant basement hill spacing. However, if inside corner crust tends to have a smaller typical basement hill spacing (i.e. a higher k_n and/or D) than outside corner crust, similar results would be expected, because more closely spaced hills produce higher basement along-track slope values. We investigate this possibility by averaging all covariance functions from inside corner and outside corner study areas (Fig. 4.10). We find that inside corner crust has a higher amplitude at zero lag than outside corner crust, with an average seafloor $\hat{H}$ of 214 m, vs. 185 m for outside corner crust. The shape of the average covariance functions is extremely similar out to a lag of 5 km, indicating that both inside corner and outside corner crust may be described with the same values of k_n and D.

Inverted values for apparent diffusivity κ show considerable variability with seafloor age (Fig. 4.11), particularly for the youngest regions studied. For the entire Rio Grande,

the mean value of κ is 0.29 ± 0.25 m^2/yr. The mean for inside corner crust (0.36 ± 0.31 m^2/yr) is higher than for outside corner crust (0.20 ± 0.11 m^2/yr), primarily due to very high inverted values of κ for three inside corner crust regions (R28, R31, and R34). We are unable to attach any special meaning to the values of κ inverted for these three regions.

Since values of κ and H inverted from inside corner crust are both higher, on average, than the values of these parameters inverted from outside corner crust, one might expect H and κ to be correlated, as we find in Chapter 3. However, we find little correlation between these parameters in the Rio Grande region (Fig. 4.12), with a correlation coefficient r of only 0.185, significant at only the $\alpha = 0.31$ level.

Uncertainties and sources of error

The inverted parameter values are subject to errors from many sources. Some of these, such as the assumptions we make about basement topography and sampling system characteristics, and the effects of compaction on the inverted values of L, hold for both the Rio Grande and Cox study areas, and are discussed later in this chapter. Here, we discuss some of the factors which contribute to uncertainties and errors in specific regions of the Rio Grande region.

The sizes of the 95% confidence bounds of the inverted values, as given in Table 4.1, are functions of N, H, L, and κ (see Fig. 3.18), as well as the general smoothness of the slope distribution function for each region. As seen in Chapter 3, confidence intervals are largest when both K and Λ are small (see Fig. 3.20 and Fig. 3.21). Inversion results from many of the near-ridge subregions here give low values of L and κ. The 95% confidence regions for these areas are large, as expected, if they can be estimated at all.

We examine the results from area R7 to help illustrate this phenomena. In Fig. 4.13, we show cross-sections through the 95% confidence region for R7. While cross-sections at fixed values of H (4.13(b)) and L (4.13(c)) seem reasonably compact, a wide range of L and H are possible if κ is low, as shown in 4.13(a). This occurs because slope distribution functions computed from low-L, low-κ models are similar in shape to some from models with very low K but high values of L and H. Thus, as shown in Fig. 4.14, the slope distribution for R7, which is best matched by a model slope distribution function

corresponding to H = 230 m, L = 15 m, and κ = 0.06 m^2/yr (K = 0.99), as given in Table 4.1, also somewhat resembles the slope distribution function produced using an H of 320 m, an L of 80 m, and a κ of 0.06 m^2/yr (K = 0.26). The relative contributions of basement and sedimented surface regions to the these models is very different, with much of the shape of the slope distribution function from the bestfitting, low-L, model resembling the shape of that of a basement model with H = 230 m, while little hint of a basement model with H = 320 m is seen in the slope distribution function computed from the H = 320 m, L = 80 m, κ = 0.06 m^2/yr surface.

We find that inverted values of L do not seem to correlate with H for regions from young (T = 3 Ma) seafloor (Fig. 4.15). The same seems to be true for most of the seafloor within the Rio Grande study area. However, we observe that, for the oldest (4.15(c)) seafloor we examine, L and H are correlated, with a correlation coefficient r of 0.9336, significant at the $\alpha < 0.01$ level.

Inversion using fixed H

Since H and L show some correlation, it seems possible that more accurate values of L and κ for all seafloor within the Rio Grande region might be obtained by fixing H based on independent knowledge of the seafloor. One possible source of a preset value of H could be RMS seafloor variability $\hat{H}$, calculated from the bathymetric data. Unfortunately, as discussed above, this value is subject to change by sedimentation (see Chapter 2) and, perhaps more importantly, long-wavelength topographic effects, especially for small T.

Another option is to assume all seafloor within the Rio Grande region actually has the same H, or that H varies only with crustal type. To evaluate these hypothesis, we reinvert data from each region, first fixing H to 205 m, the closest multiple of 5 m to $\overline{H}_{all}$, and then to either 220 m or 190 m, the closest multiples of 5 m to $\overline{H}_{in}$ and $\overline{H}_{out}$ The results of the inversion procedures are given in Figs. 4.16 and 4.17 and are listed in tables 4.2 and 4.3.

The inversion procedure is slightly modified. Since H is fixed, we may calculate the likelihoods of more finely spaced values of κ, while staying within the memory capabilities of the Sun workstations we employ for the inversion procedures. Therefore, we are able to invert for all κ between 0.01 and 1.2 m^2/yr at a resolution of 0.01 m^2/yr.

The 95% confidence bounds on L given in Table 4.2 and Table 4.3 are smaller than those given in Table 4.1. This is because much of the uncertainty in inversion results is due to correlations between L and H, as shown in figures 3.18 and 4.13. When H is fixed, the range of L which produce models with slope distribution functions which resemble a given $g_d(\theta,u)$ is also reduced, thus reducing the uncertainty of L as well as κ.

Table 4.2. Inversion results/ H preset to near $\overline{H}_{all}$.

Site	Location	N	T, m.y.	H, m	κ, m^2/yr	L, m
R1	25.92°S, 15.94°W	514	11	205	.10 +.21/-.04	36 +9/-9
R2	25.83°S, 15.47°W	417	9	205	.10 +.07/-.03	49 +13/-11
R3	25.66°S, 14.89°W	518	6	205	.30 +∞/-.13	27 +7/-7
R4	25.49°S, 14.31°W	401	3	205	.30 +∞/-.19	15 +6/-6
R7	25.19°S, 13.09°W	420	3	205	.13 +∞/-.09	7 +4/-7
R8	25.19°S, 12.64°W	446	5	205	.14 +.68/-.05	34 +9/-13
R9	25.09°S, 12.12°W	626	7.5	205	.68 +.42/-.22	61 +12/-11
R10	26.47°S, 15.92°W	480	9	205	.12 +.35/-.05	35 +9/-9
R11	26.36°S, 15.50°W	606	7	205	.28 +.49/-.10	50 +8/-10
R12	26.26°S, 15.03°W	789	5	205	.16 +.21/-.05	35 +6/-9
R13	26.13°S, 14.62°W	880	3	205	.59 +∞/-.29	21 +5/-4
R16	25.85°S, 13.41°W	831	3	205	.02 +∞/-.01	12 +3/-8
R17	25.79°S, 13.00°W	632	5	205	.23 +∞/-.10	19 +4/-6
R18	25.80°S, 12.60°W	769	7	205	.25 +∞/-.09	28 +5/-6
R19	25.78°S, 12.20°W	664	9	205	.23 +.60/-.09	38 +7/-8
R20	25.71°S, 11.81°W	655	11	205	.22 +.45/-.07	43 +8/-8
R21	26.78°S, 15.86°W	414	9	205	.12 +.11/-.04	52 +13/-12
R22	26.70°S, 15.42°W	464	7	205	.19 +.67/-.08	38 +8/-10
R23	26.62°S, 14.98°W	392	5	205	.20 +.60/-.08	34 +9/-10
R24a	26.47°S, 14.55°W	603	3	205	.21 +∞/-.10	18 +4/-7
R24b	26.69°S, 14.45°W	624	3	205	.08 +.05/-.03	37 +11/-10
R27a	26.19°S, 13.23°W	414	3	205	.11 +∞/-.05	15 +5/-7
R27b	26.41°S, 13.22°W	460	3	205	.45 +∞/-.33	5 +3/-5
R28	26.20°S, 12.92°W	555	5	205	1.2 +∞/-.88	19 +5/-5
R29	27.25°S, 15.86°W	356	11	205	.16 +.84/-.06	38 +10/-10
R30	27.20°S, 15.49°W	347	9	205	.17 +.83/-.06	37 +11/-11
R31	27.17°S, 15.04°W	249	7	205	.91 +∞/-.67	27 +11/-7
R32	27.13°S, 14.62°W	723	5	205	.39 +∞/-.18	21 +5/-5
R33	26.91°S, 14.24°W	444	3	205	.18 +∞/-.16	4 +4/-4
R34	27.15°S, 14.19°W	404	3	205	1.09 +∞/-.92	12 +5/-4
R38	26.80°S, 12.98°W	803	3	205	.05 +1.05/-.03	11 +4/-6
R39	26.83°S, 12.52°W	417	5	205	.32 +.48/-.12	48 +12/-11
R40	26.56°S, 11.84°W	594	8	205	.41 +.59/-.17	40 +9/-7

For both inversion procedures, the resulting distributions of L are more symmetric about the ridge crest, and values of L within a given age range show much less scatter, than when H is allowed to vary, as shown in Fig. 4.16 and Fig. 4.17. This is especially true

for the oldest crust in the study area, where the determinations of H are based on the smallest number of data points. This is reflected in a slight reduction in the standard error associated with all-subregion calculations of A, with an accumulation rate of 4.8 ± 0.7 m/m.y. calculated from data in Table 4.2, and of 4.9 ± 0.5 m/m.y. for the data in Table 4.3.

Table 4.3. Inversion results/ H preset to near $\overline{H}_{in}$ or $\overline{H}_{out}$

Site	Location	N	T, m.y.	H, m	κ, m^2/yr	L, m
R1	25.92°S, 15.94°W	514	11	220	.11 +.14/-.04	43 +10/-10
R2	25.83°S, 15.47°W	417	9	220	.12 +.07/-.04	58 +15/-13
R3	25.66°S, 14.89°W	518	6	220	.29 +∞/-.12	33 +7/-8
R4	25.49°S, 14.31°W	401	3	220	.21 +∞/-.12	20 +8/-8
R7	25.19°S, 13.09°W	420	3	190	.39 +∞/-.34	4 +3/-4
R8	25.19°S, 12.64°W	446	5	190	.11 +1.0/-.05	24 +7/-9
R9	25.09°S, 12.12°W	626	7.5	190	.24 +.20/-.08	51 +10/-9
R10	26.47°S, 15.92°W	480	9	190	.12 +.82/-.05	28 +7/-9
R11	26.36°S, 15.50°W	606	7	190	.26 +.57/-.09	41 +8/-8
R12	26.26°S, 15.03°W	789	5	190	.18 +.36/-.08	26 +7/-6
R13	26.13°S, 14.62°W	880	3	190	.82 +∞/-.51	17 +4/-4
R16	25.85°S, 13.41°W	831	3	220	.02 +.09/-.01	19 +4/-11
R17	25.79°S, 13.00°W	632	5	220	.21 +∞/-.09	23 +6/-4
R18	25.80°S, 12.60°W	769	7	220	.26 +.75/-.10	33 +6/-7
R19	25.78°S, 12.20°W	664	9	220	.24 +.52/-.08	45 +8/-9
R20	25.71°S, 11.81°W	655	11	220	.25 +.44/-.08	50 +9/-9
R21	26.78°S, 15.86°W	414	9	190	.11 +.11/-.04	44 +10/-11
R22	26.70°S, 15.42°W	464	7	190	.19 +.80/-.08	31 +7/-8
R23	26.62°S, 14.98°W	392	5	190	.19 +.77/-.08	28 +7/-9
R24a	26.47°S, 14.55°W	603	3	190	.28 +∞/-.15	13 +4/-5
R24b	26.69°S, 14.45°W	624	3	190	.07 +.06/-.03	27 +9/-8
R27a	26.19°S, 13.23°W	414	3	220	.10 +.96/-.05	20 +8/-9
R27b	26.41°S, 13.22°W	460	3	220	.59 +∞/-.47	7 +4/-3
R28	26.20°S, 12.92°W	555	5	220	.54 +∞/-.34	23 +6/-6
R29	27.25°S, 15.86°W	356	11	220	.17 +.80/-.07	45 +12/-11
R30	27.20°S, 15.49°W	347	9	220	.19 +.69/-.08	45 +12/-13
R31	27.17°S, 15.04°W	249	7	220	.83 +∞/-.57	32 +13/-9
R32	27.13°S, 14.62°W	723	5	220	.37 +∞/-.16	25 +6/-5
R33	26.91°S, 14.24°W	444	3	220	.02 +∞/-.01	11 +2/-11
R34	27.15°S, 14.19°W	404	3	220	.59 +∞/-.43	15 +6/-5
R38	26.80°S, 12.98°W	803	3	190	.12 +∞/-.08	6 +2/-6
R39	26.83°S, 12.52°W	417	5	190	.29 +.63/-.11	40 +10/-10
R40	26.56°S, 11.84°W	594	8	190	.25 +.71/-.10	34 +7/-7

Whether these results support a constant H for the entire Rio Grande area or an H which varies with crustal type depends on assumptions made about sediment accumulation patterns. If H is free to vary we find that the inside corner crust, represented by squares in Fig. 4.9, seems to be accumulating sediment at 5.5 ± 1.2 m/m.y. on the eastern flank and 5.0 ± 1.7 m/m.y. on the western flank, considerably more rapidly than outside corner crust accumulation rates of 4.1 ± 1.7 and 4.6 ± 1.7 m/m.y. This difference could be due to a tendency of sediments on outside corner crust to travel along abyssal valleys and into fracture zones and thus out of the subregions. Also, since outside corner crust is deeper, on average, than inside corner crust, sediments could be subject to more dissolution. Conversely, if we force both inside corner crust and outside corner crust to have H of 205 m, a reversal of this pattern occurs, with inside corner crust showing an accumulation rate of 4.0 ± 0.4 m/m.y. on the eastern flank and 4.0 ± 0.7 m/m.y. on the western flank, and outside corner crust accumulating sediment at 6.6 ± 2.6 and 5.9 ± 1.5 m/m.y. on the eastern and western flanks, respectively. This can also be explained geologically: inside corner crust stands high and is generally rough, and so may shed sediments into surrounding lows. Unfortunately, without bathymetric coverage sufficient to determine the extent of catchment basins, or more detailed imaging of sediments within the Rio Grande region to tell exactly how deep accumulations within fracture zones and other lows are, we cannot advocate one crustal type over the other as a more likely source or sink of sediment.

When we fix H near the means for inside corner and outside corner crust, we find that the difference in sediment accumulation rates between crustal types is largely eliminated. Inside corner crust is estimated to accumulate sediment at rates of 4.7 ± 0.5 and 4.8 ± 0.7 m/m.y. on the eastern and western flanks of the MAR, respectively, and outside corner crust accumulation rates are 5.3 ± 2.3 m/m.y. on the eastern flank and 4.7 ± 1.1 m/m.y. on the western flank. This relative uniformity in accumulation rate occurs because, in fixing inside-corner crust H at 220 m, inverted values of L for high-H inside corner regions such as R2 and R20 are reduced, while an outside corner H of 190 m results in increased L for outside corner regions such as R9 and R40. In the absence of proof that either inside corner crust or outside corner crust should be considered to have a greater average sediment thickness, we feel that the uniformity in sediment accumulation rates

suggests that H is a function of crustal type. H may vary somewhat for seafloor of a given crustal type, but perhaps less than the values of H presented in Table 4.1 suggest.

DATA ANALYSIS: COX REGION

The Cox near-ridge study area encompasses zero-age to 5-8 Ma seafloor located on the flanks of the Mid-Atlantic Ridge between 31° and 35.5° S, 12° and 16.25° W (see Fig. 4.1). The region consists of two major right-lateral transform faults, the Cox Transform and the Meteor Transform, as well as up to eight small discontinuities [*Fox et al.*, 1991]. Crust in the Cox region is being generated at a full rate of 35 km/m.y. [*Fox et al.*, 1991].

The Cox study area has been the site of four multibeam bathymetric (Seabeam) surveys by the *R/V Thomas Washington*, Marathon legs 10 and 13 in 1984-5 [*Fox et al.*, 1991] and Plume legs 4 and 5 in 1990 [*Neumann and Forsyth*, 1993]. Marathon Leg 13 data exhibits an along-track spacing of 250-320 m, too sparse for much of the data set to be usable. The other three cruises collected data at spacings typically between 100 and 200 m.

SCS data was not collected during these cruises. However, SCS data from the transit from DSDP sites 358 to 359 during DSDP Leg 39, which crosses the MAR to the south of the Cox near-ridge study area, shows that young seafloor in this region is generally bare, with occasional thick (> 100 m) pockets of sediment [*Neprochnov et al.*, 1977].

In Chapter 3, we find that the magnitude of the uncertainty associated with inverted parameter values varies inversely with L, and that increasing the size of study areas decreased uncertainties. In the Cox region, we seek to resolve small changes in L with T. Since sediment thicknesses are fairly low due to the young age of the crust, we construct fairly large, long, narrow subregions which extend across entire ridge flank sections. These are formed by dividing ridge-perpendicular tracklines from seafloor greater than 1.5 Ma into segments covering, generally, a 1-m.y. range in age, using the compilation of *Müller et al.* [1993]. These segments are grouped based on seafloor age and geographical position into regions labeled C1 through C26. Adjoining regions are teamed, as shown in Fig. 4.20, with each joint subregion including at least 200 km of trackline data. These subregions are inverted for parameters H, L, and κ.

Inversion technique

Covariance functions of topography within the Cox region resemble those from the Rio Grande study area, as shown in Fig. 4.21, although on average they seem to be less broad, perhaps indicating a smaller hill spacing. When compared to covariance functions following the ideal model form of *Goff and Jordan* [1988] (Fig. 4.22), most fall between curves constructed assuming k_n of 0.5 and 0.6 km^{-1} when a D of 2.05 is assumed and between values of 0.4 and 0.6 km^{-1} when a D of 2.2 is assumed. Since sedimentation tends to lower seafloor k_n values, this supports usage of a k_n of ~0.6 km^{-1} for basement topographies. A basement D of 2.2 also seems reasonable, as does an a of 3 and a ζ_s of 0°, since most tracklines run perpendicular to the MAR. Therefore, we invert topography from the Cox area using the same model topographies as employed for the Rio Grande area.

Construction of slope distribution functions from data proceeds as for Rio Grande study area, including the assumption of random, normally-distributed system noise with variance E^2 of 10 m^2, the use of a ruler length u of 300 m, a slope uncertainty cutoff e_{max} of 0.025, and a binning width w of 0.02. We also continue to use (4.4) instead of (3.11) to distribute all slope values among the appropriate bins, with $v_0 = 0.15$.

Figure 4.23 displays slope distribution functions $g_d(\theta,u)$ from the northern, middle, and southern data groupings, as shown in Fig. 4.20. As in the Rio Grande area and the ARC area of Chapter 3, $g_d(\theta,u)$ at low θ is lowest near the spreading axis, and increases off-axis, presumably in response to sedimentation.

Parameter inversion proceeds as for the Rio Grande region, with $Lik(\kappa,H,L)$ computed via (3.15) for κ between κ_{min} and κ_{max} (defined by (3.16) and (3.17)) at a spacing of $2.5\kappa_{min}$, H between 90 and 350 m at a spacing of 5 m, and L between 2 and 200 m at a spacing of 1 m, for all models for which $K \in [0.2,20]$ and $\Lambda \in [0.0156,1.25]$.

Results

Results of the inversion are given in Fig. 4.24 and are listed in Table 4.4. Sediment thickness is seen to be fairly linearly related to seafloor age (Fig. 4.25), with considerable same-age variability in L. Via (3.25), sediment accumulation rates A on the western and

eastern flanks of the MAR along each of the three segments range from 4.4 ± 0.6 to 6.8 ± 0.4 m/m.y; when the entire region is considered, A is 5.9 ± 1.0 m/m.y.

Table 4.4. Inversion results, Cox area

Site	Location	N	T, m.y.	H, m	κ, m^2/yr	L, m
C1C2	31.89°S, 14.35°W	838	4.5	190 +55/-25	.11 +.31/-.04	25 +36/-11
C2C3	31.87°S, 14.13°W	1053	3.5	175 +15/-15	.17 +∞/-.10	12 +7/-5
C3C4	31.83°S, 13.91°W	1038	2.5	**190	**0.08	**14
C5C6	31.65°S, 12.81°W	989	2.5	*210 +85/-25	*.12 +.34/-.05	*18 +45/-9
C6C7	31.62°S, 12.60°W	964	3.5	210 +40/-25	.19 +1.1/-.09	23 +20/-10
C8C9	33.09°S, 15.61°W	847	5.5	195 +35/-20	.17 +.26/-.06	30 +20/-10
C9C10	33.03°S, 15.40°W	998	4.5	195 +35/-25	.13 +.25/-.05	26 +20/-10
C10C11	32.97°S, 15.18°W	1216	3.5	195 +50/-20	.11 +.20/-.04	20 +29/-8
C11C12	32.99°S, 14.97°W	1162	2.5	**215	**0.06	**25
C13C14	32.86°S, 13.87°W	1732	2.5	**215	**0.06	**28
C14C15	32.85°S, 13.64°W	1661	3.5	195 +30/-25	.09 +.13/-.04	22 +18/-11
C15C16	32.84°S, 13.42°W	1193	4.5	185 +15/-15	.34 + ∞/-.17	17 +6/-5
C16C17	32.88°S, 13.21°W	724	5.2	200 +30/-25	.53 + ∞/-.27	33 +16/-10
C18C19	34.90°S, 16.14°W	1446	3.7	190 +20/-20	.10 +.29/-.05	15 +11/-7
C19C20	34.85°S, 15.84°W	1245	2.5	205 +30/-20	.13 + ∞/-.08	13 +12/-7
C21C22	34.68°S, 14.71°W	783	2.5	**210	**0.09	**18
C22C23	34.62°S, 14.53°W	715	3.5	**200	**0.05	**21
C23C24	34.56°S, 14.35°W	675	4.5	*190 +145/-25	*.06 +.37/-.03	*20 +102/-11
C24C25	34.51°S, 14.13°W	790	5.7	210 +65/-25	.14 +.08/-.06	38 +40/-13
C25C26	34.41°S, 13.83°W	749	7.3	205 +65/-25	.13 +.11/-.04	46 +45/-13

* Distribution of likelihood for each variable are extremely non-Gaussian, making the determination of 95% confidence bounds problematic. ** Parameters cannot be bounded. See text in previous section for explanation.

The average H value $\overline{H}_{all}$ is 199 ± 11 m, slightly lower than the value for the Rio Grande region and with only 40% of the variability. The average value of κ, $\overline{\kappa}$, is 0.14 ± 0.11 m^2/yr, also lower than the value for the Rio Grande region, but with the same amount of variability as a percentage of $\overline{\kappa}$. Inverted values of H and κ are uncorrelated.

Uncertainties and sources of error

Inversion results are subject to errors from the misestimation of basement parameters, improper modeling of the sampling characteristics of the systems which gathered the data, and the correlation of estimation error between H and L. In the Cox study area, the larger size of the subregions used leads to fairly compact error bounds, even when L is small. The decrease in the variability of H may be due to the greater sizes of the subregions as well, since slope distribution functions are smoother at high θ.

For a few of the regions, where L and κ are both low, 95% confidence intervals are indeterminable due to the similarity of the slope distribution functions to those from models with very high H and L and very low K, as is illustrated above for Rio Grande subregion R7. This probably contributes to the youngest (T = 2.5 m.y.) seafloor having a higher average value of H, 208 ± 9 m, than the rest of the Cox region.

For all T, there is considerable correlation between H and L, as shown by Fig. 4.26. This suggests that data from the Cox region might benefit by the predetermination of H prior to inversion for L and κ, as in the Rio Grande study area.

Inversion using fixed H

We assume that H is 200 m, the closest multiple of 5 m to $\overline{H}_{all}$, for the entire region. Results of this inversion procedure are given in Fig. 4.27 and in Table 4.5. We find that the linearity of the relationship between L and T throughout the Cox area is increased (Fig. 4.28), and that the range of A is tightened to between 5.2 ± 0.3 and 6.7 ± 1.3 m/m.y. The best-fitting A for the entire region is increased slightly, to 6.0 ± 0.5 m/m.y.

Table 4.5. Inversion results/ H preset to near $\overline{H}_{all}$

Site	Location	N	T, m.y.	H, m	κ, m^2/yr	L, m
C1C2	31.89°S, 14.35°W	838	4.5	200	.12 +.11/-.05	29 +8/-7
C2C3	31.87°S, 14.13°W	1053	3.5	200	.09 +.19/-.03	23 +4/-7
C3C4	31.83°S, 13.91°W	1038	2.5	200	.07 +.12/-.04	19 +6/-7
C5C6	31.65°S, 12.81°W	989	2.5	200	.13 +.85/-.06	15 +3/-6
C6C7	31.62°S, 12.60°W	964	3.5	200	.20 +.81/-.08	20 +3/-6
C8C9	33.09°S, 15.61°W	847	5.5	200	.19 +.22/-.07	32 +6/-7
C9C10	33.03°S, 15.40°W	998	4.5	200	.14 +.15/-.05	29 +5/-7
C10C11	32.97°S, 15.18°W	1216	3.5	200	.11 +.13/-.05	22 +6/-5
C11C12	32.99°S, 14.97°W	1162	2.5	200	.06 +.13/-.03	18 +4/-7
C13C14	32.86°S, 13.87°W	1732	2.5	200	.06 +.04/-.03	20 +4/-5
C14C15	32.85°S, 13.64°W	1661	3.5	200	.08 +.05/-.03	25 +4/-5
C15C16	32.84°S, 13.42°W	1193	4.5	200	.26 +.76/-.11	22 +4/-5
C16C17	32.88°S, 13.21°W	724	5.2	200	.53 +∞/-.23	33 +6/-6
C18C19	34.90°S, 16.14°W	1446	3.7	200	.08 +.10/-.03	20 +3/-5
C19C20	34.85°S, 15.84°W	1245	2.5	200	.13 +.91/-.06	12 +2/-5
C21C22	34.68°S, 14.71°W	783	2.5	200	.10 +.87/-.05	14 +4/-6
C22C23	34.62°S, 14.53°W	715	3.5	200	.05 +.18/-.02	21 +6/-9
C23C24	34.56°S, 14.35°W	675	4.5	200	.06 +.11/-.03	25 +7/-8
C24C25	34.51°S, 14.13°W	790	5.7	200	.12 +.10/-.04	33 +6/-7
C25C26	34.41°S, 13.83°W	749	7.3	200	.13 +.07/-.04	43 +8/-8

We note that A for any given ridge segment is very sensitive to the preset value of H. For example, the western flank of the middle spreading segment (subregions C8C9, C9C10, C10C11, and C11C12) has an A of 6.0 ± 2.7 m/m.y. when H is allowed to vary. The average H for this region is 200 m, the same as the fixed value of H used to compute the inversion results given in Table 4.5. Based on the values of L given in Table 4.5, fixing H at 200 m increases A for this segment to 6.2 ± 0.9 m/m.y. Along this segment, however, three of four values of H are 195 m. If we fix H for the fourth region (C11C12) at 195 m, we obtain an inverted value of L of 15 m, and an A of 5.6 ± 0.4 m/m.y. Both 195 m, which happens to be the mean of all H from the Cox region if the youngest seafloor is excluded, and 200 m, are valid estimates of H; that a 2.5% alteration in the fixed value of H changes the predicted sediment accumulation rate by 10% emphasizes the important of choosing H carefully and also the inherent uncertainty in the calculation of A.

In the Rio Grande study area, a correlation is seen between H and crustal type, with inside corner crust having an average H that is 30 m higher than for outside corner crust. To determine whether there is a similar relationship between crustal type and H in the Cox study area, we reorganize the tracklines from the middle and southern ridge flank segments into subregions based on whether they contained inside corner or outside corner crust, and invert for H, L, and κ. Results are shown in Table 4.6.

Table 4.6. Inversion results/ seafloor binned by type. I.C. is inside corner crust, O.C. is outside corner crust

	West Flank	East Flank
Middle Segment	O.C.: H = 185 +25/-15 m L = 20 +16/-7 m (A = 5.7 m/m.y.) κ = 0.13 +.16/-.05 m^2/yr I.C.: H = 215 +65/-25 m L = 24 +34/-10 m (A = 6.8 m/m.y.) κ = 0.13 +.30/-.05 m^2/yr	I.C.: H = 190 +20/-15 m L = 14 +12/-4 m (A = 4.7 m/m.y.) κ = 0.23 +∞/-.14 m^2/yr O.C.: H = 180 +15/-15 m L = 15 +9/-6 m (A = 5.0 m/m.y.) κ = 0.18 +.85/-.09 m^2/yr
Southern Segment	O.C.: H = 200 +95/-20 m L = 17 +56/-7 m (A = 5.7 m/m.y.) κ = 0.09 +.14/-.04 m^2/yr I.C.: H = 195 +20/-20 m L = 13 +8/-6 m (A = 4.3 m/m.y.) κ = 0.20 +∞/-.11 m^2/yr	I.C.: H = 205 +65/-25 m L = 26 +38/-12 m (A = 5.8 m/m.y.) κ = 0.08 +.12/-.02 m^2/yr O.C.: H = 205 +35/-25 m L = 28 +19/-11 m (A = 5.6 m/m.y.) κ = 0.11 +.09/-.04 m^2/yr

The average H for outside corner crust is found to be 192 ± 12 m, 9 m less than the inside corner crust average of 201 ± 11 m. This difference is not very significant: there is only ~70% chance that the means from inside and outside corner crust vary by 5 m, the minimum resolution at which we resolve H. There does seem to be a correlation between H and accumulation rate A for both inside corner crust and outside corner crust, suggesting that in, in some locales, H and L have been slightly underestimated, while in others they have been overestimated. However, with only four regions of each crustal type, attempting to determine H based on A is not justified.

Based on the various means employed to compute L for the Cox region, we estimate that A is roughly 6 m/m.y. for the entire region.

Effects of Compaction on Accumulation Rate

The calculation of L, and, hence, A, for the Rio Grande and Cox study areas has, to this point, ignored the effects of compaction. To estimate the productivity of surface waters, it is useful to estimate the average thickness of sediments L_u which would be present were sediments not subject to compaction and to compute uncompacted sediment accumulation rates A_u.

In Chapter 2, we derive an empirical equation (2.37) for determining the average thickness loss for a small area given its post-compaction average sediment thickness, using basement parameters appropriate for the study of North Atlantic topography. In Chapter 3, this equation is used to estimate L_u for data from the ARC. Since compaction effects seem be relatively insensitive to basement parameters, we again use (2.37) here.

For the Rio Grande study area, we favor the inverted values of L computed assuming that H is constant for a given crustal type, as listed in Table 4.3. Applying (2.37) to these values produces values of L_u which increase linearly with seafloor age (Fig. 4.29), and suggest an uncompacted sedimentation accumulation rate A_u of 5.2 ± 0.7 m/m.y. on the western flank of the MAR, 5.5 ± 0.9 m/m.y. on the eastern flank, and 5.3 ± 0.5 m/m.y. when all data from the region is considered.

For the Cox region, we have more confidence in inverted values of L computed assuming that H is everywhere 200 m, as listed in Table 4.5, than in values inverted

allowing a variable H. Applying (2.37) to the L values of Table 4.5 produces values of L_u which also increase linearly with seafloor age (Fig. 4.30), and suggest an uncompacted sedimentation accumulation rate A_u of 6.7 ± 0.9 m/m.y. on the western flank of the MAR and 6.5 ± 0.6 m/m.y. on the eastern flank. For the entire region, A_u is 6.6 ± 0.5 m/m.y, an increase of 0.6 m/m.y. over the uncompacted value.

SYSTEMATIC ERROR SOURCES

In the above analysis, we attempt to correct for error in inverted values of L and H due to possible minor misestimation of H during the inversion procedure. There are several other possible sources of error which might effect inverted values of these parameters, which we investigate in this section. First, we consider whether the use of data from both Seabeam and Hydrosweep systems seems to influence inversion results. Then, we investigate whether misestimations of k_n seem to influence results, particularly in the Rio Grande region where covariance functions span a number of possible k_n values, as displayed in Fig. 4.5. Finally, we investigate how increased smoothing of data slope distribution functions at high θ might have affected inversion results.

An additional error source is the use of a finite spacing d of 50 in the construction of the model topographies. In Chapter 3, we predict that this leads to a systematic underestimation of L of 1-2 m.

Use of multiple data sources

Inherent in our procedure is the assumption that data from different cruises can be modeled using the same filtering procedures, and thus that data from multiple cruises can be combined into single slope distribution functions. This assumption warrants investigation because Seabeam and Hydrosweep form beams with slightly different half-angle values $\delta\phi_{1/2}$, and Hydrosweep samples depths every 75-80 m, while the Seabeam data we use shows returns every 150-180 m. Ideally, we would be able to test the validity of the assumption that data sets can be safely combined by inverting data from different sources within a single subregion separately. However, between-trackline differences in seafloor character are often fairly large, so that the inverted values of H, L, and κ from any

subset of data from a subregion are likely to be different from the values associated with the subregion as a whole.

Still, serious problems with data from one source, such as an excessive amount of random noise or a tendency to have data drops over steep scarps, should be revealed by variations from norms in inversion results from subregions composed primarily of data from that source. We see no such patterns in either of the study areas. To illustrate this, in Fig. 4.31 we display inversion results from the Rio Grande study area and indicate which cruises contributed to each set of inversion results. We see no pattern of abnormally high or low values of any of the parameters corresponding to data from any particular cruise. For example, the high values of H and L from region R20 and the low values from region R1 are both drawn primarily from data from *R/V Ewing* cruise EW9011.

One reason that data sets seem to combine safely is that the spacing for all three cruises is dense enough that estimation error values e tend to be less than the binning width w of 0.02, as shown in Fig. 4.32. Data from the *R/V Ewing* cruises does tend to have smaller e values as calculated via (3.8), due to the somewhat smaller average data point spacing, but for all of the cruises errors are small enough that the width of slope distribution functions at low θ is not affected.

Effects of misestimation of sampling effects

We have assumed that the bathymetry swathmapping systems which collected the data used in this chapter smooth topography and impart a Gaussian-distributed, random system noise with a variance E^2 of 10 m^2 to the centerbeam data, and that the smoothing effects of the sampling procedure can be modeled using a Hanning taper of the form given in Chapter 3 by equations (3.1)-(3.3) [*Goff and Jordan*, 1988], with a half-angle value $\delta\phi_{1/2}$ of 0.02 rad [*Kleinrock*, 1992], as appropriate for Hydrosweep data. However, in some locales, data seems noisy enough to justify a random noise term with a variance of 25 m^2, a difference potentially large enough to cause inversion errors in L and κ (see Table 3.4). In addition, much of the data was collected with Seabeam systems, the effects of which are better modeled using a slightly larger $\delta\phi_{1/2}$ of 0.023 rad [*Goff and Jordan*, 1988].

To determine how the misestimation of sampling system variables E^2 and $\delta\phi_{1/2}$ might influence inversion results, we sample several model seafloors using 25 m^2 for E^2 and, separately, 0.023 rad for $\delta\phi_{1/2}$. Models have basement parameters H = 160 m, k_n = 0.6 km^{-1}, a = 3, D = 2.2, and ζ_s = 0°, and sediment thicknesses L of 10, 20, 30, 40, and 60 m, applied using a diffusivity κ of 0.14 m^2/yr at a rain rate F of 4 m/m.y. of model time. A ship-to-seafloor average distance h_{AV} of 3000 m is used. During the inversion, we assume an N of 800 m.

We find that increasing E^2 to 25 m^2 does not affect inversion results for L and H for the L = 10, 20, and 30 m surfaces, and results in a slight reduction to κ, to 0.12 m^2/yr. For the models with L of 40 m and 60 m, H is inverted as 165 m and L is inverted as 43 m and 63 m, respectively.

Mischoosing $\delta\phi_{1/2}$ affects H and L even less. Using a $\delta\phi_{1/2}$ of 0.023 in the filtering of model topographies results in inverted H values of 160 m for the L = 10, 20, 40, and 60 m surfaces and 155 m for the L = 30 m surface. L values show small amounts of variability for only the L = 20 m and L = 30 m surfaces, with inverted values of 21 m and 28 m respectively. Inverted values of κ are also only slightly affected.

Effects of misestimation of basement parameters

Covariance functions computed along-track for the Rio Grande region suggest that the basement k_n value of 0.6 km^{-1} used to generate the model topographies for the inversion procedures might be overestimated somewhat for at least some subregions, with an k_n of 0.5 km^{-1} or lower also perfectly reasonable (see Fig. 4.5). Also, although most tracklines we use are perpendicular to the ridge crest, some are a few degrees off of the flowline direction, particularly those over the middle ridge segment in the Cox study area.

In Chapter 3, we investigate what effect the misestimation of basement k_n would have on inversion results in the parameter range appropriate for the ARC, and find that both L and H would be underpredicted by ~10% if basement k_n is 0.5 km^{-1} instead of 0.6 km^{-1}, for H of 225 m and L between 10 and 100 m. However, in this Chapter's study areas, H is typically slightly lower, and a, ζ_s, and E^2 are also all different. Therefore, to study the effects of the overestimation of k_n on inverted parameters in a setting which models the

South Atlantic, we generate a Goff-Jordan model basement with parameters H = 200 m, k_n = 0.5 km^{-1}, a = 3, D = 2.2, and ζ_s = 0°. This basement is sedimented at a rain rate F of 4 m/m.y. for 15 m.y. of model time using a κ of 0.14 m^2/yr, and surfaces are generated at model times of 2.5, 5, 7.5, 10, and 15 m.y, corresponding to L values of 10, 20, 30, 40, and 60 m respectively. From these surfaces, slope distribution functions are calculated using the methodology of Chapter 3, letting E^2 be 10 m^2 and h_{AV} be 3000 m. During the inversion, we assume an N of 800 m.

We find that the inversion procedure estimates H values of 180 m for L of 10, 20, 30, and 60 m, and 185 m for the surface corresponding to an L of 40 m. This represents an underestimation of 10%, similar to the underestimation of H predicted based on numerical experiments in Chapter 3. These values are only slightly above 177 m, the value (via (2.32)) which best allows the distribution of the basement portions of the models to be similar to those built upon basements with parameters H = 200 m and k_n = 0.5 km^{-1}, given the other basement parameters.

We find that the inverted value of L is barely affected by the misestimation of k_n, with inversion results of 10, 20, 30, 43, and 59 m from surfaces with true L of 10, 20, 30, 40, and 60 m, respectively. Inverted values of κ also do not experience much alteration, ranging from 0.12 to 0.15 m^2/yr for all five surfaces.

The small effect of the misestimation of k_n on L assures us that this is not a significant contributor to the variations seen in L throughout the Rio Grande and Cox study areas. The effects of the misestimation of k_n on H, and hence regional values of $\overline{H}_{all}$, $\overline{H}_{in}$, and $\overline{H}_{out}$, is potentially more serious. We assume above that much of the variability in the shape of covariance functions is due to long-wavelength topographic effects to which our inversion procedure is fairly immune. In this sections, we instead estimate that the variability seen in the Rio Grande area is due solely to differences in basement k_n. We use the covariance functions to estimate the corner wave number $\hat{k}_n$ and fractal dimension $\hat{D}$ which best describe the sedimented topography, then use these values to compute the current hill spacing $\hat{\lambda}_n$ via (2.5). Then, assuming that Λ is roughly equal to inverted sediment thickness L divided by 200 m, and that basement D is 2.2, we estimate k_n by recasting (2.31) and (2.5) and substituting in for Λ and D to obtain

$$k_n = \frac{3.22(1+0.0065L)}{\hat{\lambda}_n}. \tag{4.6}$$

We use the resulting estimates of k_n to determine H such that the variability in basement slope is the same as would be expected given a k_n of 0.6 km^{-1} and the originally inverted value of H. Results are given in Table 4.7.

Table 4.7. Estimates of k_n and H, given a negligible effect of long-wavelength topography on covariance functions and L from Table 4.1.

Site	$\hat{k}_n$, km^{-1}	$\hat{D}$	$\hat{\lambda}_n$, km	k_n, km^{-1}	H, m
R1	0.45	2.05	7.57	0.525	225
R2	0.7	2.05	4.87	1.02	183
R3	0.55	2.1	6.08	0.616	196
R4	0.35	2.15	9.39	0.376	284
R7	0.4	2.2	8.06	0.438	286
R8	0.55	2.1	6.08	0.571	165
R9	0.4	2.05	8.51	0.469	195
R10	0.55	2.1	6.08	0.619	181
R11	0.5	2.1	6.69	0.569	171
R12	0.4	2.03	8.57	0.432	226
R13	0.65	2.03	5.28	0.701	189
R16	0.5	2.05	6.81	0.497	228
R17	0.25	2.2	12.9	0.298	392
R18	0.35	2.15	9.39	0.408	274
R19	0.45	2.15	7.30	0.582	235
R20	0.65	2.03	5.28	0.911	205
R21	0.45	2.05	7.57	0.569	213
R22	0.5	2.2	6.45	0.571	176
R23	0.65	2.2	4.96	0.755	159
R24a	0.45	2.2	7.17	0.522	247
R24b	0.9	2.2	3.58	1.10	135
R27a	0.45	2.2	7.17	0.508	247
R27b	0.3	2.1	11.2	0.304	362
R28	0.7	2.2	4.61	0.762	158
R29	0.45	2.1	7.44	0.540	220
R30	0.9	2.05	3.78	1.11	150
R31	0.85	2.05	4.01	1.04	178
R32	0.6	2.05	5.68	0.685	219
R33	0.6	2.2	5.37	0.615	202
R34	0.6	2.2	5.37	0.65	199
R38	0.5	2.2	6.45	0.535	222
R39	0.25	2.1	13.4	0.290	291
R40	0.4	2.1	8.37	0.447	208

The average of H in Table 4.7 is 219 ± 57 m, fairly near the value computed assuming that k_n is uniformly 0.6 km^{-1} but with far greater variability. Inside corner crust and outside corner crust have average H values of 231 ± 57 m and 204 ± 45 m,

respectively. The large distribution of values of H for crust of both types reduces the significance of the conclusion that inside corner crust and outside corner crust have different mean values. However, the difference in mean values observed, 27 m, is only slightly less than the difference observed when k_n is assumed to be 0.6 km^{-1}, indicating that a mean difference in inside corner H and outside corner H is independent of the assumption of a constant value for basement hill spacing.

In Chapter 3, we also investigate how the misestimation of ζ_s would affect inversion results, though not in the range appropriate for application to data from the South Atlantic study areas. Therefore, we here also investigate how a true ζ_s of 10° would affect inversion results, for sedimentation and basement parameters appropriate the South Atlantic seafloor investigated in this chapter. A Goff-Jordan model basement is generated with parameters H = 200 m, k_n = 0.6 km^{-1}, a = 3, D = 2.2, and ζ_s = 10°. As with the lower-k_n model above, this basement is sedimented at a rain rate F of 4 m/m.y. for 15 m.y. of model time using a diffusivity κ of 0.14 m^2/yr, and surfaces are generated at model times of 2.5, 5, 7.5, 10, and 15 m.y, corresponding to L values of 10, 20, 30, 40, and 60 m respectively. From these surfaces, slope distribution functions are calculated using the methodology of Chapter 3, letting E^2 be 10 m^2 and h_{AV} be 3000 m. During the inversion, we again assume an N of 800 m.

We find that these model surfaces had inverted values of H of either 195 m or 200 m. Inverted values of L are within two meters of the correct values, and are as likely to overpredict L as to underpredict it. Apparent diffusivity also shows little variability, with inverted values of κ ranging from 0.15 to 0.19 m^2/yr. Based on these results, we do not believe that slight variations from flowline direction have influenced inversion results from the Rio Grande and Cox study areas.

Effect of smoothing via (4.4) on inverted values

To accurately determine H, it is vital that models which correspond to inverted parameters have the same percentage of higher-slope seafloor as seen in the bathymetric data. Therefore, when computing $g_d(\theta,u)$ for the subregions in the Rio Grande and Cox study areas, we impose additional smoothing on the shapes of slope distribution functions

from data at higher values of θ by the use of equation (4.4) instead of (3.11) to compute the contribution of high slope values to individual slope bins. This smoothing produces slope distribution functions which more closely resemble those calculated from models (Fig. 4.33), allowing higher likelihood values between data and models, and better agreement between bestfitting model slope distribution functions and those calculated from data, for all θ. We find that, in practice, this smoothing alters inverted values of H by at most 10 m, with L varying by less than 4 m. Upward and downward shifts to H and L are equally likely.

One potential source of error arises from the fact that we do not subject model slope distribution functions to smoothing. To investigate the consequence of this, we apply the inversion procedure to slope distribution functions calculated using (4.4) from models generated using basement parameters H = 160 m, k_n = 0.6 km^{-1}, a = 3, D = 2.2, and ζ_s = 0°, and sediment thicknesses L of 10, 20, 30, 40, and 60 m, applied using a diffusivity κ of 0.14 m^2/yr at a rain rate F of 4 m/m.y.

We find that the smoothed slope distribution functions experience underestimations of 5 m for H for the L = 10, 20, 30, and 60 m surfaces, while H is inverted as 160 m for the L = 40 m surface. When H is underestimated, L is underestimated by ~5%. For the L = 40 m surface, however, L is overestimated by a meter. Therefore, it seems that H and L may be prone to underestimation due to the use of (4.4).

Summary of error effects

The cumulative effect of these error sources is probably a slight underestimation (~1-3 m) for all inverted values of L. This would increase A by perhaps 5%, but is tentative enough that we do not adjust our estimates of A.

Misestimation of k_n by 0.1 km^{-1} may lead to 10-20 m errors in H. However, this possibility does not alter our conclusion that inside corner crust and outside corner crust have fundamentally different typical H values.

CONCLUSIONS AND DISCUSSION

Sediment thickness variations

In both of the study areas, L increases linearly with T, within the resolution of our methodology. Accumulation rates are fairly symmetric about the MAR, averaging ~5 m/m.y. in the Rio Grande study area and ~6 m/m.y. in the Cox study area. Fixing H at regional averages and, in the Rio Grande study area, to average values related to crustal type, decreases same-age scatter in L, while only slightly altering A.

The inferred sediment accumulation rates are less than that inferred from DSDP drill sites from Legs 3 and 73 [*Maxwell et al.*, 1970; *Hsü, LaBrecque et al.*, 1984], as tabulated in Table 6.2 and Table 6.3. This is probably due both to the placement of drill holes in local maxima of sediment thickness and to local differences in surface productivity.

Discussion of the paleoceanographic implications of our results occurs in Chapter 6.

RMS height variations

Advantages of our methodology for estimating H over computation from profiles or by using the inversion methodology of *Goff and Jordan* [1988] are that we obtain a measure of basement, not seafloor, variability, and that long-wavelength topographic effects, such as subsidence due to crustal cooling, have a minimal effect on our inversion results. These advantages allow us to interpret inverted values of H geologically.

The mean values of H for the Rio Grande study area is 206 ± 29 m and for the Cox study area is 199 ± 11 m. In the Rio Grande study area, where the identification of crustal type is clear, we find that average values of H vary significantly between types: 222 ± 23 m for inside corner crust, vs. 189 ± 22 m for outside corner crust. In the Cox study area, inside corner crust also has a higher average H than outside corner crust (201 ± 11 m vs. 192 ± 12 m), but this difference is not very significant. The variation in H between crustal types in the Rio Grande study area persists even when inverted values are modified so as to account for possible variations in basement hill spacing, as in Table 4.7.

In the Rio Grande region, fixing H for inside corner and outside corner crust at 220 m and 190 m, respectively, and inverting for L and κ produces estimates of L which show

increased homogeneity on same-age crust, suggesting that, despite variations in inverted values, inside corner crust and outside corner crust have characteristic values of H which vary little throughout the region.

The strong dependence of H on crustal type suggests that H may be a measurement of the regional balance of the influence of inside corner properties such as thinner crust, blocky topography, and the surface exposure of plutonic and ultramafic rocks, and outside corner properties such as thicker crust, smaller throws on individual faults, and a greater preservation of volcanic structures generated in the neovolcanic zone [*Tucholke and Lin*, 1994]. This is not a new proposition; *Goff et al.* [1995] associated variations in along-track seafloor RMS variability (inverted using the methodology of *Goff and Jordan* [1988]) in the North Atlantic to different crustal construction regimes, with the typically high-standing topography associated with inside corner crust being rougher than lower-standing outside corner crust [*Severinghaus and Macdonald*, 1988; *Tucholke and Lin*, 1994].

This correlation suggests that some of the variability seen in H world-wide can be attributed to whether sampled crust was generated at inside or outside corners.

Apparent diffusivity

When H is free to vary, κ varies from 0.03 to 1.1 m^2/yr with an average of 0.29 ± 0.25 m^2/yr in the Rio Grande study area and from 0.06 to 0.53 m^2/yr with an average of 0.14 ± 0.11 m^2/yr in the Cox study area. When H is fixed, most values are only slightly altered. The values of κ observed in this chapter are mostly within the range observed in the North Atlantic study area discussed in Chapter 3.

Patterns exist in the distribution of κ, but it is unclear what they reflect. Younger seafloor in the Cox region (see Fig. 4.24) generally has lower κ values than older seafloor; except on the east flank of the MAR in the middle section, however, this trend is slight. In the Rio Grande study area (see Fig. 4.8), eastern subregions exhibit much less variability in κ than those to the west. And, the older regions on the east flank almost uniformly exhibit higher κ than those on the west flank. There is a slight correlation between κ and crustal type, with large values of κ inverted from several inside corner subregions.

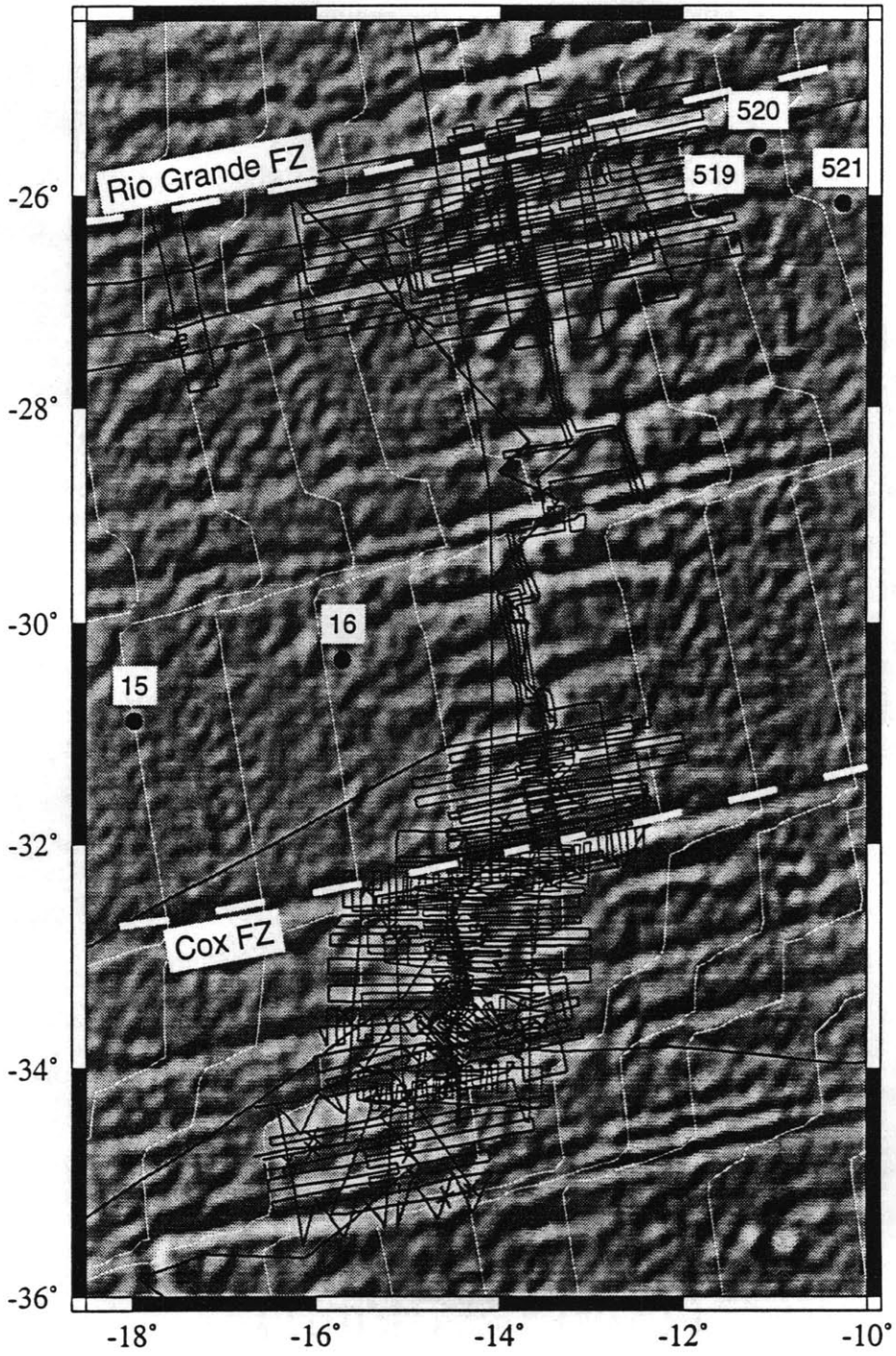

Fig. 4.1: Gray-shaded free-air gravity anomaly map of the central South Atlantic [*Sandwell and Smith*, 1995], showing tracklines for the cruises from which data is analyzed in this chapter and all local DSDP sites. White ridge-parallel lines correspond to isochrons of 5 m.y. [*Müller et al.*, 1993].

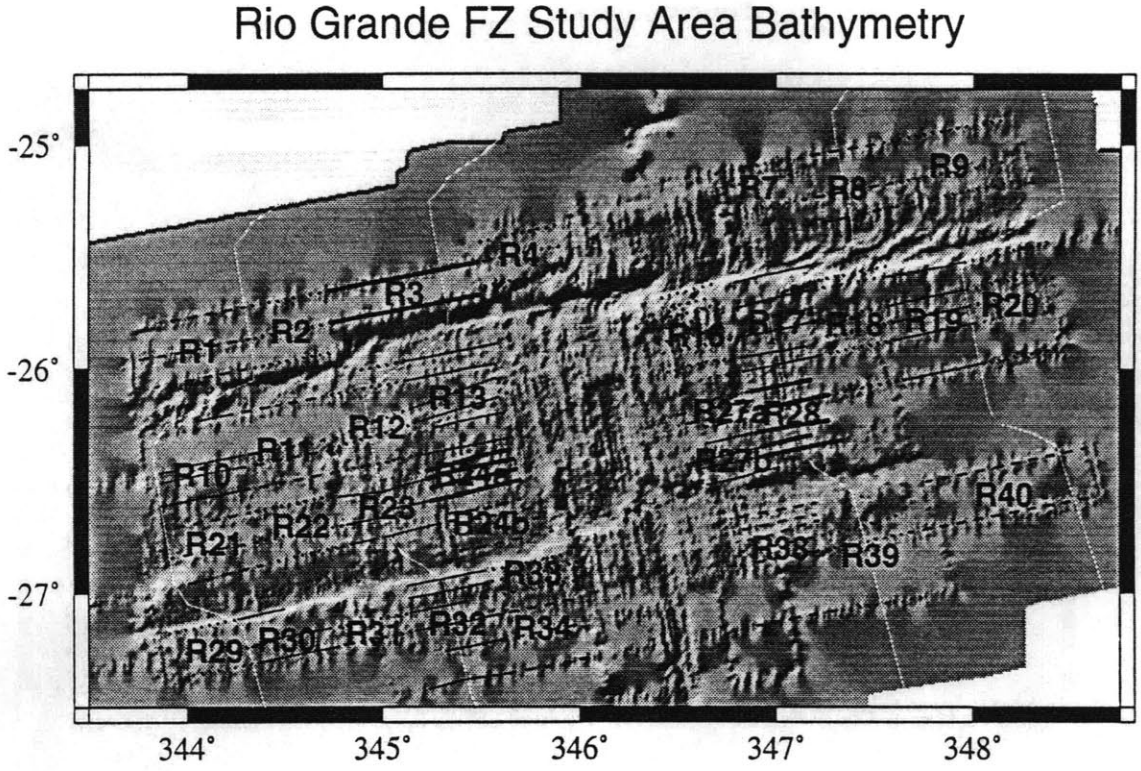

Fig. 4.2: Gray-shaded image of data in the Rio Grande near-ridge study area, gridded at an interval of 0.5 minutes, from *R/V Conrad* cruises RC2711 and RC2802 and *R/V Ewing* cruise EW9011, and trackline segments used to construct subregions, as labeled. All line segments composing a subregion are represented by the same pattern. White lines are 5 m.y. isochrons [*Müller et al.*, 1993].

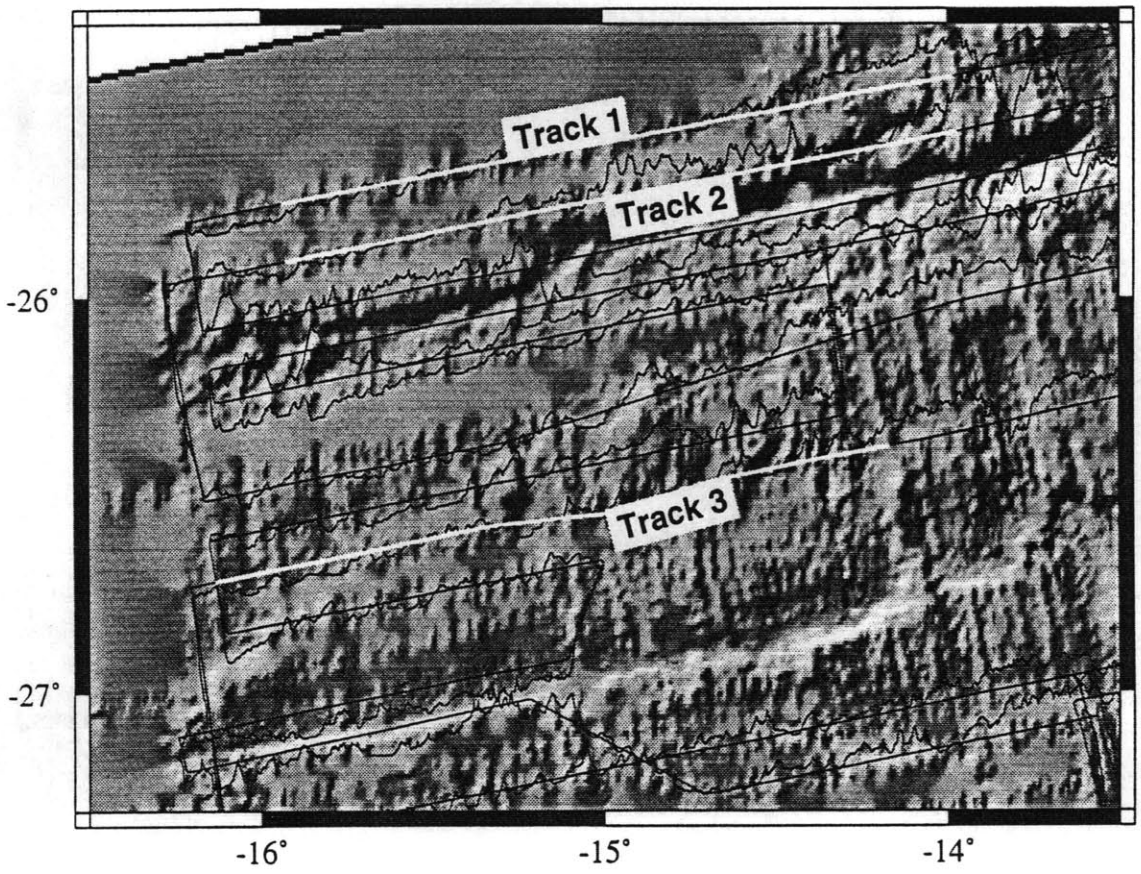

Fig. 4.3: Gray-shaded image as in Fig. 4.2, with along-track bathymetry data from cruise EW9011 shown at a vertical scale of 5000 m/inch.

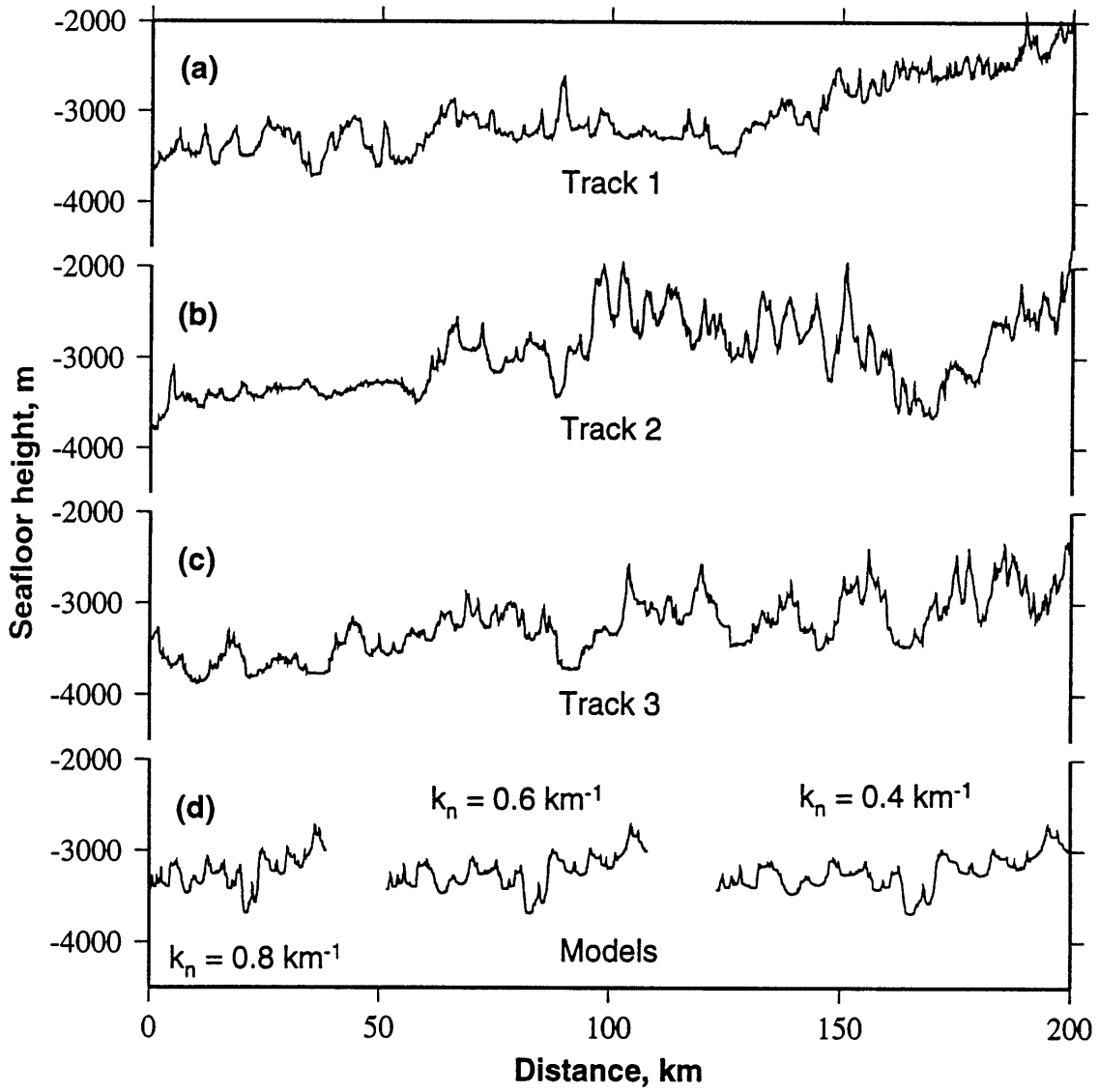

Fig. 4.4: Enlargement of along-track data from the tracklines labeled in Fig. 4.3 ((a)-(c)), and examples of tracklines through sedimented models (d), as described in the text. Vertical exaggeration is 19:1.

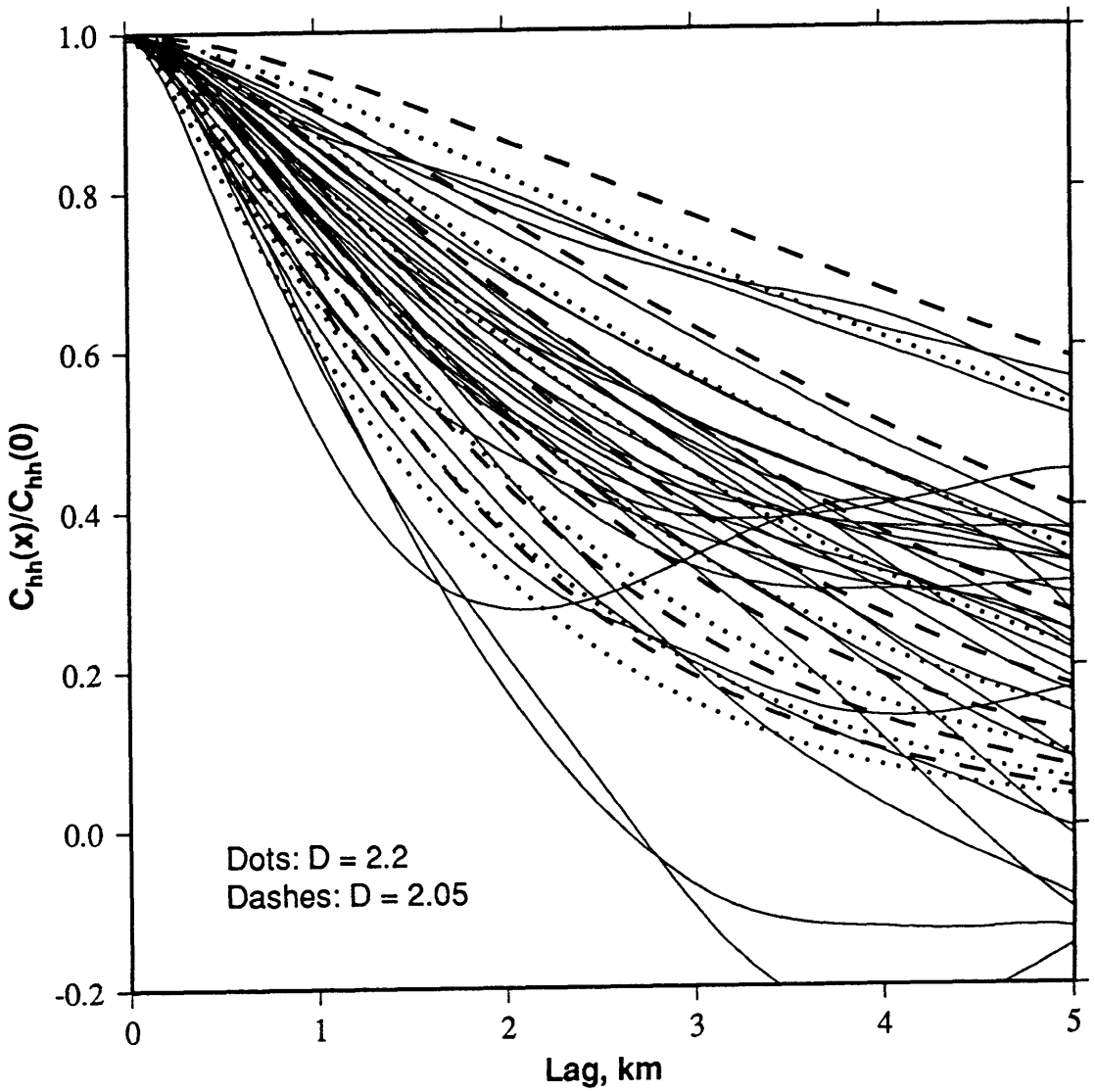

Fig. 4.5: Normalized covariance functions for the Rio Grande subregions (solid lines) and model Goff-Jordan normalized covariance functions for k_n ranging from 0.2 (uppermost functions) to 0.8 (lowermost functions) km^{-1}, for D of 2.05 (dashed lines) and 2.2 (dotted lines).

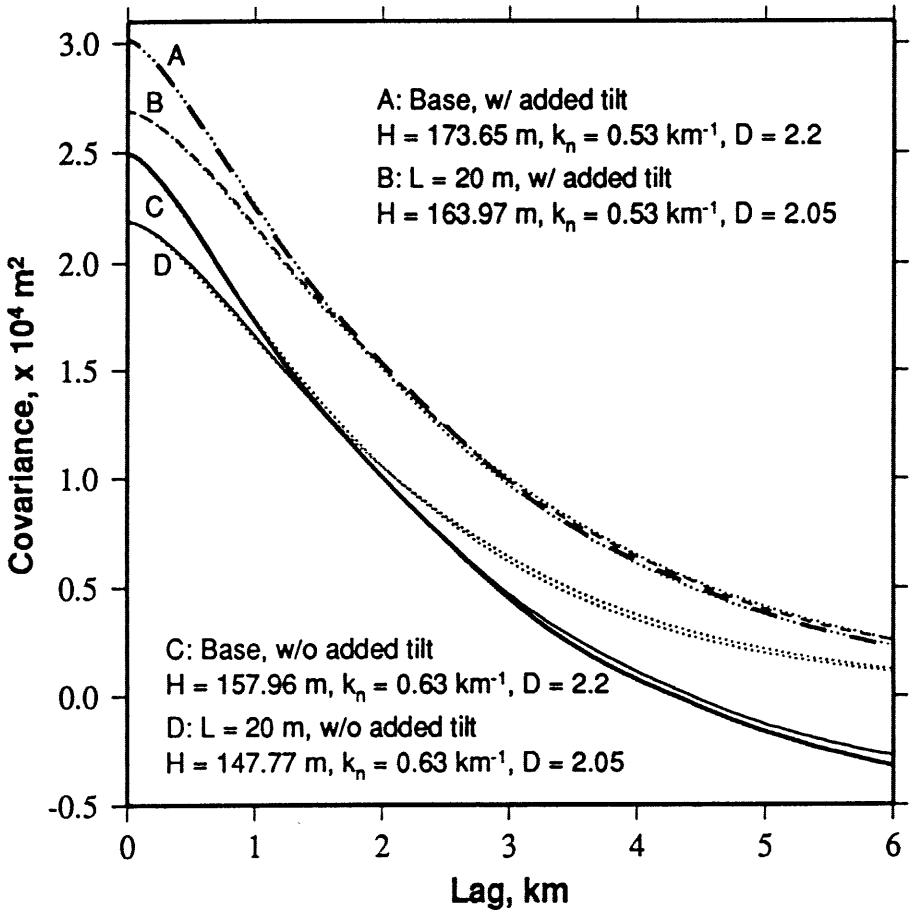

Fig. 4.6: Example of how the addition of a constant slope alters covariance functions, and, therefore, stochastic parameters as would be inverted using the methodology of *Goff and Jordan* [1988]. Lines C (thick solid line) and D (thin solid line) are covariance functions calculated from a Goff-Jordan basement model and a sedimented surface built upon this model, as described in the text. Lines A (thick dashes) and B (thin dashes) show the covariance functions of these seafloor models after the imposition of a slope of 0.005 to the surfaces. Dotted lines show best-fitting Goff-Jordan model covariance functions, corresponding to parameter values as given in the figure.

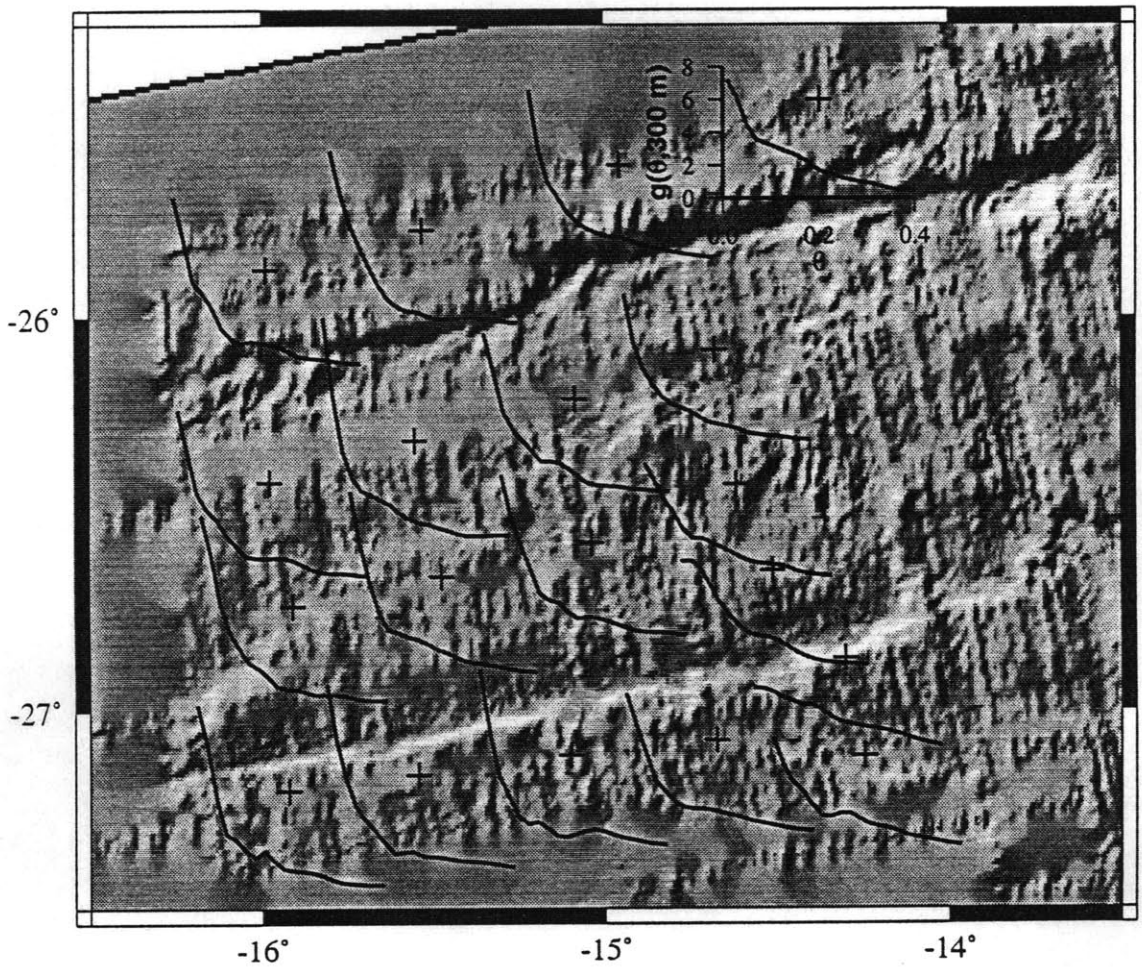

Fig. 4.7: Gray-shaded images as in Fig. 4.2 of the (a) western and (b) eastern flanks of the MAR in the vicinity of the Rio Grande Fracture Zone, and slope distribution functions calculated for the subregions given in Fig. 4.2.

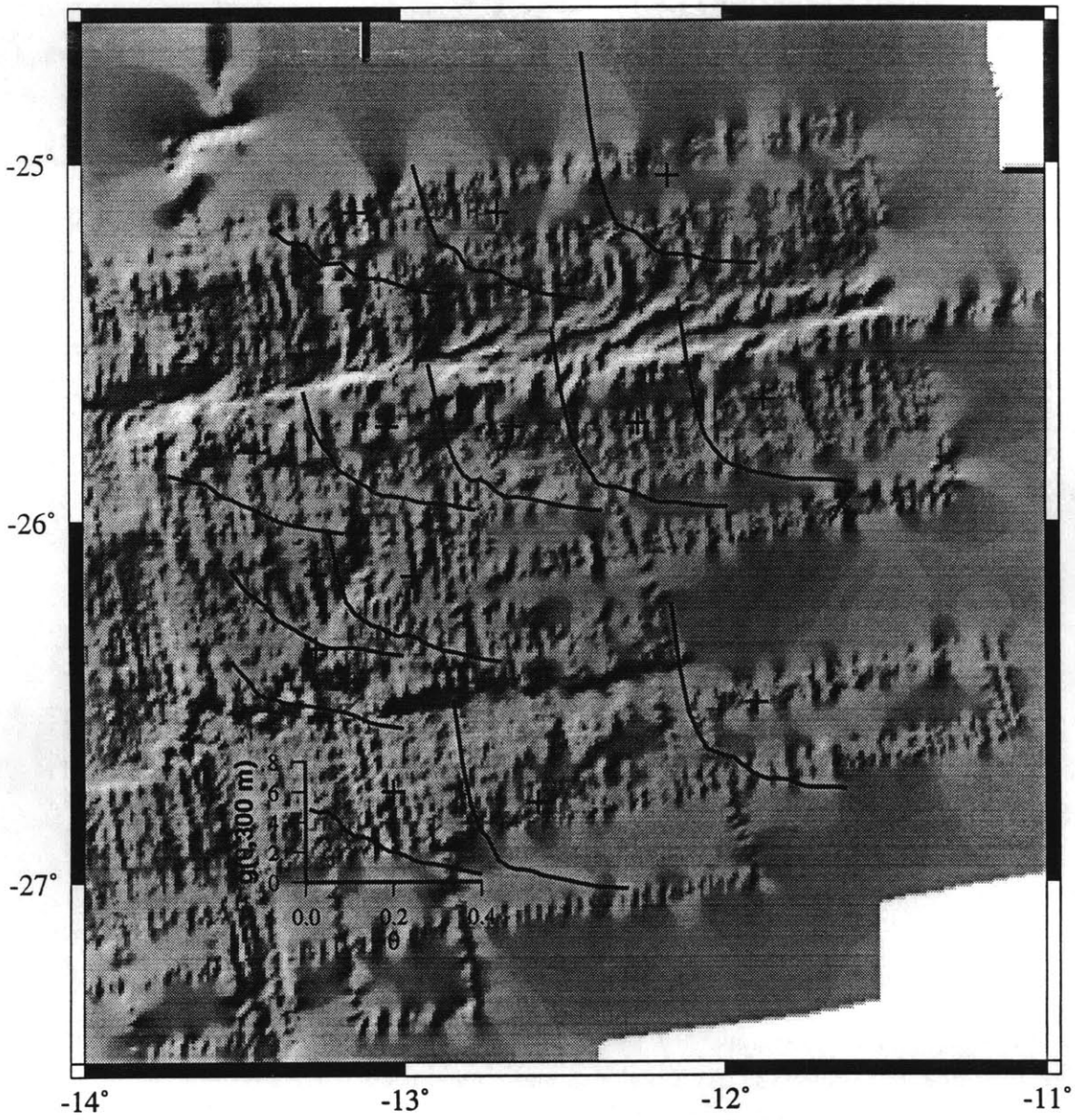

Fig. 4.7(b)

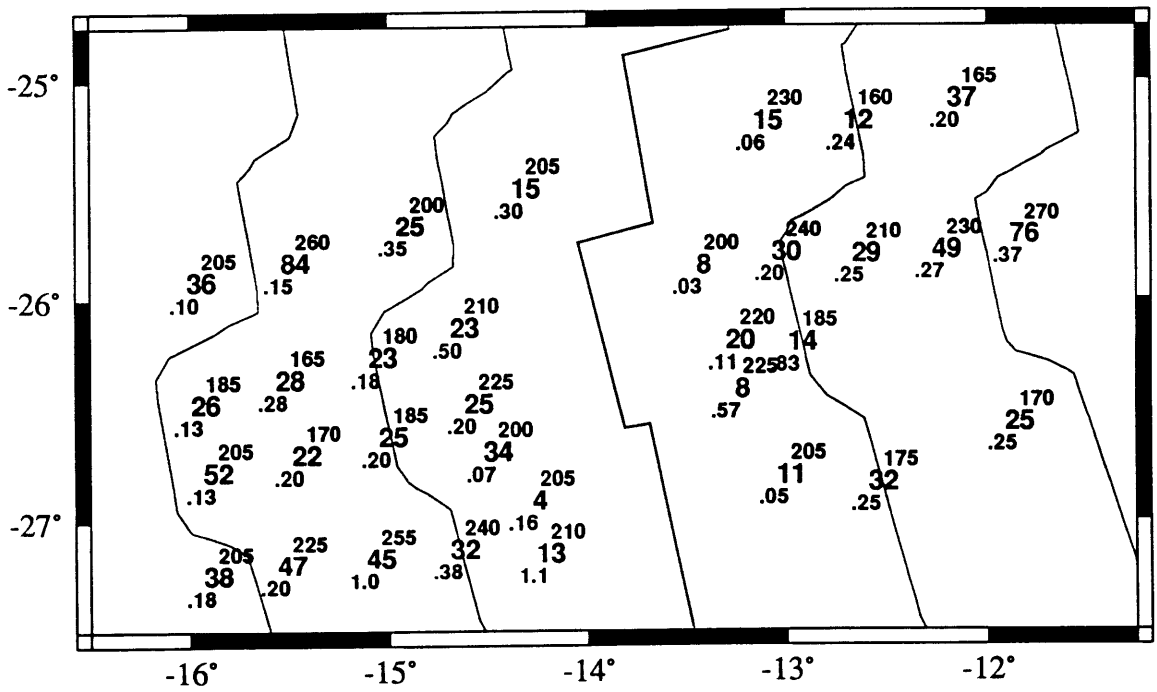

Fig. 4.8: Results of inversions for L in meters (large numbers), basement RMS height H in meters (smaller numbers above L values), and apparent diffusivity κ in m^2/yr (smaller numbers below L values), as given in Table 4.1. Thick line represents MAR, and thin lines represent 5-m.y. isochrons [*Müller et al.*, 1993].

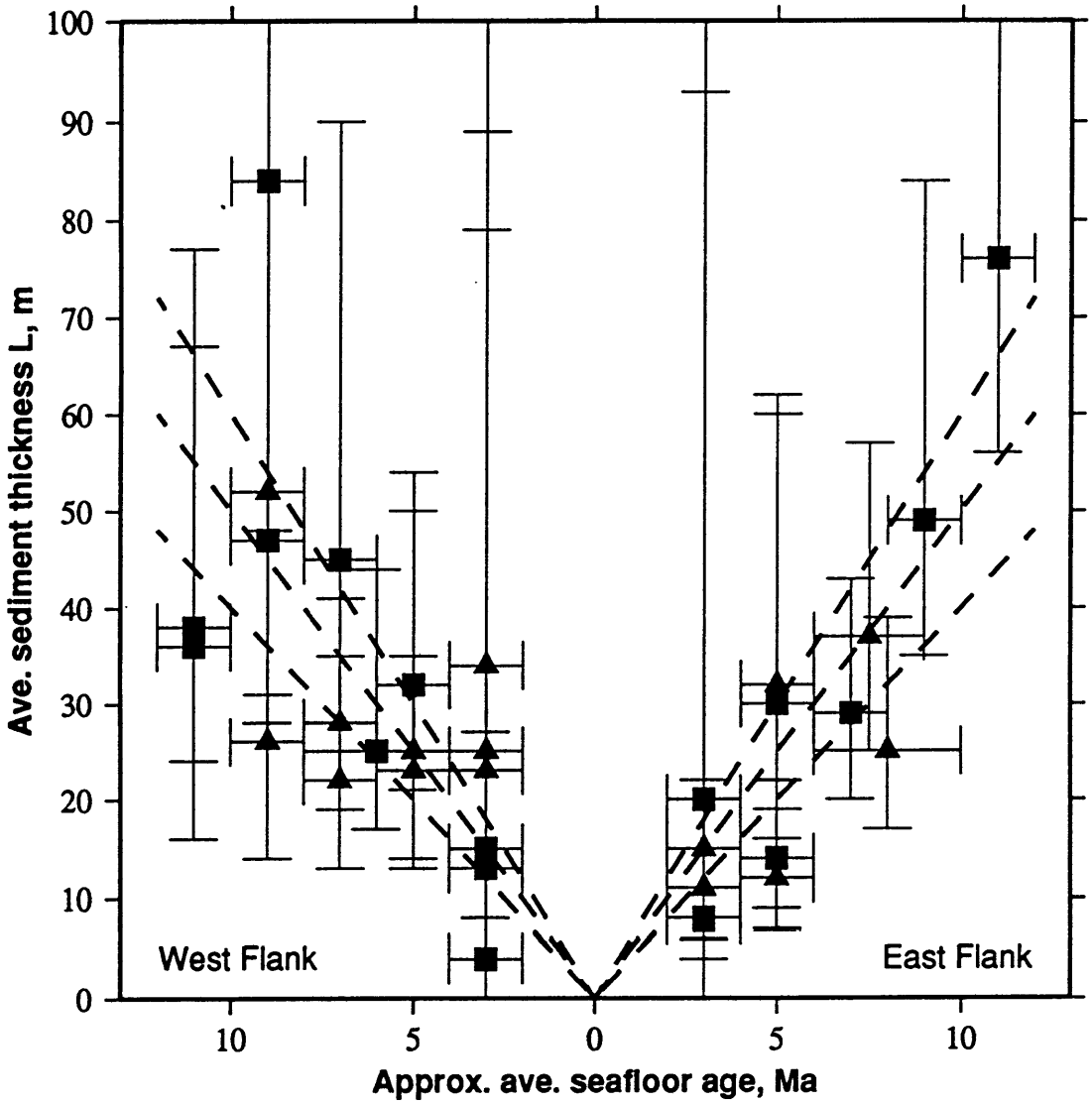

Fig. 4.9: Inverted values of L as a function of seafloor age, as given in Table 4.1. Triangles denote values derived from outside corner crust and squares denote values derived from inside corner crust. Horizontal error bars show the age range in each region, while vertical error bars give the 95% confidence intervals for L. Dashed lines correspond to constant accumulation rates of 4, 5, and 6 m/m.y.

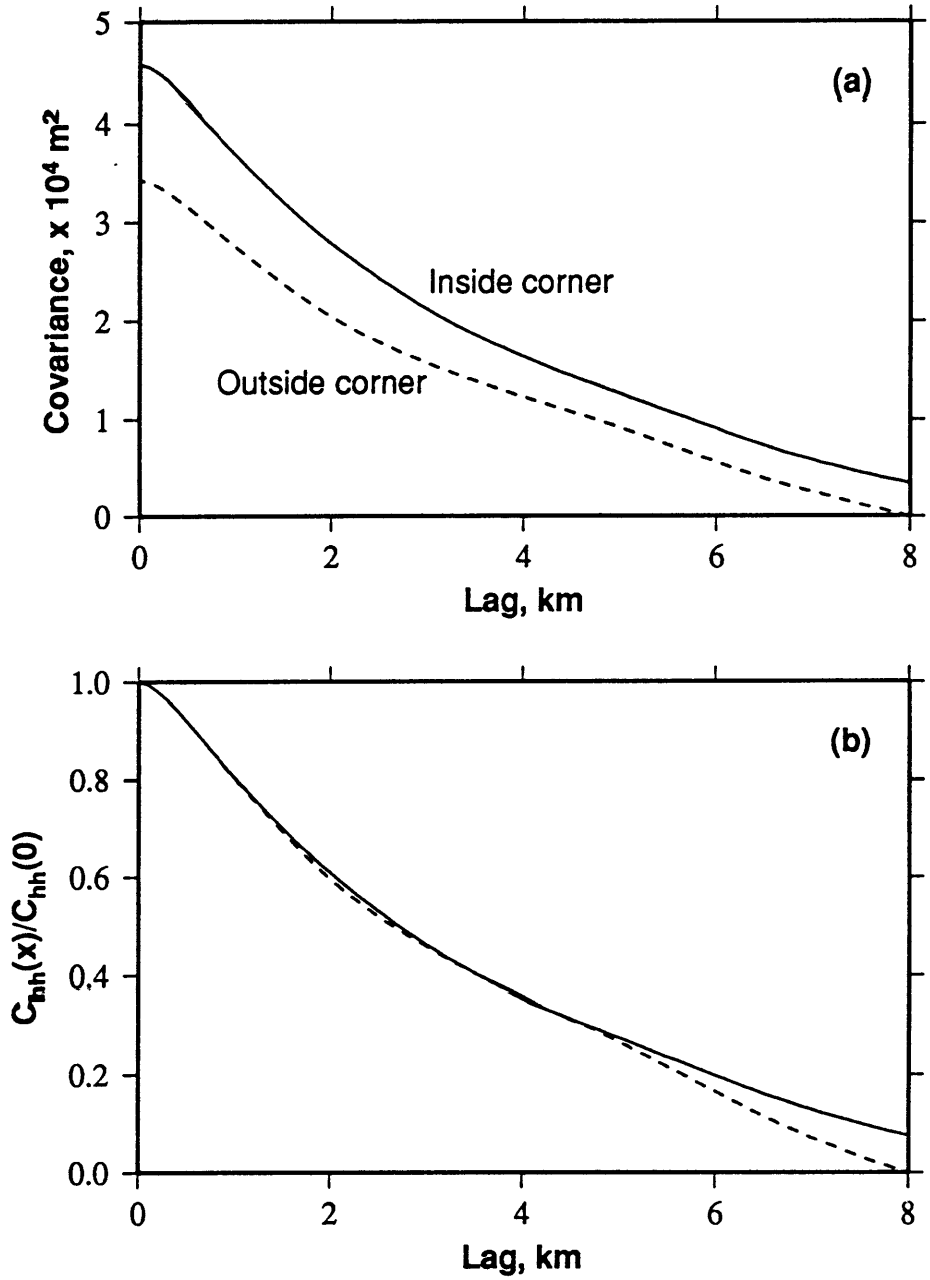

Fig. 4.10: (a) Averages of all slope distribution functions computed from all inside corner crust (solid line) and outside corner crust (dashed line) regions, showing that inside corner crust shows more topographic variability than outside corner crust. (b) Normalized form of the covariance functions shown in (a), demonstrating that inside corner crust and outside corner crust have the same mean hill spacing. Best-fitting Goff-Jordan covariance functions suggest that $\hat{k}_n = 4.8$ km^{-1} and $\hat{D} = 2.15$, making the typical hill spacing in the Rio Grande region 6.85 km (via 2.5).

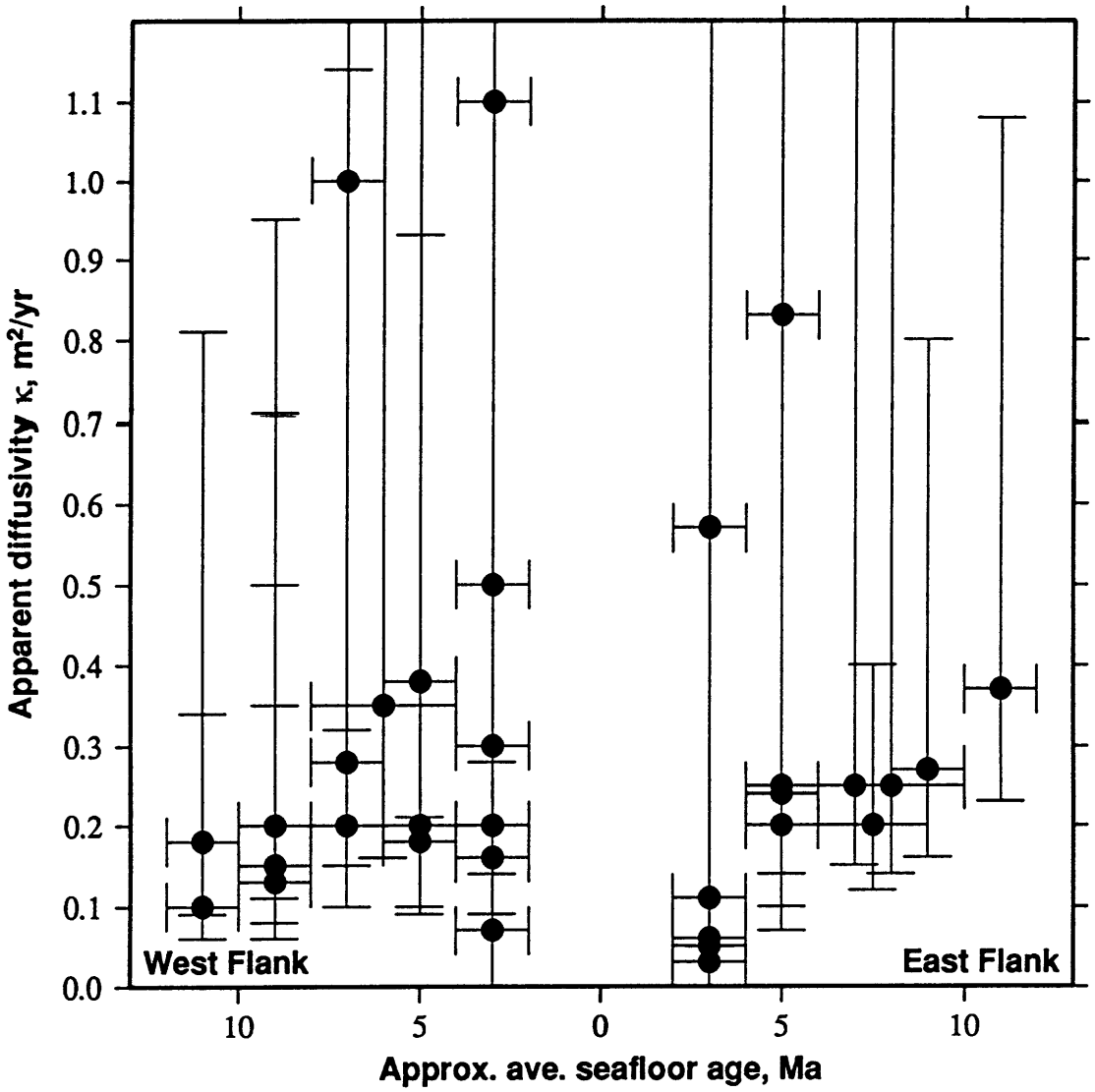

Fig. 4.11: Inverted values of κ as a function of seafloor age, as given in Table 4.1. Horizontal error bars show the age range of seafloor in each region, while vertical error bars give the 95% confidence intervals for κ.

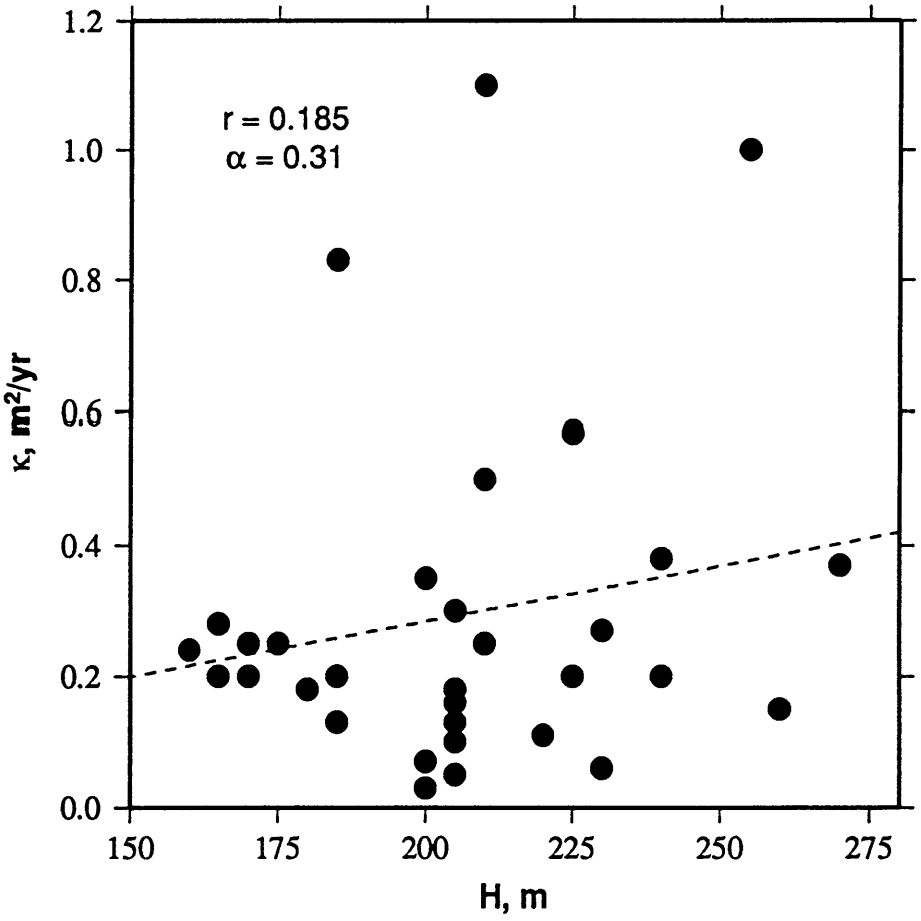

Fig. 4.12: Inverted values of κ as a function of H and best-fitting linear regression line, showing that these parameters are not significantly correlated.

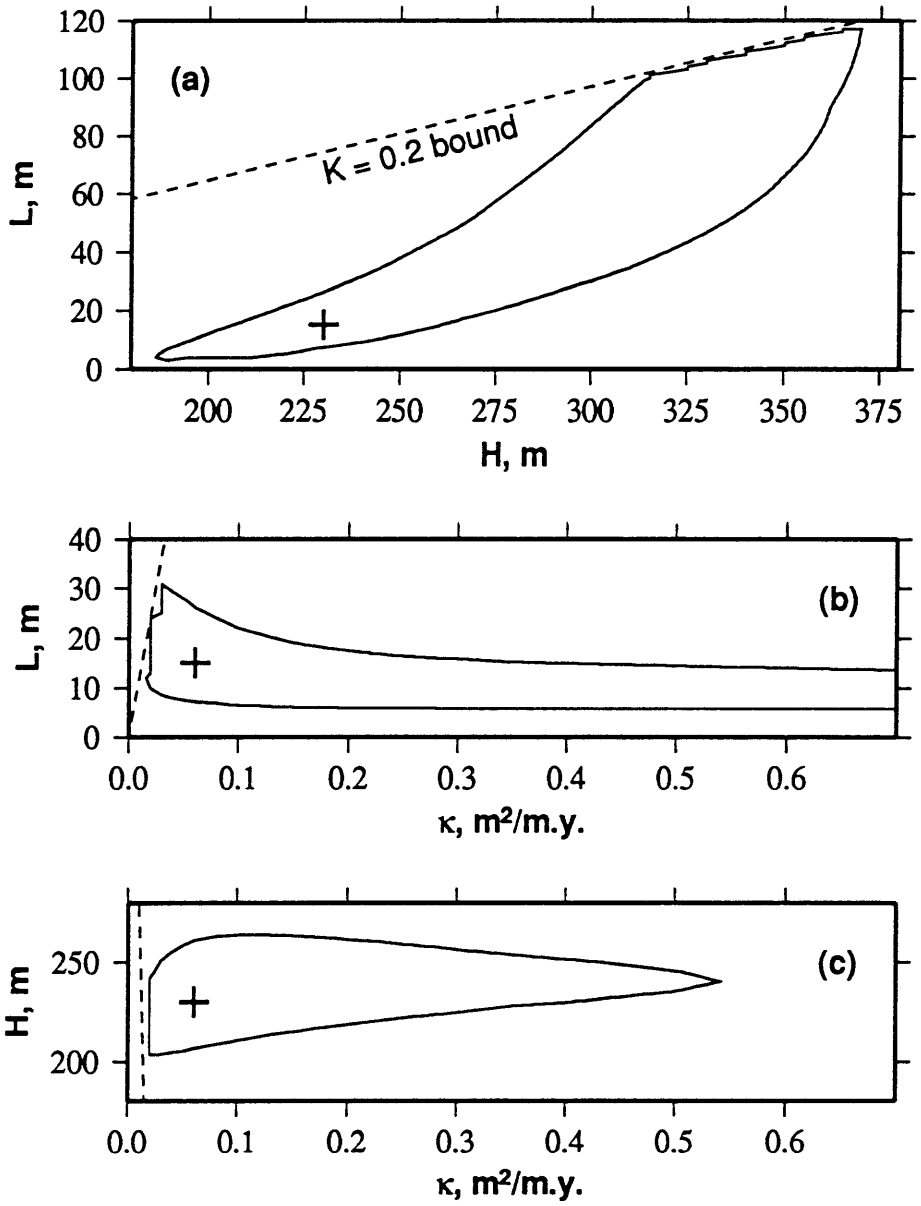

Fig. 4.13: Slices through 95% confidence region of subregion R7. (a) 95% confidence bounds on H and L and best estimate of these values (cross) at a cross-section at best κ of 0.06 m^2/yr. Dashed line shows border of model space, corresponding to the lower limit on dimensionless diffusivity K. (b) 95% confidence bounds on κ and L and best estimate of these values (cross) at a cross-section at best H of 230 m. Dashed line shows border of model space, corresponding to the lower limit on dimensionless diffusivity K. (c) 95% confidence bounds on κ and H and best estimate of these values (cross) at a cross-section at best L of 15 m. Dashed line shows border of model space, corresponding to the lower limit on dimensionless diffusivity K.

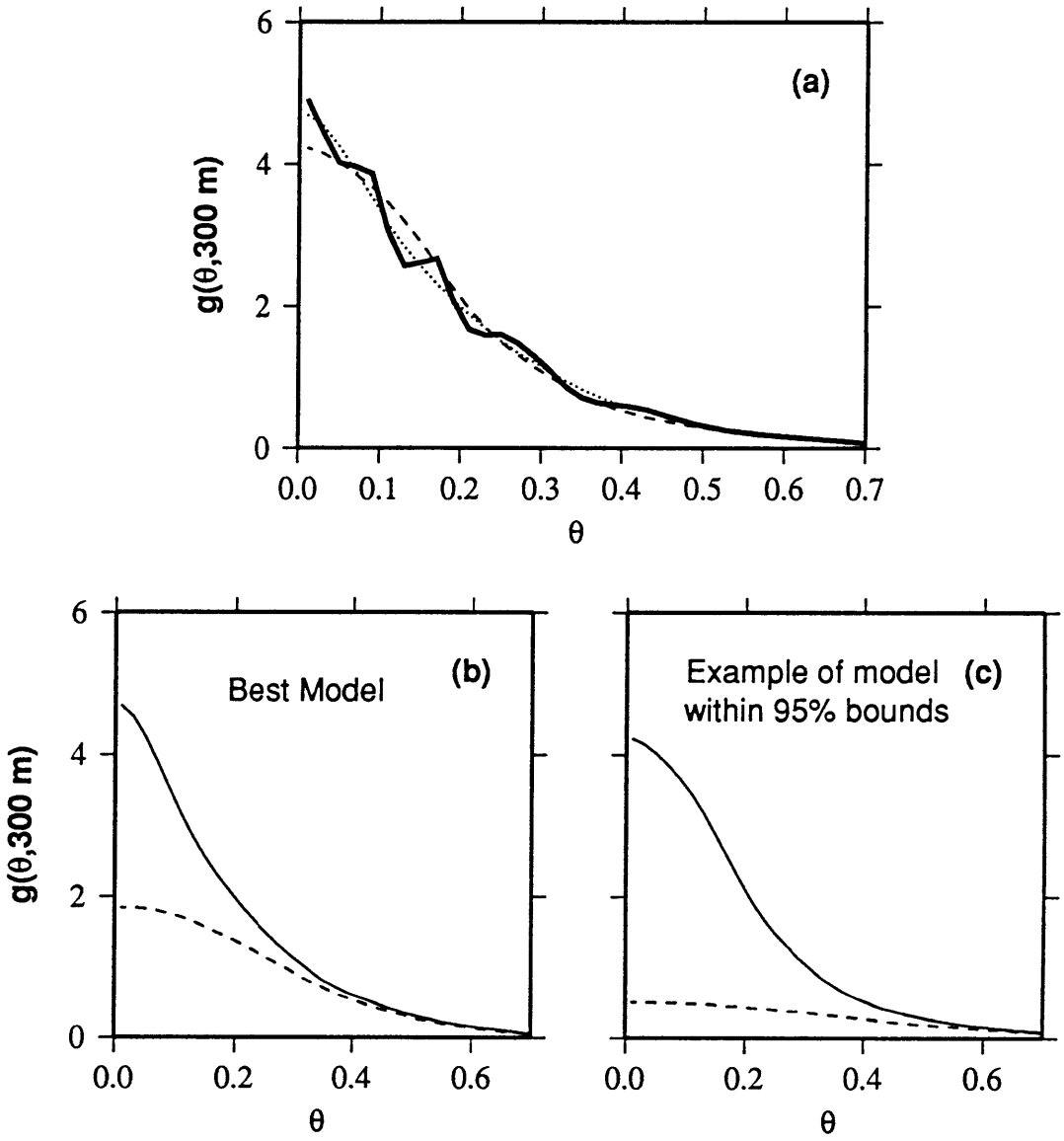

Fig. 4.14: (a) Slope distribution for subregion R7, which is best matched by a model slope distribution function corresponding to H = 230 m, L = 15 m, and κ = 0.06 m^2/yr (dotted line) but also somewhat resembles the slope distribution function produced using an H of 320 m, an L of 80 m, and a κ of 0.06 m^2/yr (dashed line), located within the 95% confidence bounds on R7 as shown in Fig. 4.13. (b) Model slope distribution functions produced using H = 230 m, L = 15 m, and κ = 0.06 m^2/yr (solid line) and the basement model where H = 230 m (dashed line), scaled such that it matches the solid line at high θ. (c) Model slope distribution functions produced using H = 320 m, L = 80 m, and κ = 0.06 m^2/yr (solid line) and the basement model where H = 320 m (dashed line), scaled such that it matches the solid line at high θ.

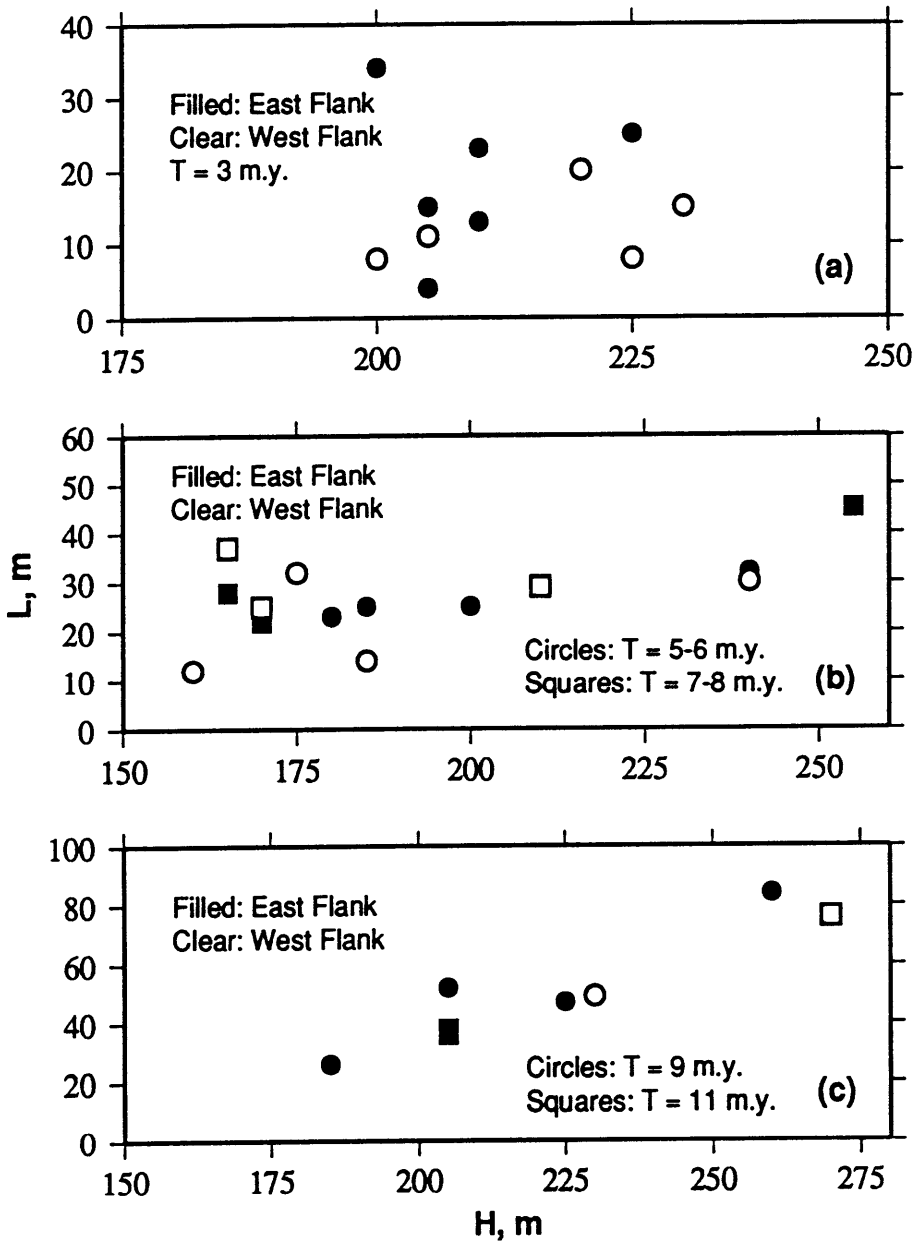

Fig. 4.15: Inverted values of H and L for the Rio Grande subregions for seafloor with average ages T of (a) 3 Ma; (b) 5-6 Ma (circles) and 7-8 Ma (squares); and (c) 9 Ma (circles) and 11 Ma (squares). The apparent correlation between H and L increases with increasing T for both east flank (filled) and west flank (clear) subregions.

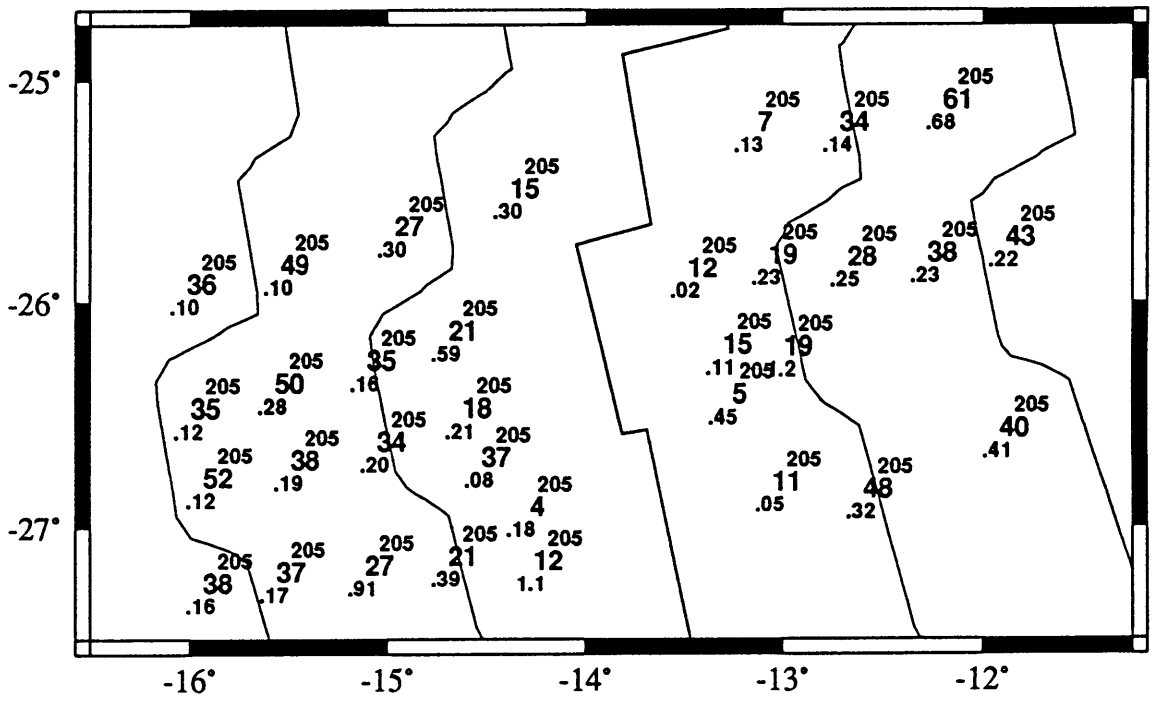

Fig. 4.16: Results of inversions for L in meters (large numbers) and apparent diffusivity κ in m^2/yr (smaller numbers below L values), with H fixed at 205 m (smaller numbers above L values), as given in Table 4.2. Thick line represents MAR, and thin lines represent 5-m.y. isochrons [*Müller et al.*, 1993].

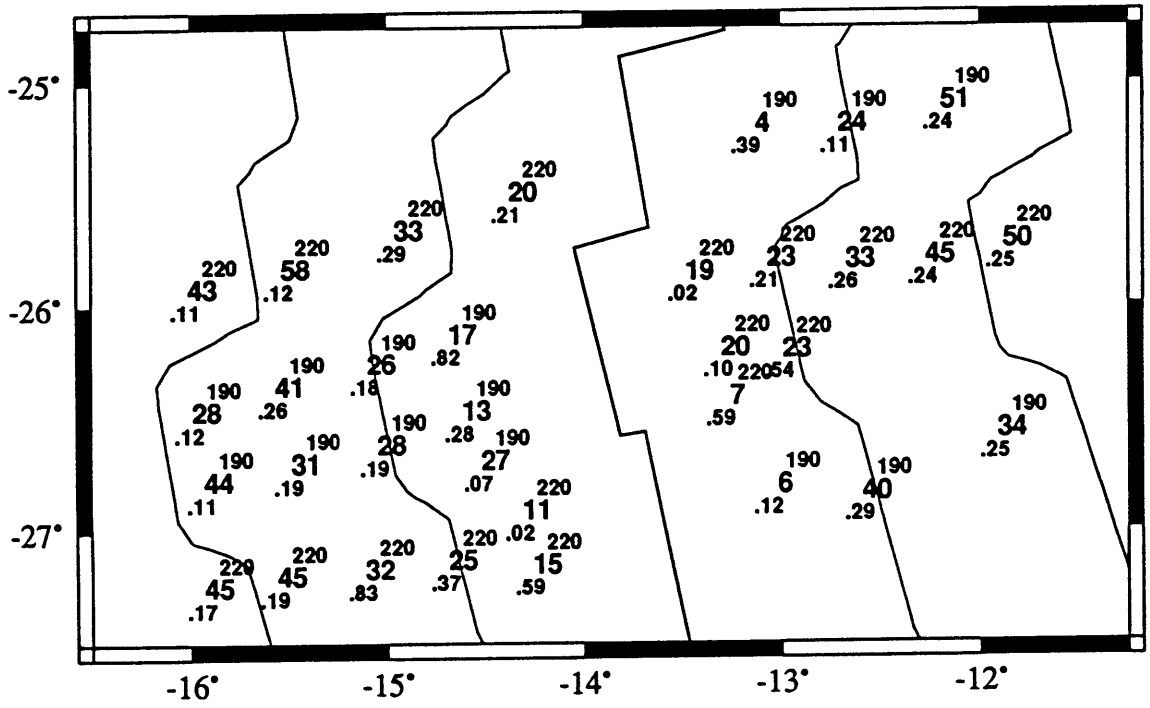

Fig. 4.17: Results of inversions for L in meters (large numbers) and apparent diffusivity κ in m^2/yr (smaller numbers below L values), with H fixed at 220 m in inside corner crust subregions and at 190 m in outside corner crust subregions (smaller numbers above L values), as given in Table 4.3. Thick line represents MAR, and thin lines represent 5-m.y. isochrons [*Müller et al.*, 1993].

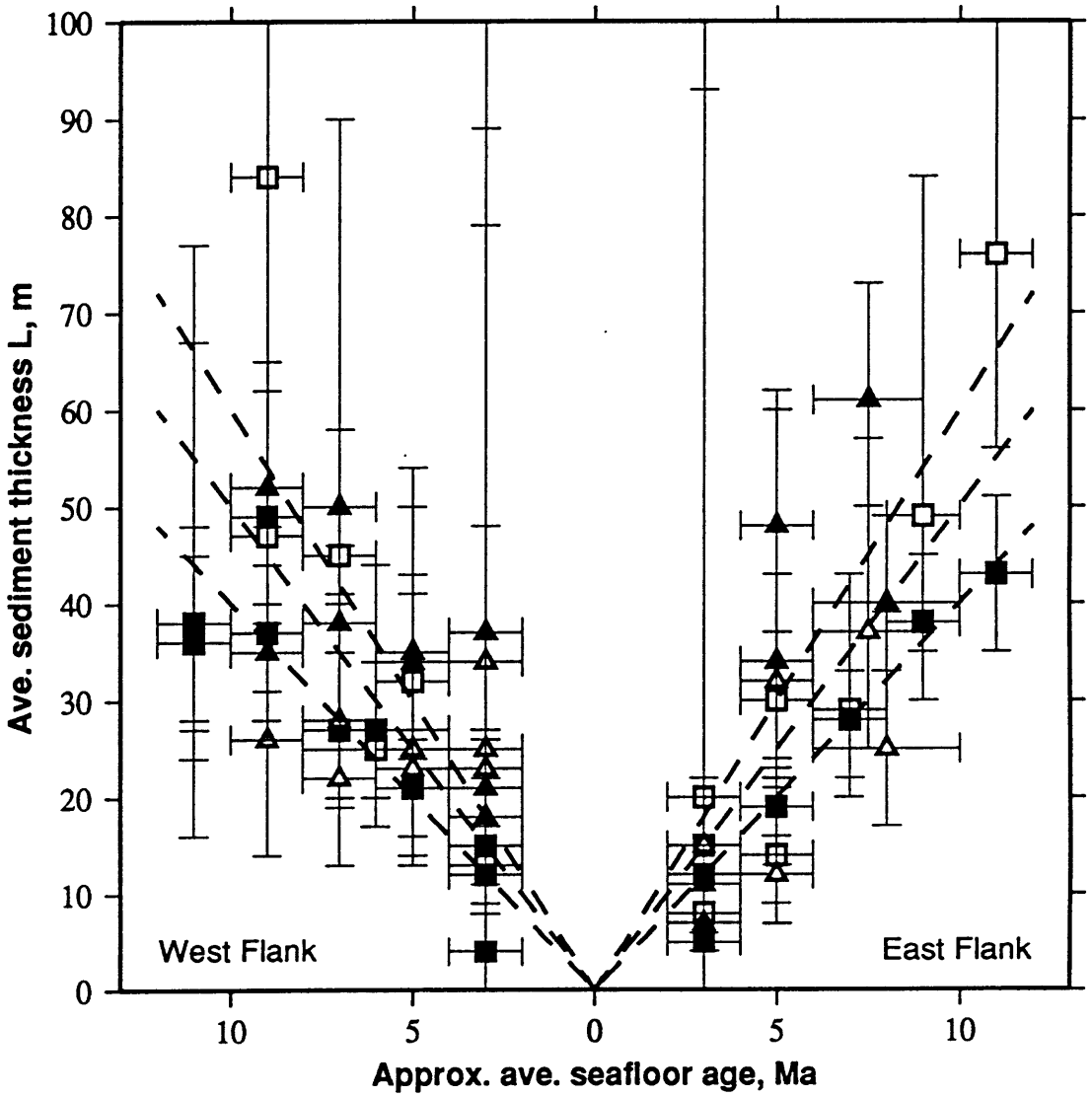

Fig. 4.18: Inverted values of L as a function of seafloor age, as given in Table 4.1 (clear symbols; H free to vary) and Table 4.2 (filled symbols; H fixed at 205 m). Triangles denote values derived from outside corner crust and squares denote values derived from inside corner crust. Horizontal error bars show the range of seafloor age in each region, while vertical error bars give the 95% confidence intervals for L. Dashed lines correspond to constant accumulation rates of 4, 5, and 6 m/m.y.

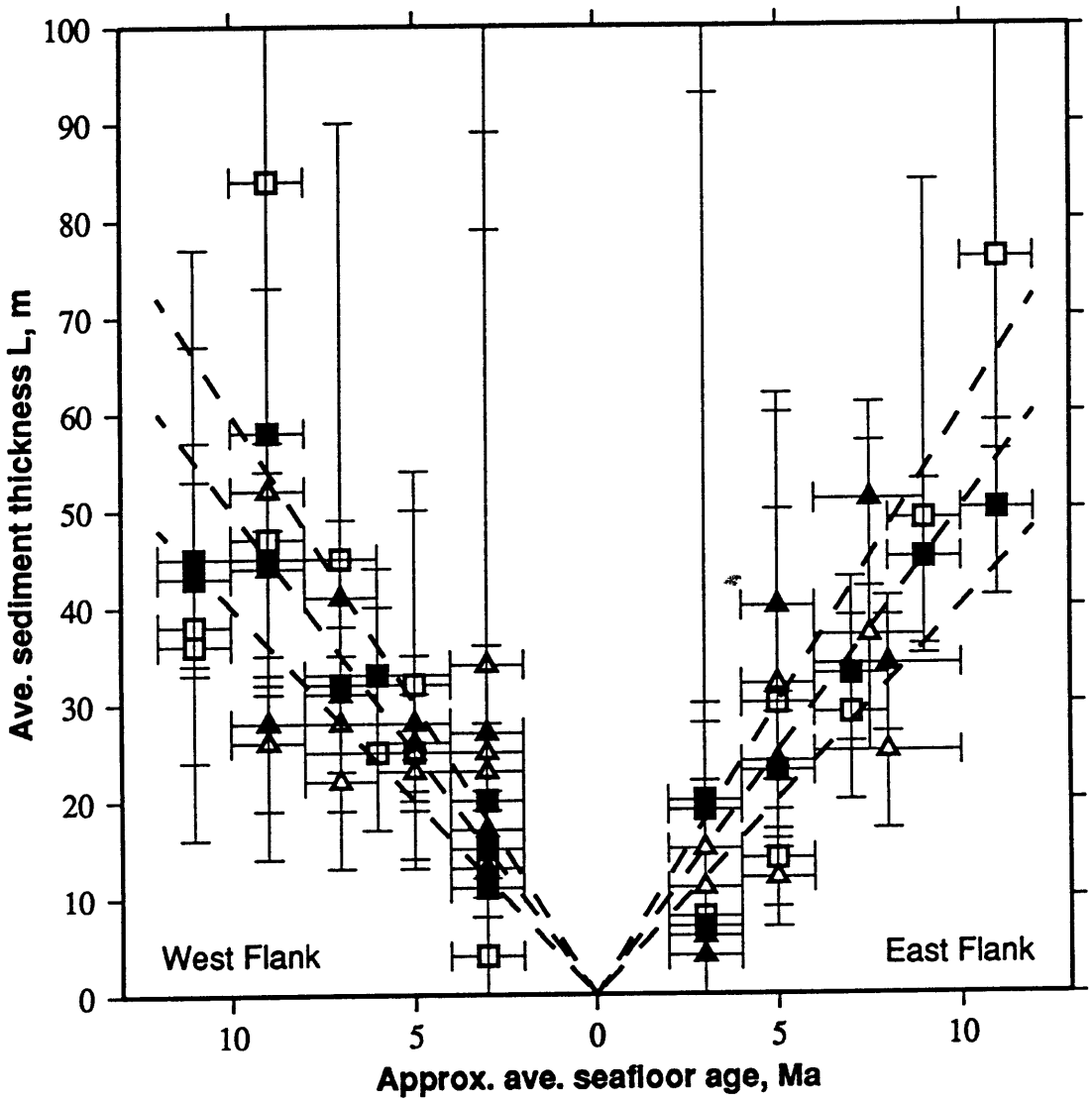

Fig. 4.19: Inverted values of L as a function of seafloor age, as given in Table 4.1 (clear symbols; H free to vary) and Table 4.3 (filled symbols; H fixed at either 190 m or 220 m). Triangles denote values derived from outside corner crust and squares denote values derived from inside corner crust. Horizontal error bars show the range of seafloor age in each region, while vertical error bars give the 95% confidence intervals for L. Dashed lines correspond to constant accumulation rates of 4, 5, and 6 m/m.y.

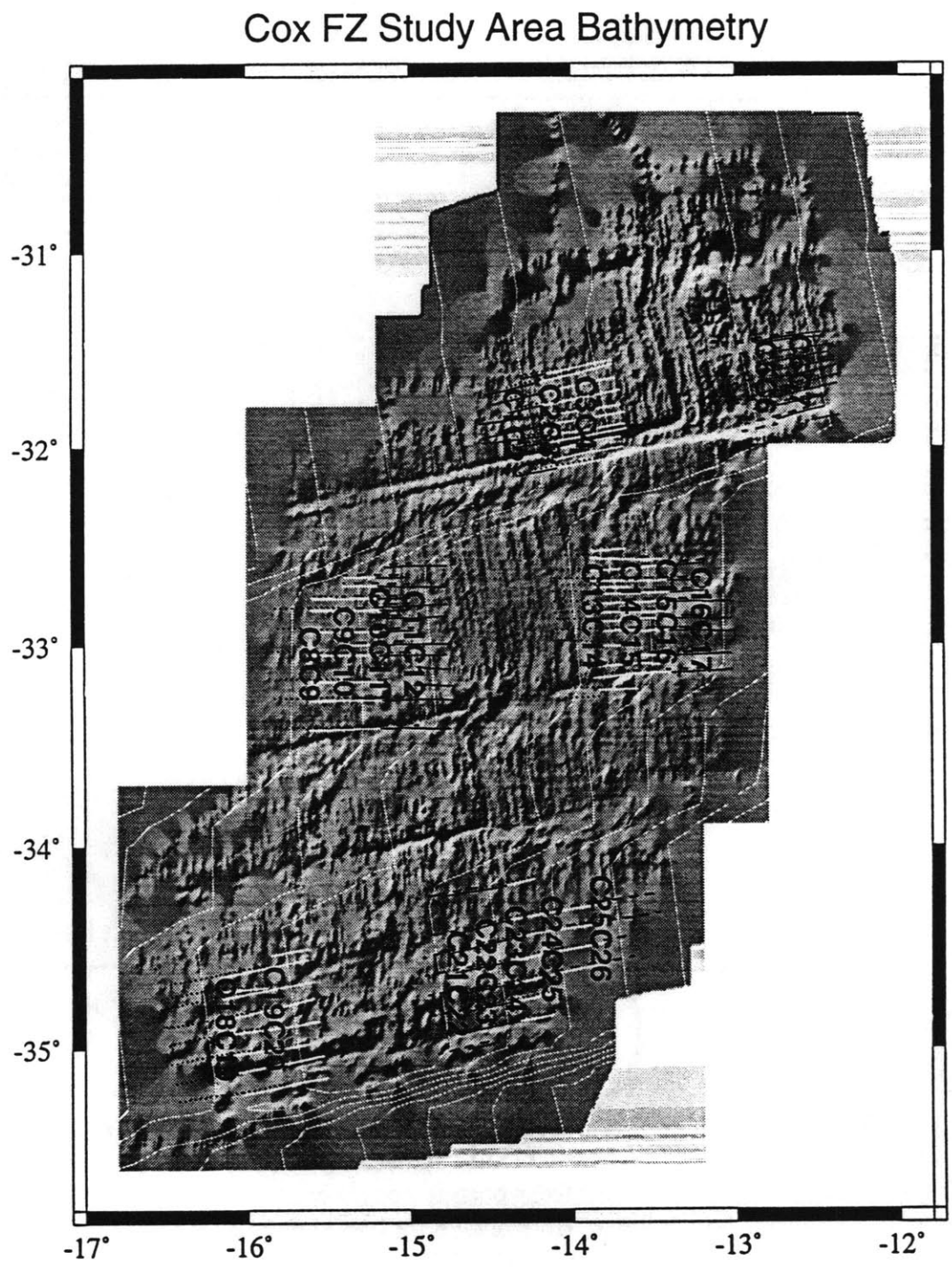

Fig. 4.20: Gray-shaded image of data in the Cox near-ridge study area, gridded at an interval of 0.5 minutes, from *R/V Washington* cruises Plume 4, Plume 5, Marathon 10, and Marathon 13, and trackline segments used to construct subregions, as labeled. Image is scaled to be comparable to Fig. 4.1. All line segments composing a region are represented by the same pattern. White lines are 2 m.y. isochrons [*Müller et al.*, 1993].

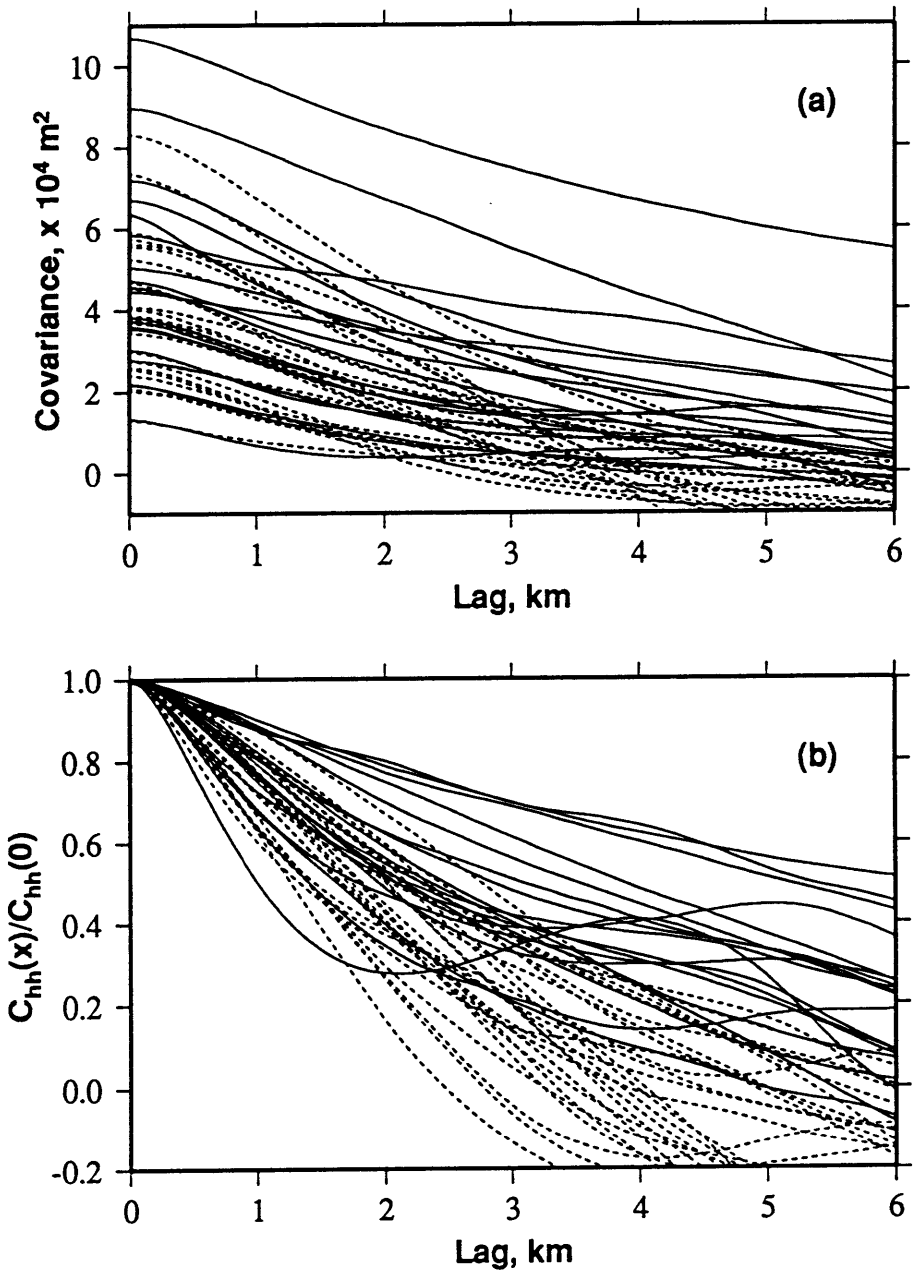

Fig. 4.21: (a) Covariance functions for the Rio Grande subregions (solid lines) and Cox subregions (dashed lines). (b) Normalized forms of the covariance functions shown in (a).

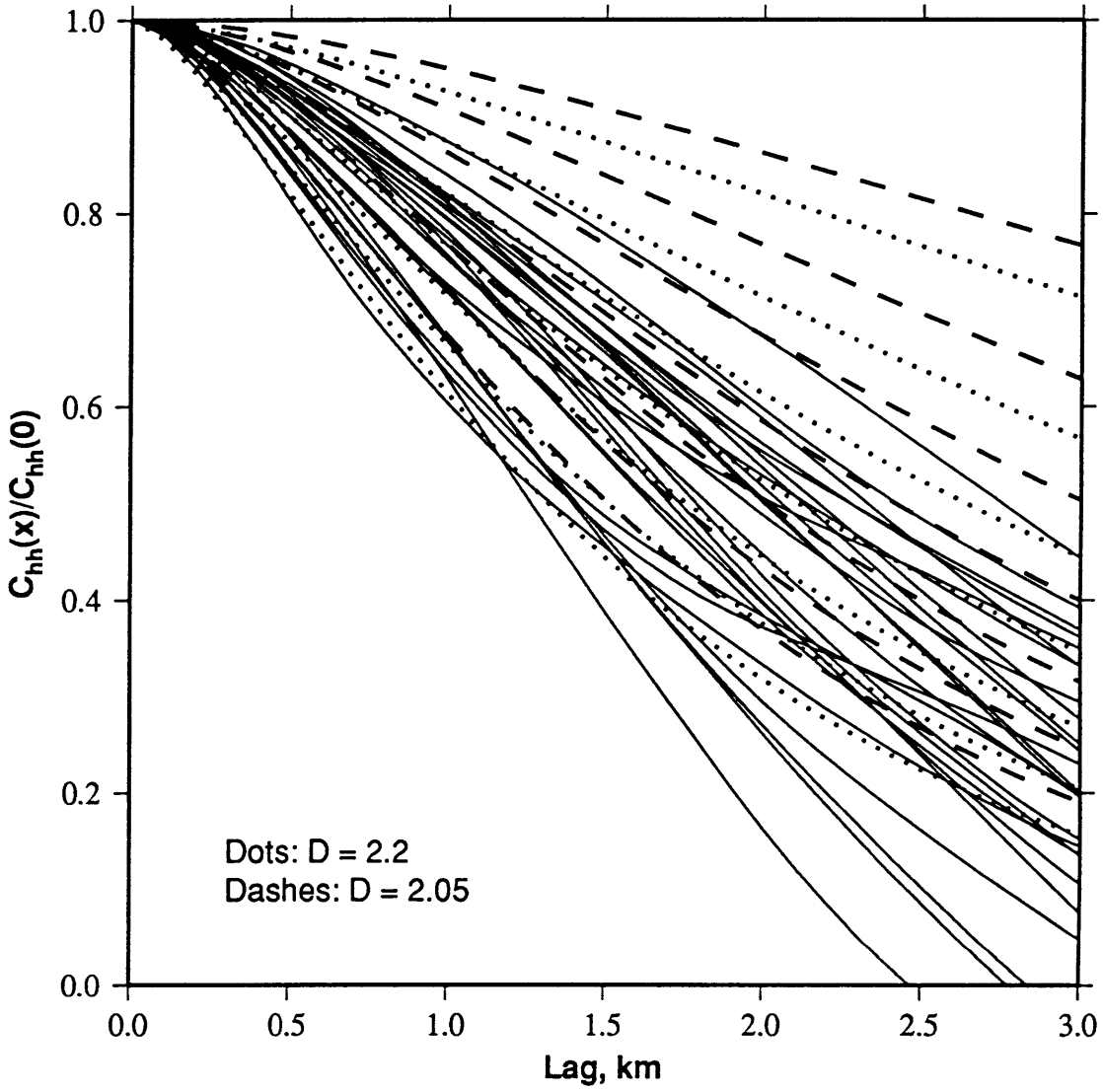

Fig. 4.22: Normalized covariance functions for the Cox subregions (solid lines) and model Goff-Jordan normalized covariance functions for k_n ranging from 0.2 (uppermost functions) to 0.8 (lowermost functions) km^{-1}, for D of 2.05 (dashed lines) and 2.2 (dotted lines).

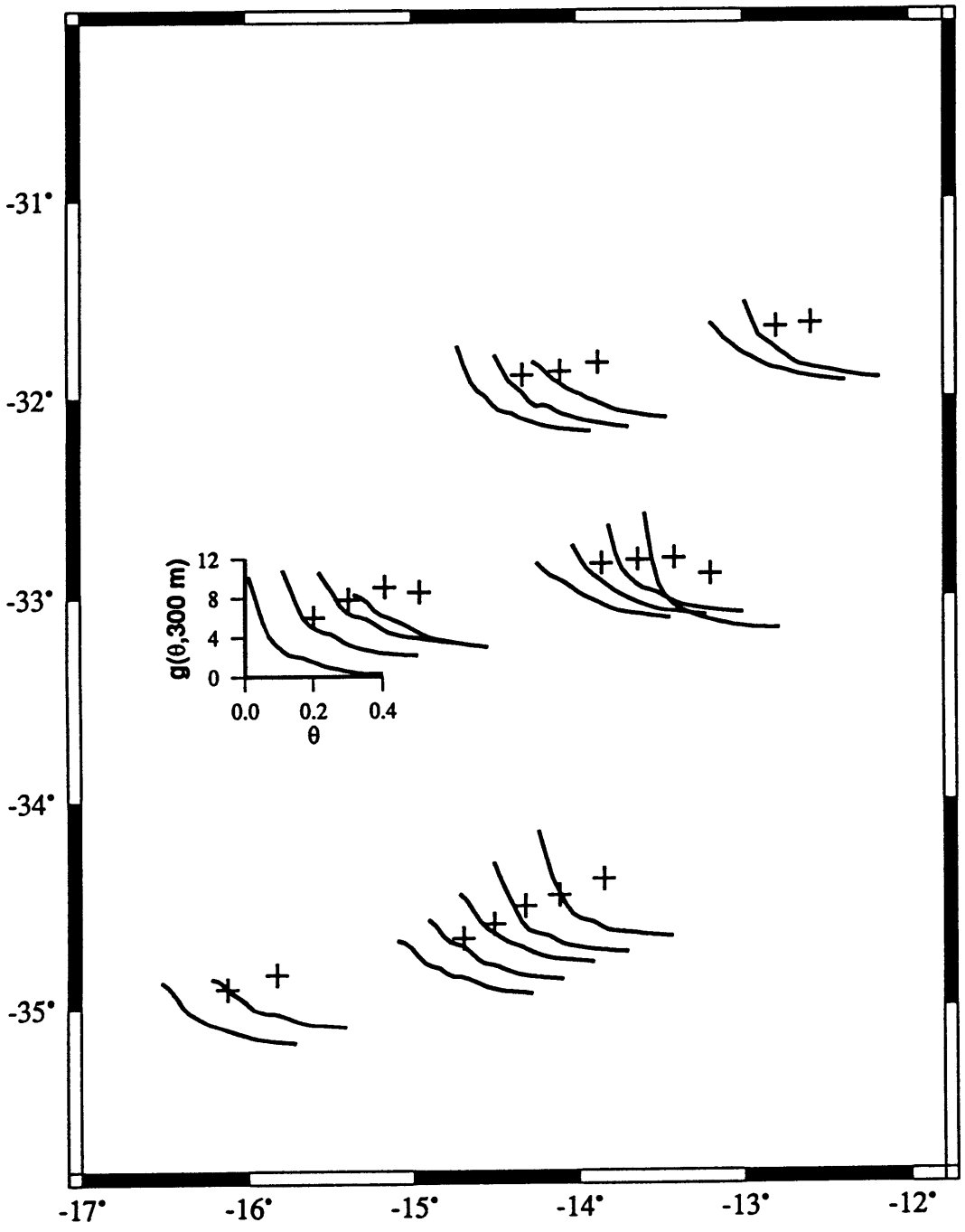

Fig. 4.23: Slope distribution functions for the Cox study area subregions as shown in Fig. 4.20.

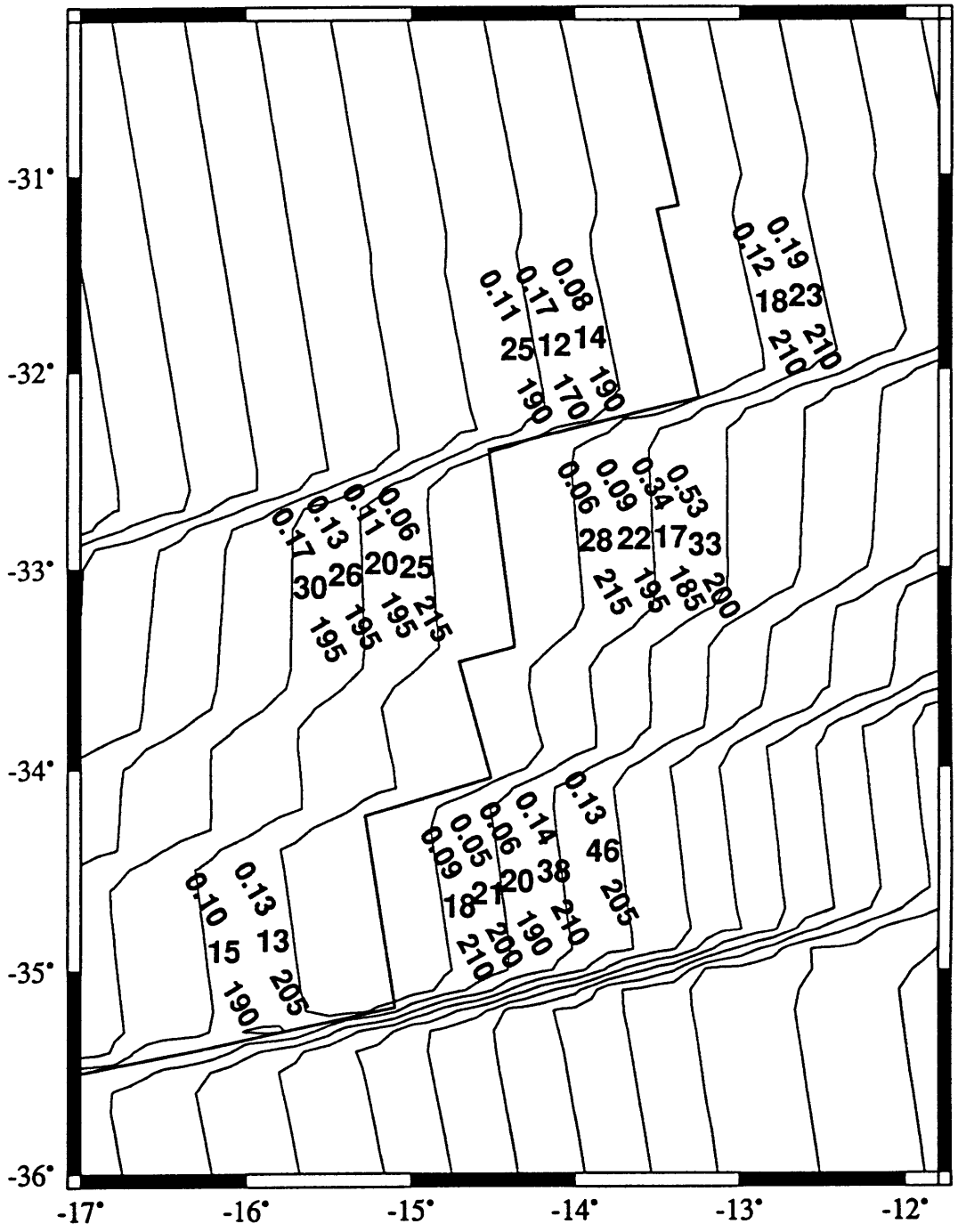

Fig 4.24: Results of inversions for L in meters (large numbers), basement RMS height H in meters (smaller numbers below L values), and apparent diffusivity κ in m^2/yr (smaller numbers above L values), as listed in Table 4.4. Thick line represents MAR, and thin lines represent 2-m.y. isochrons [*Müller et al.*, 1993].

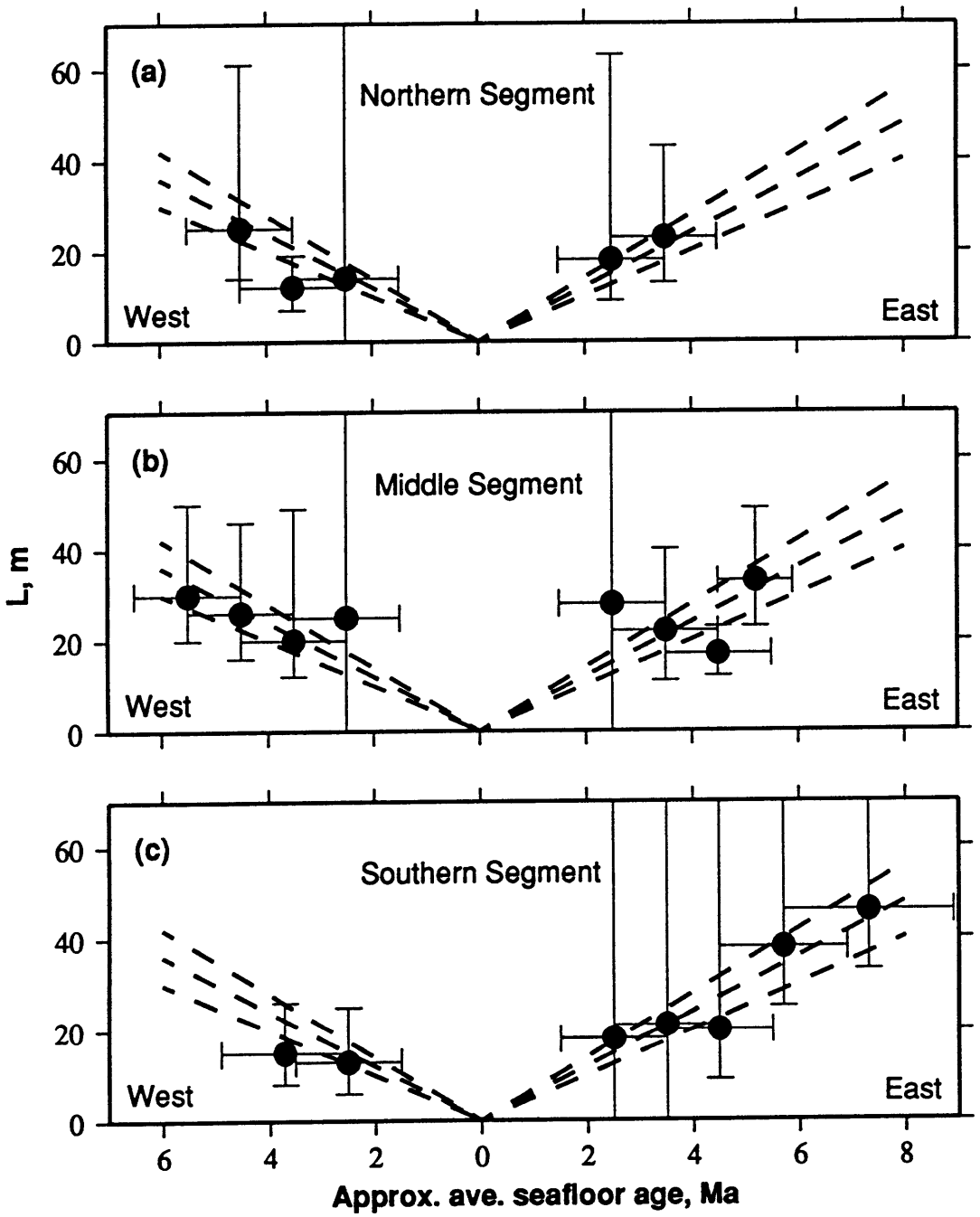

Fig. 4.25: Inverted values of L as a function of seafloor age, as given in Table 4.4, for the (a) northern, (b) middle, and (c) southern ridge segments included in the Cox study area. Horizontal error bars show the range of seafloor age in each subregion, while vertical error bars give the 95% confidence intervals for L. Dashed lines correspond to constant accumulation rates of 5, 6, and 7 m/m.y.

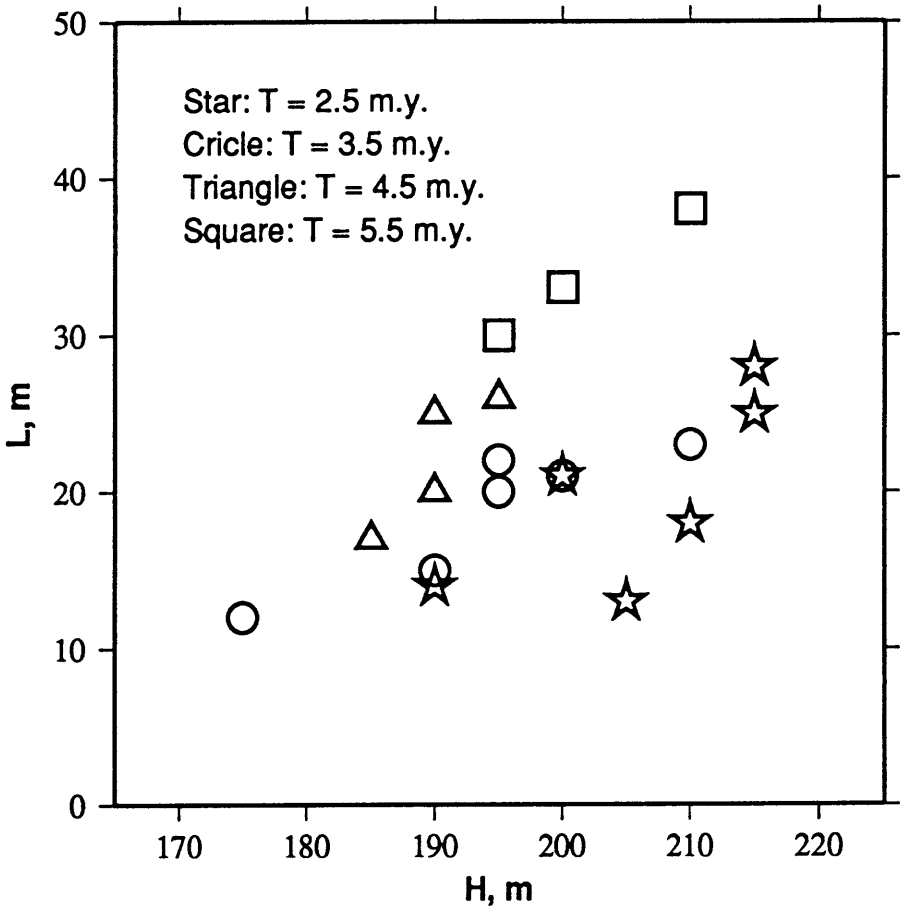

Fig. 4.26: Inverted values of H and L from the Cox study area, with subregions with T near 2.5 Ma given by stars, 3.5 Ma given by circles, 4.5 Ma given by triangles, and 5.5 Ma given by squares. A positive correlation between H and L is seen for all age ranges.

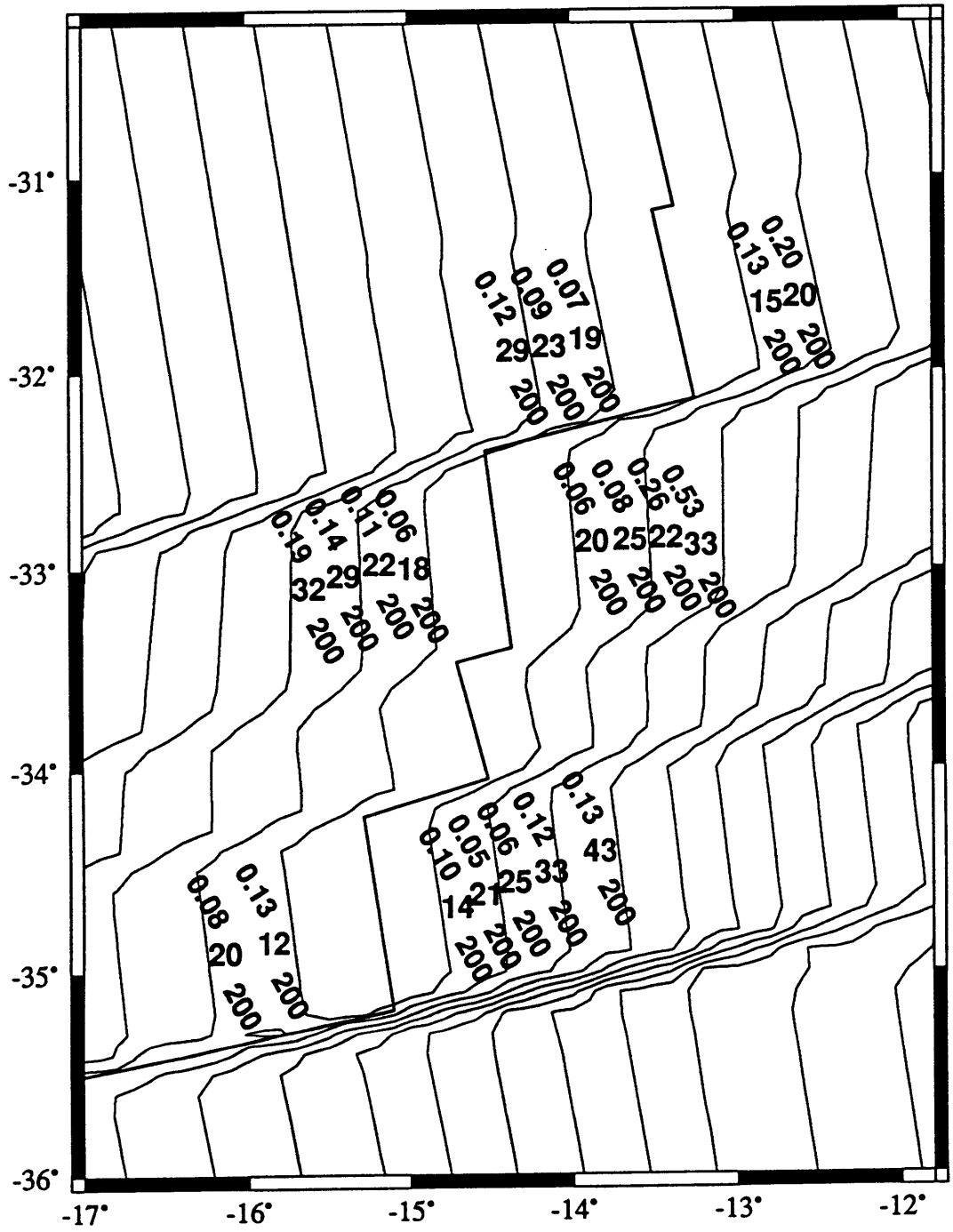

Fig 4.27: Results of inversions for L in meters (large numbers) and apparent diffusivity κ in m^2/yr (smaller numbers above L values), when basement RMS height H is fixed at 200 m (smaller numbers below L values), as listed in Table 4.5. Thick line represents MAR, and thin lines represent 2-m.y. isochrons [*Müller et al.*, 1993].

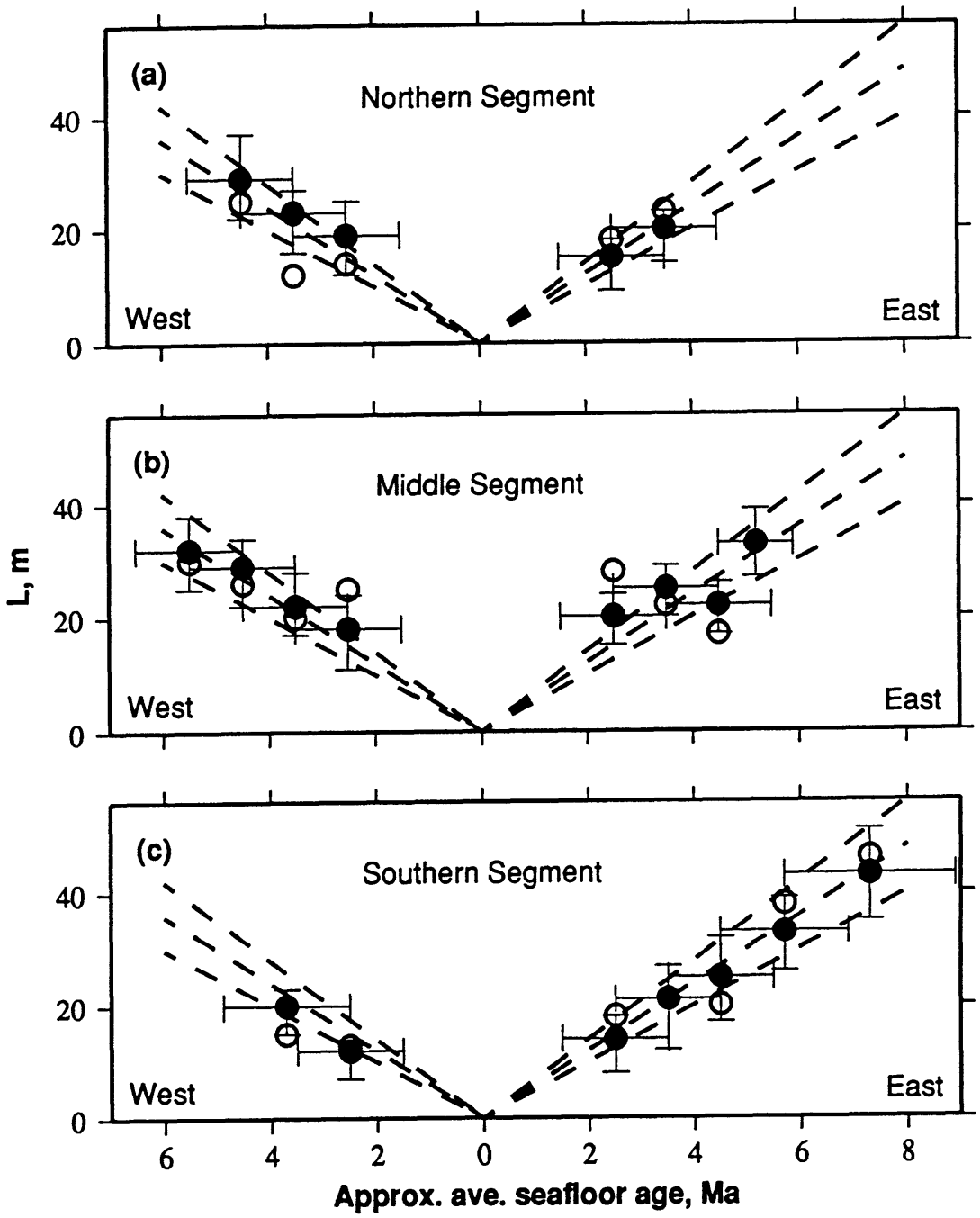

Fig. 4.28: Inverted values of L as a function of seafloor age, as given in Table 4.4 (clear symbols; H free to vary) and Table 4.5 (filled symbols; H = 200 m), for the (a) northern, (b) middle, and (c) southern ridge segments included in the Cox study area. Horizontal error bars on results obtained by fixing H show the range of seafloor age in each subregion, while vertical error bars give the 95% confidence intervals for L. Dashed lines correspond to constant accumulation rates of 5, 6, and 7 m/m.y.

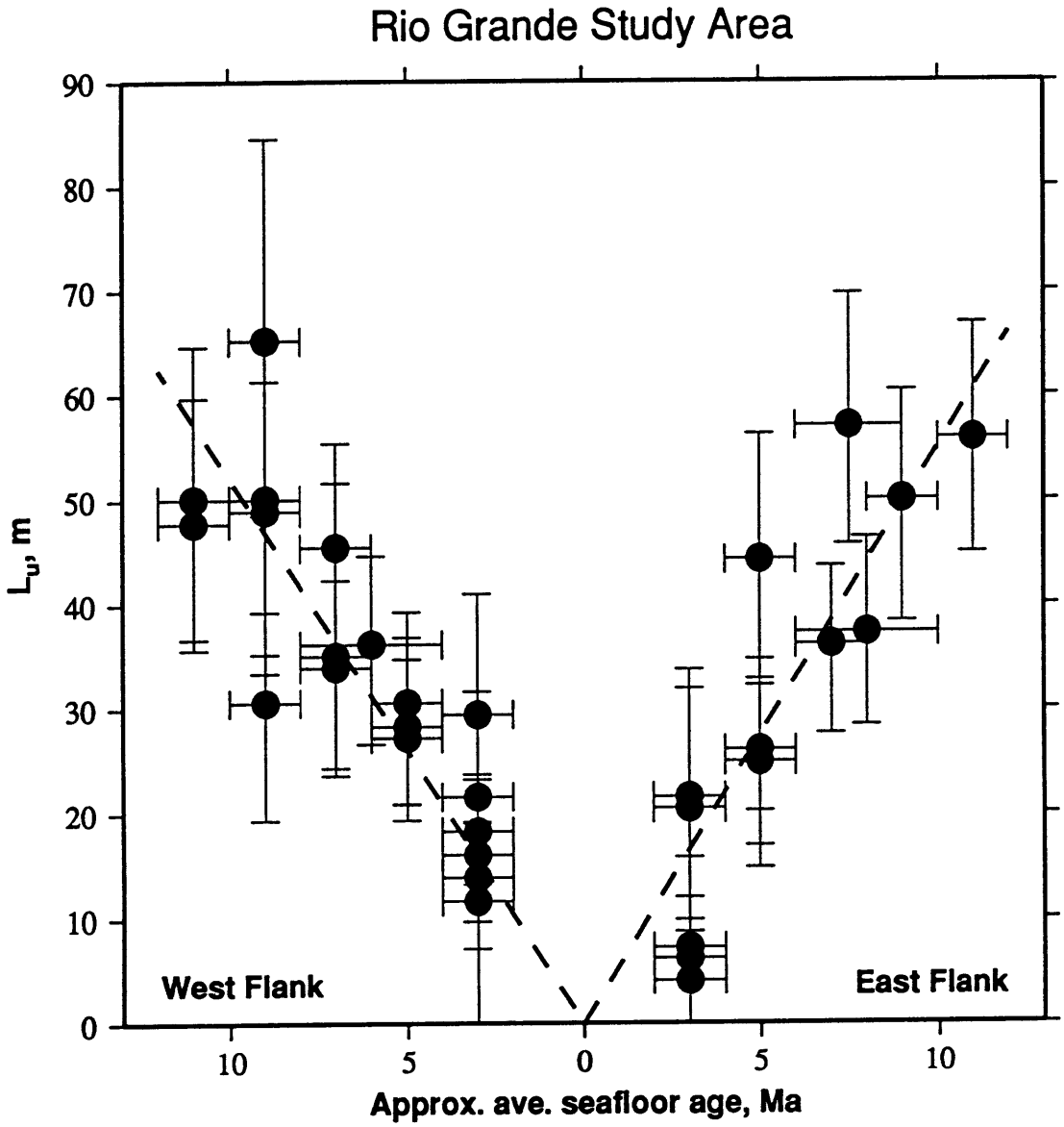

Fig. 4.29: Values of pre-compaction sediment thickness L_u computed from inverted values of L from the Rio Grande study area achieved by fixing H at values dependent on crustal type, as given in Table 4.3, and best-fitting lines (dashes) corresponding to constant accumulation rates of 5.2 m/m.y. on the western flank and 5.5 m/m.y. on the eastern flank of the MAR.

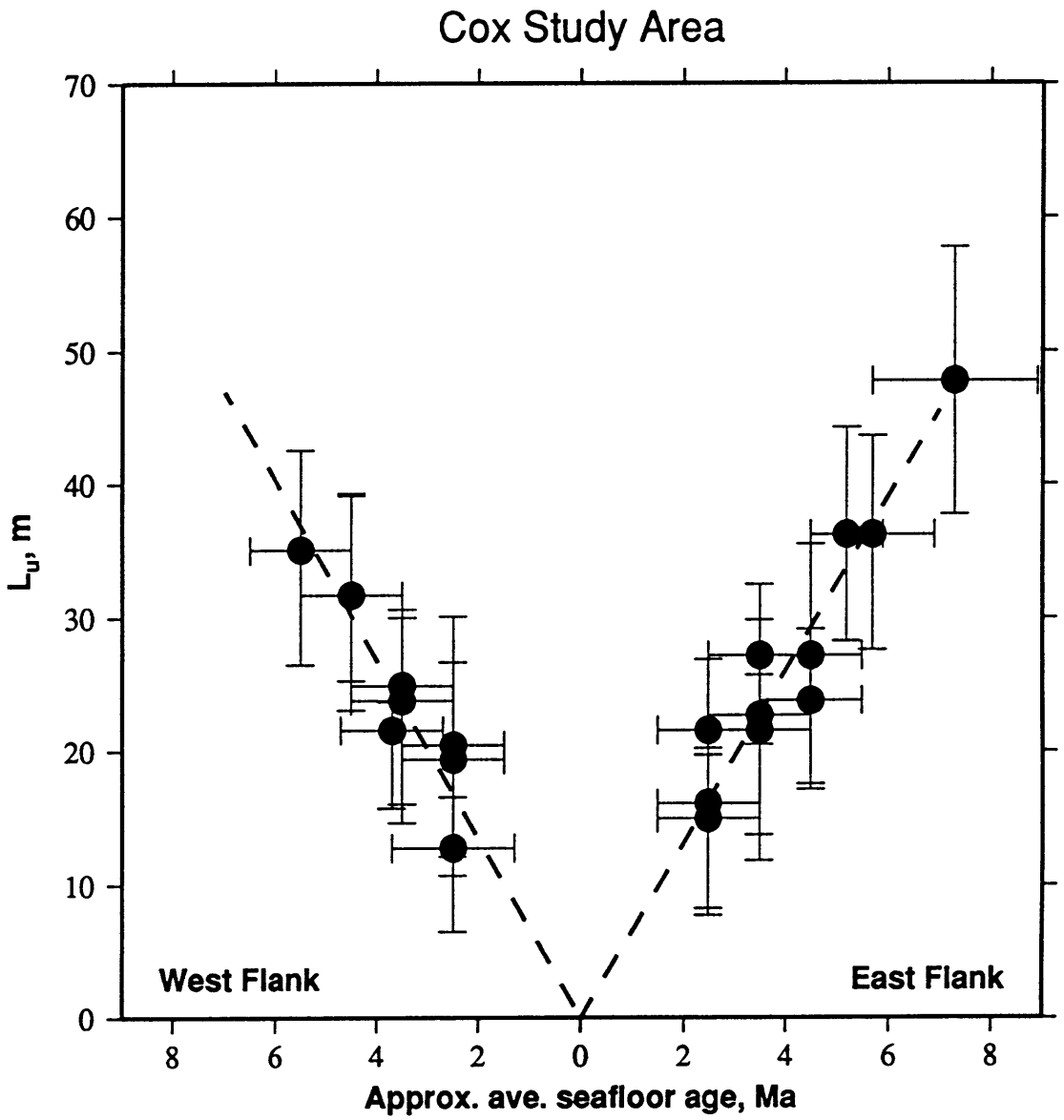

Fig. 4.30: Values of pre-compaction sediment thickness L_u computed from inverted values of L from the Cox study area achieved by fixing H at 200 m, as given in Table 4.4, and best-fitting lines (dashes) corresponding to constant accumulation rates of 6.7 m/m.y. on the western flank and 6.5 m/m.y. on the eastern flank of the MAR.

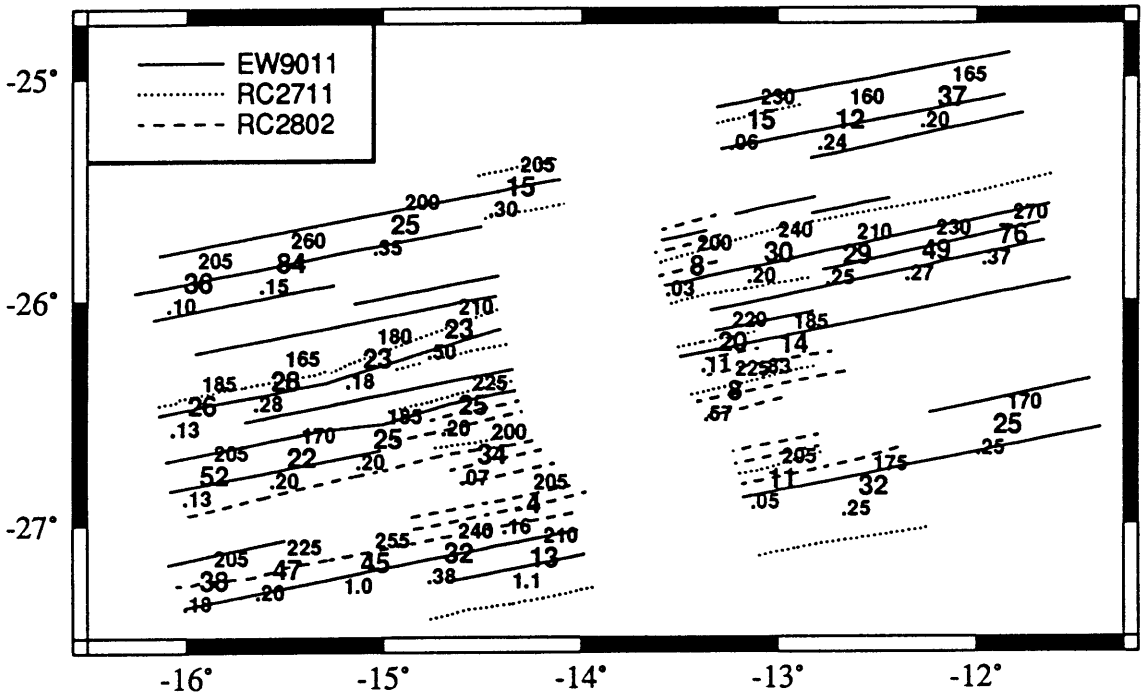

Fig. 4.31: Trackline segments used to form subregions in the Rio Grande study area, with line textures denoting data sources, as given in the figure. Inversion results, as given in Fig. 4.8, are also shown.

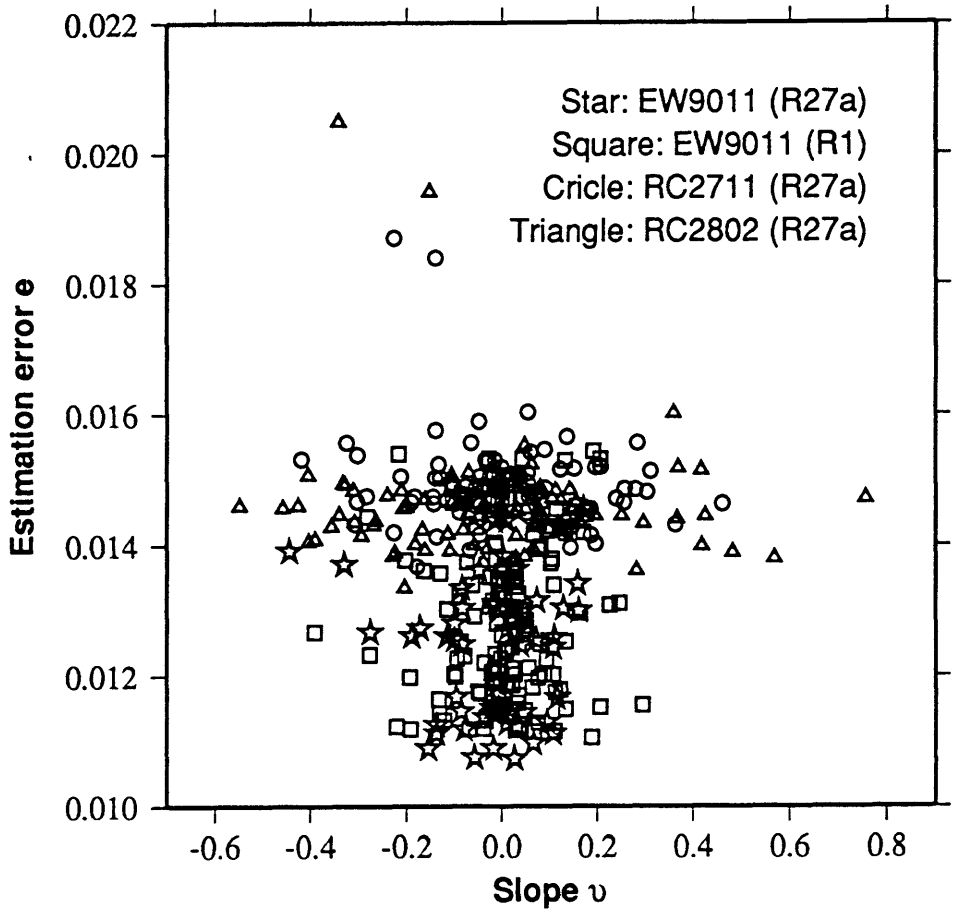

Fig. 4.32: Slope value vs. slope uncertainty for four trackline segments from Rio Grande regions R1 and R27a, as labeled in the figure. Most uncertainties for *R/V Conrad* cruises RC2711 and RC2802 are between 0.013 and 0.016, while *R/V Ewing* cruise EW9011 uncertainty values mostly fall between 0.011 and 0.015. The wide range of slopes encountered during the RC2802 segment is a function of the position of this segment over steep inside-corner topography.

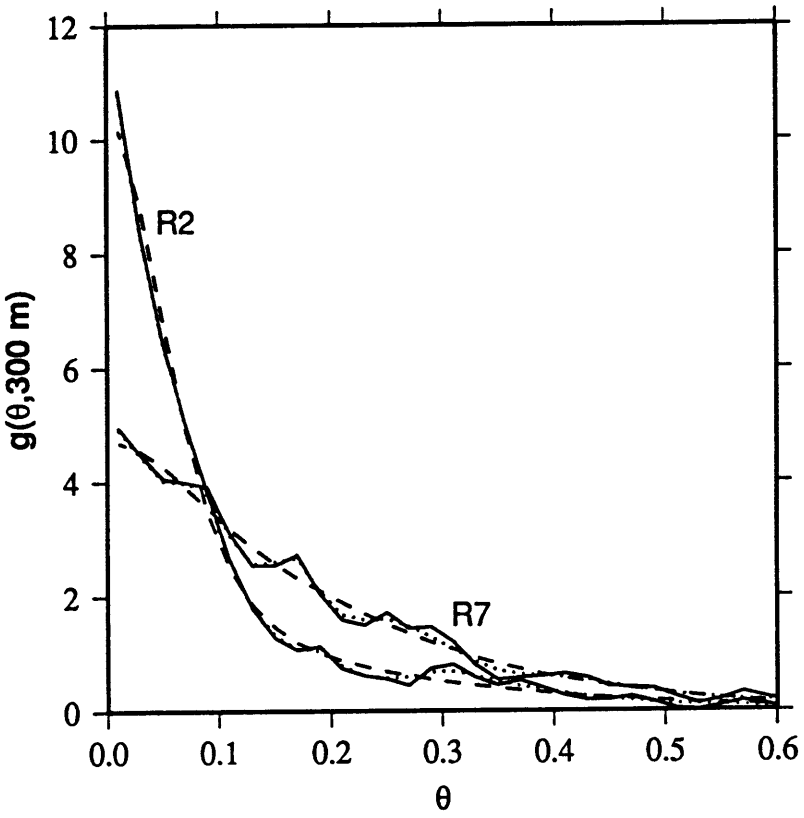

Fig. 4.33: Slope distribution functions for Rio Grande regions R2 and R7 computed without (solid lines) and with (dotted lines) high-θ smoothing via (4.4), and best-fitting model slope distribution functions computed allowing H to vary (dashed lines).

Chapter 5

Distribution of Sediment on Off-Axis Topography in the South Atlantic

INTRODUCTION

The distribution of sediment in the basins of the world ocean, combined with information about sediment composition, provides information about the rates of accumulation of sediments of various types through time. Where sediments are thick, sediment distribution information is available from seismic sources. However, where sediments are relatively thin, the seafloor is often very rough, making it difficult to image sediments. Thus, information about sediments on young seafloor, the seafloor most likely to reflect mid- to late-Cenozoic paleoceanographic changes, usually cannot be accurately estimated from wide-beam seismic data.

In Chapter 3 of this thesis, we develop a methodology for using simple models of sedimented topography to invert narrowbeam bathymetry data from sedimented abyssal hills for three parameters: RMS basement variability H, average regional sediment thickness L, and apparent diffusivity κ, a measure of how much curvature is exhibited by relatively flat stretches of topography. Using high quality, high resolution returns from the center beam of the Hydrosweep swath mapping system, which are typically available every 60-80 m along-track, we estimate these parameters for 3-29 Ma crust located on the western flank of the Mid-Atlantic Ridge (MAR) between 25.5° and 27.25° N. In Chapter 4, we apply our inversion methodology to two near-ridge study areas which span the southern MAR, using data from both Hydrosweep and Seabeam swath mapping systems.

While the North Atlantic study area extends onto upper Oligocene crust, providing a relatively long history of regional sedimentation, both of the South Atlantic study areas focused on near-ridge topography, extending onto 11 Ma crust in the more northern study area and only onto 5-8 Ma crust in the southern study area. The extent of these survey areas is typical of most near-ridge studies, which ignore "normal" off-axis seafloor.

However, in much of the world ocean, narrowbeam bathymetry data has been collected during transits to and from survey areas. In places where more detailed surveys are not available this represents a useful source of information about seafloor structure. This ever-increasing supply of data has been utilized by several authors in recent years to study variations in morphology with seafloor age [*Goff*, 1992], geographic position [e.g. *Goff*, 1991], and sediment cover (as determinable from nearby single-channel seismic (SCS) data) [*Bird and Pockalny*, 1994].

In this Chapter, we modify our inversion methodology to determine sediment thickness information from transit data as it is commonly archived. Transit lines used in this chapter run to and from the near-ridge South Atlantic study areas of Chapter 4, which both by fortune and by plan tended to follow flow lines as discernible from gravity anomaly data [*Sandwell and Smith*, 1995] (Fig. 5.1). Data used was obtained from National Geophysical Data Center (NGDC), the archives of the Lamont-Doherty Earth Observatory (LDEO), and through the RIDGE Multibeam Synthesis project.

Since each area is sampled by either single or sparsely spaced transit lines, not from surveys which cover much of the seafloor within a small region, our inversion results provide information about the amount of sediment along a particular ship track or set of ship tracks, and not necessarily about the average amount of sediment within a region. However, the values are L we obtain are probably more characteristic of a region than the thickness of sediments as obtained from drill cores, which only sample discrete points.

Although the primary goal of this chapter is to obtain information about how sediment thickness varies off-axis in the South Atlantic in regimes where SCS data is of limited utility, we also explore the limits of data quality useful for the inversion of sedimentation information. And, since some tracklines extend off-axis into regions where sediments are fairly thick, we explore the maximum amount of sediment resolvable by our methodology.

GEOLOGICAL SETTING

The flanks of the southern MAR between 20° and 40° S are primarily composed of elongated abyssal hills offset by small, irregularly spaced transform faults. Traces of non-transform discordant zones can also be seen extending off-axis. Near 35° S, 5° W,

topography off-axis is interrupted by the Walvis Ridge, a series of volcanic ridges produced by the Tristan de Cunha plume (see Fig. 5.1). Along with the MAR, the Walvis Ridge and its less dramatic western Atlantic complement, the Rio Grande Rise, divide the South Atlantic into the Argentine, Brazil, Angola, and South African basins.

Sedimentation patterns

In the moderate latitudes of the South Atlantic, calcareous oozes are currently accumulating on shallower topography, while red clays fill the deeper regions of the off-axis basins. Bottom waters are more corrosive to carbonate sediments to the west of the MAR than to the east, due to the easy passage of corrosive Antarctic bottom water (AABW) into the Argentine and Brazil basins [e.g. *Takahashi*, 1975]. As a result, the CCD is currently located at ~4000 m in the Argentine Basin, ~4500 m in the Brazil Basin, and ~5000 in the Angola Basin, based on the criteria of *Berger and Winterer* [1974].

Across-ridge differences are seen in drill cores from DSDP legs 3 and 73 (Fig. 5.1). At DSDP Site 14, located in 4340 m of water on the western flank of the MAR, no carbonates younger than lower Miocene in age were recovered, indicating that bottom waters have been corrosive to calcite since the middle Miocene. However, at DSDP Site 522, located across-ridge in 4450 m of water, and at DSDP Site 17, located on slightly younger seafloor at a depth of 4260 m, thick Pliocene and Pleistocene sequences were cored. Drill cores from both flanks of the MAR, however, show evidence that little carbonate deposited below 3500-4000 m during the Miocene has survived.

In SCS data [e.g. *Neprochnov*, 1977] it can be seen that, despite the corrosivity of bottom waters to calcite, sediments are fairly thick (greater than 100-200 m, on average) on seafloor older than 20 Ma in the Argentine Basin (see Fig. 6.28), while Eocene-Oligocene seafloor in the Brazil Basin bears much less sediment [e.g. *Gamboa and Rabinowitz*, 1981]. This difference may be attributed to greater biological productivity in surface waters [*Berger*, 1991] and/or to increased terrigenous sediment input via the nepheloid layer [*Biscaye and Eittreim*, 1977], which has led to very thick clay accumulations off the southern shelf of South America [e.g. *Divins and Rabinowitz*, 1990; *McCoy*, 1991].

Character of seafloor topography

In the moderate latitudes of the South Atlantic, ridge segmentation has been constant since ~55 Ma [*Cande et al.*, 1988; and observable in the gravity anomaly data compilation of *Sandwell and Smith*, 1995], although the relative lengths of transform offsets has varied over time. Since 45 m.y.B.P., spreading rate has gradually decreased in adjustment to global changes in tectonic plate geometries [*Cande et al.*, 1988]. Inversions of lines from *R/V Conrad* cruises RC2711 and RC2802 for *Goff-Jordan* [1988] parameters [*Goff*, 1992] show that seafloor RMS variability $\hat{H}$ decreases with crustal age, from ~200 m near-ridge to ~150 m on 45 Ma seafloor. Hill spacing $\hat{\lambda}_n$ shows an increase from ~6 km near ridge to ~11 km on 45 Ma seafloor. This correlation between spreading rate and hill height and spacing is in keeping with regional and global compilations of observations [*Krause and Menard*, 1965; *Malinverno*, 1991; *Goff*, 1991]. However, in the South Atlantic, the observed correlations may also reflect the influence of sediment on hill height and spacing, as we observe in the numerical experiments of Chapter 2 (see Fig. 2.18).

Data from 3.5 kHz systems as well as from Hydrosweep and Seabeam seem to suggest that hill heights off-axis are lower south of 30° S than to the north, both west and east of the MAR (Fig. 5.2). Seafloor older than 20 Ma in particular is much less rough than seafloor to the north.

DATA

To be useful, sparsely-spaced tracklines of narrowbeam data must be oriented close to perpendicular to hill strike direction, and be relatively continuous. The Angola Basin has been appropriately sampled by just one such cruise, *R/V Robert D. Conrad* cruise RC2711. The Brazil Basin was also sampled during cruise RC2711, as well as by to- and from-ridge transits during *Conrad* cruise RC2802. To the south, the Argentine Basin has been appropriately sampled by one transit each during *R/V Thomas Washington* cruises Plume 4, Plume 5, and Marathon 10 (see Fig. 5.1).

Data available from these transit lines ranges greatly in quality. For the transit line through the Angola Basin, the entire swath as collected by Seabeam was available, although only the centerbeam value is used in the inversion process. Data from this cruise

has a spacing of ~240 m, just under the resolution limit we find usable in Chapter 3. For the other regions, only one-minute averages of centerbeam returns are used. These data sets contain bathymetry information at spacings of 250 m to 400 m or greater.

Centerbeam data from cruises RC2711, RC2802, and Marathon 10 were available from both LDEO and NGDC, while Plume 4 and Plume 5 data sets were available solely from NGDC. The data from these sources show slight differences, with listed seafloor coordinates offset by roughly 10 m and with differences in depth of 1-3 m. Along-track point-to-point differences in height tend to be less than a meter, however, and are in part a consequence of differences in the resolution at which the data sets are stored, with the NGDC data precise to the nearest tenth of a meter and LDEO data provided only to the nearest meter. Due to ease of use, we use data from LDEO where possible.

INVERSION PROCEDURE

The inversion of data for basement and sedimentological information follows the form of Chapter 3, with several important differences, detailed below.

Construction of model topographies

Sedimented models are constructed upon the basement used in Chapter 4 to model near-ridge seafloor in the South Atlantic. This basement is a 51.1×51.1 km^2 Goff-Jordan model [*Goff and Jordan*, 1988], discretized with a data point spacing d of 50 m, constructed using model Goff-Jordan parameters $H = 160$ m, $k_n = 0.6$ km^{-1}, $k_s = 0.2$ km^{-1} (so that $a = 3$), $D = 2.2$, and $\zeta_s = 0°$. We sediment this basement at a constant rate F of 4 m/m.y. for 50 m.y. of model time, using diffusivities κ of 0.014, 0.024, 0.04, 0.08, 0.14, 0.24, 0.4, 0.8, and 1.4 m^2/yr. Surfaces are recorded at model times of 0.625, 1.25, 2.5, 3.75, 5, 7.5, 10, 15, 20, 25, 30, 37.5, and 50 m.y., corresponding to average sediment thicknesses L of 2.5, 5, 10, 15, 20, 30, 40, 60, 80, 100, 120, 150, and 200 m. By (2.21) and (2.23), these sedimented surfaces can be used to produce models for any H and k_n (given $a = 3$, $D = 2.2$, and $\zeta_s = 0°$) for non-dimensional $K \in \{0.2, 0.34, 0.57, 1.14, 2.0, 3.4, 5.7, 11.4, 20.0\}$ and $\Lambda \in \{0.0156, 0.0312, 0.0625, 0.0935, 0.125, 0.188, 0.25, 0.375, 0.5, 0.625, 0.75, 0.9375, 1.25\}$, where Λ is non-dimensional

sediment thickness given by (2.21). Keeping k_n fixed at 0.6 km^{-1}, we let H = 160/m_i m, for $m_i \in \{0.4,0.45,0.5..1.95\}$. This produces models for H from 82.05 to 450 m.

Computation of slope distribution functions

We compute slope distribution functions from models, denoted $g_m(\theta,u,\kappa,H,L)$, and from data, $g_d(\theta,u)$, as in Chapter 3 and Chapter 4, with high-θ smoothing applied via (4.4) to functions calculated from both data and model topographies. Binning width w is set at 0.02, system noise is assumed to be random and normally distributed with a variance E^2 of 10 m^2 as in Chapter 4, and we again use a beam half-width $\delta\phi_{1/2}$ of 0.02 rad when simulating multibeam sampling via (3.1)-(3.3).

The sparse along-track spacing of the data, when compared to the data evaluated in Chapter 3 and Chapter 4, leads to large spacings ξ between data points and places where slope is measured. This produces large slope uncertainties e, via (3.8), when a ruler length u of 300 m is used. Therefore, we use a higher u of 500 m.

Since the data point spacing seen in individual segments of trackline range from roughly 250 m to 400 m, the range of computed e varies between data sets, and shows correlation with the average data point spacing of the sets, as displayed in Fig. 5.3 for 18-20 Ma seafloor from all seven tracklines used. Since e is often greater than w, this could affect slope distribution functions at low θ enough to influence inverted values of L and κ. Therefore, prior to the construction of slope histograms, we linearly sample all along-track data at a spacing of 350 m, then hand-delete all points located within data gaps greater than 0.5-0.6 km. This degrades all the data, preventing data-quality differences from being reflected in slope distribution functions. A side-effect of this procedure is a reduction of the highest slope values, as shown in Fig. 5.4, complicating the inversion for H.

When computing slope distribution functions from model topographies, we sample models every 350 m, letting ξ_1 = -400 m, ξ_2 = -50 m, ξ_3 = 300 m, ξ_4 = -200 m, ξ_5 = 150, and ξ_6 = 500 m. Model slope distribution functions generated using these ξ_j and a u of 500 m span a lower range of θ than those using the ξ_j of Chapter 3 and Chapter 4 and a u of 300 m, as shown in Fig. 5.5 for slope distribution functions from models sedimented at a rate of 4 m/m.y. using κ of 0.04 and 0.14 m^2/yr for model times of 2.5, 5, 10, and 20

m.y. (L = 10, 20, 40, and 80 m). Amplitude at high θ decreases as u increases, as described by equation (2.32). In contrast, increasing u increases the range of slopes encountered in the flatter regions of model topographies.

Data inversion process

For each slope distribution from data $g_d(\theta,u)$, initial estimates of H, L, and κ are made; then, minimum and maximum κ values κ_{min} and κ_{max} are selected. For κ between κ_{min} and κ_{max} measured at an interval of $2.5\kappa_{min}$, H between 85 and 400 m measured at an interval of 5 m, and L between 3 and 200 m measured at an interval of 1 m, $Lik(\kappa,H,L)$ is calculated via (3.15) for all models for which $K \in [0.2,20]$ and $\Lambda \in [0.0156,1.25]$. Where K is less than 0.2 or Λ is less than 0.0156 or greater than 1.25, we set $Lik(\kappa,H,L)$ to 0. Where K is greater than 20 and Λ is between 0.0156 and 1.25, we set $Lik(\kappa,H,L)$ to the value associated with the maximum possible κ given H and L, as in Chapter 3.

As in Chapter 3 and Chapter 4, it is necessary to interpolate between defined slope distribution functions to compute (3.15) for many κ, H, and L. This is again achieved using the methodology described in Appendix B. Inversion errors are also calculated following the methodology given in Chapter 3.

The use of a u of 500 m adversely affects our ability to resolve precise values of H, L, and κ. This may be seen in scaled likelihood functions for H, L, and κ obtained by inverting $g_m(\theta,u,\kappa,H,L)$ corresponding to model surfaces generated at a rate of 4 m/m.y. for 10 m.y. of model time (L = 40 m) using κ of 0.04 m^2/yr (Fig. 5.6) and 0.14 m^2/yr (Fig. 5.7), assuming a total data point quantity N of 800. For both values of κ displayed, the likelihood functions generated using u = 500 are wider than those generated using a u of 300 m, and thus 95% uncertainty bounds are larger. We find that bounds on κ are particularly sensitive to u.

ANGOLA BASIN

The Angola Basin was sampled off-axis by cruise RC2711, labeled in Fig. 5.1 as RC2711-1. This trackline extends from near the MAR through Rio Grande regions R18, R19, and R20, eastward, covering seafloor from 6 to 40 m.y. in age (Fig. 5.8). Near-

ridge, this trackline is very rough, with inverted $\hat{H}$ of ~250-300 m [*Goff*, 1992] on seafloor younger than 17-18 Ma. Past this point, the topography along-track, though still hilly, becomes less variable. The transition from high-$\hat{H}$ to lower-$\hat{H}$ character occurs as the trackline veers slightly to the south of the crest of an inside corner high, observable in the gravity data in Fig. 5.8.

To analyze this data set, the trackline is divided into segments covering 2 m.y. of crustal generation, as determined from *Müller et al.* [1993] (see Fig. 5.8). West to east, these sections are labeled Z1 (6-8 Ma seafloor) to Z17 (38-40 Ma seafloor). Each subregion of the trackline is processed as described above so that the data point spacing is exactly 350 m except where gaps in the original data occur. Data from 3 or 4 adjacent segments is combined, and slope distribution functions are calculated. These functions, given in Fig. 5.9, show increasing amplitude at low θ with seafloor age, and gradual decrease in amplitude at high θ with seafloor age, with the oldest seafloor having virtually no high-θ signal.

Results

The results of the inversion procedure are given in Table 5.1, and model slope distribution functions corresponding to these values are displayed in Fig. 5.9. The inversion results show considerable scatter in L and H, while κ decreases dramatically with seafloor age. We also list $\tilde{H}$, the RMS variability of the topography within each subregion after the subtraction of the best-fitting linear trend. The 95% confidence bounds for most of the inverted variables cover most of model space, where they may be determined at all, and so are not listed.

Table 5.1. Inversion results, Angola Basin trackline

Site	Center Location	N	T, m.y.	H, m	κ, m^2/yr	L, m	$\tilde{H}$, m
Z1Z2Z3Z4	25.52°S, 12.04°W	332	10	210	0.31	12	254
Z3Z4Z5Z6	25.35°S, 11.17°W	357	14	215	0.56	31	245
Z5Z6Z7Z8	25.13°S, 10.30°W	361	18	200	0.19	49	235
Z7Z8Z9Z10	24.94°S, 9.43°W	361	22	145	0.048	24	129
Z9Z10Z11Z12	24.76°S, 8.56°W	358	26	195	0.020	52	160
Z11Z12Z13Z14	24.63°S, 7.68°W	360	30	235	0.030	86	193
Z13Z14Z15Z16	24.49°S, 6.78°W	386	34	165	0.038	45	167
Z15Z16Z17	24.40°S, 6.04°W	302	37	100	0.017	13	123

The inverted value of L for subregion Z1Z2Z3Z4, 12 m, is much lower than the values inverted in Chapter 4 for the Rio Grande subregions which contain the trackline. This probably occurs because the trackline travels through the highest part of the subregions, and is devoid of the level regions seen along the other tracklines, as shown in Fig. 5.10 for segment Z3, which is part of near-ridge subregion R20. The gradual increase in L with seafloor age between Z1Z2Z3Z4 and Z5Z6Z7Z8 probably reflects the transition of the shiptrack from the highstanding topography into lower regions (see Fig. 5.8), or the gradual accumulation of less mobile sediments or talus in valleys.

Since sedimentation reduces the RMS variability of topography, $\tilde{H}$ should ideally be some fraction of L less than H (see Chapter 2). For the three nearest-ridge subregions, however, H is considerably lower than $\tilde{H}$, suggesting that inverted values of H, and thus L, may be too low for the three nearest-ridge subregions. Further off-axis, H and L are correlated, suggesting that the inverted values for these regions are also suspect. In Chapter 4, we had success in inverting for L where some constraints on H could be applied. Using this technique, we investigate the possibility that H near-axis is actually somewhat higher than the inverted values given above, and whether off-axis regions are better modeled using parameters obtained when H is fixed at predetermined values related to spreading rate and crustal type.

Adjustments to results: younger seafloor

In Chapter 4 of this thesis we find that, for inside corner crust in the Rio Grande study area, a fixed H of 220 m produces inverted L values which show much less variability with age than values obtained when H is free to vary, leading us to advance 220 m as the typical RMS variability of inside corner crust locally. This value, however, is influenced by gentler topography located towards the middles of spreading segments, and a higher value might be appropriate for the peaks of inside corner highs that make up subregions Z1Z2Z3Z4, Z3Z4Z5Z6, and Z5Z6Z7Z8. Therefore, we here experiment with using H values of 240, 260, and 280 m, as well as 220 m, and invert for L and κ. Results are shown in Table 5.2.

Table 5.2. Inversion results/ H fixed at various high values

Site	T, m.y.	H, m	κ, m^2/yr	L, m
Z1Z2Z3Z4	10	220	0.38 +∞/-.28	15 +8/-7
		240	0.22 +∞/-.21	21 +11/-8
		260	0.015 +∞/-0.005	57 +11/-34
		280	0.017 +∞/-0.002	82 +13/-50
Z3Z4Z5Z6	14	220	>0.60**	33 +10/-9**
		240	>0.68**	41 +12/-10**
		260	>0.67**	50 +13/-12**
		280	0.46 +∞/-.36	57 +18/-9
Z5Z6Z7Z8	18	220	0.19 +∞/-.11	62 -12/+15
		240	0.20 +∞/-.10	76 -14/+18
		260	0.22 +∞/-.12	91 +21/-17
		280	0.24 +∞/-.14	108 +23/-21

** Non-dimensional diffusivity for these inverted values of κ and L correspond to a dimensionless diffusivity K of 20 (as defined by (2.22)), the maximum value of K modeled. Thus, κ here is probably higher than the inverted values.

Fits between data slope distribution functions and those from models become progressively poorer as H increases, as shown in Fig. 5.11 for subregions Z1Z2Z3Z4 and Z5Z6Z7Z8. Particularly for subregion Z1Z2Z3Z4, the higher-H functions seem to vary in basic form from that of the models, although profiles from model topographies generated using the best inverted parameters and those associated with an H of 280 m seem equally reasonable visually (Fig. 5.12). The opposite seems to hold for region Z5Z6Z7Z8: slope distribution functions from the best model and from models with H of 240 and 280 m and associated inversion results all seem to reasonably follow the form of the slope distribution function as calculated from data. However, the topography itself, though shown to be lineated perpendicular to the trackline by the entire swath of data, seems not to compare well to tracklines through sedimented models generated with parameters near either the best possible model parameters or those associated with an H of 280 m (Fig. 5.13).

Based on these inconclusive findings, we favor the values of H, L, and κ as given in Table 5.1, for the three nearest-ridge regions. However, we caution that these describe only the along-track seafloor, not regional sediment distribution patterns, due to the atypical nature of the topography sampled.

Adjustments to results: older seafloor

For the five subregions located further off-axis, an H appropriate to inside corner crust in general seems appropriate. This H has probably increased through time along the

trackline, however, due to the slowing of spreading along this section of the MAR since 45 m.y.B.P. [*Cande et al.*, 1988]. Using the poles and angular spreading rates of *Cande et al.*, [1988] and the relationship between observed seafloor variability and spreading rate as quantified by *Malinverno* [1991], given by (4.5), scaled so that the predicted H for 0-age seafloor is 220 m as in Chapter 4, we estimate H for the five eastern subregions. Using these values, we invert for L and κ. Results are given in Table 5.3.

Table 5.3. Inversion results/ H fixed so that $H(T=0)$ is 220 m.

Site	T, m.y.	H, m	κ, m^2/yr	L, m
Z7Z8Z9Z10	22	210	0.045 +0.055/-0.014	81 +21/-22
Z9Z10Z11Z12	26	205	0.022 +0.024/-0.009	61 +18/-19
Z11Z12Z13Z14	30	205	0.025 +0.040/-0.009	57 +16/-18
Z13Z14Z15Z16	34	205	0.048 +0.044/-0.018	83 +23/-20
Z15Z16Z17	37	200	0.020 +0.023/-0.004	194**

** Inverted value of L too close to the maximum considered value to compute 95% confidence bounds.

Fits between data slope distribution functions and those from models with the values of Table 5.3 are good for subregions Z7Z8Z9Z10, Z9Z10Z11Z12, Z11Z12Z13Z14, and Z13Z14Z15Z16, but poor for subregion Z15Z16Z17. As an example, the slope distribution functions from Z11Z12Z13Z14 and Z15Z16Z17 and slope distribution functions which correspond to the best model parameters and model parameters as in Table 5.3, are shown in Fig. 5.14. For subregion Z11Z12Z13Z14, slope distribution functions corresponding to the best H of 235 m and the estimated H of 205 m seem to both have forms close to that slope distribution function calculated from data. One reservation is that the slope of the slope distribution functions at very low θ is not as steep as is seen in the data. This is unavoidable, however, because the model inversion results are influenced by the slope break seen in $g_d(\theta,u)$ for Z11Z12Z13Z14 at θ = 0.1. Similarities in $g_m(\theta,u,\kappa,H,L)$ shown in Fig. 5.14(a) make it difficult to determine whether the original inverted values of Table 5.1 or the results computed using fixed values of H in Table 5.3 are more accurate. Visually comparing profiles from model topographies generated using parameters near the best inverted values and near those associated with an H of 205 m, we also find that both seem equally reasonable (Fig. 5.15), although both seem to have ponds which are just slightly too curved, perhaps a consequence of the inability of the model slope distribution functions to match the data slope distribution function at very low θ.

For subregion Z15Z16Z17, the bestfitting model slope distribution function matches that of the data extremely closely, as shown in Fig. 5.14(b), and profiles through models generated using values near those of the best model for this region have the character of the topographic data (Fig. 5.16). In contrast, the match between $g_m(\theta,u,\kappa,H,L)$ corresponding to the inversion results when H is fixed at 200 m and $g_d(\theta,u)$ for Z15Z16Z17 is poor, and profiles through model topographies generated using values near the inverted parameters do not resemble the bathymetric data (Fig. 5.16(c)). This occurs because, to reduce the amplitude of slope distribution functions to near 0 for θ greater than 0.3 when H is large, the basement must be almost completely covered, which occurs when L is high. At the same time, the slope distribution function is fairly wide at low θ, which corresponds to a low κ. Thus, the predicted topography is high in amplitude and very smooth. This is very difference in appearance from the data as shown in Fig. 5.16(a).

Based on these results, we suspect that the actual amount of sediment along the off-ridge trackline is probably between the values stated in Tables 5.1 and 5.3 for subregions Z7Z8Z9Z10, Z9Z10Z11Z12, Z11Z12Z13Z14, and Z13Z14Z15Z16, and is near the value of Table 5.1 for subregion Z15Z16Z17. These estimates are summarized in Fig. 5.17. The implications of these values of L are discussed below and in Chapter 6.

Effect of data degradation on inversion results

A possible source of error in our inversion results is the data degradation performed prior to the construction of slope distribution functions. As shown in Fig. 5.4 for segment Z7, this process tends to lower the range of slopes encountered. This effect can be seen by comparing slope distribution functions computed with and without presampling, as shown by Fig. 5.18 for subregion Z5Z6Z7Z8. The slope distribution function computed from presampled data has less amplitude at high θ, as expected, and correspondingly greater amplitude at low θ. These differences result in slightly different inverted parameter values, with inversion of the non-presampled slope distribution function producing an estimated H of 210 m, L of 49 m, and κ of 0.12 m^2/yr, in contrast to Table 5.1 values of 200 m for H, 49 m for L, and 0.19 m^2/yr for κ. This suggests that the inversion results, particularly for L, are not much affected by the presampling process.

BRAZIL BASIN

On the opposite side of the MAR from the Angola Basin trackline, three parallel tracklines along which Seabeam data was collected extend westward, beginning on ~5-10 Ma seafloor, across much of the Brazil Basin. Nearer the MAR, these lines can be continued onto other shiptracks, so that seafloor between 2 Ma and 46 Ma is sampled almost continuously.

We analyze data from these tracklines by dividing each into segments covering 2 m.y. of crustal generation, as determined from *Müller et al.* [1993] (Fig. 5.19). East to west, these sections are labeled J1 (2-4 Ma seafloor) to J22 (44-46 Ma seafloor). Each subregion of the trackline is processed as described above so that the data point spacing is exactly 350 m except where gaps in the original data occur. Then, data from pairs of adjacent segments is combined for the calculation of the slope distribution functions. These functions, given in Fig. 5.20 at the same scale as given for the Angola Basin slope distribution functions of Fig. 5.9, show the amplitude of slope distribution functions at low θ increasing with seafloor age, as in the Angola Basin.

Results

The results of the inversion procedure are given in Table 5.4, and correspond to the dashed lines in Fig. 5.20. Approximate lower bounds of 95% confidence intervals are determinable for all inverted values, and where both lower and upper bounds are provided, both confidence bounds are well constrained. No obvious pattern emerges indicating what slope distribution function forms are most and least prone to being poorly constrained.

The four nearest-ridge sections show a small range in H, and an L which increases linearly with seafloor age, albeit at a rate A of 3.8 ± 1.1 m/m.y. (via (3.25)), lower than the rate of 4.8 ± 1.2 m/m.y. we obtain from the analysis of data on the western flank in MAR in the Rio Grande study area in Chapter 4. On 12-36 Ma seafloor, sediment thicknesses are generally ~30 m, although several subregions yield higher values of L, correlating with high inverted values of H (e.g. subregions J10J11 and J11J12). On older seafloor,

corresponding to subsegments J17 through J20, L is somewhat higher, while the two most easterly regions show lower values of L and correspondingly lower values of H.

Table 5.4. Inversion results, Brazil Basin tracklines

Site	Center Location	N	T, m.y.	H, m	κ, m^2/yr	L, m
J1J2	26.72°S, 14.56°W	487	4	180 +50/-20	1.07 +∞/-1.02	14 +37/-7
J2J3	26.80°S, 15.14°W	487	6	175 +35/-20	0.89 +∞/-.84	17 +18/-7
J3J4	26.80°S, 15.53°W	497	8	175 +140/-25	0.062 +∞/-.017	28 +∞/-20
J4J5	26.88°S, 15.91°W	451	10	185 +135/-35	0.047 +.185/-.017	44 +∞/-30
J5J6	26.94°S, 16.30°W	418	12	185 +120/-25	0.062 +∞/-.017	33 +113/-16
J6J7	26.98°S, 16.67°W	419	14	205 +140/-30	0.056 +∞/-.016	35 +128/-18
J7J8	27.05°S, 17.01°W	406	16	195 +160/-30	0.028 +∞/-.008	32 +∞/-20
J8J9	27.12°S, 17.37°W	419	18	165 +95/-25	0.026 +∞/-.011	24 +96/-15
J9J10	27.18°S, 17.81°W	535	20	160 +125/-25	0.019 +.056/-.007	37 +∞/-20
J10J11	27.22°S, 18.31°W	642	22	260 +65/-55	0.045 +.040/-.023	130 +∞/-60
J11J12	27.27°S, 18.87°W	665	24	220 +120/-35	0.020 +.030/-.007	68 +∞/-30
J12J13	27.31°S, 19.43°W	672	26	175 +125/-30	0.014 +.036/-.008	38 +∞/-20
J13J14	27.32°S, 20.01°W	620	28	185 +120/-35	0.017 +.038/-.007	50 +∞/-30
J14J15	27.34°S, 20.61°W	571	30	170 +75/-25	0.026 +∞/-.006	33 +77/-17
J15J16	27.41°S, 21.10°W	579	32	155 +30/-20	0.031 +∞/-.011	30 +26/-13
J16J17	27.47°S, 21.52°W	552	34	145 +70/-20	0.021 +.059/-.008	30 +79/-14
J17J18	27.50°S, 22.23°W	540	36	180 +85/-35	0.024 +.037/-.009	78 +∞/-40
J18J19	27.50°S, 22.67°W	535	38	160 +75/-40	0.019 +.032/-.009	80 +∞/-40
J19J20	27.50°S, 22.96°W	560	40	160 +70/-40	0.023 +.032/-.013	82 +∞/-50
J20J21	27.52°S, 23.46°W	630	42	145 +85/-25	0.015 +.027/-.005	43 +123/-23
J21J22	27.53°S, 24.00°W	616	44	130 +80/-10	0.035 +∞/-.025	16 +86/-5

The observed correlation between L and H suggests that better estimates of L might be determined by fixing H at a reasonable value prior to inversion. Since the two northern tracklines considered, RC2802-1 and RC2802-2, traverse outside corner crust, and the third, RC271102, though primarily on inside corner crust, mostly avoids the roughest, highest-standing parts of its segment (see Fig. 5.19), we fix H at values appropriate for outside corner crust. These are determined by assuming that H near-ridge is 190 m as in Chapter 4, with off-axis variations determined using the poles and angular spreading rates of *Cande et al.* [1988] and the relationship between observed seafloor variability and spreading rate of *Malinverno* [1991], given by (4.5), scaled so that the predicted H for 0-age seafloor is 190 m. Using the resulting estimates of H, we invert for L and κ.

Results are given in Table 5.5. Inverted values of L show much less along-track variability than those given in Table 5.4, as shown in Fig. 5.21. Near-ridge, an A of 4.5 ± 0.7 m/m.y. is predicted, only slightly below the Chapter 4 value. Additionally, models

generated using values near those inverted from both high-L and low-L subregions resemble trackline data at scale lengths greater than one kilometer. This is demonstrated in Fig. 5.22 for high-L subregion J18J19 and in Fig. 5.23 for low-L subregion J6J7. Thus, we believe that the inversion results as presented in Table 5.5 describe the distribution of sediments better than those of Table 5.4.

Table 5.5. Inversion results/ H fixed so that $H(T=0)$ is 190 m.

Site	Center Location	N	T, m.y.	H, m	κ, m^2/yr	L, m
J1J2	26.72°S, 14.56°W	487	4	190	0.79 +∞/-.7	17 +7/-5
J2J3	26.80°S, 15.14°W	487	6	190	0.25 +∞/-.15	24 +6/-7
J3J4	26.80°S, 15.53°W	497	8	190	0.058 +.142/-.025	40 +12/-14
J4J5	26.88°S, 15.91°W	451	10	185	0.048 +.082/-.018	44 +12/-14
J5J6	26.94°S, 16.30°W	418	12	185	0.063 +∞/-.023	33 +9/-11
J6J7	26.98°S, 16.67°W	419	14	185	0.085 +∞/-.045	23 +7/-8
J7J8	27.05°S, 17.01°W	406	16	185	0.038 +∞/-.018	24 +8/-10
J8J9	27.12°S, 17.37°W	419	18	185	0.025 +.057/-.012	38 +13/-13
J9J10	27.18°S, 17.81°W	535	20	180	0.022 +.014/-.007	57 +14/-14
J10J11	27.22°S, 18.31°W	642	22	180	0.020 +.014/-.006	46 +9/-12
J11J12	27.27°S, 18.87°W	665	24	180	0.015 +.024/-.006	33 +9/-10
J12J13	27.31°S, 19.43°W	672	26	180	0.013 +.010/-.005	44 +11/-12
J13J14	27.32°S, 20.01°W	620	28	180	0.016 +.012/-.006	46 +12/-12
J14J15	27.34°S, 20.61°W	571	30	180	0.026 +.055/-.010	40 +10/-11
J15J16	27.41°S, 21.10°W	579	32	180	0.031 +.050/-.010	48 +11/-12
J16J17	27.47°S, 21.52°W	552	34	180	0.023 +.018/-.007	62 +14/-15
J17J18	27.50°S, 22.23°W	540	36	175	0.023 +.010/-.007	72 +14/-15
J18J19	27.50°S, 22.67°W	535	38	170	0.023 +.008/-.007	90 +19/-13
J19J20	27.50°S, 22.96°W	560	40	165	0.025 +.007/-.007	89 +17/-14
J20J21	27.52°S, 23.46°W	630	42	165	0.019 +.008/-.005	65 +12/-13
J21J22	27.53°S, 24.00°W	616	44	170	0.013 +.010/-.005	51 +14/-13

The implications of the pattern of L seen in tables 5.4 and 5.5 for temporal changes in water chemistry and sediment rain rate are delayed until Chapter 6.

ARGENTINE BASIN

Roughly a thousand kilometers south of the trio of Brazil Basin tracklines, three tracklines collected by the *R/V Thomas Washington* during cruises to and from the Cox study area of Chapter 4 extend westward across the South Atlantic (Fig. 5.24). We utilize the portions of these tracklines extending from 6-7 Ma seafloor out onto 38 Ma seafloor. To analyze this data, we divide tracklines into segments covering 2 m.y. of crustal generation, as determined from *Müller et al.* [1993]. East to west, these sections are

labeled W1 (6-8 Ma seafloor) to W16 (36-38 Ma seafloor). Each subregion of the trackline is processed as described above so that the data point spacing is exactly 350 m except where gaps in the original data occurred. Then, we combine data from pairs of adjacent segments for the calculation of the slope distribution functions, shown in Fig. 5.25. As in the Angola and Brazil basins, slope distribution functions show an increase in amplitude at low θ with seafloor age. This trend continues out to subregion W13W14, with the two westernmost regions showing a slight decrease in amplitude at low θ. For seafloor of any given age, the amplitude of the slope distribution functions at low θ is higher in the Argentine Basin than in the other regions studied in this chapter.

Results

The results of the inversion procedure are given in Table 5.6, and correspond to the dashed lines in Fig. 5.25. For the entire region, fits between model slope distribution functions and those from data are fairly good. 95% confidence bounds are determinable for most values of H, L, and κ, limited only by the upper limit of 200 m placed on L.

Table 5.6. Inversion results, Argentine Basin tracklines

Site	Center Location	N	T, m.y.	H, m	κ, m^2/yr	L, m
W1W2	35.41°S, 17.81°W	387	8	190 +85/-35	0.31 +∞/-.1	56 +83/-22
W2W3	35.68°S, 18.51°W	446	10	205 +75/-30	0.32 +∞/-.1	81 +85/-27
W3W4	35.72°S, 19.01°W	493	12	170 +80/-25	0.16 +∞/-.04	59 +84/-20
W4W5	35.79°S, 19.55°W	471	14	145 +60/-25	0.08 +.23/-.03	42 +62/-18
W5W6	35.81°S, 20.07°W	463	16	165 +70/-30	0.10 +.17/-.05	60 +82/-25
W6W7	35.88°S, 20.59°W	438	18	175 +80/-35	0.10 +.16/-.04	*88 +112+/-30
W7W8	35.94°S, 21.23°W	455	20	115 +90/-15	0.03 +.10/-.01	54 +140/-21
W8W9	35.80°S, 21.57°W	564	22	115 +90/-10	0.03 +.11/-.01	*50 +150+/-10
W9W10	35.76°S, 22.02°W	608	24	115 +80/-15	0.04 +.10/-.01	54 +115/-16
W10W11	35.79°S, 22.59°W	597	26	135 +50/-35	0.07 +.08/-.04	*107 +93+/-50
W11JW12	35.84°S, 23.20°W	581	28	130 +55/-30	0.05 +.08/-.02	*96 +104+/-40
W12W13	35.81°S, 23.76°W	599	30	170 +25/-40	0.11 +.05/-.05	*158 +42+/-40
W13W14	35.89°S, 24.35°W	545	32	195 +15/-30	0.15 +.08/-.05	*192 +8+/-20
W14W15	36.06°S, 25.08°W	468	34	205 +35/-40	0.15 +.17/-.07	*154 +46+/-30
W15W16	36.03°S, 25.59°W	491	36	135 +75/-25	0.05 +.10/-.02	63 +96/-26

* Shape of likelihood functions suggests that the 95% confidence bounds on L is definable, but that the upper bound is above the maximum considered value of 200 m. Lower bounds on L for these values are approximate.

Despite the goodness of fit seen for inverted parameters, the correlation between L and H overwhelms attempts to discern patterns in sediment thickness and H. Therefore, as

with the analysis of Angola and Brazil basin data, we fix H at values which seem geologically reasonable, and invert for L and κ.

The tracklines examined traverse seafloor generated at spreading segments bounded north and south by right-lateral transform zones and non-transform offsets. Therefore, crust along each segment is outside corner to the north and inside corner to the south. Near ridge, in the Cox study area, we find that, in this situation, inside corner crust and outside corner crust have only slightly different characteristic H values, and that fixing H at 200 m for all data produces inverted values of L which seem reasonable. However, there is some indication that a slightly lower H might be equally appropriate.

Due to this uncertainty as to the best possible value of H at $T = 0$, we fix H for each subregion at two values, the first chosen such that the zero-age estimate of H is 200 m and the second such that the zero-age estimate is 190 m, the value we use for the analysis of Brazil Basin tracklines above. As above, this is done by appropriately scaling the estimates of H as a function of spreading rate predicted by *Malinverno* [1991] (given via (4.5)), using the poles and angular spreading rates of *Cande et al.* [1988]. A slight modification of the inversion algorithm as described above is that L values as high as 240 m are considered, for Λ below the upper limit of 1.25.

Results are given in Table 5.7 and Table 5.8, and are shown in Fig. 5.26.

Table 5.7. Inversion results, H fixed so that $H(T=0)$ is 200 m.

Site	Center Location	N	T, m.y.	H, m	κ, m^2/yr	L, m
W1W2	35.41°S, 17.81°W	387	8	200	0.32 +∞/-.1	64 +14/-13
W2W3	35.68°S, 18.51°W	446	10	195	0.29 +∞/-.1	72 +13/-13
W3W4	35.72°S, 19.01°W	493	12	195	0.19 +.54/-.06	83 +14/-17
W4W5	35.79°S, 19.55°W	471	14	195	0.14 +.09/-.04	91 +18/-18
W5W6	35.81°S, 20.07°W	463	16	195	0.12 +.10/-.03	91 +17/-18
W6W7	35.88°S, 20.59°W	438	18	195	0.12 +.06/-.03	112 +21/-19
W7W8	35.94°S, 21.23°W	455	20	190	0.10 +.03/-.03	166 +28/-28
W8W9	35.80°S, 21.57°W	564	22	190	0.10 +.03/-.02	160 +23/-26
W9W10	35.76°S, 22.02°W	608	24	190	0.12 +.04/-.03	154 +29/-17
W10W11	35.79°S, 22.59°W	597	26	185	0.12 +.05/-.02	200 +30/-34
W11JW12	35.84°S, 23.20°W	581	28	185	0.10 +.05/-.01	201 +21/-37
W12W13	35.81°S, 23.76°W	599	30	185	0.13 +.03/-.03	186 +25/-22
W13W14	35.89°S, 24.35°W	545	32	185	0.14 +.04/-.03	170 +26/-20
W14W15	36.06°S, 25.08°W	468	34	185	0.12 +.06/-.03	128 +19/-19
W15W16	36.03°S, 25.59°W	491	36	180	0.09 +.06/-.02	119 +16/-20

Table 5.8. Inversion results, H fixed so that $H(T=0)$ is 190 m.

Site	Center Location	N	T, m.y.	H, m	κ, m^2/yr	L, m
W1W2	35.41°S, 17.81°W	387	8	190	0.32 +∞/-.1	56 +12/-11
W2W3	35.68°S, 18.51°W	446	10	185	0.27 +∞/-.1	64 +11/-13
W3W4	35.72°S, 19.01°W	493	12	185	0.17 +.56/-.05	73 +13/-15
W4W5	35.79°S, 19.55°W	471	14	185	0.12 +.10/-.04	80 +17/-16
W5W6	35.81°S, 20.07°W	463	16	185	0.12 +.08/-.04	80 +16/-16
W6W7	35.88°S, 20.59°W	438	18	185	0.11 +.05/-.03	100 +18/-18
W7W8	35.94°S, 21.23°W	455	20	180	0.09 +.03/-.03	147 +28/-23
W8W9	35.80°S, 21.57°W	564	22	180	0.09 +.02/-.02	141 +21/-20
W9W10	35.76°S, 22.02°W	608	24	180	0.11 +.03/-.03	138 +26/-25
W10W11	35.79°S, 22.59°W	597	26	180	0.12 +.04/-.03	190 +22/-32
W11JW12	35.84°S, 23.20°W	581	28	175	0.10 +.03/-.02	181 +22/-32
W12W13	35.81°S, 23.76°W	599	30	175	0.12 +.02/-.03	167 +27/-19
W13W14	35.89°S, 24.35°W	545	32	175	0.12 +.04/-.02	154 +23/-18
W14W15	36.06°S, 25.08°W	468	34	175	0.10 +.06/-.02	116 +16/-19
W15W16	36.03°S, 25.59°W	491	36	175	0.08 +.06/-.02	112 +16/-18

Inversion results for 8 Ma seafloor imply near-ridge accumulation rates of 8 m/m.y. using the values of Table 5.7 and 7 m/m.y. using the values of Table 5.8. These values are above the rate of 6.2 ± 0.8 m/m.y. seen in the near-ridge Cox study area data, depicted by the dashed line in Fig. 5.26. Though the difference in near-ridge rates could be simply a function of track placement, we feel that the values as given in Table 5.7 are probably too high, and advance the values as given in Table 5.8 as being more probable.

The largest differences between original inverted H values and the values assumed in Table 5.7 and 5.8 occur in subregions W7W8, W8W9, and W9W10, making the assumption of higher H values most suspect for these subregions. We find that the topographic data from these subregions compares reasonably well, at longer wavelengths, with models generated using values near the inverted parameters from Table 5.8, as shown in Fig. 5.28. The original parameters generated when H is free to vary (Table 5.6), however, seem to produce models which better resemble the data at shorter wavelength. This is particularly clear when models are expanded, as shown in Fig. 5.28. The high-H model of 5.28(c) has none of the 1-2 km-scale topographic roughness obvious from the data. This would seem to suggest that the low-H, low-L values of Table 5.6 are more accurate for these subregions. However, SCS data collected nearby suggests that L is high on seafloor older than 20 Ma. This implies that our inversion methodology may be inadequate for analyzing data from this regime; this is discussed further below.

Values of L inverted for the oldest seafloor we considered are lower than those from 20-32 Ma seafloor. This correlates with the crossing of several seamounts, as shown in Fig. 5.24, and so is probably not relevant to the regional distribution of sediment.

CONCLUSIONS AND DISCUSSION

Sediment thickness

The resulting values of L determined by the inversion procedures conducted in this and the previous chapter are given in Fig. 5.29, along with sediment thicknesses encountered at local DSDP sites. We find that our estimates of average sediment thickness tend to be lower than the thicknesses found at drill sites. This is probably a function of the inhomogeneous distribution of sediments common to rough topography. The 3.5 kHz data available for the DSDP Leg 3 sites is not of high enough quality to determine how much post-deposition transport sediments might have been subjected to, and whether slumped structures are present, so we cannot attach any significance to differences between our inversion results and the thicknesses of sediments found at Leg 3 drill sites.

During Leg 73, SCS data of high quality was collected [*Hsü, LaBrecque et al.*, 1984]. Sites 519 and 520 (off scale in Fig. 5.29, with a thickness of 449 m) are clearly located in thick sediment ponds, so comparison of these values with our inversion results is not warranted. At Site 522, as shown in Fig. 5.30, sediments seem to have undergone little post-depositional transport, suggesting that the sediment thickness encountered at that location, 150 m, is equal to the regional average thickness. Our inversion results suggest that the seafloor sampled along the trackline we utilize in the Angola basin, portions of which are shown in Fig. 5.30, has an average sediment thickness of only 13 m, reflecting either a problem with the inversion methodology or a difference in local accumulation rate over a fairly short geographic distance; this is discussed in Chapter 6.

The setting of Site 521 is unclear, so while the measured depths of drill cores at that site, 71 and 84 m, are not much higher than we predict for 16 Ma seafloor in the modeling exercises of Chapter 6 (see Fig. 6.27), this does not necessarily support our inversion results.

Results from the Brazil and Argentine basins suggest that sediment accumulates more gradually in the northern region than to the south, with differences in sediment thickness between the basins increasing off-axis. We have confidence in the accuracy of our results from the Brazil Basin when H is predetermined (Table 5.5), due to the general agreement between data and models produced using values near those of inverted parameters, as shown in Fig. 5.22 and Fig. 5.23, and because the near-ridge sediment accumulation rate A is 4.5 ± 0.7 m/m.y., similar to that of the Rio Grande region of Chapter 4. Off-ridge sedimentation patterns probably reflect temporal variations in sediment rain rate and oceanic chemistry; this is addressed in detail in Chapter 6.

Results from the Argentine Basin agree reasonably well with near-ridge data. However, we are wary of inversion results from seafloor greater than 15-20 Ma. SCS data from the Argentine Basin suggest that sediment thicknesses might easily average 200 m on 20 Ma seafloor, and increase steadily with increasing seafloor age [e.g. *Neprochnov*, 1977] (see Fig. 6.28). We find that, where seafloor is heavily sedimented and basement outcrops are rare, the seafloor tends to exhibit low-amplitude waves, which we do not numerically model. Therefore, inverting topography which contains such features becomes problematic.

Inversion results from the Angola Basin are derived from only one trackline, which seems to be atypical for seafloor younger than 20 Ma. Therefore, results from this data may not be generally applicable to the basin as a whole. However, sediment thickness does seem to steadily increase with seafloor age. Data from presumably more normal crust further off-axis implies an accumulation rate somewhere between those of the Brazil and Argentine basins.

Apparent diffusivity

Inverted values of apparent diffusivity are not discussed above because, as in chapters 3 and 4, we have been unsuccessful in attaching geological meaning to them. Some patterns are observed in our inversion results, however, which we present here.

In Fig. 5.31, we show relationships between inverted parameters obtained when H is free to vary. We find that, particularly in the Angola and Brazil basins, κ is highest near-

ridge and decreases off axis, as shown in Fig. 5.31(a). Since nearer-ridge values are similar to those seen in Chapter 4, we do not believe that variations made to the inversion methodology in this chapter are at fault. One possible cause for the decrease in κ with T might be a correlation between κ and H, which does seem to exist (Fig. 5.31(b)), since H shows some reduction with increasing T (Fig. 5.31(c)). Another possibility is that sediment redistribution processes do not produce very flat ponds unless turbidity currents are active, and thus that where F is low or 0, ponds will maintain a small but measurable amount of curvature through time. Since most sedimentation in Brazil Basin in particular probably occurs when the seafloor is young, if no redistribution occurs then measured κ will decrease as T increases. This would result in a relatively invariant dimensionless diffusivity K through time. In actuality, all three basins show variability in K which is somewhat coherent (Fig. 5.31(d)). The only clear correlation seems to be between F and κ (Fig. 5.31(e)), which may indicate that sediment redistribution processes might not able to keep up with sedimentation processes, even in relatively low-F environments.

A potential drawback to trying to determine the controls using values inverted when H is free to vary is that they are probably subject to misestimation of H and, consequently, L. In Fig. 5.32, we display the relationships of Fig. 5.31 using our favored inversion results for each basin, as described in the figure caption. The negative correlation between seafloor age and κ persists (Fig. 5.32(a)), as does the positive correlation between κ and H (Fig. 5.32(b)). These relationships could be due to the imposed relationship between H and T, as given in Fig. 5.32(c). Variations in K with time continue to show coherence between basins (Fig. 5.32(d)), and the strongest correlation continues to be between F and κ (Fig. 5.32(e)). Thus, fixing H influences inverted values of κ for individual subregions, but does not result in changes in the pattern of distribution of κ. This contrasts with L, which shows a negative correlation with fixed H values (Fig. 5.32(f)), a reflection of the generally positive relationship between L and T and the imposed negative correlation between H and T.

The observed variations seen in inverted values of κ clearly show patterns, but we remain unsure of what these patterns are reflecting. We suspect that detailed near-bottom bathymetry studies, combined with sediment sampling, would help clarify this issue.

Limits to the utility of the inversion methodology

In this chapter, we use 1-minute averages of bathymetric data, collected along transit lines, to study how changes to topography suggest that sediment thickness varies on the flanks of the southern MAR. When H is free to vary, the poor resolution of slope distribution functions at high θ leads to high variability in this parameter, and thus a lack of confidence in inverted values of L and κ as well. However, when we have some knowledge of H, the agreement between values of L obtained in this chapter and in Chapter 4 where study areas overlap suggests that our inversion results are fairly accurate. An important caveat, however, is that our inversion results hold only for the seafloor directly beneath tracklines, which may not be typical of the crust with a region.

As L approaches H, at least in the Argentine Basin, the character of the interaction between basement topography and sediment seems to change, with sedimented surfaces showing morphology not related to basement outcrops. These features are absent from our models, and make our inversion procedure, as it is now constructed, inadequate for estimating H, L, and κ when L is near H.

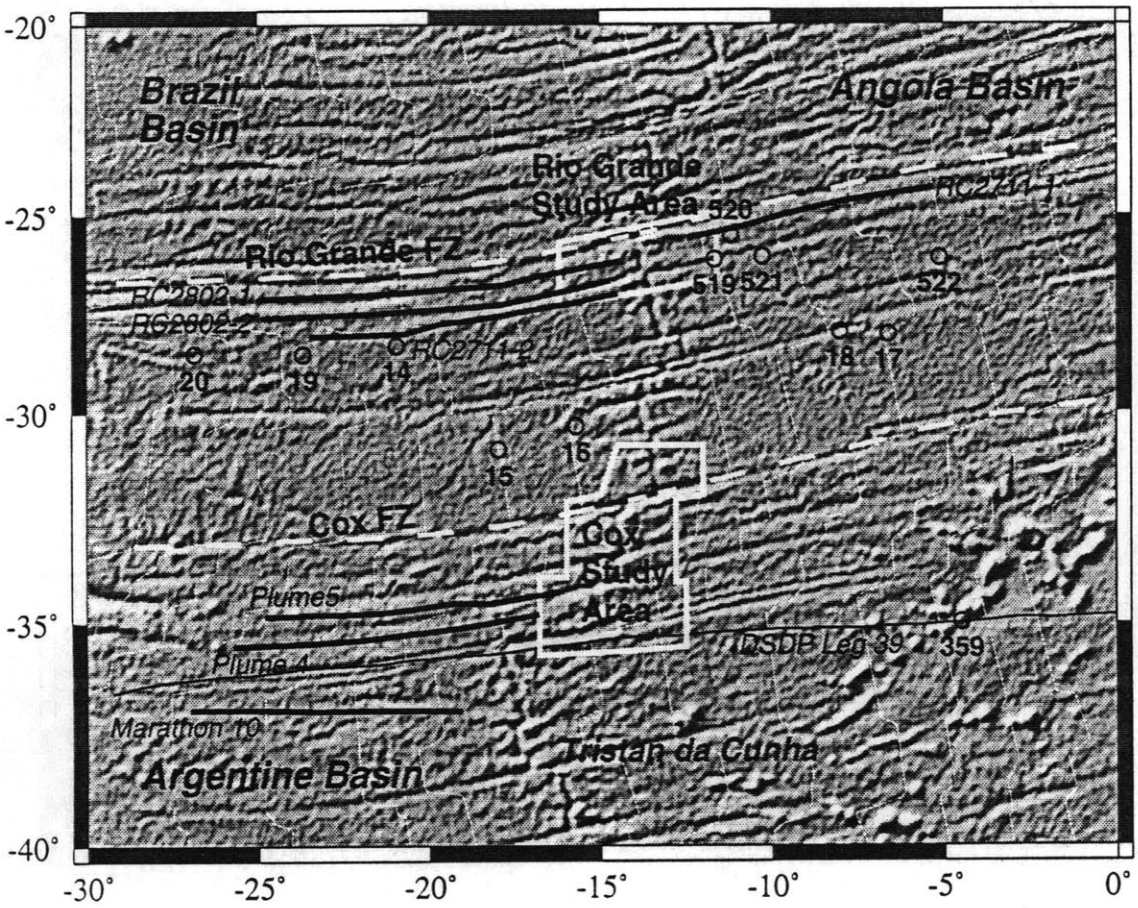

Fig. 5.1: Gray-shaded free-air gravity anomaly map of the central South Atlantic [*Sandwell and Smith*, 1995], showing all local DSDP sites, the near-ridge study areas discussed in Chapter 4, and off-axis lines used to invert for sediment thickness and apparent diffusivity (thick black lines). The thin black line is the region-spanning trackline of DSDP Leg 39, along which SCS data was collected. White ridge-parallel lines correspond to isochrons of 10 m.y. [*Müller et al.*, 1993].

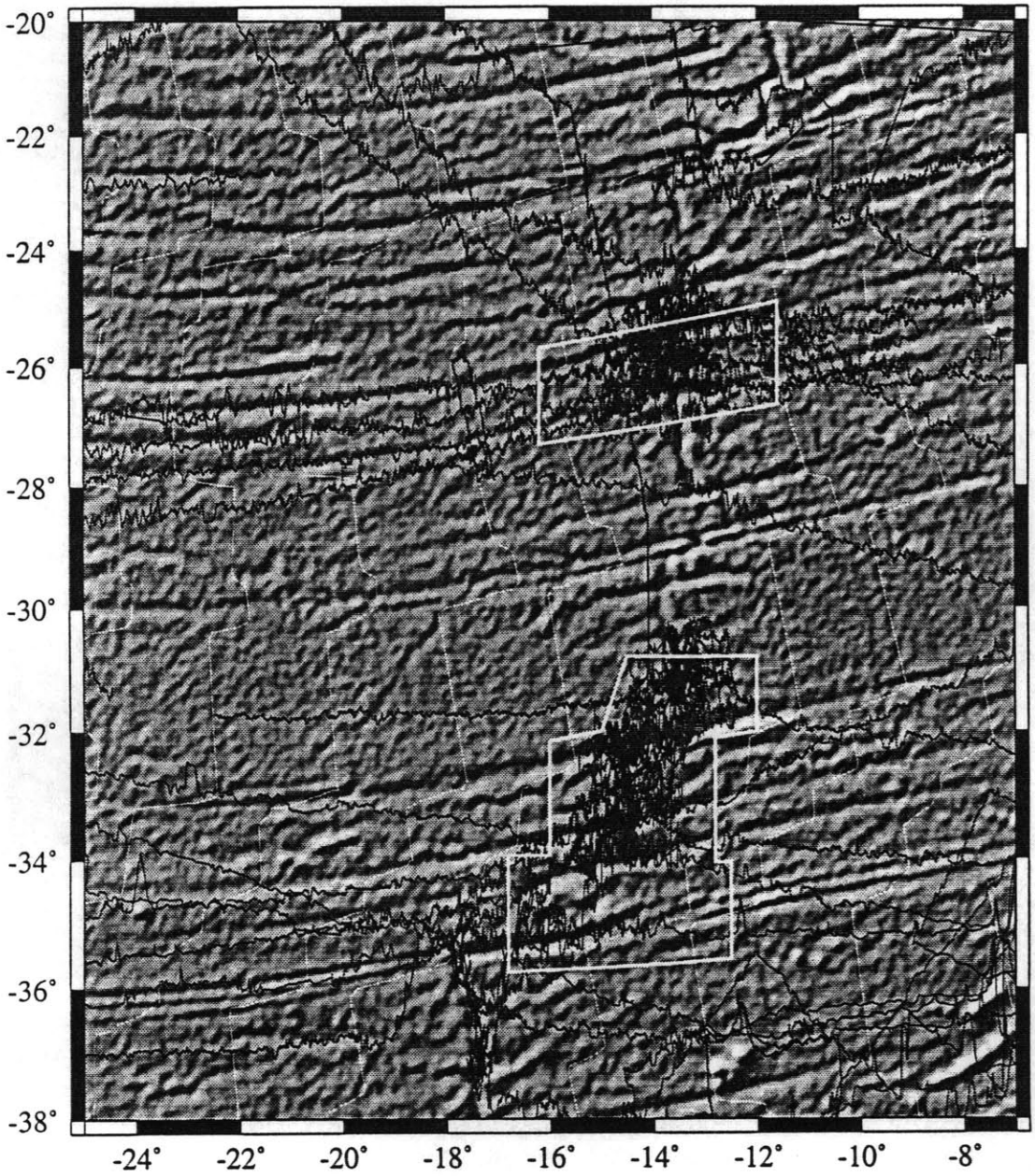

Fig. 5.2: Gray-shaded free-air gravity anomaly map of the central South Atlantic [*Sandwell and Smith*, 1995], showing a number of shiptracks through the area along which bathymetric data (multibeam or 3.5 or 12 kHz echosounder) was collected. Outlines of the near-ridge study areas are given for scale. White ridge-parallel lines correspond to isochrons of 10 m.y. [*Müller et al.*, 1993]. A noticeable decrease in bathymetric variability west of the 20-30 Ma isochrons is seen in the character of seafloor bathymetry south of 30° S. Bathymetry along ship tracks is plotted about a 4000 m mean, with a horizontal scale of 8000 m per inch.

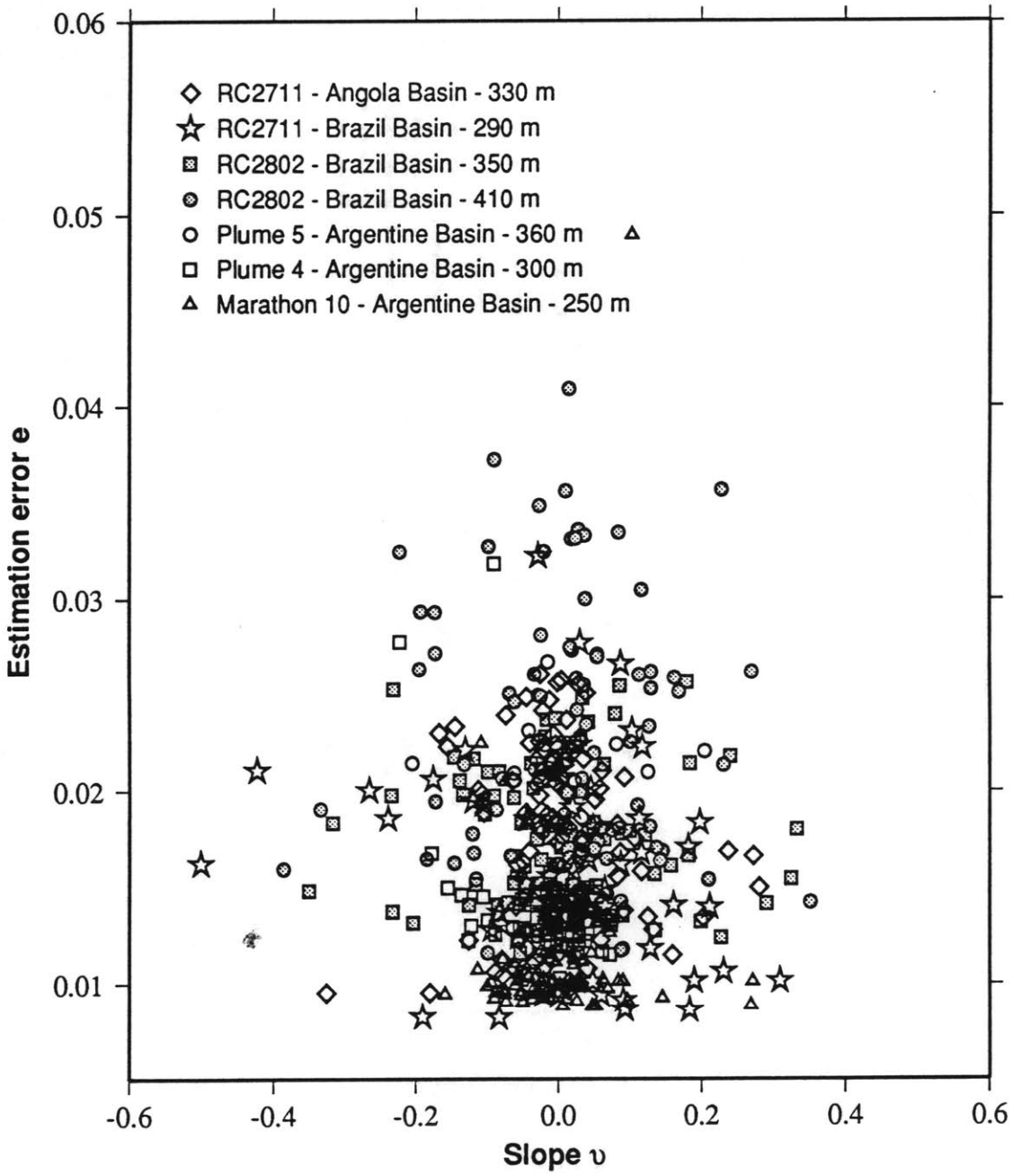

Fig. 5.3: Estimated values of slope υ and error e for all 18-20 Ma seafloor from all tracklines considered in this chapter, as calculated using equations (3.6) and (3.8). No correlation between e and υ is evident. However, less densely sampled tracklines tend to have higher values of e.

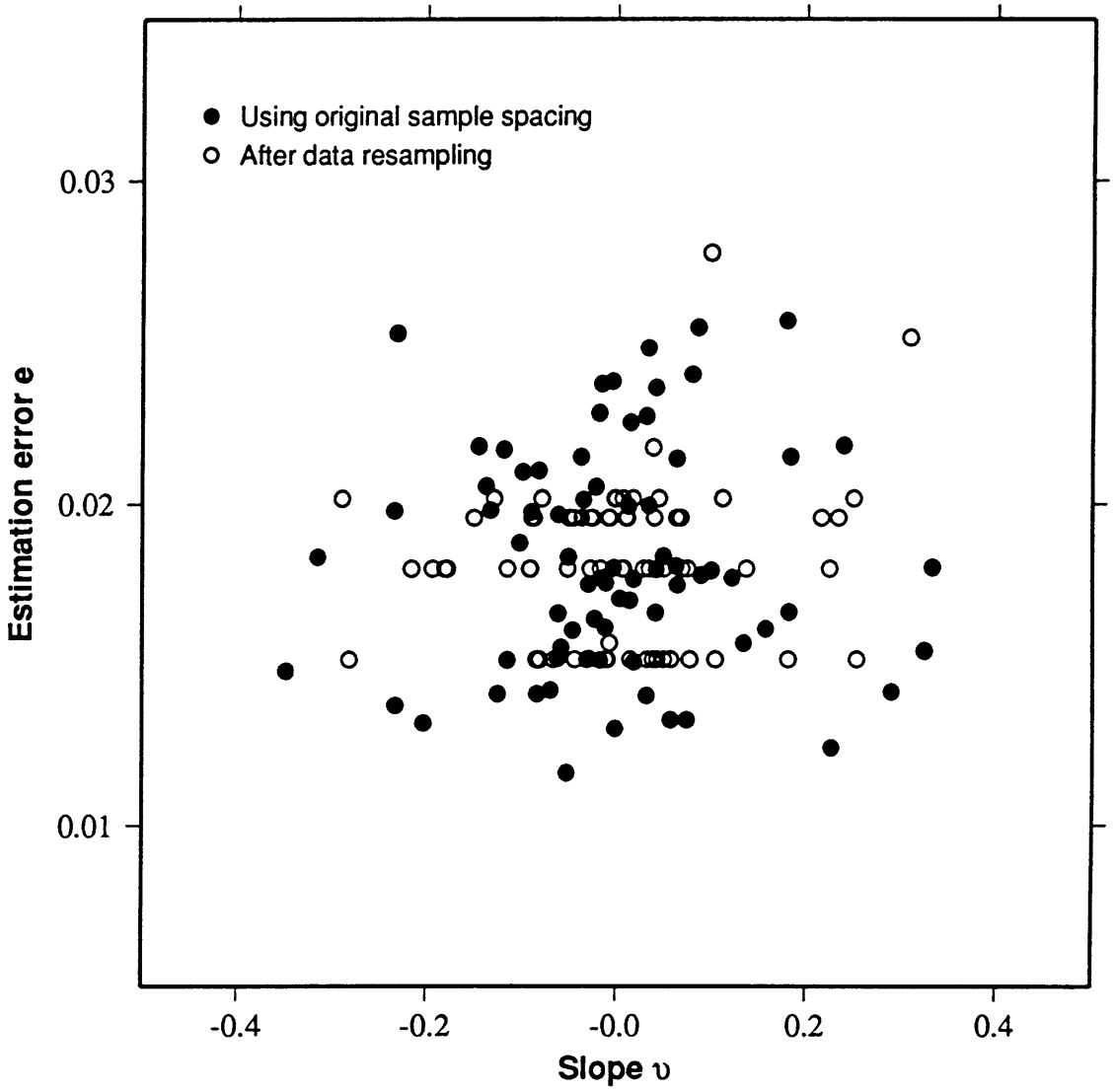

Fig. 5.4: Estimated values of slope υ and error e for 18-20 Ma seafloor from the southern trackline from cruise RC2802 (RC2802-2 in Fig. 5.1), before (black circles) and after (white circles) resampling as described in the text.

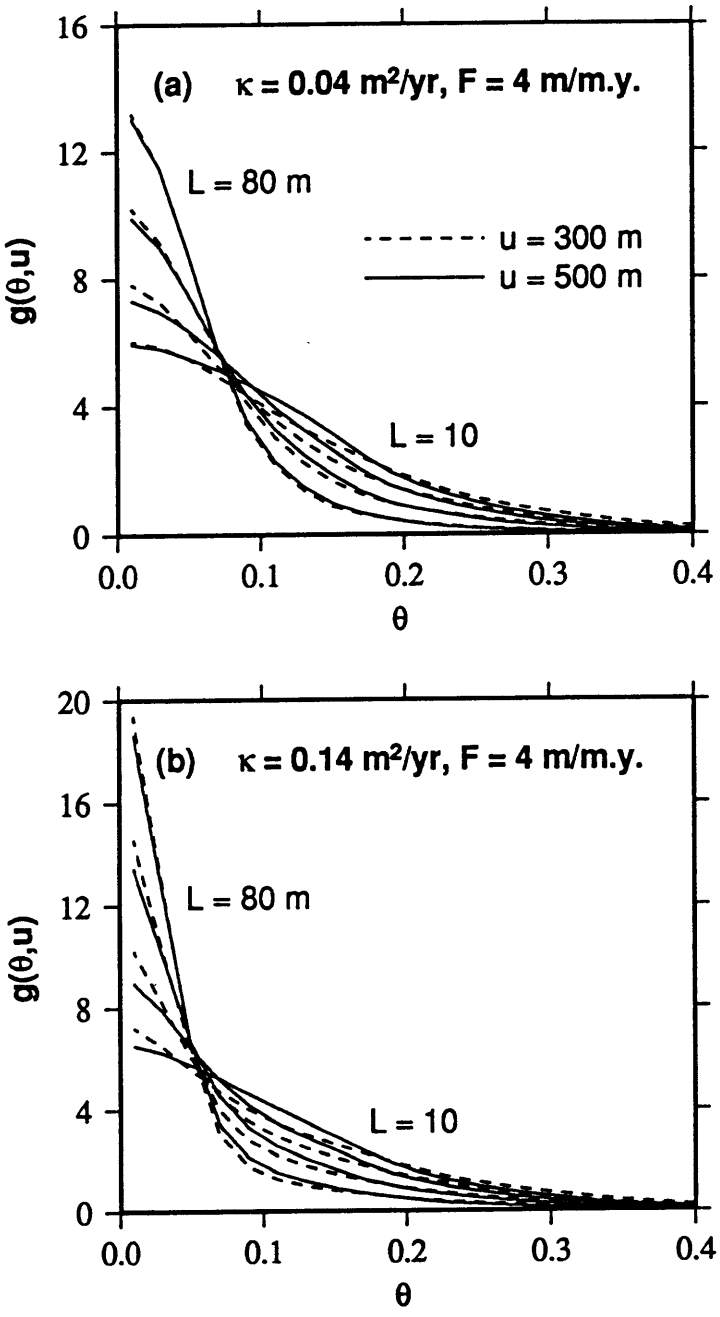

Fig. 5.5: Slope distribution functions calculated from model bathymetries generated using basement parameters H = 160 m, k_n = 0.6 km^{-1}, a = 3, ζ_s = 0, and D = 2.2, sedimented at a rate of 4 m/m.y. using apparent diffusivity values κ of (a) 0.04 and (b) 0.14 (b) m^2/yr, for 2.5, 5, 10, and 20 m.y. of model time (L = 10, 20, 40, and 80 m, respectively), sampled using u of 300 m (dashed lines) as in previous chapters and a u of 500 m (solid lines), the value used in this chapter.

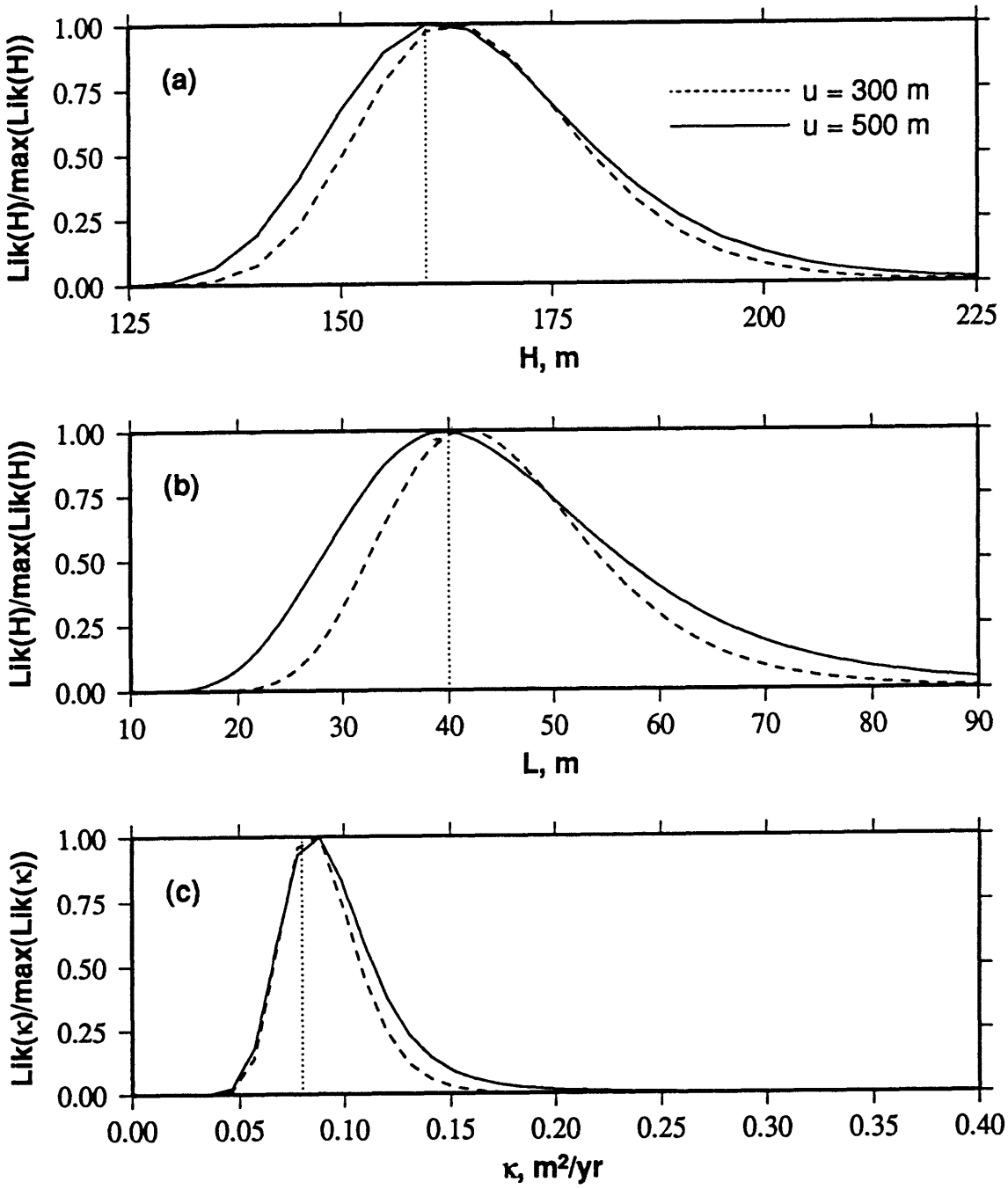

Fig. 5.6: Normalized likelihood functions for (a) H, (b) L, and (c) κ, from the inversion of slope distribution functions from a model topography generated using the basement parameters of Fig. 5.5, an F of 4 m/m.y., and a κ of 0.08 m^2/yr, for 10 m.y. of model time (L = 40 m), using u of 300 m (dashed lines) and 500 m (solid lines) and an N of 800.

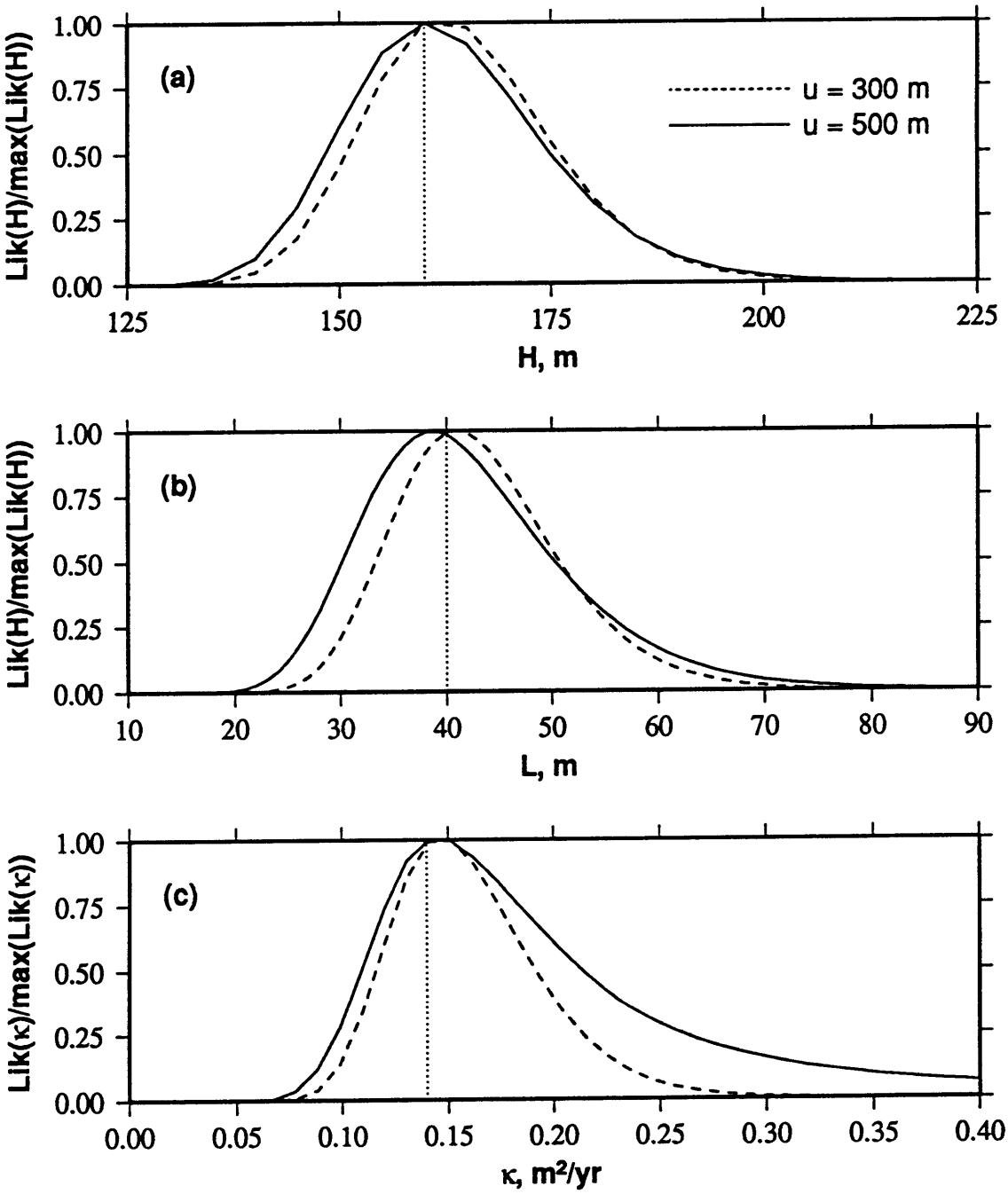

Fig. 5.7: Normalized likelihood functions for (a) H, (b) L, and (c) κ, from the inversion of slope distribution functions from a model topography generated using the basement parameters of Fig. 5.5, an F of 4 m/m.y., and a κ of 0.14 m^2/yr, for 10 m.y. of model time (L = 40 m), using u of 300 m (dashed lines) and 500 m (solid lines) and an N of 800.

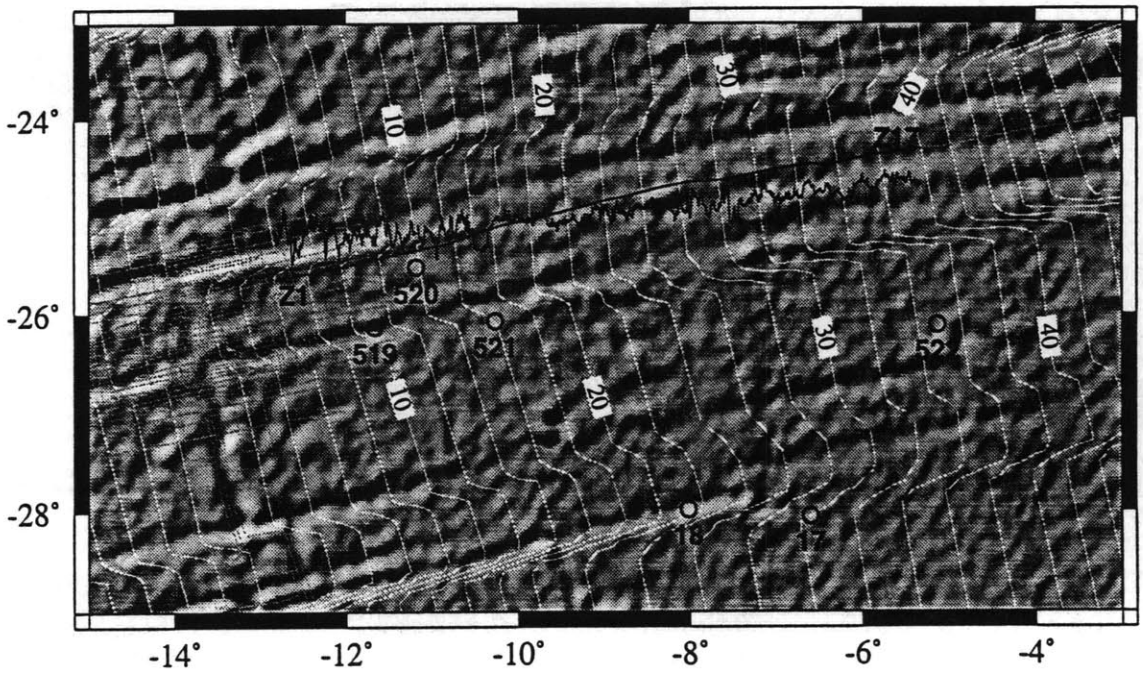

Fig. 5.8: Gray-shaded gravity anomaly map of the eastern flank of the MAR in the vicinity of the Angola Basin trackline and local DSDP drill sites. White ridge-parallel lines correspond to isochrons of 2 m.y. [*Müller et al.*, 1993]. Bathymetry along ship tracks is plotted about a 4000 m mean, with a horizontal scale of 5000 m per inch. Terminal segments Z1 and Z17 are labeled. The remaining segments are associated with 2-m.y. lengths of seafloor between Z1 and Z17.

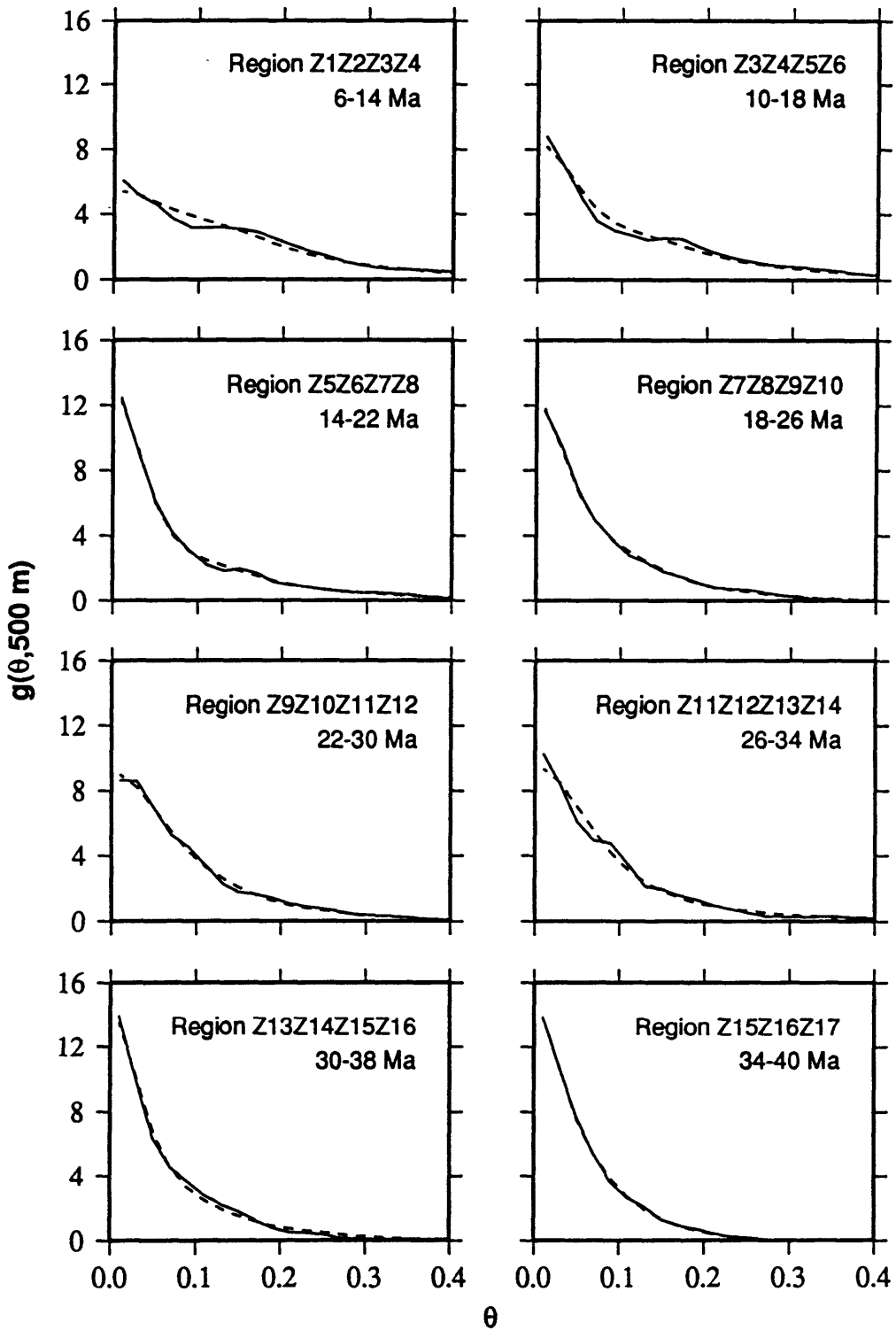

Fig. 5.9: Slope distribution functions computed from subregions in the Angola Basin (solid lines) and from best-fitting models (dashed lines), as labeled.

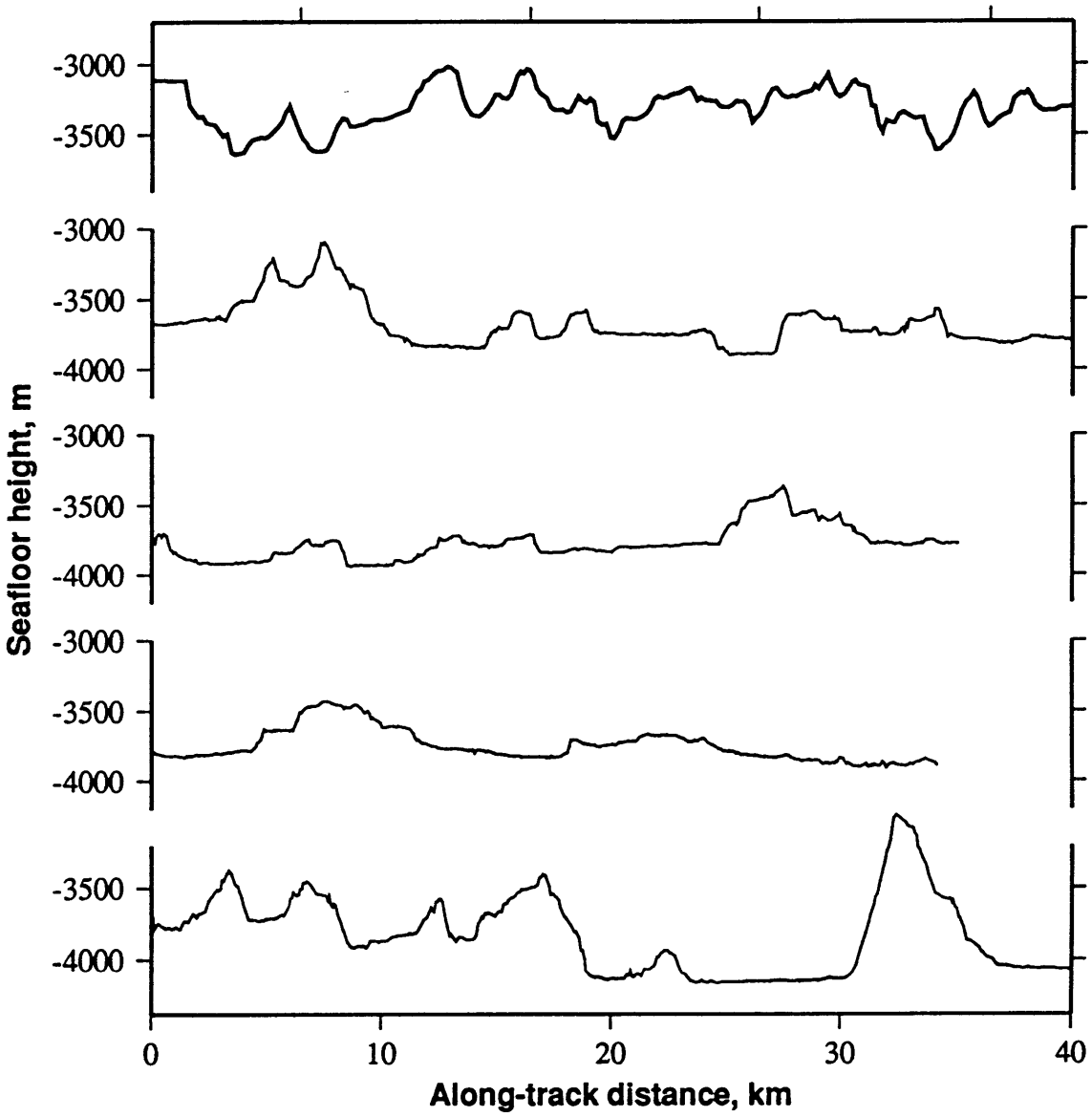

Fig. 5.10: Portions of along-track profiles for the five ship tracks which compose Rio Grande study area subregion R20. The uppermost, bold profile corresponds to segment Z3 in this chapter. Vertical exaggeration is 6:1.

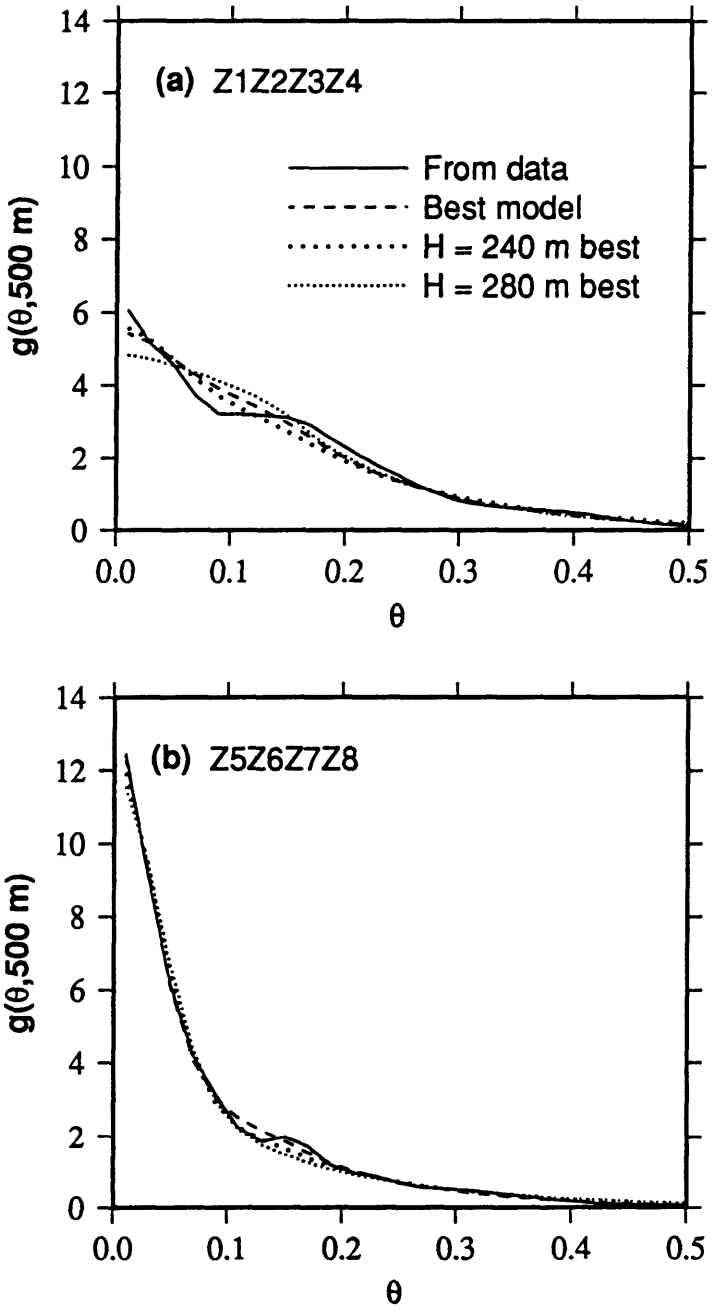

Fig. 5.11: Slope distribution functions computed from Angola Basin subregions (a) Z1Z2Z3Z4 and (b) Z5Z6Z7Z8 (solid lines), best-fitting models (dashed lines), models calculated when H is fixed at 240 m (large dotted line) and models calculated when H is fixed at 280 m (small dotted line).

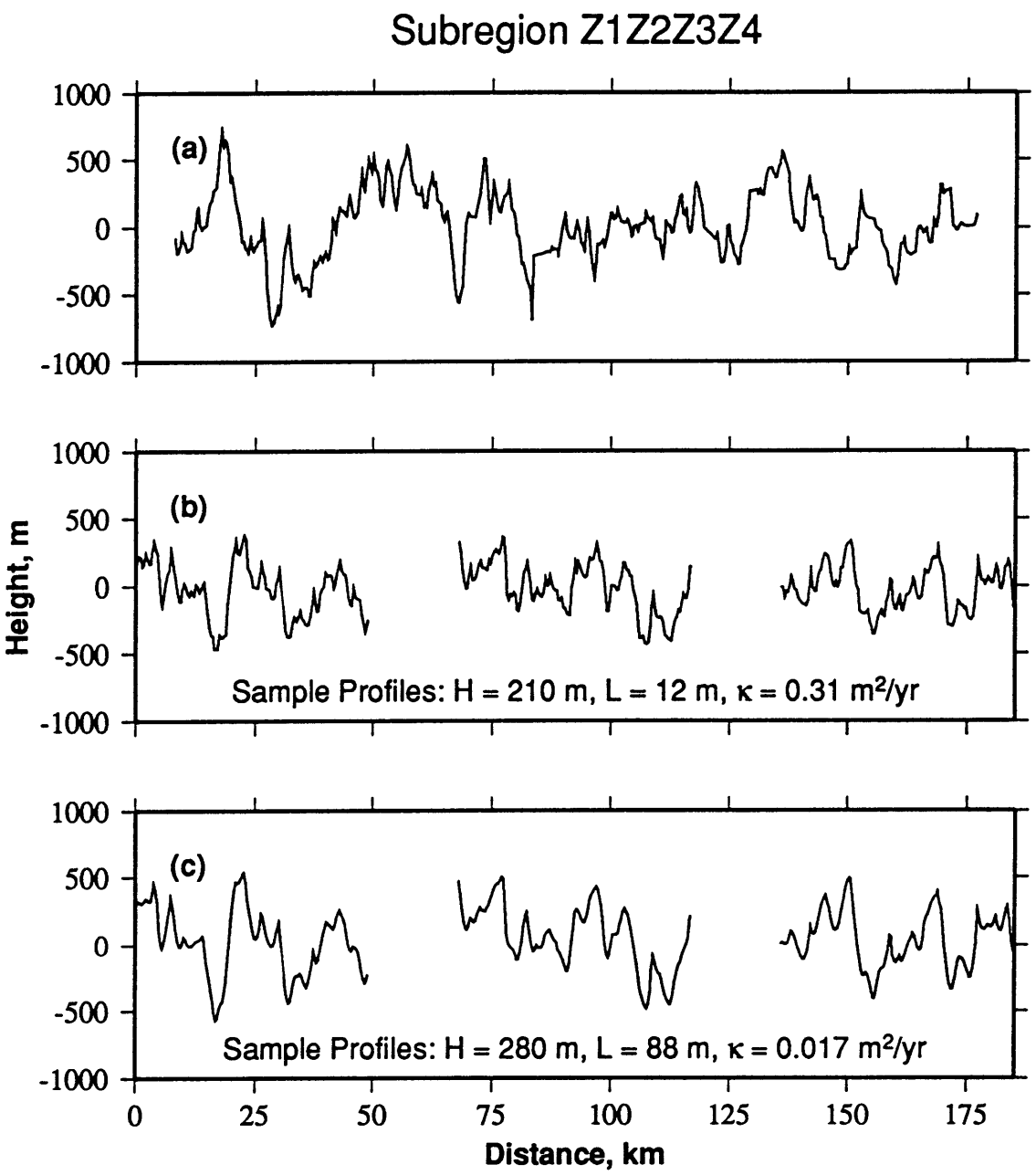

Fig. 5.12: (a) Angola basin trackline Z1Z2Z3Z4, after the subtraction of the best-fitting linear trend. (b) Sample tracklines through models generated using similar parameters to those listed for this subregion in Table 5.1 Models are smoothed to simulate the multibeam system which collected the data, and sampled at a spacing of 350 m. (c) Same as (b), using values of Table 5.2. Vertical exaggeration is 28:1.

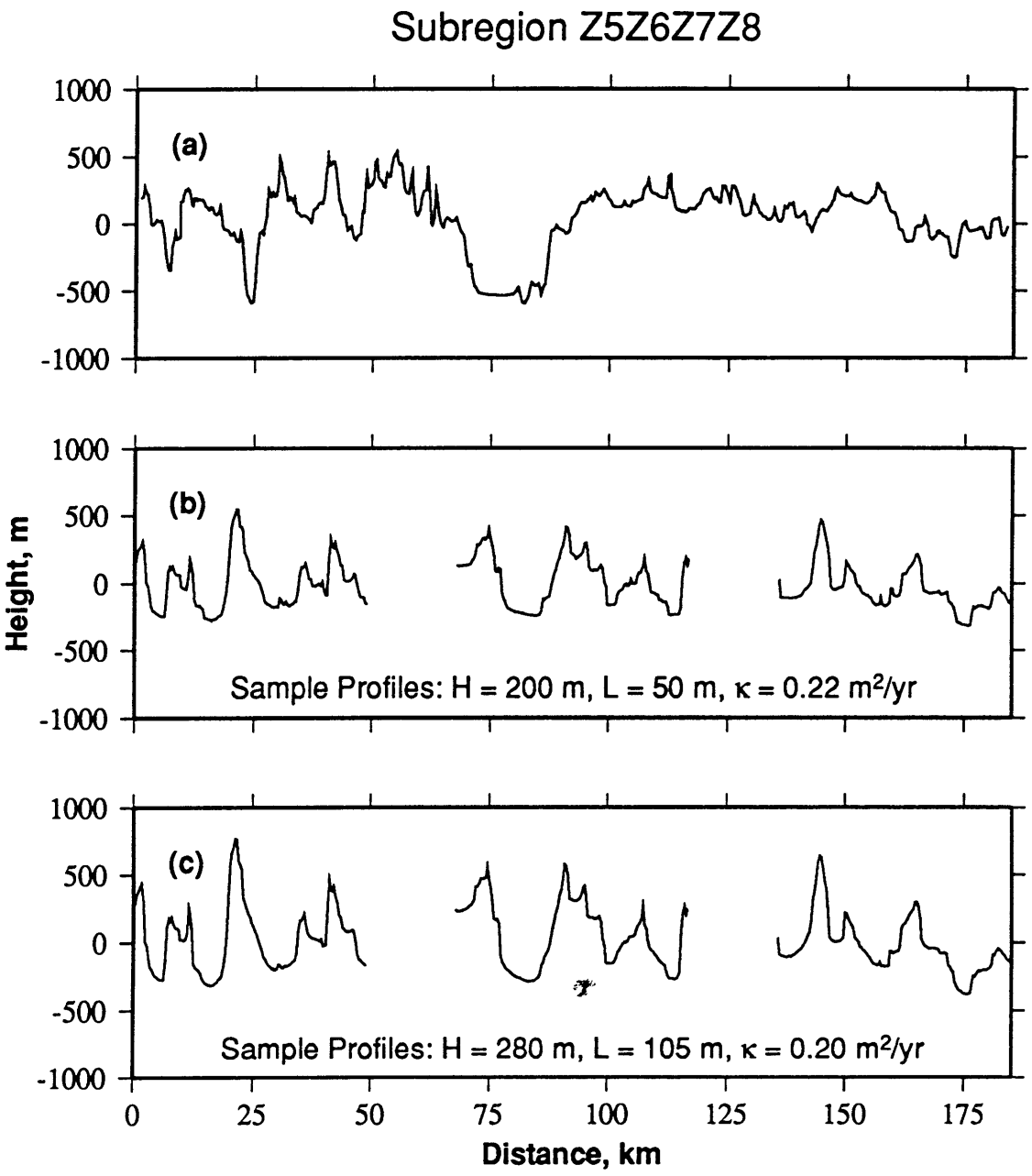

Fig. 5.13: (a) Angola basin trackline Z5Z6Z7Z8, after the subtraction of the best-fitting linear trend. (b) Sample tracklines through models generated using similar parameters to those listed for this subregion in Table 5.1 Models are smoothed to simulate the multibeam system which collected the data, and sampled at a spacing of 350 m. (c) Same as (b), using values of Table 5.2. Vertical exaggeration is 28:1.

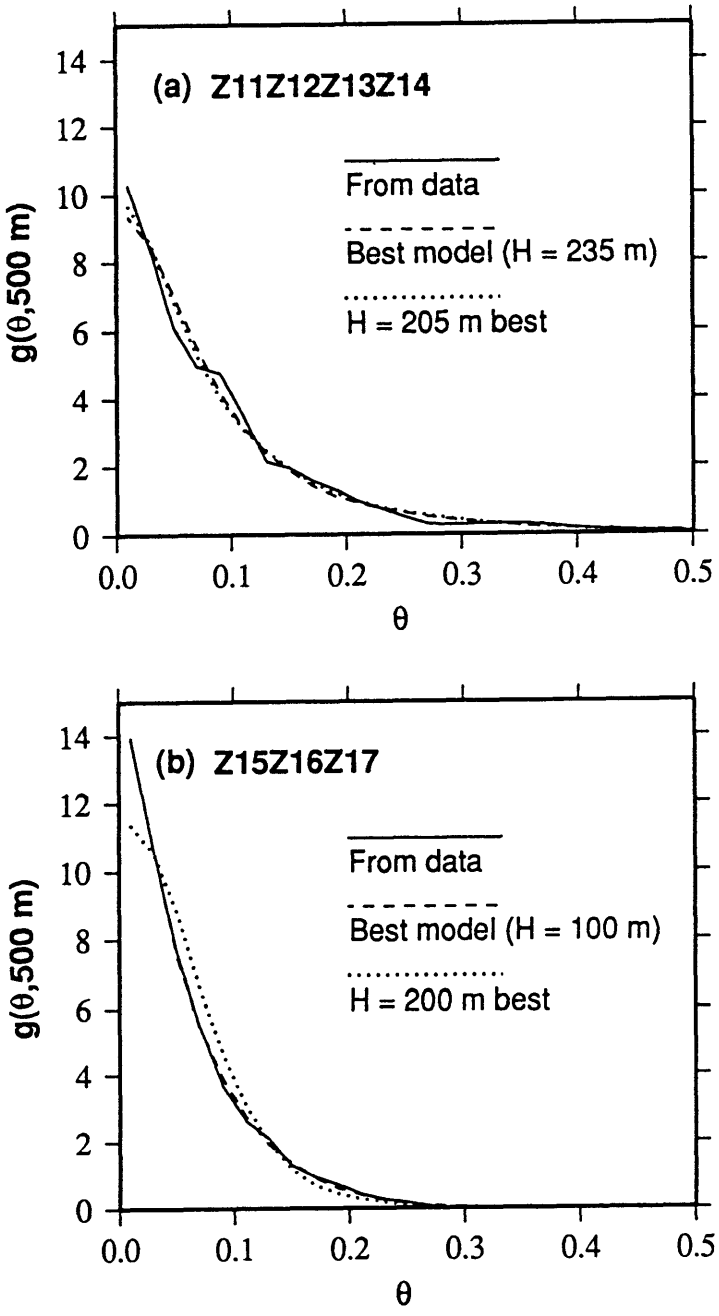

Fig. 5.14: Slope distribution functions computed from Angola Basin subregions (a) Z11Z12Z13Z14 and (b) Z15Z16Z17Z (solid lines), best-fitting models (dashed lines), and models calculated when H is fixed at values calculated using a scaled form of the relationship of *Malinverno* [1991] (equation (4.6)) (dotted line).

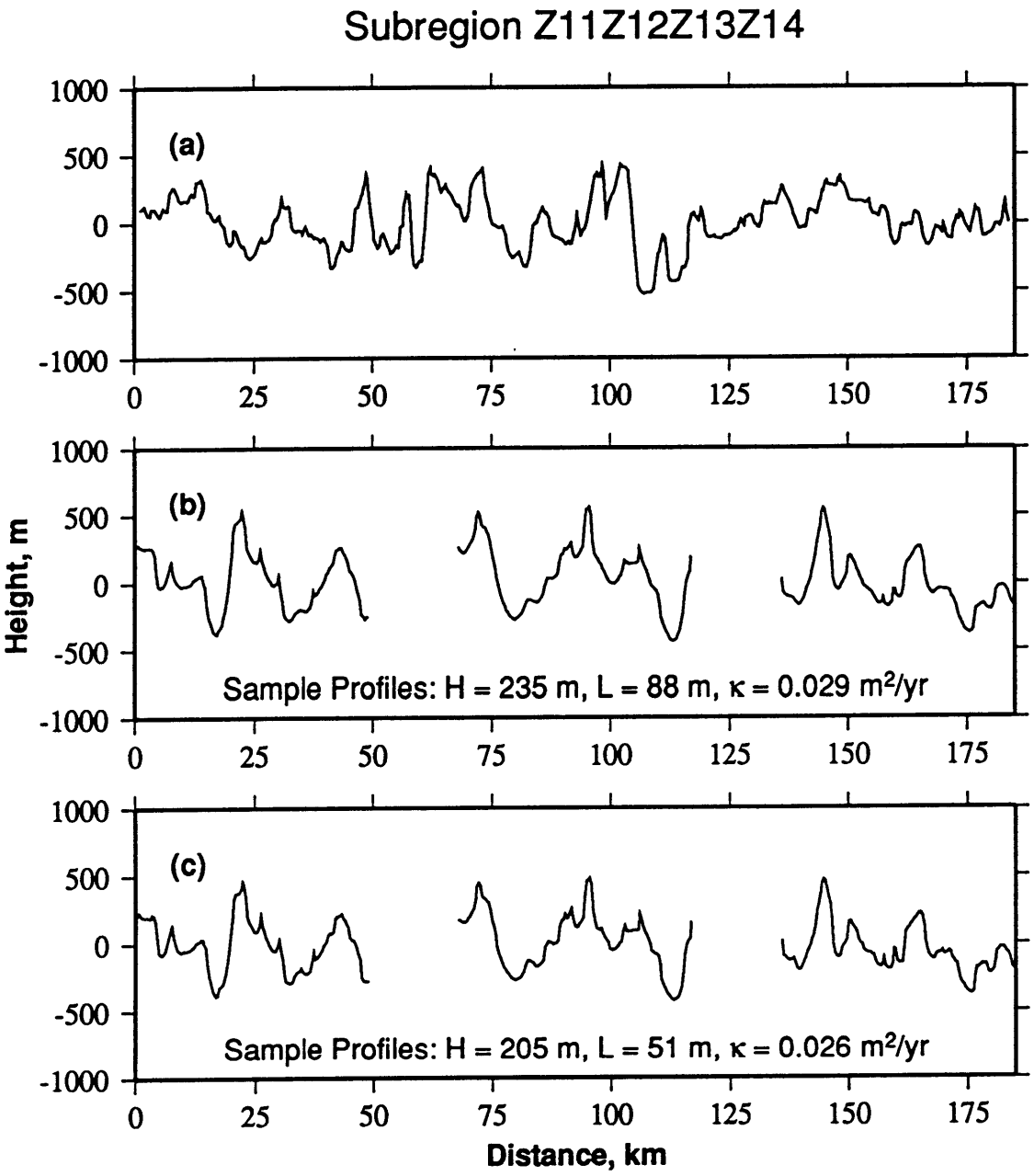

Fig. 5.15: (a) Angola basin trackline Z11Z12Z13Z14, after the subtraction of the best-fitting linear trend. (b) Sample tracklines through models generated using similar parameters to those listed for this subregion in Table 5.1 Models are smoothed to simulate the multibeam system which collected the data, and sampled at a spacing of 350 m. (c) Same as (b), using values of Table 5.3. Vertical exaggeration is 28:1.

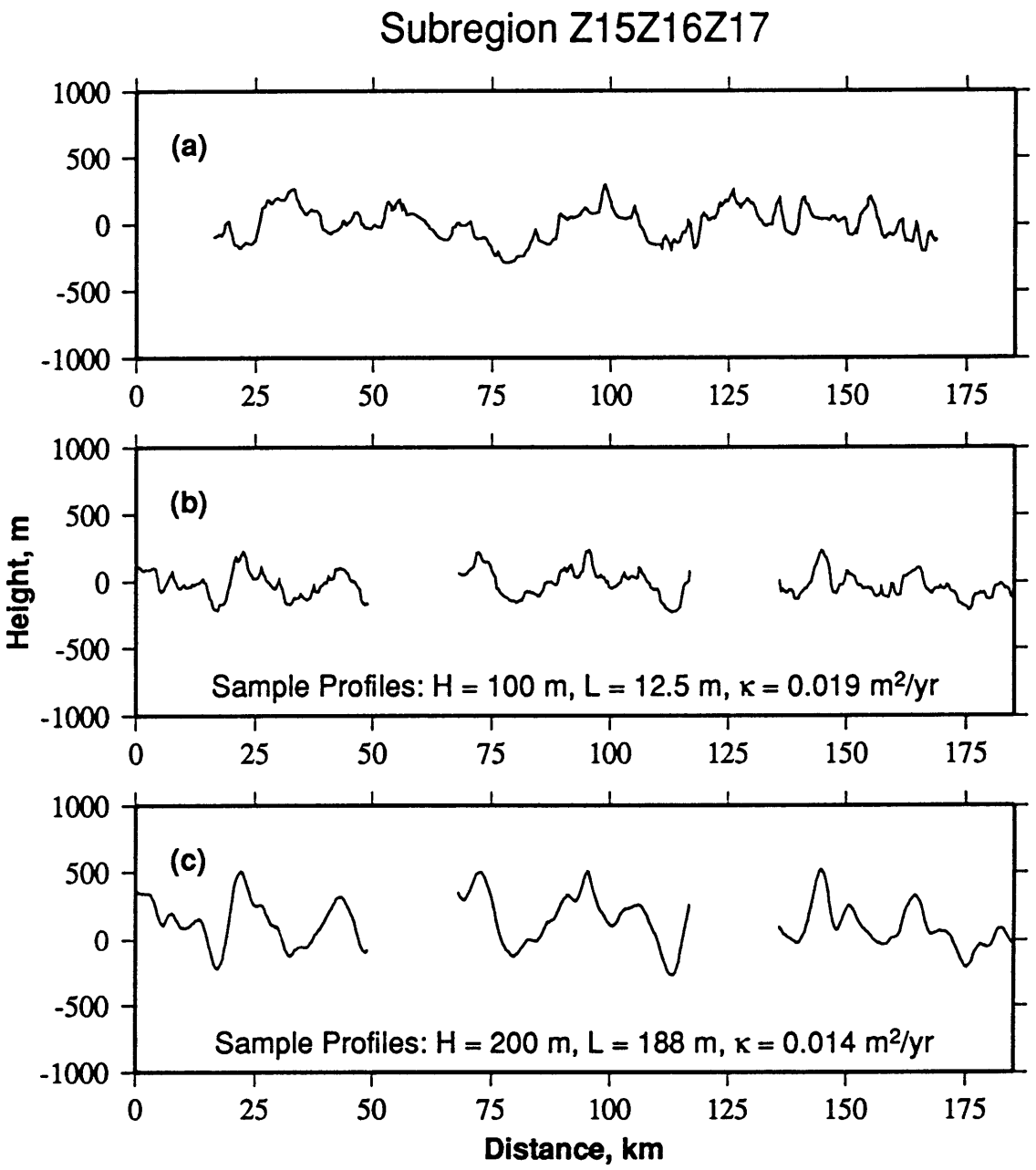

Fig. 5.16: Angola basin trackline Z15Z16Z17, after the subtraction of the best-fitting linear trend. (b) Sample tracklines through models generated using similar parameters to those listed for this subregion in Table 5.1 Models are smoothed to simulate the multibeam system which collected the data, and sampled at a spacing of 350 m. (c) Same as (b), using values of Table 5.3. Vertical exaggeration is 28:1.

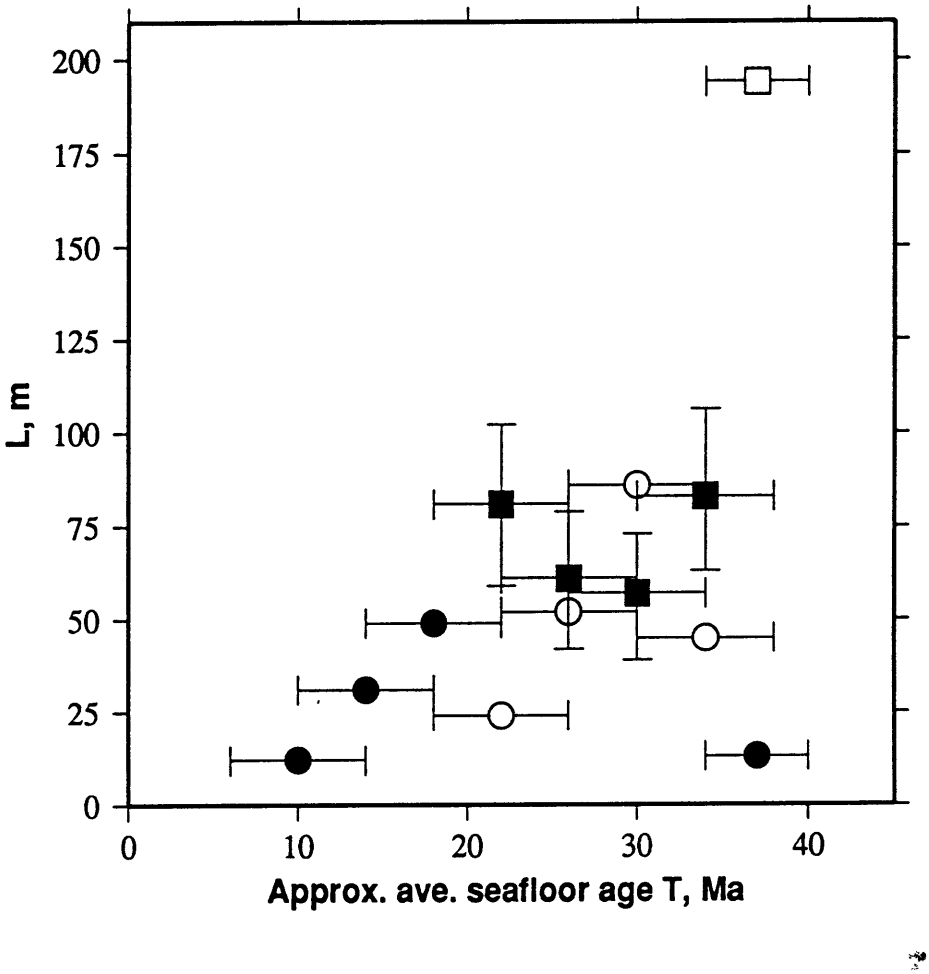

Fig. 5.17: Inverted values of L as a function of T for Angola Basin subregions. Circles represent values as given in Table 5.1, and squares represent values from Table 5.3. Black symbols represent our preferred inversion results for each subregion. Horizontal bars represent the age range of data incorporated in each subregion. Vertical bars are given for the four inversion results of Table 5.3 in which we have a reasonable amount of confidence. For the oldest seafloor considered, the great difference between L as given in Table 5.1 and Table 5.3 causes us to have little confidence in either value, although forward modeling results as shown in Fig. 5.16 seem to indicate that L is relatively low for this region.

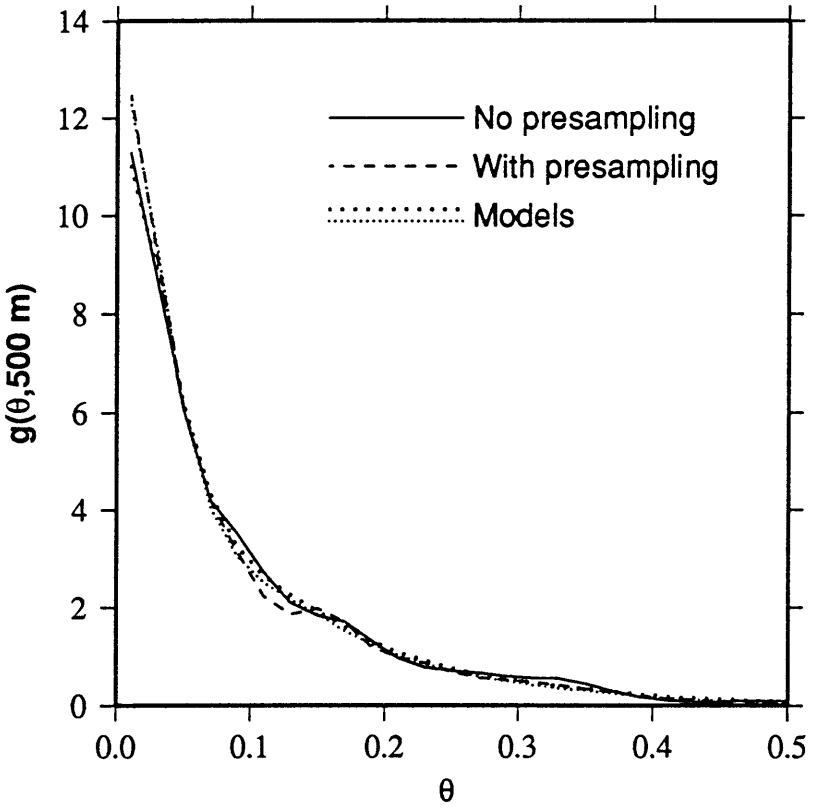

Fig. 5.18: Comparison of slope distribution functions for subregion Z5Z6Z7Z8 generated before (solid line) and after (dashed line) data presampling, and best-fitting model slope distribution functions (dotted lines).

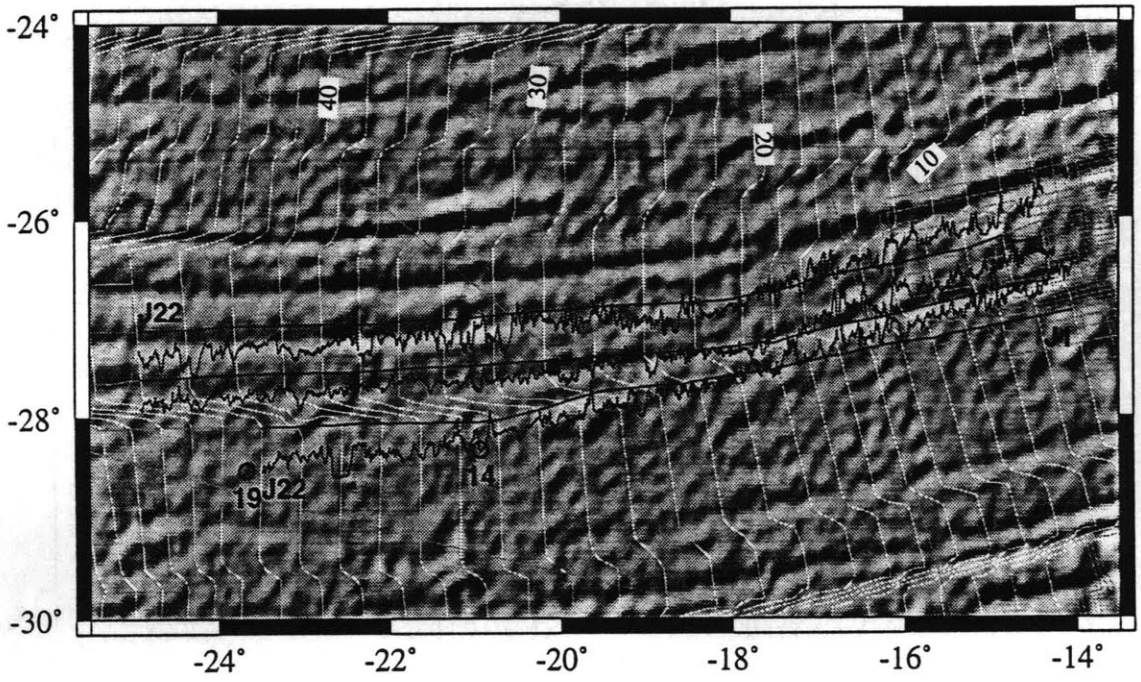

Fig. 5.19: Gray-shaded gravity anomaly map of the western flank of the MAR in the vicinity of the Brazil Basin tracklines and local DSDP drill sites. White ridge-parallel lines correspond to isochrons of 2 m.y. [*Müller et al.*, 1993]. Bathymetry along ship tracks is plotted about a 4000 m mean, with a horizontal scale of 5000 m per inch. Terminal segments J1 and J22 span 2-m.y. lengths of each trackline, as labeled. The remaining segments are associated with 2-m.y. lengths of seafloor between J1 and J22.

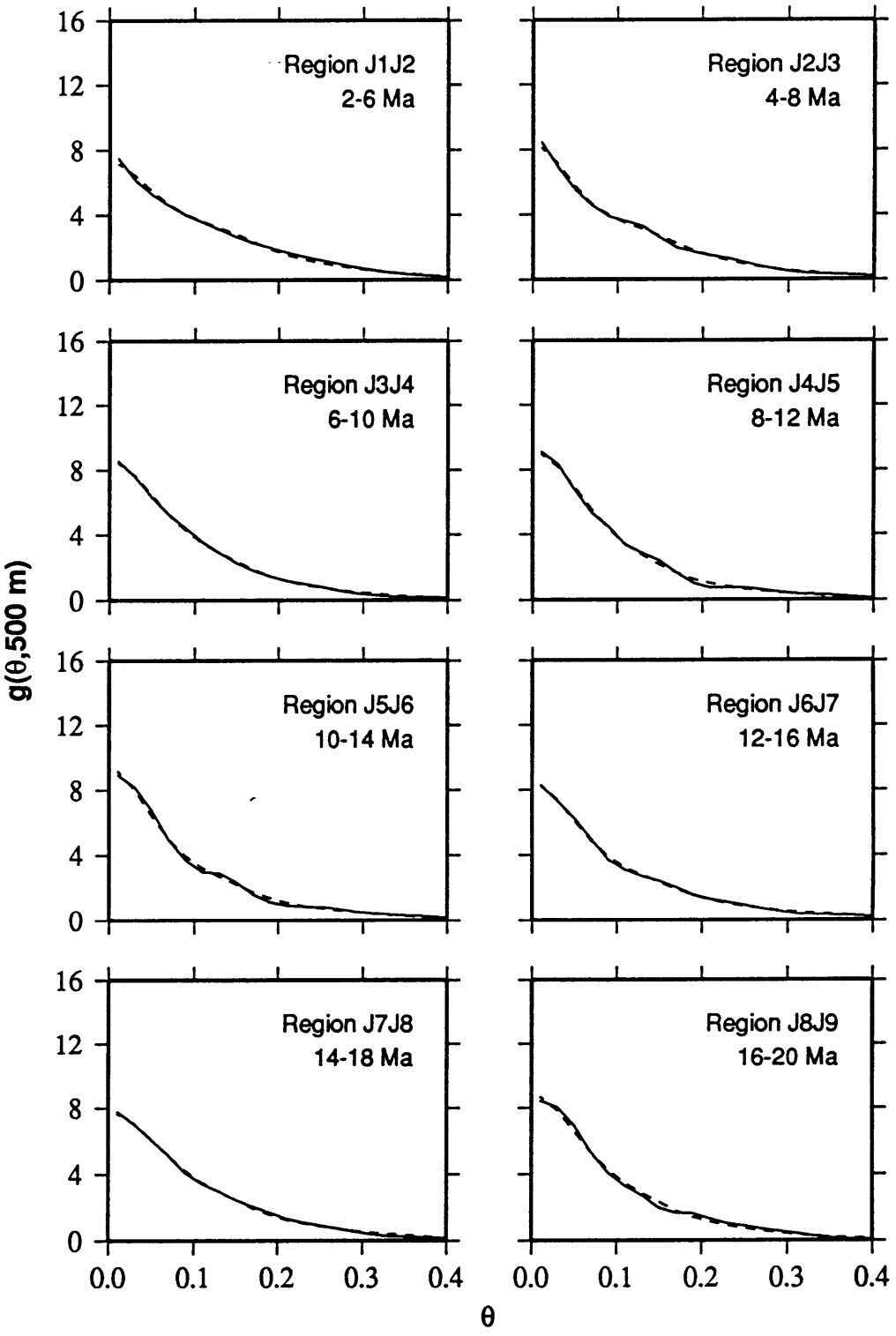

Fig. 5.20: Slope distribution functions computed from subregions in the Brazil Basin (solid lines) and from best-fitting models (dashed lines), as labeled.

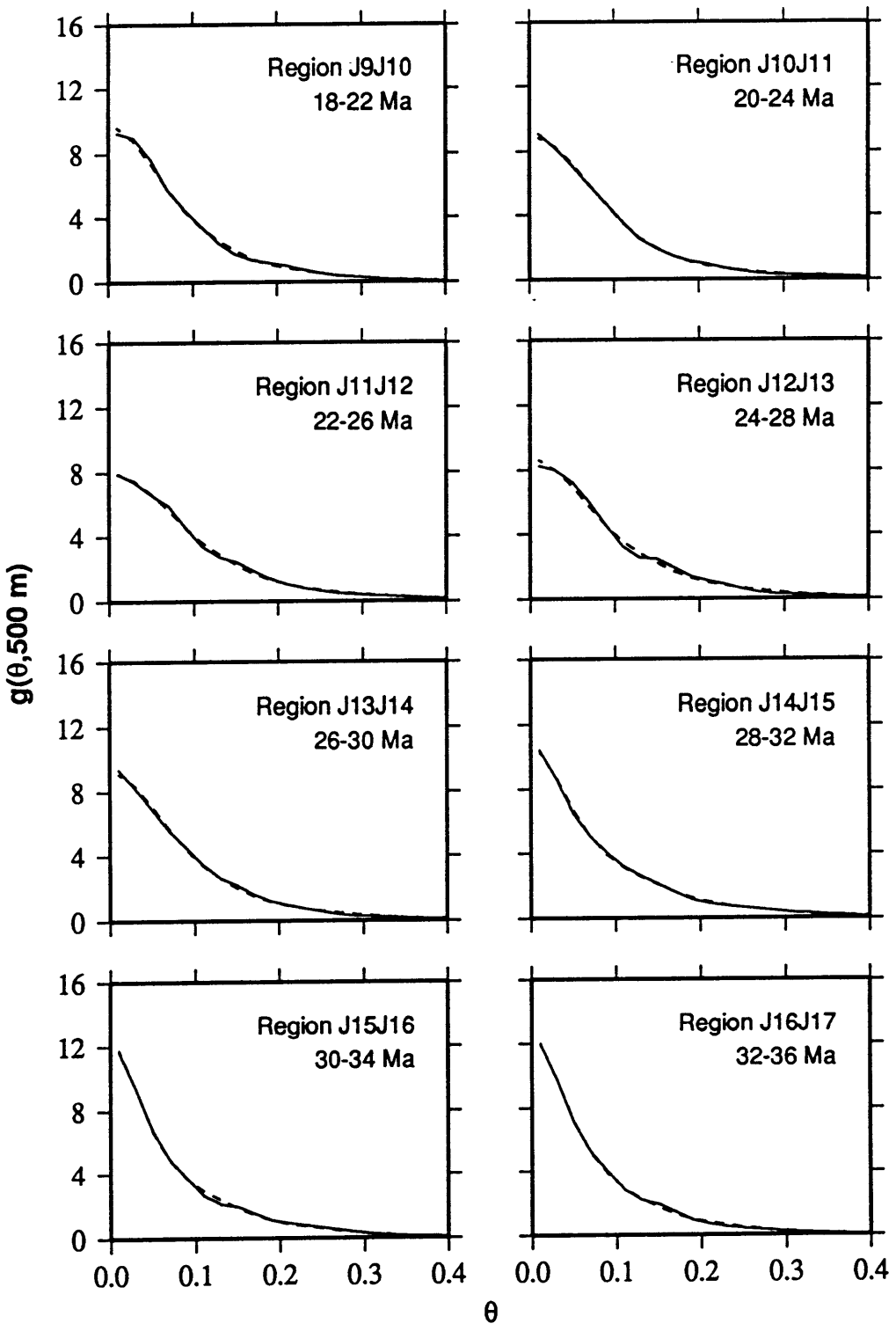
Region J9J10
18-22 Ma
Region J10J11
20-24 Ma
Region J11J12
22-26 Ma
Region J12J13
24-28 Ma
Region J13J14
26-30 Ma
Region J14J15
28-32 Ma
Region J15J16
30-34 Ma
Region J16J17
32-36 Ma
g(θ,500 m)
θ
0
4
8
12
16
0.0
0.1
0.2
0.3
0.4

Fig. 5.20 cont.

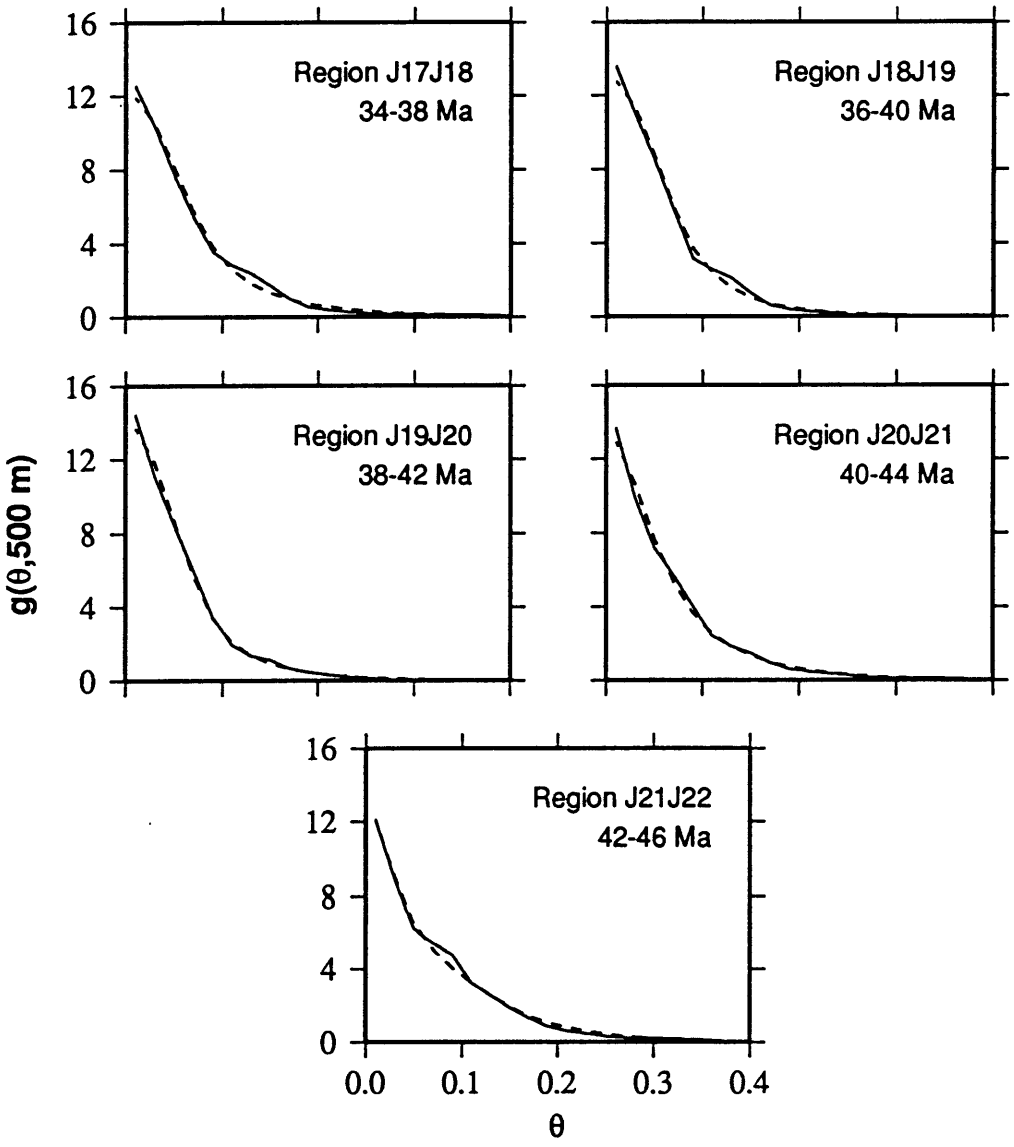
Region J17J18
34-38 Ma
Region J18J19
36-40 Ma
Region J19J20
38-42 Ma
Region J20J21
40-44 Ma
Region J21J22
42-46 Ma
g(θ,500 m)
θ
0
4
8
12
16
0.0
0.1
0.2
0.3
0.4

Fig. 5.20 cont.

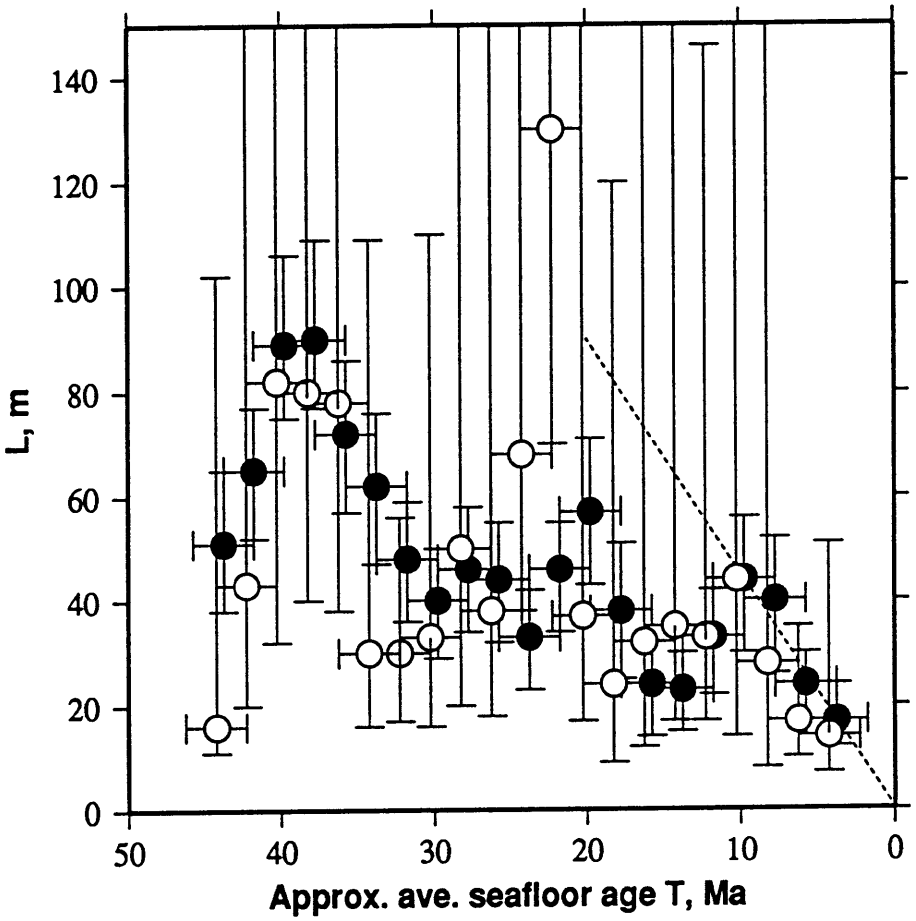

Fig. 5.21: Inverted values of L as a function of T for Brazil Basin subregions. Clear circles represent values as given in Table 5.4, and black circles represent values from Table 5.5, in which we have greater confidence. Horizontal bars represent the age range of data incorporated in each subregion. Vertical bars represent the 95% confidence bounds. Dashed line corresponds to a constant accumulation rate of 4.5 m/m.y.

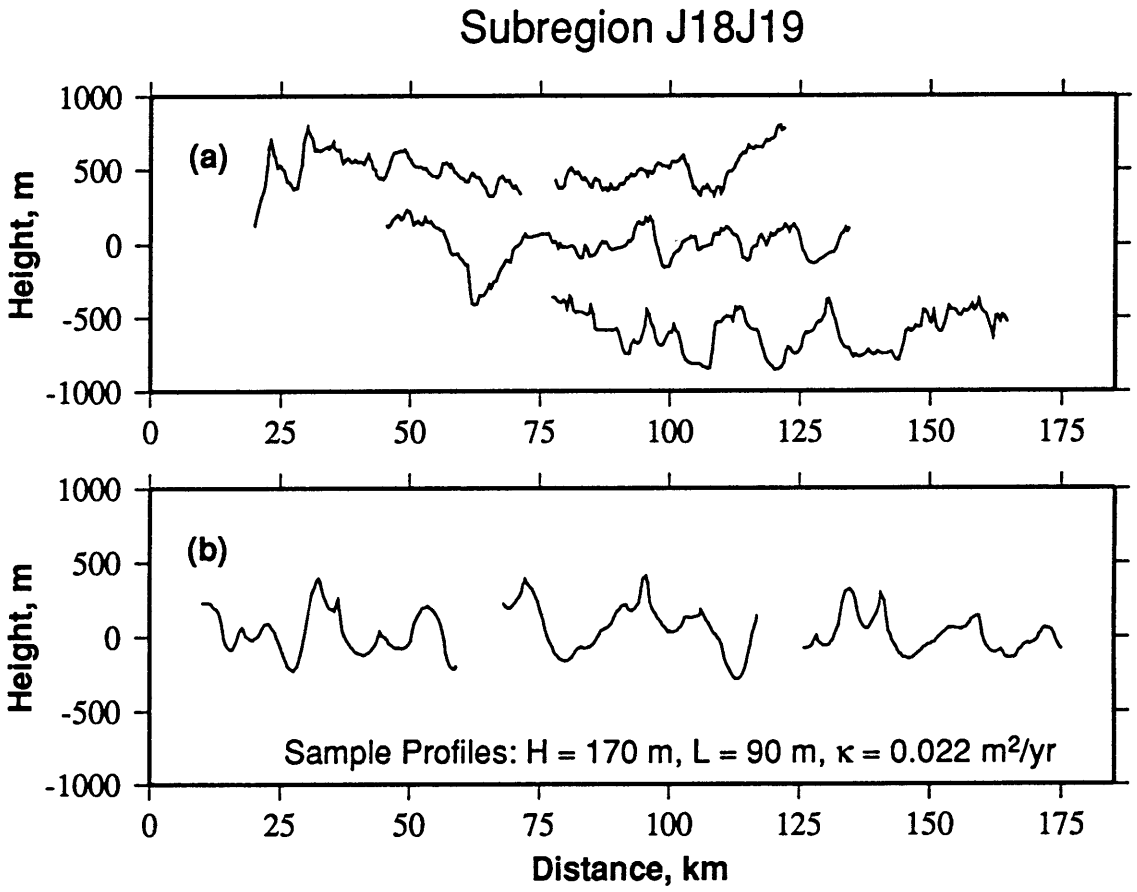

Fig. 5.22: (a) Tracklines forming Brazil Basin subregion J18J19, after the subtraction of the best-fitting linear trends. (b) Sample tracklines through models generated using similar parameters to those listed for this subregion in Table 5.5. Models are smoothed to simulate the multibeam system which collected the data, and sampled at a spacing of 350 m. Vertical exaggeration is 28:1.

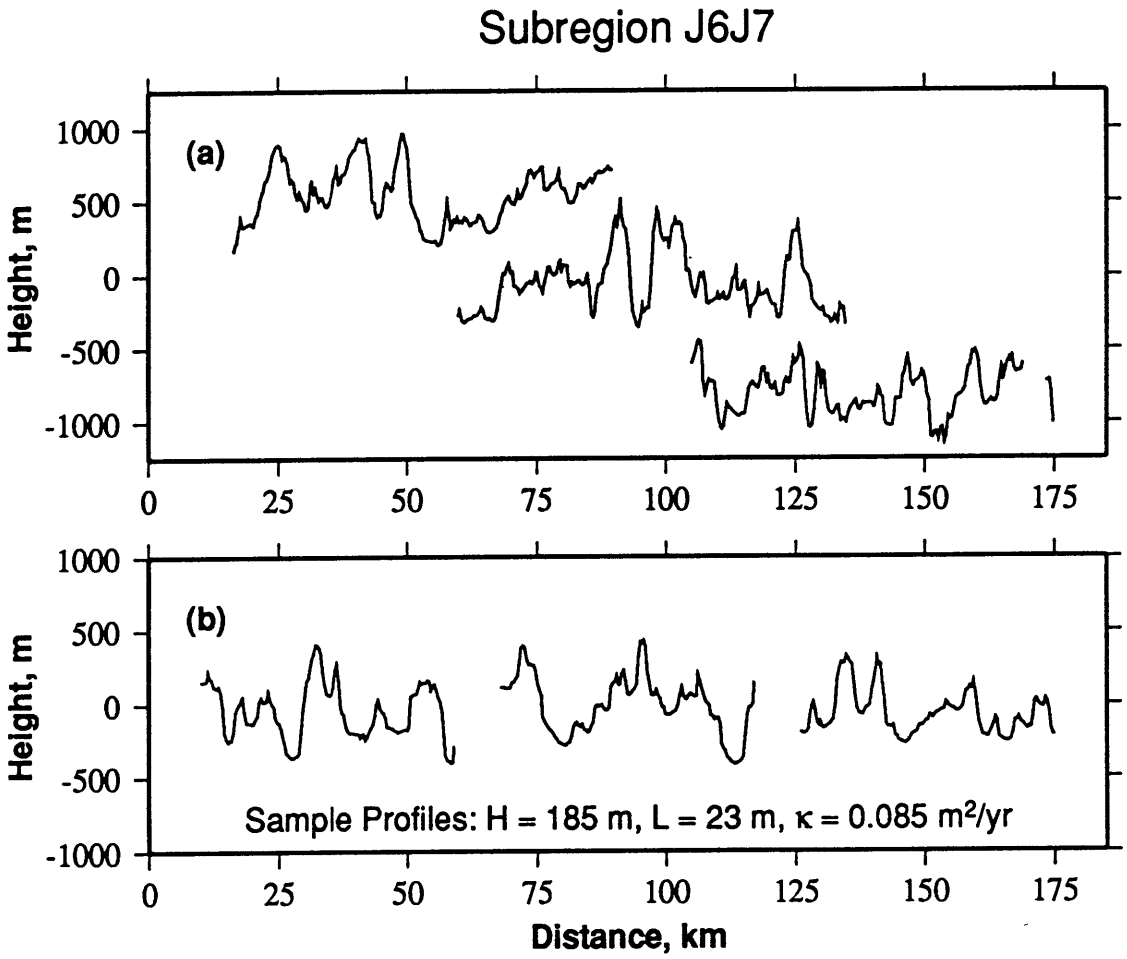

Fig. 5.23: (a) Tracklines forming Brazil Basin subregion J6J7, after the subtraction of the best-fitting linear trends. (b) Sample tracklines through models generated using similar parameters to those listed for this subregion in Table 5.5 Models are smoothed to simulate the multibeam system which collected the data, and sampled at a spacing of 350 m. Vertical exaggeration is 28:1.

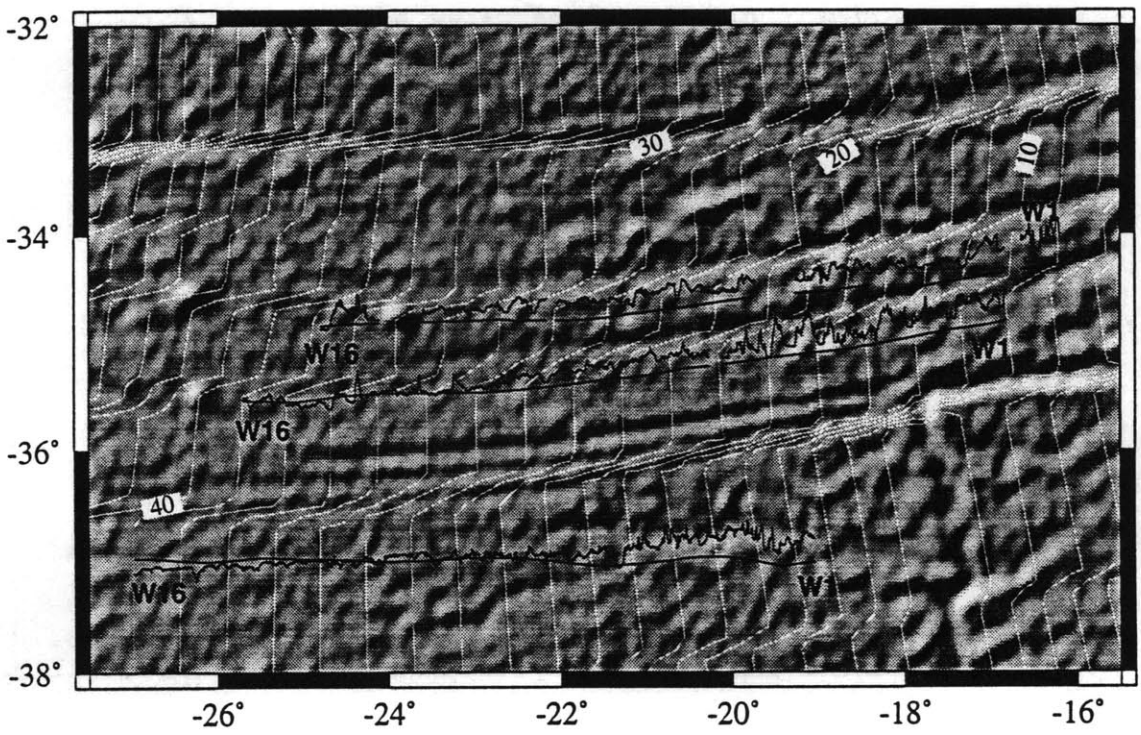

Fig. 5.24: Gray-shaded gravity anomaly map of the western flank of the MAR in the vicinity of the Argentine Basin tracklines. White ridge-parallel lines correspond to isochrons of 2 m.y. [*Müller et al.*, 1993]. Bathymetry along ship tracks is plotted about a 4000 m mean, with a horizontal scale of 5000 m per inch. Terminal segments W1 and W16 span 2-m.y. lengths of each trackline, as labeled. The remaining segments are associated with 2-m.y. lengths of seafloor between W1 and W16 segments.

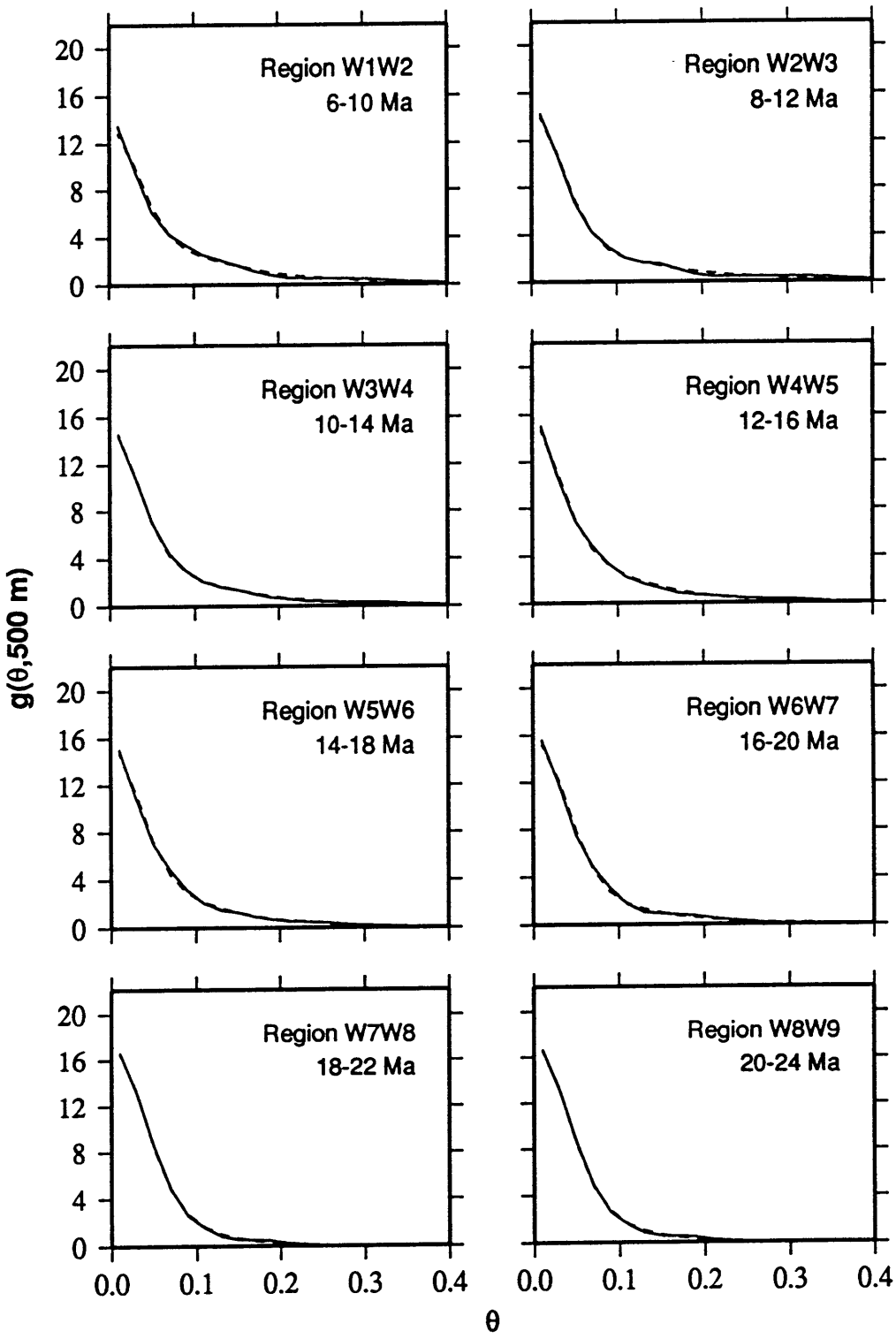

Fig. 5.25: Slope distribution functions computed from subregions in the Argentine Basin (solid lines) and from best-fitting models (dashed lines), as labeled.

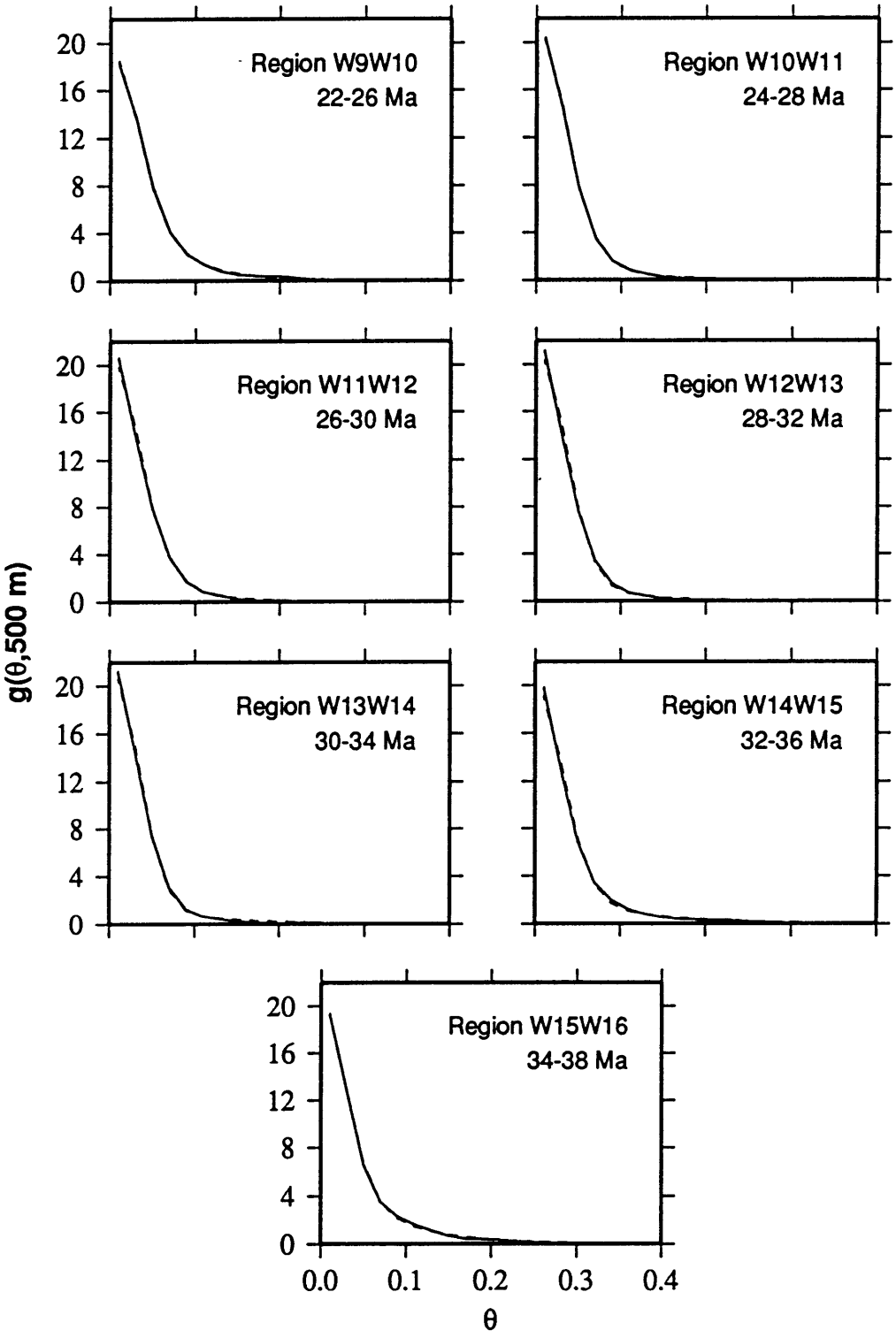
Region W9W10
22-26 Ma
Region W10W11
24-28 Ma
Region W11W12
26-30 Ma
Region W12W13
28-32 Ma
Region W13W14
30-34 Ma
Region W14W15
32-36 Ma
Region W15W16
34-38 Ma
g(θ,500 m)
θ
0
4
8
12
16
20
0.0
0.1
0.2
0.3
0.4

Fig. 5.25 cont.

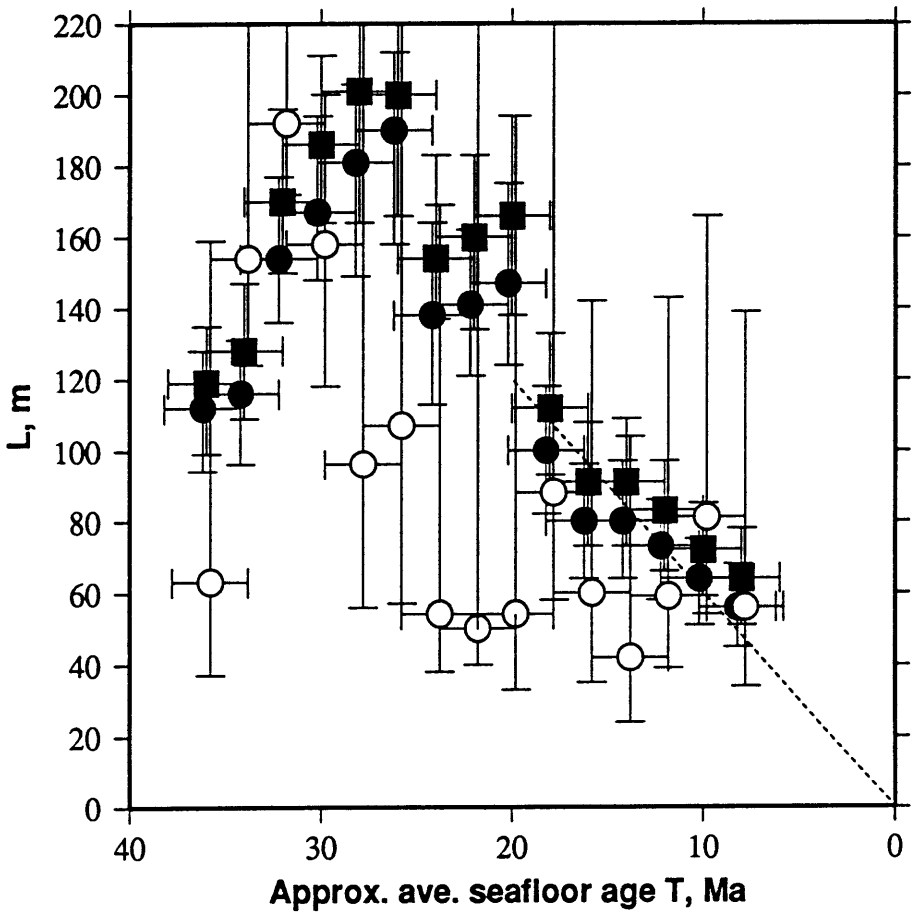

Fig. 5.26: Inverted values of L as a function of T for Argentine Basin subregions. Clear circles represent values as given in Table 5.6, black squares represent values from Table 5.7, and black circles represent values from Table 5.8. Horizontal bars represent the age range of data incorporated in each subregion. Vertical bars represent the 95% confidence bounds. Dashed line corresponds to a constant accumulation rate of 6 m/m.y.

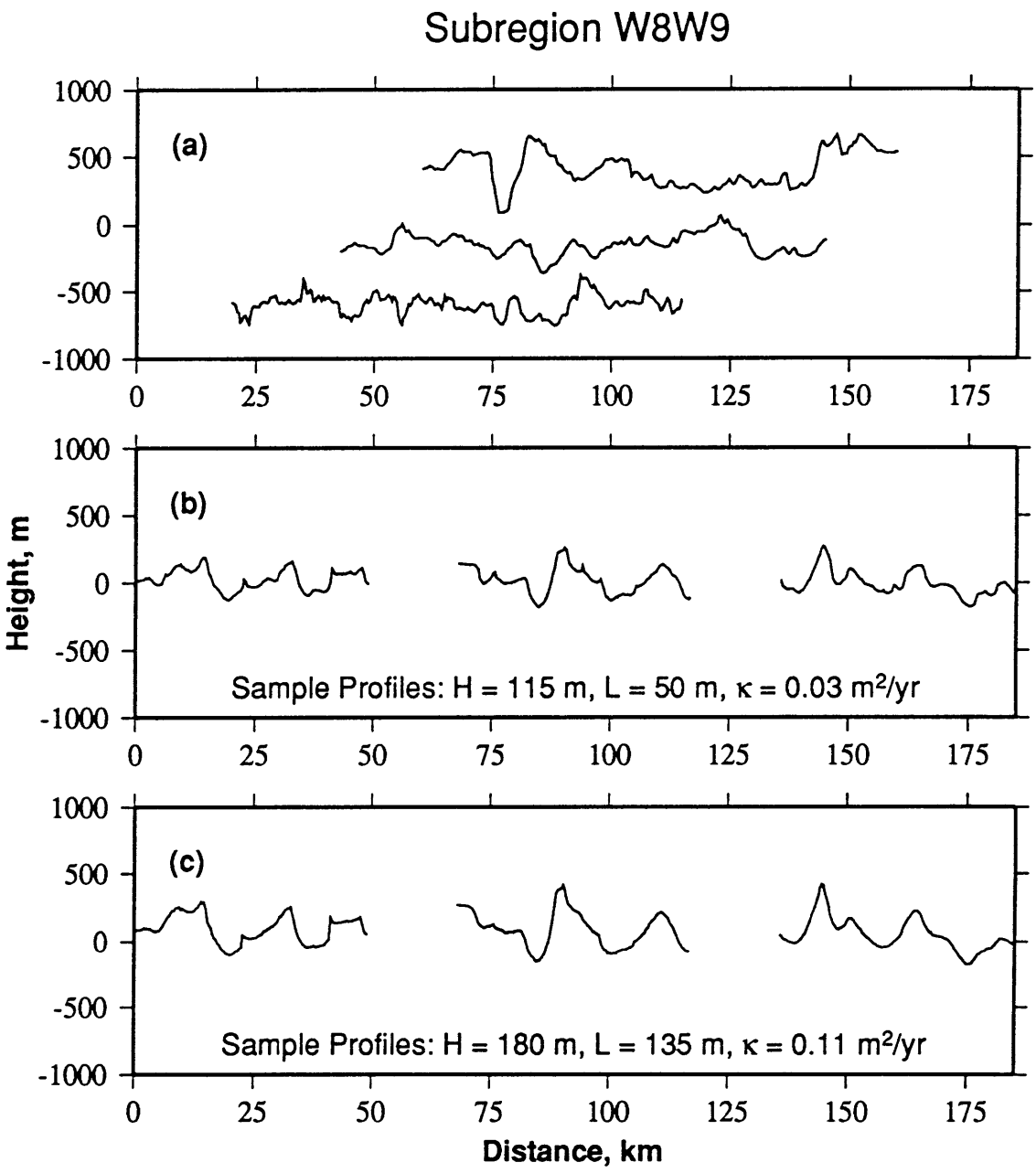

Fig. 5.27: (a) Tracklines forming Argentine Basin subregion W8W9, after the subtraction of the best-fitting linear trends. (b) Sample tracklines through models generated using similar parameters to those listed for this subregion in Table 5.6. Models are smoothed to simulate the multibeam system which collected the data, and sampled at a spacing of 350 m. (c) Same as (b), for values in Table 5.8. Vertical exaggeration is 28:1.

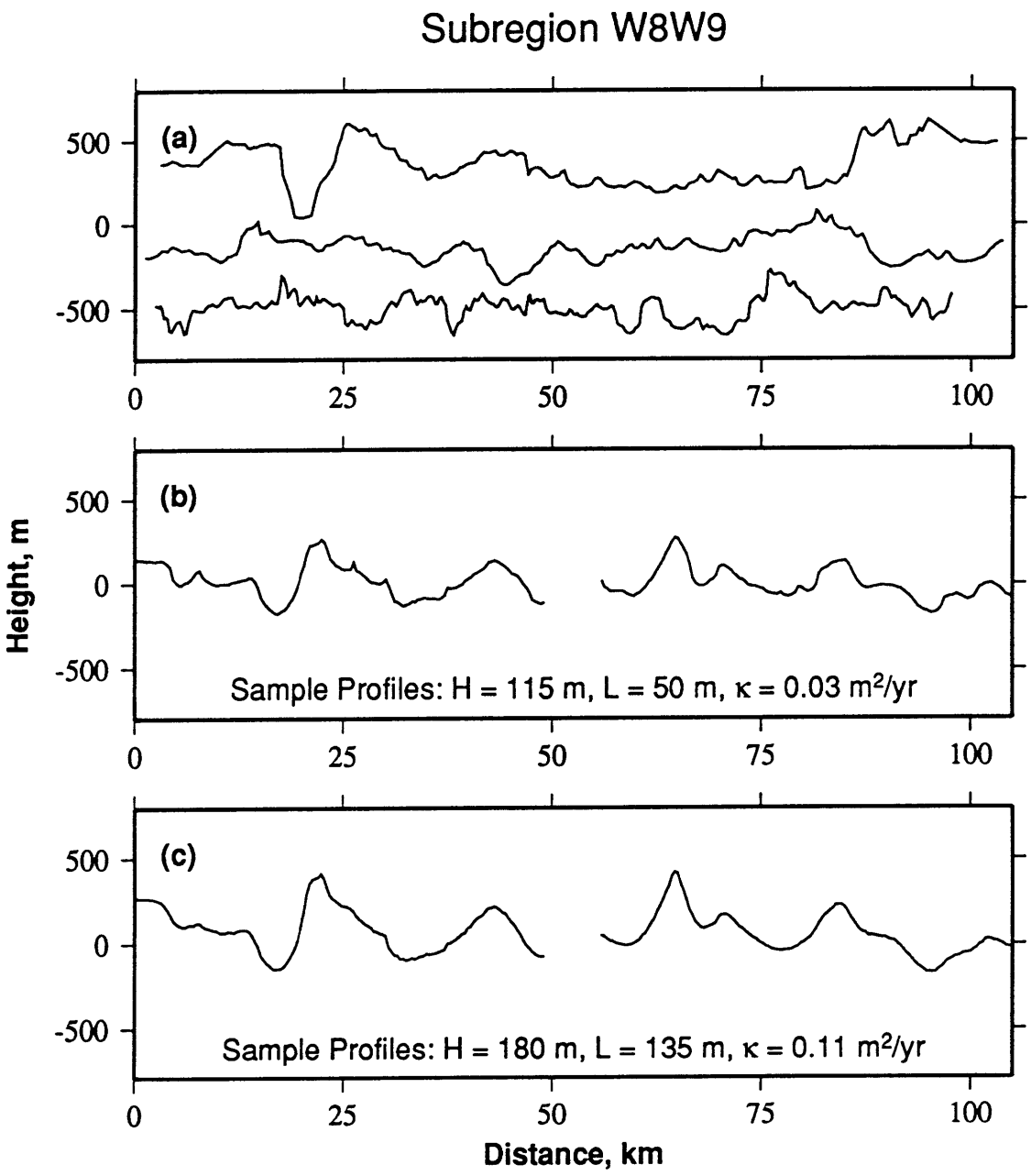

Fig. 5.28: Enlargement of 5.27. Vertical exaggeration is 20:1.

Fig. 5.29: Inverted values of L as a function of T from this chapter and Chapter 4, and depth to basement at nearby DSDP sites. Horizontal bars represent the age range of data incorporated in each subregion. (a) Results from Brazil Basin subregions and western Rio Grande subregions of Chapter 4. Clear circles represent values as given in Table 5.4, and black circles represent values from Table 5.5, in which we have greater confidence. Clear squares represent values from western subregions listed in Chapter 4 Table 4.1, for which H is free to vary, and gray squares represent values from these regions when H is fixed according to seafloor type, as in Table 4.3. (b) Results from Angola Basin subregions and eastern Rio Grande subregions of Chapter 4. Clear circles represent values as given in Table 5.1, and black circles represent values from Table 5.3, in which H is fixed prior to inversion for L and κ (omitting the value from the easternmost region). Clear squares represent values from western subregions listed in Chapter 4 Table 4.1, for which H is free to vary, and gray squares represent values from these regions when H is fixed according to seafloor type, as in Table 4.3. (c) Inverted values of L as a function of T for Argentine Basin subregions and western Cox subregions of Chapter 4. Clear circles represent values as given in Table 5.6, gray circles represent values from Table 5.7, and black circles represent values from Table 5.8. Clear squares represent values from western subregions listed in Chapter 4 Table 4.4, for which H is free to vary, and gray squares represent values from these regions when H is fixed according to seafloor type, as in Table 4.5. The paleoceanographic implications of the inversion results presented in this figure are discussed in Chapter 6.

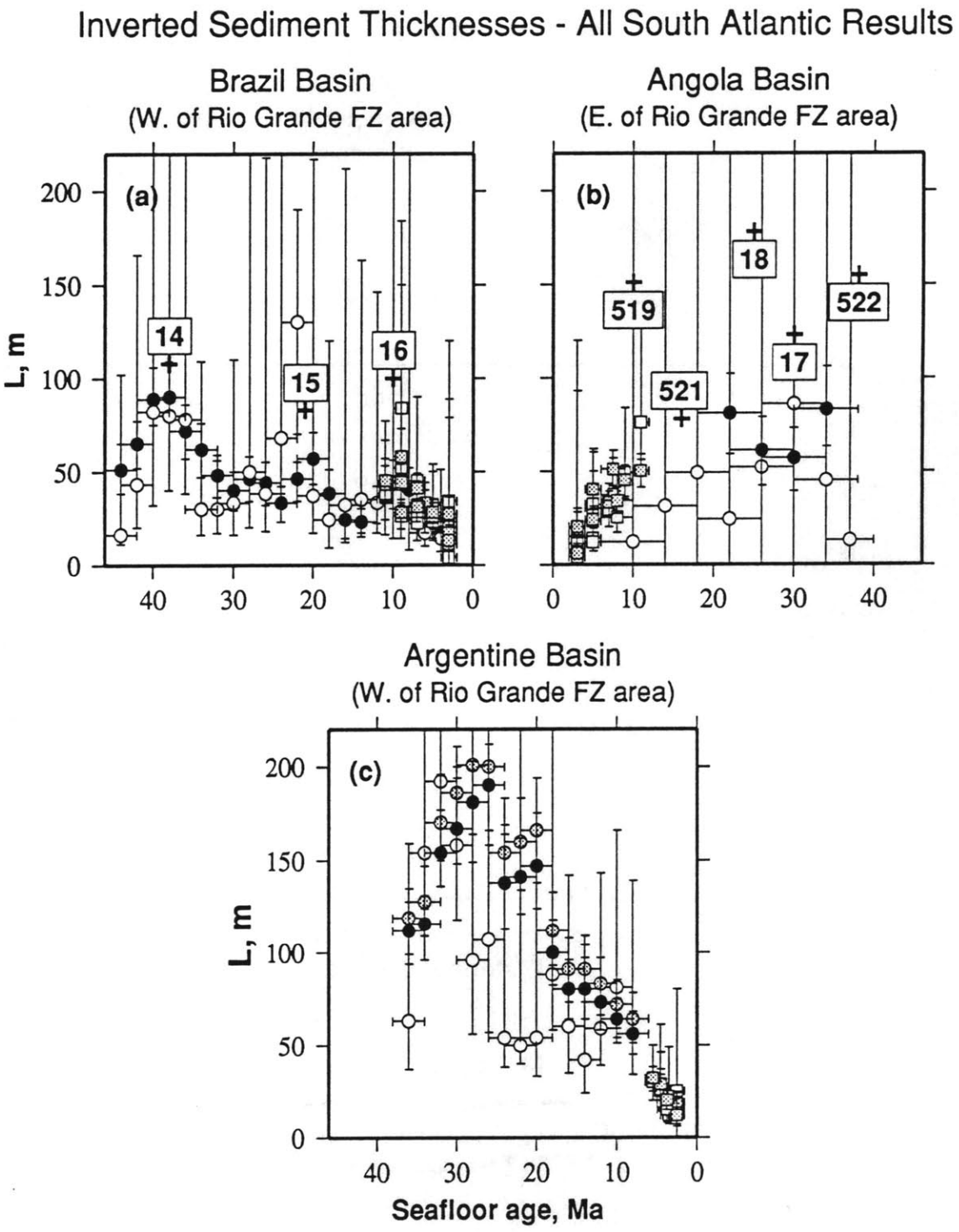
Inverted Sediment Thicknesses - All South Atlantic Results
Brazil Basin
(W. of Rio Grande FZ area)
Angola Basin
(E. of Rio Grande FZ area)
Argentine Basin
(W. of Rio Grande FZ area)
(a)
(b)
(c)
14
15
16
519
521
18
17
522
L, m
Seafloor age, Ma
0
50
100
150
200
40
30
20
10
0

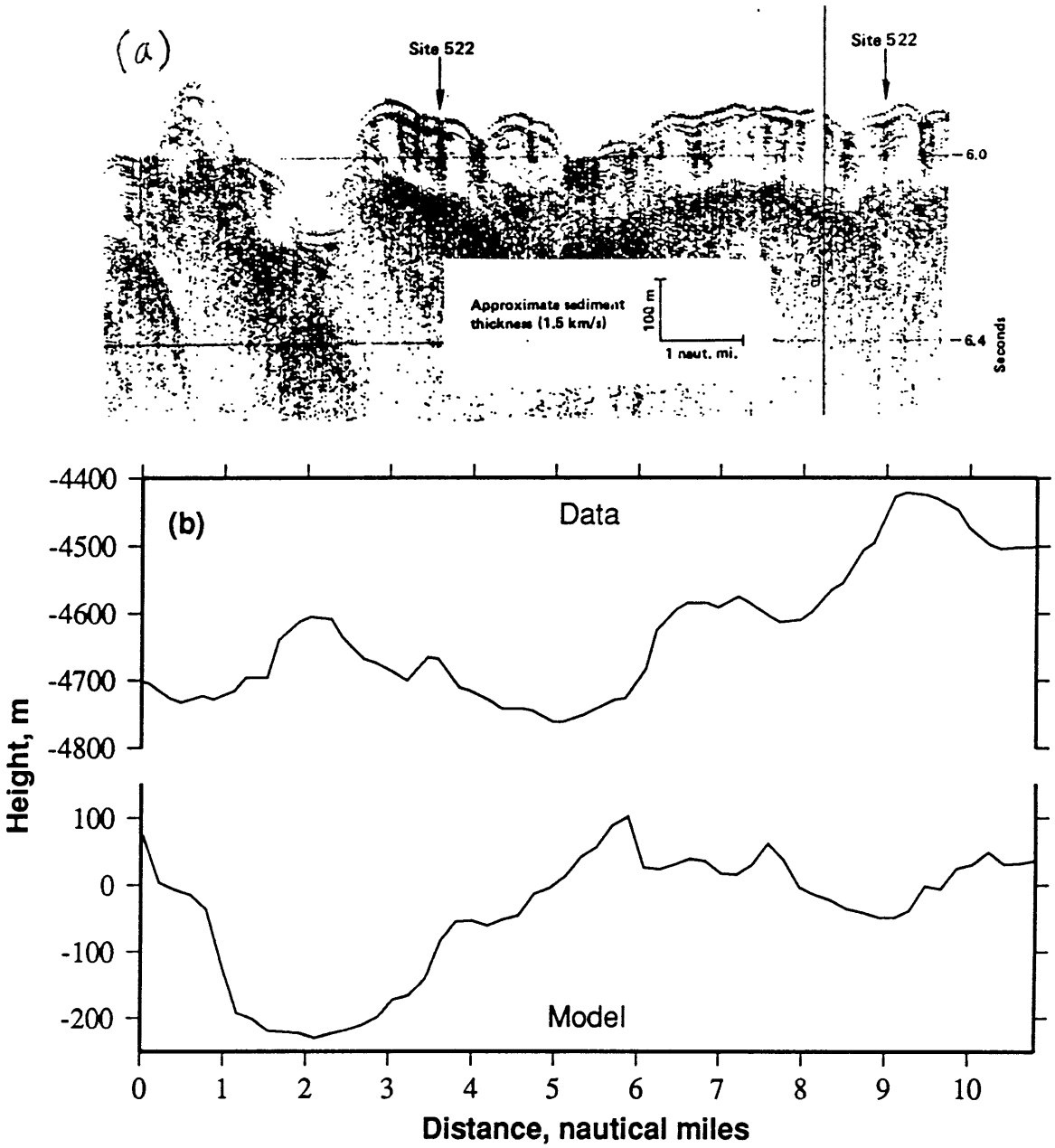

Fig. 5.30: SCS data collected near DSDP Site 522 (a) and portions of segment Z15 (b) which crosses same-age seafloor several hundred kilometers to the northwest, shown at the same scale. Vertical exaggeration is 15:1.

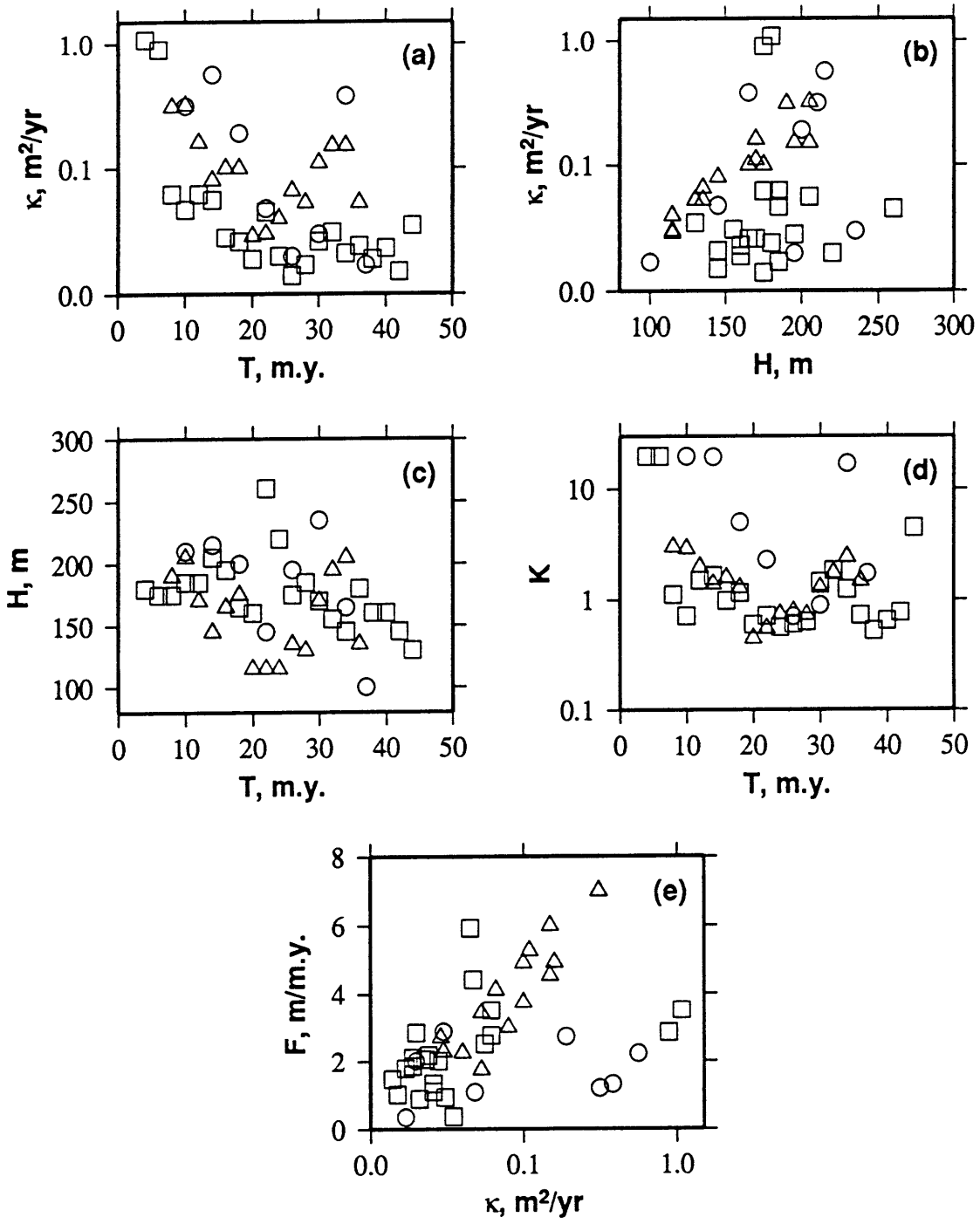

Fig. 5.31: Relationships between inverted parameters (κ, L, H), calculated parameters (F and K) and seafloor age T, for Angola Basin (circles), Brazil Basin (squares) and Argentine Basin (triangles) subregions, as labeled, as obtained when all κ, L, and H are all allowed to vary.

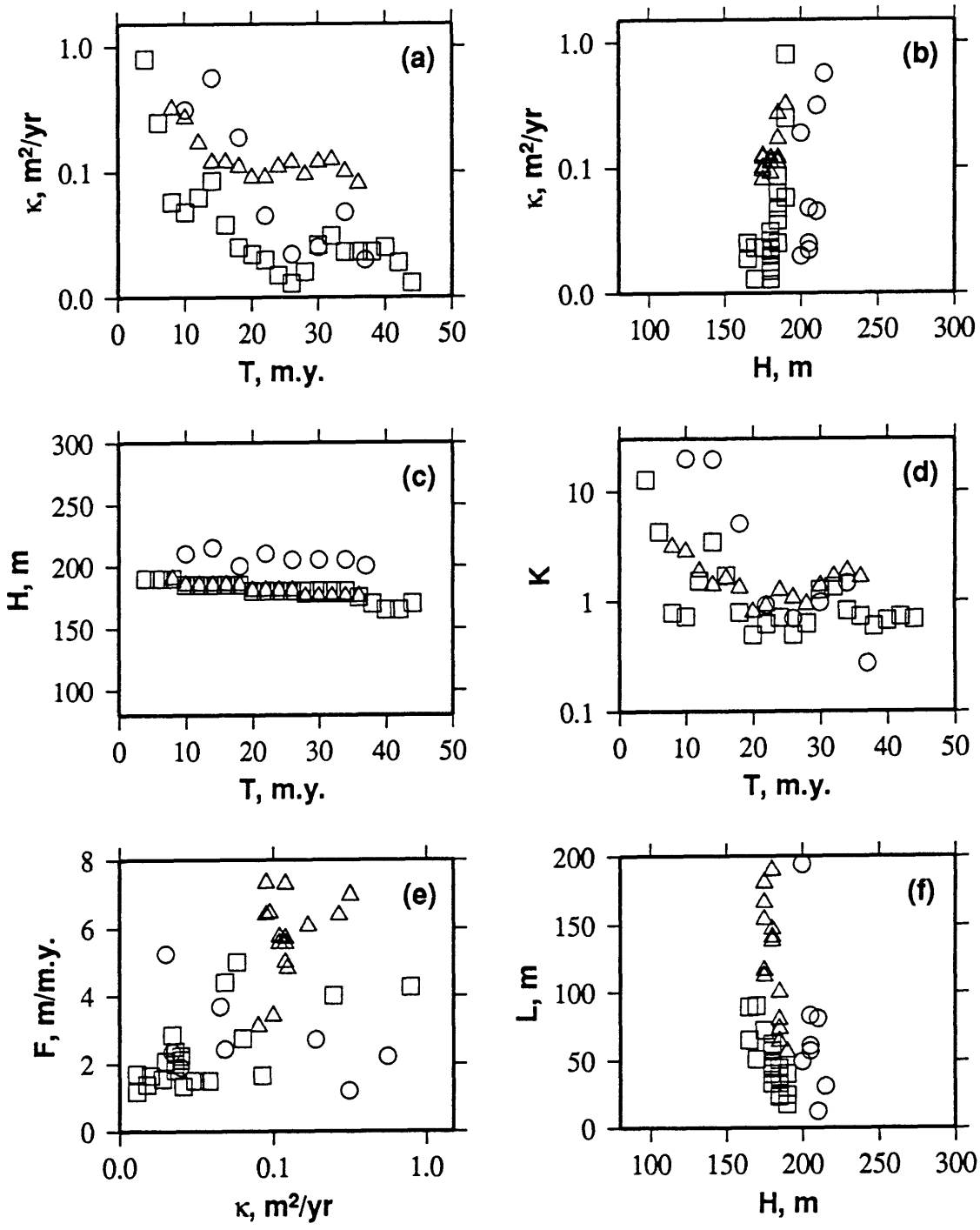

Fig. 5.32: Relationships between favored inverted parameters (κ, L, H), calculated parameters (F and K) and seafloor age T, for Angola Basin (circles), Brazil Basin (squares) and Argentine Basin (triangles) subregions, as labeled. The Brazil Basin and Argentine Basin values are as given in Table 5.4 and Table 5.8, respectively, and result from fixing H at predetermined values. The Angola Basin values used correspond to those in Table 5.1 for the three western subregions and to those in Table 5.3 for the five eastern subregions.

Chapter 6

Atlantic Paleoceanography Since the Oligocene: Constraints from Sediment Thickness Estimates

INTRODUCTION

In the first chapter of this thesis, we list several outstanding questions of marine sedimentology, relevant to the understanding of marine productivity and ocean chemistry now and in the past: How rapidly is sediment accumulating near-ridge in the current ocean? How does this rate vary geographically? How has this rate varied through time? In ensuing chapters, we develop methodologies for inverting bathymetric data for information about sedimentation as well as basement topography. This information allows us to (among other things) estimate average rates of sediment accumulation on young seafloor in the North Atlantic and South Atlantic oceans during the past 5-10 m.y.

How sediment accumulation rates have varied prior to the late Miocene is harder to address, but must be understood to determine how biological productivity, chemistry, and circulation pattern have varied in the central gyres of the Atlantic during the Cenozoic. Much of what is currently accepted about past surface currents, nutrient supply levels, and the production and flow of bottom waters is based on data gathered from piston cores and deep sea drill hole cores. Unfortunately, the portion of seafloor sampled remains small, and information about sediment composition and particularly about sediment accumulation rate obtained from cores may be dependent on purely local or regional phenomena (see Chapter 2). The study of Miocene sedimentation in particular is complicated by the absence of Miocene sediments from many sites. Thus, while the initiation of vigorous Antarctic Bottom Water (AABW) flow is fairly well established as following the onset of permanent glaciation on Eastern Antarctica after ~15 m.y.B.P. [e.g. *Flower and Kennett*, 1994], there is no general agreement on the response of bulk ocean productivity to AABW production and associated invigoration of surface ocean circulation systems [e.g. *Thunell and Belyea*,

1982], or on the sensitivity of biological productivity and ocean chemistry to earlier changes in bottom water sources.

If high-resolution isochron, sediment isopach, and bathymetry maps were available for the entire ocean floor, differences in sediment thickness between nearby regions could be related to differences in the depths or ages of the regions, leading to detailed histories of regional controls of sedimentation. This is consistent with the goal of a "horizontal" time-slice approach to the study of sedimentation patterns advanced by *Davies et al.* [1995]. With few exceptions (e.g. *Jaroslow and Tucholke* [1995], *Jaroslow* [1997]), however, detailed two-dimensional sediment thickness information has not been available.

The methodology for estimating sediment thickness which we develop in this thesis provides a new source of information about the distribution of sediments on the ocean floor. In this chapter, we use the results of the inversion of near- and off-axis bathymetric data for average regional sediment thickness from chapters 3, 4, and 5 (Fig. 6.1) to study sediment accumulation in the central North and South Atlantic oceans. To relate observations of sediment thickness to possible models of ocean chemistry and sediment rain rate and composition, we introduce a numerical model of regional sediment accumulation which incorporates the effects of calcite dissolution on the total average thickness of sediment in a region. Our simple model assumes that the dissolution rate of calcite increases linearly with depth below some threshold, which we term the *U*-lysocline. This depth can be hundreds of meters above the foraminiferal and coccolith lysoclines, as commonly identified by changes in calcite percentage or the degree of preservation of microfossils.

Since the resolution of the sediment thickness information we obtain in previous chapters is relatively coarse, we are unable to resolve changes at timescales finer than a few million years, much too long to address changes related to individual glacial cycles but short enough to study epoch- and sub-epoch-scale phenomena.

We begin this chapter by reviewing the controls on sedimentation in the central gyres of the Atlantic. Then, we develop our forward model of sediment accumulation, and explore the effects of a number of calcite dissolution models, downward sediment rain rates, sediment compositions, and values of seafloor RMS variability on sedimentation

patterns. In concert with DSDP drill core data, we then use the forward model of sediment accumulation to evaluate proposed models of sediment rain rate, composition, and calcite dissolution for the central North Atlantic since the early Miocene and the central South Atlantic since the end of the Eocene, given the inversion results of chapters 4 and 5.

ATLANTIC SEDIMENTATION

Since the end of the Eocene, the Atlantic basins have been accumulating carbonate sediments in shallower regions and clays in deeper regions, while siliceous sediments are absent from the geologic record of moderate latitudes [*Thiede et al.*, 1981]. Rates of sediment accumulation have been governed by sediment supply, sediment composition, and the corrosivity of bottom waters.

Table 6.1. Summary of near-ridge drill hole data - North Atlantic

Site	Age[1], Ma	Depth, m	Thickness, m	Example % $CaCO_3$	Accumulation Rate, m/m.y.
9	101	4981	835	40[#] or 9[@]	40, Pliocene to Recent
10	77	4697 (4460) (4040)	459	90[#] or 67[@] 0-100[#] or 62[@] 80[#] or 53[@]	8, Pliocene to Recent 1.2, Oligocene and Miocene 2.5, Middle and Upper Eocene
11	15	3556 (2550)	284	99[#] or 83[@] 100[#] or 52[@]	14, Pleistocene 16, Miocene
332	3	1810	105-149	99[#] or 91[@]	30, U. Pliocene and Pleistocene
333	3	1666	219	98[#] or 93[@]	74, U. Pliocene and Pleistocene
334	9	2619	254	97[#] or 90[@]	24, Pleistocene
335	16	3188 (2890)	450	98[#] or 88[@] 100[#] or 96[@]	100, Pleistocene 35, Pliocene and Miocene
395	7	4484	93	49[#] or 79[@] or 73[*]	8, Pleistocene
396	13	4450	125	75[#] or 80[@] or 62[*]	10, Pleistocene
410	10	2980 (2220)	340	89[@] or 70[*] 94[@] or 100[*]	66, Quaternary 40, Upper Miocene

[1]: From *Müller et al.* [1993].

[#]: Via X-Ray Diffraction, from *Rex* [1970a] for sites 9, 10, and 11; *Zemmels et al.* [1977] for sites 332, 333, 334, and 335; and from *Timofeev et al.* [1979] for sites 396 and 396.

[@]: Via Carbon/Carbonate analysis, from *Peterson et al.* [1970] for sites 9, 10, and 11; from *Bode* [1977] for sites 332, 333, 334, and 335; from *Bode* [1979] for sites 395 and 396; and from *White and Bode* [1979] for Site 410.

[*]: Via Carbonate Bomb technique, from *Melson, Rabinowitz et al.* [1979] for sites 395 and 396; and from *Luyendyk, Cann et al.* [1979] for Site 410.

(): Backtracked depth, calculated assuming that seafloor depth = $B_0 + 350T^{1/2}$ [*Parsons and Sclater*, 1977], with B_0 chosen based on present seafloor depth.

Table 6.2. Summary of near-ridge drill hole data - SW Atlantic

Site	Age[1], Ma	Depth, m	Thickness, m	Example % $CaCO_3$	Accumulation Rate, m/m.y.
14	35	4346	108	85# or 53@	2, Lower Miocene
		(3270)		98# or 76@	1, Upper Oligocene
		(2880)		99# or 75@	4.5, U. Oligocene to U. Eocene
15	20	3938	83	99# or 81@	12, Pleistocene
		(3680)		99# or 91@	6, L. Pliocene to U. Miocene
		(3420)		75# or 80@	3, M. Miocene to L. Miocene
16	9	3526	176	99# or 88@	18, Pleistocene to L. Pliocene
		(3080)		99# or 93@	12, L. Pliocene to U. Miocene
		(2480)		99.5# or 90@	10, Upper Miocene
19	47	4685	141	33# or 0@	1, Pleistocene
		(3850)		80# or 22-65@	3.5, Upper Oligocene
		(3730)		98# or 77@	6, L. and U. Oligocene
		(3340)		98# or 71@	3, Upper Eocene
20	67	~4450	91	-	0.2, Pleistocene
		(4130)		38-88# or 62@	0.3, Pliocene
		(3800)		0#@	0, Miocene
		(3630)		60# or 22-88@	1.5, Upper Oligocene
		(3400)		99# or 71@	4, Lower Oligocene
				80# or 31@	2, Upper to Middle Eocene
513	35	4373	380	0@	18.5, Pleistocene to U. Pliocene
		(4280)		0@	33, L. Pliocene
		(4080)		0@	35, U. Miocene
		(3900)		1-27@	?, Miocene
		(3290)		59@	11, U. Oligocene
		(2800)		55@	19, L. Oligocene
514	37	4318	-	0@	~30, Pleistocene to Pliocene

[1]: From *Müller et al.* [1993].
#: Via X-Ray Diffraction, from *Rex* [1970b].
@: Via Carbon/Carbonate analysis, from *Pimm* [1970] for site 14, 15, 16, 19, and 20, and from *Ludwig, Krasheninikov et al.* [1983] for sites 513 and 514.
(): as in Table 6.1.

Approximately 40 Deep Sea Drilling Project (DSDP) and Ocean Drilling Project (ODP) sites are located off-axis within the central gyres of the Atlantic basins, as shown in Fig. 6.1. In tables 6.1-6.3, we summarize sediment accumulation rate and composition information gathered from the sites nearest the Mid-Atlantic Ridge (MAR). A total of four different methods for determining the amount of calcite within samples are represented. Highest values are associated with measurement via X-Ray diffraction, while the other three methods used - carbon/carbonate analysis, the carbon bomb technique, and the modified volumetric chemical method - tend to produce similar, usually lower, values for a given core. In this chapter, we use the results of carbon/carbonate analyses.

Table 6.3. Summary of near-ridge drill hole data - SE Atlantic

Site	Age[1], Ma	Depth, m	Thickness, m	Example % $CaCO_3$	Accumulation Rate, m/m.y.
17	30	4270	123	99[#] or 84[@]	5, Pleistocene
		(4140)		100[#] or 83[@]	4.5, Lower Pliocene
		(3960)		-	-, Upper Miocene
		(3460)		98-99[#] or 75[@]	3, Lower Miocene
		(2960)		100[#] or 88[@]	4 (?), Upper Oligocene
18	21	3980	178	100[#] or 83[@]	?, Pleistocene
		(2730)		99[#] or 86[@]	8, Lower Miocene
359	54	1658	?	93[$] or 94[@]	?, Lower Pliocene
		?		70[$] or 88[@]	?, Middle Miocene
519	11	3769	152	90[*] or 86[@]	95, Pleistocene
		(3600)		90[*] or 92[@]	25, Pliocene
		(3100)		94[*] or 88[@]	7, Upper Miocene
520	14	4217	449	75[*] or 79[@]	46, Pliocene and Pleistocene
		(3690)		25-75[*] or 63[@]	30, Upper Miocene
		(3510)		0-80[*] or 26-74[@]	<1, Upper to Middle Miocene
521	16	4125	71-84	88[*] or 83[@]	10, U. Pliocene and Pleistocene
		(3890)		85[*] or 90[@]	5, L. Pliocene to U. Miocene
		(3510)		40[*] or 28-87[@]	2, Upper and Middle Miocene
		(3330)		80[*] or 83[@]	10, Middle Miocene
522	35	4456	150	60-95[*] or 63 (var.)[@]	9, Pliocene and Pleistocene
		(3990)		0-50[*] or 27[@]	1, Miocene
		(3380)		85[*] or 87[@]	5, Upper Oligocene
		(2880)		90[*] or 89[@]	9, Lower Oligocene
523	48	4572	190	85 (var.)[@]	6, Pliocene and Pleistocene
		(4070)		2-58[@]	<1, Miocene and U. Oligocene
		(3700)		76[@]	3, Upper Oligocene
		(3460)		86[@]	2-7, Lower Oligocene

[1]: From *Müller et al.* [1993].
[#]: Via X-Ray Diffraction, from *Rex* [1970b] for sites 17 and 18.
[@]: Via Carbon/Carbonate analysis, from *Pimm* [1970] for sites 17 and 18; from *Scott* [1977] for Site 359; and from *Bode* [1984] for sites 519, 520, 521, and 522.
[*]: Via Carbonate Bomb technique, from *Hsü, LaBrecque et al.*, [1984] for sites 519, 520, 521, and 522.
[$]: Modified volumetric chemical method, *Supko, Perch-Nielsen et al.* [1977] for Site 359.
(): as in Table 6.1.
(var.): indicates the presence of considerable down-core variability.

Biological productivity

Biological paleoproductivity in the Atlantic basins since the end of the Eocene has been addressed by a number of workers, often resulting in contradictory conclusions. *Diester-Haass* [1995] studied cores from ODP Site 689 on the Maud Rise using coarse fraction analysis, and found that productivity was generally low in the Weddell Sea during the middle Eocene, but increased during the late Eocene into the early Oligocene. The

magnetic properties of sediments at DSDP Site 522 in the Angola Basin also identify an increase in South Atlantic productivity at the Eocene/Oligocene boundary [*Hartl et al.*, 1995] at more temperate latitudes, and *Hallock et al.* [1991] theorized that productivity increased through the Oligocene, based on foraminiferal evolutionary patterns throughout the Paleogene. In contrast, *Keller et al.* [1992] interpreted vertical $\delta^{13}C$ gradients between surface and subsurface foraminiferal species as indicative of a general decrease in primary biological productivity beginning in the Eocene and extending through the Oligocene.

Since the middle Miocene, sediment accumulation rates have risen steadily world-wide, when averaged over several million years [e.g. *Davies and Worsley*, 1981; *Hay et al.*, 1988], in part probably due to increased levels of calcite preservation worldwide [e.g. *Van Andel*, 1975] but also attributable to increased continental erosion and the contribution of organic and inorganic material directly to the deep ocean due to a generally low sea level and periodic extreme sea-level lowstands [e.g. *Haq et al.*, 1987]. There is some agreement that productivity was reduced in the early and middle Miocene and has since increased, contributing to increased accumulation rates, though the degree and the precise timing of the increase are not well understood. Based on surface-to-deep $\delta^{13}C$ gradients observed at drill sites in the southern ocean, *Wright et al.* [1991] speculated that nutrient levels were only 1/2 to 1/3 of modern levels during the early and middle Miocene, while *Delaney* [1990] asserted that the oceanic phosphorous inventory was 80% of current levels during that time. Vigorous AABW flow is fairly well established as following the formation of permanent glaciation on Eastern Antarctica after ~15 m.y.B.P. [e.g. *Flower and Kennett*, 1994], resulting in invigoration of surface ocean circulation systems, increased upwelling [e.g. *Thunell and Belyea*, 1982], and perhaps increased productivity as early as the early middle Miocene. Global compilations of $\delta^{13}C$ data also suggest an increase in productivity beginning ~15 m.y.B.P. [*Renard*, 1986; *Shackleton*, 1987], perhaps in response to the exhumation of buried carbon by strong bottom currents [e.g. *Tucholke and Mountain*, 1986].

Calcite dissolution

Calcite dissolution occurs at all depths in the ocean due to the presence of reactive CO_2 and O_2 in seafloor sediments The concentration of CO_3^{2-} in the water column decreases with depth, causing the rate of dissolution of calcareous tests to increase. The foraminiferal and coccolith lysoclines are identified as depths at which the degree of preservation of these nannofossils decreases dramatically, with the coccolith lysocline usually lying several hundred meters below the foraminiferal lysocline. The exact placement of the foraminiferal lysocline is determined by the needs of individual researchers. It may be identified by a change in the percentage of calcite present in surface sediments [e.g. *Farrell and Prell*, 1989], by a change in the degree of dissolution of individual calcareous tests [e.g. *Thunell*, 1982; *Hsü et al.*, 1984], or experimentally by observing the rate of dissolution to samples suspended at various levels in the water column [e.g. *Peterson*, 1966]. *Broeker and Takahashi* [1978] find that all of these methods often place the foraminiferal lysocline within a few hundred meters of where the carbonate ion concentration equals an (increasing) function of water depth.

The Carbonate Compensation Depth (CCD) is identified as the bottom of the zone in which dissolution occurs, such that the dissolution rate of calcite is equal to the rate at which calcite is supplied through the water column. In some studies, the CCD is placed at the shallowest depth at which surface sediments are devoid of calcite [e.g. *Biscaye et al.*, 1976]; other researchers allow 20-30% of surface sediments to be calcite at the CCD [e.g. *Tucholke and Mountain*, 1986; *Hsü et al.*, 1984]. Differing criteria can result in CCD placements for a given area which are separated by hundreds of meters; for example, *Biscaye et al.* [1976] place the current CCD of the western North Atlantic at below 6000 m, while *Tucholke and Mountain* [1986] place it at ~5400 m.

Analysis of DSDP cores reveals long-wavelength correlations in CCD curves for the Atlantic, Pacific, and Indian Ocean basins [e.g. *Van Andel*, 1975]. The CCD was generally high in the Paleocene and Eocene, followed by a world-wide deepening at the Eocene-Oligocene boundary, a rise at the beginning of the Miocene, and finally a deepening to all-Cenozoic lows around 5-10 m.y.B.P. These first-order variations are thought to correspond to the transgression and regression of oceans onto continents, with flooded

shelves acting as sinks of calcite, resulting in increased undersaturation in CO_3^{2-} in deep water and a shallowing of the lysocline and CCD [*Berger and Winterer*, 1974; *Hsü et al.*, 1984]. In particular, the extreme depth of the CCD in the Atlantic since the Pliocene is probably due to North Atlantic glaciations and the accompanying lower sea level and increased continental erosion, which increased the concentration of CO_3^{2-} throughout the water column, allowing calcite to be preserved at great depths [*Davies and Worsley*, 1981].

In detail, however, CCD curves from throughout the world ocean differ greatly. Within the Atlantic Basin, detailed CCD curves generated for the late Eocene-present for the western North Atlantic [*Tucholke and Vogt*, 1979; *Tucholke and Mountain*, 1986] and the Angola Basin [*Hsü et al.*, 1984] reflect differing paleoceanographic environments between the basins (Fig. 6.2). Both regimes, as interpreted by *Tucholke and Mountain* [1986] and *Hsü et al.* [1984], show CCDs of ~3600-4000 m at ~40 m.y.B.P., gradually deepening to 4400-4500 at ~30 m.y.B.P. More recently, the curves show divergence. In the western North Atlantic, constraints from drill holes show that the CCD may have been as shallow as 3500 m between 30 and 15 m.y.B.P., though the data do not preclude a CCD as deep as 4500 m during that time. The CCD then deepened to 5000 m from 15 to 5 m.y.B.P. Since 5 m.y.B.P., it has experienced variations in amplitude of 300-500 m, but has always stayed deeper than 5000 m. In contrast, the CCD in the Angola Basin, as constrained by the degree of dissolution in sediments at 6 DSDP drill sites near 30° S, shallowed to ~3700 m from 30 to ~22 m.y.B.P., but shows a local maximum in depth at 15 m.y.B.P., the time of the CCD minimum in the western North Atlantic. Since the middle Miocene, the Angola Basin CCD shows two minima, shallowing to 3000 m at 12 m.y.B.P. and 3700 m at 6-7 m.y.B.P. Since 5 m.y.B.P., the CCD has varied between 4600 and 4700 m, 300-600 m shallower than post-Miocene CCD values in the western North Atlantic.

Bottom water flow

Current geographical variations in CCD signature are thought to be functions of variations in bottom water flow patterns. AABW in particular is rich in biogenic CO_2, and is therefore corrosive to calcite, leading to increased calcite dissolution in the Argentine Basin [e.g. *Takahashi*, 1975]. To enter the Brazil Basin, however, AABW must flow

through the Vema Channel at 30° S. The Angola Basin is further isolated: AABW must flow through the Vema and Romanche fracture zones into the eastern North Atlantic and then back southward. In the Argentine and Brazil basins, the boundary between North Atlantic Deep Water (NADW) and AABW corresponds to the position of the foraminiferal lysocline as defined by *Thunell* [1982]. In the North Atlantic and the Angola Basin, the boundary between NADW and AABW is less distinct [*Thunell*, 1982].

There is evidence for early NADW-AABW production as far back as 57-60 m.y.B.P. causing erosion in the western North Atlantic [*Mountain and Miller*, 1992]. The next pulse of NADW production probably began ~36 m.y.B.P., near the Eocene-Oligocene boundary [*Miller and Tucholke*, 1983]; AABW flow over the Maude Rise (DSDP site 689) has been identified in uppermost Eocene sediments [*Diester-Haass*, 1995], and was well established in the Brazil Basin by 32 m.y.B.P., based on bottom current deposits at DSDP Site 515 [*Johnson*, 1985]. At DSDP Site 522 in the Angola Basin, the presence of the AABW-associated foraminifera species *Nuttallides umboniferus* in 30-31 Ma sediments deposited at a paloedepth of 3100 m may indicate increased AABW flow [*Hsü et al.*, 1984]. There is no evidence (that we know of) to suggest that AABW was produced in large amounts between 30 and 15 m.y.B.P., but production seems to have resumed after 15 m.y.B.P., corresponding to the initiation of stable East Antarctic glaciation at 14.8 m.y.B.P. [*Flower and Kennett*, 1994].

Vigorous AABW production, combined with the effects of a generally high sea level concentrating biological productivity away from the central gyres, may be the causes of CCD minima at 15 m.y.B.P. in the western North Atlantic and 12 m.y.B.P. in the Angola Basin [*Hsü et al.*, 1984]. However, the link between cooler climates at high latitudes and bottom water vigor does not hold for the Northern hemisphere. Production of NADW decreases greatly during glacial periods [*Raymo et al.*, 1992] because the salinity of the North Atlantic decreases enough that cold northern waters are not dense enough to sink.

MODELING TIME- AND DEPTH-DEPENDENT SEDIMENT ACCUMULATION

To use the patterns of sedimentation we observed in chapters 3, 4, and 5 to add to our understanding of sediment accumulation in the Atlantic, we numerically model regional

sediment accumulation through time, incorporating the effects of calcite dissolution on the total average thickness of sediment in a region. Our model is different in form from models of calcite dissolution in the current ocean, which rely on knowledge of the ocean's chemistry, particularly how the concentration of CO_3^{2-} varies with depth [e.g. *Sjöberg*, 1976; *Keir*, 1980]. Instead, our model makes use of knowledge of the CCD through time, a widely available source of information about the past ocean.

Thermodynamic models of calcite dissolution

The rate at which calcareous pelagic sediments accumulate is dependent on the rain rate through the water column, the concentration of CO_3^{2-} in bottom waters, the amount of reactive CO_2 and O_2 present in young sediments, the rate of burial, and the susceptibility of the sediment to further dissolution by interstitial waters [e.g. *Heath and Culberson*, 1970; *Emerson and Bender*, 1981; *Archer*, 1991]. Often, models of calcite dissolution in the current ocean are driven primarily by variations to $\left[CO_3^{2-}\right]$ and the solubility constant of calcite with depth in the water column, which are taken as the most important controls of calcite dissolution rate (although *Archer* and coworkers argue that the amount of organic carbon in sediments may be of primary importance [e.g. *Emerson and Archer*, 1990; *Archer*, 1996b].)

Sjöberg [1976] and *Rickard and Sjöberg* [1983] parameterize the rate of dissolution of calcite in seawater $r_{\%}$ (in %/day) as

$$r_{\%} = k_{\%}\left(1 - \frac{\left[Ca^{2+}\right]^n\left[CO_3^{2-}\right]^n}{K'_{sp}(z)^n}\right) \tag{6.1}$$

where $K'_{sp}(z)$ is the solubility constant of calcite at depth z, $k_{\%}$ depends on $\left[Ca^{2+}\right]$ and $\left[SO_4^{2-}\right]$, and n is a function of $\left[Mg^{2+}\right]/\left[Ca^{2+}\right]$ (typically 0.5 for sea water). Alternatively, *Keir* [1980] and *Acker et al.* [1987], among others, favor the form

$$r_{\%} = k_{\%}\left(1 - \frac{\left[Ca^{2+}\right]\left[CO_3^{2-}\right]}{K'_{sp}(z)}\right)^n. \tag{6.2}$$

In *Morse* [1978], experimental results placed n between 2.7 and 4.3, while the rate constant $k_{\%}$ varies between species of foraminifera. Refinements to dissolution rate models include the explicit parameterization of the effect of organic CO_2 [e.g. *Hales et al.*, 1994].

To use (6.1) or (6.2) to model calcite dissolution, we must know both the concentration of CO_3^{2-} with depth and the form of $K'_{sp}(z)$. *Broeker and Takahashi* [1978] find that if the solubility constant is related to depth via

$$K'_{sp}(z) = 90\exp(0.16(z-4))\left[Ca^{2+}\right], \tag{6.3}$$

an increased rate of calcite dissolution is generally predicted within 100-200 m of where the foraminiferal lysocline is identified, thus allowing the usage of (6.1) or (6.2) to compute $r_{\%}$ in the current ocean. Unfortunately, absent knowledge of paleo values of $\left[CO_3^{2-}\right]$, we cannot use these equations to calculate sediment dissolution rates in the past.

The predicted relationship between $\left[CO_3^{2-}\right]$ and $r_{\%}$, calcite accumulation rate, and $\%CaCO_3$ embodied by these equations is demonstrated in Fig. 6.3. In this example we allow $\left[CO_3^{2-}\right]$ to vary linearly with depth between 4 and 6 km, with a concentration of ~108 μM/kg at 4 km and of ~98 μM/kg at 6 km, similar to what has been observed for the North Atlantic [*Broeker and Takahashi*, 1978], and assume a sediment rain rate of 5 m/m.y., of which 90% is calcite. Using (6.2) and letting $k_{\%}$ = 7.177 %/day and n = 4.54 [*Kier*, 1980], we find that $r_{\%}$ is predicted to accelerate with depth. Conversely, using (6.1), an n of 0.5, and choosing a $k_{\%}$ of 0.01 %/day for ease of comparison, the rate of dissolution is predicted to increase linearly with depth (Fig. 6.3 (a)).

To study how calcite accumulation rate and sediment composition are affected by (6.1) and (6.2) we must make assumptions about the volume of sediment subject to dissolution at any given time. This is an area of active research, and *in situ* studies show that dissolution by pore waters is an important, complex process [e.g. *Sayles*, 1985; *Hales and Emerson*, 1996]. Here, for purposes of illustration, we assume that all dissolution occurs within the upper centimeter of sediment, that dissolution is uniformly active within this layer, and that there is no sediment mixing. These assumptions are made to minimize the amount of dissolution occurring as a function of $r_{\%}$, yet still lead to the focusing of changing sediment accumulation rates into a narrow band of depths (Fig. 6.3(b)), which in this example correspond to those depths for which $r_{\%}$ is near 0.0001 %/day. The

percentage of surface sediment which is calcite changes from the rain value of 90% to 0 within a narrow band of depths (Fig. 6.3(c)). The range of these depths varies between dissolution models, but the dissolution patterns are qualitatively very similar, implying that sediment composition data is rather useless for determining whether (6.1) or (6.2) best models calcite dissolution patterns. We find that the band of depths through which calcite percentage decreases is much narrower than is found in nature [e.g. *Biscaye et al.*, 1976].

Although this modeling exercise is dependent on several somewhat arbitrarily chosen assumptions, it underscores that, as a practical matter, both (6.1) and (6.2) do equally well (or poorly) at describing how dissolution varies with water depth. When studying ancient regimes, the only information available is, typically, the observed CCD, with detailed foraminiferal lysoclines available for a few locations (e.g. the Angola Basin [*Hsü et al.*, 1984]). Therefore, equations such as (6.1) and (6.2) are inadequate for our purposes.

Forward model of sediment accumulation paleorate

We assume that the amount of calcite within the rain of pelagic sediment which accumulates instead of dissolving varies linearly with position between the CCD and some upper boundary [e.g. *Heath and Culberson*, 1970; *Berger et al.*, 1982]. This qualitatively resembles the form of the functions given in Fig. 6.3(b) for both (6.1) and (6.2), though in general we assume that the amount of dissolution experienced by sediments varies across a wider range of depths. We term the upper boundary the *U*-lysocline; ideally, this level coincides with the foraminiferal lysocline. Thus, the rate of sediment accumulation at paleotime t and depth z has the form

$$R(z,t) = \begin{cases} R_r(t) + R_c(t), & z < z_{lys}(t) \\ R_r(t) + R_c(t)\left(1 - \left(\dfrac{z - z_{lys}(t)}{z_{ccd}(t) - z_{lys}(t)}\right)\right), & z_{lys}(t) \le z \le z_{ccd}(t) \\ R_r(t), & z > z_{ccd}(t) \end{cases} \qquad (6.4)$$

where $R_c(t)$ and $R_r(t)$ are the rain rates of calcite and refractory material, respectively, $z_{lys}(t)$ is the *U*-lysocline, and $z_{ccd}(t)$ is the CCD. Like (6.1) and (6.2), (6.4) does not explicitly parameterize the potentially important effects of organic CO_2, bioturbation, or interstitial water circulation on dissolution.

As illustrated in Fig. 6.4, the sediment accumulation rate and sediment calcite percentages predicted by (6.4) are comparable to those of (6.1) and (6.2). This figure also illustrates that the *U*-lysocline may be placed high above a lysocline identified based on calcite percentage in sediments. Where calcite makes up a very large percentage of the sediment rain, a considerable amount must be removed from sediments before the percentage of calcite in surface sediments is decreased by more than a few percent. Thus, in the example in Fig. 6.4, sediment which is originally 95% calcite does not experience sufficient dissolution to have a composition of 90% calcite unless it lies more than halfway between the *U*-lysocline and the CCD. If the 90%-calcite surface were being used to identify the lysocline, much of the region beneath the *U*-lysocline would not be included.

The average rate at which sediment accumulates in a region is the integral of the sediment accumulation rates for the range of local seafloor depths, which is parameterized by the RMS variability of topography H. If H is large, the range of depths at which sediment is deposited is wide enough to influence how much sediment ultimately accumulates in a region. If the variability of depths of sediment deposition within a region is ignored, sediment accumulation will be overestimated when average seafloor depth $B(\tau)$ is near the lysocline and underestimated when $B(\tau)$ is near the CCD.

For typical Gaussian seafloor topography (e.g. *Goff and Jordan* [1988]), the distribution function for seafloor of age τ is approximated by

$$p(H,\tau,z) = \frac{1}{H\sqrt{2\pi}} e^{\left(-(z-B(\tau))^2/2H^2\right)}. \tag{6.5}$$

Therefore, the average sediment rain rate $\overline{R}(t,\tau,H)$ on a region of seafloor of age τ at paleotime t is

$$\overline{R}(t,\tau,H) = \int_0^\infty p(H,\tau,z)R(z,t)dz \tag{6.6}$$

and the amount of sediment currently on seafloor of age T can be estimated as

$$L(T,H) = \int_T^0 \overline{R}(\varsigma,\varsigma-T,H)d\varsigma. \tag{6.7}$$

Mean seafloor depth $B(\tau)$ has the form

$$B(\tau) = B_0 + B_1\sqrt{\tau} - L, \tag{6.8}$$

where τ is measured in m.y. When analyzing data, we choose B_0 and B_1 which best fit the available bathymetry. When exploring the effects of various model parameters on sediment thickness, we let B_0 = 2500 m and B_1 = 350 m [*Parsons and Sclater*, 1977].

Sensitivity of L to model parameters

To explore the sensitivity of L to model parameters, we apply our sediment accumulation model for 30 m.y. of model time, except where otherwise noted, using a variety of $R_c(t)$, $R_r(t)$, $z_{lys}(t)$, $z_{ccd}(t)$, and H. In Fig. 6.5 - 6.10, we show the resulting expected average sediment thicknesses as a function of seafloor age. Included in panel (b) of the figures is the subsidence history for 5, 10, 15, 20, 25, and 30 Ma model seafloor, which can be followed by tracing the thin dashed lines shown from the date of seafloor generation to the present.

The basic interactions between sediment rain rate, sediment composition, and the position of the U-lysocline and CCD are shown in the relationship between seafloor age and sediment thickness of Model 1 (Fig. 6.5). For this model, we assume a constant total rain rate $R_t(t)$ of 5 m/m.y., of which 90% is dissolvable calcite (i.e. $R_c(t)$ = 4.5 m/m.y., $R_r(t)$ = 0.5 m/m.y.) The CCD and U-lysocline are also constant, at 4500 m and 3500 m, respectively. We assume an H of 300 m. Since most young seafloor resides above the U-lysocline, sediment initially accumulates at near 5 m/m.y. As the seafloor ages, more seafloor subsides below the U-lysocline, and, eventually, the CCD, so the average rate at which sediment accumulates declines as the seafloor ages. After 30 m.y. of model time, the average depth of topography is greater than 4800 m, and the average sediment accumulation rate approaches $R_r(t)$.

The timing of the transition of accumulation rate from equaling $R_t(t)$ to $R_r(t)$ is sensitive to the position of the lysocline within the water column. If the U-lysocline in the scenario of Model 1 is lowered to 4000 m (Model 2, Fig. 6.5), the sediment accumulation rate remains ~5 m/m.y. for 11-12 m.y., as opposed to 6-7 m.y., and approaches $R_r(t)$ more slowly, resulting in the accumulation of a total of 15 m more sediment after 30 m.y. of model time. Conversely, if the zone in which dissolution occurs in the deep oceans is doubled in size from that of Model 1, such that the U-lysocline resides at 2500 m and the

CCD at 4500 m, much of the sediment arriving on the seafloor is subject to dissolution even on very young crust, and the sediment accumulation rate approaches $R_r(t)$ quickly (Model 3, Fig. 6.5).

If the total rain rate at the *U*-lysocline is variable, models are more complex. For models 4 and 5, shown in Fig. 6.6, we assume a constant CCD of 4500 m and *U*-lysocline of 3500 m, a sediment composition of 90% calcite, 10% refractory material, and an *H* of 300 m, as in Model 1. However, for Model 4, we assume that the seafloor is subject to a total sediment rain rate $R_t(t)$ of 2 m/m.y. for the first 15 m.y. of the model run, and 5 m/m.y. for the next 15 m.y., while in Model 5 we assume an initial $R_t(t)$ of 5 m/m.y. followed by 15 m.y. of an $R_t(t)$ of 3 m/m.y. In Model 4, where the more recent rain rates are higher, the average sediment thickness for 0 - 15 Ma seafloor is the same as for Model 1, since the conditions of the two models are identical. However, topography older than 15 Ma in Model 4 receives little sediment when young, so that the average sediment thickness on older topography decreases slightly with increasing seafloor age. In contrast, Model 5 shows that a high initial $R_t(t)$ followed by a lower total rain rate causes sediment thickness to increase steadily with seafloor age. Data which followed this pattern might be incorrectly interpreted as indicative of a constant sediment accumulation rate of 2.5 m/m.y., perhaps due to a constant $R_t(t)$, if the dissolution of calcite is ignored.

As seen in Fig. 6.2, the position of the CCD can vary by over a kilometer in depth over a few million years. With models 6 and 7 (Fig. 6.7), we explore the consequences of abrupt changes in the depth of the CCD from 4000 m to 5000 m at 15 Ma, as opposed to a constant CCD at 4500 m as in Model 1, with *U*-lysoclines fixed 1000 m (Model 6) and 2000 m (Model 7) shallower than the CCD. As in Model 1, the sediment rain rate $R_t(t)$ is fixed at 5 m/m.y., the composition of the sediment is 90% calcite and 10% refractory material, and *H* is 300 m. We find that the deepening of the CCD at 15 Ma has an effect similar to an increase in the sediment rain rate, increasing the rate at which sediment accumulates on all but the youngest seafloor, particularly when the distance between the CCD and *U*-lysocline is large.

Through models 8 and 9, we find that the average sediment thickness on older seafloor is sensitive to sediment composition, especially when the CCD and lysocline are

relatively shallow. In Model 8 (Fig. 6.8), we assume a sediment composition of 95% calcite, and the $R_t(t)$, CCD, U-lysocline, and H of Model 3. This causes a relative decrease in sediment accumulation on older seafloor, and an eventual sediment accumulation rate of only 0.25 m/m.y. Likewise, a decrease in the calcite composition to 80% causes an increase in sediment accumulation on older seafloor and an eventual sediment accumulation rate of 1 m/m.y. (Model 9, Fig. 6.8).

With Model 10 (Fig. 6.9) we explore the result of assuming that the RMS variability of topography does not affect the rate at which sediment accumulates by letting $H = 0$; other parameters are as in Model 1. Sediment accumulation is modeled for 40 m.y. When H is greater than 0, as in Model 1, we estimate that some seafloor is subject to calcite dissolution even when the average depth is shallower than the U-lysocline, leading to a lower rate of accumulation on young seafloor than is predicted for Model 10. As the seafloor subsides, the mean depth of the seafloor passes through the U-lysocline, and the Model 1 seafloor accumulates sediment slightly more rapidly than the Model 10 seafloor, but not rapidly enough to make up all of the difference in accumulation amounts until the mean seafloor depth sinks below the CCD. When this occurs, Model 1 seafloor continues to accumulate some calcite, but Model 10 accumulates only refractory material. For seafloor older than ~33 Ma, we find that Model 10 predicts less sediment than Model 1.

In some locales, average sediment thickness decreases with increasing seafloor age [e.g. *Jaroslow and Tucholke*, 1991; *Webb and Jordan*, 1993]. Model 4 (Fig. 6.6) shows this effect, caused by an initially low $R_t(t)$ followed by a higher total rain rate. When $R_c(t)$ and $R_r(t)$ are constant through time, there may also be a decrease to L with increasing seafloor age. For example, a slight downward bend to the sediment accumulation pattern occurs in Model 7 (Fig. 6.7), caused by a shallow initial CCD and U-lysocline followed by deepenings of these surfaces. Although the downward trend of Model 7 is slight, large decreases in L with increasing seafloor age are possible in regimes where $R_c(t)$ and $R_r(t)$ are constant if the CCD or U-lysocline trends with the subsidence curve, such that sediments on seafloor older than a certain age have always been subject to more dissolution than sediments on slightly younger seafloor. With Model 11 (Fig. 6.10), we illustrate this by placing the CCD for the most recent 15 m.y. of model time along the

subsidence curve for 15 Ma seafloor, and keeping the CCD constant for the prior 15 m.y. of model time at 2750 m (the mean depth predicted for 0.5-Ma seafloor). The *U*-lysocline is placed 500 m above the CCD, *H* is set to 300 m, and sediment rain rate and composition are as in Model 1. With this configuration, the sediment accumulation model predicts a sharp decrease in sediment thickness for *T* between 12 and 15 Ma. For seafloor greater than 15 Ma, *L* increases at refractory rain rate of 0.5 m/m.y.

SEDIMENT ACCUMULATION ON YOUNG NORTH ATLANTIC SEAFLOOR

Seismic surveys have mapped out the general distribution of sediments in the North Atlantic [*Tucholke*, 1986; *Tucholke and Uchupi*, 1990]: thick accumulations exist near continents, sediments are generally thin near the MAR, and a gradual increase in sediment thickness, roughly corresponding to increasing seafloor age, takes place between the MAR crest and the continental rises. Near-ridge sediments are fairly thick south of 10° N due to the high productivity of surface waters beneath the equatorial divergence zone. Near-ridge sediments also show an increase in thickness with latitude north of 30° N.

In Chapter 3, we estimate the sediment thickness *L* from basin-centered regions within the ONR Acoustic Research Corridor (ARC), located on 0-29 Ma seafloor on the western flank of the Mid-Atlantic Ridge north of the Kane Fracture Zone (25.5° - 27.25° N, 44.5° - 49° W). The inverted values of *L*, after correction for the effects of compaction (see Fig. 3.44), combined with our forward sediment accumulation model, allow us to address central questions about sedimentation within the central gyre of the North Atlantic: (1) What is the current sediment rain rate? (2) What is the initial composition of sediment prior to any seafloor dissolution? (3) At what depth does the undersaturation of bottom waters in CO_3^{2-} begin to increase the rate at which calcite is dissolved, and does this depth coincide with the calcite lysocline of *Broeker and Takahashi* [1978]? (4) How has sediment rain rate varied with time during the late Cenozoic? (5) How rapidly are sediments currently accumulating in the North Atlantic at various depths?

When modeling sediment accumulation, we assume that *H* is 300 m, slightly larger than the values of *H* we inverted in Chapter 3. We use a B_0 of 1600 m and B_1 of 560 m,

based on the mean seafloor depths of the hill-centered study areas along the southern segment of Chapter 3 (Fig. 6.11).

Current sediment rain rate

Drill core data from near-ridge sediments have been collected at several locations (see Fig. 6.1) and used to construct basin-wide estimates of past CCD values (see Fig. 6.2). Drill cores from DSDP sites 335, 395, and 396 indicate that nannofossil ooze has accumulated in the central gyre of the North Atlantic for at least the past 10-13 m.y. [*Aumento, Melson et al.*, 1977; *Melson, Rabinowitz et al.*, 1978]. Sediment accumulation rates from near-ridge drill holes range from 8 to 100 m/m.y. (see Table 6.1), with the range of rates reflecting both post-depositional transport and variable rates of dissolution (see Chapter 2). Since all drill holes seem to have been sited over local topographic lows, this data suggest that the average sediment accumulation rate since the Miocene has been no higher than 8 m/m.y. Other studies of worldwide sediment accumulation patterns place the accumulation rate in the central North Atlantic at 2-2.5 g/cm^2/k.y. [*Archer*, 1996b; *Jahnke*, 1996], equivalent to 13-16 m/m.y. assuming a sediment density of 1600 kg/m^3.

Our inverted values of L from basin-centered regions within the ARC allow us to address the issue of sediment accumulation rate without concern for the effects of post-depositional transport. Via (4.5), inversion results from Chapter 3 suggest a sediment accumulation rate of 6.3 ± 2.5 m/m.y. for the past 10 m.y. This rate is reduced to 5.9 ± 2.0 m/m.y. if suspect data from subregion B31 is ignored. Assuming that most of the seafloor used to determine this rate resides above the foraminiferal lysocline, we here estimate that the total rain rate is currently 6 m/m.y. when averaged over several million years. This rate is somewhat lower than the published accumulation rates given above, probably due to sampling biases in the published studies. We suspect that, if anything, we overestimate the sediment rain rate, because the sediment thicknesses we inverted in Chapter 3 are more likely to be too high than too low, based on comparisons with single channel seismic data [*Jaroslow and Tucholke*, 1995; *Jaroslow*, 1997].

Lysocline depth and sediment composition

Broeker and Takahashi [1978], referencing Geochemical Ocean Sections Study (GEOSECS) data and the foraminiferal dissolution interpretations of *Kipp* [1976], place the current foraminiferal lysocline in the western North Atlantic at 4800 ± 100 m, roughly 500 m above the current CCD of *Tucholke and Mountain* [1986]. More recently, *Archer* [1996a], also working with GEOSECS data, has placed saturation depth of calcite in the North Atlantic at 4100 m. However, the decrease in calcite content with depth seen in Table 6.1 suggests that calcite dissolution begins higher in the water column.

If we assume that calcite dissolution patterns follow (6.4), for any time t the amount of calcite in deposited sediments should follow

$$\frac{\%CaCO_3}{1-\%CaCO_3} = \left(\frac{R_c(t)}{R_r(t)}\right)\left(\frac{z_{ccd}(t)-z}{z_{ccd}(t)-z_{lys}(t)}\right). \tag{6.9}$$

Casting the most recent calcite composition data from Table 6.1 into the form of (6.9) and determining $\left(R_c(t)/R_r(t)\right)\left(z_{ccd}(t)/\left(z_{ccd}(t)-z_{lys}(t)\right)\right)$ and $\left(R_c(t)/R_r(t)\right)/\left(z_{ccd}(t)-z_{lys}(t)\right)$ via least-squares, we find that the current CCD is placed near 5050 m, even ignoring data from Site 9. If we assume that, as suggested by the Site 332 findings, sediment is originally 93% calcite, the *U*-lysocline is predicted to be a shallow 1000 m. In contrast, a deeper *U*-lysocline of 4050 m would require the pelagic rain to be 23% refractory, which clearly is inconsistent with the data. An intermediate pelagic rain refractory composition of 10 to 12% corresponds to a *U*-lysocline between 2200 and 2700 m above the CCD; an example of the fit between the data of Table 6.1 and the theoretical sediment composition curve when pelagic rain is 88% calcite is given in Fig. 6.12.

The inverted values of L from Chapter 3 suggest a shallow *U*-lysocline as well. Using the CCD of *Tucholke and Mountain* [1986] and placing the *U*-lysocline 500 m above the CCD, as per *Broeker and Takahashi* [1978], we find that if 90%-calcite sediment rained into the ARC at a rate of 6 m/m.y. for the past 15 m.y., we predict that 65 m of sediment accumulates during this time on 25 Ma seafloor, considerably more than is suggested by our inversion results, as shown in Fig. 6.13. Increasing the distance between the CCD and the *U*-lysocline to 1000 m decreases the amount accumulated to 55 m, still more than we

believe resides on 25 Ma seafloor in the ARC. Only a *U*-lysocline/CCD separation of 1500 m or greater adequately prevents an excessive amount of sediment from accumulating.

These results are not much altered by assuming that the CCD for the past 5 m.y. has been a constant 5050 m, the current CCD estimated from the amount of calcite seen in surface sediments, as discussed above.

Based on these results, we estimate that the rate of calcite dissolution in the North Atlantic currently increases at a depth of around 3.5 km, and we suggest that this denotes the surface of the foraminiferal lysocline. A placement of the *U*-lysocline even this high in water column leads to an overestimation of the calcite percentage, however (see Fig. 6.12).

Sediment rain paleorates

In Fig. 6.14, we show that, even allowing a large separation between the CCD and *U*-lysocline of 1500 or 2000 m, a constant sediment rain rate and composition since the Oligocene would have resulted in more sediment accumulating in the western part of the ARC than we estimate in Chapter 3, given the CCD of *Tucholke and Mountain* [1986]. In addition, the CCD during the early and middle Miocene is not well constrained, and could have been as deep as 4500 m, based on sediments at DSDP Site 386 on the Bermuda Rise [*Tucholke and Vogt*, 1979]. This would allow still more sediment accumulation on older crust. Therefore, it seems likely that sediment rain rates were lower within the ARC prior to the middle or late Miocene.

The timing of a rise from a lower sediment rain rate to our current estimate of 6 m/m.y., and the sediment rain rate prior to the rise, are not uniquely determinable from our sediment thickness estimates. In Fig. 6.15, we suggest a range of possible sediment rain rate histories and resulting sediment accumulation patterns, computed assuming the CCD of *Tucholke and Mountain* [1986]. The *U*-lysocline is pinned 1800 m above the CCD, and the sediment rain is taken to have a constant calcite content of 90%. We find that the longer a rain rate increase to 6 m/m.y. is delayed, the higher the rain rate may be before the increase. We are unable to determine whether the rise in sediment rain rate occurred rapidly, or took place over millions of years.

Flower and Kennett [1994] identify 14.8 Ma as a boundary between ocean-climate systems, after which permanent Antarctic glaciation intensified AABW flow, leading to increased upwelling in the eastern Atlantic. However, other authors [*Delaney*, 1990; *Wright et al.*, 1991] suggest low productivity conditions may have persisted through the middle Miocene. Our analysis does not allow us to resolve this matter.

Alternate hypothesis: a shallow CCD prior to the late Miocene

As an alternative to variable sediment rain rates, we also explore whether CCD and *U*-lysocline curves exist which could model the observed variations in sediment thickness given a constant sediment rain rate for the past 30 m.y. We find that if we shoal the CCD slightly between 0 and 15 m.y.B.P., hold the CCD constant at ~3200 m during the prior 15 m.y., maintain a constant 1800 m spacing between the *U*-lysocline and the CCD, and allow 90% of the 6 m/m.y. of sediment rain to be calcite, sediment accumulation patterns are predicted which somewhat resemble the data, as shown in Fig. 6.16. Results improve if the percentage of refractory material is decreased to 5%. Such variations to the CCD are in contradiction of observations at DSDP drill sites, particularly Site 10, however.

Current accumulation rates

Given a total sediment rain rate $R_t(t)$ of 6 m/m.y., an initial calcite content of 90%, a CCD at 5300 m, and a *U*-lysocline at 3500 m and the above defined values for B_0 and B_1, sediment is currently accumulating within the ARC at mean-depth-dependent rates given in Fig. 6.17.

SEDIMENT ACCUMULATION ON YOUNG SOUTH ATLANTIC SEAFLOOR

More so than the western North Atlantic, the South Atlantic might be expected to reflect the effects of changing AABW circulation intensities and patterns and associated variations in upwelling and, hence, surface water biological productivity. Toward this end, several DSDP and ODP legs have been devoted to studying sedimentation in high latitudes, on the margins of South America and Africa, and within the central gyre. Among these

cruises, DSDP legs 3 and 73 drilled at 12 sites located on thinly sedimented abyssal hills between 25° and 31° S, 0° and 30° W [*Maxwell et al.*, 1970; *Hsü, LaBrecque et al.*, 1984] (see Fig. 6.1).

Despite the attention focused on South Atlantic sedimentation, some of the same fundamental questions remain about controls of sedimentation in the central gyre of the South Atlantic as in the North Atlantic. Sediment thickness inversion estimates from densely-sampled near-ridge regions and from basin-spanning tracklines allow us to address these, although with less certainty in our conclusions than we achieve in our analyses of North Atlantic data.

Our inversion of bathymetric data in Chapter 4 reveals symmetric sedimentation about the MAR on young seafloor. When corrected via (2.37) for the effects of post-depositional compaction, current sediment accumulation rates of 5.3 ± 0.5 m/m.y. near 26° S and 6.6 ± 0.5 m/m.y. near 33° S are suggested. DSDP leg 3 and 73 drill sites confirm that local sediment accumulation rates have been less than 10 m/m.y., with the exception of intervals which contain sediment transported by slumps or slides [*Maxwell et al.*, 1970; *Hsü, LaBrecque et al.*, 1984].

Information about off-axis sedimentation is presented in Chapter 5, though coverage limitations and data quality concerns constrain our confidence in the inverted values of L. Keeping in mind the limitations of the data, however, we are able to use inverted values for off-axis sediment thickness, corrected via (2.37) for the effects of compaction, in concert with the near-ridge results of Chapter 4 and with data from DSDP drill sites and other studies of sedimentation in the central regions of the South Atlantic, to study sedimentation in the Angola, Brazil, and Argentine basins.

Current CCD, U-lysocline, and sediment composition

The current CCD in the Angola, Brazil, and Argentine basins, as defined by the depth at which calcite is absent from surface sediments, varies between basins due to AABW flow restrictions. This is reflected in the composition of sediments as recovered at DSDP drill sites, as given in Table 6.2 and Table 6.3 and shown in Fig. 6.18.

Using the surface sediment composition data to determine the proper placement of the current CCD via recasting the data in the form of (6.9) produces unsatisfactory results. In the Angola Basin, the relatively high calcite compositions seen at sites 522 and 523 lead to the placement of the CCD at an unreasonably deep 5300 m.

Hsü et al. [1984] place the current CCD of the Angola Basin near 4700 m and the foraminiferal lysocline ~150 higher in the water column. If we assume that the *Hsü et al.* [1984] CCD represents the depth at which surface sediments have a calcite composition of 30% and that their foraminiferal lysocline represents the 75% calcite composition level, the zero-calcite depth is placed at 4725 m, and the *U*-lysocline is placed at a depth of 4180 m if the sediment is originally 90% calcite or at 3810 m if the sediment is originally 94% calcite. As shown in Fig. 6.19, these values predict slightly too much calcite in surface sediments.

In the Brazil Basin, the CCD is shallower than the present depth of DSDP Site 19, which sits at 4685 m, and is deeper than the 3938-m Site 15. Unfortunately, disturbed cores make the determination of the calcite composition of any post-Pliocene calcareous deposition difficult at DSDP sites 14 and 20, the two DSDP Leg 3 sites with depths between these extremes. Thus, only sites 15 and 16 can be used for calculating the position of the CCD and *U*-lysocline via recasting the data in the form of (6.9). This method produces a CCD estimate of 4500 m and a *U*-lysocline of 3300 m if an original calcite composition of 90% is assumed or a *U*-lysocline of 2400 if an original calcite composition of 94% is assumed. While this estimate of CCD is based on only two data points, it is within the range of possible CCD values, so we take it as the current CCD for the Brazil Basin in the modeling to follow.

In the Argentine Basin, the CCD is clearly shallower than 4300 m, based on the absence of calcite from core-top sediments at DSDP sites 513 and 514. We are unable to speculate as to possible *U*-lysocline positions or original calcite compositions based on available DSDP data.

Sediment rain rates since the late Miocene

If dissolution effects were unimportant above roughly 4000 m, the current sediment accumulation rates on the flanks of the Mid-Atlantic Ridge would be equal to the current

sediment rain rates. However, according to *Hsü et al.* [1984], prior to 5 m.y.B.P., the foraminiferal lysocline was very shallow (see Fig. 6.2), implying that even sediments deposited near the MAR crest were subject to some calcite dissolution at that time.

Using the sediment thickness inversion results from Chapter 4, we constrain the sediment rain rate on the eastern and western flanks of the MAR since the late Miocene at ~26° S and ~33° S using our forward model of sediment accumulation. We assume that sediment is 94% calcite and 6% refractory matter, based on results from Site 359. For each of the four regions we examine, we allow the CCD and *U*-lysocline to follow both the CCD and foraminiferal lysocline of *Hsü et al.* [1984] as modified to reflect local conditions, and also surfaces that place the CCD at the 30% calcite level and the foraminiferal lysocline at the 75% calcite level. For this and all subsequent *U*-lysocline models, where modifications to the *U*-lysocline would place it shallower than 2000 m, it is defined to be 2000 m. We assume that seafloor subsidence follows the form of (6.8), with B_0 and B_1 determined separately for each region, using depths adjusted by mean inverted values of L. The adjusted mean seafloor depths and best-fitting subsidence curves for all near-ridge regions studied are shown in Fig. 6.20. Based on the inversion results of chapters 4 and 5, we take H to be 200 m.

For near-ridge regions in the Angola Basin near 26° S (the Rio Grande study area of Chapter 4), we find that the CCD and foraminiferal lysocline of *Hsü et al.* [1984], when taken to be the CCD and *U*-lysocline, are consistent with a constant total sediment rain rate $R_t(t)$ of 5.5 ± 0.9 m/m.y, as shown in Fig. 6.21. When the CCD is lowered and the *U*-lysocline is raised as described above, we find a higher constant $R_t(t)$ is needed to match the data; we show the result of a constant $R_t(t)$ of 7.0 m/m.y. The data are slightly better modeled by allowing $R_t(t)$ to vary, transiting from 10 m/m.y. before 5 m.y.B.P. to 4 m/m.y. after 3 m.y.B.P.

For modeling sediment accumulation patterns in near-MAR portions of the Brazil Basin (Fig. 6.22), we adjust the CCD and foraminiferal lysocline of *Hsü et al.* [1984] upwards by 200 m for the past 5 m.y., to reflect the higher CCD estimated from the calcite composition data seen at Brazil Basin DSDP sites 15 and 16, as discussed above; this has

no effect on near-ridge accumulation estimates, but becomes important when modeling regions further off-axis.

We find that, within the Brazil Basin, if we take the adjusted CCD and foraminiferal lysocline of *Hsü et al.* [1984] as the CCD and *U*-lysocline, an $R_t(t)$ of 5.2 m/m.y. models the data fairly well, as estimated in Chapter 4. When the CCD is deepened and the *U*-lysocline is shallowed as described above, we find a higher constant $R_t(t)$ of ~6.7 m/m.y. is needed to match the data. Unlike in the Angola Basin, a lowering of $R_t(t)$ during the past 3 m.y. is not suggested.

When modeling sediment accumulation patterns in near-MAR portions of the Argentine Basin (Fig. 6.23), we adjust the CCD and foraminiferal lysocline of *Hsü et al.* [1984] upwards by 400 m for the past 5 m.y., so that the current CCD is near 4300 m. As in the Brazil Basin to the north, this has no effect on near-ridge accumulation estimates. We find that a constant $R_t(t)$ of 6.7 m/m.y. well-models the accumulation patterns seen in data from the western portion of the Cox study area of Chapter 4, using either CCD/*U*-lysocline combination. The near-ridge data do not cross onto old enough seafloor to allow us to determine if a post-Miocene drop in $R_t(t)$ is likely to have occurred.

Slightly older seafloor is sampled on the eastern flank of the MAR in the Cox study area, but again we are unable to determine whether a post-Miocene drop in $R_t(t)$ is required to well-model the data, as shown in Fig. 6.24. We find that a constant $R_t(t)$ of 6.5 m/m.y. does an adequate job of modeling the accumulation patterns, using either the CCD and foraminiferal lysocline of *Hsü et al.* [1984] or the expanded CCD and *U*-lysocline. We do find that a higher rate of 8 m/m.y. prior to 3 m.y.B.P. produces a slightly better fit to the data, but given the scatter seen in the data this improvement in fit is not necessarily indicative of a post-Miocene reduction in sediment rain rate.

We find that if calcite dissolution starts shallow enough to allow the foraminiferal lysocline of *Hsü et al.* [1984] to represent the surface at which 94%-calcite sediment is reduced to containing 75% calcite, all four South Atlantic near-ridge regions we model may have experienced total rain rains of 6.5-7 m/m.y. Thus, the north-south variation in sediment accumulation rate seen in Chapter 4 is not necessarily indicative of a higher sediment rain rate in the Cox study area than in the Rio Grande study area for the past 10

m.y. However, since models which allow a rather low sediment rain rate of 4 m/m.y. for the past 3 m.y., preceded by a period of higher rates, are not precluded by the data for the Rio Grande study area, while $R_t(t)$ for the Cox study areas have definitely been above 6 m/m.y. for the past 3 Ma, we also cannot state that rain rates have been geographically uniform in the South Atlantic since the late Miocene.

The sediment rain rates we estimate for near-ridge regions are much lower than the sediment accumulation rate of 9 m/m.y for the past 4-5 m.y observed at nearby DSDP Site 522. This site is located on a high-standing region of low-relief late Eocene (~37-38 Ma) seafloor [*Hsü, LaBrecque et al.*, 1984]. (The less accurate seafloor age compilation of *Müller et al.* [1993], used in Table 6.3, gives a slightly younger age.) It differs from most ridge flank seafloor in that it does not appear, based on single-channel seismic records (see Fig. 5.30), to have experienced appreciable amounts of lateral sediment transport, though the presence of thicker sediments in nearby valleys than on hillsides indicates that some preferential downslope transport has occurred. Thus, the sediment accumulation rate represents a minimum value of $R_t(t)$.

As would be expected from its depth, Pliocene and Pleistocene sediments at Site 522 have experienced significant amounts of calcite dissolution. In Table 6.3, we give the calcite percent found in the uppermost section of core sampled; the range of calcite compositions seen in post-Miocene samples from Site 522 suggest that 54% of the original calcite has dissolved since initial deposition, if an original sediment composition of 94% calcite us assumed. Given the post-Miocene accumulation rate of 9 m/m.y., this implies an $R_t(t)$ of above 18 m/m.y.

The difference between $R_t(t)$ within the Rio Grande study area and at Site 522 has proven difficult to explain. Site 522 lies outside the high-productivity area associated with upwelling in the Benguela current along the western coast of Africa [e.g. *Pokras and Molfino*, 1986], and the global compilation of primary biological productivity of *Antoine et al.* [1996] suggests that the ocean at Site 522 is less productive than in the Rio Grande study area.

Off-axis sedimentation: Brazil Basin

The Rio Grande Rise formally separates the Argentine Basin from the Brazil Basin to the north. However, since the Rio Grande rise has no expression near the MAR, we define 30° S as the boundary between the basins on young, near-ridge seafloor.

To explore the sediment thickness patterns on seafloor in the Brazil Basin, we compare inverted values of L derive from off-ridge surveys in Chapter 5, corrected for the effects of compaction via (2.37), to sediment accumulation models. We present values of L obtained both when additional model parameters RMS basement variability H and sediment apparent diffusivity κ are allowed to vary, and when H is fixed at a value determined by seafloor spreading rate and near-ridge basement roughness, as described in Chapter 5, prior to inverting for L and κ. We anticipate that the values of L obtained by these methods bracket a range in which the actual average sediment thickness for a region probably lies.

As with the models of the previous section, we assume that sediment is 94% calcite and 6% refractory. We assume that seafloor subsidence follows the form of (6.8), with B_0 and B_1 chosen to be 2590 m and 330 m, respectively, based on the mean depths of the seafloor adjusted by mean inverted values of L, as above. We again take the typical basement variability H to be 200 m. As above, we adjust the CCD and foraminiferal lysocline of *Hsü et al.* [1984] for the past 5 m.y. upwards by 200 m.

If the CCD and U-lysocline follow the modified forms of the CCD and foraminiferal lysocline of *Hsü et al.* [1984], then a constant $R_t(t)$ of the near-ridge value of 5.2 m/m.y. overpredicts sediment thickness on most of the off-ridge seafloor, as shown in Fig. 6.25. If we redefine the CCD and U-lysocline such that the modified forms of the CCD and foraminiferal lysoclines of *Hsü et al.* [1984] represent surfaces at which the sediment is 30% and 90% calcite, respectively, near-ridge data suggests a $R_t(t)$ of 5.5 m/m.y. We find that, although sediment on 15 Ma seafloor undergoes a bit more dissolution in this model, the increase in $R_t(t)$ offsets this effect. Even more dissolution occurs to sediments on 15 Ma seafloor if we redefine the CCD and U-lysocline such that the modified forms of the CCD and foraminiferal lysoclines of *Hsü et al.* [1984] represent surfaces at which the sediment is 30% and 75% calcite, respectively. However, the higher $R_t(t)$ of 6.7 m/m.y.

required based on near-ridge sediment accumulation patterns again offsets much of the dissolution to sediment on 15 Ma seafloor. In addition, the very high *U*-lysocline that this model imposes prior to 15 m.y.B.P. causes the accumulations of sediment on older seafloor to be too low.

We find that modeling sediment accumulation patterns in the Brazil Basin requires modifications to our CCD/*U*-lysocline placements as well as a variable $R_t(t)$. In Fig. 6.26, we show the results of models in which the modified CCD of *Hsü et al.* [1984] represents the surface at which sediment is 30% calcite, as above, and the modified foraminiferal lysocline of *Hsü et al.* [1984] represents the surface at which the sediment is 75% calcite between 0 and 20.5 m.y.B.P., 85% between 20.5 and 24.5 m.y.B.P., and 90% prior to 24.5 m.y.B.P, when the placement of the foraminiferal lysocline by *Hsü et al.* [1984] is most uncertain. This in effect places the *U*-lysocline roughly 500 to 1000 m above the CCD throughout the time period modeled. Using this CCD and *U*-lysocline, a constant sediment rain rate of 5.5 m/m.y. is shown to still fit none of the data particularly well. However, if $R_t(t)$ is lowered to 1 m/m.y. between 10 and 17 m.y.B.P. and is 8 m.y.B.P. before 30 m.y.B.P., the predicted sediment accumulation pattern reflects some of the features evident in the inverted values of *L*. While this model produces, perhaps, the best agreement with inversion results, we find that the proposed formulation of $R_t(t)$ which we found best models sediment accumulation patterns in the North Atlantic ARC also well-models off-axis sedimentation patterns in the Brazil Basin, particularly if the sediment rain rate is allowed to be a high 8 m/m.y. prior to 29 m.y.B.P.

In summary, inversion results from the Brazil Basin suggest that if calcite dissolution does not occur above the foraminiferal lysocline of *Hsü et al.* [1984], the sediment accumulation patterns inverted in Chapter 5 cannot be modeled using a constant $R_t(t)$. If we allow dissolution to begin at shallower depths, less sediment accumulates on middle Miocene-age seafloor, allowing marginally better fits to data. However, in order for less sediment to be present on 15 Ma seafloor than on 10 Ma seafloor, as our inverted values of *L* suggest, $R_t(t)$ must have been lower during the middle Miocene than its average since the end of the Miocene. The extent of the time that $R_t(t)$ was low cannot be determined

from this data, however. We also find that $R_t(t)$ seems to have been higher prior to 30 Ma than at any time thereafter.

We note that the models we present do not predict the low values of L we invert for 42-45 Ma seafloor. This could reflect a misplaced CCD or U-lysocline or a low $R_t(t)$ prior to 40 m.y.B.P.; since the proposed CCD and foraminiferal lysocline of *Hsü et al.* [1984] are poorly constrained for seafloor of this age, we have chosen not to attempt to model this region of seafloor.

Off-axis sedimentation: Angola Basin

In the Angola Basin, many of the results of the inversion process from off-axis data are somewhat problematic, as discussed in Chapter 5. However, matches between models and actual topography suggest that estimates from subregions Z7Z8Z9Z10, Z9Z10Z11Z12, Z11Z12Z13Z14, and Z13Z14Z15Z16, as computed both when H is free to vary and when H is preset at geologically reasonable values, constrain the average thickness of sediment on 20-33 Ma seafloor reasonably well. Using these values, as corrected via (2.37) for the effects of compaction, we employ our forward model of sediment accumulation to determine whether biological productivity has been constant, when averaged over several million year time intervals, or has exhibited long-time-scale variability.

We again assume that sediment is 94% calcite and 6% refractory, that H is 200 m, and that seafloor subsidence follows the form of (6.8). Based on the mean depths of 20-38 Ma seafloor adjusted by mean inverted values of L, we take B_0 and B_1 to be 2660 m and 360 m, respectively. These values place the zero-age seafloor at a slightly different mean depth than in the across-ridge Brazil Basin, probably reflecting the normal variability in seafloor depths along flow lines. Since the sediment accumulation model is very sensitive to seafloor depth, it is very important that the values of B_0 and B_1 used well-model the along-track depths of the seafloor, so no attempt is made to impose uniformity in subsidence histories between regions.

Due to the lack of constraint for accumulation models for seafloor with ages between 11 and 22 Ma and the wide range of possible L values for older seafloor, we find that a number of configurations of $R_t(t)$ are permitted, as shown in Fig. 6.27. If we take the

CCD and foraminiferal lysocline of *Hsü et al.* [1984] to be the model CCD and *U*-lysocline, the computed best near-ridge $R_t(t)$ of 5.5 m/m.y. produces a pattern of sediment accumulation which conforms to the range of estimated L values fairly well. If we take the CCD and foraminiferal lysocline of *Hsü et al.* [1984] to represent the 30% and 75% calcite surfaces, respectively, and assume an $R_t(t)$ of 7 m/m.y., lower sediment accumulations are predicted, but not so low as to rule out the model. Finally, if we take the CCD of *Hsü et al.* [1984] to represent the 30% calcite surface and the foraminiferal lysocline to represent a variable calcite percentage as described for the Brazil Basin, the variable forms of $R_t(t)$ which best fit the North Atlantic ARC and the Brazil Basin both also are not counter indicated by the data. Of all the models we consider, the model optimized for the Brazil Basin, with its period of low sediment rain rate between 10 and 17 m.y.B.P., seems to best model the Angola Basin as well.

In summary, off-axis data analyzed in the Angola Basin generally support sediment rain rates of the range valid for local near-axis regions. None of the models examined predict sediment thicknesses of ~160 m for late Eocene seafloor, such as are seen at nearby DSDP Site 522.

Off-axis sedimentation: Argentine Basin

The Argentine Basin currently bares the full brunt of AABW flow. Yet, sediment thickness maps constructed from seismic data show that, at least on seafloor generated before 25 - 30 Ma, sediments lie thicker than in the Brazil or Angola basins [*Divins and Rabinowitz*, 1990] due to greater biological productivity in surface waters [*Berger*, 1991; *Antoine et al.*, 1996] and/or to terrigenous sediment input from the Antarctic margin via the nepheloid layer [*Biscaye*, 1965].

As discussed in Chapter 5, we are somewhat suspicious of our inversion results from seafloor greater than 20 Ma. As shown by single channel seismic data from DSDP Leg 39 [*Neprochnov et al.*, 1977] (Fig. 6.28), sediments are quite thick on seafloor older than 20 Ma, to the extent that slope distribution functions contain samples of very little area rough enough to reflect the stochastic character of the basement topography. Fixing H prior to inversion for L and κ produces estimates of L which are probably closer to the actual

amount of sediment present than the values obtained when allowing H to vary, but the inverted values of L are sensitive to the values of H chosen (see Table 5.7 and Table 5.8). Where sediments are very thick, such as prior to 0800 on December 6, 1974 in the DSDP Leg 39 along-track SCS data (Fig. 6.28), the seafloor has what appear to be current-generated features large enough to affect slope measurements which occur when L is near the RMS variability of the basement topography. Therefore, we have no confidence in our inversion results from seafloor greater than 25-30 Ma.

The relatively low values of L inverted from ~35 Ma seafloor result from the passage of the tracklines used over high-slope seamounts, and probably do not reflect trends in average sediment thickness.

To determine whether the somewhat shallower seafloor of the Argentine Basin, coupled with near-ridge sediment rain rates which may slightly higher than those active to the north, explain the pattern of inverted sediment thickness as determined in Chapter 5, as corrected for the effects of compaction via (2.37), we again apply our forward sedimentation model. We take the CCD and U-lysocline to be the CCD and foraminiferal lysocline of *Hsü et al.* [1984], modified by raising the post-Miocene CCD and lysocline by 400 m, in response to the lack of calcite in core top sediments at DSDP sites 513 and 514. We use an H of 200 m, and take B_0 and B_1 to be 2580 m and 270 m, respectively, determined as in the Argentine and Brazil basins, with the inclusion of depth data from near-ridge regions to better constrain the inversion for B_0 and B_1. These values reflect that seafloor sampled in the Argentine Basin is shallower than that of the Brazil Basin; a depth anomaly on seafloor greater than 40 Ma is thought to be due primarily to crustal thickening by the Tristan de Cuhna plume [*Ito and Lin*, 1995], and we suspect that this plume has some influence on younger crust as well. Some of the shallowing may also be due to an underestimation of sediment thickness on older seafloor.

For purposes of comparison with results from the Brazil Basin, we again take the sediment to be 94% calcite and 6% refractory. We find that the near-ridge sediment rain rate $R_t(t)$ of 6.7 m/m.y. is not high enough to account for the thickness of sediments observed further off-axis, as shown in Fig. 6.29. Allowing more of the sediment to be refractory would improve the agreement between the model and inverted L values from 10-

18 Ma seafloor. If the lysocline and CCD shallowed as much as predicted by *Hsü et al.* [1984], the refractory composition of sediment during the middle Miocene would have to be ~5 m/m.y.

We suspect that much of the sediment on the Miocene-age seafloor in the Argentine Basin is clay transmitted northward by AABW [*Biscaye*, 1965]; the nepheloid layer is documented as particle-rich as far east as 30° W at 30° S [*Biscaye and Eittreim*, 1977], and sediment cores from DSDP sites 357 and 358 (see Fig. 6.1) show evidence of rapidly-accumulating clays, at rates above 10-20 m/m.y [*Supko and Perch-Nielsen et al.*, 1977]. We suspect, however, that little clay penetrates further east than 20° W, since the sedimentation east of 20° W is fairly symmetric about the MAR.

SUMMARY OF CONCLUSIONS

By comparing sediment thickness estimates inverted from bathymetric data from rough topography beneath the central gyres of the North Atlantic and South Atlantic oceans to model results, we explore possible sediment rain rate histories, CCD curves, and depths at which calcite dissolution rates markedly increase (the *U*-lysocline). Our results seem to suggest that productivity is currently relatively uniform throughout the central gyres. Current intra-gyre sediment rain rates, which range from roughly 5 to 7 m/m.y., seem to have been in place only since ~10 m.y.B.P., somewhat after the intensification of AABW flow as identified by *Flower and Kennett* [1994]. Levels of productivity similar to that of the current ocean seem to prevailed prior to the middle Miocene, but we are unable to determine whether the decrease in productivity occurred at the end of the early Miocene or possibly as early as the end of the early Oligocene. During the Miocene low-productivity period, sediment rain rates seem to have been 15-50% of current values.

Our modeling results suggest that dissolution begins over a kilometer above the CCD in the South Atlantic and almost 2 km above the CCD in the North Atlantic. This places the current start to dissolution high above the foraminiferal lysocline as estimated by *Broeker and Takahashi* [1978] or *Archer* [1996a].

In most of the regions we examine, terrigenous sedimentation has been relatively unimportant. However, although 12-20 Ma seafloor in the Brazil Basin bears little

sediment, seafloor of this age in the Argentine Basin seems to have accrued sediment at greater than the current near-ridge rate. We suspect that this is due to the influx of clays from the south.

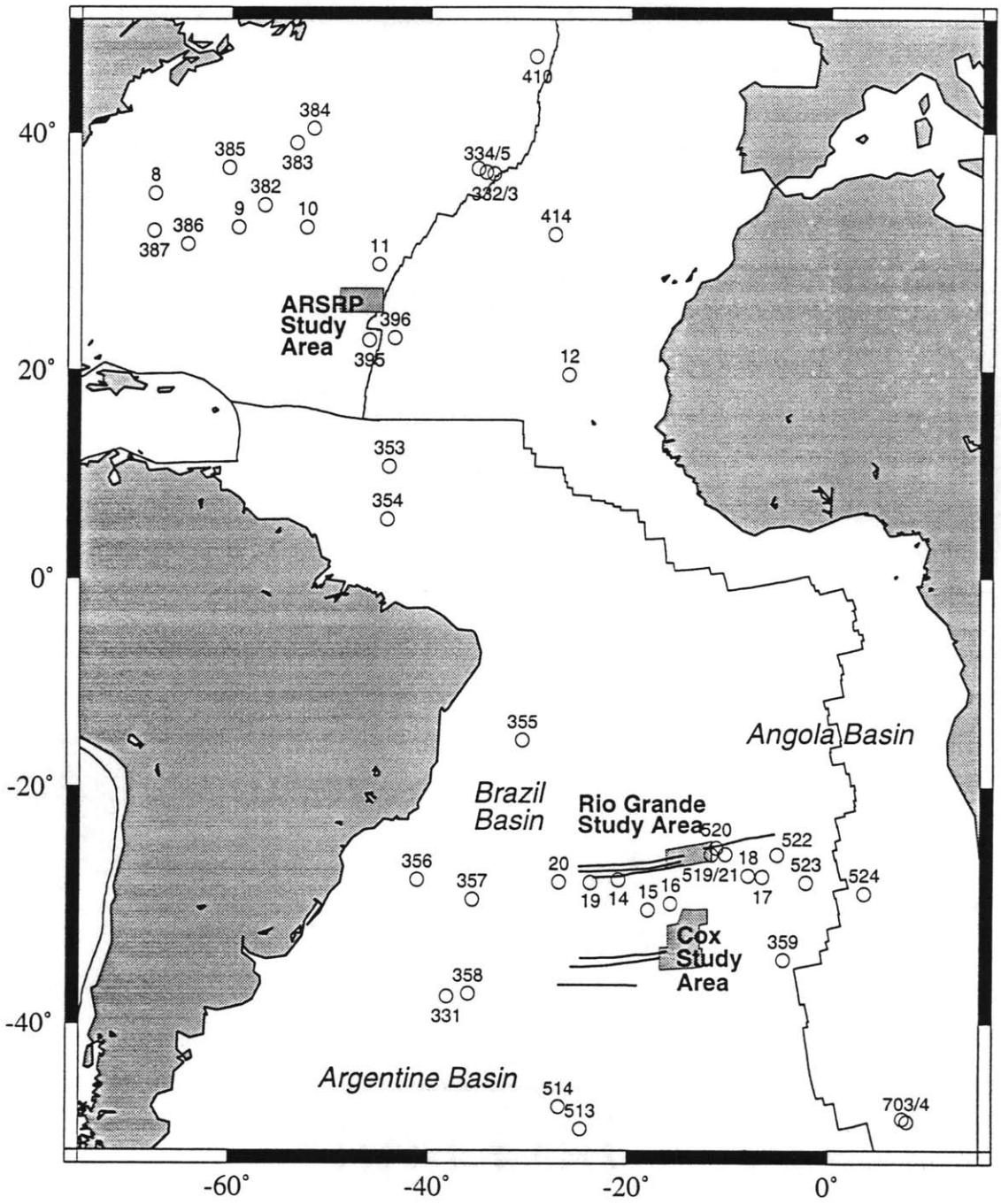

Fig. 6.1 Location map showing all study areas and tracklines where sediment thickness is estimated in previous chapters, and all drill sites referenced in the text.

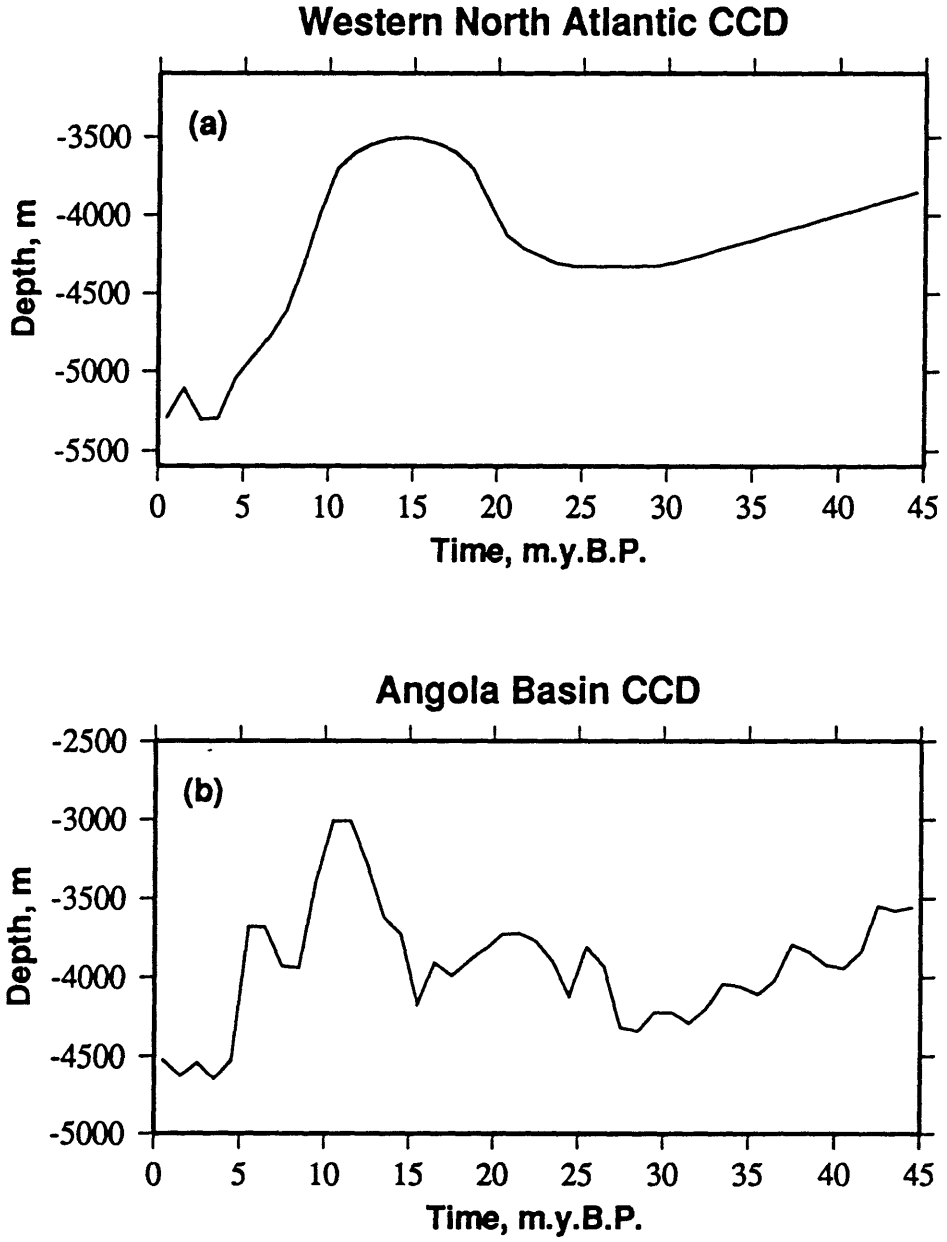

Fig. 6.2: CCD curves estimated for the Atlantic Basin. (a) Western North Atlantic CCD curve of *Tucholke and Mountain* [1986]. (b) Angola Basin CCD of *Hsü et al.* [1984].

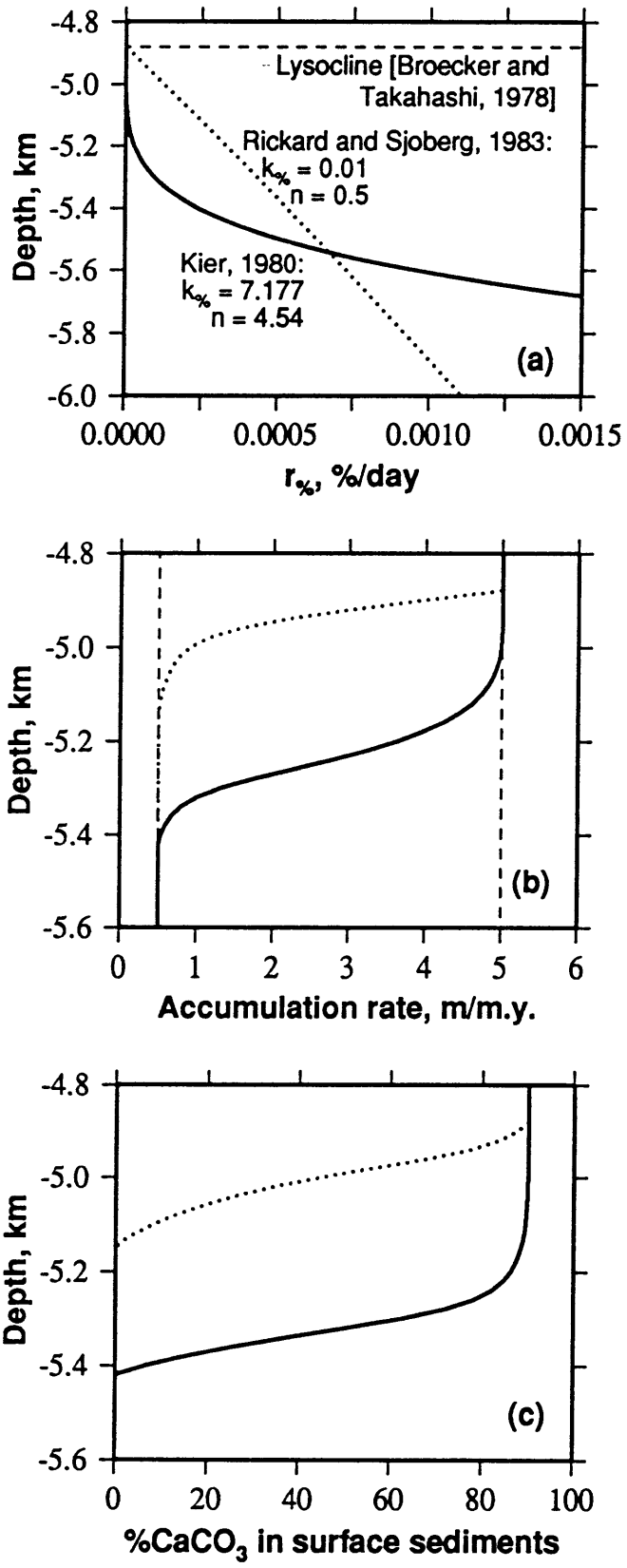

Fig. 6.3 (a) Estimates of calcite dissolution rates, in %/day, using the equations of *Rickard and Sjöberg* [1983] and *Kier* [1980], as presented in the text by equations (6.1) and (6.2). (b) Accumulation rate predicted by (a), given the thickness of the layer of sediment susceptible to dissolution as described in the text. (c) Surface sediment percent calcite, given (b).

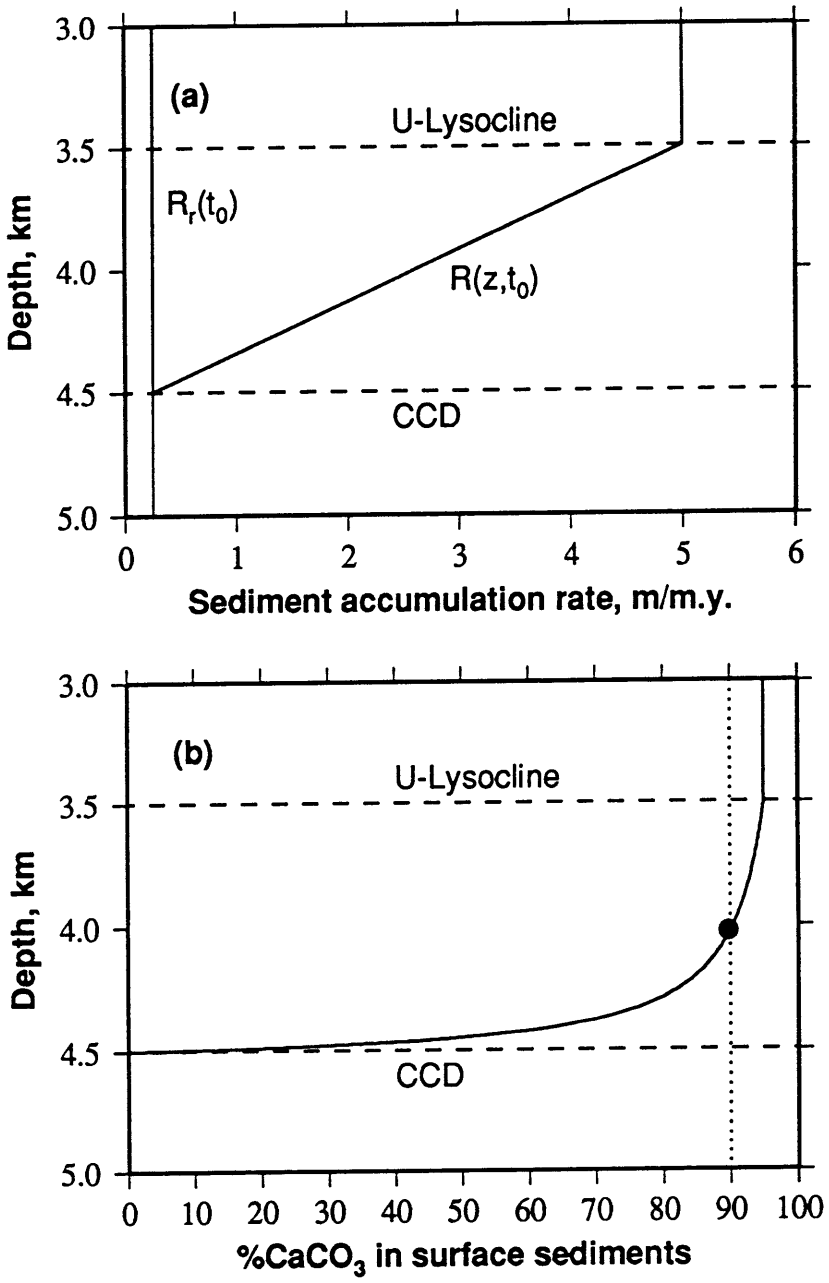

Fig. 6.4: (a) Relationship between the *U*-lysocline, CCD, refractory sediment rain rate $R_r(t)$, and predicted sediment accumulation rate at depth z. (b) Relationship between the *U*-lysocline, CCD, and percent calcite in deposited sediments, given the sediment rain rate structure of (a). Dot represents the depth where the calcite lysocline might be identified if a calcite percentage of 90% or less were used as the primary selection criteria.

Fig. 6.5: Sediment accumulation patterns predicted given a constant sediment rain rate structure and CCD and a variety of *U*-lysoclines, for models 1, 2, and 3 described in the text. (a) Refractory and total sediment rain rates used: $R_r(t)$ = 0.5 m/m.y., $R_t(t)$ = 5.0 m/m.y. (b) Bottom solid line represents CCD, set at 4500 m. Dashed line, upper solid line, and dotted line represent *U*-lysoclines set at 4000, 3500, and 2500 m, respectively. Thinner dashed lines represent the subsidence history of 5, 10, 15, 20, 25, and 30 Ma seafloor in this model. (c) Predicted sediment thicknesses as a function of seafloor age using the sediment rain rates of (a) and the lysoclines of (b), with the solid line resulting from the use of the lysocline of Model 1, the dashed line resulting from the use of the lysocline of Model 2, and the dotted line resulting from the use of the lysocline of Model 3.

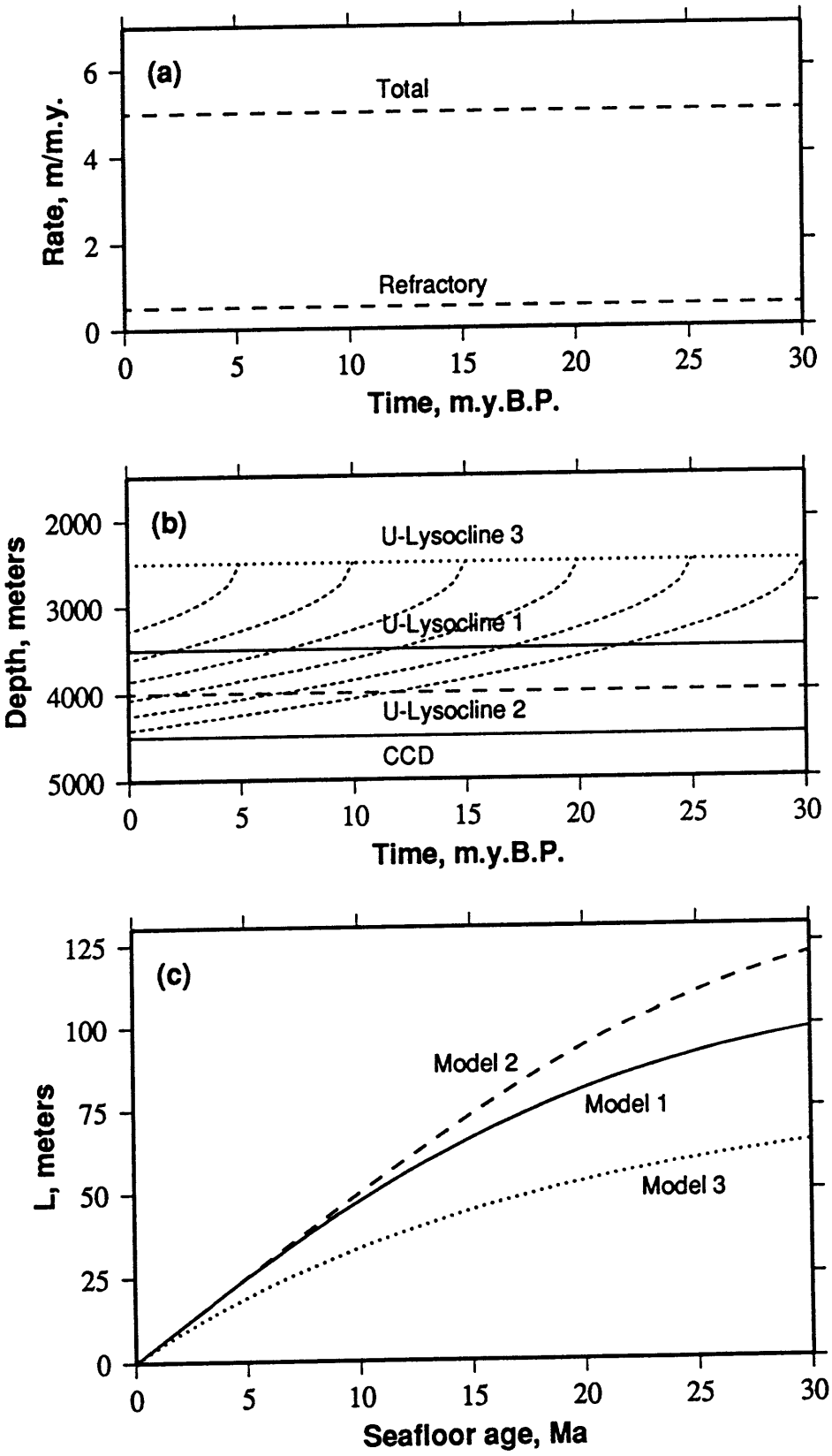
(a)
Total
Refractory
Rate, m/m.y.
0
2
4
6
0
5
10
15
20
25
30
Time, m.y.B.P.
(b)
U-Lysocline 3
U-Lysocline 1
U-Lysocline 2
CCD
Depth, meters
2000
3000
4000
5000
0
5
10
15
20
25
30
Time, m.y.B.P.
(c)
Model 2
Model 1
Model 3
L, meters
0
25
50
75
100
125
0
5
10
15
20
25
30
Seafloor age, Ma

Fig. 6.6: Sediment accumulation patterns predicted by variable sediment rain rates and a constant CCD and *U*-lysocline, for models 4 and 5 described in the text. (a) Refractory and total sediment rain rates used. For Model 4, $R_r(t)$ = 0.5 m/m.y. and $R_t(t)$ = 5.0 m/m.y. between 0 and 15 m.y.B.P., and $R_r(t)$ = 0.2 m/m.y. and $R_t(t)$ = 2.0 m/m.y. between 15 and 30 m.y.B.P. For Model 5, these are reversed. (b) Thicker dashed lines are the CCD, set at 4500 m, and the *U*-lysocline, set at 3500 m. Thinner dashed lines represent the subsidence history of 5, 10, 15, 20, 25, and 30 Ma seafloor in this model. (c) Predicted sediment thicknesses as a function of seafloor age from the sediment rain rates of (a) and the CCD and *U*-lysocline of (b). The solid line results from the use of the rain rates of Model 4 and the dashed line resulting from the rain rates of Model 5.

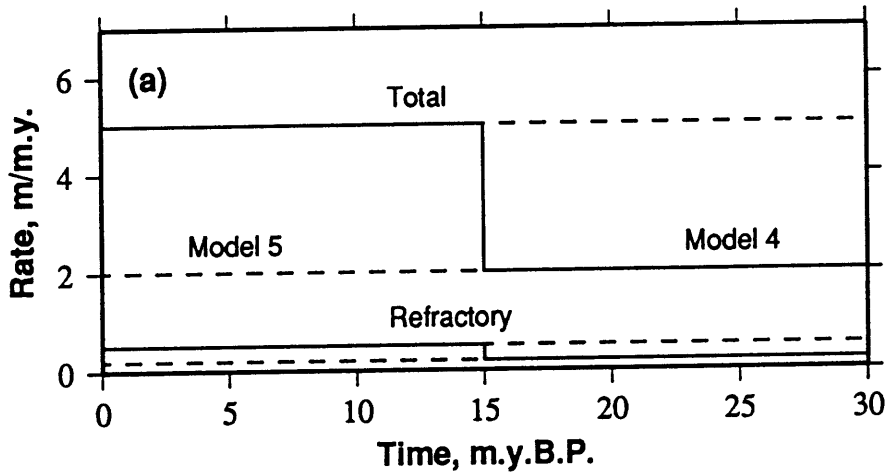
(a)
Total
Model 5
Model 4
Refractory
Rate, m/m.y.
0
2
4
6
0
5
10
15
20
25
30
Time, m.y.B.P.

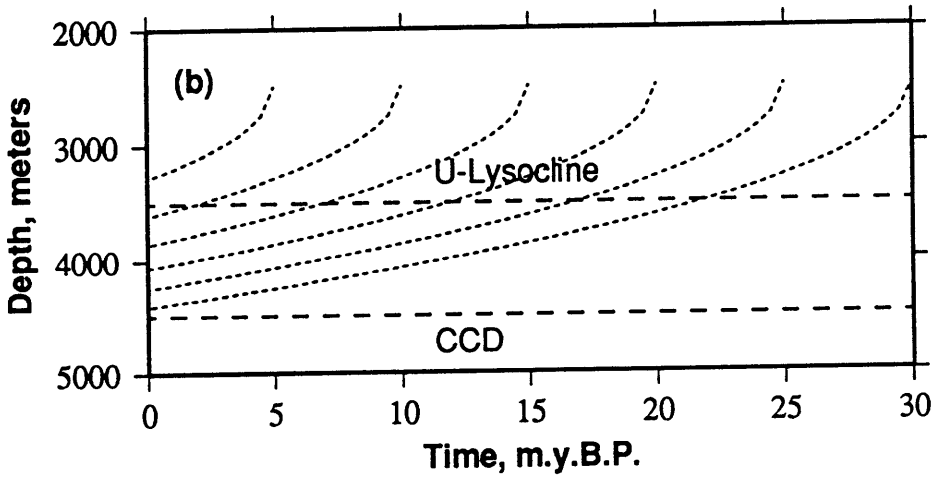
(b)
U-Lysocline
CCD
Depth, meters
2000
3000
4000
5000
0
5
10
15
20
25
30
Time, m.y.B.P.

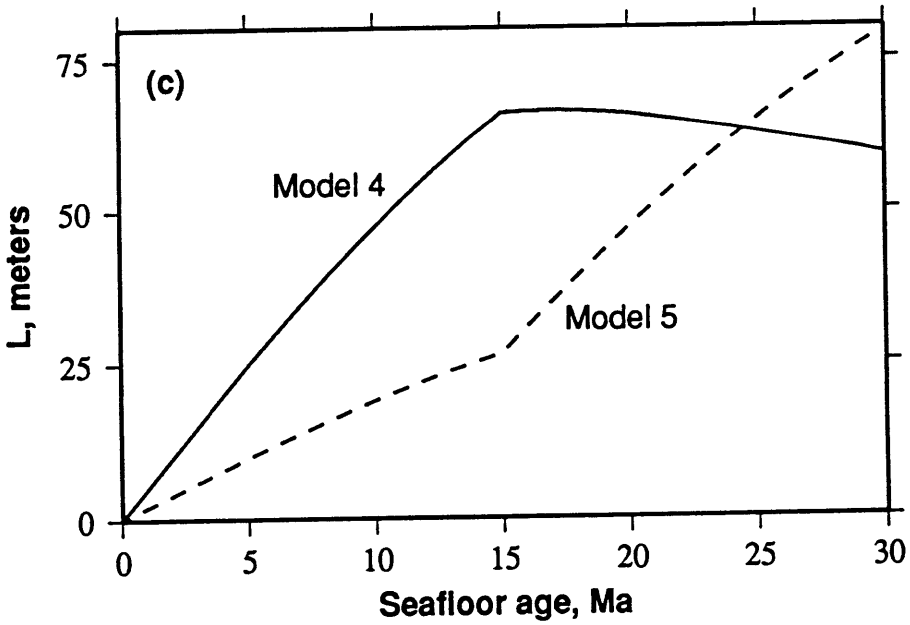
(c)
Model 4
Model 5
L, meters
0
25
50
75
0
5
10
15
20
25
30
Seafloor age, Ma

Fig. 6.7: Sediment accumulation patterns predicted given constant sediment rain rates and time-variable CCD and *U*-lysoclines, for models 6 and 7 described in the text. (a) Refractory and total sediment rain rates used are 0.5 m/m.y. for $R_r(t)$ and 5.0 m/m.y. for $R_t(t)$. (b) Bottom solid line represents CCD, set at 5000 m between 0 and 15 m.y.B.P. and at 4000 m between 15 and 30 m.y.B.P. Upper solid line represents the lysocline of Model 6, set at 4000 m between 0 and 15 m.y.B.P. and at 3000 m between 15 and 30 m.y.B.P. Thicker dashed line represents the lysocline of Model 7, set at 3000 m between 0 and 15 m.y.B.P. and at 2000 m between 15 and 30 m.y.B.P. Thinner dashed lines represent the subsidence history of 5, 10, 15, 20, 25, and 30 Ma seafloor in this model. (c) Predicted sediment thicknesses as a function of seafloor age using the rain rates of (a) and the *U*-lysoclines of (b) , with the solid line resulting from the use of *U*-Lysocline 6 (Model 6), and the dashed line resulting from the use of *U*-Lysocline 7 (Model 7). Also shown is the predicted sediment thicknesses associated with Model 1 (dotted line).

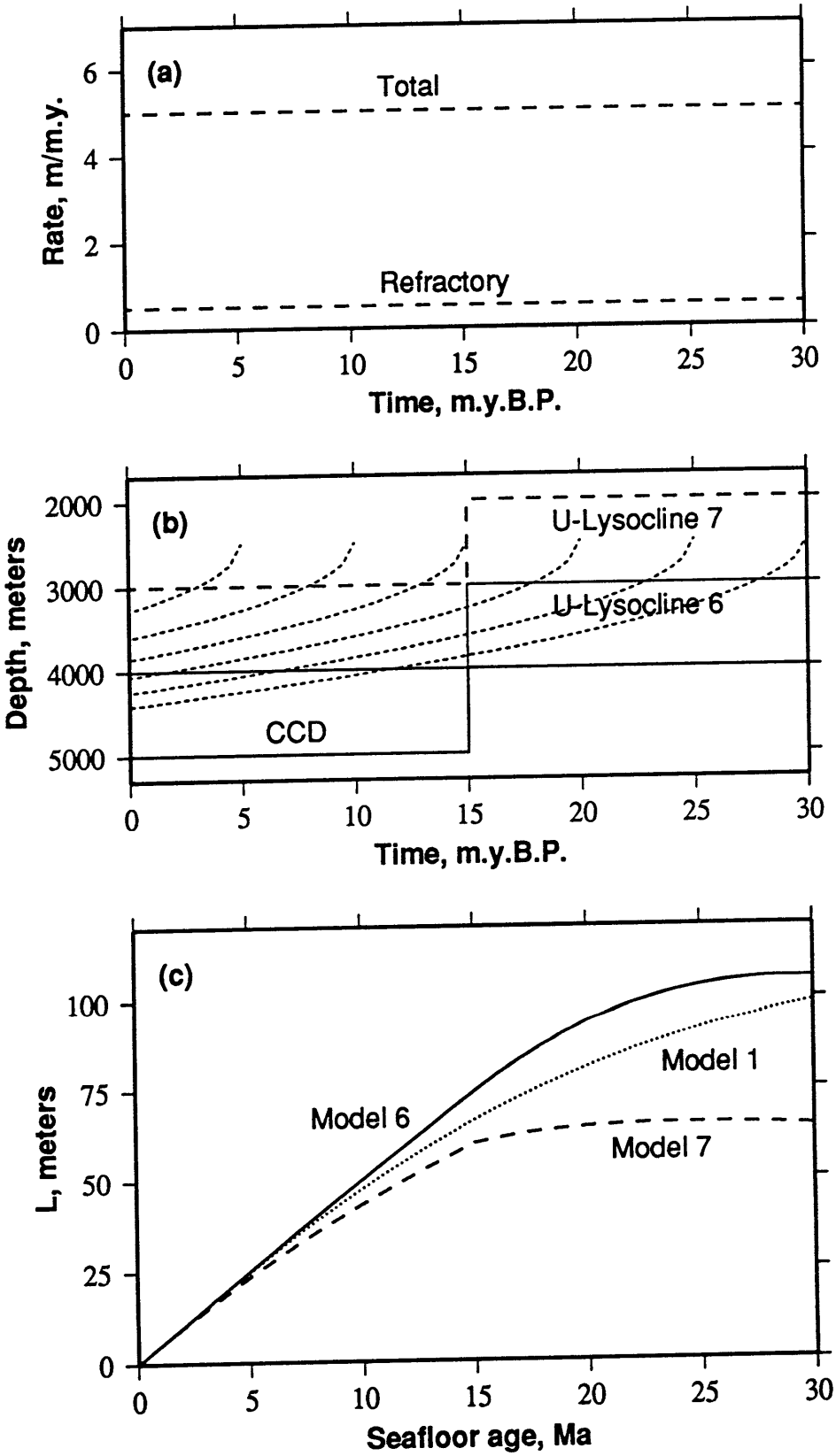
(a)
Total
Refractory
Rate, m/m.y.
0
2
4
6
0
5
10
15
20
25
30
Time, m.y.B.P.
(b)
U-Lysocline 7
U-Lysocline 6
CCD
Depth, meters
2000
3000
4000
5000
0
5
10
15
20
25
30
Time, m.y.B.P.
(c)
Model 1
Model 6
Model 7
L, meters
0
25
50
75
100
0
5
10
15
20
25
30
Seafloor age, Ma

Fig. 6.8: Sediment accumulation patterns predicted given a constant total sediment rain rate but a variable $R_r(t)$, for models 8 and 9 described in the text, as compared to Model 3. (a) Variable refractory sediment rain rates $R_r(t)$ used: 0.25 m/m.y. (Model 8, solid line) and 1 m/m.y. (Model 9, dashed line) m/m.y. Also shown by the dotted line is an $R_r(t)$ of 0.5 m/m.y. for Model 3. The total sediment rain rate $R_t(t)$ for these models is 5 m/m.y. (b) Bottom thicker dashed line represents CCD, set at 4500 m, and upper thicker dashed line represents the U-lysocline, set at 2500 m. Thinner dashed lines represent the subsidence history of 5, 10, 15, 20, 25, and 30 Ma seafloor. (c) Predicted sediment thicknesses as a function of seafloor age using the sediment rain rates of (a) and the lysocline and CCD of (b), with the solid line corresponding to Model 8, the dashed line corresponding to Model 9, and the dotted line corresponding to Model 3 of Fig. 6.5 (for comparison.)

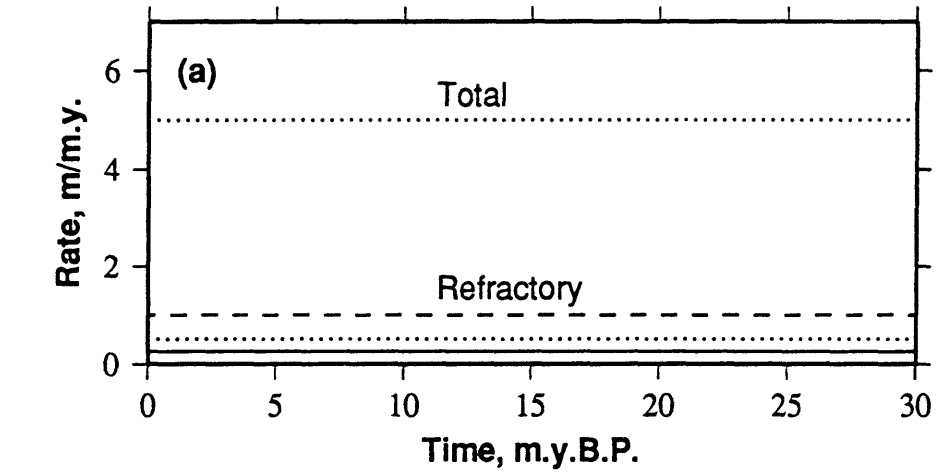
(a)
Total
Refractory
Rate, m/m.y.
0
2
4
6
0
5
10
15
20
25
30
Time, m.y.B.P.

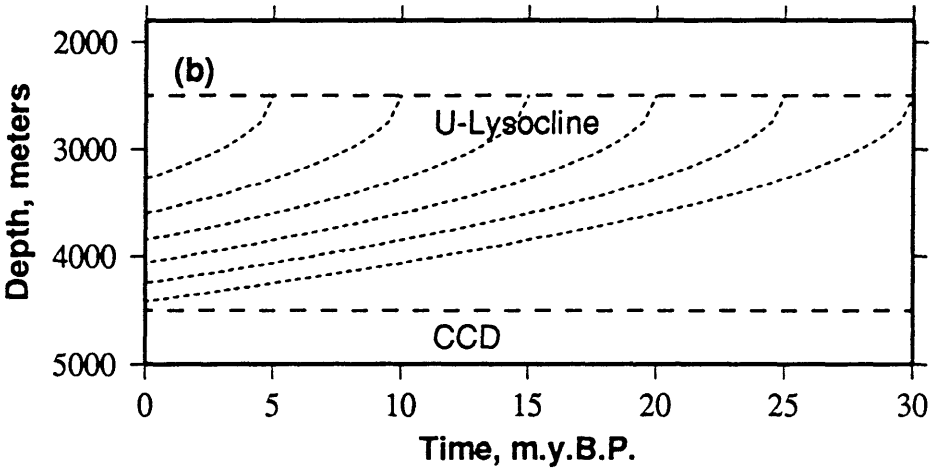
(b)
U-Lysocline
CCD
Depth, meters
2000
3000
4000
5000
0
5
10
15
20
25
30
Time, m.y.B.P.

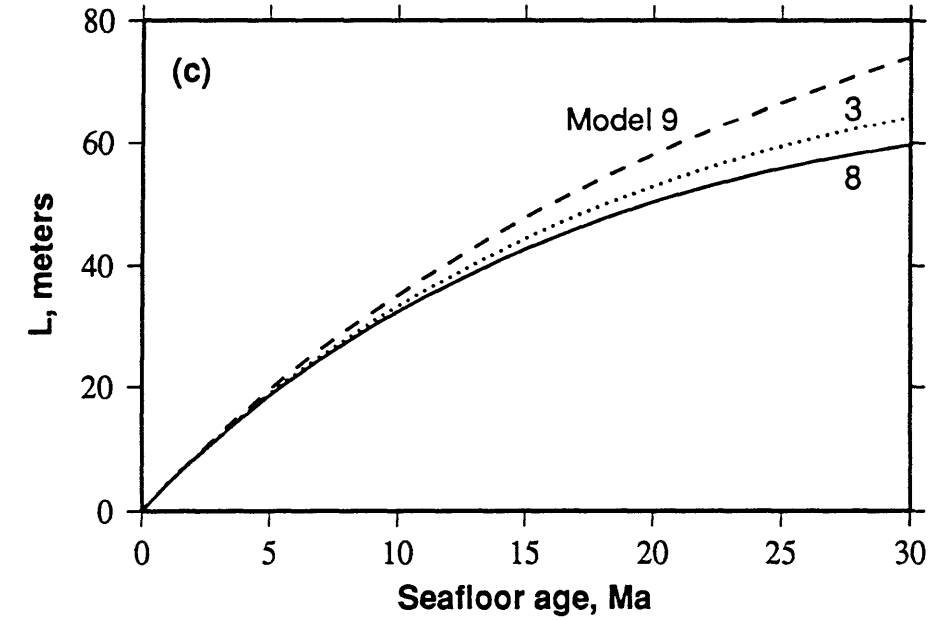
(c)
Model 9
3
8
L, meters
0
20
40
60
80
0
5
10
15
20
25
30
Seafloor age, Ma

Fig. 6.9: Sediment accumulation patterns predicted given a constant sediment rain rate structure, CCD, and *U*-lysocline, computed using an H of 0, appropriate for modeling level topography or the sedimentation history at a single location, as described in the text (Model 10). (a) Refractory and total sediment rain rates used are 0.5 m/m.y. for $R_r(t)$ and 5.0 m/m.y. for $R_t(t)$. (b) Bottom thicker dashed line represents CCD, set at 4500 m, and upper thicker dashed line represents the *U*-lysocline, set at 2500 m. Thinner dashed lines represent the subsidence history of 5, 10, 15, 20, 25, 30, 35 and 40 Ma seafloor. (c) Predicted sediment thicknesses as a function of seafloor age using the sediment rain rates of (a) and the *U*-lysocline and CCD of (b) with the solid line resulting from the use of an H of 0 m (Model 10) and the dotted line produced using an H of 300 m, as in Model 1 of Fig. 6.5.

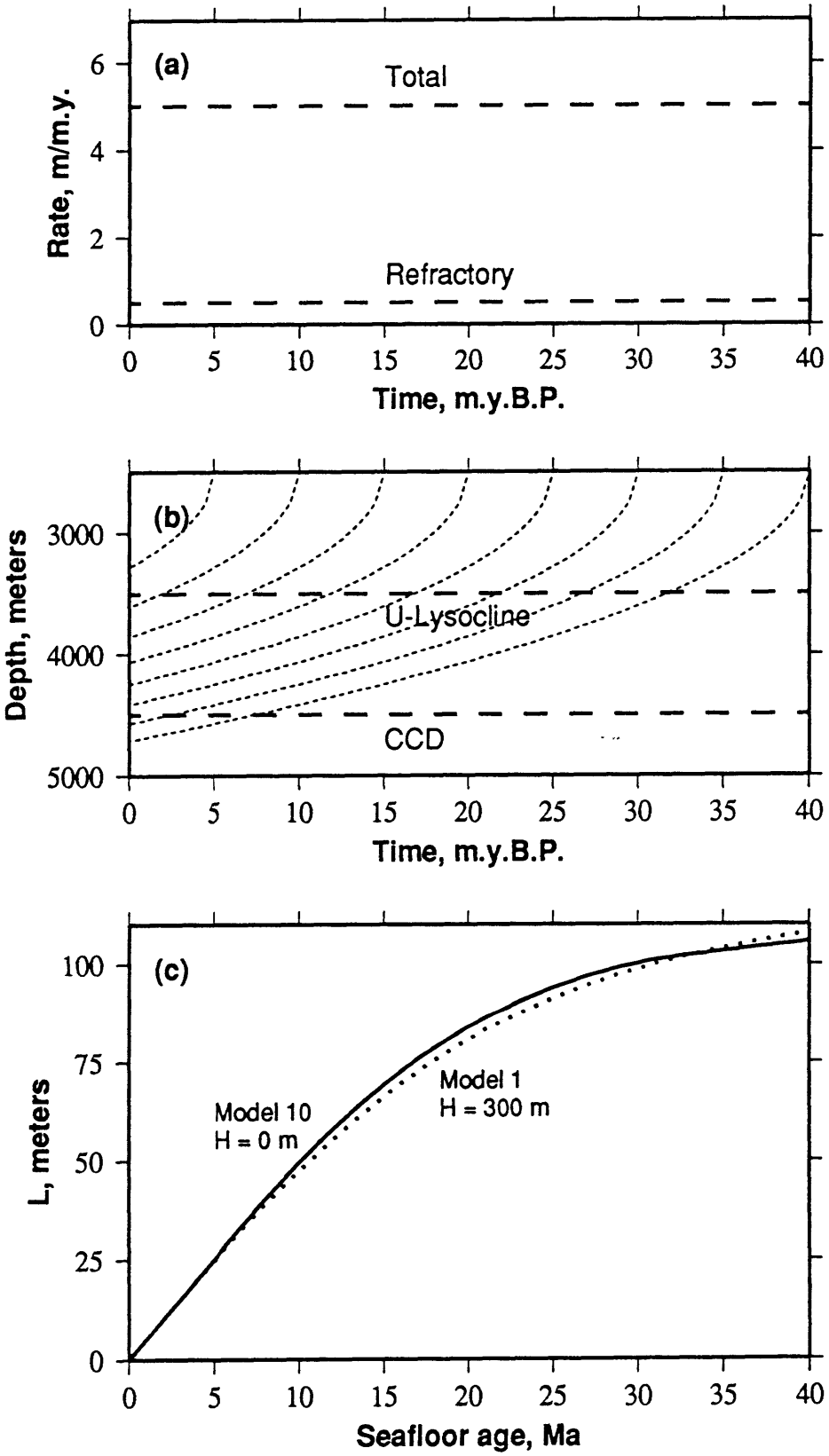
(a)
Total
Refractory
Rate, m/m.y.
0
2
4
6
0
5
10
15
20
25
30
35
40
Time, m.y.B.P.
(b)
U-Lysocline
CCD
Depth, meters
3000
4000
5000
0
5
10
15
20
25
30
35
40
Time, m.y.B.P.
(c)
Model 10
H = 0 m
Model 1
H = 300 m
L, meters
0
25
50
75
100
0
5
10
15
20
25
30
35
40
Seafloor age, Ma

Fig. 6.10: Sediment accumulation patterns predicted given a constant sediment rain rate structure and a CCD and *U*-lysocline designed to produce greater sediment thicknesses on 10 Ma seafloor than on 15 Ma seafloor, described in the text as Model 11. (a) Refractory and total sediment rain rates used: $R_r(t)$ = 0.5 m/m.y., $R_t(t)$ = 5.0 m/m.y. (b) Bottom solid line represents CCD, designed such that between 0 and 14.5 m.y.B.P. it followed the subsidence curve predicted for 15 Ma seafloor. Before 14.5 m.y.B.P., the CCD is at 2747 m. The *U*-lysocline, given by the higher solid line, is located 500 m above the CCD. Thin dashed lines represent the subsidence history of 5, 10, 15, 20, 25, and 30 Ma seafloor. (c) Predicted sediment thicknesses as a function of seafloor age using the sediment rain rates of (a) and the lysocline and CCD of (b).

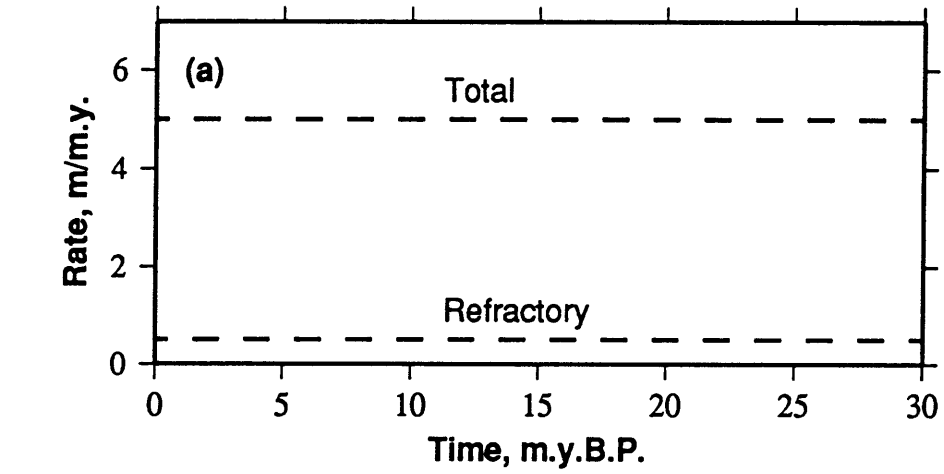
(a)
Total
Refractory
Rate, m/m.y.
0
2
4
6
0
5
10
15
20
25
30
Time, m.y.B.P.

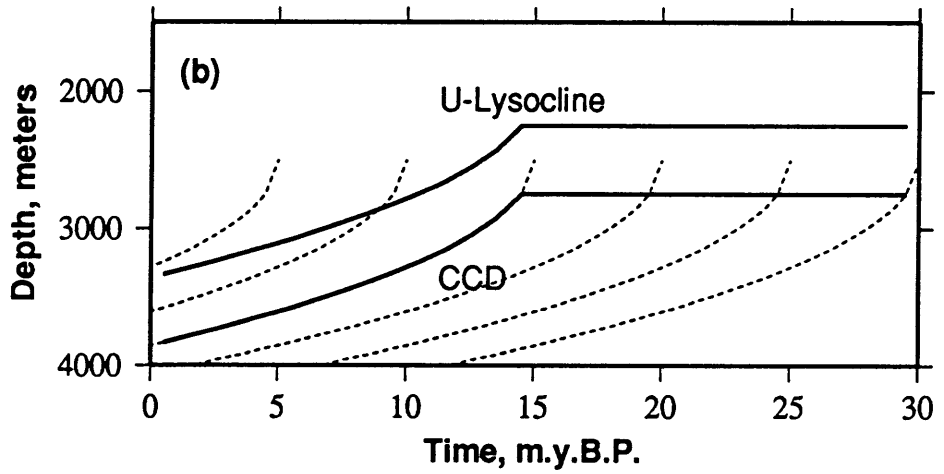
(b)
U-Lysocline
CCD
Depth, meters
2000
3000
4000
0
5
10
15
20
25
30
Time, m.y.B.P.

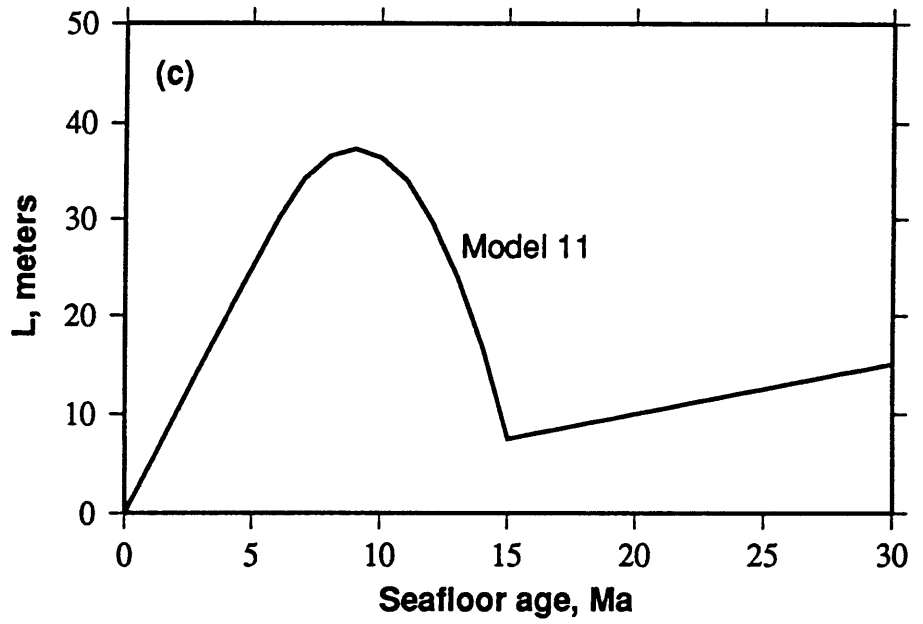
(c)
Model 11
L, meters
0
10
20
30
40
50
0
5
10
15
20
25
30
Seafloor age, Ma

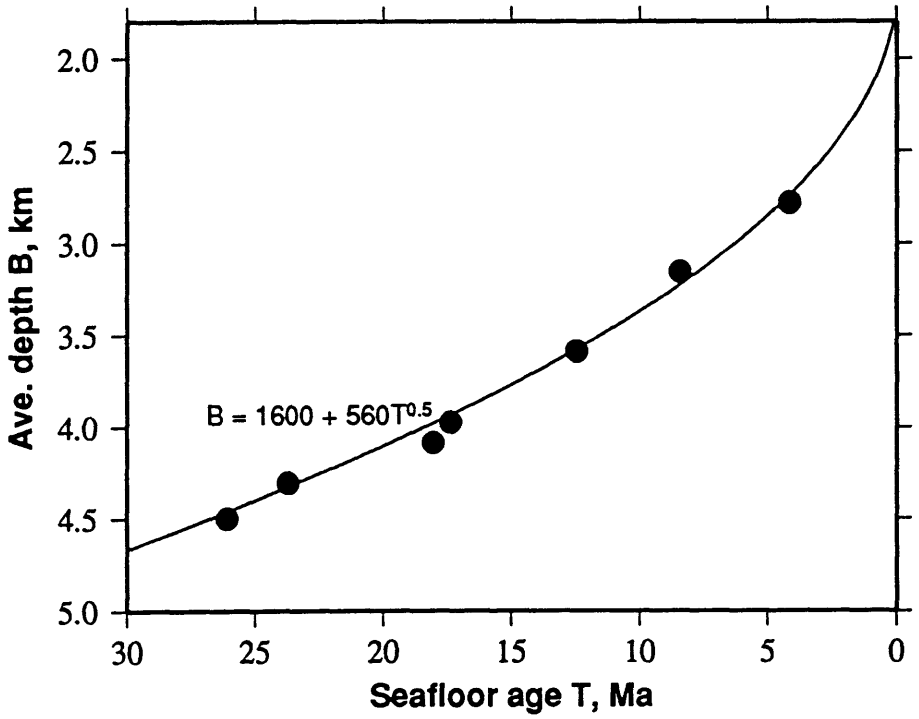

Fig. 6.11: Average seafloor depths for seafloor of varying ages for hill-centered subregions along the southern spreading center of the ARC, as described in Chapter 3 (dots) and best-fitting subsidence curve (dashed line).

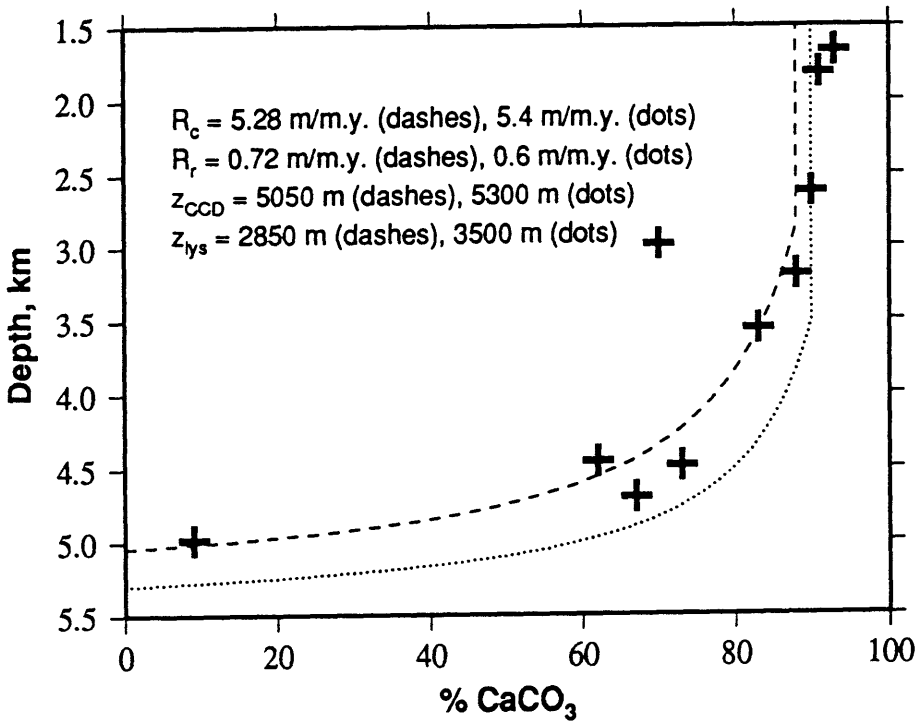

Fig. 6.12: Percent calcite observed in near-surface sediments from the DSDP sites listed in Table 6.1 (crosses), and predicted percent calcite based on (6.4) using (1) an original calcite composition of 88% and the CCD and *U*-lysocline estimated by casting composition data into the form of (6.9) (dashed line); and (2) an original calcite composition of 90%, a CCD of 5300 m, and a *U*-lysocline of 3500 m (dotted line).

Fig. 6.13: Amount of sediment accumulated during the past 15 m.y. in the North Atlantic, compared to compaction-corrected inverted values of L from basin-centered regions of Chapter 3. (a) Refractory and total sediment rain rates used: $R_r(t)$ = 0.6 m/m.y., $R_t(t)$ = 6.0 m/m.y. for 0-15 Ma seafloor, based on trend seen on 0-10 Ma seafloor. (b) Solid line represents CCD of *Tucholke and Mountain* [1986]. Dotted lines represent candidate U-lysoclines, lying 500, 1000, 1500, and 2000 m above the CCD. (c) Predicted sediment distributions using the sediment rain rates of (a) and the U-lysoclines of (b), compared to inverted values of L. The lowermost line corresponds to the most shallow U-lysocline, with deeper U-lysoclines allowing increasingly more sediment accumulation on older seafloor.

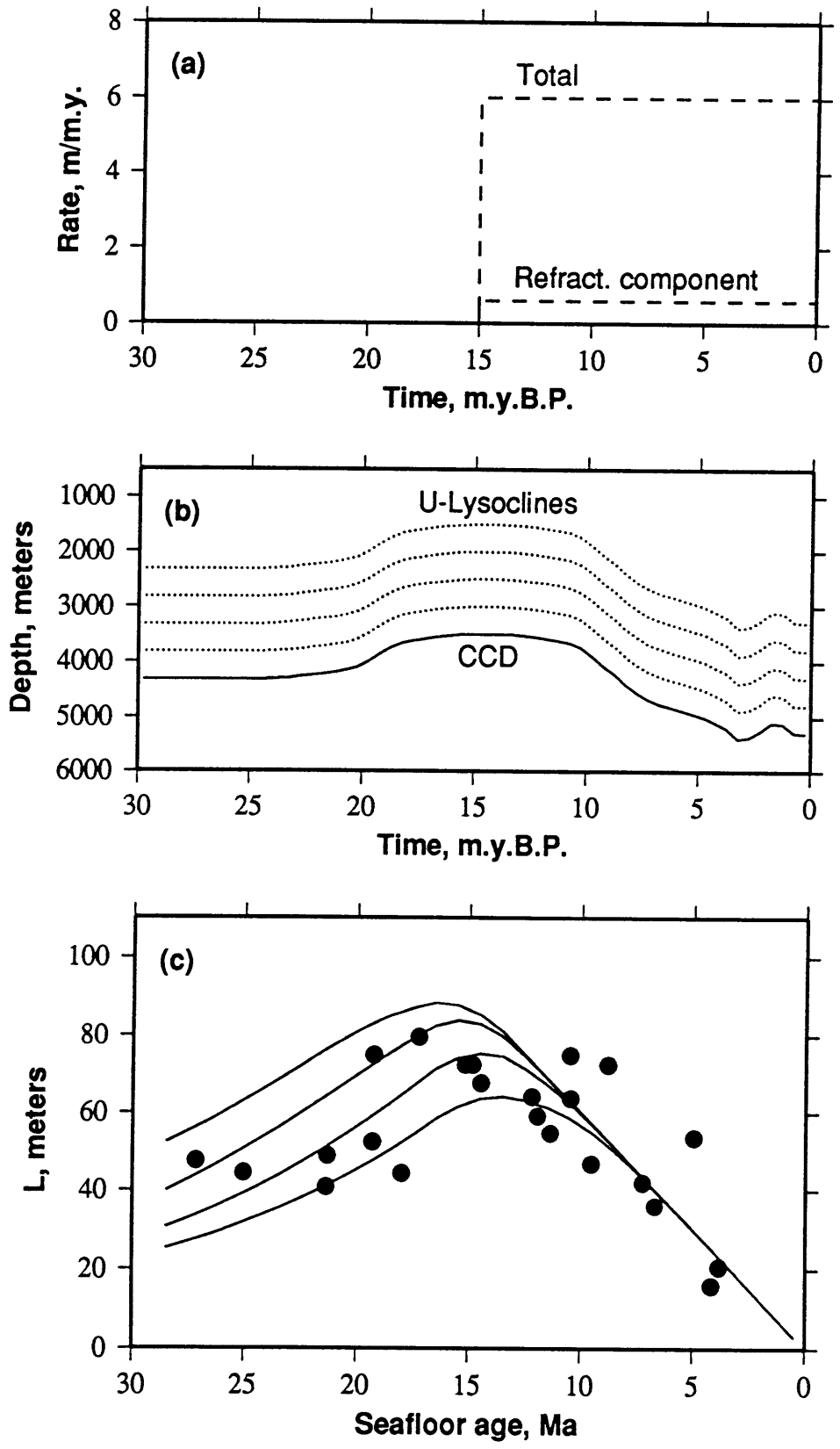
(a)
Total
Refract. component
Rate, m/m.y.
Time, m.y.B.P.
(b)
U-Lysoclines
CCD
Depth, meters
Time, m.y.B.P.
(c)
L, meters
Seafloor age, Ma

Fig. 6.14: Amount of sediment predicted for the ARC assuming a constant sediment rain rate for 30 m.y., compared to compaction-corrected inverted values of L from basin-centered regions of Chapter 3. (a) Refractory and total sediment rain rates used: $R_r(t)$ = 0.6 m/m.y., $R_t(t)$ = 6.0 m/m.y. for 0-30 Ma seafloor, based on trend seen on 0-10 Ma seafloor. (b) Solid line represents CCD of *Tucholke and Mountain* [1986]. Dotted lines represent candidate U-lysoclines, lying 500, 1000, 1500, and 2000 m above the CCD. (c) Predicted sediment distributions using the sediment rain rates of (a) and the U-lysoclines of (b), compared to inverted values of L. The lowermost line corresponds to the most shallow U-lysocline, with deeper U-lysoclines allowing increasingly more sediment accumulation on older seafloor.

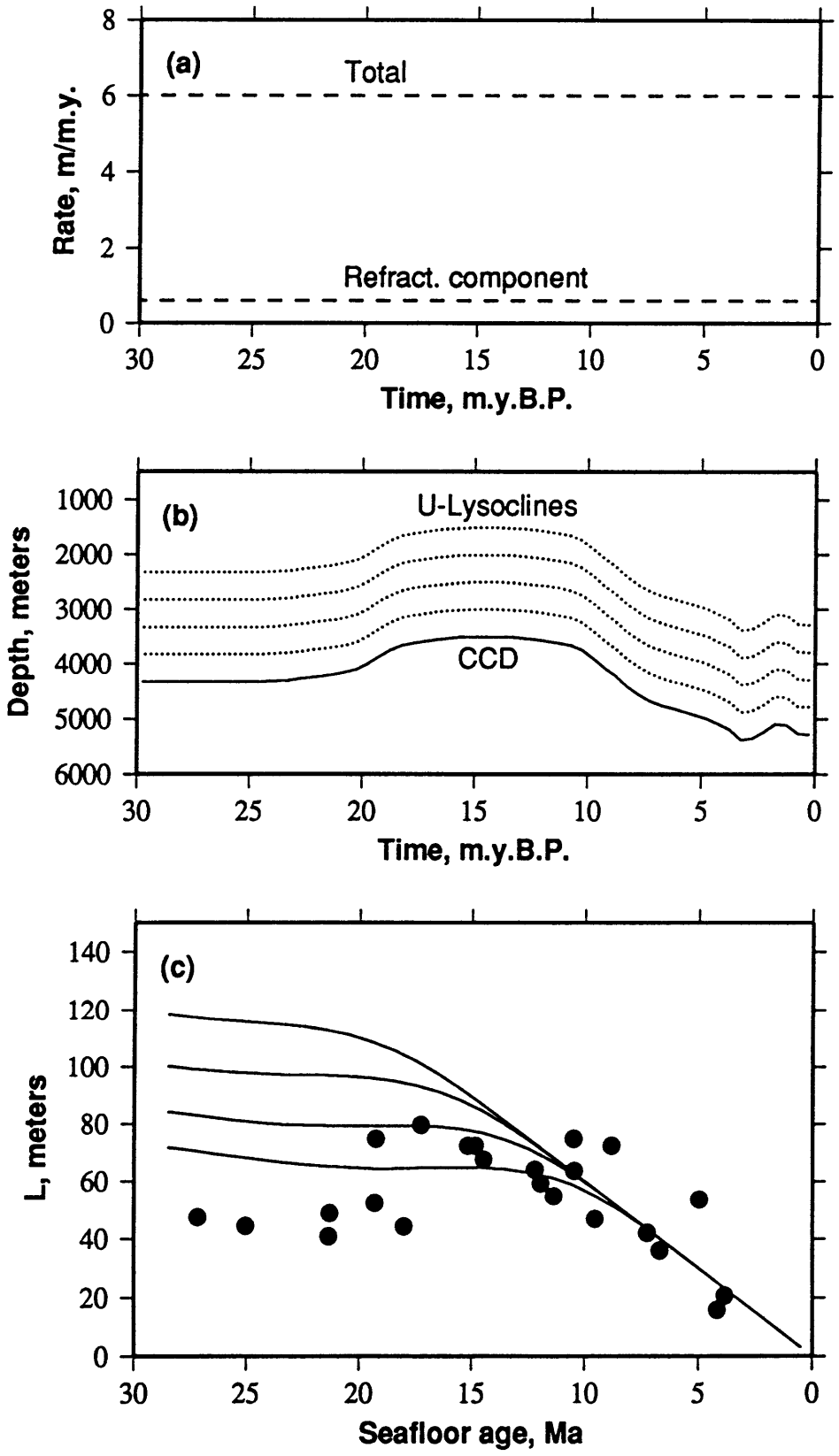
(a)
Total
Refract. component
Rate, m/m.y.
8
6
4
2
0
30
25
20
15
10
5
0
Time, m.y.B.P.
(b)
U-Lysoclines
CCD
Depth, meters
1000
2000
3000
4000
5000
6000
30
25
20
15
10
5
0
Time, m.y.B.P.
(c)
L, meters
140
120
100
80
60
40
20
0
30
25
20
15
10
5
0
Seafloor age, Ma

Fig. 6.15: Results of possible models, compared to compaction-corrected inverted values of L from basin-centered regions of Chapter 3. (a) Refractory and total sediment rain rates used in the models. Dashed lines correspond to an $R_r(t)$ of 0.15 m/m.y. and an $R_t(t)$ of 1.5 m/m.y. prior to 13 m.y.B.P., and of 0.6 m/m.y. and 6.0 m/m.y., respectively, since 13 m.y.B.P. Dotted lines correspond to an $R_r(t)$ of 0.3 m/m.y. and an $R_t(t)$ of 3.0 m/m.y. prior to 10 m.y.B.P., and of 0.6 m/m.y. and 6.0 m/m.y., respectively, since 10 m.y.B.P. Thin solid lines correspond to an $R_r(t)$ of 0.1 m/m.y. and an $R_t(t)$ of 1.0 m/m.y. prior to 15 m.y.B.P., and of 0.6 m/m.y. and 6.0 m/m.y., respectively, since 15 m.y.B.P. Thick solid lines correspond to an $R_r(t)$ of 0.2 m/m.y. and an $R_t(t)$ of 2.0 m/m.y. prior to 15 m.y.B.P., a gradual increase in $R_r(t)$ and $R_t(t)$ between 15 and 11 m.y.B.P., and an $R_r(t)$ and $R_t(t)$ of 0.6 m/m.y. and 6.0 m/m.y., respectively, since 11 m.y.B.P. (b) Lower solid line represents CCD of *Tucholke and Mountain* [1986]. Upper solid line represents the U-lysocline, placed 1800 m above the CCD. Thin dashed lines represent the subsidence history of 5, 10, 15, 20, 25, and 30 Ma seafloor. (c) Predicted sediment thicknesses as a function of seafloor age using the sediment rain rates of (a) and the U-lysocline and CCD of (b). Texture of lines corresponds to texture of sediment rain rates used.

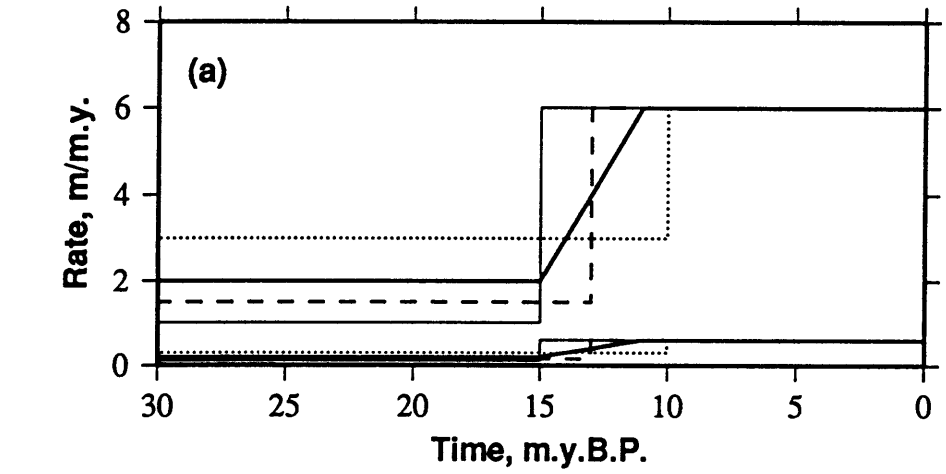
(a)
Rate, m/m.y.
8
6
4
2
0
30
25
20
15
10
5
0
Time, m.y.B.P.

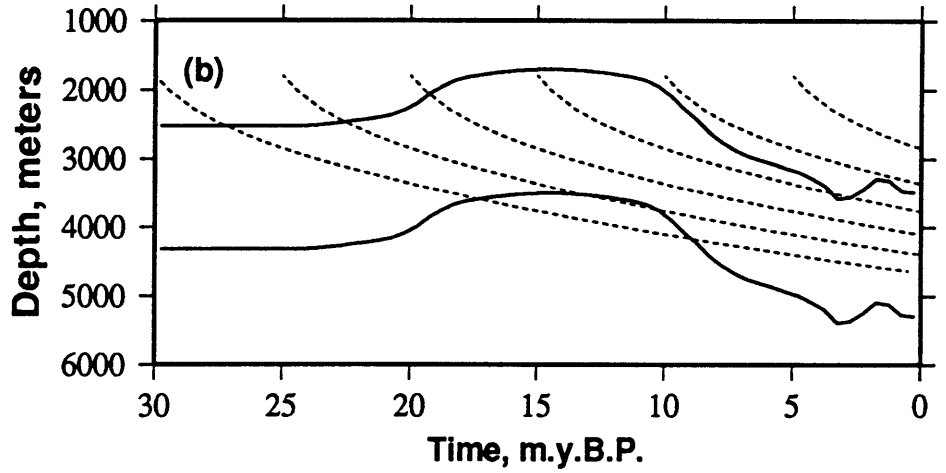
(b)
Depth, meters
1000
2000
3000
4000
5000
6000
30
25
20
15
10
5
0
Time, m.y.B.P.

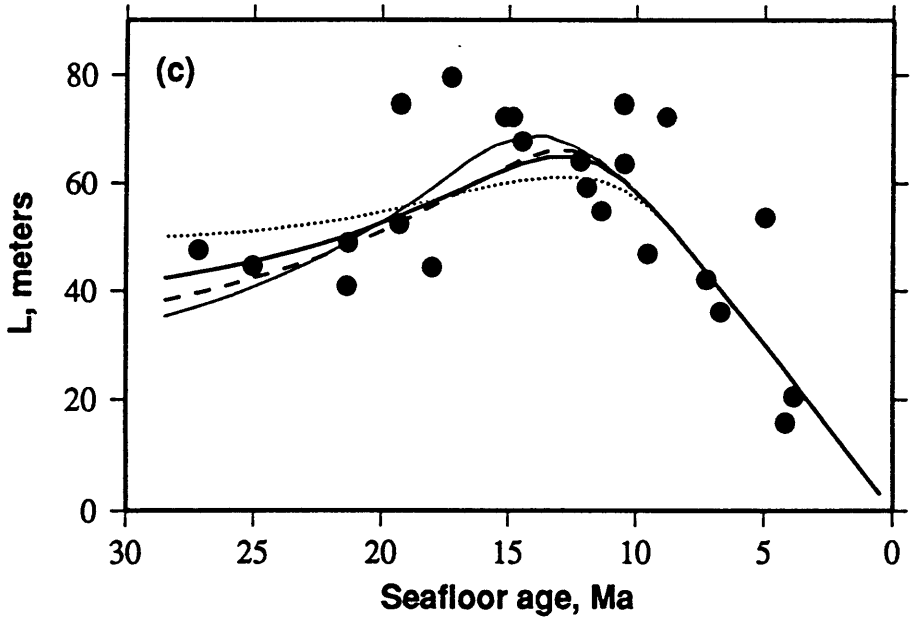
(c)
L, meters
80
60
40
20
0
30
25
20
15
10
5
0
Seafloor age, Ma

Fig. 6.16: Results of possible models, compared to compaction-corrected inverted values of L from basin-centered regions of Chapter 3, constructed using CCD and U-lysocline which assume bottom water was more corrosive to calcite than estimated by *Tucholke and Mountain* [1986]. (a) Refractory and total sediment rain rates used in the models. Dashed lines correspond to a $R_r(t)$ of 0.6 m/m.y. and an $R_t(t)$ of 6.0 m/m.y. Dotted lines correspond to a $R_r(t)$ of 0.3 m/m.y. and an $R_t(t)$ of 6.0 m/m.y. (b) Lower solid line represents CCD, altered from that of *Tucholke and Mountain* [1986]. Upper solid lines represents the U-lysocline, placed 1800 m above the CCD. Thin dashed lines represent the subsidence history of 5, 10, 15, 20, 25, and 30 Ma seafloor. (c) Predicted sediment thicknesses as a function of seafloor age using the sediment rain rates of (a) and the U-lysocline and CCD of (b). Line texture corresponds to the sediment rain rates used.

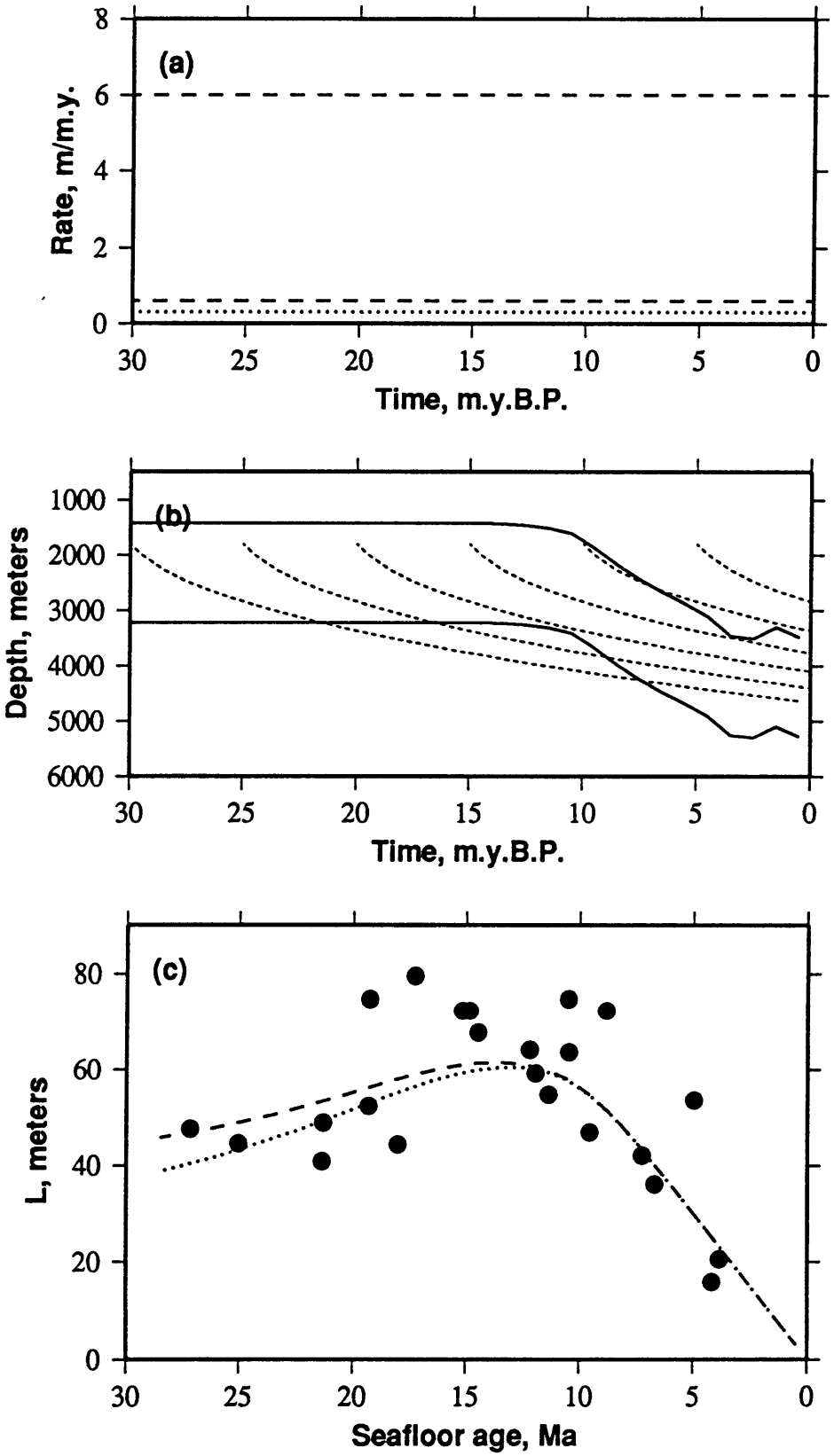
(a)
Rate, m/m.y.
8
6
4
2
0
30
25
20
15
10
5
0
Time, m.y.B.P.
(b)
Depth, meters
1000
2000
3000
4000
5000
6000
30
25
20
15
10
5
0
Time, m.y.B.P.
(c)
L, meters
80
60
40
20
0
30
25
20
15
10
5
0
Seafloor age, Ma

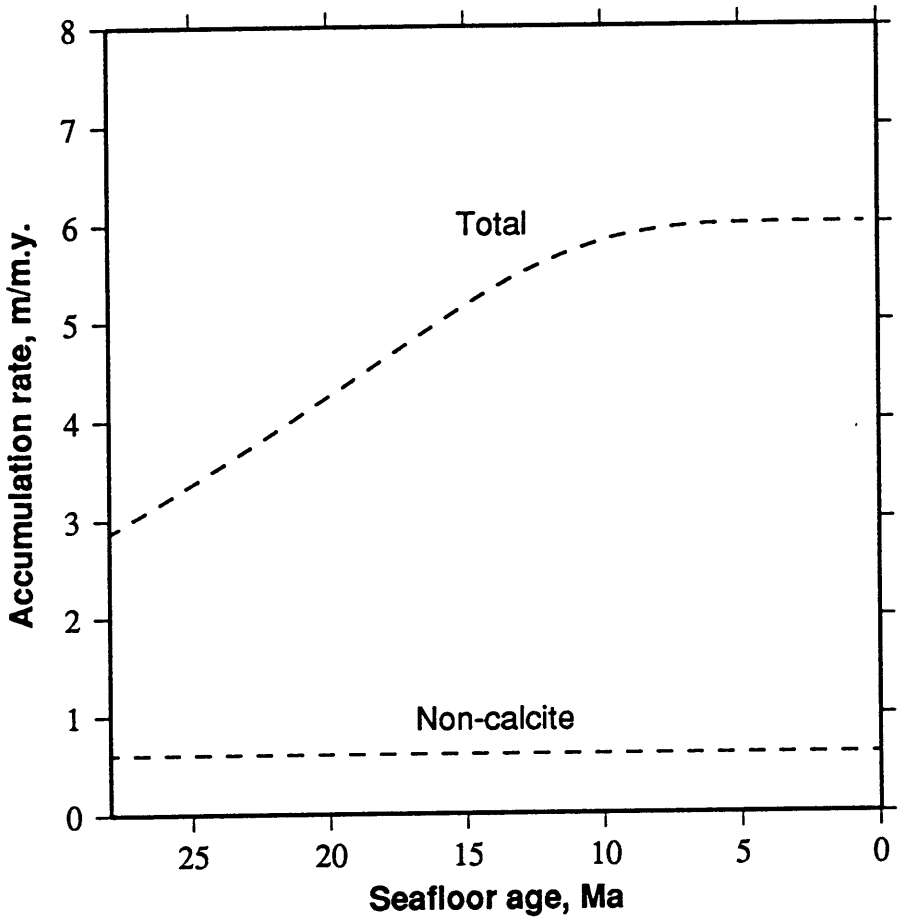

Fig. 6.17: The predicted sediment accumulation rate at present for 0-30 Ma seafloor in the ARC, assuming a $R_r(t)$ and $R_c(t)$ of 0.6 and 5.4 m/m.y., respectively.

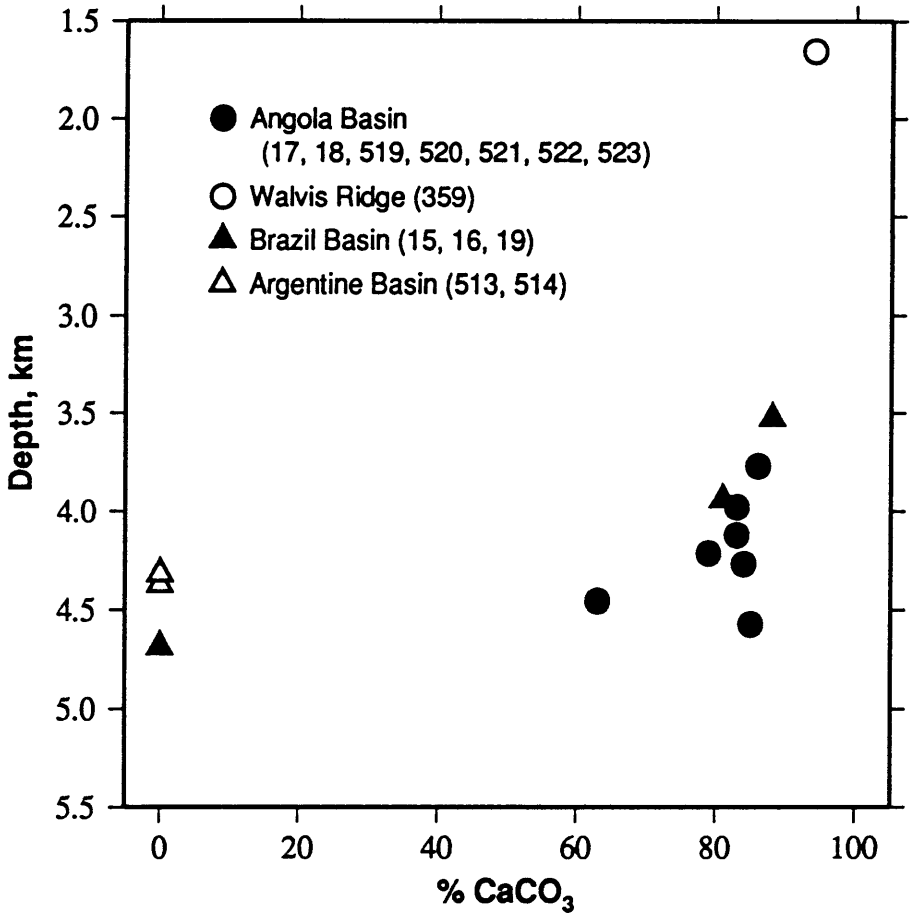

Fig. 6.18: Percent calcite observed in near-surface sediments from the DSDP sites listed in Table 6.2 and Table 6.3, as labeled.

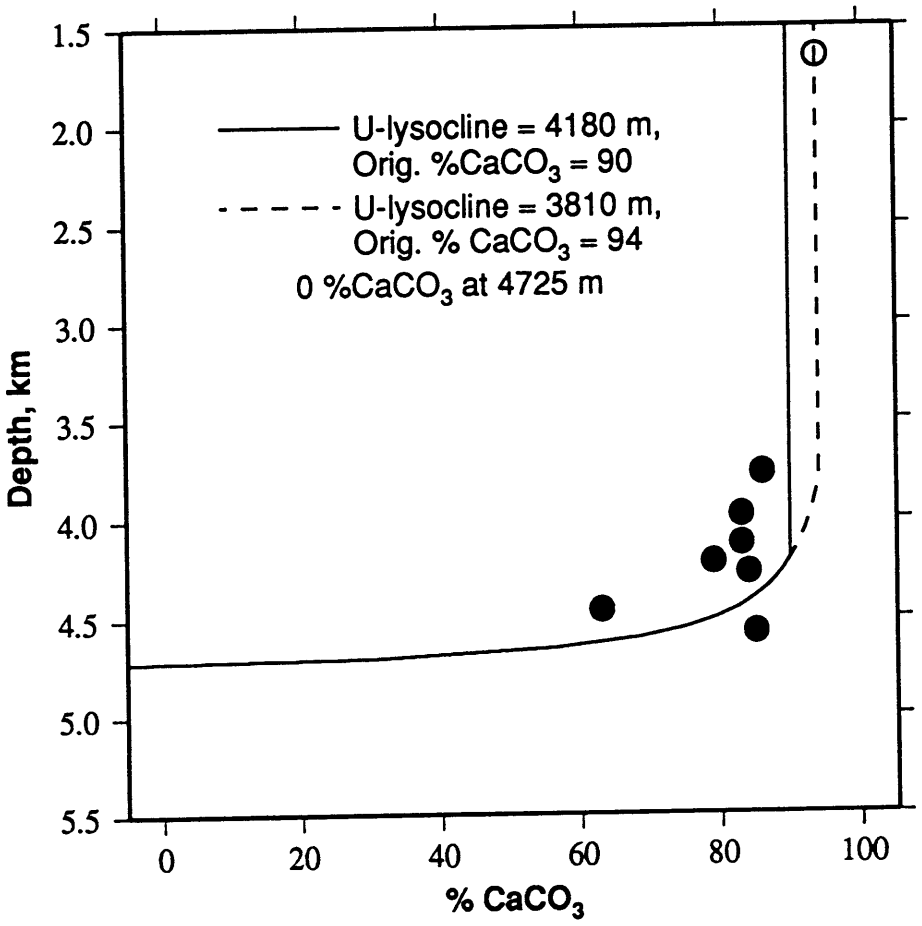

Fig. 6.19: Percent calcite observed in near-surface sediments from the DSDP sites listed in Table 6.3, with data from locations within the Angola Basin given by filled circles and Walvis Ridge site 359 represented by an open circle, and predicted percent calcite based on (6.4) such that the current CCD of *Hsü et al.* [1984] represents the surface at which sediments are 30% calcite and the foraminiferal lysocline represents the surface at which sediments are 75% calcite, for (1) an original calcite composition of 90% (solid line); and (2) an original calcite composition of 94% (dashed line).

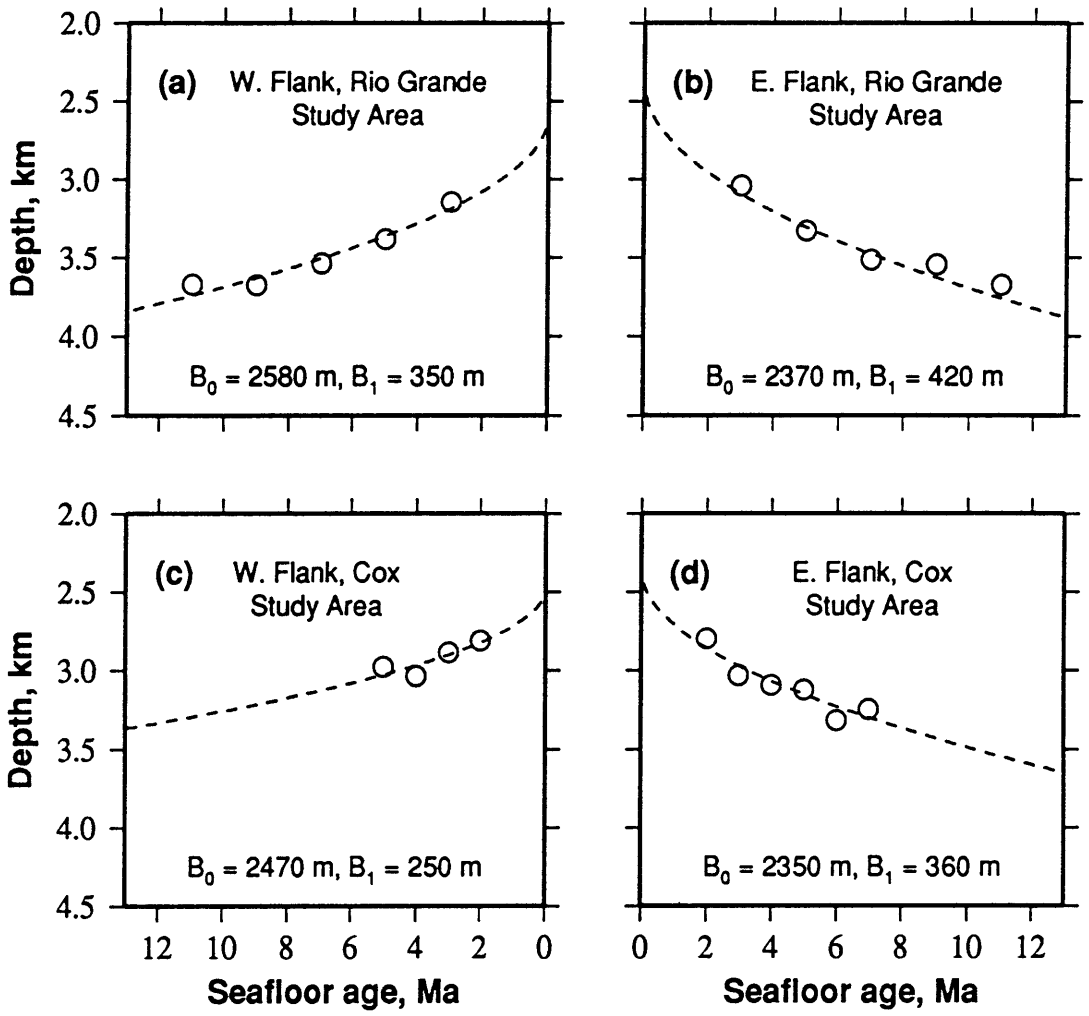

Fig. 6.20: Average seafloor depths for seafloor of varying ages for near-ridge South Atlantic subregions as described in Chapter 4 (open circles) and best-fitting subsidence curves for each region (dashed lines), for (a) the western flank of the MAR in the Rio Grande study area; (b) the eastern flank of the MAR in the Rio Grande study area; (c) the western flank of the MAR in the Cox study area; and (d) the eastern flank of the MAR in the Cox study area.

Fig. 6.21: Results of possible models, compared to compaction-corrected inverted values of L from the eastern flank of the MAR in the Rio Grande study area (Chapter 4). (a) Refractory and total sediment rain rates used in the models. Solid line corresponds to a constant $R_t(t)$ of 5.5 m/m.y., of which 6% is refractory ($R_r(t)$ = 0.33 m/m.y.) Dashed line corresponds to a constant $R_t(t)$ of 7.0 m/m.y., of which 6% is refractory ($R_r(t)$ = 0.42 m/m.y.) Dotted line corresponds to an $R_t(t)$ of 10.0 m/m.y. prior to 5 m.y.B.P., followed by a decrease to 4 m/m.y. by 3 m.y.B.P. The refractory rain rate is assumed to remain 6% of the total rate, such that $R_r(t)$ = 0.6 m/m prior to 5 m.y.B.P., 0.42 m/m.y. at 4 m.y.B.P., and 0.24 m/m.y. by 3 m.y.B.P. (b) Solid lines represent the CCD and foraminiferal lysocline of *Hsü et al.* [1984]. Dotted lines show the placement of the CCD and U-lysocline which allow the CCD and foraminiferal lysocline of *Hsü et al.* [1984] to represent surfaces at which sediments are 30% calcite and 75% calcite, respectively, given an initial calcite composition of 94%, constrained as described in the text. Thin dashed lines represent the subsidence history of 5, 10, and 15 Ma seafloor. (c) Filled circles represent compaction-corrected inverted values of L from the eastern half of the Rio Grande study area, associated with fixed values of H based on crustal type as discussed in Chapter 4. Error bars represent 95% confidence bounds on these values. Lines correspond to predicted sediment thickness using the sediment rain rates of (a), with the texture of lines corresponding to texture of sediment rain rates used. The CCD and foraminiferal lysocline of *Hsü et al.* [1984] were used as the CCD and U-lysocline for the generation of the model represented by the solid line, while the other two models were generated using the CCD and U-lysocline represented by dotted lines in (b).

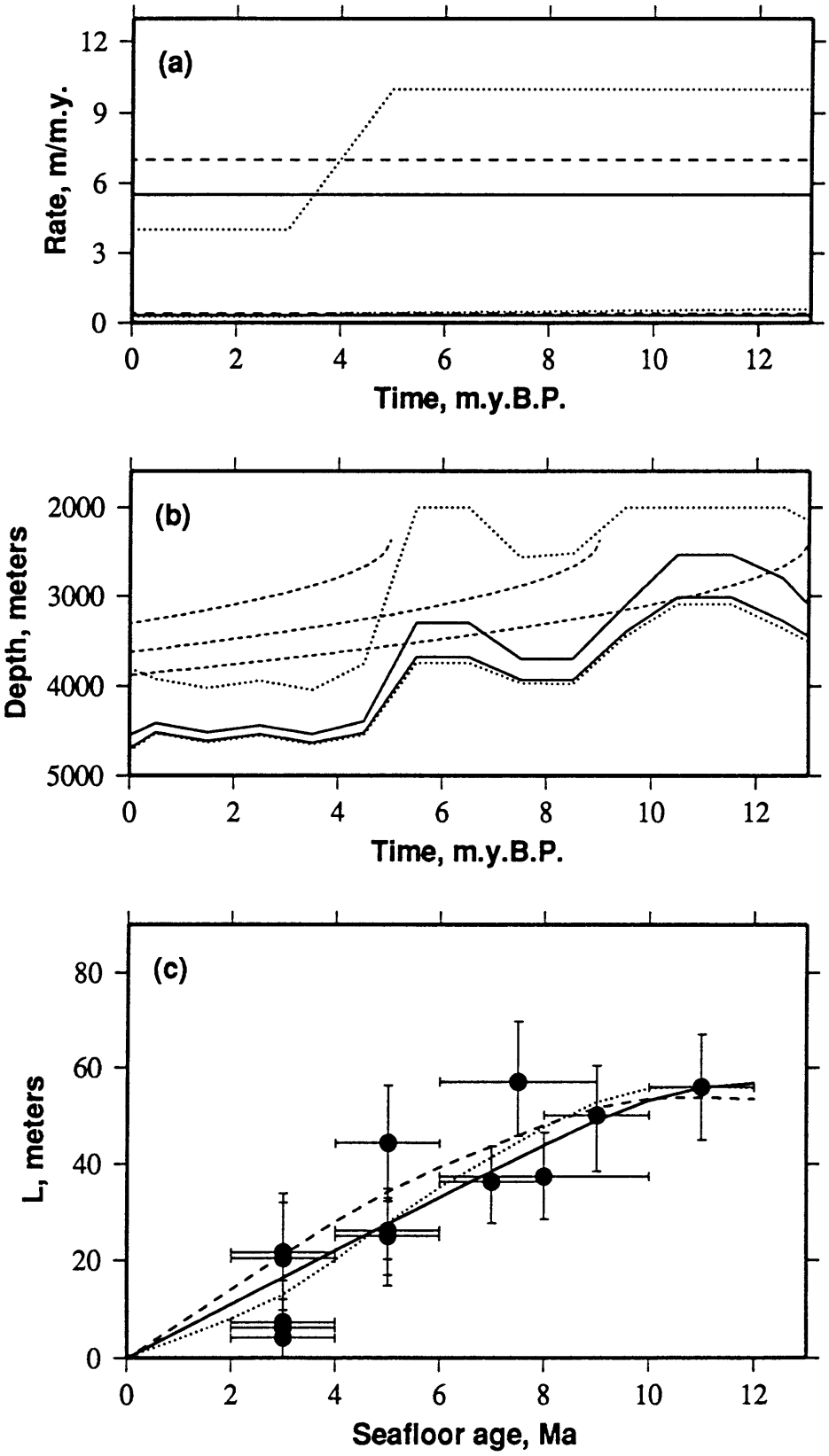
(a)
Rate, m/m.y.
12
9
6
3
0
0
2
4
6
8
10
12
Time, m.y.B.P.
(b)
Depth, meters
2000
3000
4000
5000
0
2
4
6
8
10
12
Time, m.y.B.P.
(c)
L, meters
80
60
40
20
0
0
2
4
6
8
10
12
Seafloor age, Ma

Fig. 6.22: Results of possible models, compared to compaction-corrected inverted values of L from the western flank of the MAR in the Rio Grande study area (Chapter 4). (a) Refractory and total sediment rain rates used in the models. Solid line corresponds to a constant $R_t(t)$ of 5.2 m/m.y., of which 6% is refractory ($R_r(t)$ = 0.312 m/m.y.) Dashed line corresponds to a constant $R_t(t)$ of 6.7 m/m.y., of which 6% is refractory ($R_r(t)$ = 0.402 m/m.y.) Dotted line corresponds to an $R_t(t)$ of 10.0 m/m.y. prior to 5 m.y.B.P., followed by a decrease to 4 m/m.y. by 3 m.y.B.P. The refractory rain rate is assumed to remain 6% of the total rate, such that $R_r(t)$ = 0.6 m/m prior to 5 m.y.B.P., 0.42 m/m.y. at 4 m.y.B.P., and 0.24 m/m.y. by 3 m.y.B.P. (b) Solid lines represent the CCD and foraminiferal lysocline of *Hsü et al.* [1984], modified as described in the text. Dotted lines show the placement of the CCD and U-lysocline which allow the modified CCD and foraminiferal lysocline of *Hsü et al.* [1984] to represent surfaces at which sediments are 30% calcite and 75% calcite, respectively, given an initial calcite composition of 94%. Thin dashed lines represent the subsidence history of 5, 10, and 15 Ma seafloor, constrained as described in the text. (c) Filled circles represent compaction-corrected inverted values of L from the western half of the Rio Grande study area, associated with fixed values of H based on crustal type as discussed in Chapter 4. Error bars represent 95% confidence bounds on these values. Lines correspond to predicted sediment thickness using the sediment rain rates of (a), with the texture of lines corresponding to texture of sediment rain rates used. The CCD and foraminiferal lysocline of *Hsü et al.* [1984] were used as the CCD and U-lysocline for the generation of the model represented by the solid line, while the other two models were generated using the CCD and U-lysocline represented by dotted lines in (b).

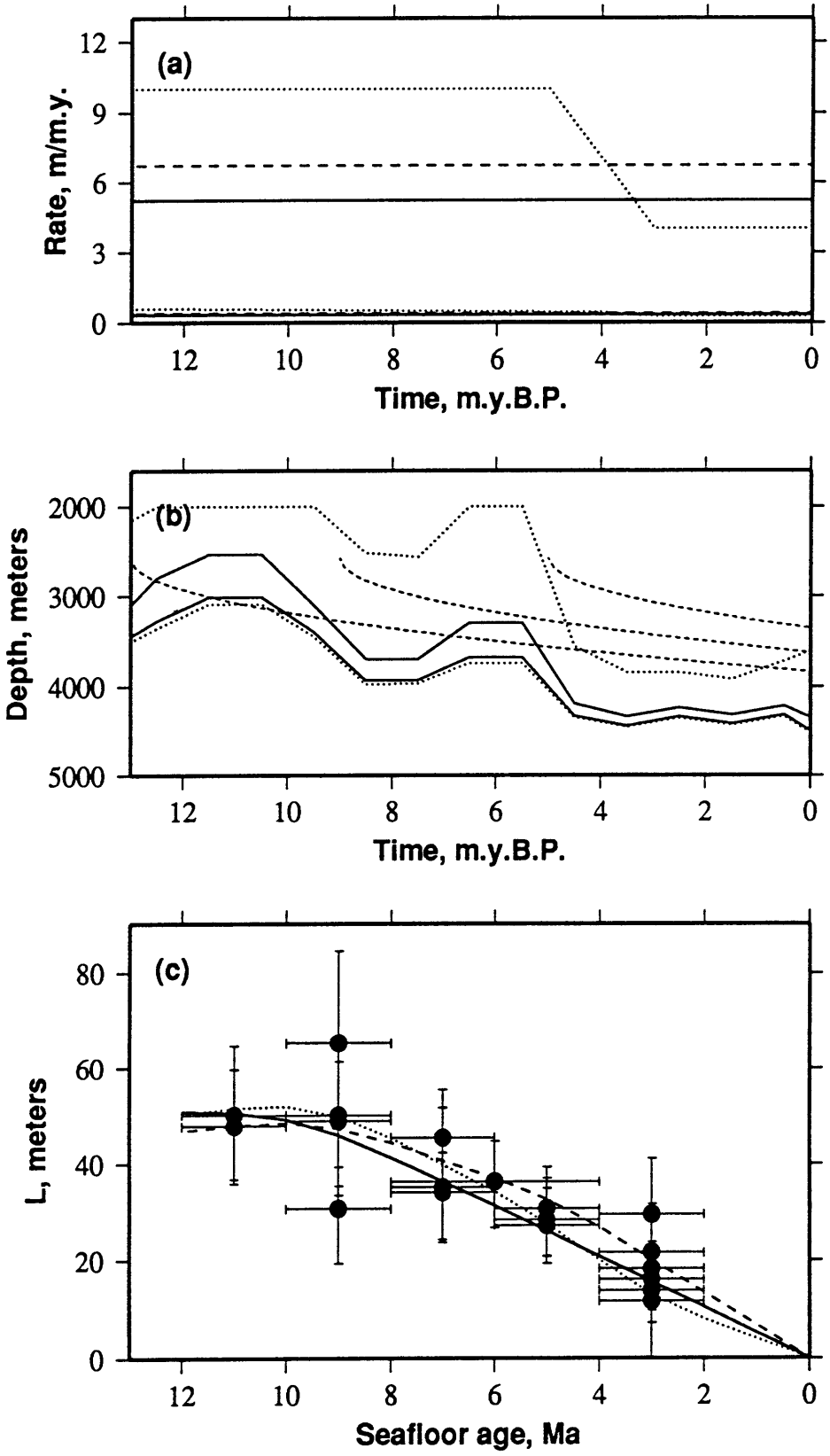
(a)
Rate, m/m.y.
12
9
6
3
0
12
10
8
6
4
2
0
Time, m.y.B.P.
(b)
Depth, meters
2000
3000
4000
5000
12
10
8
6
4
2
0
Time, m.y.B.P.
(c)
L, meters
80
60
40
20
0
12
10
8
6
4
2
0
Seafloor age, Ma

Fig. 6.23: Results of possible models, compared to compaction-corrected inverted values of L from the western flank of the MAR in the Cox study area (Chapter 4), which lies within the Argentine Basin. (a) Refractory and total sediment rain rates of 6.7 and 0.402 m/m.y., respectively. (b) Solid lines represent the CCD and foraminiferal lysocline of *Hsü et al.* [1984], modified as described in the text. Dotted lines show the placement of the CCD and U-lysocline which allow the modified CCD and foraminiferal lysocline of *Hsü et al.* [1984] to represent surfaces at which sediments are 30% calcite and 75% calcite, respectively, given an initial calcite composition of 94%, constrained as described in the text. Thin dashed lines represent the subsidence history of 5, 10, and 15 Ma seafloor. (c) Filled circles represent compaction-corrected inverted values of L from the western half of the Cox study area, associated with fixed values of H based on crustal type as discussed in Chapter 4. Error bars represent 95% confidence bounds on these values. Lines correspond to predicted sediment thickness using the sediment rain rates of (a). The CCD and foraminiferal lysocline of *Hsü et al.* [1984] were used as the CCD and U-lysocline for the generation of the model represented by the solid line, while the dashed line corresponds to the model generated using the CCD and U-lysocline represented by dotted lines in (b).

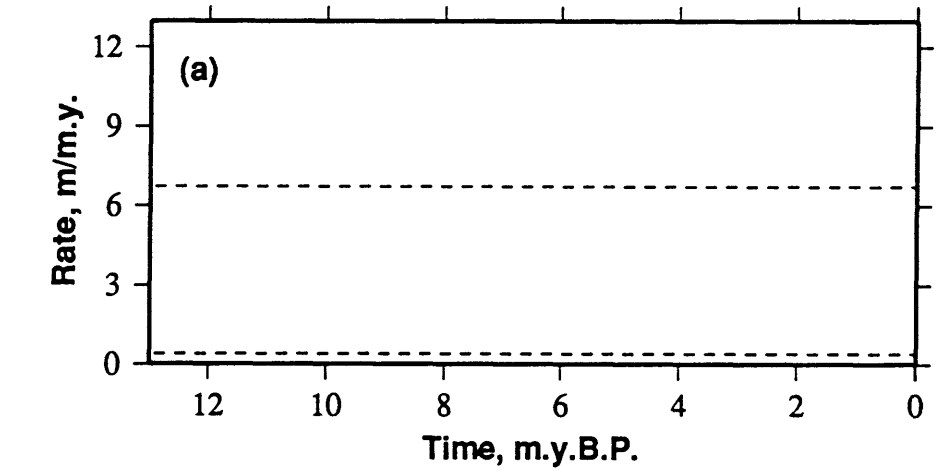
(a)
Rate, m/m.y.
12
9
6
3
0
12
10
8
6
4
2
0
Time, m.y.B.P.

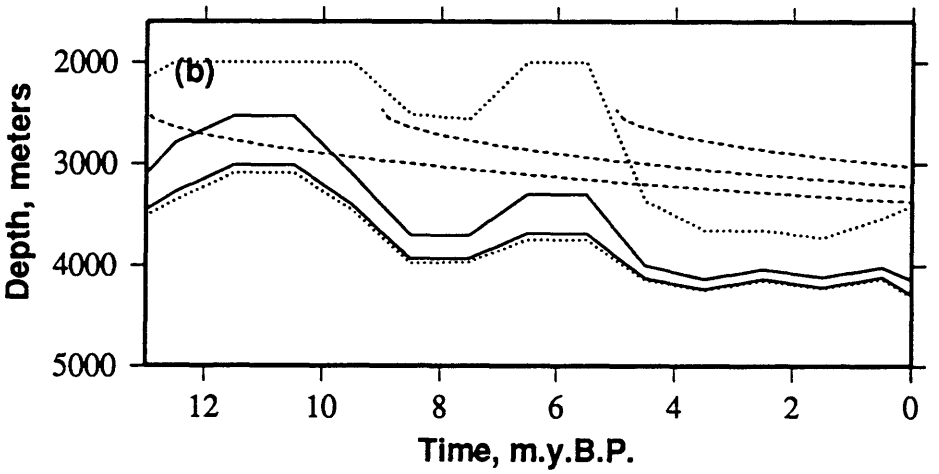
(b)
Depth, meters
2000
3000
4000
5000
12
10
8
6
4
2
0
Time, m.y.B.P.

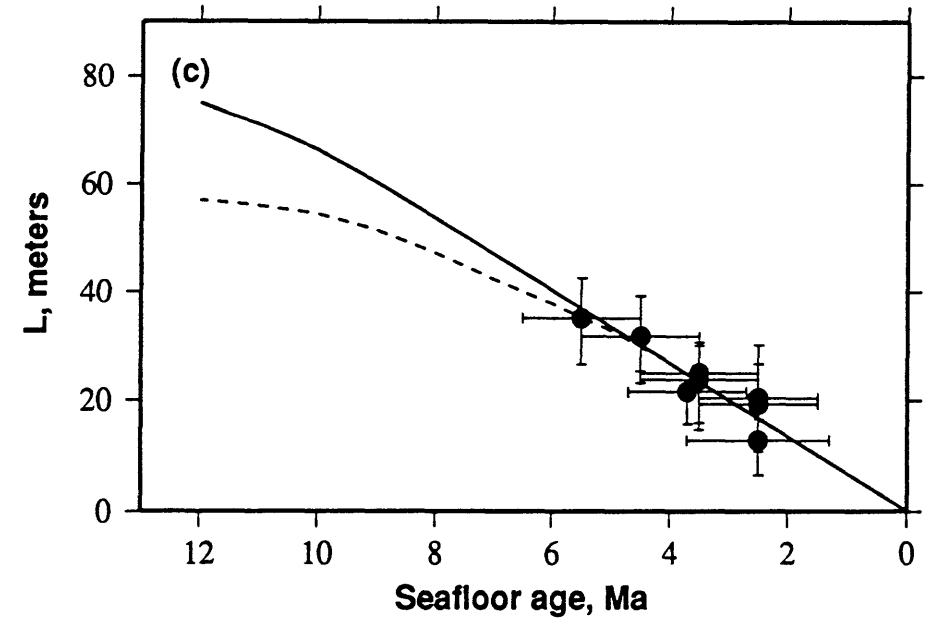
(c)
L, meters
80
60
40
20
0
12
10
8
6
4
2
0
Seafloor age, Ma

Fig. 6.24: Results of possible models, compared to compaction-corrected inverted values of L from the eastern flank of the MAR in the Cox study area (Chapter 4), which lies within the Angola Basin. (a) Solid lines shows constant refractory and total sediment rain rates of 6.5 and 0.39 m/m.y., respectively. Dotted lines show an $R_t(t)$ of 8.0 m/m.y. prior to 3 m.y.B.P. and an $R_t(t)$ of 6.5 m/m.y. thereafter. The refractory rain rate is assumed to be 6% of $R_t(t)$. (b) Solid lines represent the CCD and foraminiferal lysocline of *Hsü et al.* [1984]. Dotted lines show the placement of the CCD and U-lysocline which allow the CCD and foraminiferal lysocline of *Hsü et al.* [1984] to represent surfaces at which sediments are 30% calcite and 75% calcite, respectively, given an initial calcite composition of 94%, constrained as described in the text. Thin dashed lines represent the subsidence history of 5, 10, and 15 Ma seafloor. (c) Filled circles represent compaction-corrected inverted values of L from the eastern half of the Cox study area, associated with fixed values of H based on crustal type as discussed in Chapter 4. Error bars represent 95% confidence bounds on these values. Lines correspond to predicted sediment thickness using the sediment rain rates of (a). The constant $R_t(t)$ and the CCD and foraminiferal lysocline of *Hsü et al.* [1984] were used as the CCD and U-lysocline for the generation of the model represented by the solid line, while the other line corresponds to the model generated using the CCD and U-lysocline represented by dotted lines in (b). The constant $R_t(t)$ produced the sediment accumulation pattern represented by the dashed line, and the variable $R_t(t)$ produced the sediment accumulation pattern represented by the dotted line.

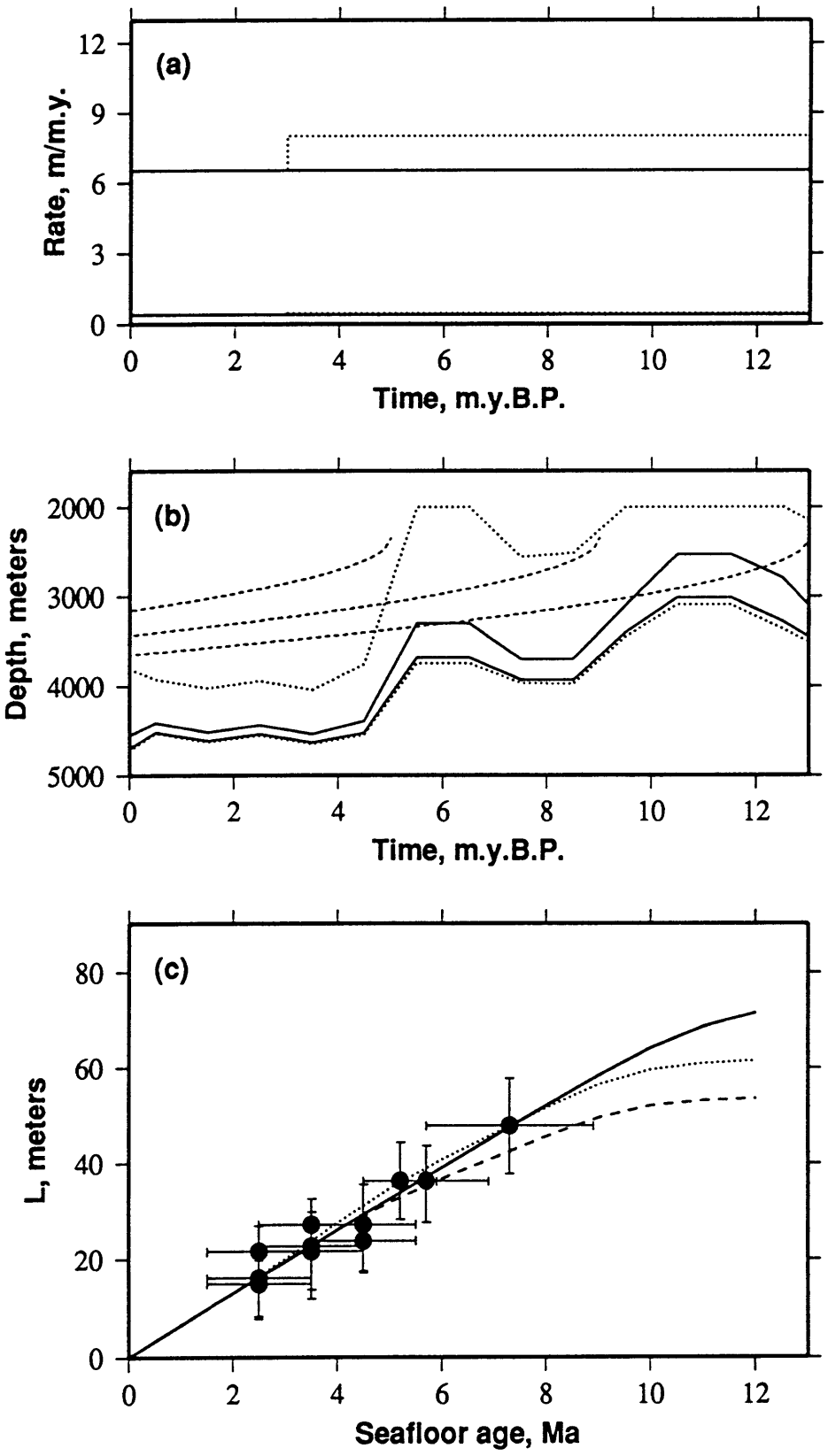
(a)
Rate, m/m.y.
12
9
6
3
0
0
2
4
6
8
10
12
Time, m.y.B.P.
(b)
Depth, meters
2000
3000
4000
5000
0
2
4
6
8
10
12
Time, m.y.B.P.
(c)
L, meters
80
60
40
20
0
0
2
4
6
8
10
12
Seafloor age, Ma

Fig. 6.25: Results of possible models, compared to compaction-corrected inverted values of L from the Brazil Basin in Chapter 4 (near-ridge) and Chapter 5 (off-axis). (a) Refractory and total sediment rain rates used in the models. Dashed lines correspond to a constant $R_t(t)$ of 6.7 m/m.y. and a $R_r(t)$ of 0.402 m/m.y. Dotted lines correspond to a constant $R_t(t)$ of 5.5 m/m.y. and a $R_r(t)$ of 0.33 m/m.y. Solid lines correspond to a constant $R_t(t)$ of 5.2 m/m.y. and a $R_r(t)$ of 0.312 m/m.y. (b) Solid lines represent the CCD and foraminiferal lysocline of *Hsü et al.* [1984], modified as described in the text. Dotted lines show the placement of the CCD and U-lysocline which allow the modified CCD and foraminiferal lysocline of *Hsü et al.* [1984] to represent surfaces at which sediments are 30% calcite and 90% calcite, respectively, given an initial calcite composition of 94%. Dashed lines show the placement of the CCD and U-lysocline which allow the modified CCD and foraminiferal lysocline of *Hsü et al.* [1984] to represent surfaces at which sediments are 30% calcite and 75% calcite, respectively, given an initial calcite composition of 94%, constrained as described in the text. Thin dashed lines represent the subsidence history of 5, 10, 15, 20, 25, 30, 35, 40, and 45 Ma seafloor. (c) Filled squares represent inverted values from the western half of the Rio Grande study area associated with fixed values of H based on crustal type, as discussed in Chapter 4. Clear circles represent inverted values from Brazil Basin subregions of Chapter 5, as computed when H is allowed to vary. Black circles represent inverted values determined when H is preset at reasonable values for outside corner crust, as described in Chapter 5. Error bars represent 95% confidence intervals. Lines represent accumulation models generated using sediment rain rates of (a) and the U-lysoclines and CCDs of (b). Texture of each line indicates which sediment rain rate model, U-lysocline, and CCD is used in its production.

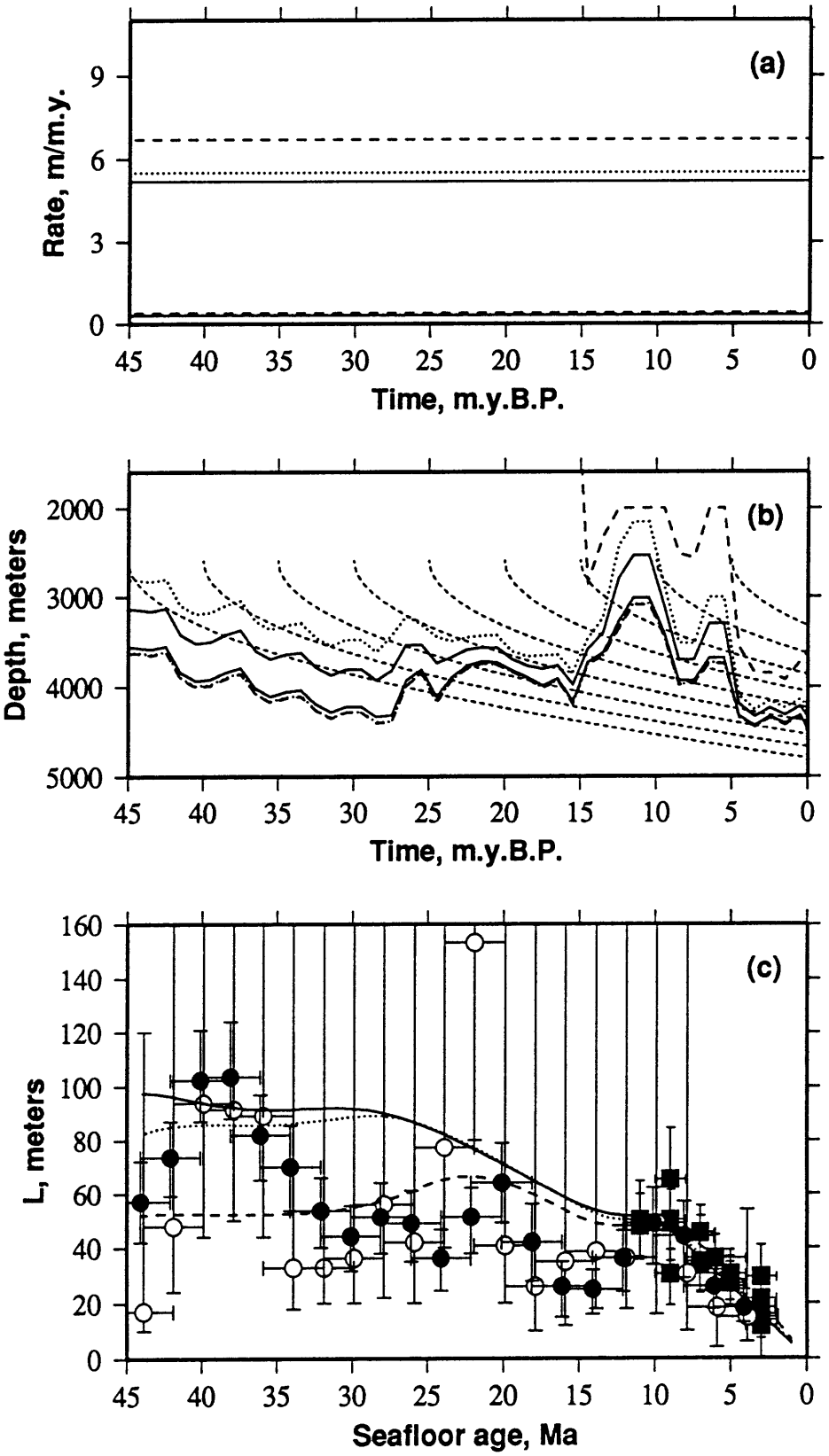
(a)
Rate, m/m.y.
9
6
3
0
45 40 35 30 25 20 15 10 5 0
Time, m.y.B.P.
(b)
Depth, meters
2000
3000
4000
5000
45 40 35 30 25 20 15 10 5 0
Time, m.y.B.P.
(c)
L, meters
160
140
120
100
80
60
40
20
0
45 40 35 30 25 20 15 10 5 0
Seafloor age, Ma

Fig. 6.26: Results of possible models, compared to compaction-corrected inverted values of L from the Brazil Basin in Chapter 4 (near-ridge) and Chapter 5 (off-axis). (a) Refractory and total sediment rain rates used in the models. Solid lines correspond to a constant $R_t(t)$ of 5.5 m/m.y. and a $R_r(t)$ of 0.33 m/m.y. Dashed lines correspond an $R_t(t)$ of 8.0 m/m.y. and an $R_r(t)$ of 0.48 m/m.y between 45 and 30 m.y.B.P., an $R_t(t)$ of 5.5 m/m.y. and an $R_r(t)$ of 0.33 m/m.y between 30 and 17 m.y.B.P. and between 10 and 0 m.y.B.P., and an $R_t(t)$ of 1.0 m/m.y. and an $R_r(t)$ of 0.06 m/m.y between 17 and 10 m.y.B.P. Dotted lines correspond an $R_t(t)$ of 8.0 m/m.y. and an $R_r(t)$ of 0.48 m/m.y between 45 and 29 m.y.B.P., an $R_t(t)$ of 2.0 m/m.y. and an $R_r(t)$ of 0.12 m/m.y between 29 and 15 m.y.B.P., a gradual increase in $R_t(t)$ and $R_r(t)$ between 15 and 11 m.y.B.P., and an $R_t(t)$ and $R_r(t)$ of 6.0 m/m.y. and 0.36 m/m.y., respectively, since 11 m.y.B.P. (b) Lines show the placement of the CCD and U-lysocline which allow the modified (as described in the text) CCD of *Hsü et al.* [1984] to represent surfaces at which sediments are 30% calcite, and the foraminiferal lysocline of *Hsü et al.* [1984] to represent surfaces at which sediments are a variable amount of calcite, given an initial calcite composition of 94%. This variable amount is 75% between 0 and 20.5 m.y.B.P., 85% between 20.5 and 24.5 m.y.B.P., and 90% prior to 24.5 m.y.B.P, constrained as described in the text. Thin dashed lines represent the subsidence history of 5, 10, 15, 20, 25, 30, 35, 40, and 45 Ma seafloor. (c) Filled squares represent inverted values from the western half of the Rio Grande study area associated with fixed values of H based on crustal type, as discussed in Chapter 4. Clear circles represent inverted values from Brazil Basin subregions of Chapter 5, as computed when H is allowed to vary. Black circles represent inverted values determined when H is preset at reasonable values for outside corner crust, as described in Chapter 5. Error bars represent 95% confidence intervals. Lines represent accumulation models generated using sediment rain rates of (a) and the U-lysocline and CCD of (b). Texture of each line indicates which sediment rain rate model is used in its production.

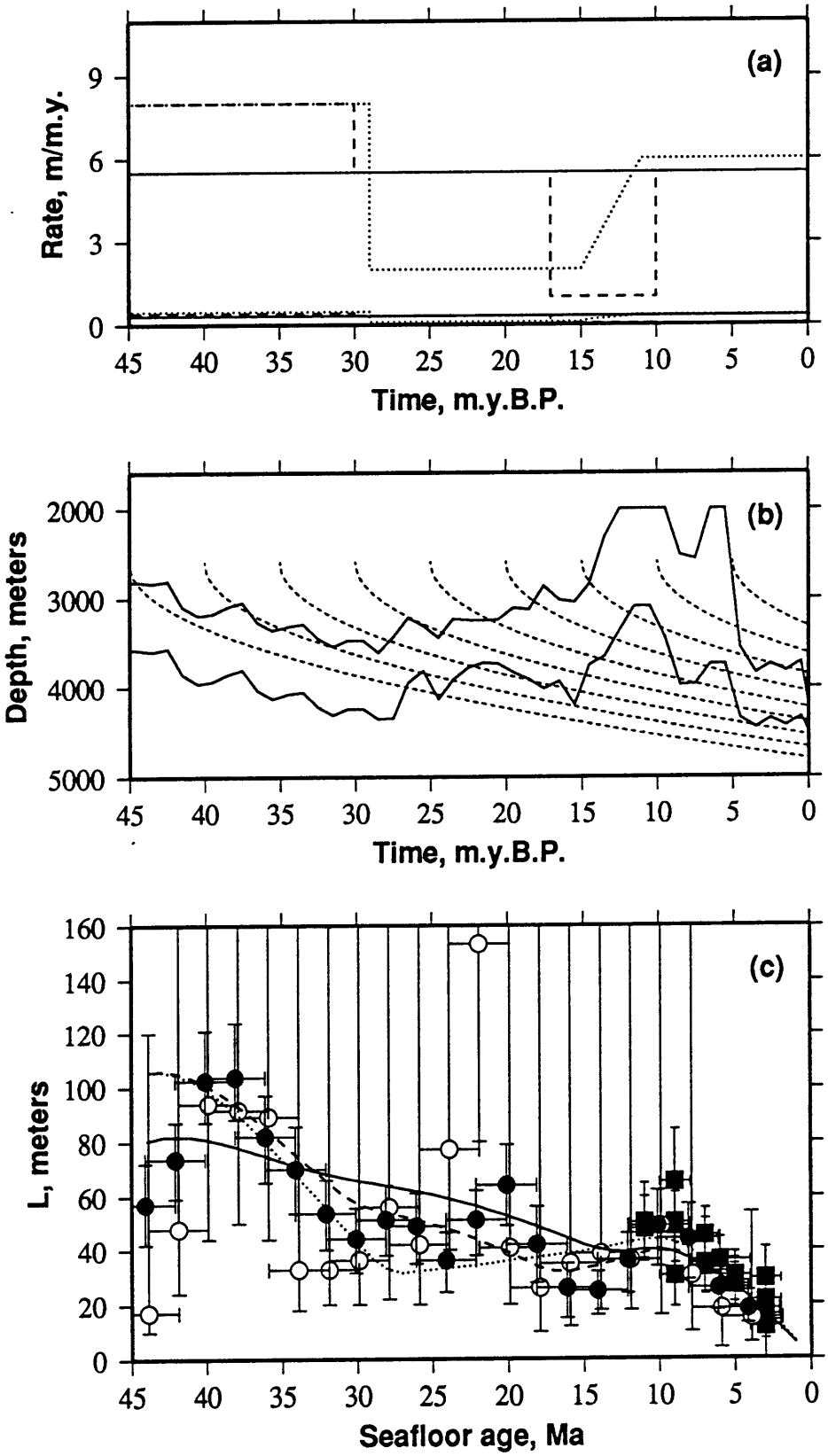
(a)
Rate, m/m.y.
9
6
3
0
45 40 35 30 25 20 15 10 5 0
Time, m.y.B.P.
(b)
Depth, meters
2000
3000
4000
5000
45 40 35 30 25 20 15 10 5 0
Time, m.y.B.P.
(c)
L, meters
160
140
120
100
80
60
40
20
0
45 40 35 30 25 20 15 10 5 0
Seafloor age, Ma

Fig. 6.27: Results of possible models, compared to compaction-corrected inverted values of L from near 30° S in the Angola Basin as given in Chapter 4 (near-ridge) and Chapter 5 (off-axis). (a) Refractory and total sediment rain rates used. Thin solid lines correspond to a constant $R_t(t)$ of 5.5 m/m.y. and $R_r(t)$ of 0.33 m/m.y. Dashed lines correspond to a constant $R_t(t)$ of 7.0 m/m.y. and $R_r(t)$ of 0.42 m/m.y. Dotted lines correspond to an $R_t(t)$ of 8.0 m/m.y. and an $R_r(t)$ of 0.48 m/m.y between 40 and 30 m.y.B.P., an $R_t(t)$ of 5.5 m/m.y. and an $R_r(t)$ of 0.33 m/m.y between 30 and 17, and between 10 and 0, m.y.B.P., and an $R_t(t)$ of 1.0 m/m.y. and an $R_r(t)$ of 0.06 m/m.y between 17 and 10 m.y.B.P. Thick solid lines correspond to an $R_t(t)$ of 8.0 m/m.y. and an $R_r(t)$ of 0.48 m/m.y between 40 and 29 m.y.B.P., an $R_t(t)$ of 2.0 m/m.y. and an $R_r(t)$ of 0.12 m/m.y between 29 and 15 m.y.B.P., gradually increasing $R_t(t)$ and $R_r(t)$ between 15 and 11 m.y.B.P., and $R_t(t)$ and $R_r(t)$ of 6.0 m/m.y. and 0.36 m/m.y., respectively, since 11 m.y.B.P. (b) Solid lines represent the CCD and foraminiferal lysocline of *Hsü et al.* [1984]. Dashed lines show the placement of the CCD and *U*-lysocline which allow the CCD and foraminiferal lysocline of *Hsü et al.* [1984] to represent surfaces at which sediments are 30% calcite and 75% calcite, respectively, given an initial calcite composition of 94%; where this would place the *U*-lysocline shallower than 2 km, it is defined to be 2 km. Dotted show the placement of the CCD and *U*-lysocline which allow the CCD of *Hsü et al.* [1984] to represent surfaces at which sediments are 30% calcite, and the foraminiferal lysocline of *Hsü et al.* [1984] to represent surfaces at which sediments are a variable amount of calcite, given an initial calcite composition of 94%. This variable amount is 75% between 0 and 20.5 m.y.B.P., 85% between 20.5 and 24.5 m.y.B.P., and 90% prior to 24.5 m.y.B.P. Where this would place the *U*-lysocline shallower than 2 km, it is defined to be 2 km. Thin dashed lines represent the subsidence history of 5, 10, 15, 20, 25, 30, 35, and 40 Ma seafloor. (c) Filled squares represent inverted values from the eastern half of the Rio Grande study area associated with fixed values of H based on crustal type, as discussed in Chapter 4. Clear circles represent inverted values from Angola Basin subregions of Chapter 5, as computed when H is allowed to vary. Black circles represent inverted values determined when H is preset at reasonable values for inside corner crust, as described in Chapter 5. Error bars represent 95% confidence intervals. Lines represent accumulation models generated using sediment rain rates of (a) and the *U*-lysocline and CCD of (b). Texture of each line indicates which sediment rain rate model is used in its production. The CCD and *U*-lysocline represented by the solid lines in (b) were used to generate the model represented by the thin solid line. The CCD and *U*-lysocline represented by the dashed lines in (b) were used to generate the model represented by the dashed line. The CCD and *U*-lysocline represented by the dotted lines in (b) were used to generate the models represented by the dotted and thick solid lines.

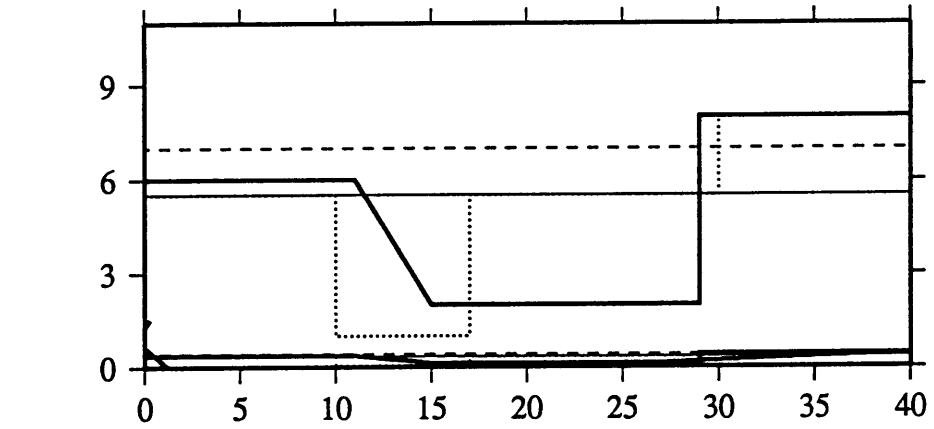
9
6
3
0
0
5
10
15
20
25
30
35
40

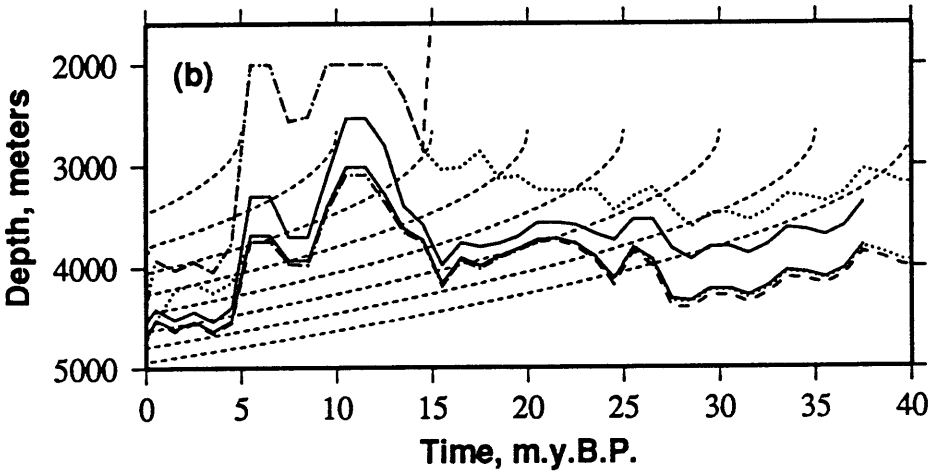
(b)
Depth, meters
2000
3000
4000
5000
0
5
10
15
20
25
30
35
40
Time, m.y.B.P.

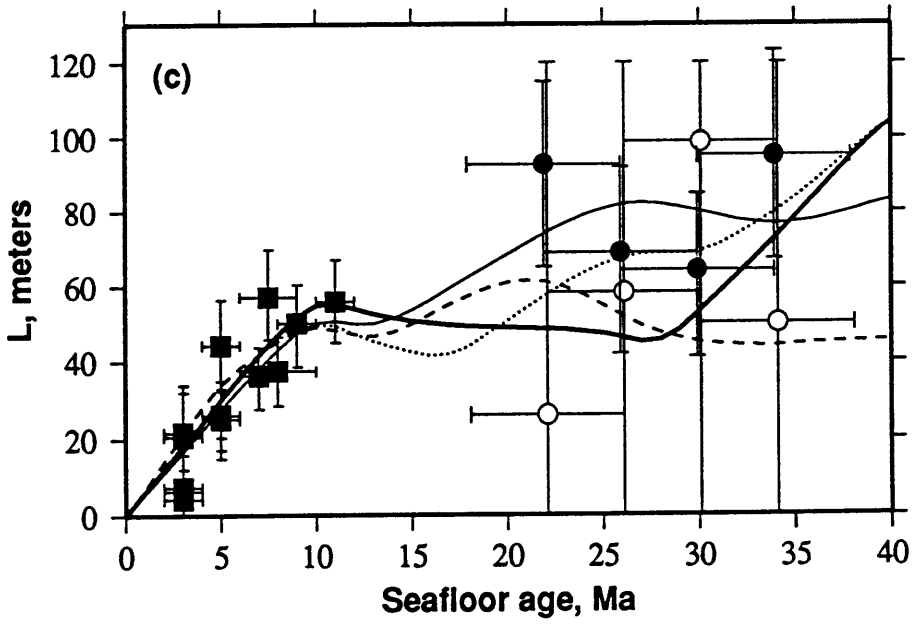
(c)
L, meters
120
100
80
60
40
20
0
0
5
10
15
20
25
30
35
40
Seafloor age, Ma

Fig. 6.28: Single channel seismic data from DSDP Leg 39 [*Neprochnov et al.*, 1977], and seafloor ages from *Müller et al.* [1993]. Note that the 25-30 Ma high-standing hills seem to be completely filled with sediment, and that sediment on seafloor greater than 30 Ma displays current-generated features which are not directly related to the bottom topography.

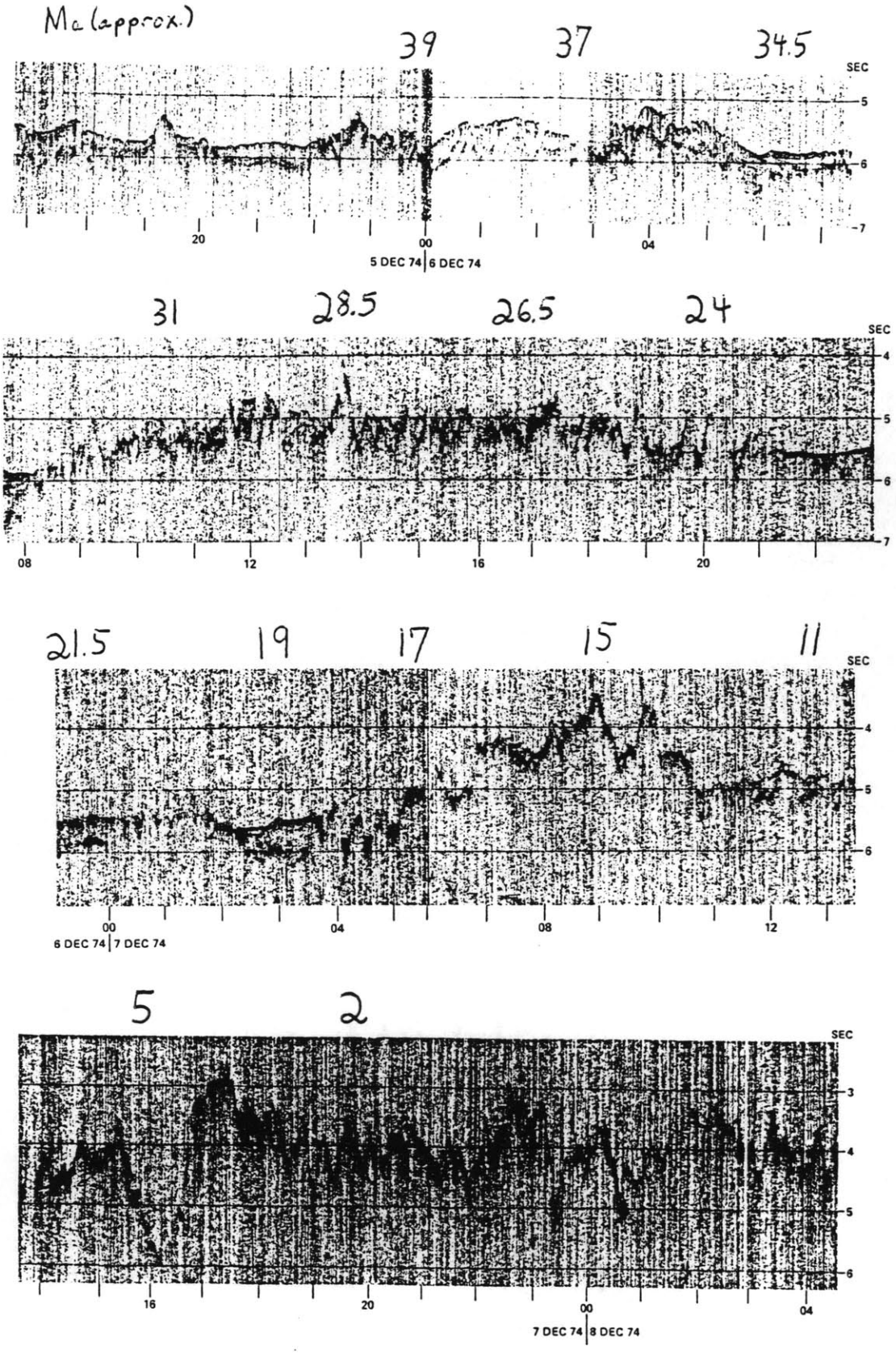
Mc (approx.)
39
37
34.5
SEC
5
6
7
20
00
04
5 DEC 74 | 6 DEC 74
31
28.5
26.5
24
SEC
4
5
6
7
08
12
16
20
21.5
19
17
15
11
SEC
4
5
6
00
04
08
12
6 DEC 74 | 7 DEC 74
5
2
SEC
3
4
5
6
16
20
00
04
7 DEC 74 | 8 DEC 74

Fig. 6.29: Results of possible model, compared to compaction-corrected inverted values of L from the Argentine Basin from Chapter 4 (near-ridge) and Chapter 5 (off-axis). (a) Refractory and total sediment rain rates used in the model: $R_t(t)$ = 7.0 m/m.y., $R_r(t)$ = 0.42 m/m.y. (b) CCD and foraminiferal lysocline of *Hsü et al.* [1984], adjusted such that these curves are 400 m higher during the past 5 m.y.. Thin dashed lines represent the subsidence history of 5, 10, 15, 20, 25, 30, 35, and 40 Ma seafloor. (c) Filled squares represent inverted values from the western half of the Cox study area associated with fixed values of H based on crustal type. White circles represent inverted values from Argentine Basin subregions of Chapter 5, as computed when H is allowed to vary. Black circles represent inverted values determined when H is preset at reasonable values (such that the H of 0-age seafloor is take to be 190 m), as described in Chapter 5. Error bars represent 95% confidence intervals. Line represents accumulation model generated using sediment rain rates of (a) and the U-lysocline and CCD of (b).

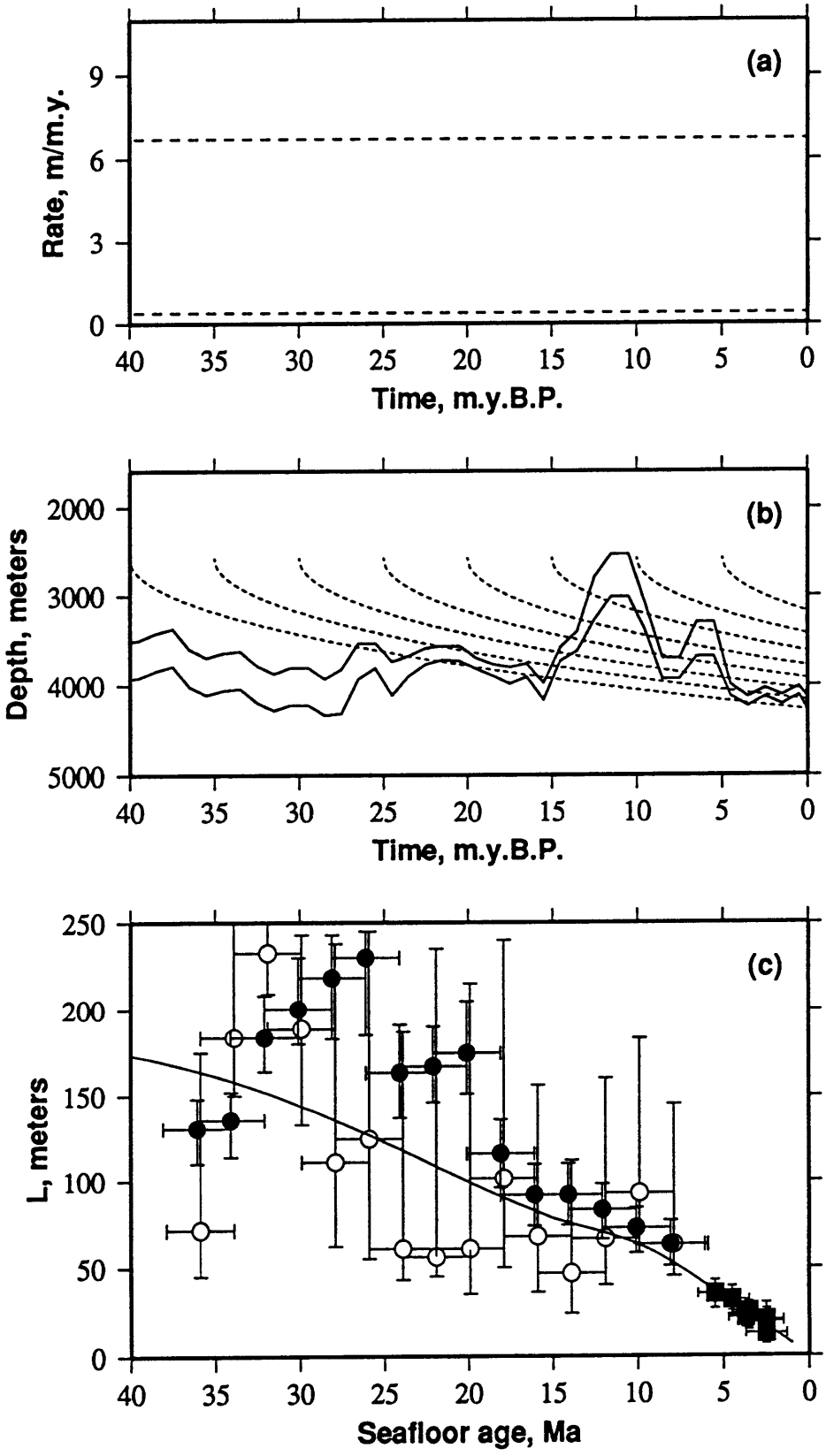
(a)
Rate, m/m.y.
9
6
3
0
40
35
30
25
20
15
10
5
0
Time, m.y.B.P.
(b)
Depth, meters
2000
3000
4000
5000
40
35
30
25
20
15
10
5
0
Time, m.y.B.P.
(c)
L, meters
250
200
150
100
50
0
40
35
30
25
20
15
10
5
0
Seafloor age, Ma

Appendix A: Forward Sedimentation Algorithm

To numerically sediment model topographies, model bathymetries $b(\mathbf{x})$ are discretized onto an even grid of cells with spacing d. To insure that sediment volume $v(\mathbf{x},t)$ is always non-negative, the volumes v_{in} and v_{out} of sediments transported into and out of cells during each timestep k are considered separately, with

$$v_{i,j}^{k+1} = v_{i,j}^{k} + \left(v_{in,i,j}^{k} - v_{out,i,j}^{k}\right) + n \tag{A.1}$$

where $n = F\Delta t d^2$ is the amount of sediment added to a cell from the water column. Potential outward volume $\hat{v}_{out}$ is computed first, by

$$\hat{v}_{\text{out},i,j}^{k} = \kappa\Delta t \sum_{\substack{a=-1,+1 \\ b=-1,+1}} \begin{cases} h_{i,j}^{k} - h_{i-a,j-b}^{k}, & h_{i,j}^{k} > h_{i-a,j-b}^{k} \\ 0, & h_{i,j}^{k} \le h_{i-a,j-b}^{k}, \end{cases} \tag{A.2}$$

where $h_{i,j}^{k}$ is the seafloor height at location (i,j) at the start of timestep k. If $\hat{v}_{out}$ is less than the amount of sediment available then $v_{out} = \hat{v}_{out}$; if not enough sediment is available, due to the non-erodibility of bedrock,

$$v_{out} = \beta\hat{v}_{out}, \tag{A.3}$$

where

$$\beta_{i,j}^{k} = \left(v_{i,j}^{k} + n\right) \Big/ \hat{v}_{\text{out},i,j}^{k}. \tag{A.4}$$

The volume transported into each cell is then given by

$$v_{in,i,j}^{k} = \kappa\Delta t \sum_{\substack{a=-1,+1 \\ b=-1,+1}} \begin{cases} \beta_{i-a,j-b}^{k}\left(h_{i-a,j-b}^{k} - h_{i,j}^{k}\right), & h_{i,j}^{k} < h_{i-a,j-b}^{k} \\ 0, & h_{i,j}^{k} \ge h_{i-a,j-b}^{k}. \end{cases} \tag{A.5}$$

To determine optimal timestep Δt, we recast (2.12) as

$$h_{i.j}^{k+1} = h_{i.j}^{k+1}\left(\frac{\kappa\Delta t}{d^2}\right)\left(h_{i+1.j}^{k} + h_{i-1.j}^{k} + h_{i.j+1}^{k} + h_{i.j-1}^{k} - 4h_{i.j}^{k}\right) + F_{i.j}^{k}\Delta t. \tag{A.6}$$

Letting $\mu = \kappa\Delta t/d^2$, this becomes

$$h_{i.j}^{k+1} = \mu\left(h_{i+1.j}^{k} + h_{i-1.j}^{k} + h_{i.j+1}^{k} + h_{i.j-1}^{k} - 4h_{i.j}^{k}\right) + (1-4\mu)h_{i.j}^{k} + F_{i.j}^{k}\Delta t. \tag{A.7}$$

Although solutions to (A.7) will converge as $t \to \infty$ for $\mu \le 0.25$ [*Gerald and Wheatley*, 1984, p.477], accuracy at small t is improved by using $\mu = 0.2$, the highest value for which the center of a spike of material subject to diffusion will always be a maximum. Therefore, we use timestep $\Delta t = 0.2d^2/\kappa$.

Appendix B: Interpolation of Slope Distribution Functions

Slope distribution functions $g_m(\theta,u,\kappa,H,L)$ are calculated from only a limited number of sedimented model toporaphies. Where $g_m(\theta,u,\kappa,H,L)$ is not precalculated, it is estimated during the inversion procedure as

$$\begin{aligned} g_m(\theta,u,\kappa,H,L) = {} & \alpha\beta\gamma g_m\left(\theta,u,\kappa(K_l,H_l,\Lambda_l)_l,H_l,\Lambda_l H_l\right) \\ & +(1-\alpha)\beta\gamma g_m\left(\theta,u,\kappa(K_u,H_l,\Lambda_l),H_l,\Lambda_l H_l\right) \\ & +\alpha(1-\beta)\gamma g_m\left(\theta,u,\kappa(K_l,H_u,\Lambda_l),H_u,\Lambda_l H_u\right) \\ & +(1-\alpha)(1-\beta)\gamma g_m\left(\theta,u,\kappa(K_u,H_u,\Lambda_l),H_u,\Lambda_l H_u\right) \\ & +\alpha\beta(1-\gamma)g_m\left(\theta,u,\kappa(K_l,H_l,\Lambda_u),H_l,\Lambda_u H_l\right) \\ & +(1-\alpha)\beta(1-\gamma)g_m\left(\theta,u,\kappa(K_u,H_l,\Lambda_u),H_l,\Lambda_u H_l\right) \\ & +\alpha(1-\beta)(1-\gamma)g_m\left(\theta,u,\kappa(K_l,H_u,\Lambda_u),H_u,\Lambda_u H_u\right) \\ & +(1-\alpha)(1-\beta)(1-\gamma)g_m\left(\theta,u,\kappa(K_u,H_u,\Lambda_u),H_u,\Lambda_u H_u\right), \end{aligned} \tag{B.1}$$

where H_u and H_l are the nearest values of H for which $g_m(\theta,u,\kappa,H,L)$ is precalculated, Λ_u and Λ_l are the nearest values of Λ for which $g_m(\theta,u,\kappa,H,L)$ is precalculated, and K_u and K_l are the nearest values for which $g_m(\theta,u,\kappa,H,L)$ is precalculated. We define $\kappa(K,H,\Lambda)$ as $K(\Lambda H/T)/\left(H0.36km^{-2}\right)$. The scaling parameters α, β, and γ are defined as

$$\alpha = 1-\frac{\log(K_m/K_l)}{\log(K_u/K_l)}, \tag{B.2}$$

$$\beta = 1-\left(\frac{H_u H_l}{H_u-H_l}\right)\left(\frac{H-H_l}{H_l H}\right), \tag{B.3}$$

and

$$\gamma = 1-\frac{\log((L/H)/\Lambda_l)}{\log(\Lambda_u/\Lambda_l)}. \tag{B.4}$$

REFERENCES

Abbott, D., W. Menke, M. Hobart, and R. Anderson, Evidence for excess pore pressures in Southwest Indian Ocean sediments, *J. Geophys. Res.*, *86*, 1813-1827, 1981.

Abbott, D., W. Menke, M. Hobart, R. N. Anderson, and R. W. Embley, Correlated sediment thickness, temperature gradient and excess pore pressure in a marine fault block basin, *Geophys. Res. Lett.*, *11*, 485-488, 1984.

Acker, J. G., R. H. Byrne, S. Ben-Yaakov, R. A. Feely, and P. R. Betzer, The effect of pressure on aragonite dissolution rates in seawater, *Geochem. et Cosmochim. Acta*, *51*, 2171-2175, 1987.

Antoine, D., J.-M. André, and A. Morel, Oceanic primary production 2. Estimation at global scale from satellite (coastal zone color scanner) chlorophyll, *Global Biogeochem. Cycles*, *10*, 57-69, 1996.

Archer, D., Modeling the calcite lysocline, *J. Geophys. Res.*, *96*, 17,037-17,050, 1991.

Archer, D. An atlas of the distribution of calcium carbonate sediments in the deep sea, *Global Biogeochem. Cycles*, *10*, 159-174, 1996a.

Archer, D. A data-driven model of the global calcite lysocline, *Global Biogeochem. Cycles*, *10*, 511-516, 1996b.

Audet, D. M., Modelling of porosity evolution and mechanical compaction of calcareous sediments, *Sedimentology*, *42*, 355-373, 1995.

Aumento, F., W. G. Melson et al., *Init. Repts. DSDP*, *37*, U.S. Government Printing Office, Washington, D.C., 1977.

Bard, P.-Y. and M. Bouchon, The two-dimensional resonance of sediment-filled valleys, *Bull. Seis. Soc. Am.*, *75*, 519-541, 1985.

Bell, T. H., Statistical features of sea-floor topography, *Deep-Sea Res.*, *22*, 883-892, 1975.

Berger, W. H. and E. L. Winterer, Plate stratigraphy and the fluctuating carbonate line, *Spec. Publs int. Ass. Sediment.*, *1*, 11-48, 1974.

Berger, W. H., M.-C. Bonneau, and F. L. Parker, Foraminifera on the deep-sea floor: lysocline and dissolution rate, *Oceanol. Acta*, *5*, 249-258, 1982.

Berger, W. H., Produktivität des Ozeans aus geologischer Sicht: Denkmodelle und Beispiele, *Z. dt. geol. Ges.*, *142*, 149-178, 1991.

Bird, R. T. and R. A. Pockalny, Late Cretaceous and Cenozoic seafloor and oceanic basement roughness: Spreading rate, crustal age and sediment thickness correlations, *Earth. Planet. Sci. Lett.*, *123*, 239-254, 1994.

Biscaye, P. E., Mineralogy and sedimentation of Recent deep-sea clay in the Atlantic Ocean and adjacent seas and oceans, *Geol. Soc. Am. Bull.*, *76*, 803-832, 1965.

Biscaye, P. E., V. Kolla, and K. K. Turekian, Distribution of calcium carbonate in the surface sediments of the Atlantic Ocean, *J. Geophys. Res.*, *81*, 2,595-2,603, 1976.

Biscaye, P. E. and S. L. Eittreim, Suspended articulate loads and transports in the nepheloid layer of the abyssal Atlantic Ocean, *Mar. Geol.*, *23*, 155-172, 1977.

Bode, G. W., Grain-size and carbon/carbonate analyses, Leg 37, in Aumento, F., W. G. Melson et al., *Init. Repts. DSDP*, *37*, U.S. Government Printing Office, Washington, D.C., 637-639, 1977.

Bode, G. W., Grain-size and carbon/carbonate analyses, Leg 45, in Melson, W. G., P. D. Rabinowitz et al., *Init. Repts. DSDP*, *45*, U.S. Government Printing Office, Washington, D.C., 379-380, 1979.

Bode, G. W., Appendix I. Carbon and carbonate analyses, in Hsü, K. J., J. L. LaBrecque et al., *Init. Repts. DSDP*, *73*, U.S. Government Printing Office, Washington, D.C., 789-790, 1984.

Broecker, W. S. and T. Takahashi, The relationship between lysocline depth and *in situ* carbonate ion concentration, *Deep-Sea Res.*, *25*, 65-95, 1978.

Cande, S., J. L. LaBrecque, and W. B. Haxby, Plate kinematics of the South Atlantic: Chron 34 to present, *J. Geophys. Res.*, *93*, 13,479-13,492, 1988.

Cao, S. and I. Lerche, A quantitative model of dynamical sediment deposition and erosion in three dimensions, *Comp. Geosci.*, *20*, 635-663, 1994.

Carbotte, S., S. M. Welch, and K. C. Macdonald, Spreading rates, rift propagation, and fracture zone offset histories during the past 5 my on the Mid-Atlantic Ridge; 25°-27°30'S and 31°-34°30' S, *Mar. Geophys. Res.*, *13*, 51-80, 1991.

Cochran, J. R., J. A. Goff, A. Malinverno, D. J. Fornari, C. Keeley, and X. Wang, Morphology of a "superfast" mid-ocean ridge crest and flanks: The East Pacific Rise, 7° - 9° S, *Mar. Geophys. Res.*, *15*, 65-76, 1993.

Culling, W. E. H., Analytical theory of erosion, *J. Geol.*, *68*, 336-344, 1960.

Dade, W. B. and H. E. Huppert, Predicting the geometry of channelized deep-sea turbidites, *Geology*, *22*, 645-648, 1994.

Davies, T. A. and T. R. Worsley, Paleoenvironmental implications of oceanic carbonate sedimentation rates, in *The Deep Sea Drilling Project: a Decade of Progress, SEPM Special Publication 32*, ed. by J. E. Warme, R. G. Douglas and E. L. Winterer, 169-179, 1981.

Davies, T. A., R. B. Kidd, and A. T. S. Ramsay, A time-slice approach to the history of Cenozoic sedimentation in the Indian Ocean, *Sed. Geol.*, *96*, 157-179, 1995.

DeGroot, M. H., *Probability and Statistics, 2nd Edition*, Addison-Wesley Publishing Co., 1986.

Delaney, M. L., Miocene benthic foraminiferal Cd/Ca records: South Atlantic and western equatorial Pacific, *Paleoceanography*, *5*, 743-760, 1990.

Diester-Haass, L., Middle Eocene to early Oligocene paleoceanography of the Antarctic Ocean (Maud Rise, ODP Leg 113, Site 689): change from a low to a high productivity ocean, *Palaeogeogr., Palaeoclimatol., Palaeoecol.*, *113*, 311-334, 1995.

Divins, D. L. and P. D. Rabinowitz, Thickness of sedimentary cover. Sheet 3. South Atlantic, in *International Geological-Geophysical Atlas of the Atlantic Ocean*, ed. by G. B. Udintsev, Intergovernmental Oceanographic Committee (of UNESCO), Ac. Sc. USSR, 126-127, 1989-1990.

Ellis, D. B. and T. C. Moore Jr., Calcium carbonate, opal and quartz in Holocene sediments and the calcium compensation level in the South Atlantic Ocean, *J. Mar. Res.*, 31, 210-227, 1973.

Embley, R. M. and R. Jacobi, Distribution and morphology of large submarine sediment slides and slumps on Atlantic continental margins, *Mar. Geotech.*, *2*, 205-228, 1977.

Emerson, S. R. and D. Archer, Calcium carbonate preservation in the ocean, *Phil. Trans. R. Soc. Lond. A.*, *331*, 29-40, 1990.

Emerson, S. and M. Bender, Carbon fluxes at the sediment-water interface of the deep-sea: calcium carbonate preservation, *J. Mar. Res.*, *39*, 139-162, 1981.

Emerson, S. R. and D. Archer, Calcium carbonate preservation in the ocean, *Phil. Trans. R. Soc. Lond.*, *A 331*, 29-40, 1990.

Farrell, J. W. and W. L. Prell, Climatic changes and $CaCO_3$ preservation: an 800,000 year bathymetric reconstruction of the from the central equatorial Pacific ocean, *Paleoceanography*, *4*, 447-466, 1989.

Flemings, P. B. and T. E. Jordan, A synthetic stratigraphic model for foreland basin development, *J. Geophys. Res.*, *94*, 3851-3866, 1989.

Flood, R. D., Studies of deep-sea sedimentary microtopography in the North Atlantic Ocean, unpublished manuscript (doctoral thesis), 1978.

Flower, B. P. and J. P. Kennett, The middle Miocene climatic transition: East Antarctic ice sheet development, deep ocean circulation and global carbon cycling, *Palaeogeogr., Palaeoclimatol., Palaeoecol.*, *108*, 537-555, 1994.

Fox, C. G. and D. E. Hayes, Quantitative methods for analyzing the roughness of the seafloor, *Rev. Geophys.*, *23*, 1-48, 1985.

Fox, P. J., N. R. Grindlay, and K. C. Macdonald, The Mid-Atlantic Ridge (31°S-34°30'S): Temporal and spatial variations of accretionary processes, *Mar. Geophys. Res.*, *13*, 1-20, 1991.

Gamboa, L. A. P. and P. D. Rabinowitz, The Rio Grande fracture zone in the western South Atlantic and its tectonic implications, *Earth Plan. Sci. Lett.*, *52*, 410-418, 1981.

Gerald, C. F. and P. O. Wheatley, *Applied Numerical Analysis, 3rd Edition*, Addison-Wesley Publishing Co., 1984.

Goff, J. A., and T. H. Jordan, Stochastic Modeling of Seafloor Morphology: Inversion of Sea Beam data for second-order statistics, *J. Geophys. Res.*, *93*, 13,589-13,608, 1988.

Goff, J. A., A global and regional stochastic analysis of near-ridge abyssal hill morphology, *J. Geophys. Res.*, *96*, 21,713-21,737, 1991.

Goff, J. A., T. H. Jordan, M. H. Edwards, and D. J. Fornari, Comparison of a stochastic seafloor model with SeaMARC II bathymetry and Sea Beam data near the East Pacific Rise 13°-15°N, *J. Geophys. Res., 96*, 3867-3885, 1991.

Goff, J. A. and M. C. Kleinrock, Quantitative comparison of bathymetric survey systems, *Geophys. Res. Lett., 18*, 1253-1256, 1991.

Goff, J. A., Quantitative characterization of abyssal hill morphology along flow lines in the Atlantic Ocean, *J. Geophys. Res., 97*, 9,183-9,202, 1992.

Goff, J. A., A utilitarian approach to modeling non-Gaussian characteristics of a topographic field, *J. Geophys. Res., 96*, 19,635-19,647, 1993.

Goff, J. A., A. Malinverno, D. J. Fornari, and J. R. Cochran, Abyssal hill segmentation: Quantitative analysis for the East Pacific Rise 7° - 9°S, *J. Geophys. Res., 98*, 13,851-13,862, 1993.

Goff, J. A., B. E. Tucholke, J. Lin, G. E. Jaroslow, and M. C. Kleinrock, Quantitative analysis of abyssal hills in the Atlantic Ocean: A correlation between inferred crustal thickness and extensional faulting, *J. Geophys. Res., 100*, 22,509-22,522, 1995.

Gould, W. J., R. Hendry, and H. E. Huppert, An abyssal topographic experiment, *Deep-Sea Res., 28A*, 409-440, 1981.

Grindlay, N. R. and P. J. Fox, Segmentation of the Southern Mid-Atlantic Ridge (abstract), *Eos Trans. AGU, 72* (44), Fall Meeting suppl., 471, 1991.

Grindlay, N. R., P. J. Fox, and P. R. Vogt, Morphology and tectonics of the Mid-Atlantic Ridge (25° - 27°30' S) from Sea Beam and magnetic data, *J. Geophys. Res., 97*, 6,983-7,010, 1992.

Gross, T. F. and W. B. Dade, Suspended sediment storm modeling, *Mar. Geol., 99*, 343-360, 1991.

Grousset, F. E. and R. Chesselet, The Holocene sedimentary regime in the northern Mid-Atlantic Ridge region, *Earth Plan. Sci. Lett., 78*, 271-287, 1986.

Haq, B. U., J. Hardenbol, and P. R. Vail, Chronology of fluctuating sea levels since the Triassic, *Science, 235*, 1156-1167, 1987.

Hales, B., S. Emerson, and D. Archer, Respiration and dissolution in the sediments of the western North Atlantic: estimates from models of in situ microelectrode measurements of porewater oxygen and pH, *Deep-Sea Res. I, 41*, 695-719, 1994.

Hales, B., and S. Emerson, Calcite dissolution in sediments of the Ontong-Java Plateau: In situ measurements of pore water O_2 and *p*H, *Global Biogeochem. Cycles, 10*, 527-541, 1996.

Hallock, P., I. P. Silva, and A. Boersma, Similarities between planktonic and larger foraminiferal evolutionary trends through Paleogene paleoceanographic changes, *Palaeogreogr., Palaeoclimatol., Palaeoecol., 83*, 49-64, 1991.

Hartl, P., L. Tauxe, and T. Herbert, Earliest Oligocene increase in South Atlantic productivity as interpreted from "rock magnetics" at Deep Sea Drilling Project Site 522, *Paleoceanography*, *10*, 311-325, 1995.

Hay, W. W., J. L. Sloan II, and C. N. Wold, Mass/age distribution and composition of sediments on the ocean floor and the global rate of sediment subduction, *J. Geophys. Res.*, *93*, 14,933-14,940, 1988.

Heath, G. R. and C. Culberson, Calcite: degree of saturation, rate of dissolution, and the compensation depth in the deep oceans, *Geol. Soc. Am. Bull.*, *81*, 3157-3160, 1970.

Heezen, B. C. and C. D. Hollister, *The Face of the Deep*, Oxford University Press, New York, 1971.

Howard, A. D., W. E. Dietrich, and M. A. Seidl, Modeling fluvial erosion on regional to continental scales, *J. Geophys. Res.*, *99*, 13,971-13,986, 1994.

Hsü, K. J., J. L. LaBrecque et al., *Init. Repts. DSDP*, *73*, U.S. Government Printing Office, Washington, D.C., 1984.

Hsü, K. J., J. A. McKenzie, H. Oberhänsli, and R. C. Wright, South Atlantic Cenozoic paleoceanography, in Hsü, K. J., J. L. LaBrecque et al., *Init. Repts. DSDP*, *73*, U.S. Government Printing Office, Washington, D.C., 771-785, 1984.

Ito, G. and J. Lin, Oceanic spreading center-hotspot interactions: Constraints from along-isochron bathymetric and gravity anomalies, *Geology*, *23*, 657-660, 1995.

Jackson, D. R. and D. P. Winebrenner, Application of the composite roughness model to high-frequency bottom backscatter, *J. Acoust. Soc. Am.*, *79*, 1410-1422, 1986.

Jahnke, R. A., The global ocean flux of particulate organic carbon: Areal distribution and magnitude, *Global Biogeochem. Cycles*, *10*, 71-88, 1996.

Jaroslow, G. and B. E. Tucholke, Echo character of the Mid-Atlantic Ridge flank in the region of the Acoustic Reverberation Corridor, Bottom/Subbottom Acoustic Reverberation Special Research Program, 1991 Fall Research Symposium, Woods Hole, MA, p. 15, 1991.

Jaroslow, G. E. and B. E. Tucholke, Mesozoic-Cenozoic sedimentation in the Kane fracture zone, western North Atlantic, and uplift history of the Bermuda Rise, *Geol. Soc. Am. Bull.*, *106*, 319-337, 1994.

Jaroslow, G. E., and B. E. Tucholke, Detailed mapping of sediment distribution in the Acoustic Reverberation Corridor, Acoustic Reverberation Special Research Program, 1995 Research Symposium, Woods Hole, MA, 1995.

Jaroslow, G. E., The Geological Record of Oceanic Crustal Accretion and Tectonism at Slow-Spreading Ridges, Ph.D. Thesis, Massachusetts Institute of Technology/Woods Hole Oceanographic Institution Joint Program in Oceanography, 210 pp., 1997.

Johnson, D. A. and T. C. Johnson, Sediment redistribution by bottom currents in the central Pacific, *Deep-Sea Res.*, *17*, 157-169, 1970.

Johnson, D. A., Abyssal teleconnections II. Initiation of Antarctic Bottom Water flow in the southwestern Atlantic, in *South Atlantic Paleoceanography*, ed. by. K. J. Hsü and H. J. Weissert, Cambridge University Press, p. 243-281, 1985.

Kastens, K. A., K. C. Macdonald, S. P. Miller, and P. J. Fox, Deep-tow studies of the Vema fracture zone; 2, Evidence for tectonism and bottom currents in the sediments of the transform valley floor, *J. Geophys. Res.*, *91*, 3355-3367, 1986.

Keir, R. J., The dissolution kinetics of biogenic calcium carbonates in seawater, *Geochem. et Cosmochim. Acta*, *44*, 241-252, 1980.

Keller, G., N. MacLeod, and E. Barrera, Eocene-Oligocene faunal turnover in planktic foraminifera, and Antarctic glaciation, in *Eocene-Oligocene Climatic and Biotic Evolution*, ed. by D. R. Prothero and W. A. Berggren, 218-244, 1992.

Kipp, N. G., New transfer function for estimating past sea surface conditions from sea bed distribution of planktonic foraminiferal assemblages in the North Atlantic, *Geol. Soc. Am., Mem.*, *145*, ed. by R. Kline and J. Hays, 3-41, 1976.

Kleinrock, Martin C., Capabilities of some systems used to survey the deep-sea floor, in *CRC Handbook of Geophysical Exploration at Sea*, ed. by R. A. Geyer, 35-83, 1992.

Komar, P. D., Relative significance of head and body spill from a channelized turbidity current, *Geol. Soc. Am. Bull.*, *83*, 1151-1156, 1972.

Komar, P. D. and C. E. Reimers, Grain shape effects on settling rates, *J. Geol.*, *86*, 193-209, 1978.

Kooi, H. and C. Beaumont, Escarpment evolution on high-elevation rifted margins: Insights derived from a surface processes model that combines diffusion, advection, and reaction, *J. Geophys. Res.*, *99*, 12,191-12,209, 1994.

Koons, The topographic evolution of collisional mountain belts: a numerical look at the Southern Alps, New Zealand, *Am. J. Sci.*, *289*, 1041-1069, 1989.

Kowsmann, R. O., Coarse components in the surface sediments of the Panama Basin, *J. Geol.*, *81*, 473-494, 1973.

Krause, D. C. and H. W. Menard, Depth distribution and bathymetric classification of some sea-floor profiles, *Mar. Geol.*, *3*, 169-193, 1965.

Kuptsov, V. M. and L. I. Barteneva, Rate of Late Quaternary sediment accumulation in the Reykjanes Rift at 58° N, *Oceanology*, *28*, 618-622, 1988.

Le Pichon, X., Models and structure of the oceanic crust, *Tectonophys.*, *7*, 385-401, 1969.

Lisitzin, Alexander P., "Sedimentation in the World Ocean", *SEPM Spec. Publ. 17*, 1 - 218, 1972.

Ludwig, W. J., V. A. Krasheninnikov, et al., *Init. Repts. DSDP*, *71*, U. S. Government Printing Office, Washington, D.C., 1983.

Luyendyk, B. P., J. R. Cann et al., *Init. Repts. DSDP*, *49*, U. S. Government Printing Office, Washington, D.C., 1979.

Macario, A., W. F. Haxby, J. A. Goff, W. B. F. Ryan, S. C. Cande, and C. A. Raymond, Flow line variations in abyssal hill morphology for the Pacific-Antarctic Rise at 65° S, *J. Geophys. Res.*, *99*, 17,921-17,934, 1994.

Magde, L. S. and D. K. Smith, Seamount volcanism at the Reykjanes Ridge: Relationship to the Iceland hot spot, *J. Geophys. Res.*, *100*, 8449-8468, 1995.

Makris, N. C. and J. M. Berkson, Long-range backscatter from the Mid-Atlantic Ridge, *J. Acoust. Soc. Am.*, *95*, 1865-1881, 1994.

Malinverno, A. and L. E. Gilbert, A stochastic model for the creation of abyssal hill topography at a slow spreading center, *J. Geophys. Res.*, *94*, 1665-1675, 1989.

Malinverno, A. Inverse square-root dependence of mid-ocean ridge flank roughness on spreading rate, *Nature*, *352*, 58-60, 1991.

Malinverno, A. and P. Cowie, Normal faulting and the topographic roughness of mid-ocean ridge flanks, *J. Geophys. Res.*, *98*, 17,921-17,939, 1993.

Marks, N. S., Sedimentation on new ocean crust: the Mid-Atlantic Ridge at 37° N, *Mar. Geol.*, *43*, 65-82, 1981.

Maxwell, A. E. et al., *Init. Repts. DSDP*, *3*, U.S. Government Printing Office, Washington, D.C., 1970.

McCave, I. N. and S. A. Swift, A physical model for the rate of deposition of fine-grained sediments in the deep sea, *Geol. Soc. Am. Bull.*, *87*, 541-546, 1976.

McCave, I. N. and B. E. Tucholke, Deep current-controlled sedimentation in the western North Atlantic, in Vogt, P. R. and B. E. Tucholke, eds., *The Geology of North America, Volume M, The Western North Atlantic Region*, 451-468, 1986.

McCoy, F. W., Southern ocean sediments: Circum-Antarctic to 30°S, in *Marine Geological and Geophysical Atlas of the Circum-Antarctic to 30°S*, Ed. D. E. Hayes, 37-46, 1991.

McKean, J. A., W. E. Dietrich, R. C. Finkel, J. R. Southon, and M. W. Caffee, Quantification of soil production and downslope creep rates from cosmogenic ^{10}Be accumulations on a hillslope profile, *Geology*, *21*, 343-346, 1993

McKenzie, D. P. and C. Bowin, The relationship between bathymetry and gravity in the Atlantic Ocean, *J. Geophys. Res.*, *81*, 1903-1915, 1976.

McLean, S. R., Theoretical modelling of deep ocean sediment transport, *Mar. Geol.*, *66*, 243-265, 1985.

McLean, S. R. and J. Yean, Velocity and stress in the deep-ocean boundary layer, *J. Phys. Ocean.*, *17*, 1356-1365, 1987.

Melson, W. G., P. D. Rabinowitz et al., *Init. Repts. DSDP*, *45*, U. S. Government Printing Office, Washington, D. C., 1979.

Menard, H. W., Sea floor spreading, topography and the second layer, *Science*, *157*, 923-924, 1967.

Mitchell, N. C., A model for attenuation of backscatter due to sediment accumulations and its application to determine sediment thicknesses with GLORIA sidescan sonar, *J. Geophys. Res.*, *98*, 22,477-22,493, 1993.

Mitchell, N. C., Diffusion transport model for pelagic sediments on the Mid-Atlantic Ridge, *J. Geophys. Res.*, *100*, 19,991-20,009, 1995.

Mitchell, N. C., Creep in pelagic sediments and potential for morphologic dating of marine fault scarps, *Geophys. Res. Lett.*, *23*, 483-486, 1996.

Moore, D. G., Submarine slumps, *J. Sediment. Petrol.*, *31*, 343-357, 1961.

Moore, T. C. Jr., G. R. Heath, and R. O. Kowsmann, Biogenic sediments of the Panama Basin, *J. Geol.*, *81*, 458-472, 1973.

Morse, J. W., Dissolution kinetics of calcium carbonate in sea water. IV: The near-equilibrium dissolution kinetics of calcium carbonate-rich sea sediments, *Am. J. Sci.*, *278*, 344-353, 1978

Montgomery, D. R. and W. E. Deitrich, Landscape dissection and drainage area-slope thresholds, *Process Models and Theoretical Geomorphology*, Ed. M. J. Kirkby, John Wiley and Sons Ltd., 221-246, 1994.

Mountain, G. S. and K. G. Miller, Seismic and geological evidence for early Paleogene deepwater circulation in the western North Atlantic, *Paleoceanography*, *7*, 423-439, 1992.

Müller, R. D., W. R. Roest, J.-Y. Royer, L. M. Gahagan, and J. G. Sclater, A digital age map of the ocean floor, SIO Reference Series 93-30, 1993.

Neprochnov, Y. P., L. R. Merklin, and P. R. Supko, Underway geophysical measurements, Leg 39, Deep Sea Drilling Project, in Supko, P. R., K. Perch-Nielsen et al., *Init. Repts. DSDP*, *39*, U. S. Government Printing Office, Washington, D. C., 971-1043, 1977.

Neumann, G. A. and D. W. Forsyth, The paradox of the axial profile: Isostatic compensation along the axis of the Mid-Atlantic Ridge?, *J. Geophys. Res.*, *98*, 17,891-17,910, 1993.

Parker, G., Conditions for the ignition of catastrophically erosive turbidity currents, *Mar. Geol.*, *46*, 307-327, 1982.

Parker, G., M. Garcia, F. Fukushima, and W. Yu, Experiments on turbidity currents over an erodible bed, *J. Hydrol. Res.*, *25*, 123-147, 1987.

Parsons, B. and J. G. Sclater, An analysis of the variation of ocean floor bathymetry and heat flow with age, *J. Geophys. Res.*, 82, 803-827, 1977.

Peterson, M. N. A., Calcite: Rates of dissolution in a vertical profile in the central Pacific, *Science*, *154*, 1542-1544, 1966.

Peterson, M. N. A., et al., *Init. Repts. DSDP*, *2*, U. S. Government Printing Office, Washington, D. C., 1970.

Pimm, A. C., Carbon carbonate results, Leg 3, in Maxwell, A. E. et al., *Init. Repts. DSDP*, *3*, U.S. Government Printing Office, Washington, D.C., 495-507, 1970.

Pokras, E. and B. Molfino, Oceanographic control of diatum abundances and species distributions in surface sediments of the tropical and southeast Atlantic, *Mar. Micropaleontol.*, *10*, 165-188, 1986.

Pykhov, N. V., The conditions and causes of disturbances of the stability of sediments on the ocean floor, *Oceanol.*, *13*, 238-241, 1972.

Raymo, M. E., D. Hodell, and E. Jansen, Response of deep ocean circulation to initiation of northern hemisphere glaciation (3-2 Ma), *Paleoceanography*, *7*, 645-672, 1992.

Renard, M., Pelagic carbonate chemostratigraphy (Sr, Mg, 18O, 13C), *Mar. Micropaleontol.*, 10, 117-164, 1986.

Rex, R. W., X-Ray mineralogy studies - Leg 2, in Peterson, M. N. A., et al., *Init. Repts. DSDP*, *2*, U.S. Government Printing Office, Washington, D.C., 329-348, 1970a.

Rex, R. W., X-Ray mineralogy studies - Leg 3, in Maxwell, A. E. et al., *Init. Repts. DSDP*, *3*, U.S. Government Printing Office, Washington, D.C., 509-581, 1970b.

Richardson, M. J., M. Wimbush and L. Mayer, Exceptionally strong near-bottom flows on the continental rise of Nova Scotia, *Science*, *213*, 887-888, 1981.

Rickard, D. and E. L. Sjöberg, Mixed kinetic control of calcite dissolution rates, *Amer. J. Sci.*, *283*, 815-830, 1983.

Robertsson, J. O. A. and A. Levander, A numerical study of seafloor scattering, *J. Acoust. Soc. Am.*, *97*, 3532-3546, 1995.

Robertsson, J. O. A., K. Hollinger, A. Levander, J. A. Goff, H. F. Webb and B. E. Tucholke, A numerical analysis of ocean acoustic reverberation data from the proximity of the Mid-Atlantic Ridge, submitted to *J. Acoust. Soc. Am.*, January 1996.

Rona, P. A., R. N. Harbison, and S. A. Bush, Abyssal hills of the eastern central North Atlantic, *Mar. Geol.*, *16*, 275-292, 1974.

Rosenbloom, N A. and R. S. Anderson, Hillslope and channel evolution in a marine terraced landscape, Santa Cruz, California, *J. Geophys. Res.*, 99, 13,591-13,608, 1994.Rossi, S., F. Westall and J. Mascle, The geomorphology of the Southwest Guinea Margin: tectonic, volcanic, mass movement and bottom current influences, *Mar. Geol.*, *105*, 225-240, 1992.

Ruddiman, W. F. and L. K. Glover, Vertical mixing of ice-rafted volcanic ash in North Atlantic sediments, *Geol. Soc. Am. Bull.*, *83*, 2817-2835, 1972.

Sandwell, D. T. and W. H. F. Smith, Marine gravity from satellite altimetry (poster), The Geological Data Center, Scripps Inst. of Oceanography, (digital file, v. 7.2), 1995.

Sayles, F. L., $CaCO_3$ solubility in marine sediments: Evidence for equilibrium and non-equilibrium behavior, *Geochem. et Cosmochim. Acta*, 49, 877-888, 1985.

Scott, B., Grain-size and carbon/carbonate analyses, Leg 39, in Supko, P. R., K. Perch-Nielsen et al., *Init. Repts. DSDP, 39*, U. S. Government Printing Office, Washington D. C., 501-504, 1977.

Severinghaus, J. P. and K. C. Macdonald, High inside corners at ridge-transform intersections, *Mar. Geophys. Res., 9*, 353-367, 1988.

Shackleton, N. J., The carbon isotope record of the Cenozoic: history of organic carbon burial and of oxygen in the ocean and atmosphere, in *Marine Petroleum Source Rocks*, ed. by J. Brooks and A. J. Fleet, *Geological Society Special Publ. 26*, 423-434, 1987.

Shaw, P. R. and D. K. Smith, Robust description of statistically heterogeneous seafloor topography through its slope distribution, *J. Geophys. Res., 95*, 8705-8722, 1990.

Shaw, P. R. and J. Lin, Causes and consequences of variations in faulting style at the Mid-Atlantic Ridge, *J. Geophys. Res., 98*, 21,839-21,851, 1993.

Sjöberg, E. L., A fundamental equation for calcite dissolution kinematics, *Geochem. et Cosmochim. Acta*, 40, 441-447, 1976.

Smith, D. K. and T. H. Jordan, Seamount statistics in the Pacific Ocean, *J. Geophys. Res., 93*, 2899-2918, 1988.

Smith, D. K. and J. R. Caan, The role of seamount volcanism in crustal construction at the Mid-Atlantic Ridge (24° N - 30° N), *J. Geophys. Res., 97*, 1645-1658, 1992.

Supko, P. R., K. Perch-Nielsen et al., *Init. Repts. DSDP, 39*, U. S. Government Printing Office, Washington, D. C., 1977.

Swift, Stephen A., Holocene rate of sediment accumulation in the Panama Basin, eastern Equatorial Pacific: Pelagic sedimentation and lateral transport, *J. Geol., 85*, 301-319, 1977.

Takahashi, T., Carbonate chemistry of sea water and the calcite compensation depth in the ocean, in Sliter, A. W., A. W. H. Bé, and W. Berger, eds., *Dissolution of Deep Sea Carbonates, Spec. Publ. 13*, 11-26, Cushman Found. for Foraminiferal Res., Washington, D.C., 1975.

Thiede, J., J.-E. Strand, and T. Agdestein, The distribution of major pelagic sediment components in the Mesozoic and Cenozoic North Atlantic Ocean, *SEPM Spec. Publ. 32*, 67 - 90, 1981.

Thunell, R. C., Carbonate dissolution and abyssal hydrography in the Atlantic Ocean, Mar. Geology, 47, 165-180, 1982.

Thunell, R. and P. Belyea, Neogene planktonic foraminiferal biogeography of the Atlantic Ocean, *Micropaleontology, 28*, 381-398, 1982.

Timofeev, P. P., I. M. Varentsov, M. A. Rateev, and N. V. Renngarten, Lithology, mineralogy, and geochemistry of upper Cenozoic sediments at 23°N near the Mid-Atlantic Ridge, drilled on Leg 45, in Melson, W. G., P. D. Rabinowitz et al., *Init.*

Repts. DSDP, 45, U. S. Government Printing Office, Washington, D. C., 323-347, 1979.

Tucholke, B. E. and P. R. Vogt, Western North Atlantic: sedimentary evolution and aspects of tectonic history, in Tucholke, B. E., P. R. Vogt, et al., *Init. Repts. DSDP, 43*, U. S. Government Printing Office, Washington, D. C., 791-825, 1979.

Tucholke, B. E, Structure of basement and distribution of sediments in the western North Atlantic Ocean, in Vogt, P. R. and B. E. Tucholke, eds., *The Geology of North America, Volume M, The Western North Atlantic Region*, 331-340, 1986.

Tucholke, B. E. and G. S. Mountain, Tertiary paleoceanography of the western North Atlantic ocean, in Vogt, P. R. and B. E. Tucholke, eds., *The Geology of North America, Volume M, The Western North Atlantic Region*, 631-650, 1986.

Tucholke, B. E. and H. Schouten, Kane Fracture Zone, *Mar. Geophys. Res., 10*, 1-40, 1988.

Tucholke, B. E. and E. Uchupi, Thickness of sedimentary cover. Sheet 2, in *International Geological-Geophysical Atlas of the Atlantic Ocean*, ed. by G. B. Udintsev, Intergovernmental Oceanographic Committee (of UNESCO), Ac. Sc. USSR, 124-125, 1989-1990.

Tucholke, B. E., J. Lin, and M. C. Kleinrock, Crustal structure of spreading segments on the western flank of the Mid-Atlantic Ridge at 25°25'N to 27°10'N (abstract), *Eos Trans. AGU, 73* (43), Fall Meeting Suppl., 537-538, 1992.

Tucholke, B. E., and J. Lin, A geological model for the structure of ridge segments in slow spreading ocean crust, *J. Geophys. Res.*, 99, 11,937-11,958, 1994.

Tucholke, B. E., W. K. Stewart, and M. C. Kleinrock, Long-term denudation of ocean crust in the central North Atlantic Ocean, *Geology*, in press, 1997.

van Andel, Tj. and P. D. Komar, Ponded sediments of the mid-Atlantic Ridge between 22° and 23° North latitude., *Geol. Soc. Am. Bull., 80*, 1163-1190, 1969.

van Andel, Tj. H., Texture and dispersal of sediments in the Panama Basin, *J. Geol., 81*, 434-457, 1973.

van Andel, Tj. H., Mesozoic/Cenozoic calcite compensation depth and the global distribution of calcareous sediments, *Earth Plan. Sci. Lett., 26*, 187-194, 1975.

Webb, H. F. and T. H. Jordan, Quantifying the distribution and transport of pelagic sediments on young abyssal hills, *Geophys. Res. Lett., 20*, 2203-2206, 1993.

White, S, M. and G. W. Bode, Grain-size and carbon/carbonate analyses, Leg 49, in Luyendyk, B. P., J. R. Cann et al., *Init. Repts. DSDP, 49*, U. S. Government Printing Office, Washington, D. C., 873-882, 1979.

Wolfe, C. J., M. K. McNutt, and R. S. Detrick, The Marquesas Archipelagic Apron: Seismic stratigraphy and implications for volcano growth, mass wasting, and crustal underplating, *J. Geophys. Res., 99*, 13,591-13,608, 1994.

Wright, J. D., K. G. Miller, and R. G. Fairbanks, Evolution of modern deepwater circulation: evidence from the late Miocene Southern Ocean, *Paleoceanography*, *6*, 275-290, 1991.

Zahn, R., K. Winn, and M. Sarnthein, Benthic foraminiferal C-13 and accumulation rates of organic carbon: Uvigerina peregrina group and Cibicidoides wuellerstorfi, *Paleoceanography*, *1*, 7-42, 1986.

Zemmels, I., P. J. Harrold, and H. E. Cook, X-ray mineralogy data from the FAMOUS area of the Mid-Atlantic Ridge - Leg 37 Deep Sea Drilling Project, in Aumento, F., W. G. Melson et al., *Init. Repts. DSDP*, *37*, U. S. Government Printing Office, Washington, D. C., 895-903, 1977.